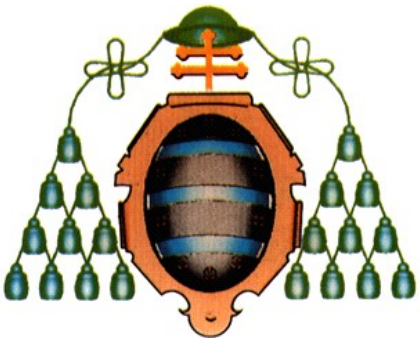

UNIVERSIDAD DE OVIEDO

Programa de Doctorado de Ciencia y Tecnología de Materiales

METAL-ORGANIC COORDINATION POLYMERS BASED ON RUTHENIUM CARBOXYLATES: SYNTHESIS, CHARACTERIZATION AND APPLICATIONS

TESIS DOCTORAL

Alla Dikhtiarenko

September 2015

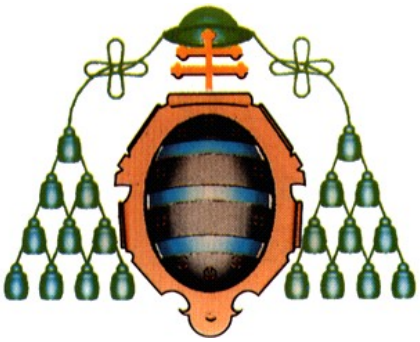

UNIVERSIDAD DE OVIEDO

Programa de Doctorado de Ciencia y Tecnología de Materiales

METAL-ORGANIC COORDINATION POLYMERS BASED ON RUTHENIUM CARBOXYLATES: SYNTHESIS, CHARACTERIZATION AND APPLICATIONS

TESIS DOCTORAL

José Gimeno Heredia

José Rubén García Menéndez

RESUMEN DEL CONTENIDO DE TESIS DOCTORAL

1.- Título de la Tesis	
Español: Polímeros de Coordinación Metal-Orgánicos Basados en Carboxilatos de Rutenio: Síntesis, Caracterización y Aplicaciones.	Inglés: Metal-Organic Coordination Polymers Based on Ruthenium Carboxylates: Synthesis, Characterization and Applications

2.- Autora	
Nombre: Alla Dikhtiarenko	NIE:
Programa de Doctorado: Ciencia y Tecnología de Materiales (Interdepartamental) (RD 778)	
Órgano responsable: Departamento de Ciencia de los Materiales e Ingeniería Metalúrgica	

RESUMEN (en español)

La presente Tesis Doctoral se centra en el estudio de polímeros de coordinación basados en carboxilatos de rutenio, abarcando tanto la preparación de redes extendidas metal-orgánicas con buen comportamiento estructural como la caracterización y evaluación de sus propiedades. Se exploraron diversas estrategias sintéticas con el fin de obtener redes poliméricas basadas en carboxilatos de rutenio mediante *i*) interacción directa entre una sal inorgánica de rutenio y ácidos carboxílicos, y *ii*) procedimientos indirectos, donde la construcción de la red polimérica tuvo lugar a partir de unidades moleculares pre-construidas. Cuando se utilizó como unidad elemental constructiva un acetato trinuclear de rutenio, donde los ligandos acetato son susceptibles de ser reemplazados por enlazadores carboxílicos multidentados, la capacidad reductora de éstos dio lugar a la formación de una especie trinuclear de rutenio con valencia mixta, que fue caracterizada estructuralmente, y utilizada como catalizador en varias transformaciones orgánicas. Se ha demostrado que, mediante estrategias de síntesis indirecta, usando oxalato de rutenio(III) como unidad prediseñada para la construcción de redes poliméricas extendidas, es posible aislar compuestos de dimensionalidad controlada (2D o 3D). En consecuencia, se han obtenido polímeros de coordinación heterometálicos bidimensionales, $\{[K(18\text{-crown-6})]_3[M^{II}{}_3(H_2O)_4[Ru(C_2O_4)_3]_3]\}_n$ (M^{II} = Fe, Co, Mn, Cu, Zn), con propiedades magnéticas y catalíticas. Mediante el uso del metaloligando $[Ru(C_2O_4)_3]^{3-}$ y plantillas catiónicas homoquirales, se logró aislar una familia de polímeros de coordinación tridimensionales, $\{[M^{II}(bpy)_3][Na/LiRu(C_2O_4)_3]\}_n$ (bpy = 2,2´-bipiridina; M^{II} = Fe, Co, Ni), con interesantes interacciones electrostáticas entre la red aniónica y la plantilla molecular catiónica que, mostrando fenómenos de transición de espín, son eficientes en la foto-reducción de CO_2 bajo irradiación ultravioleta. Finalmente, se prepararon polímeros de coordinación tridimensionales de fórmulas $\{[Zn(bpy)_3](H_2O)[LiRu(C_2O_4)_3]\}_n$ y $\{[Z^{II}(bpy)_3][Na/LiRu(C_2O_4)_3]\}_n$ (Z^{II} = Zn, Cu, Ru, Os), destacando entre sus propiedades la actividad catalítica en la fotolisis del agua.

RESUMEN (en Inglés)

The Doctoral Thesis is focused on the study of coordination polymers based on the ruthenium carboxylates covering the preparation of extended metal-organic networks with enhanced structural behaviour, their characterization and the evaluation of properties. In order to obtain the polymeric networks based on the ruthenium carboxylates, variety of synthetic approaches have been explored: *i*) direct interaction between an inorganic ruthenium salt and carboxylic acids, and *ii*) indirect procedures, by which the polymeric networks are built up from predesigned molecular units. As the trinuclear ruthenium acetate was used as an elemental building unit intending that the acetate ligands can be replaced by multidentate carboxylic linkers, the reductive power of latter leads to the formation of a trinuclear mixed-valence ruthenium cluster that was structurally characterized and used as a catalyst in various organic transformations. As was shown, the extended polymeric nets of controllable dimensionalities (2D or 3D) can be constructed by using the indirect approach with Ru(III) oxalate as a predesigned unit. As a result, heterometallic 2D-coordination polymers $\{[K(18\text{-crown-}6)]_3[M^{II}_3(H_2O)_4[Ru(C_2O_4)_3]_3]\}_n$ (M^{II} = Fe, Co, Mn, Cu, Zn) with magnetic and catalytic properties have been obtained. It has been managed to isolate a family of three-dimensional coordination polymers $\{[M^{II}(bpy)_3][Na/LiRu(C_2O_4)_3]\}_n$ (bpy = 2,2´-bipiridina; M^{II} = Fe, Co, Ni) with interesting electrostatic interaction between the anionic network and the molecular cationic template, exhibiting the spin-crossover phenomena and being effective in the photo-reduction of CO_2 under the UV-light. Finally, the three-dimensional coordination polymers of a formula $\{[Zn(bpy)_3](H_2O)[LiRu(C_2O_4)_3]\}_n$ y $\{[Z^{II}(bpy)_3][Na/LiRu(C_2O_4)_3]\}_n$ (Z^{II} = Zn, Cu, Ru, Os) have been prepared, which demonstrate a catalytic activity in the water splitting reaction among their properties.

SR. DIRECTOR DE DEPARTAMENTO DE CIENCIA DE LOS MATERIALES E INGENIERIA METALURGICA

Contenidos

Resumen

El diseño racional de polímeros de coordinación y redes metal-orgánicas ha experimentado recientemente gran desarrollo debido a sus potenciales aplicaciones, especialmente como catalizadores heterogéneos. A pesar de la gran evolución sufrida por estos materiales, la investigación en este campo continúa asentada en la construcción racional de polímeros de coordinación con características estructurales específicas y propiedades concretas, donde la elección juiciosa de los bloques de construcción juega un papel determinante. Esta Tesis Doctoral se enmarca dentro del contexto conceptual de la química de coordinación y, en particular, se centra en el estudio de polímeros de coordinación basados en carboxilatos de rutenio, abarcando tanto la preparación de redes extendidas metal-orgánicas con buenas propiedades estructurales como la caracterización y evaluación de sus propiedades.

Se exploraron diversas estrategias sintéticas con el fin de obtener redes poliméricas basadas en carboxilatos de rutenio. La interacción directa entre una sal inorgánica de rutenio y ácidos carboxílicos que actúan como enlazadores orgánicos demostró la tendencia de éstos a actuar como reductores, obteniéndose partículas de rutenio elemental de tamaño nanométrico. Posteriormente, se exploraron estrategias sintéticas indirectas, donde la construcción de la red polimérica tiene lugar a partir de unidades moleculares pre-construidas. Cuando se utilizó como unidad elemental constructiva un acetato trinuclear de rutenio, donde los ligandos acetato son susceptibles de ser reemplazados por enlazadores carboxílicos multidentados, la capacidad reductora de éstos dio lugar a la formación de una especie trinuclear de rutenio con valencia mixta, que fue caracterizada estructuralmente, y utilizada como catalizador en varias transformaciones orgánicas. Cuando se eligió el oxalato de rutenio(III) como unidad prediseñada para la construcción de las redes poliméricas extendidas, se sintetizaron redes poliméricas de dimensionalidad controlada (2D o 3D), aislándose una serie de polímeros de coordinación heterometálicos bidimensionales, $\{[K(18\text{-crown-}6)]_3[M^{II}{}_3(H_2O)_4[Ru(C_2O_4)_3]_3]\}_n$ (M^{II} = Fe, Co, Mn, Cu, Zn), donde un esqueleto aniónico hexagonal genera espacios interlaminares ocupados por especies catiónicas, $[K(18\text{-crown-}6)]^+$, con propiedades magnéticas y catalíticas. Mediante el uso del metaloligando $[Ru(C_2O_4)_3]^{3-}$ y plantillas catiónicas homoquirales, se logró aislar una familia de polímeros de coordinación tridimensionales, $\{[M^{II}(bpy)_3][M^{I}Ru(C_2O_4)_3]\}_n$ (bpy = 2,2´-bipiridina; M^{II} = Fe, Co, Ni; M^{I} = Na, Li), con interesantes interacciones electrostáticas entre la red aniónica y la plantilla molecular catiónica que, mostrando fenómenos de transición de espín, son eficientes en la foto-reducción de CO_2 bajo irradiación ultravioleta. Por último, esta Tesis recoge la síntesis y caracterización estructural de polímeros de coordinación de fórmulas $\{[Zn(bpy)_3](H_2O)[LiRu(C_2O_4)_3]\}_n$ y $\{[Z^{II}(bpy)_3][M^{I}Ru(C_2O_4)_3]\}_n$ (bpy = 2,2´-bipyridyl; Z^{II} = Zn, Cu, Ru, Os; M^{I} = Na, Li), que constituyen una familia de redes poliméricas tridimensionales resultado del autoensamblaje de un metaloligando, $[Ru(C_2O_4)_3]^{3-}$, una plantilla catiónica, $[Z^{II}(bpy)_3]^{2+}$, y un metal alcalino, destacando entre sus propiedades la actividad catalítica de uno de sus miembros en la fotolisis del agua.

Abstract

Rational design of coordination polymers and metal-organic networks was recently experienced great development due to their potential applications, especially as heterogeneous catalysts. Despite of considerable evolution undergone by these materials, research in this field continues to be focused on the rational construction of coordination polymers with specific structural characteristics and certain properties, where the judicious choice of building blocks plays a decisive role. This Doctoral Thesis has been developed under the conceptual context of coordination chemistry and, particularly, focuses on a study of coordination polymers based on ruthenium carboxylate, having covered the preparation of extended metal-organic networks with good structural properties as well as their characterization and evaluation.

Various synthetic strategies of obtaining of ruthenium carboxylates-based polymeric networks were explored.

Direct interaction between an inorganic salt of ruthenium and carboxylic acids that act as organic linkers along with their tendency to behave as reducing agents yields of ruthenium(0) particles of nanometric size. Subsequently, the indirect synthetic approaches where the polymeric network assembling takes place from pre-built molecular units were explored. As the trinuclear ruthenium acetate was used as an elemental building unit intending that the acetate ligands can be replaced by multidentate carboxylic linkers, the reductive power of latter leads to the formation of a trinuclear mixed-valence ruthenium cluster that was structurally characterized and used as a catalyst in various organic transformations. As the ruthenium(III) oxalate had been chosen as a predesigned building unit, the polymeric networks of controllable dimensionalities (2D or 3D) were synthesized. As a result, a series of bidimensional heterometallic coordination polymers of $\{[K(18\text{-crown-}6)]_3[M^{II}{}_3(H_2O)_4[Ru(C_2O_4)_3]_3]\}_n$ (M^{II} = Fe, Co, Mn, Cu, Zn) have been obtained, where molecular cationic species of $[K(18\text{-crown-}6)]^+$ reside in the interlaminar space of the hexagonal anionic frameworks exhibiting magnetic and catalytic properties. It has been managed to isolate a family of three-dimensional coordination polymers $\{[M^{II}(bpy)_3][Na/LiRu(C_2O_4)_3]\}_n$ (bpy = 2,2´-bipyridine; M^{II} = Fe, Co, Ni) with interesting electrostatic interaction between the anionic network and the molecular cationic template, exhibiting the spin-crossover phenomena and being effective in the photo-reduction of CO_2 under the UV-light. Finally, the current work contains the synthesis and structural characterization of coordination polymers of formulas $\{[Zn(bpy)_3](H_2O)[LiRu(C_2O_4)_3]\}_n$ and $\{[Z^{II}(bpy)_3][Na/LiRu(C_2O_4)_3]\}_n$ (Z^{II} = Zn, Cu, Ru, Os) which constitute a family of three-dimensional polymeric networks formed through self-assembly of $[Ru(C_2O_4)_3]^{3-}$ metaloligand with $[Z^{II}(bpy)_3]^{2+}$ molecular template and an alkali metal cation, highlighting among their properties the catalytic activity of one of their members in the water photo-splitting reaction.

Índices de Calidad

De acuerdo con el Reglamento de los Estudios de Doctorado aprobado por el Consejo de Gobierno de la Universidad de Oviedo el 17 de Junio de 2013 (Boletín Oficial del Principado de Asturias Nº 146, de 25-06-2013), para presentar la Tesis Doctoral como Compendio de Publicaciones es necesario incluir en la presente Memoria un informe con el factor de impacto de las publicaciones presentadas, junto con un detalle informativo sobre la calidad de las mismas, basado en el índice de impacto y en la posición que ocupa la revista científica dentro de una determinada categoría.

El informe correspondiente a los índices de impacto de las revistas en las que se han publicado, o están en trámite de publicación, los artículos que forman parte de la presente Memoria de Tesis Doctoral se resume en la siguiente Tabla:

Relación de las publicaciones derivadas de la presente Tesis Doctoral (datos obtenidos de Journal Citations Reports®)

Revista / Referencia	Índice de Impacto	Área	Posición (Cuartil)	
Journal of Alloys and Compounds / **2012**, *536*, S437–S440 /	***2.999*** (JCR 2014)	Chemistry, Physical	47/139	(Q2)
		Material Science	48/259	(Q1)
		Metallurgy & Metallurgical Engineering	4/74	(Q1)
Acta Crystallographica Section E – Structure Reports / **2012**, *68*, 713–714 /	***0.347*** (JCR 2011)	Crystallography	24/25	(Q4)
Inorganic Chemistry / **2013**, *52*, 3933–3941 /	***4.762*** (JCR 2014)	Chemistry, Inorganic & Nuclear	4/44	(Q1)
Journal of Nanoscience and Nanotechnology / **2015** (in press) /	***1.556*** (JCR 2014)	Chemistry, Multidisciplinary	74/157	(Q2)
		Materials Science, Multidisciplinary	133/259	(Q3)
		Nanoscience & Nanotechnology	48/79	(Q3)
		Physics, Applied	73/143	(Q3)
		Physics, Condensed Matter	41/67	(Q3)
Chemical Communications / **2015** (submitted) /	***6.834*** (JCR 2014)	Chemistry	20/157	(Q1)
Dalton Transactions / **2015** (in preparation) /	***4.197*** (JCR 2014)	Chemistry, Inorganic & Nuclear	5/44	(Q1)
Inorganica Chimica Acta / **2015** (in preparation) /	***2.046*** (JCR 2014)	Chemistry, Inorganic & Nuclear	16/44	(Q2)
Crystal Growth & Design / **2015** (in preparation) /	***4.891*** (JCR 2014)	Chemistry, Multidisciplinary	24/157	(Q1)
		Crystallography	1/23	(Q1)
		Materials Science, Multidisciplinary	31/259	(Q1)

Capítulo I

Introducción

1.1. Materiales Porosos Multifuncionales

Los materiales porosos multifuncionales representan una clase muy importante de sólidos, cuyo predominio es innegable en el progreso tecnológico mundial. Actualmente, dichos materiales se han convertido en una parte integral de nuestra sociedad debido a sus numerosas aplicaciones.

Hasta ahora, las zeolitas,[1] redes puramente inorgánicas, constituían el grupo de materiales funcionales porosos más destacados y utilizados debido a sus aplicaciones en campos tan variados como el refino del petróleo,[2,3] la catálisis heterogénea,[4–6] el intercambio iónico (reblandecimiento de agua y su purificación),[7–9] o la adsorción selectiva de gases, propiedades todas ellas derivadas de la naturaleza aniónica y la estructura abierta de sus redes cristalinas. Sin embargo, en general, la utilización de las zeolitas se ha limitado a su aplicación en moléculas pequeñas debido a la restricción del tamaño de sus poros y cavidades ($\leq$ 1 nm),[10] así como por su limitada funcionalización[11] y composición química.[12]

En las últimas dos décadas, la búsqueda de nuevos materiales porosos multifuncionales ha avanzado considerablemente debido al desarrollo de polímeros de coordinación (*Coordination Polymers*, *CPs*) basados en redes extendidas de iones metálicos o complejos polinucleares coordinados a ligandos polidentados. Estos materiales sólidos, cristalinos o amorfos presentan una amplia variedad de características estructurales y pueden ser tanto porosos como no porosos. De especial relevancia son aquellos materiales porosos, ya que pueden ser utilizados en una amplia variedad de procesos, con la ventaja adicional de que existe la posibilidad de sintetizar estructuras con características pre-diseñadas. Mediante elección de ligandos de geometría y longitud adecuadas, es posible construir poros de un tamaño pre-determinado, al tiempo que se pueden crear entornos particulares mediante la adecuada funcionalización de los ligandos, propiciando que reacciones imposibles de llevarse a cabo en disolución puedan transcurrir en el espacio poroso Por otro lado, por comparación con la robusta red de las zeolitas, la flexibilidad de los *CPs* permite el comportamiento dinámico de su red porosa, lo que facilita modificaciones estructurales (intercambio del huésped o reacciones químicas dentro del poro) sin pérdida de su integridad estructural.

Estos materiales poliméricos son fácilmente modulables ya que la existencia de entidades constituidas por compuestos de coordinación permite seleccionar un gran número de metales y la incorporación de grupos funcionales en los ligandos facilitando el proceso de cristalización. La posibilidad de generar materiales de alta porosidad y elevadas áreas superficiales específicas han

(1) C. Baerlocher, L. B. McCusker, *Database of Zeolite Structures*, 2008; http://www.iza-structure.org/databases
(2) I. E. Maxwell, W. H. J. Stok, *Stud. Surf. Sci. Catal*., **2001**, *137*, 747–819.
(3) A. Corma, *NATO ASI Series. Zeolite Microporous Solids: Synthesis, Structure, and Reactivity*, **1992**, *352*, 373–436.
(4) R. Gläser, J. Weitkamp, *Springer Ser. Chem. Phys*., **2004**, *75*, 159–212.
(5) R. P. Claridge, N. L. Lancaster, R. W. Millar, R. B. Moodie, J. P. B. Sandall, *J. Chem. Soc. Perkin Trans*., **2001**, *2*, 197–200.
(6) G. Hourdin, A. Germain, C. Moreau, F. Fajula. *Catal. Lett*., **2000**, *69*, 241–244.
(7) S. M. Kuznicki, T. W. Langner, J. S. Curran, V. A. Bell, *US Pat. Appl*. US 20020077245, **2002**.
(8) S. M. Kuznicki, V. A. Bell, T. W. Langner, J. S. Curran, *US Pat. Appl*. US 20020074293, **2002**.
(9) R. Le Van Mao, N. T. Vu, S. Xiao, A. Ramsaran, *J. Chem. Mater*., **1994**, *4*, 1143–1147.
(10) J. L. Paillaud, B. Harbuzaru, J. Patarin, N. Bats, *Science*, **2004**, *304*, 990–992.
(11) K. Yamamoto, Y. Sakata, Y. Nohara, Y. Takahashi, T. Tatsumi, *Science*, **2003**, *300*, 470–472.
(12) A. K. Cheetham, G, Férey, T. Loiseau, *Angew. Chem. Int. Ed*., **1999**, *38*, 3268–3292.

introducido nuevas posibilidades en aplicaciones tradicionales de los sólidos inorgánicos microporosos, tales como la catálisis heterogénea, la separación y almacenamiento de gases, la captación selectiva de especies, etc.[13–15]

La incorporación de moléculas orgánicas en los *CPs* ofrece múltiples posibilidades de alteración más o menos sutil de las propiedades del material, realizando cambios basados en las dimensiones y la forma del ligando (que variará los ángulos de enlace en los entornos de coordinación) o su funcionalización (la decoración del ligando mediante nuevos grupos funcionales que modifican su comportamiento químico). Por otro lado la presencia de compuestos de coordinación (componente inorgánica) seguirá proporcionando potencialidades similares a las de las zeolitas, incluyendo estabilidad térmica y mecánica,[13] así como propiedades ópticas y electrónicas.

1.2. Antecedentes de los Polímeros de Coordinación

El primer ejemplo de síntesis en el laboratorio de un polímero de coordinación se remonta a más de doscientos años atrás. Entre 1704 y 1705, Berlín vio surgir un nuevo colorante, que desarrollado por Dippel y Diesbach, alcanzaría fama mundial con el nombre de "azul de Prusia", del que actualmente se conocen muchas otras variantes, incluido el "azul de Delft", representándose la estructura cristalina de su principio activo, $Fe_4[Fe(CN)_6]_3{\cdot}xH_2O$, en la Figura 1.2-1a.[16] Casi dos siglos después, se describió la síntesis de un nuevo polímero de coordinación, $[Ni(NH_3)(CN)_2]{\cdot}C_6H_6$,[17] denominado complejo de Hofmann, obtenido en forma de monocristales mediante difusión lenta de benceno a través de una disolución amoniacal de cianuro de níquel (II). Aunque Pfeiffer (1927) y Feigl (1944) especularon acerca de su orden estructural, proponiendo ambos una naturaleza monómera, solamente a mediados del siglo XX fue posible la determinación de la estructura cristalina de este compuesto,[18] estableciéndose que su empaquetamiento cristalino conduce a una red polimérica cuadrada donde átomos de níquel se enlazan, a través de grupos cianuro, originando canales capaces de acomodar a las moléculas de benceno (Figura 1.2-1b). Hace poco más de una centuria, Walker y Hawthorne[19] lograron la expansión del espacio interlaminar del complejo de Hofmann mediante la introducción de *n*-alquilaminas y, posteriormente, Iwamoto *et al.*[20,21] describieron una gran variedad de complejos tipo Hofmann que, formulados como $[M_1M_2(NH_3)_2(CN)_4]{\cdot}nX$ (donde M_1 = Ni, Zn, Cd, Cu, Mn, Fe, Co; M_2 = Ni, Pd, Pt; X = benceno, anilina, pirrol, tiofeno), pudieron sistematizarse estructuralmente mediante tres unidades básicas de construcción: $[Ni(NH_3)_2]^{2+}$, $[Ni(CN)_4]^{2-}$, y C_6H_6. Probablemente, sean estos estudios una de las bases más sólidas en las que se asientan los métodos de construcción racional de polímeros de coordinación, que se han mostrado tan fructíferos en el pasado más reciente.

(13) U. Mueller, M. Schubert, F. Teich, H. Puetter, K. Schierle-Arndt, J. Pastre, *J. Mater. Chem*., **2006**, *16*, 626–636.
(14) M. E. Kosal, J. Chou, S. R. Wilson, K. S. Suslick, *Nat. Mater*., **2002**, *1*, 118–121.
(15) J. L. C. Rowsell, O. M. Yaghi, *Angew. Chem. Int. Ed*., **2005**, *44*, 4670–4679.
(16) H. Buser, D. Schwarzenbach, W. Petter, A. Ludi, *Inorg. Chem*., **1977**, *16*, 2704–2710.
(17) K. A. Hofmann, F. Küspert, *Anorg. Chem*., **1897**, *15*, 204–207.
(18) J. H. Rayner, H. M. Powell, *J. Chem. Soc*., **1952**, 319–328.
(19) G. F. Walker, D. G. Hawthorne, *Trans. Faraday Soc.*, **1967**, *63*, 166–174.
(20) T. Iwamoto, T. Miyoshi, T. Miyamoto, Y. Sasaki, S. Fujiwara, *Bull. Chem. Soc. Jpn*., **1967**, *40*, 1174–1178.
(21) T. Iwamoto, T. Nakano, M. Morita, T. Miyoshi, T. Miyamoto, Y. Sasaki, *Inorg. Chim. Acta*, **1968**, *2*, 313–316.

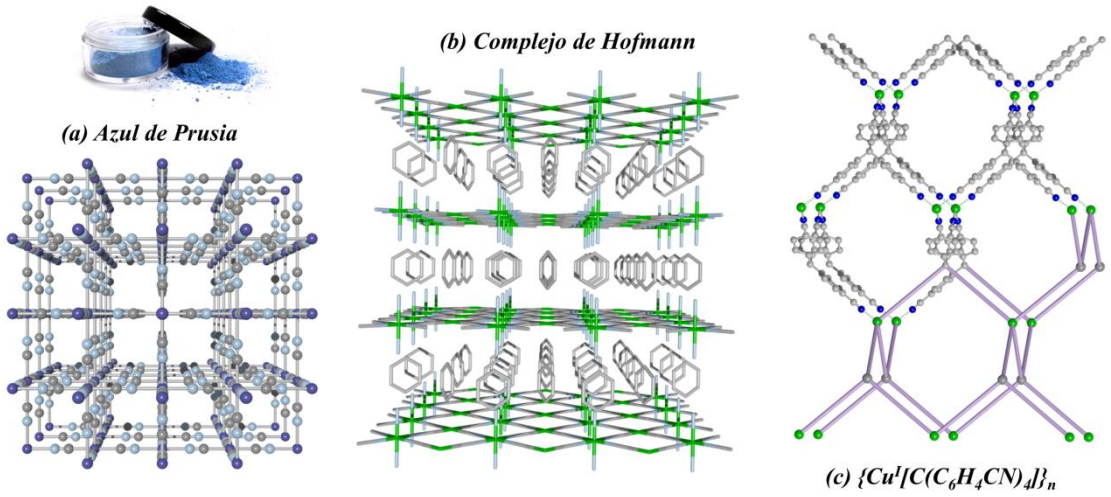

Figura 1.2-1 *(a) Estructura cristalina del colorante industrial azul de Prusia. (b) Estructura cristalina del complejo de Hofmann $[Ni(NH_3)(CN)_2]\cdot C_6H_6$. (c) Estructura adamantina de $\{Cu^I[C(C_6H_4CN)_4]\}_n$ y su representación topológica.*

En 1977, se describió la síntesis de una serie de polímeros de coordinación que, conteniendo diaminas aromáticas de diferente longitud, son capaces de encapsular selectivamente moléculas neutras. Por ejemplo, [Ni(4,4´-bipiridina)$Ni(CN)_4$] es activo frente a benceno, naftaleno, di- y tri-clorometano, o metanol, pero no frente a fenantreno o tetracloruro de carbono.[22] Posteriormente, se expandieron las variedades del complejo de Hofmann a los derivados de especies como 1,2-diaminopropano, dimetilamina, o 1,ω-diaminoalcanos,[23–25] contribuyendo enormemente al desarrollo de la química de los complejos tipo Hofmann, y señalando a los polímeros de coordinación como una nueva clase de materiales objeto de diseño molecular.

Aunque en el periodo 1970-80, se sintetizaron y caracterizaron estructuralmente una gran variedad de polímeros de coordinación, centrándose su estudio fenomenológico en la inclusión molecular y el magnetismo, es especialmente destacable el trabajo de Hoskins y Robson,[26] que recoge el primer ejemplo de red polimérica abierta construida por iones Cu^I enlazados mediante ligandos orgánicos tetradentatos, originando una red tridimensional. En $[Cu^I(CH_3CN)_4]^+$, la sustitución de acetonitrilo por 4,4´,4´´,4-tetracianotetrafenilmetano condujo a una red infinita, $\{Cu^I[C(C_6H_4CN)_4]\}_n$, construida por centros tetraédricos enlazados por unidades lineales (Figura 1.2-1c). La estructura diamantina resultante contiene cavidades similares a las del adamantano (volumen aproximado de 700 $Å^3$), ocupando su red polimérica un tercio del volumen total del cristal. De esta manera, se estableció una nueva vía de síntesis que hizo posible el diseño de nuevos sólidos, con grandes canales y cavidades, siguiendo una estrategia combinatoria, utilizando ligandos orgánicos de diferentes tamaños y formas.[26,27] A partir de ese momento, se introdujo el concepto sintético de "nodo-espaciador", incluido en la mayor parte de los caminos elegidos actualmente para el diseño de nuevos polímeros de coordinación.

(22) Y. Mathey, C. Mazières, R. Setton, *Inorg. Nucl. Chem. Lett.*, **1977**, *13*, 1–3.
(23) S. Nishikiori, T. Iwamoto, Y. Yoshino, *Bull. Chem. Soc. Jpn.*, **1980**, *53*, 2236–2240.
(24) S. Nishikiori, T. Iwamoto, *Chem. Lett.*, **1983**, 1129–1130.
(25) T. Hasegawa, S. Nishikiori, T. Iwamoto, *Chem. Lett.*, **1985**, 1659–1662.
(26) B. F. Hoskins, R. Robson, *J. Am. Chem. Soc.*, **1989**, *111*, 5962–5964.
(27) M. Fujita, J. Yazaki, K. Ogura, *J. Am. Chem. Soc.*, **1990**, *112*, 5645–5647.

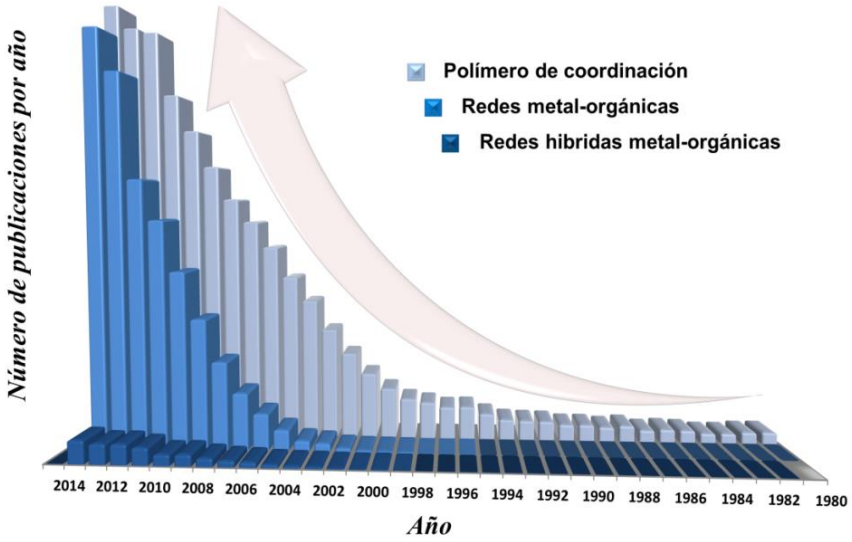

Figura 1.2-2 *Evolución anual del número de publicaciones (desde 1980) que contienen los conceptos "Hybrid Metal-Organic Frames", "Metal-Organic Frameworks" o "Coordination Polymer" (datos obtenidos usando SciFinder-2015).*

A partir de los años 1960, los polímeros de coordinación emergieron en el área de la química de coordinación como un nuevo grupo de materiales que, como se muestra en la Figura 1.2-2, han sido objeto de interés creciente hasta constituir un relevante campo de investigación entre los materiales funcionales, incluyendo la síntesis, caracterización, e ingeniería estructural de compuestos con muy diversas topologías y aplicaciones.

1.3. Clasificación y Definiciones

En general, los Polímeros de Coordinación (*CPs*) se definen como compuestos con estructura extendida, al menos en una dimensión,[28,29] en los que sus constituyentes, orgánicos e inorgánicos se unen mediante enlaces de coordinación, constituyendo una red polimérica.[30] Esta clasificación excluye tanto a los sistemas moleculares como a los oligoméricos. Una familia especial de *CPs* conocida como redes metal-orgánicas (*Metal-Organic Frameworks, MOFs)* son materiales cristalinos y porosos con estructura extendida en tres dimensiones,[31,32] y con enlaces metal-ligando robustos. Estos materiales se distinguen de las redes híbridas inorgánicas, donde las estructuras extendidas se construyen por conectividad entre partes puramente inorgánicas, resultando en múltiples enlaces **M-X-M**, donde **X** puede ser un átomo (O, Cl, N, S) o especies aniónicas como $[SiO_4]^{2-}$ $[PO_4]^{3-}$, $[SO_4]^{2-}$, etc. Por tanto de acuerdo con la anterior definición los *MOFs* son una subclase de la familia más amplia de Polímeros de Coordinación.

En el año 2012,[33] la IUPAC constituyó un grupo de trabajo supranacional con el objetivo de unificar los criterios de definición de estos materiales[34] proponiendo la clasificación jerárquica que se refleja en la Figura 1.3-1.[35]

(28) C. N. R. Rao, A. K. Cheetham, A. Thirumurugan, *J. Phys.: Condens. Matter*., **2008**, *20*, 083202(1)–(21).
(29) A. K. Cheetham, C. N. R. Rao, R. K. Feller, *Chem. Commun*., **2006**, 4780–4795.
(30) C. Janiak, *Dalton Trans.*, **2003**, 2781–2804.
(31) O. M. Yaghi, G. Li, H. Li, *Nature*, **1995**, *378*, 703–706.
(32) O. M. Yaghi, H. Li, *J. Am. Chem. Soc*., **1995**, *117*, 10401–10402.
(33) S. R. Batten, N. R. Champness, X.-M. Chen, J. Garcia-Martinez, S. Kitagawa, L. Öhrström, M. O'Keeffe, M. P. Suh, J. Reedijk, *Cryst. Eng. Comm.*, **2012**, *14*, 3001–3004.
(34) K. Biradha, A. Ramanan, J. J. Vittal, *Cryst. Growth Des*., **2009**, *9*, 2969–2970.

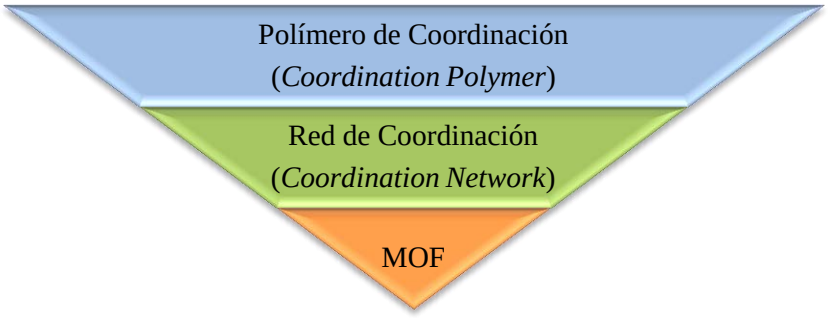

Figura 1.3-1 *Clasificación jerárquica propuesta por la IUPAC para los polímeros de coordinación, las redes de coordinación y las redes metal-orgánicas.*

El término más general es "polímero de coordinación" (*Coordination Polymer*), considerándose a las "redes de coordinación" (*Coordination Networks*) un subgrupo de los polímeros de coordinación y, a su vez, a las "redes metal-orgánicas" (*Metal-Organic Frameworks, MOFs*) un subgrupo de las redes de coordinación, de acuerdo con las siguientes definiciones:

- ✓ *Coordination Polymer* es un compuesto de coordinación que se extiende mediante la repetición de entidades de coordinación en una, dos o tres dimensiones. Los polímeros de coordinación no necesariamente deben ser cristalinos y, en algunos casos (por ejemplo, muchos carboxilatos), pueden ser considerados sales. Además, cuando se utiliza este término, debe tenerse en cuenta la definición de la IUPAC para "polímero" (sustancia macromolecular, constituida por una molécula de elevada masa molecular cuya estructura puede ser descrita por repetición múltiple de unidades derivadas de moléculas de baja masa molecular). Adicionalmente, la "entidad de coordinación" se define como un ion o molécula neutra, generalmente un centro metálico, unido a una serie de ligandos.

Por ejemplo, compuesto de cobalto(II) enlazado por 4,4´-bipiridinas forma cadena polimérica extendida en una dimensión es representante clásico de un polímero de coordinación (Figura 1.3-2).[36]

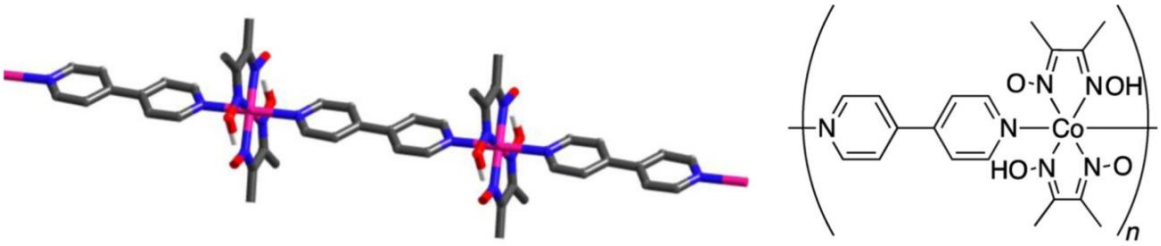

Figura 1.3-2 *Ejemplo representativo de polímero de coordinación con la estructura de cadena extendida en una dimensión.*[36]

- ✓ *Coordination Network* es un polímero de coordinación que se extiende en una dimensión mediante la repetición de entidades de coordinación, existiendo enlaces cruzados entre dos o más cadenas individuales, bucles o espirales. También incluye a compuestos de coordinación que se extienden por repetición de entidades de coordinación en dos o tres dimensiones.

(35) S. R. Batten, N. R. Champness, X.-M. Chen, J. Garcia-Martinez, S. Kitagawa, L. Öhrström, M. O'Keeffe, M. Paik Suh, J. Reedijk, *Pure Appl. Chem.*, **2013**, *85*, 1715–1724.
(36) F. Kubel, J. Strahle, *Z. Naturforsch., B: Chem. Sci*., **1982**, 37, 272–275.

Como ejemplos representativos, en Figura 1.3-3 y Figura 1.3-4 se muestran las redes de coordinación formadas mediante enlaces cruzados entre cadenas individuales (Figura 1.3-3a),[37] bucles (Figura 1.3-3b)[38] o espirales (Figura 1.3-4a).[39]

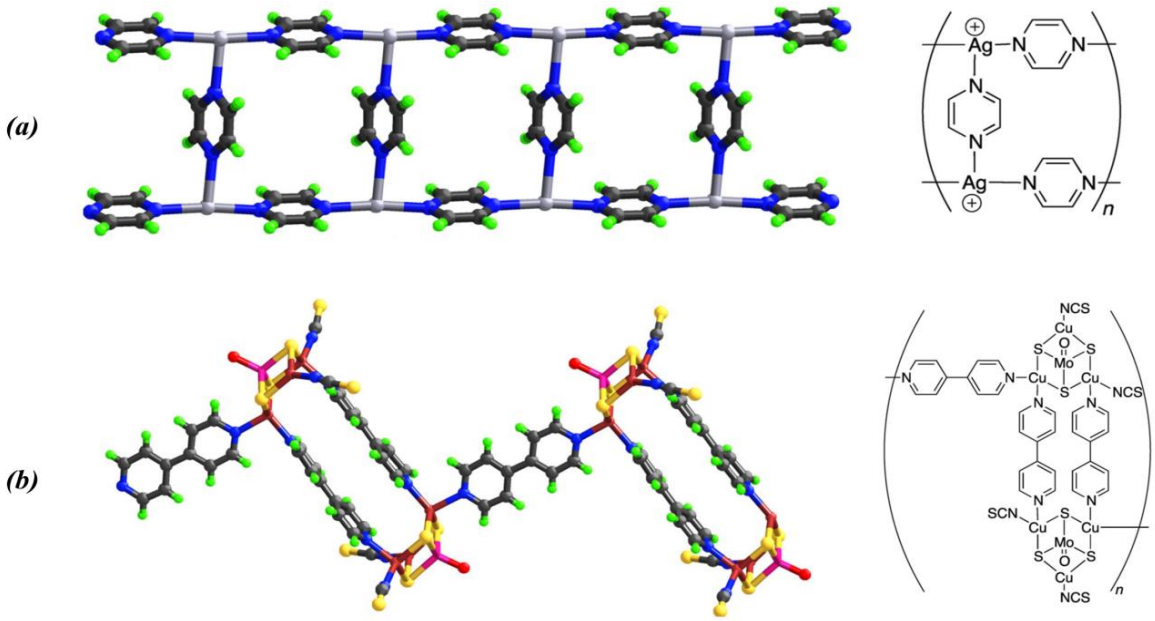

Figura 1.3-3 *Ejemplos representativos de redes de coordinación formadas mediante enlaces cruzados entre (a) cadenas[37] o (b) bucles individuales.[38]*

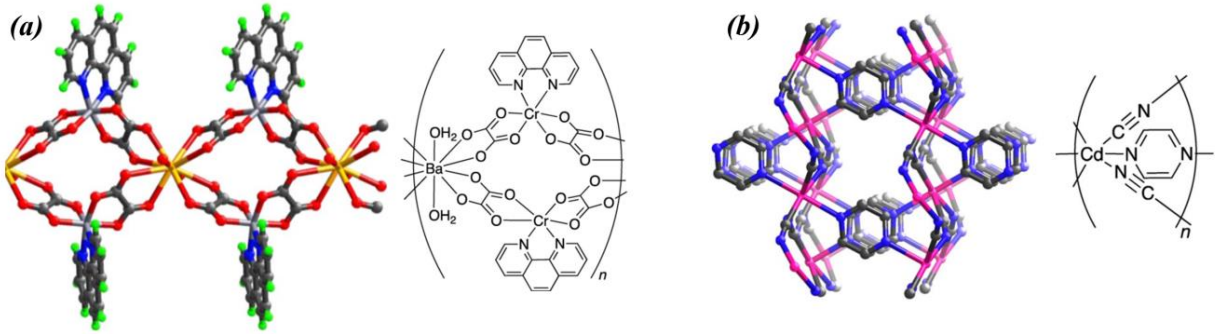

Figura 1.3-4 *Ejemplos representativos de redes de coordinación formadas mediante enlaces cruzados entre (a) espirales individuales extendiéndose en una dimensión[39] y (b) la red de coordinación formada mediante extensión en tres dimensiones.[40]*

Además, en la Figura 1.3-4b se representa el ejemplo clásico de la red de coordinación tres-dimensional y también se considera como el polímero de coordinación.[40]

✓ *Metal-Organic Framework* es una red de coordinación porosa o potencialmente porosa. Debido al hecho de que muchos de estos sistemas se comportan de forma dinámica, pudiendo

(37) D. Venkataraman, S. Lee, J. S. Moore, P. Zhang, K. A. Hirsch, G. B. Gardner, A. C. Covey, C. L. Prentice, *Chem. Mater*., **1996**, *8*, 2030–2040.
(38) J.-X. Chen, X.-Y. Tang, Y. Chen, W.-H. Zhang, L.-L. Li, R.-X. Yuan, Y. Zhang, J.-P. Lang, *Cryst. Growth Des*., **2009**, *9*, 1461–1469.
(39) K. Larsson, *Acta Cryst*., **2001**, *E57*, m195–m197.
(40) B. F. Abrahams, M. J. Hardie, B. F. Hoskins, R. Robson, E. E. Sutherland, *J. Chem. Soc., Chem. Commun*., **1994**, 1049–1050.

observarse cambios estructurales en la generación de porosidad por evacuación de especies ocluidas en las cavidades estructurales (huecos potenciales) bajo factores externos (habitualmente temperatura o presión), las redes metal-orgánicas pueden ser no cristalinas.

Uno de los primeros ejemplos de *MOF*, inicialmente no considerado como una red metal-orgánica, se representa en la Figura 1.3-5a.[41] Adicionalmente, en la Figura 1.3-5b se muestra un típico MOF, reportado por grupo de Yaghi y conocido como MOF-5.[42]

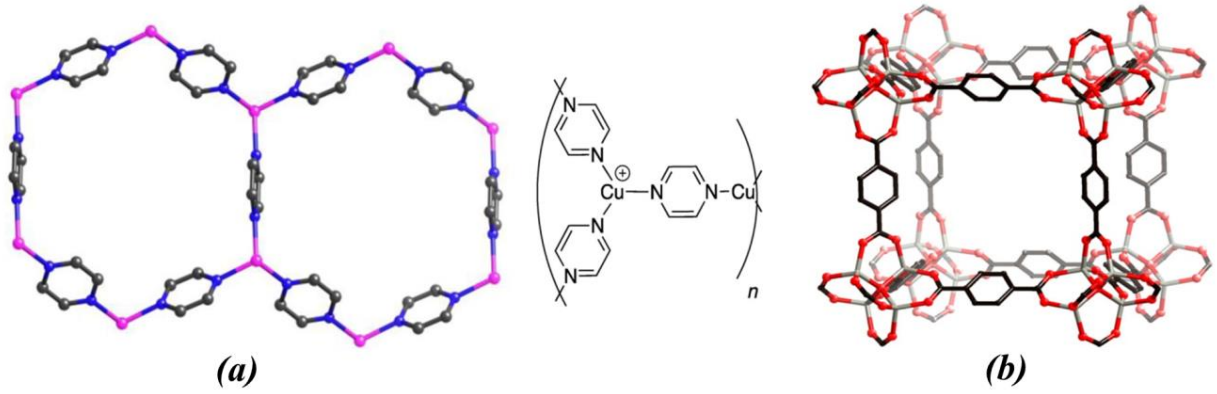

Figura 1.3-5 *Ejemplos representativos de los MOFs (a) {[Cu(C$_4$H$_4$N$_2$)$_{1.5}$(CH$_3$CN)]PF$_6$·0.5C$_3$H$_6$O}$_n$ [41] (moléculas de disolventes y aniones fueron omitidos) y (b) arquetípico MOF-5.*[42]

En la Figura 1.3-6 se visualizan los conceptos anteriores, incluyendo además tres propuestas de clasificación de las "redes metal-orgánicas" atendiendo, respectivamente, a (*i*) características topológicas (código alfabético propuesto por el grupo de O'Keeffe),[43] (*ii*) composicionales (habitualmente, en función de la naturaleza química del ligando-enlazador o de la carga de la red), o (*iii*) fenomenológicas (esencialmente, considerando sus propiedades más relevantes).

La clasificación basada en la naturaleza del ligando conector ha sido utilizada previamente con profusión. Como ejemplo, se pueden citar las familias de *MOFs* con ligandos derivados del imidazol y estructura relacionada con las zeolitas, conocidas como *ZIFs* (*Zeolitic Imidazolate Framework*),[44] o las redes metal-orgánicas basadas en polioxometalatos (POM-MOFs).[45]

Aceptando el uso de esta terminología, la IUPAC recomienda el análisis preciso de la topología de la red de cada compuesto para facilitar su comparación con otros materiales porosos y asignar racionalmente el grupo de compuestos al que pertenece. Además, la IUPAC recomienda evitar el uso del término "materiales híbridos metal-orgánicos" (*Hybrid Organic–Inorganic Materials*),[35] precedente histórico de *MOF*, argumentando que "material híbrido" tiene un uso muy extendido en procesos sol-gel para describir materiales completamente diferentes de los que constituyen las redes metal-orgánicas.

(41) S. Kitagawa, M. Munakata, T. Tanimura, *Inorg. Chem.*, **1992**, *31*, 1714–1717.
(42) H. Li, M. Eddaoudi, M. O'Keeffe, O. M. Yaghi, *Nature*, **1999**, *402*, 276–279.
(43) M. O'Keeffe, M. A. Peskov, S. Ramsden, O. M. Yaghi, *Acc. Chem. Res.*, **2008**, *41*, 1782–1789.
(44) M. Eddaoudi, D. F. Sava, J. F. Eubank, K. Adil, V. Guillerm, *Chem. Soc. Rev.*, **2015**, *44*, 228–249.
(45) H. N. Miras, L. Vilà-Nadal, L. Cronin, *Chem. Soc. Rev.*, **2014**, *43*, 5679–5699.

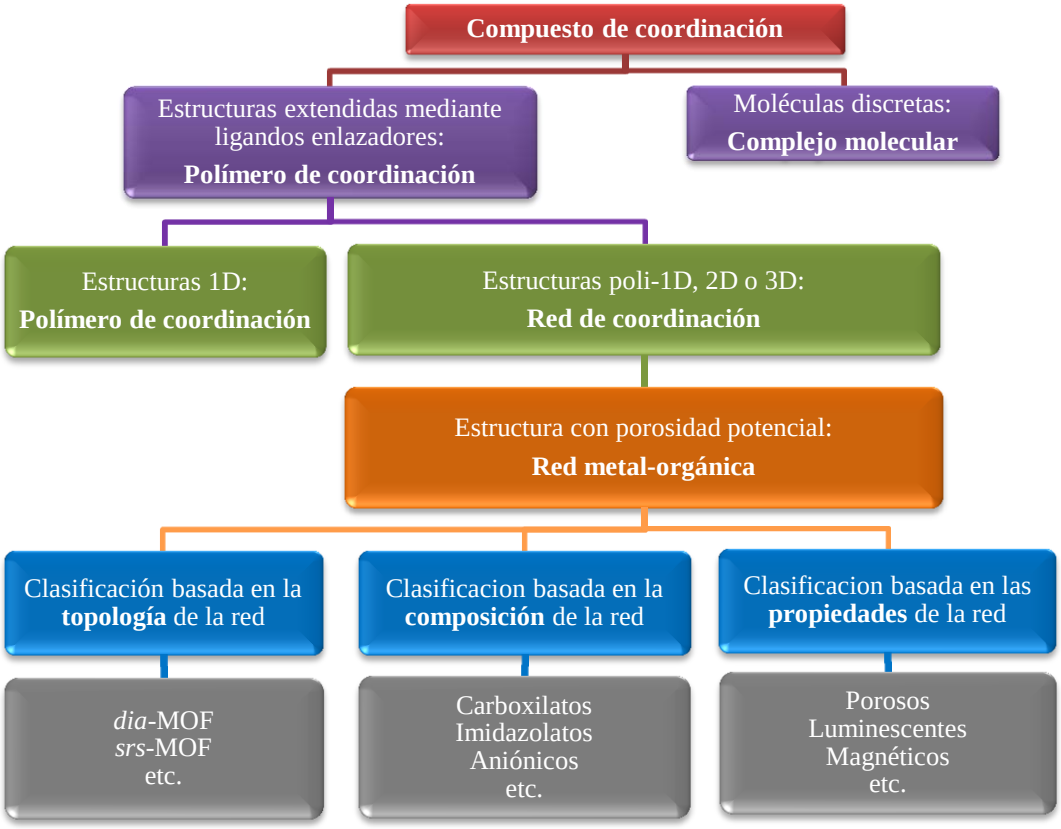

Figura 1.3-6 *Clasificación jerárquica ampliada de los polímeros de coordinación, las redes de coordinación y las redes metal-orgánicas (opciones adicionales para la subsiguiente clasificación de las redes metal-orgánicas se presentan en la parte inferior del esquema).*

1.4. Propiedades y Aplicaciones

El enorme interés de la comunidad científica e industrial hacia a las redes metal-orgánicas (*MOFs*) surge de sus interesantes aplicaciones potenciales.[46,47] La propiedad clave para muchas de ellas es la microporosidad característica de este tipo de materiales, unido al hecho de que la presencia cooperativa de componentes orgánicos e inorgánicos permite obtener estructuras muy diversas, con diferentes formas, tamaño y ambiente químico en los poros, resumiéndose algunas de sus propiedades más relevantes, junto con sus aplicaciones más destacadas, en la Figura 1.4.

Una de las propiedades más exploradas en los *MOFs* ha sido su capacidad para encapsular selectivamente muy diversas especies, tanto neutras como cargadas (en función de que la red del compuesto sea neutra, aniónica o catiónica), que van desde especies inorgánicas (gases, aniones, cationes) hasta compuestos orgánicos, incluyendo medicamentos. Así, el área de mayor demanda de *MOFs* quizá sea la separación y almacenamiento de gases,[48] ligada a la investigación en el campo de las energías renovables. En este ámbito, las redes metal-orgánicas han demostrado potencialidad como depósitos seguros para almacenamiento de hidrógeno[49,50] o

(46) A. U. Czaja, N. Trukhan, U. Müller, *Chem. Soc. Rev.*, **2009**, *38*, 1284–1293.
(47) C. Sanchez, P. Belleville, M. Popall, L. Nicole, *Chem. Soc. Rev.*, **2011**, *40*, 696–753.
(48) J.-R. Li, R. J. Kuppler, H.-C. Zhou, *Chem. Soc. Rev.*, **2009**, *38*, 1477–1504.
(49) L. J. Murray, M. Dincă, J. R. Long, *Chem. Soc. Rev.*, **2009**, *38*, 1294–1314.
(50) M. P. Suh, H. J. Park, T. K. Prasad, D.-W. Lim, *Chem. Rev.*, **2012**, *112*, 782–835.

metano,[51,52] al tiempo que la simulación del comportamiento de estos materiales en la adsorción de diferentes gases, llevó a un enorme desarrollo en la capacidad de predicción de las propiedades deseadas en nuevos compuestos.[53]

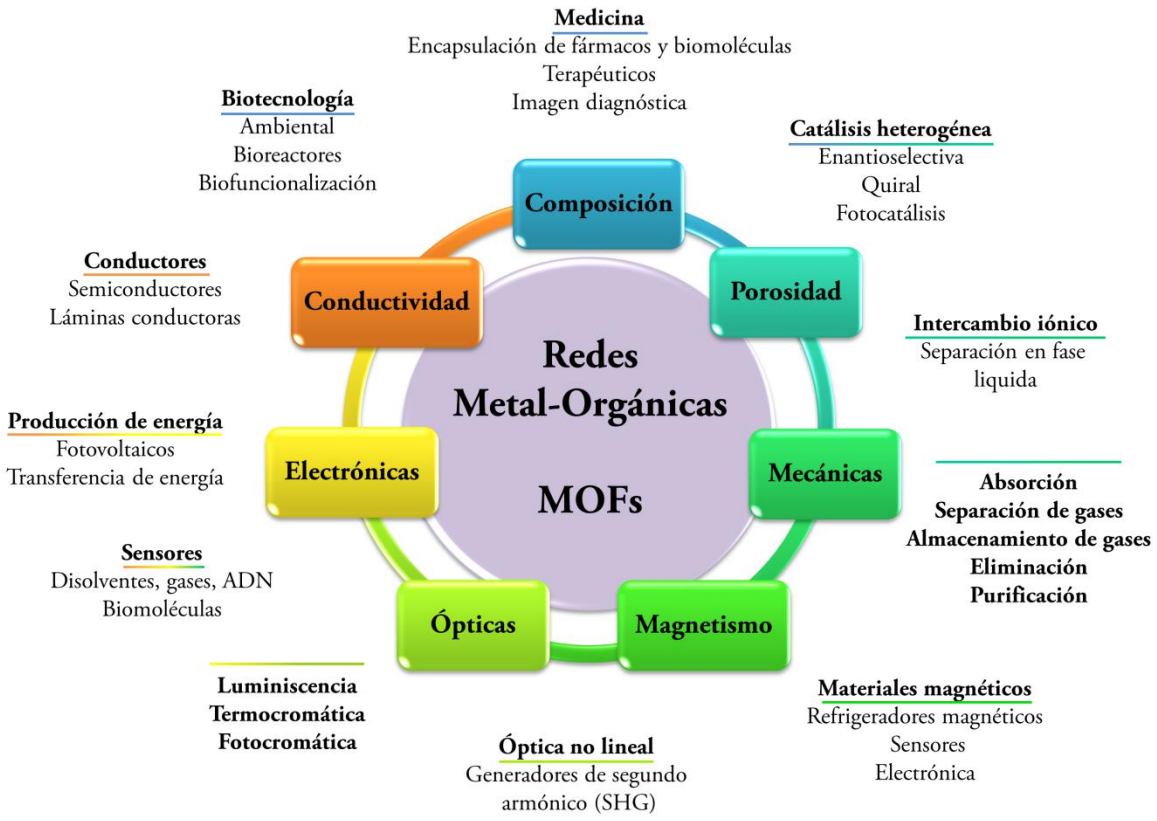

Figura 1.4 *Selección de propiedades y aplicaciones de las redes metal-orgánicas.*

Además, las redes metal-orgánicas han sido recomendadas como matrices eficientes para la captación de hidrocarburos,[54] al tiempo que, debido a la posibilidad de controlar la reactividad y las propiedades de estos materiales mediante su reactividad en estado sólido o transformaciones estructurales,[55] en particular el comportamiento dinámico de algunas redes metal-orgánicas flexibles,[56] fue posible explorar estos materiales como tamices moleculares en la separación de dióxido de carbono en mezclas gaseosas,[57–59] incluido el biogás.[60] Aunque los *MOFs* también se aplican con éxito en la purificación del aire[61] y en la separación y eliminación de gases tóxicos,[62] las aplicaciones de las redes metal-orgánicas no se limitan a operaciones de separación en fase

(51) T. A. Makal, J.-R. Li, W. Lu, H.-C. Zhou, *Chem. Soc. Rev.*, **2012**, *41*, 7761–7779.
(52) Y. He, W. Zhou, G. Qian, B. Chen, *Chem. Soc. Rev.*, **2014**, *43*, 5657–5678.
(53) R. B. Getman, Y.-S. Bae, C. E. Wilmer, R. Q. Snurr, *Chem. Rev.*, **2012**, *112*, 703–723.
(54) H. Wu, Q. Gong, D. H. Olson, J. Li, *Chem. Rev.*, **2012**, *112*, 836–868.
(55) G. K. Kole, J. J. Vittal, *Chem. Soc. Rev.*, **2013**, *42*, 1755–1775.
(56) G. Férey, C. Serre, *Chem. Soc. Rev.*, **2009**, *38*, 1380–1399.
(57) K. Sumida, D. L. Rogow, J. A. Mason, T. M. McDonald, E. D. Bloch, Z. R. Herm, T.-H. Bae, J. R. Long, *Chem. Rev.*, **2012**, *112*, 734–781.
(58) J. Liu, P. K. Thallapally, B. P. McGrail, D. R. Brown, J. Liu, *Chem. Soc. Rev.*, **2012**, *41*, 2308–2322.
(59) G. Férey, C. Serre, T. Devic, G. Maurin, H. Jobic, P. L. Llewellyn, G. De Weireld, A. Vimont, M. Daturi, J.-S. Chang, *Chem. Soc. Rev.*, **2011**, *40*, 550–562.
(60) S. Chaemchuen, N. A. Kabir, K. Zhou, F. Verpoort, *Chem. Soc. Rev.*, **2013**, *42*, 9304–9332.
(61) J. B. DeCoste, G. W. Peterson, *Chem. Rev.*, **2014**, *114*, 5695–5727.
(62) E. Barea, C. Montoro, J. A. R. Navarro, *Chem. Soc. Rev.*, **2014**, *43*, 5419–5430.

gaseosa, ya que también encuentran acomodo como materiales funcionales[63] en la separación de contaminantes en fase liquida,[64] incluyendo medios acuosos,[65,66] siendo remarcable la capacidad de las redes metal-orgánicas para actuar selectivamente en procesos de intercambio iónico.[67]

Las propiedades magnéticas de las redes metal-orgánicas son un campo emergente en las investigaciones actuales,[68,69] siendo, en este ámbito, destacables dos tipos de familias: las redes poliméricas con orden magnético de largo alcance y las que presentan transición de espín. Ambos fenómenos, que son vitales para el almacenamiento de datos en la electrónica industrial, se unen a los fenómenos magnéticos observados en algunas redes metal-orgánicas que han sido propuestas para su utilización en el diseño de refrigeradores magnéticos.[70]

Los *MOFs* también han recibido mucha atención en la búsqueda de nuevos materiales ferroeléctricos, fundamentalmente debido a la posibilidad de controlar su comportamiento a través de las características de la especie huésped que habitualmente completa la red polimérica.[71] Además, la coexistencia o acoplamiento entre ferroelectricidad y otras propiedades físicas (o químicas), tales como el magnetismo, la porosidad, la quiralidad, la foto-sensibilidad y las propiedades ópticas dan lugar a fenómenos físicos complejos e interesantes con capacidad de ser utilizados en la tecnología actual, con especial incidencia en la fabricación de dispositivos electrónicos y optoelectrónicos,[72–74] sin olvidar que la posibilidad de incorporar grupos funcionales en la estructura porosa del *MOF* hace que este tipo de materiales sean enormemente prometedores como conductores protónicos.[75,76]

Por otro lado, en la actualidad, las redes metal-orgánicas con propiedades luminiscentes son materiales aún intrigantes, que combinan su alta estabilidad térmica, en comparación con la de los ligandos orgánicos aislados, con la capacidad de alterar la longitud de onda de emisión mediante la coordinación al centro metálico.[77–80] Así, la elección del enlazador orgánico y los centros metálicos adecuados en las redes poliméricas se ha mostrado como una vía eficiente para la construcción de nuevos materiales electroluminiscentes con interesantes aplicaciones potenciales, incluyendo aportaciones en el campo de los diodos emisores de luz (LEDs).[77] Además, los *MOFs* luminiscentes se han posicionado como sensores químicos,[81] siendo explorados algunos de ellos en la detección de compuestos explosivos,[82] mientras las redes

(63) J.-R. Li, J. Sculley, H.-C. Zhou, *Chem. Rev*., **2012**, *112*, 869–932.
(64) B. Van de Voorde, B. Bueken, J. Denayer, D. De Vos, *Chem. Soc. Rev*., **2014**, *43*, 5766–5788.
(65) N. C. Burtch, H. Jasuja, K. S. Walton, *Chem. Rev*., **2014**, *114*, 10575–10612.
(66) J. Canivet, A. Fateeva, Y. Guo, B. Coasne, D. Farrusseng, *Chem. Soc. Rev*., **2014**, *43*, 5594–5617.
(67) C. K. Brozek, M. Dincă, *Chem. Soc. Rev*., **2014**, *43*, 5456–5467.
(68) E. Coronado, G. Mínguez Espallargas, *Chem. Soc. Rev*., **2013**, *42*, 1525–1539.
(69) M. Kurmoo, *Chem. Soc. Rev*., **2009**, *38*, 1353–1379.
(70) Y.-Z. Zheng, G.-J. Zhou, Z. Zheng, R. E. P. Winpenny, *Chem. Soc. Rev*., **2014**, *43*, 1462–1475.
(71) W. Zhang, R.-G. Xiong, *Chem. Rev.*, **2012**, *112*, 1163–1195.
(72) P. Falcaro, R. Ricco, C. M. Doherty, K. Liang, A. J. Hill, M. J. Styles, *Chem. Soc. Rev*., **2014**, *43*, 5513–5560.
(73) T. Hang, W. Zhang, H.-Y. Ye, R.-G. Xiong, *Chem. Soc. Rev*., **2011**, *40*, 3577–3598.
(74) V. Stavila, A. A. Talin, M. D. Allendorf, *Chem. Soc. Rev*., **2014**, *43*, 5994–6010.
(75) P. Ramaswamy, N. E. Wong, G. K. H. Shimizu, *Chem. Soc. Rev*., *2014*, **43**, 5913–5932.
(76) T. Yamada, K. Otsubo, R. Makiura, H. Kitagawa, *Chem. Soc. Rev*., **2013**, *42*, 6655–6669.
(77) J. Heine, K. Müller-Buschbaum, *Chem. Soc. Rev*., **2013**, *42*, 9232–9242.
(78) Y. Cui, Y. Yue, G. Qian, B. Chen, *Chem. Rev*., **2012**, *112*, 1126–1162.
(79) M. D. Allendorf, C. A. Bauer, R. K. Bhakta, R. J. T. Houk, *Chem. Soc. Rev*., **2009**, *38*, 1330–1352.
(80) J. Rocha, L. D. Carlos, F. A. Almeida Paz, D. Ananias, *Chem. Soc. Rev*., **2011**, *40*, 926–940.
(81) L. E. Kreno, K. Leong, O. K. Farha, M. Allendorf, R. P. Van Duyne, J. T. Hupp, *Chem. Rev*., **2012**, *112*, 1105–1125.
(82) Z. Hu, B. J. Deibert, J. Li, *Chem. Soc. Rev*., **2014**, *43*, 5815–5840.

metal-orgánicas con estructuras no centrosimétricas con actividad óptica no lineal han sido implementadas en tecnologías fotónicas, incluyendo moduladores ópticos de alta velocidad, interruptores ópticos ultrarrápidos y medios de almacenamiento de datos ópticos de alta densidad.[83]

Las propiedades mecánicas de las redes metal-orgánicas, tales como la dureza y elasticidad, se encuentran en una posición intermedia entre las de los materiales puramente orgánicos y las de las cerámicas inorgánicas y los materiales metálicos.[84] Dichas propiedades, que deben ser consideradas en el diseño práctico de sensores o de sistemas para la separación de gases, también deben ser tenidas en cuenta en el uso de los *MOFs* porosos como tamices moleculares, que hace posible su utilización en aplicaciones biotecnológicas.[85,86] Así, debido a que las enzimas, las proteínas y el ADN son muy sensibles a su entorno local, perdiendo fácilmente su funcionalidad, la incorporación de estas biomoléculas a las estructuras porosas versátiles de las redes metal-orgánicas consigue ofrecer la protección necesaria para su conservación y añade un mayor número de funcionalidades para el diseño de bioreactores de última generación y biosensores para aplicaciones ambientales y biotecnológicas.[87] Además, el carácter dual hidrofílico-hidrofóbico de algunos *MOFs* biocompatibles, y la presencia en sus estructuras de centros metálicos accesibles con carácter ácido tipo Lewis, hace que estos materiales se hayan posicionado como candidatos a la encapsulación de biomoléculas terapéuticas, ya que algunos de ellos poseen canales y poros suficientemente grandes para incorporar las moléculas de fármaco y, posteriormente, proceder a su liberación controlada en condiciones fisiológicas,[88] siendo posible aumentar la eficiencia terapéutica mediante la entrega de las moléculas activas en centros específicos del receptor por una vía más precisa y proporcionada. También, los *MOFs* pueden mostrar actividad terapéutica mediante la incorporación de la especie activa a la red polimérica como (*i*) enlazador orgánico, que se libera como molécula bioactiva por degradación del sólido, o como (*ii*) metal activo que puede ser utilizado en técnicas de imagen diagnóstica o como agente de contraste.[89]

El diseño de redes metal-orgánicas para aplicaciones catalíticas constituye un fértil campo de la investigación.[90,91] La naturaleza porosa de estos materiales, junto a la presencia en sus estructuras de centros metálicos potencialmente activos en catálisis, especialmente selectivos en términos de tamaño y forma de los substratos, posiciona a las redes metal-orgánicas entre los mejores materiales para realizar conversiones catalíticas heterogéneas.[92] Frecuentemente, los poros en los *MOFs* se encuentran bien ordenados y poseen tamaños definidos, adecuados para acoger moléculas pequeñas presentes en las reacciones químicas, proporcionando además oportunidades para inmovilizar catalizadores moleculares[93] o para encapsular nanopartículas

(83) C. Wang, T. Zhang, W. Lin, *Chem. Rev.*, **2012**, *112*, 1084–1104.
(84) J. C. Tan, A. K. Cheetham, *Chem. Soc. Rev*., **2011**, *40*, 1059–1080.
(85) P. Horcajada, R. Gref, T. Baati, P. K. Allan, G. Maurin, P. Couvreur, G. Férey, R. E. Morris, C. Serre, *Chem. Rev*., **2012**, *112*, 1232–1268.
(86) J. Shi, Y. Jiang, X. Wang, H. Wu, D. Yang, F. Pan, Y. Su, Z. Jiang, *Chem. Soc. Rev*., **2014**, *43*, 5192–5210.
(87) J. H. Jung, J. H. Lee, J. R. Silverman, G. John, *Chem. Soc. Rev*., **2013**, *42*, 924–936.
(88) C.-Y. Sun,C. Qin, X.-L. Wang, Z.-M. Su, *Expert Opin. Drug Delivery*, **2013**, *10*, 89–101.
(89) J. Della Rocca, D. Liu, W. Lin, *Acc. Chem. Res*., **2011**, *44*, 957–968.
(90) J. Gascon, A. Corma, F. Kapteijn, F. X. Llabrés i Xamena, *ACS Catal*., **2014**, *4*, 361–378.
(91) A. Corma, H. García, F. X. Llabrés i Xamena, *Chem. Rev.*, **2010**, *110*, 4606–4655.
(92) J. Y. Lee, O. K. Farha, J. Roberts, K. A. Scheidt, S. T. Nguyen, J. T. Hupp, *Chem. Soc. Rev*., **2009**, *38*, 1450–1459.
(93) J. Liu, L. Chen, H. Cui, J. Zhang, L. Zhang, C.-Y. Su, *Chem. Soc. Rev*., **2014**, *43*, 6011–6061.

metálicas que, a su vez, también pueden ser utilizadas como centros catalíticamente activos.[94,95] Por otro lado, el entorno de los poros puede ser modificado mediante la incorporación directa de funcionalidades adicionales en la red polimérica. De esta manera, cavidades prediseñadas y funcionalizadas pueden actuar como microreactores catalíticos para conversiones específicas, por ejemplo, en reacciones de polimerización.[96]

Como se ha mencionado anteriormente, la actividad catalítica de un *MOF* puede ser promovida por (*i*) los centros metálicos nodales utilizados en la construcción de la red polimérica o por (*ii*) los centros metálicos que contienen los ligandos enlazadores (metaloligandos). En este sentido, cabe destacar aquellas redes metal-orgánicas que, constituidas por motivos estructurales o ligandos quirales, resultan en redes poliméricas quirales, cuyo sistema poroso puede ser eficiente en procesos catalíticos enantioselectivos y de catálisis asimétrica.[97,98]

Entre las principales ventajas ofrecidas por las redes metal-orgánicas como catalizadores heterogéneos destacan su fácil reciclaje, su estabilidad, y su selectividad con respecto al tamaño y la forma del substrato, habiendo sido propuestas para su uso en muchas reacciones, incluyendo hidrogenación, oxidación, transesterificación, alquilación, cianosililación, arilación, reacciones de acoplamiento C–C y C–heteroatomo, o en la síntesis de heterociclos que contienen nitrógeno,[99,100] y más recientemente en fotocatálisis heterogénea.[101]

En la búsqueda de nuevos materiales adecuados para el almacenamiento de energía fotónica, los *MOFs* se han mostrado recomendables como catalizadores prometedores para su exploración en tecnologías relacionadas con energías renovables y ecológicas, en especial en los campos de la fotocatálisis y la fotosíntesis. Las redes metal-orgánicas son fotocatalizadores eficientes en una amplia variedad de procesos, tales como la fotogeneración de hidrógeno a partir de agua (*water splitting*), la oxidación del agua, la fotoreducción del dióxido de carbono, la fotodegradación oxidativa de compuestos orgánicos, o algunas transformaciones orgánicas.[102] De esta manera, los *MOFs* proporcionan una ruta atractiva hacia la conversión y el almacenamiento de la energía solar.

1.5. Diseño Racional: Unidades de Construcción y Concepto de Síntesis Reticular

Debido a la relación directa entre la estructura y las propiedades de un material, el diseño racional de las redes metal-orgánicas (*MOFs*) es un punto crucial para la síntesis de estructuras microcristalinas con las propiedades deseadas. La mayor ventaja de las redes metal-orgánicas, en comparación con los polímeros orgánicos y los materiales microporosos inorgánicos, es la posibilidad a diseñar sistemáticamente sus estructuras a través de una elección juiciosa de las "unidades de construcción"; es decir, del enlazador orgánico (*linker*) y el metal o clúster metálico. La optimización del tamaño, geometría y forma del poro, la distribución de los grupos funcionales, y otras muchas propiedades adecuadas para aplicaciones específicas, puede ser

(94) H. R. Moon, D.-W. Lim, M. P. Suh, *Chem. Soc. Rev*., **2013**, *42*, 1807–1824.
(95) A. Dhakshinamoorthy, H. Garcia, *Chem. Soc. Rev*., **2012**, *41*, 5262–5284.
(96) T. Uemura, N. Yanai, S. Kitagawa, *Chem. Soc. Rev*., **2009**, *38*, 1228–1236.
(97) L. Ma, C. Abney, W. Lin, *Chem. Soc. Rev*., **2009**, *38*, 1248–1256.
(98) M. Yoon, R. Srirambalaji, K. Kim, *Chem. Rev*., **2012**, *112*, 1196–1231.
(99) A. Dhakshinamoorthy, A. M. Asiri, H. Garcia, *Chem. Soc. Rev*., **2015**, *44*, 1922–1947.
(100) A. Dhakshinamoorthy, H. Garcia, *Chem. Soc. Rev*., **2014**, *43*, 5750–5765.
(101) T. Zhang, W. Lin, In *Metal-Organic Frameworks for Photonic Applications*; Vol. 157: Structure and Bonding, Springer, Berlin, **2014**, 89–104.
(102) T. Zhang, W. Lin, *Chem. Soc. Rev*., **2014**, *43*, 5982–5993.

alcanzada considerando: (*i*) las características del ligando, tales como geometría, forma, ángulo entre centros dentados, y la naturaleza química de grupos dentados; (*ii*) la naturaleza química del metal, geometría del entorno coordinativo y número de coordinación; (*iii*) los moduladores, disolventes y *templates*;[103] y (*iv*) los grupos funcionales no coordinativos presentes en la estructura del enlazador.[104]

1.5.1. Características del Ligando

En las estructuras poliméricas de las redes metal-orgánicas, el ligando conector realiza la función de puente entre centros metálicos, participando en enlaces covalentes que estabilizan la carcasa polimérica resultante. Considerando que la mayoría de las redes metal-orgánicas son estructuras extendidas en dos o tres dimensiones, para su construcción es imprescindible el uso de ligandos multidentados. Dependiendo del número de centros coordinativos y de los átomos donantes presentes en el ligando, el enlazador puede nombrarse como *mono-*, *bi-*, *tri-* or *tetra-*tópico(Figura 1.5.1-1).[30]

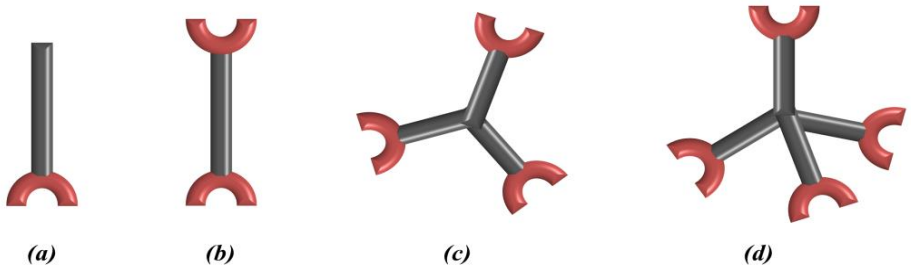

Figura 1.5.1-1 *Representación esquemática de los centros potencialmente coordinativos en los enlazadores: (a) mono-, (b) bi-, (c) tri- o (d) tetra-tópico.*

Resulta reseñable que el número de átomos dadores del ligando conector determina el grado de expansión de la red. Además, el diseño de redes poliméricas con distintas topologías y geometría porosa variada puede lograrse ajustando la relación angular entre los átomos dadores del ligando conector.[105]

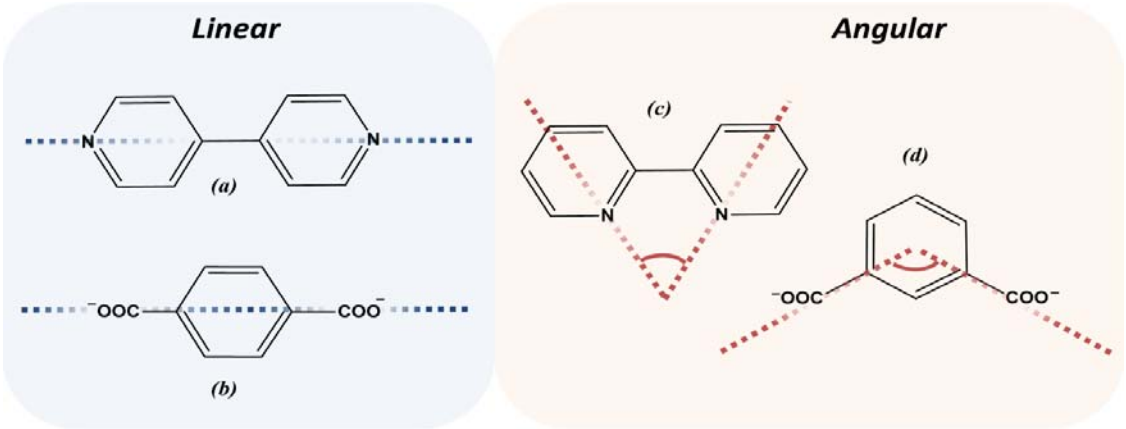

Figura 1.5.1-2 *Ejemplos representativos de enlazadores bi-dentados con diferente angulosidad entre centros coordinantes. Lineales: (a) 4,4´-bipiridina y (b) benceno-1,4-dicarboxílato. Angulares: (c) 2,2´-bipiridina y (d) benceno-1,3-dicarboxilato.*

(103) Z. Zhang, M. J. Zaworotko, *Chem. Soc. Rev*., **2014**, *43*, 5444–5455.
(104) T. R. Cook, Y.-R. Zheng, P. J. Stang, *Chem. Rev*., **2013**, *113*, 734–777.
(105) M. D. Allendorf, V. Stavila, *Cryst. Eng. Comm*, **2015**, *17*, 229–246.

Como ejemplo, en la Figura 1.5.1-2 se representan algunos ligandos conectores bidentados con diferentes ángulos de coordinación, como ilustración de los más comunes en la construcción de *CPs* y *MOFs*.

Otra característica del ligando conector que debe ser considerada en el diseño de redes metal-orgánicas es su carga eléctrica, clasificándose como neutros y aniónicos (Figura 1.5.1-3). Los ligandos neutros coordinados a centros metálicos positivos originan redes catiónicas, que requieren una especie molecular aniónica (*template* o molécula huésped) para garantizar la neutralidad del sistema. A su vez, los ligandos aniónicos constituyen redes metal-orgánicas neutras o cargadas negativamente, siendo necesaria en este último caso la incorporación de especies huésped de naturaleza catiónica.

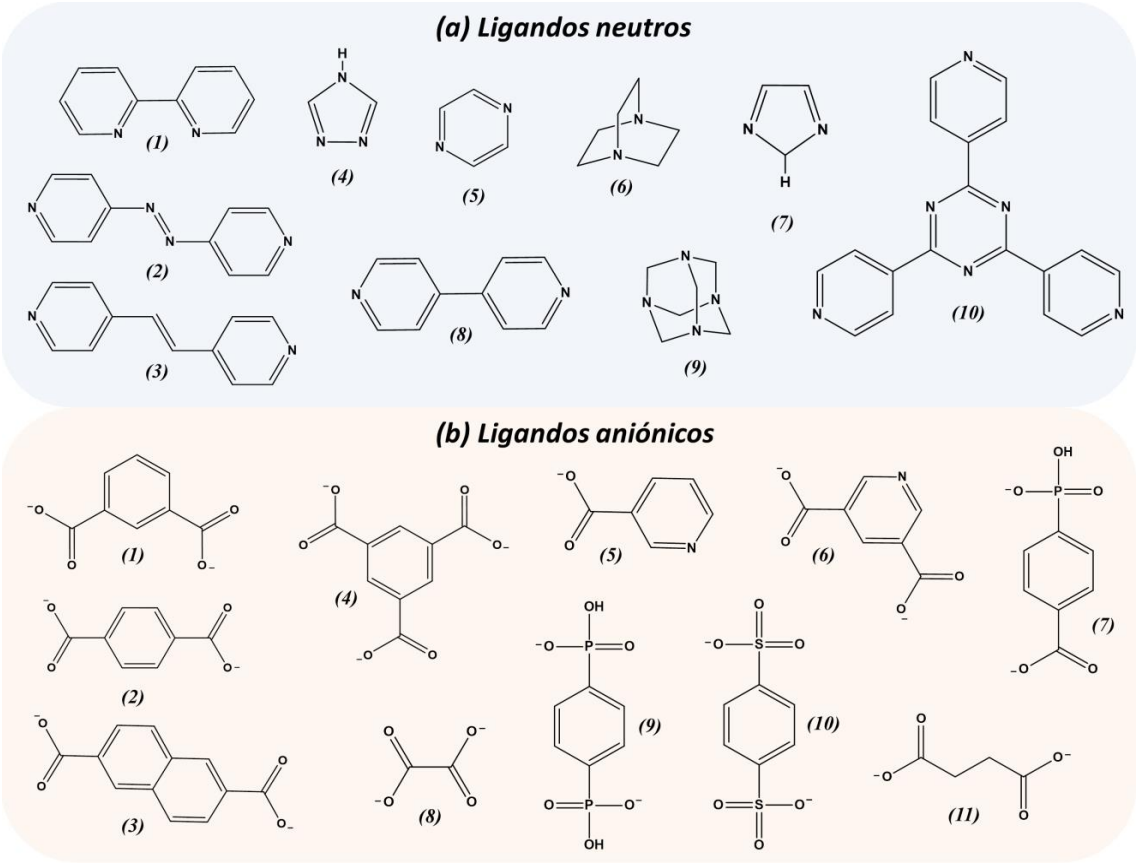

Figura 1.5.1-3 *Algunos ejemplos de ligandos (a) neutros y (b) aniónicos usados en la construcción de las redes metal-orgánicas.*

En función de su capacidad de deformación, los ligandos conectores pueden clasificarse en rígidos (véanse algunos ejemplos en la Figura 1.5.1-3b (1-7,9,10)) y flexibles (Figura 1.5.1-3b (8,11)),[106] siendo importante destacar que es la naturaleza química del átomo dador capacidad para formar uno sólo o múltiples enlaces covalentes, lo que determina la red metal-orgánica originada, su topología y sus propiedades.[107] La gran variedad de topologías descritas en la bibliografía ha sido posible como consecuencia de que en la construcción y diseño de las redes metal-orgánicas extendidas se ha realizado usando múltiples enlazadores con grupos

(106) Z.-J. Lin, J. Lü, M. Hong, R. Cao, *Chem. Soc. Rev*., **2014**, *43*, 5867–5895.
(107) W. Lu, Z. Wei, Z.-Y. Gu, T.-F. Liu, J. Park, J. Park, J. Tian, M. Zhang, Q. Zhang, T. Gentle III, M. Bosch, H.-C. Zhou, *Chem. Soc. Rev*., **2014**, *43*, 5561–5593.

coordinantes de naturaleza química variada. Entre otros muchos ejemplos de enlazadores, han sido utilizados azoles,[108] aminoácidos derivados de triazoles,[109] fosfonatos,[110] sulfonatos,[111] porfirinas,[112] rotaxanos,[113] carboxilatos,[114] y ligandos multifuncionales conteniendo grupos coordinantes de naturaleza química diferente (Figura 1.5.1-3b (5-7)).[115]

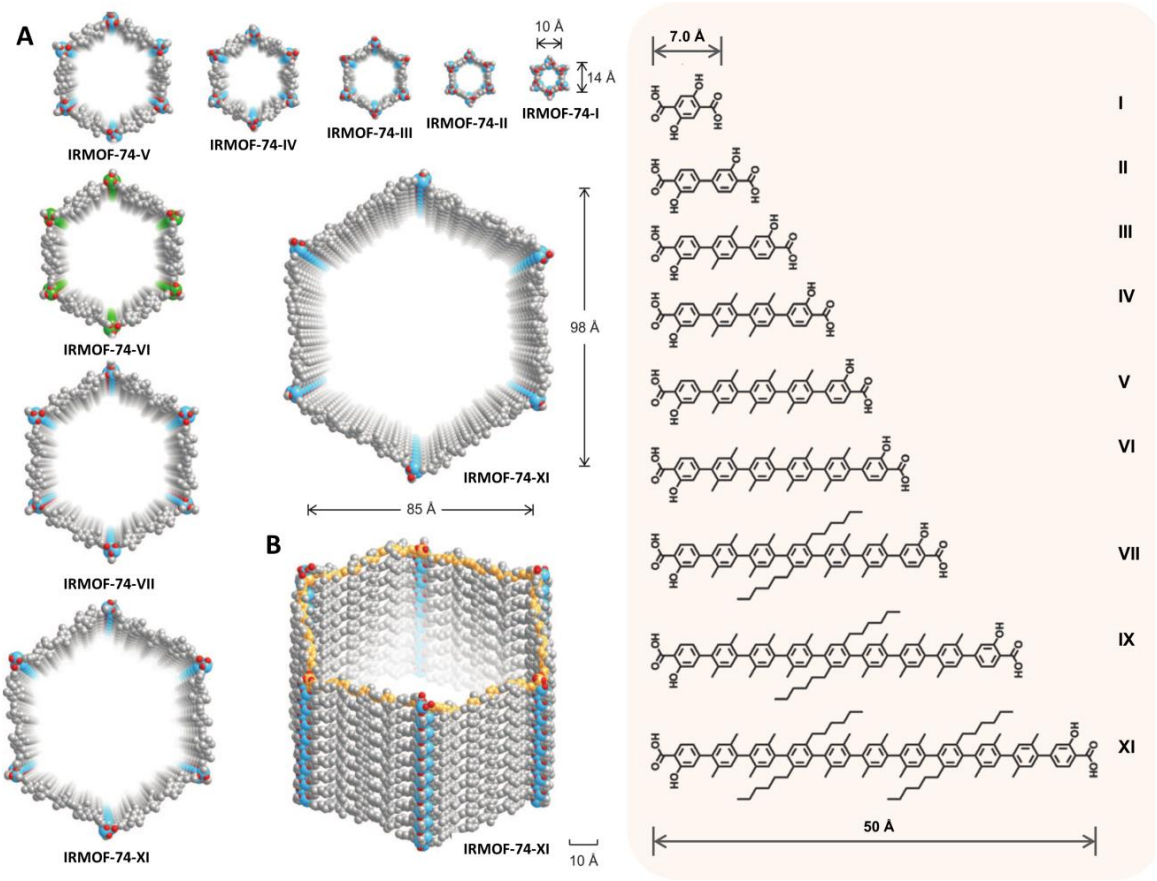

Figura 1.5.1-4 *(A) Representación de los canales hexagonales característicos de las estructuras de la familia IRMOF-74, desde el más pequeño (IRMOF-74-I) hasta el más grande (IRMOF-74-XI), junto con los ligandos usados en su construcción (de I a IX). (B) Visión lateral del canal hexagonal del anillo de 282 átomos que determina la porosidad del IRMOF-74-XI.*

Aunque la forma y la geometría del ligando conector determina las características topológicas de la red resultante, el tamaño de sus poros puede ser variado sistemáticamente utilizando el concepto de "síntesis reticular" (*Reticular Synthesis*), propiciando cambios en el tamaño de los poros desde unos pocos angstroms a varios nanómetros, simplemente cambiando las dimensiones del ligando orgánico utilizado.[116,117]

(108) J.-P. Zhang, Y.-B. Zhang, J.-B. Lin, X.-M. Chen, *Chem. Rev.*, **2012**, *112*, 1001–1033.
(109) A. D. Naik, M. M. Dîrtu, A. P. Railliet, J. Marchand-Brynaert, Y. Garcia, *Polymers*, **2011**, *3*, 1750–1775.
(110) K. J. Gagnon, H. P. Perry, A. Clearfield, *Chem. Rev.*, **2012**, *112*, 1034–1054.
(111) G. K. H. Shimizu, R. Vaidhyanathan, J. M. Taylor, *Chem. Soc. Rev.*, **2009**, *38*, 1430–1449.
(112) W.-Y. Gao, M. Chrzanowski, S. Ma, *Chem. Soc. Rev.*, **2014**, *43*, 5841–5866.
(113) V. N. Vukotic, S. J. Loeb, *Chem. Soc. Rev.*, **2012**, *41*, 5896–5906.
(114) Y. He, B. Li, M. O'Keeffe, B. Chen, *Chem. Soc. Rev.*, **2014**, *43*, 5618–5656.
(115) F. A. Almeida Paz, J. P. C. Tome, J. Klinowski, J. A. S. Cavaleiro, S. M. F. Vilela, J. Rocha, *Chem. Soc. Rev.*, **2012**, *41*, 1088–1110.
(116) O. M. Yaghi, M. O'Keeffe, N. W. Ockwig, H. K. Chae, M. Eddaoudi, J. Kim, *Nature*, **2003**, *423*, 705–714.

Como ejemplo, los IRMOF-74 constituyen una familia de compuestos *isoreticulares*, análogos al MOF-74, en los que el tamaño de poro va desde los 14 Å hasta los 98 Å en función del número de anillos aromáticos del enlazador orgánico (Figura 1.5.1-4).[118]

Se conocen otros muchos ejemplos de las familias de *MOFs* isoreticulares constituidos por los ligandos de idéntica topología, pero de la longitud variada, que preservan la topología general de la red. Entre ellos, cabe citar MOF-180 y MOF-200, prototipos de MOF-177, PCN-6 y MOF-399, análogos de HKUST-1 (MOF-199), o NU-110 y PCN-66 con redes ultra-porosas definidas por el motivo $[Cu_3(TDPAT)]_n$.[119]

Con el objeto de introducir funcionalidades adicionales a las redes metal-orgánicas, también se contempla la construcción de redes constituidas por ligandos modificables a *posteriori* de forma que, mediante reacciones post-sintéticas sea posible introducir en una red prediseñada aquellos grupos funcionales que no es factible incorporar en procesos de síntesis directa.[120]

Los ligandos carboxílicos son los enlazadores más populares en la síntesis de redes metal-orgánicas funcionales debido a su habilidad a formar más de un enlace de coordinación, pudiendo actuar simultáneamente en modo coordinativo monodentado, bidentado o quelato, y bis-monodentado (Figura 1.5.1-5), aumentando de esta manera aumentar las posibilidades de formación de nuevas redes poliméricas. El grupo carboxílico es capaz de actuar en múltiples modos de coordinación, formando enlaces covalentes con un centro metálico o con múltiples centros metálicos, propiciando en este caso la formación de clústeres polinucleares que constituyen la base estructural de la carcasa de muchos *MOFs*.

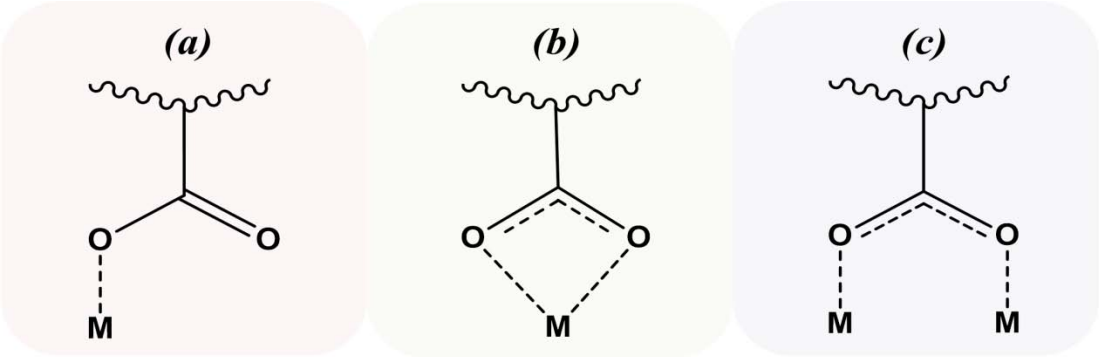

Figura 1.5.1-5 *Modos de coordinación más comunes del grupo carboxílico: (a) monodentado, (b) bidentado o quelato, (c) bis-monodentado.*

Además, la fuerza de los enlaces covalentes formados mediante coordinación a centros metálicos proporcionan a la red polimérica resultante la estabilidad necesaria para mantener su integridad durante los procesos de evacuación de los disolventes acomodados en los poros o canales de la estructura, permitiendo realizar la activación del material para la exploración de sus aplicaciones potenciales (adsorción, catálisis, etc).

(117) M. Eddaoudi, J. Kim, N. Rosi, D. Vodak, J. Wachter, M. O'Keeffe, O. M. Yaghi, *Science*, **2002**, *295*, 469–472.

(118) H. Deng, S. Grunder, K. E. Cordova, C. Valente, H. Furukawa, M. Hmadeh, F. Gándara, A. C. Whalley, Z. Liu, S. Asahina, H. Kazumori, M. O'Keeffe, O. Terasaki, J. F. Stoddart, O. M. Yaghi, *Science*, **2012**, *336*, 1018–1023.

(119) H. Furukawa, K. E. Cordova, M. O'Keeffe, O. M. Yaghi, *Science*, **2013**, *341*, 1230444(1)–(12).

(120) S. M. Cohen, *Chem. Rev*., **2012**, *112*, 970–1000.

1.5.2. Características del Metal o Clúster Metálico

La utilización de centros metálicos en la construcción de las redes metal-orgánicas hace que estas presenten múltiples ventajas en comparación con los polímeros puramente orgánicos o las redes que se organizan mediante interacciones no covalentes. Los enlaces covalentes establecidos entre metal y ligando poseen mayor direccionalidad que otras interacciones más débiles, al tiempo que la disponibilidad para establecer ángulos de enlace ortogonales (90°) favorece la construcción de arquitecturas poliméricas. Además, la capacidad de los ligandos terminales de restringir el número de sitios coordinativos del metal, junto a la posibilidad de alterar su tamaño y flexibilidad, unido a las variaciones energéticas del campo de los ligandos, y a sus variados modos de coordinación, proporciona una amplia gama de posibilidades de construcción de arquitecturas peculiares.[30]

Los centros metálicos en las redes metal-orgánicas pueden ser considerados como juntas construccionales para los ligandos conectores. En cierto modo, la forma y geometría del entorno de coordinación del centro metálico puede controlar la direccionalidad, el grado de expansión y la geometría de la red metal-orgánica.

Los metales más comúnmente utilizados para la síntesis de *MOFs* son elementos de transición que, en función de su configuración electrónica o su estado de oxidación, pueden formar especies con variadas simetrías e índices de coordinación, incluyendo geometrías lineales, curvadas, trigonales, plano-cuadradas, tetragonales, piramidales, prismáticas, octaédricas, y muchas otras variaciones distorsionadas, para el entorno coordinativo del metal (Figura 1.5.2-1).[121]

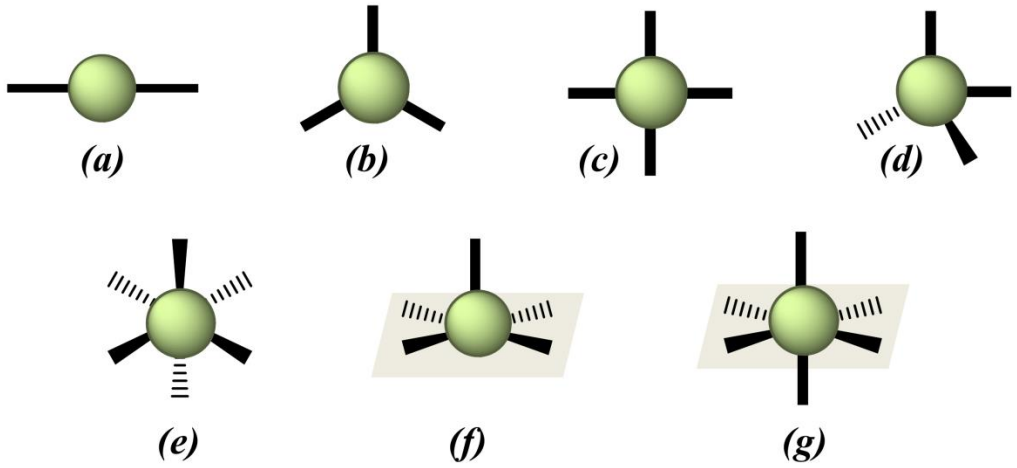

Figura 1.5.2-1 *Geometrías más frecuentes para el entorno coordinativo de los metales de transición.*

Como se ha mencionado anteriormente, la coordinación en modo quelato de un ligando bidentado a menudo resulta en la formación de agregados superiores que definen la estructura de la red metal-orgánica. En este contexto, estos complejos precursores de nuevas especies poliméricas suelen ser denominadas como "unidades de construcción secundarias" (*Secondary Building Units, SBUs*), término popularizado por el grupo de Yaghi.[122] Cuando estas *SBUs* se

(121) S. R. Batten, S. M. Neville, D. R. Turner, In *Coordination Polymers: Design, Analysis and Application*; The Royal Society of Chemistry, Cambridge, UK, 2009.
(122) M. Eddaoudi, D. B. Moler, H. Li, B. Chen, T. M. Reineke, M. O'Keeffe, O. M. Yaghi, *Acc. Chem. Res*., **2001**, *34*, 319–330.

unen entre sí, por ejemplo, vía enlazadores carboxílicos multidentados, originan redes metal-orgánicas con estructura rígida. Algunos tipos de *SBUs* se muestran en la Figura 1.5.2-2, incluyendo la llamada *paddlewheel* (*a*) con cuatro sitios coordinativos mediante los que se extiende la red polimérica y dos sitios terminales, trímeros trigonales prismáticos (*b*, *e*) que con un oxo-centro incorporan tres ligandos terminales, nodos cúbicos con ocho sitios coordinativos y un oxo-centro (*c*, *f*, *g*), nodos octaédricos tipo "acetato de zinc" (*d*), y nodos cubo-octaédricos con doce sitios coordinativos (*h*).[123]

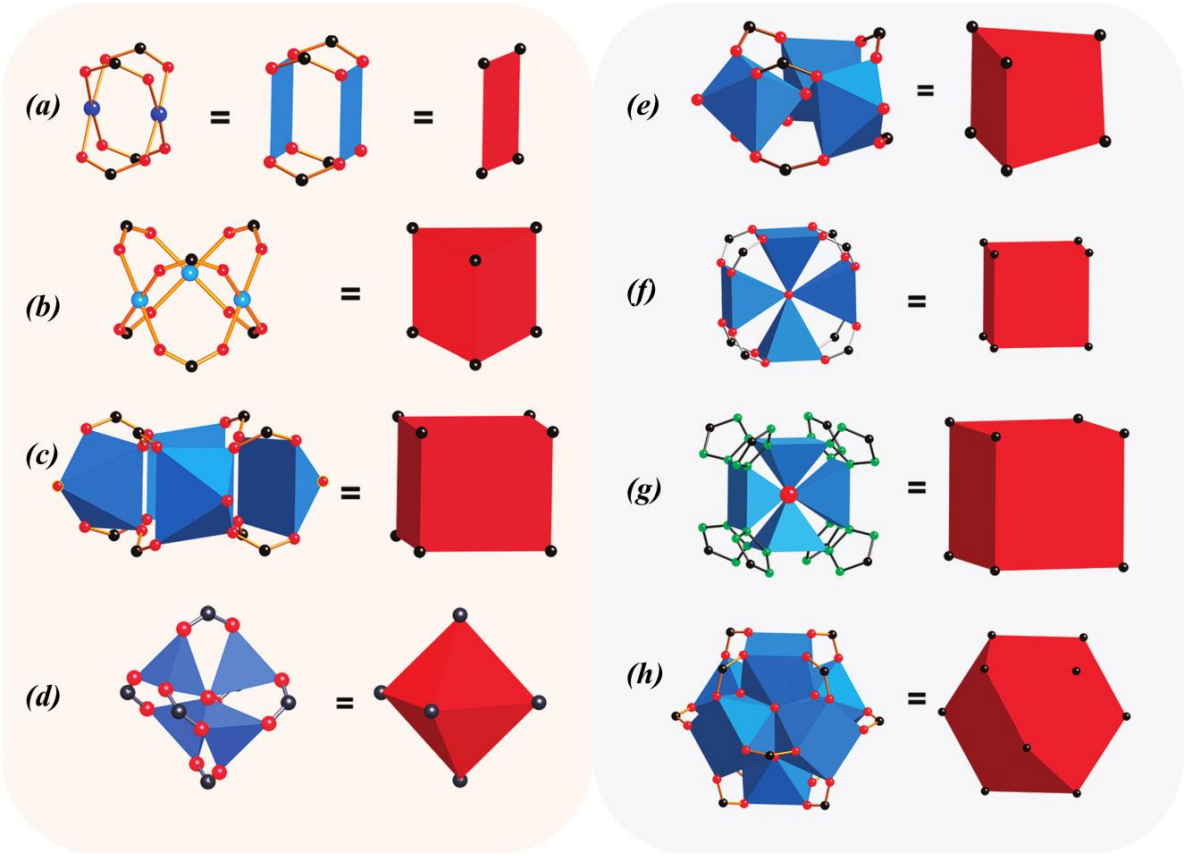

Figura 1.5.2-2 *Ejemplos de clústeres metálicos como unidades de construcción secundarias (SBUs), sus modos de coordinación y sus geometrías.*

En general, las *SBUs* se forman en fase líquida durante el proceso de preparación de la red polimérica siendo, en general, las condiciones de síntesis (temperatura, pH, etc.) específicas para cada tipo de *SBU*. La forma y geometría de las *SBUs* determina los puntos de extensión donde ellas se conectan mediante los enlazadores orgánicos. De esta manera, las *SBUs* actúan como nodos rígidos en la construcción de las redes metal-orgánicas. En los casos en los que contienen ligandos terminales, por ejemplo agua, coordinados al clúster, el número de nodos puede variar mediante intercambio de estos ligandos terminales por ligandos conectores, al tiempo que dichos grupos pueden ser canjeados por otros grupos terminales provocando la funcionalización de la red metal-orgánica. Por lo tanto, las *SBUs* son los ladrillos prediseñados

(123) D. J. Tranchemontagne, J. L. Mendoza-Cortés, M. O'Keeffe, O. M. Yaghi, *Chem. Soc. Rev.*, **2009**, *38*, 1257–1283.

que permiten la accede a una geometría y conectividad específica, permitiendo racionalizar el diseño de estructuras poliméricas con las topologías y aplicaciones particulares.[124]

En algunos casos, los clústeres metálicos de las redes metal-orgánicas constituyen cadenas infinitas o anillos de varios miembros, denominándose entonces "bloques de construcción supramolecular" (*Supermolecular Building Blocks, SBBs*).[125] Más recientemente, complementando el concepto de unidades constructivas supramoleculares, el grupo de Eddaoudi introdujo el término "capas de construcción supramolecular" (*Supermolecular Building Layers, SBLs*) para definir redes metal-orgánicas laminares pilareadas con un elevado grado de complejidad.[126]

1.5.3. Diseño y Caracterización Topológica

Como se ha mencionado anteriormente, cada red metal-orgánica necesariamente contiene, al menos, dos componentes en su estructura: un ligando y un centro metálico. Mientras la complejidad de las unidades constructivas puede variar, las redes poliméricas con estructuras complicadas a menudo pueden reducirse a redes más simples (*Nets*).[127,128] La práctica de simplificación topológica hace posible obtener una mejor compresión de la forma en la que los constituyentes se organizan en la red polimérica y, por lo tanto, proporciona una manera a sistematizar el diseño de un material con un cierto conjunto de propiedades. En la actualidad, la metodología de simplificación de estructuras cristalinas a más redes simples se utiliza frecuentemente para el análisis de las redes metal-orgánicas y su comparación con otros materiales funcionales inorgánicos.[129]

La característica fundamental más importante para el análisis topológico de una red polimérica es el número de sitios coordinativos disponibles en los centros metálicos o en las *SBUs*, la orientación relativa de estos sitios en el conjunto, el número de sitios coordinativos del ligando, el modo de coordinación que exhiben y la angulosidad relativa entre dichos sitios.

Una "red simple" (*Net*) es una representación de la estructura del polímero de coordinación mediante "nodos" (*Nodes*), cada uno de cuales está conectado a otros tres o más nodos mediante "espaciadores lineares" (*Rods*). Generalmente en la representación simplificada de una red metal-orgánica, como nodo se considera un centro metálico, o un clúster metálico, que actúa como unidad de construcción. Las características geométricas del entorno de coordinación del metal, o del clúster metálico, junto con las características geométricas del enlazador, definen la conectividad del nodo.[130] En la mayoría de las redes metal-orgánicas, el enlazador actúa como espaciador lineal, pero en los casos en los que el espaciador une tres o más nodos, también debe representarse como un nodo. Además, entre las bases de simplificación de las redes metal-orgánicas, debe considerarse el concepto de "red aumentada" (*Augmented Net*) introducido por O'Keeffe.[131] En una red aumentada, cada nodo es reemplazado por un poliedro o

(124) M. O'Keeffe, O. M. Yaghi, *Chem. Rev.*, **2012**, *112*, 675–702.
(125) J. J. Perry IV, J. A. Perman, M. J. Zaworotko, *Chem. Soc. Rev*., **2009**, *38*, 1400–1417.
(126) V. Guillerm, D. Kim, J. F. Eubank, R. Luebke, X. Liu, K. Adil, M. S. Lah, M. Eddaoudi, *Chem. Soc. Rev*., **2014**, *43*, 6141–6172.
(127) O. Delgado-Friedrichs, O'Keeffe, *J. Solid State Chem.*, **2005**, *178*, 2480–2485.
(128) O. Delgado-Friedrichs, M. D. Foster, M. O'Keeffe, D. M. Proserpio, M. M. J. Treacy, O. M. Yaghi, *J. Solid State Chem.*, **2005**, *178*, 2533–2554.
(129) S. Natarajan, Partha Mahata, *Chem. Soc. Rev*., **2009**, *38*, 2304–2318.
(130) M. Li, D. Li, M. O'Keeffe, O. M. Yaghi, *Chem. Rev*., **2014**, *114*, 1343–1370.
(131) M. O'Keeffe, *Z. Kristallogr*., **1991**, *196*, 21–37.

un polígono con la misma conectividad que el nodo original. Una estructura derivada de una red aumentada se denomina "red decorada" (*Decorated Net*).

La metodología basada en el uso de redes simples para el análisis y clasificación de estructuras cristalinas complejas tiene sus orígenes en la década de los años 1950, cuando Wells describió estructuralmente los polímeros inorgánicos por reducción de sus componentes a los simples nodos y espaciadores lineares.[132,133] En las estructuras de las redes metal-orgánicas, un nodo representa su entorno geométrico particular (tetraédrico = 4, octaédrico = 6, cubico = 8, etc.) por conexiones a un número fijo de puntos relacionados.[129] De esta manera, las estructuras poliméricas pueden ser representadas matemáticamente como una matriz periódica de los nodos. Por lo tanto, la topología de una red simple dependerá del número de nodos de cada estructura particular. La conexión secuencial del nodo se define como un camino cerrado alrededor de un vértice, que se conoce como circuito. Una red se determina por el circuito más corto alrededor del nodo y puede ser considerado como el anillo fundamental para describir la estructura.

Según la clasificación de Wells, una red con sólo un tipo de nodo y de anillo (red uniforme) puede ser representada por la notación (*n, p*), donde *p* es número de enlaces (conexiones) del nodo y *n* es tamaño del anillo más pequeño que se origina del nodo. Por ejemplo, aplicando esta descripción, la estructura laminar tipo de panal de abeja (Figura 1.5.3-1a) se representa por la red uniforme (*6,3*) donde *n* = 6 (anillo hexagonal) y *p* = 3 (nodo con tres conexiones), mientras en el caso de la estructura diamantina la red simple es (*6,4*) (Figura 1.5.3-1b).

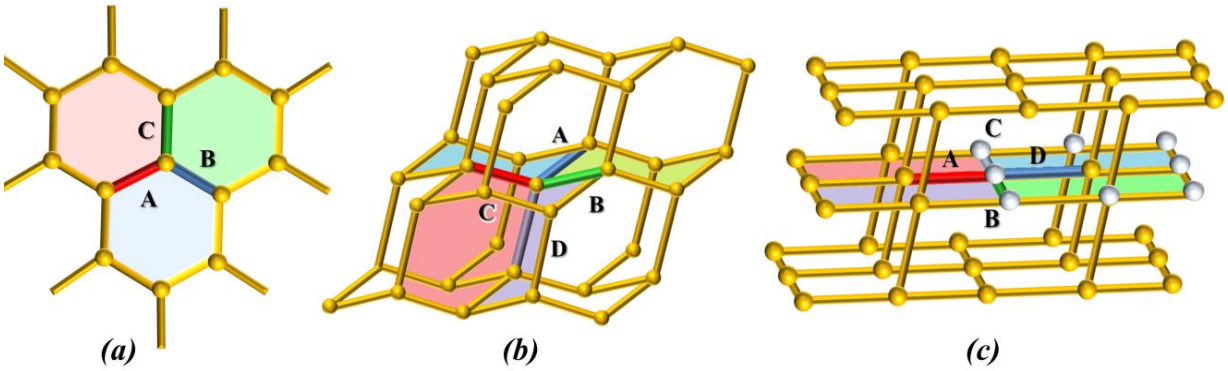

Figura 1.5.3-1 *Ilustración de la notación Schläfli para las redes simplificadas de (a) una estructura laminar tipo panal de abeja (espaciadores lineares de diferentes colores – aristas A (rojo), B (azul), C (verde) y anillos hexagonales uniformes), (b) una estructura tri-dimensional diamantina (anillos de seis miembros coloreados, y cuatro aristas – A (azul), B (verde), C (rojo), D (morado)), y (c) estructura tri-dimensional con dos tipos de circuitos cortos (las áreas coloreadas representan circuitos de seis miembros, los nodos plateados representan un circuito de ocho miembros, y aristas coloreadas – A (rojo), B (verde), C (morado), D (azul)).*

En casos más complejos, donde existen nodos de diferentes tipos, la representación de la red se modifica según la notación $N(1)^{P1}.N(2)^{P2}.N(3)^{P3}\ldots$, donde N(*i*) son los tamaños de los circuitos más pequeños que se originan de cada nodo. Los circuitos se representan en orden ascendente [N(1) < N(2) < N(3) < …] junto a sus superíndices (*Pi*), que representan el número de circuitos diferentes originados por cada nodo. De esta manera, la conectividad total del nodo puede ser determinada usando la ecuación:

(132) A. F. Wells, *Acta Crystallogr.*, **1954**, *7*, 535–544.
(133) A. F. Wells, *Acta Crystallogr.*, **1954**, *7*, 545–554.

$$p = \tfrac{1}{2} + \left(\tfrac{1}{4} + 2\sum Pi\right)^{1/2}, \text{ donde } \quad \sum Pi = p(p-1)/2$$

El valor Σ*Pi* puede determinarse a partir del número de ángulos formados en la extensión de cada nodo y definidos por un par de aristas. En consecuencia, las redes de 3, 4 y 6 nodos tendrán 3, 6 y 15 ángulos. Como ejemplo, en la Figura 1.5.3-1c se representa una estructura tri-dimensional con dos tipos diferentes de circuitos cortos localizados en un nodo con conectividad cuatro. El nodo y las cuatro aristas (A, B, C, D) correspondientes forman seis ángulos, cinco de los cuales (AB, AC, CD, DB, AD) forman parte de los circuitos cortos de seis miembros, mientras BC forma parte del circuito de ocho miembros (representado en la Figura 1.5.3-1c por nodos plateados). De esta manera, la red simplificada, considerando N(1) = 6, *P1* = 5, N(2) = 8, *P2* = 1, la conectividad del nodo p = 4 y la conectividad total Σ*Pi* = *P1* + *P2* = 6, se describe como (6^5,*8*). Este tipo de notación de la red simplificada se conoce como "símbolo puntual" (Wells) o "símbolo Schläfli".

Otra vía alternativa para describir las redes complejas es usar los símbolos Schläfli extendidos, conocidos como "símbolos de vértices". La nomenclatura expresada en términos de símbolos de vértices requiere la definición del anillo fundamental y el circuito más corto. Los anillos fundamentales son los anillos más pequeños existentes en la red, los cuales no pueden ser subdivididos, mientras los círculos más cortos son caminos que se definen por el ángulo formado entre las aristas de un nodo. De esta manera, la representación de una red usando símbolos de vértices se expresa como $A_{Q1}.B_{Q2}.C_{Q3}\ldots$ (donde A, B, C … representan el tamaño de los anillos fundamentales asociados con los ángulos, mientras Q1, Q2, Q3 indican el número de los anillos fundamentales asociados con un ángulo en particular). Como ejemplo, en el caso de la estructura diamantina representada en Figura 1.5.3-1b, que se forma por un nodo de cuatro conexiones definiendo seis ángulos ($A_{Q1}.B_{Q2}.C_{Q3}.D_{Q4}.E_{Q5}.F_{Q6}$), utilizando los símbolos de vértices, la red simple se describe como $6_2.6_2.6_2.6_2.6_2.6_2$, remarcando que cada ángulo está asociado con dos anillos fundamentales de seis miembros.

Mientras es posible describir las características de la red mediante símbolos puntuales o de vértices, sus espacios vacíos (canales o cajas) deben describirse por "azulejos poliédricos" (*Tiles*). La metodología mediante la cual se describe la geometría de los canales o cajas de una red simplificada mediante azulejos poliédricos (*Tilling*) fue propuesta por el grupo de Friedrichs,[134] utilizándose ampliamente para la caracterización, clasificación, análisis y diseño de los poros y canales de las redes metal-orgánicas. En ella, el espacio de las cavidades o sus superficies se representan como cubiertas de azulejos poligonales (zonas bi-dimensionales) o de forma general como poliedros representando el espacio euclídeo de la cavidad.[135,136] En caso de un espacio bi-dimensional, los azulejos que lo representan comparten aristas, debido a lo cual los mosaicos formados en el proceso de reconstrucción de los huecos de la red se denomina "borde-borde" (*edge-to-edge*). En el caso de espacios tri-dimensionales, los azulejos compartirán caras, por lo que el mosaico originado se denominará "cara-cara" (*face-to-face*). Habitualmente, cada tipo de red se caracteriza por poseer una geometría de mosaico propia, "mosaico natural" (*Natural tilling*), en el que las geometrías de los azulejos reflejan la simetría de la red (Figura 1.5.3-2a–d).

(134) O. Delgado Friedrichs, D. H. Huson, *Discrete Comput. Geom*., **2000**, *24*, 279–292.
(135) O. Delgado-Friedrichs, M. O'Keeffe, O. M. Yaghi, *Phys. Chem. Chem. Phys*., **2007**, *9*, 1035–1043.
(136) M. O'Keeffe, *APL. Mater*., **2014**, *2*, 124106(1)–(6).

La propiedad básica que caracteriza a un mosaico es su transitividad (*Transitivity*), que se define por cuatro números enteros, *pqrs*, donde *p* es el número de vértices diferentes no relacionados por simetría, *q* es el número de tipos de aristas, *r* el de caras, y *s* el de azulejos. La transitividad refleja la regularidad de la estructura porosa de la red y, en consecuencia, las redes más regulares tendrán una transitividad de 1111, mientras que a medida que disminuye la regularidad aumenta la transitividad (Figura 1.5.3-2e–f). Como caso particular, para estructuras donde los mosaicos representan espacios bi-dimensionales, la transitividad se expresa solamente por tres números, *pqr*.

Las redes simplificadas, clasificadas mediante símbolos puntuales o de vértice, facilitan su comparación topológica con redes idénticas o similares previamente conocidas. Para facilitar dicha comparación, algunas estructuras que pertenecen a un determinado tipo de red se nombran usando una notación de tres letras que indica su similitud topológica con una red conocida. Por ejemplo, la red metal-orgánica con topología **hcb** (*honeycomb*) se asimila con una red tipo panal de abeja, mientras que la red

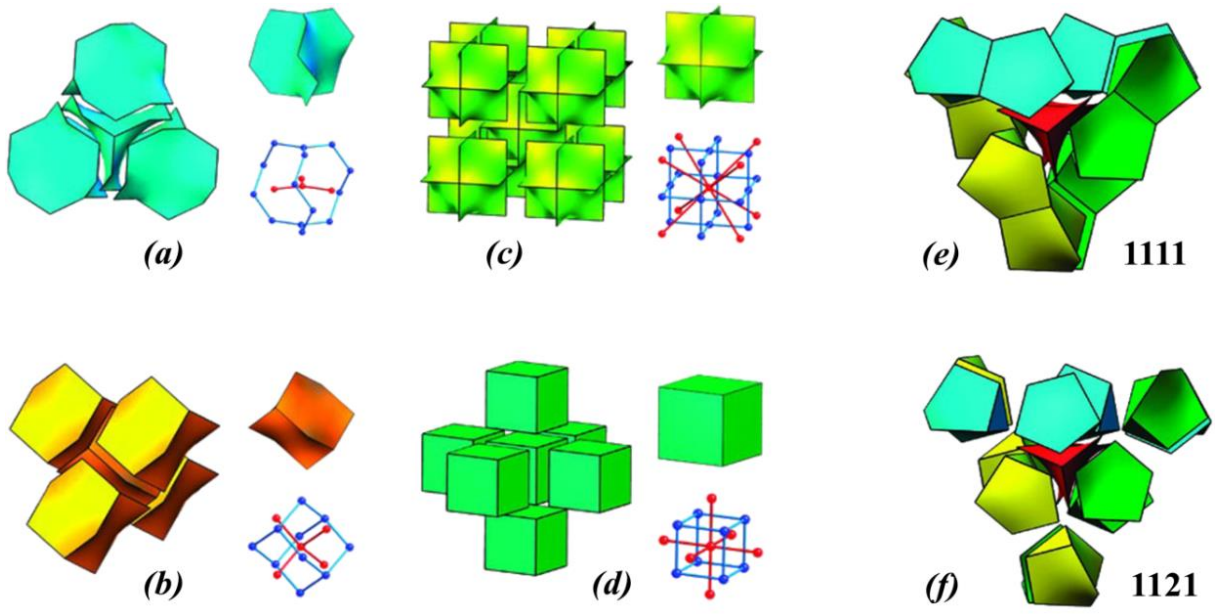

Figura 1.5.3-2 *Ejemplos (a–d) de mosaicos naturales y geometrías de azulejos de diferentes redes, y (e–f) empaquetamiento de mosaicos de diferente transitividad.*

tipo **dia** (*diamond*) indica empaquetamiento diamantino. Esta nomenclatura ha sido recomendada como una clasificación uniforme,[137] análoga a los códigos IUPAC para los diferentes tipos de redes poliméricas de las zeolitas, representadas por tres letras mayúsculas (SOD para sodalita, etc.).[138]

Una herramienta útil para búsqueda de topologías de redes simplificadas es la base de datos *Reticular Chemistry Structure Research* (*RCSR*).[43] Además, programas automatizados como Systre,[139] Olex[140] o TOPOS[141] incluyen algoritmos matemáticos para la simplificación, análisis y asignación del tipo de topología de cada red.

(137) V. A. Blatov, M. O'Keeffe, D. M. Proserpio, *Cryst. Eng. Comm*, **2010**, *12*, 44–48.
(138) http://izasc.ethz.ch/fmi/xsl/IZA-SC/ft.xsl
(139) O. Delgado-Friedrichs, M. O'Keeffe, *Acta Cryst.*, **2003**, *A59*, 351–360.
(140) O. V. Dolomanov, A. J. Blake, N. R.Champness, M. Schröder, *J. Appl. Cryst.*, **2003**, *36*, 1283–1284.
(141) V. A. Blatov, A. P. Shevchenko, D. M. Proserpio, *Cryst. Growth Des.*, **2014**, *14*, 3576–3586.

1.6. Métodos y Estrategias Sintéticas

1.6.1. Métodos clásicos

Generalmente, la mayoría de las redes metal-orgánicas conocidas se han sintetizado aplicando estrategias clásicas de síntesis, en las que las arquitecturas poliméricas se obtienen por mezcla de disoluciones de una sal del metal y un ligando orgánico.[142] Como resultado de la reacción, espontáneamente se forman enlaces metal-ligando, generando el producto cinéticamente y/o termodinámicamente más favorable. Debido a que los enlaces de coordinación son el paso clave para formación de la red polimérica, este proceso a menudo se denomina "autoensamblaje coordinativo" (*Coordination-driven self-assembly*). En este tipo de síntesis, para un mismo sistema en estudio, pueden obtenerse redes metal-orgánicas de estructura y/o composición diferente variando algunas de las variables experimentales (temperatura, concentración, presión, relación de reactivos, disolventes, pH, etc), como consecuencia de que las unidades de construcción secundarias (*SBUs*), que determinan la topología de la red polimérica, al formarse *in-situ* durante la reacción de autoensamblaje, dependen de las condiciones de reacción.[143] Además de factores químicos y composicionales, es necesario controlar la temperatura y la presión, en adición a las velocidades de calentamiento y enfriamiento del sistema. Las diferentes formas de control de la síntesis de las redes metal-orgánicas llevó a la aparición de diferentes métodos de síntesis: solvotermal, solvotermal asistido por microondas, electroquímico, mecanoquímico, sonoquímico, evaporación lenta, difusión lenta, reacción directa, etc.[144,145]

Método solvotermal. Desde los años 1960, el método hidrotermal se ha utilizado ampliamente para la síntesis de un buen número de familias de materiales funcionales. Un proceso hidrotermal requiere el uso de agua como un medio de reacción. El proceso de cristalización, que habitualmente transcurre en un recipiente de teflón cerrado herméticamente e insertado en una carcasa de acero, tiene lugar a temperaturas moderadas (100–200 ºC) y presiones autogeneradas por el vapor que emana de la disolución. Cuando, en lugar de agua, se utiliza un disolvente orgánico como medio de reacción, la estrategia sintética se denomina "solvotermal". Los procedimientos solvo/hidrotermales son el método más común y ampliamente utilizado en la síntesis de polímeros de coordinación.

Método solvotermal asistido por microondas. La síntesis asistida por microondas es un método rápido para la preparación de redes metal-orgánicas. La síntesis transcurre de forma análoga a como se describió en el párrafo anterior, con la única variación de que el calentamiento de la solución se consigue mediante emisión de microondas. La rapidez con que se alcanza el producto final de la reacción hace que, generalmente, éste esté constituido por cristales de tamaño nanométrico.[146]

Método electroquímico. La síntesis electroquímica es un método rápido y fácilmente reproducible para preparación de redes metal-orgánicas. No requiere el aporte de sales metálicas, ofreciendo la posibilidad de producir de forma continua muestras altamente cristalinas, lo que resulta ventajoso a escala industrial. El principio básico del método se basa en proporcionar el

(142) N. Stock, S. Biswas, *Chem. Rev*., **2012**, *112*, 933–969.
(143) J. L. C. Rowsell, O. M. Yaghi, *Micropor. Mesopor. Mat*., **2004**, *73*, 3–14.
(144) C. Dey, T. Kundu, B. P. Biswal, A. Mallick, R. Banerjee, *Acta Cryst.*, **2014**, *B70*, 3–10.
(145) S.-i. Noro, S. Kitagawa, T. Akutagawa, T. Nakamura, *Prog. Polym. Sci.*, **2009**, *34*, 240–279.
(146) J. Klinowski, F. A. Almeida Paz, P. Silva, J. Rocha, *Dalton Trans*., **2011**, *40*, 321–330.

ion metálico, por disolución anódica, a una disolución reactante que contiene el enlazador orgánico.[147]

Método mecanoquímico. La síntesis mecanoquímica no requiere el uso de disolventes, ya que la reacción entre la sal metálica y el enlazador orgánico ocurre mediante la aplicación de una fuerza mecánica. La simplicidad de este método, que además es económico y respetuoso al medio ambiente, ha recibido recientemente una considerable atención, habiendo sido aplicado eficientemente en la síntesis rápida de *MOFs* mediante "molienda asistida por líquidos" (*Liquid-assisted grinding, LAG*), donde se añade una pequeña cantidad de disolvente a una mezcla de reactivos sólidos.[148,149]

Método sonoquímico. Dado que las moléculas pueden sufrir modificaciones químicas debido a la aplicación de radiación ultrasónica (20 kHz – 10 MHz), los ultrasonidos inducen cambios químicos o físicos debido a un proceso de cavitación, que implica la formación, crecimiento y colapso instantáneo de partículas sólidas o burbujas en fase liquida. De esta manera, dentro de la solución reactante aparecen puntos calientes locales de tiempos de vida cortos, caracterizados por altas temperaturas y presiones, por lo que condiciones extremas creadas bajo radiación ultrasónica pueden promover reacciones químicas produciendo múltiples centros de cristalización. El método sonoquímico proporciona la posibilidad a generar centros de nucleación homogéneos y reducir considerablemente el tiempo de cristalización comparando con métodos hidrotermales convencionales.

Método de evaporación lenta. El método de evaporación lenta es un proceso convencional de preparación de *MOFs* que no requiere la aplicación de ninguna fuente de energía. Aunque tiene la ventaja de que la reacción transcurre a temperatura ambiente, su mayor desventaja radica en que requiere mayores tiempos de reacción comparados con otros métodos convencionales bien conocidos. Cuando se utiliza la evaporación lenta, una disolución con los compuestos de partida se concentra por evaporación espontanea del disolvente a una temperatura predeterminada. A veces, el proceso implica mezclas de disolventes, que aumentan la solubilidad de los reactivos y/o aceleraran el proceso de evaporación.

Método de difusión lenta. Este método se basa en la capacidad de dos disoluciones de difundir en sentido contrario, contiendo por separado la sal del metal y el ligando que generaran la red metal-orgánica. Generalmente, se usa para crecer cristales grandes, de alta calidad, para su estudio mediante técnicas de difracción de monocristal.[150] La vía más simple a realizar un experimento de contradifusión es, en un tubo de ensayo o un vial, añadir cuidosamente una disolución sobre la otra. A menudo, entre ambas, se sitúa una capa de disolvente puro, que actúa como separación entre las dos fases liquidas. Un procedimiento más sofisticado incluye la adición de geles como fases intermedias, que actúan como retardadores de la difusión. La desventaja mayor de este método es la incertidumbre en el tiempo requerido para la obtención de cristales, que puede ir desde unas pocas horas a muchos meses.

Método de precipitación directa. Este procedimiento se caracteriza por la adición rápida de una solución conteniendo la sal metálica a otra que contiene el ligando. La presión suele ser la

(147) A. Martinez Joaristi, J. Juan-Alcañiz, P. Serra-Crespo, F. Kapteijn, J. Gascon, *Cryst. Growth Des*., **2012**, *12*, 3489–3498.

(148) T. Friščić, *Chem. Soc. Rev*., **2012**, *41*, 3493–3510.

(149) S. L. James, C. J. Adams, C. Bolm, D. Braga, P. Collier, T. Friščić, F. Grepioni, K. D. M. Harris, G. Hyett, W. Jones, A. Krebs, J. Mack, L. Maini, A. G. Orpen, I. P. Parkin, W. C. Shearouse, J. W. Steed, D. C. Waddell, *Chem. Soc. Rev*., **2012**, *41*, 413–447.

(150) R. Cudney, S. Patel, A. McPherson, *Acta Cryst*., **1994**, *D50*, 479–483.

atmosférica y la temperatura puede ser variable, utilizándose en ocasiones condiciones de reflujo. Este método simple es el más evidente, fácilmente reproducible y energéticamente muy económico.

1.6.2. Métodos Alternativos

Como se ha comentado ya, la mayoría de las redes metal-orgánicas se sintetizan mediante reacción directa entre la sal inorgánica del metal y un enlazador orgánico. Sin embargo, existen algunas otras rutas alternativas, entre las que son destacables la modificaciones post-sintéticas,[151] o las estrategias de síntesis usando compuestos precursores seleccionados, como oxo-clusters,[152,153] o metaloligandos.[154]

1.6.2.1. Compuestos Precursores

El uso de precursores (*Precursor Approach*) implica la utilización de complejos de coordinación polinucleares pre-construidos, conteniendo funcionalidades similares o idénticas a las de la red metal-orgánica que se pretende sintetizar.[155] Al tiempo que los precursores polinucleares deben mantener su integridad estructural en el medio de reacción, el intercambio de los ligandos monodentados de los precursores moleculares con los enlazadores polidentados debe generar una red polimérica extendida. Por ejemplo, la sustitución del ligando acetato en un complejo trinuclear de hierro(III) por los enlazadores bidentados tales como fumarato, naftaleno-2,6-dicarboxilato o muconato fue el camino para la formación de las redes poliméricas de los compuestos MIL-88, MIL-88C y MIL-89,[156,157] confirmándose mediante datos de EXAFS obtenidos *in situ* que, durante la cristalización del MIL-89, las unidades constructivas del acetato trinuclear de hierro permanecen intactas.[158]

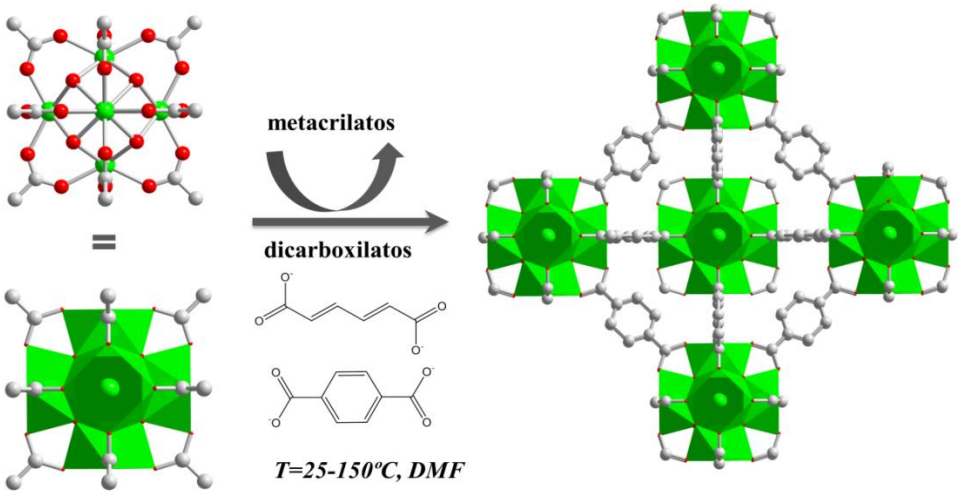

Figura 1.6.2.1-1 *Esquema del proceso de síntesis del polímero de coordinación UiO-66(Zr) a partir de un oxo-clúster de zirconio.*

(151) P. Deria, J. E. Mondloch, O. Karagiaridi, W. Bury, J. T. Hupp, O. K. Farha, *Chem. Soc. Rev*., **2014**, *43*, 5896–5912.
(152) U. Schubert, *Chem. Soc. Rev*., **2011**, *40*, 575–582.
(153) L. Rozes, C. Sanchez, *Chem. Soc. Rev*., **2011**, *40*, 1006–1030.
(154) G. Kumar, R. Gupta, *Chem. Soc. Rev*., **2013**, *42*, 9403–9453.
(155) Y. Han, J.-R. Li, Y. Xiea, G. Guo, *Chem. Soc. Rev*., **2014**, *43*, 5952–5981.
(156) C. Serre, F. Millange, S. Surblé, G. Férey, *Angew. Chem., Int. Ed*., **2004**, *43*, 6285–6289.
(157) S. Surblé, C. Serre, C. Mellot-Draznieks, F. Millange, G. Férey, *Chem. Commun*., **2006**, 284–286.
(158) S. Surblé, F. Millange, C. Serre, G. Férey, R. I. Walton, *Chem. Commun*., **2006**, 1518–1520.

Aplicando una estrategia similar, se ha logrado obtener la estructura polimérica UiO-66 partiendo de un oxo-clúster de metacrilato de zirconio, $[Zr_6O_4(OH)_4(OMc)_{12}]$, sustituyendo los ligandos monocarboxílicos por dicarboxílicos (muconato y tereftalato) (Figura 1.6.2.1-1).[159]
Entre otros muchos ejemplos, las redes poliméricas Zn-MOF-5 y Be-MOF-5 se han preparado a partir de oxo-clústeres tetranucleares de acetato de zinc y berilio, $[(M_4(\mu_4\text{-}O)(OAc)_6)]$.[160] Sin embargo, se conocen pocos ejemplos de polímeros de coordinación basados en carboxilatos de rutenio, todos ellos sintetizados usando compuestos precursores.[161–164] Así, Mori *et al.* aislaron redes poliméricas tri-dimensionales de composición $\{Ru_2^{II,III}(fuma)_2Cl\}_n$, $\{Ru_2^{II,III}(muco)_2Cl\}_n$ y $\{Ru_2^{II,III}(BDC)_2Cl\}_n$ mediante reacción de intercambio de ligandos entre un acetato binuclear de rutenio de valencia mixta, $[Ru_2^{II,III}(OAc)_4Cl]$, y ácidos carboxílicos (fuma = ácido fumárico, muco = ácido mucónico y BDC = ácido tereftálico).[165,166] En todas las redes resultantes, la unidad dímera, $[Ru^{II}Ru^{III}]$, se enlaza por puentes carboxilato extendiendo la red en dos dimisiones, mientras el cloruro actúa también como puente entre los dímeros de rutenio extendiendo la red en una tercera dimensión (Figura 1.6.2.1-2).

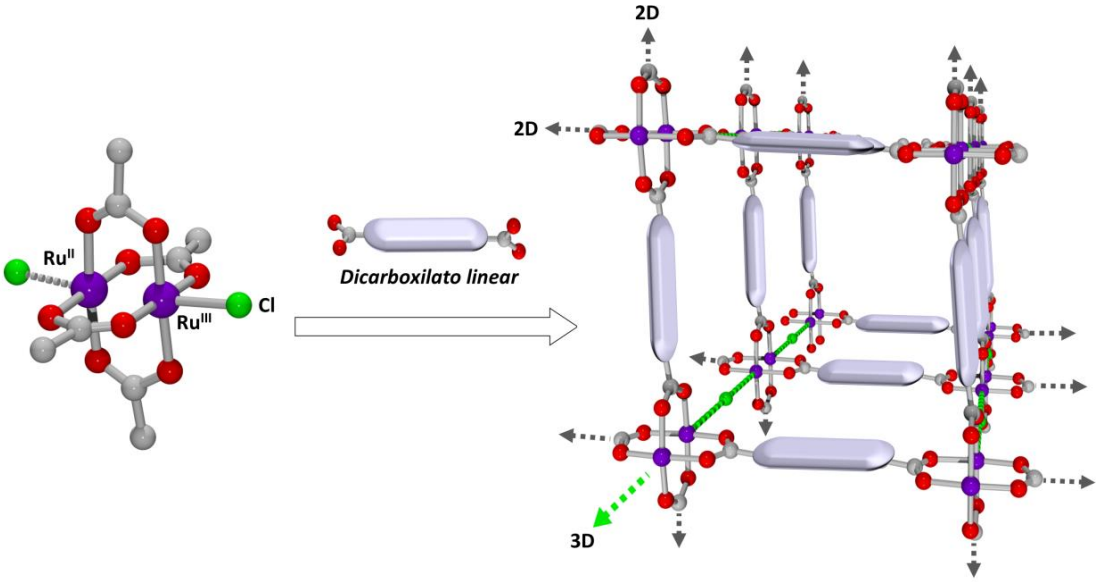

Figura 1.6.2.1-2 *Representación esquemática de la formación de una red polimérica tri-dimensional mediante intercambio de ligandos.*

Entre las propiedades que muestran estas redes poliméricas se encuentra su capacidad para adsorber (O_2, N_2 y Ar) a temperaturas inferiores a 200 K. Además, su capacidad de adsorción es función del tamaño de sus poros, que varía con la longitud del enlazador carboxílico elegido. Usando la misma estrategia de la síntesis, Ribero *et al.* han añadido un nuevo miembro a esta familia de *CPs*, $\{Ru_2^{II,III}(adip)_2Cl\}_n$ (adip = adipato), siendo destacable el elevado valor de su área superficial específica (281 $m^2 \cdot g^{-1}$) debida mayoritariamente a su porosidad intracristalina.[167]

(159) V. Guillerm, S. Gross, C. Serre, T. Devic, M. Bauer, G. Férey, *Chem. Commun*., **2010**, *46*, 767–769.
(160) S. Hausdorf, F. Baitalow, T. Böhle, D. Rafaja, F. O. R. L. Mertens, *J. Am. Chem. Soc*., **2010**, *132*, 10978–10981.
(161) M. A. S. Aquino, *Coord. Chem. Rev*., **2004**, *248*, 1025–1045.
(162) W. Mori, S. Takamizawa, *J. Solid State Chem*., **2000**, *152*, 120–129.
(163) W. Mori, T. Sato, C. N. Kato, T. Takei, T. Ohmura, *Chem. Rec*., **2005**, *5*, 336–351.
(164) W. Mori, T. Sato, T. Ohmura, C. N. Kato, T. Takei, *J. Solid State Chem*., **2005**, *178*, 2555–2573.
(165) S. Takamizawa, K. Yamaguchi, W. Mori, *Inorg. Chem. Commun*., **1998**, *1*, 177–178.
(166) S. Takamizawa, T. Ohmura, Y. Yamaguchi, W. Mori, *Mol. Cryst. Liq. Cryst*., **2000**, *342*, 199–204.
(167) G. Ribeiro, F. M. Vichi, D. O. Silva, *J. Mol. Struct.*, **2008**, *890*, 209–214.

La metodología del intercambio de ligandos en complejos precursores se ha popularizado en la síntesis de polímeros de coordinación basados en la unidad dímera $[Ru^{II}Ru^{II}]$.[168] Alguna de las redes resultantes, $\{Ru_2^{II,II}(BDC)_2\}_n$ y $\{Ru_2^{II,II}(BPDC)_2\}_n$ poseen estructuras bidimensionales, mientras otras, $\{Ru_2^{II,II}(BDC)_2(dabco)\}_n$ y $\{Ru_2^{II,II}(BPDC)_2(dabco)\}_n$ (dabco = 1,4-diazabicilo[2,2,2]octano; BPDC = ácido bifenil-4,4´-dicarboxilico), resultaron ser tridimensionales (la estructura bidimensional constituida por puentes de los carboxilatos se extiende en una tercera dimensión mediante el enlazador dabco). Estos compuestos presentan estructura cristalina porosa (diámetro de poro *ca.* 8.5 Å) con un volumen de microporos más elevado en los compuestos 3D que en los 2D, aumentando en ambas casos cuando lo hace la longitud del enlazador. Es destacable que estos polímeros de coordinación muestran elevada actividad catalítica en la reacción de la hidrogenación de etileno a etano a temperatura de 50 °C, alcanzando la conversión total en 120–324 min, siendo más eficientes los compuestos 3D que los 2D.

El interés hacia los polímeros de coordinación microporosos basados en unidades diméricas de rutenio como catalizadores heterogéneos dio origen a interesantes estudios realizados por Mori *et al.*,[169,170] donde se describió la elevada actividad catalítica de un nuevo MOF, $\{[Ru_2^{II,III}(H_2TCPP)](BF_4)\}_n$ (H_2TCPP = 4,4′,4″,4‴-(21H,23H-porfin-5,10,15,20-tetrail)tetrakis acido benzoico), en la oxidación heterogénea de alcoholes primarios alifáticos con aire a temperatura ambiente.

Es destacable que el primer ejemplo de reducción fotoquímica de agua con formación de hidrógeno molecular fue descrita usando un polímero de coordinación poroso, donde la reacción estaba promovida por $\{Ru_2^{II,II}(BPDC)_2\}_n$ en presencia de $[Ru(bpy)_3]^{2+}$, MV^{2+} y Na_2EDTA (bpy = 2,2´-bipiridine, MV^{2+} = N,N´-dimetil-4,4´-bipiridinio, EDTA = ácido etilendiaminotetraacético).[171] El polímero de coordinación, $\{Ru_2^{II,II}(BPDC)_2\}_n$, preparado por tratamiento del acetato dinuclear de rutenio, $[Ru_2^{II,III}(OAc)_4]$, con ácido tereftálico, fue capaz de producir 41 µmol H_2 después de 4 horas bajo la irradiación (TON = 8.16) mostrando mayor actividad que el catalizador inorgánico más eficiente en la fotoreducción del agua (TiO_2).

La estrategia de síntesis usando compuestos precursores presenta ventajas en comparación con los procesos de síntesis convencional, entre las que se incluyen un mayor control sobre la naturaleza y la topología del producto final, así como la posibilidad de trabajar en condiciones de síntesis más suaves (temperaturas y presiones más reducidas). Además, dada la diversidad de compuestos precursores de carboxilatos de rutenio, es ésta una ruta muy versátil para la síntesis de nuevos polímeros de coordinación basados en rutenio.

1.6.2.2. Metaloligandos

El uso de metaloligandos (*Metalloligands Approach*) en la síntesis de nuevas redes metal-orgánicas recibe actualmente mucha atención, siendo ampliamente utilizada en la preparación de polímeros de coordinación heterometálicos,[172] utilizándose complejos de coordinación moleculares (metaloligandos) con grupos donantes que permiten la coordinación de

(168) T. Ohmura, W. Mori, H. Hiraga, M. Ono, Y. Nishimoto, *Chem. Lett*., **2003**, *32*, 468–469.
(169) C. N. Kato, W. Mori, *C. R. Chimie*, **2007**, *10*, 284–294.
(170) C. N. Kato, M. Ono, T. Hino, T. Ohmura, W. Mori, *Catal. Commun*., **2006**, *7*, 673–677.
(171) Y. Kataoka, K. Sato, Y. Miyazaki, K. Masuda, H. Tanaka, S. Naito, W. Mori, *Energy Environ. Sci*., **2009**, *2*, 397–400.
(172) J. D. Evans, C. J. Sumby, C. J. Doonan, *Chem. Soc. Rev*., **2014**, *43*, 5933–5951.

un segundo ion metálico, de manera que es posible construir una red polimérica de estructura específica con las propiedades deseadas (Figura 1.6.2.2),[112,173] permitiendo la selección del metaloligando el control sobre la estequiometria y la geometría de la red polimérica resultante.

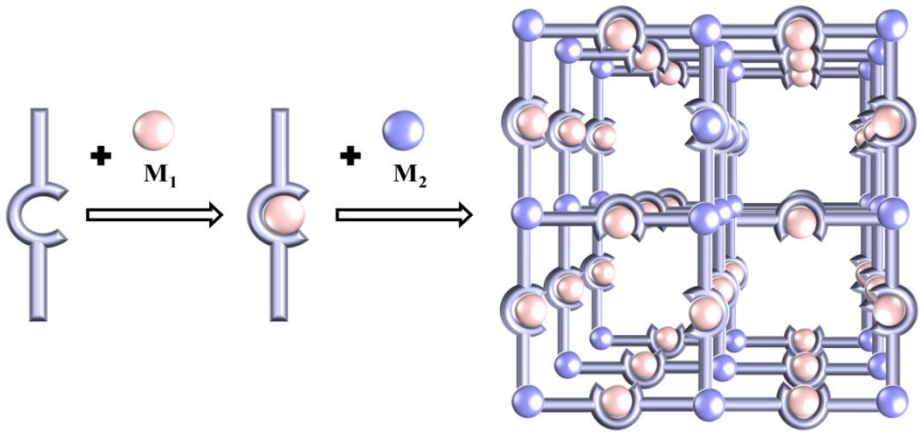

Figura 1.6.2.2 *Representación esquemática de la estrategia de síntesis usando metaloligandos.*

Este procedimiento permite obtener materiales con los centros metálicos insaturados que, posteriormente, pueden ser utilizados en la coordinación de moléculas huésped o en procesos catalíticos.[174]

1.6.2.2.1. Anión *Tris*-Oxalato como Metaloligando

El anión oxalato se muestra como un ligando muy versátil en la síntesis de polímeros de coordinación heterometálicos, pudiendo actuar como el ligando *mono*-, *bi*-, *tri*- o *tetra*-dentado (Figura 1.6.2.2.1-1).[175]

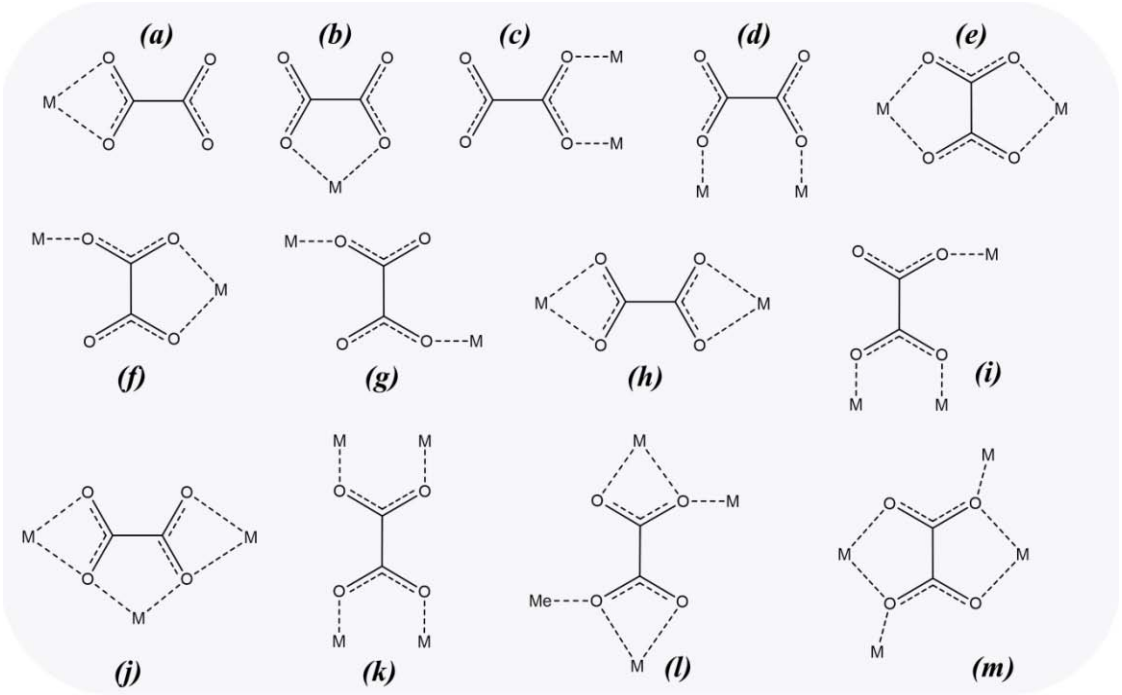

Figura 1.6.2.2.1-1 *Modos de coordinación del ligando oxalato: (a–b) monodentado, (c–h) bidentado, (i–j) tridentado, y (k–m) tetradentado.*

(173) S. Kitagawa, S.-i. Noro, T. Nakamura, *Chem. Commun*., **2006**, 701–707.
(174) M. C. Das, S. Xiang, Z. Zhang, B. Chen, *Angew. Chem., Int. Ed*., **2011**, *50*, 10510–10520.
(175) G. Marinescu, M. Andruh, F. Lloret, M. Julve, *Coord. Chem. Rev*., **2011**, *255*, 161–185.

En presencia de cationes trivalentes de metales de transición, el anión oxalato (*ox*, $C_2O_4^{2-}$) puede formar el anión quiral *tris*-quelato, $[M^{III}(ox)_3]^{3-}$, con la simetría D_3, que puede actuar como unidad de construcción primaria, originando redes poliméricas extendidas.[176–182] La combinación de este metaloligando con un segundo ion puede proporcionar la formación de redes aniónicas heteronucleares extendidas en dos dimensiones caracterizadas por las fórmulas generales $\{M_1^{I}M_2^{III}(ox)_3^{-}\}_n$ o $\{M_1^{II}M_2^{III}(ox)_3^{-}\}_n$ (M_1^{I} = Na; M_1^{II} = Cr^{2+}, Mn^{2+}, Fe^{2+}, Co^{2+}, Ni^{2+}, Cu^{2+}, Zn^{2+}; M_2^{III} = Cr^{3+}, Fe^{3+}, V^{3+}, Mn^{3+}, Ru^{3+}), donde el catión molecular $[XR_4]^+$ (*X* = N, P, As; *R* = C_6H_5 (Ph), *n*-C_2H_5, *n*-C_3H_7, *n*-C_4H_9, *n*-C_5H_{11}, $C_6H_5CH_2$, $[(C_6H_5)_3PNP(C_6H_5)_3]_{0.25}$, $N(CH_3)_3Ph$), $[M_3^{III}Cp_2]$ (donde M_3^{III} = Co^{3+}, Fe^{3+}; *Cp* = pentametilciclopentadienilo) o [K(18-crown-6)] actúa como *template* imprescindible para contrarrestar la carga negativa de la red.[183–204]

La distancia interlaminar en compuestos bidimensionales, y la dimensionalidad (2D o 3D) de la red polimérica, están determinadas por el tipo del plantilla molecular y por la quiralidad del metaloligando. Usualmente, las redes 2D se generan por combinación de un

(176) S. J. Garibay, J. R. Stork, S. M. Cohen, In *Progress in Inorganic Chemistry*; Vol. 56, John Wiley & Sons, Inc., New Jersey, **2009**, 335–378.
(177) M. Pilkington, M. Gross, P. Franz, M. Biner, S. Decurtins, H. Stoeckli-Evans, A. Neels, *J. Solid. State. Chem.*, **2001**, *159*, 262–267.
(178) S. Decurtins, H. W. Schmalle, P. Schneuwly, R. Pellaux, J. Ensling, *Mol. Cryst. Liq. Cryst*., **1995**, *273*, 167–174.
(179) S. Decurtins, H. W. Schmalle, R. Pellaux, P. Fischer, A. Hauser, *Mol. Cryst. Liq. Cryst*., **1997**, *305*, 227–237.
(180) R. Clément, S. Decurtins, M. Gruselle, C. Train, *Monatsh. Chem*., **2003**, *134*, 117–135.
(181) S. Decurtins, H. Schmalle, R. Pellaux, *New J. Chem*., **1998**, *22*, 117–121.
(182) R. Pellaux, H. W. Schmalle, S. Decurtins, P. Fischer, F. Fauth, B. Ouladdiaf, T. Hauss, *Phisica B*, **1997**, *234–236*, 783–784.
(183) H. Tamaki, Z. J. Zhong, N. Matsumoto, S. Kida, M. Koikawa, N. Achiwa, Y. Hashimoto, H. Okawa, *J. Am. Chem. Soc*., **1992**, *114*, 6974−6979.
(184) S. G. Carling, C. Mathonière, P. Day, K. M. A. Malik, S. J. Coles, M. B. Hursthouse, *J. Chem. Soc*., *Dalton. Trans.*, **1996**, 1839–1843.
(185) I. D. Watts, S. G. Carling, P. Day, *J. Chem. Soc., Dalton Trans*., **2002**, 1429–1434.
(186) Z. J. Zhong, N. Matsumoto, H. Okawa, S. Kida, *Chem. Lett*., **1990**, *19*, 87–90.
(187) S. Decurtins, H. W. Schmalle, H. R. Oswald, A. Linden, J. Ensling, P. Gutlich, A. Hauser, *Inorg. Chim. Acta*, **1994**, *216*, 65–73.
(188) R. P. Farrell, T. W. Hambley, P. A. Lay, *Inorg. Chem*., **1995**, *34*, 757–758.
(189) R. Pellaux, H. W. Schmalle, R. Huber, P. Fischer, T. Hauss, B. Ouladdiaf, S. Decurtins, *Inorg. Chem*., **1997**, *36*, 2301–2308.
(190) E. Coronado, R. J. Galán-Mascarós, C. J. Gómez-García, J. M. Martínez-Agudo, E. Martínez-Ferrero, J. C. Waerenborgh, M. Almeida, *J. Solid State Chem*., **2001**, *159*, 391−402.
(191) J. Larionova, B. Mombelli, J. Sanchiz, O. Kahn, *Inorg. Chem*., **1998**, *37*, 679−684.
(192) E. Coronado, J. R. Galán-Mascarós, C. Martí-Gastaldo, *J. Mater. Chem*., **2006**, *16*, 2685−2689.
(193) C. Mathonière, K. J. Nuttall, S. G. Carling, P. Day, *Inorg. Chem*., **1996**, *35*, 1201−1206.
(194) K. S. Min, A. L. Rhinegold, J. S. Miller, *Inorg. Chem*. **2005**, *44*, 8433−8441.
(195) N. S. Ovenesyan, V. D. Makhaev, S. M. Aldoshin, P. Gredin, K. Boubekeur, C. Train, M. Gruselle, *Dalton Trans*., **2005**, 3101−3107.
(196) E. Coronado, J. R. Galán-Mascarós, C. Martí-Gastaldo, J. C. Waerenborgh, P. Gaczyński, *Inorg. Chem*., **2008**, *47*, 6829−6839.
(197) E. Coronado, J. R. Galán-Mascarós, C. Martí-Gastaldo, *Inorg. Chem*., **2006**, *45*, 1882−1884.
(198) R. Andrés, M. Gruselle, B Malézieux, M. Verdaguer, J. Vaissermann, *Inorg. Chem*., **1999**, *38*, 4637−4646.
(199) E. Coronado, J. R. Galán-Mascarós, C. Martí-Gastaldo, *J. Am. Chem. Soc*., **2010**, *132*, 5456−5468.
(200) E. Coronado, J. R. Galán-Mascarós, C. Martí-Gastaldo, *J. Am. Chem. Soc*., **2008**, *130*, 14987−14989.
(201) E. Coronado, J. R. Galán-Mascarós, C. J. Gómez-García, C. Martí-Gastaldo, *Inorg. Chem.*, **2005**, *44*, 6197−6202.
(202) E. Coronado, J. R. Galán-Mascarós, C. Martí-Gastaldo, *Inorg. Chem*., **2007**, *46*, 8108−8110.
(203) E. Coronado, J. R. Galán-Mascarós, C. Martí-Gastaldo, *Inorg. Chim. Acta*, **2008**, *361*, 4017−4023.
(204) E. Coronado, J. R. Galán-Mascarós, C. Martí-Gastaldo, *Polyhedron*, **2007**, *26*, 2101−2104.

metaloligando racémico con la sal de un metal de transición divalente, formando una red polimérica aquiral donde se alternan unidades *tris*-oxalato Δ y Λ, dando lugar a estructuras hexagonales tipo "panal de abeja", que pueden incorporar cationes en su espacio interlaminar (Figura 1.6.2.2.1-2a).

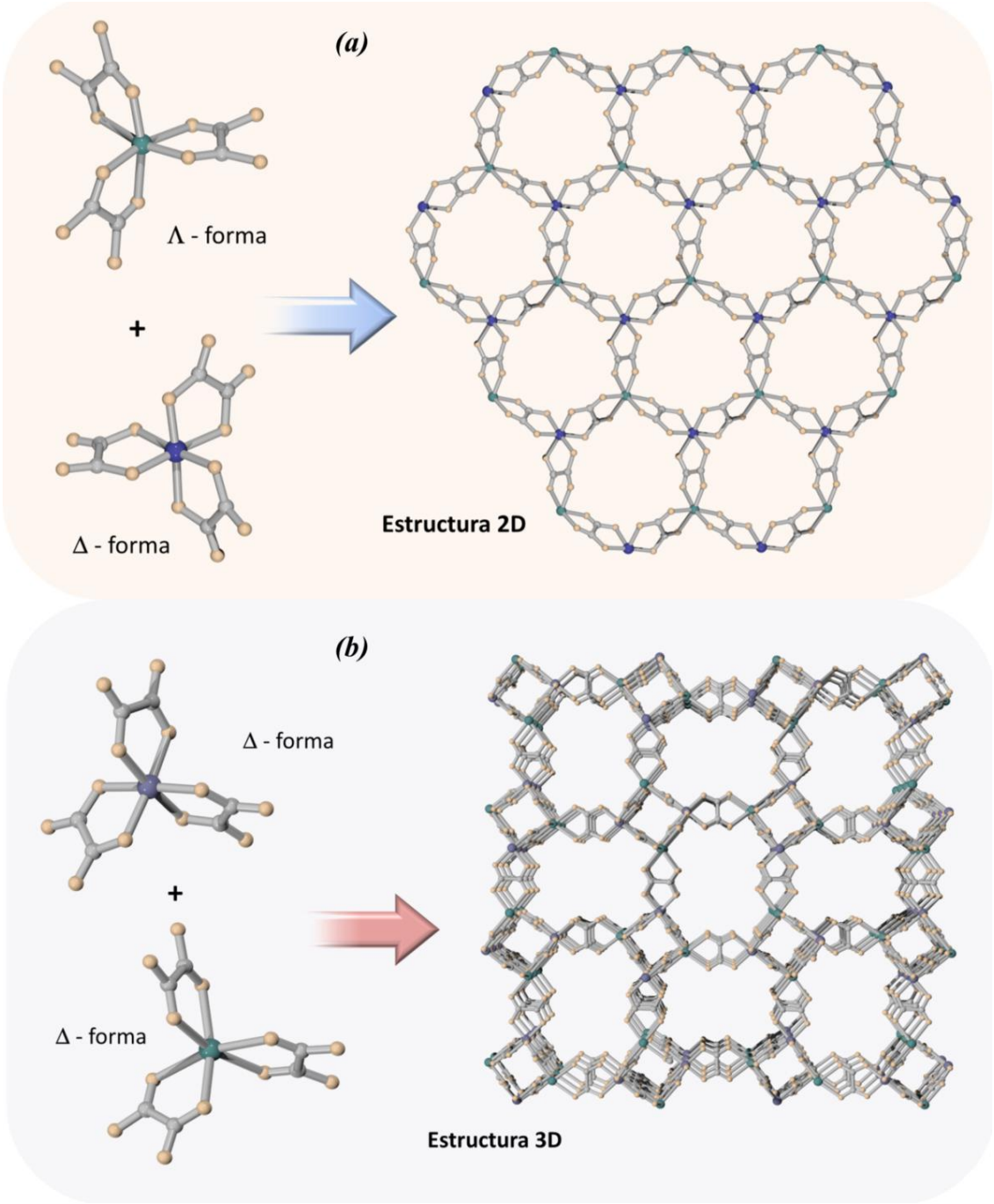

Figura 1.6.2.2.1-2 *Representación esquemática de la formación de redes poliméricas: (a) red 2D a partir de unidades de construcción tris-oxalato en Λ- y Δ-configuración, y (b) red 3D a partir de tris-oxalatos homoquirales en Λ-Λ o Δ-Δ configuración.*

Por otro lado, la organización helicoidal de los centros conectores octaédricos homoquirales, adaptando unidades *tris*-oxalato en secuencias $\Lambda M_1–\Lambda M_2$ o $\Delta M_1–\Delta M_2$, provoca la formación de las estructuras tridimensionales (Figura 1.6.2.2.1-2b), que formuladas como

$\{[M_1^{I}M_2^{III}(ox)_3]^{2-}\}_n$,[198,205–221] $\{[M_1^{II}M_2^{III}(ox)_3]^{-}\}_n$,[222–228] o $\{[(M_1^{II})_2(ox)_3]^{2-}\}_n$ [211,214,222,229–231] (donde M_1^{I} =Na^+, Li^+, K^+; M_1^{II} = Cu^{2+}, Mn^{2+}, Fe^{2+}, Co^{2+}, Ni^{2+}, Zn^{2+}; M_2^{III} = Rh^{3+}, Cr^{3+}, Al^{3+}, Ru^{3+}, Co^{3+}, Ni^{3+}, Fe^{3+}) se corresponden con redes aniónicas quirales de tipo ***srs***[232] con cavidades en las que residen cationes moleculares. La carga del cation molecular debe ser igual a la de la subunidad aniónica, $[M_1M_2(ox)_3]^{x-}$ (x = 1 o 2), por lo que el *template* catiónico debe que ser mono- o di-positivo. Entre las plantillas moleculares di-positivas, se conocen complejos moleculares con simetría D_3 o quasi-D_3 tales como $[M^{II}(phen)_3]^{2+}$ [211,212,215] o $[M^{II}(bpy)_3]^{2+}$ (donde M^{II} = Co^{2+}, Zn^{2+}, Ru^{2+}, Ni^{2+}, Fe^{2+}; *phen* = fenantrolina; *bpy* = 2,2´-bipiridina),[205–207,210,213,214,222,229,231] y sistemas del tipo $[M^{III}(bpy)_3][ClO_4]^{2+}$,[208,209,211,216–218,220,221,230] $[M^{III}(bpy)_3][BF_4]^{2+}$,[211] y $[M^{III}(bpy)_3][PF_6]^{2+}$,[211] (donde M^{III} = Cr^{3+}, Rh^{3+}, Ru^{3+}, Co^{3+}, Os^{3+}; *bpy* = 2,2´-bipiridina). Cuando la carga de la red aniónica es igual a uno, la plantilla catiónica puede ser $[M^{II}(bpy)_3][ClO_4]^{+}$,[223,225–227] o un complejo monopositivo octaédrico con simetría quasi-D_3 tal como $[M^{II}(bpy)_2(ppy)]^{+}$ o

(205) R. Pellaux, S. Decurtins, H. W. Schmalle, *Acta Cryst.*, **1999**, *C55*, 1075–1079.
(206) S. Rabaste, N. Amstutz, A. Hauser, A. Pillonnet, *Appl. Phys. Lett.*, **2005**, *87*, 251904(1)–(3).
(207) R. Sieber, S. Decurtins, H. Stoeckli-Evans, C. Wilson, J. A. K. Howard, S. C. Capelli, A. Hauser, *Chem. Eur. J.*, **2000**, *6*, 361–368.
(208) M. Milos, P. Pal, A. Hauser, *Chem. Phys. Chem.*, **2010**, *11*, 3161–3166.
(209) A. Hauser, H. Riesen, R. Pellaux, S. Decurtins, *Chem. Phys. Lett*., **1996**, *261*, 313–317.
(210) P. Roman, C. Guzman-Miralles, A. Luque, *Dalton Trans*., **1996**, 20, 3985–3989.
(211) S. Decurtins, H. W. Schmalle, R. Pellaux, P. Schneuwly, A. Hauser, *Inorg. Chem*., **1996**, *35*, 1451–1460.
(212) P.-z. Li, X.-m. Lu, B. Liu, S. Wang, X.-j. Wang, *Inorg. Chem*., **2007**, *46*, 5823–5825.
(213) M. Milos, T. Penhouet, P. Pal, A. Hauser, *Inorg. Chem*., **2010**, *49*, 3402–3408.
(214) S. Decurtins, H. W. Schmalle, P. Schneuwly, J. Ensling, P. Gütlich, *J. Am. Chem. Soc*., **1994**, *116*, 9521–9528.
(215) K. R. Butler, M. R. Snow, *J. Chem. Soc. A*, **1971**, *4*, 565–569.
(216) M. Milos, A. Hauser, *J. Luminescence*, **2009**, *129*, 1901–1904.
(217) M. Milos, A. Hauser, *J. Luminescence*, **2013**, *133*, 15–20.
(218) V. S. Langford, M. E. von Arx, A. Hauser, *J. Phys. Chem. A*, **1999**, *103*, 7161–7169.
(219) M. E. von Arx, E. Burattini, A. Hauser, L. van Pieterson, R. Pellaux, S. Decurtins, *J. Phys. Chem. A*, **2000**, *104*, 883–893.
(220) M. E. von Arx, V. S. Langford, U. Oetliker, A. Hauser, *J. Phys. Chem. A*, **2002**, *106*, 7099–7105.
(221) M. E. von Arx, A. Hauser, H. Riesen, R. Pellaux, S. Decurtins, *Phys. Rev. B*, **1996**, *54*, 15800–15807.
(222) F. Pointillart, C. Train, M. Gruselle, F. Villain, H. W. Schmalle, D. Talbot, P. Gredin, S. Decurtins, M. Verdaguer, *Chem. Mater*., **2004**, *16*, 832–841.
(223) M. Gruselle, R. Andres, B. Malezieux, M. Brissard, C. Train, M. Verdaguer, *Chirality*, **2001**, *13*, 712–714.
(224) M. Brissard, M. Gruselle, B. Malézieux, R. Thouvenot, C. Guyard-Duhayon, O. Convert, *Eur. J. Inorg. Chem*., **2001**, *7*, 1745–1751.
(225) E. Coronado, J. R. Galán-Mascarós, C. J. Gómez-García, E. Martínez-Ferrero, M. Almeida, J. C. Waerenborgh, *Eur. J. Inorg. Chem*., **2005**, *11*, 2064–2070.
(226) E. Coronado, J. R. Galán-Mascarós, C. J. Gómez-García, J. M. Martínez-Agudo, *Inorg. Chem*., **2001**, *40*, 113–120.
(227) R. Andrés , M. Brissard, M. Gruselle, C. Train, J. Vaissermann, B. Malézieux, J.-P. Jamet, M. Verdaguer, *Inorg. Chem*., **2001**, *40*, 4633–4640.
(228) M. Clemente-León, E. Coronado, C. J. Gómez-García, A. Soriano-Portillo, *Inorg. Chem*., **2006**, *45*, 5653–5660.
(229) S. Decurtins, H. W. Schmalle, P. Schneuwly, H. R. Oswald, *Inorg. Chem*., **1993**, *32*, 1888–1892.
(230) M. Hernández-Molina, C. Ruiz-Pérez, F. Lloret, M. Julve, *Inorg. Chem*., **1998**, *37*, 4131–4135.
(231) Y. Li, Z.-X. Zhang, K.-C. Li, W.-D. Song, Q.-S. Li, *Inorg. Chem. Commun*., **2007**, *10*, 1557–1560.
(232) N. W. Ockwig, O. Delgado-Friedrichs, M. O'Keeffe, O. M. Yaghi, *Acc. Chem. Res*., **2005**, *38*, 176–182.

$[M^{II}(bpy)_2(quo)]^+$ (donde M^{II} = Ru^{2+}, Ir^{2+}; *bpy* = 2,2´-bipiridina; *ppy* = 2-fenilpiridina; *quo* = 8-hidroxiquinoleato).[223,224,227,228]

La quiralidad del metaloligando *tris*-oxalato (Δ- o Λ-) hace posible prediseñar la actividad óptica del polímero de coordinación resultante, mientras en algunas ocasiones los metaloligandos racémicos resuelven espontáneamente en uno de sus isómeros durante la cristalización del polímero de coordinación, dando lugar a formación de redes 3D enantioméricamente puras.[214]

Como se ha mencionado anteriormente, la forma de la plantilla catiónica puede determinar la formación de redes poliméricas de diferente dimensionalidad. Un ejemplo representativo de este hecho es la síntesis de la red 3D heterometálica $\{[KCr(ox)_3]^{2-}\}_n$ a partir de $[Cu(trans[14]dieno]^{2+}$ (trans[14]dieno = 5,7,7,12,14,14-hexametil-1,4,8,11-tetraazaciclotetradeca-4-11-dieno). En ella, K^+ y Cr^{3+} se encuentran en un entorno octaédrico, mientras el Cu^{2+} se coordina por un oxigeno proveniente del grupo oxalato originando canales helicoidales de dimensiones aproximadas de 21 × 9 $Å^2$.[233] Esta red polimérica es del tipo ***ths***, mientras las estructuras mencionadas previamente poseían redes quirales tipo ***srs***.

Las familias de compuestos laminares caracterizadas por la presencia de unidades octaédricas $[M^{III}(ox)_3]^{3-}$ (M^{III} = Cr^{3+} o Fe^{3+}) presentan propiedades magnéticas. Las redes $\{A[M^{II}Cr(ox)_3]\}_n$ (A = catión monopositivo) generalmente son ferromagnéticas,[183] mientras las redes heterometálicas constituidas por $[Fe(ox)_3]^{3-}$ en combinación con algunos metales de transición suelen originar comportamientos antiferromagnéticos y ferrimagnéticos.[184,193]

La plantilla molecular, además de ser un componente determinante de las características estructurales del material y de añadir nuevas funcionalidades a la red polimérica, puede influir en sus propiedades magnéticas. Como ejemplos, mencionar el trabajo de Armentano *et al.*,[234] que demostró cómo las dimensiones de la plantilla (sustitución del catión $MeNH_3^+$ por los más voluminosos $Me_2NH_2^+$ o $EtNH_3^+$) provoca cambios en la temperatura de transición magnética cercanos a los 20 K, algunos compuestos bidimensionales con orden magnético de alto rango debido a naturaleza paramagnética de la especie catiónica integrada en la red aniónica,[235] o las redes metal-orgánicas 3D en las que la plantilla molecular $[M^{II}(bpy)_3]^{2+}$ (M^{II} =Ni^{2+}, Fe^{2+}, Co^{2+}) o $[Cr(bpy)_3]^{3+}$ actúa en combinación con una red aniónica para-, antiferro- o ferro-magnética.[214,226,227]

Otra de las propiedades atractivas de las redes metal-orgánicas bidimensionales basadas en *tris*-oxalatos es su conductividad eléctrica. Los grupos de Kurmoto y Coronado han aislado polímeros de coordinación incorporando en el espacio interlaminar el catión BEDT-TFF (bis(etileneditio)tetratiafulvalene), demostrándose la coexistencia de orden magnético de largo alcance y conductividad eléctrica en el compuesto $\{[BEDT\text{-}TFF]_3[MnCr(ox)_3]\}_n$,[236] así como la capacidad del compuesto $\{[BEDT\text{-}TFF]_3[(H_2O)Fe(ox)_3]\}_n$ de preservar su superconductividad a temperaturas bajas.[237]

(233) H.-Y. Shen, W.-M. Bu, D.-Z. Liao, Z.-H. Jiang, S.-P. Yan, G.-L. Wang, *Inorg. Chem*., **2000**, *39*, 2239–2242.

(234) D. Armentano, G. De Munno, T. F. Mastropietro, D. M. Proserpio, M. Julve, F. Lloret, *Inorg. Chem*., **2004**, *43*, 5177–5179.

(235) E. Coronado, J. R. Galán-Mascarós, C. J. Gómez-García, J. M. Martínez-Agudo, *Adv. Mater*., **1999**, *11*, 558–561.

(236) E. Coronado, J. R. Galán-Mascarós, C. J. Gómez-García, V. Laukhin, *Nature*, **2000**, *408*, 447–449.

(237) M. Kurmoo, A. W. Graham, P. Day, S. J. Coles, M. B. Hursthouse, J. L. Caulfield, J. Singleton, F. L. Pratt, W. Hayes, *J. Am. Chem. Soc*., **1995**, *117*, 12209–12217.

Las redes metal-orgánicas formadas por *tris*-oxalatos también presentan relevantes propiedades ópticas.[238] La posibilidad de construir redes poliméricas mediante selección razonada de sus unidades constructivas, controlando además su quiralidad, ofrece evidentes posibilidades para el diseño de materiales con propiedades en el campo del dicroísmo magneto-quiral. Por ejemplo, polímeros de coordinación heterometálicos, ópticamente activos, de estructura bidimensional o tridimensional, formados por unidades Δ o Λ $[Cr(ox)_3]^{3-}$ exhiben efecto Cotton.[198,239]

La construcción de los polímeros de coordinación 3D bimetálicos ópticamente activos, basados en ligandos oxalato, es posible mediante el uso de unidades de construcción aniónicas o de plantillas catiónicas ópticamente activas. De esta manera, se han obtenido las redes $\{A[M_1M_2(ox)_3]\}_n$ ($M_1 = M_2 = Mn^{2+}$; $M_1 = Mn^{2+}$, Ni^{2+}, Fe^{2+}, Cu^{2+}; $M_2 = Cr^{3+}$, Co^{3+}, Fe^{3+}) con A = $[Ru(bpy)_3]^{2+}$, $[Ru(bpy)_2(ppy)]^{+}$ en las formas Δ o Λ enantioméricamente puras,[198,224,227] con dicroísmo magneto-quiral.

Adicionalmente, las sistemas laminares ofrecen la oportunidad de incorporar en su espacio interlaminar cromóforos catiónicos hiperpolarizables que, empaquetados en un modo no-centrosimétrico, proporcionan a la estructura cristalina un comportamiento no-lineal, haciéndolos útiles como materiales generadores de segundo armónico. Así, el grupo de Clément,[240–242] ha sintetizado una familia de compuestos laminares, $\{A[M_1^{II}Cr(ox)_3](S)\}_n$ ($M_1^{II} = Mn^{2+}$, Ni^{2+}, Fe^{2+}, Cu^{2+}, Co^{2+}; S = disolvente) que contienen diferentes *templates* catiónicos hiperpolarizables cromóforos análogos de stilbazolio (*stilbasolium*), algunos de los cuáles mostraron comportamiento óptico no-lineal. Además, la incorporación de especies fotoactivas en el espacio interlaminar de las redes poliméricas de metal-oxalatos puede conducir al diseño de nuevos interruptores fotosensibles. Como ejemplo, la incorporación del compuesto catiónico spiropiran (*spiropyran*, *SP*) como plantilla interlaminar produjo un nuevo polímero de coordinación, $\{(SP)[MnCr(ox)_3]\}_n$,[243] con extraordinarias propiedades ópticas, ya que se comporta como material cromóforo en el que el cambio conformacional reversible de spiropiran (SP, forma cerrada) a merocianina (MC, forma abierta) tiene lugar bajo irradiación con la luz visible (cierre) o UV (apertura).[244] Es interesante destacar que ambas conformaciones, SP y MC, son térmicamente estables, probablemente debido a que la fortaleza de la interacción entre las partes aniónica y catiónica de la estructura eleva la barrera energética entre ellas, obstaculizando su interconversión.

Finalmente, destacar la existencia de procesos de transferencia de energía en redes 3D basadas en *tris*-oxalatos conteniendo especies huésped. La plantilla molecular $[M(bpy)_3]^{x+}$ (x =1–3) puede ser incorporada a la red aniónica de modo que, dependiendo de las energías relativas de los estados excitados de ambos cromóforos, se produce la transferencia de energía desde el huésped catiónico, $[M(bpy)_3]^{x+}$(x =1–3), que actúa como donor, a la red aniónica,

(238) A. Hauser, M. E. Von Arx, R. Pellaux, S. Decurtins, *Mol. Cryst. Liq. Cryst*., **1996**, *286*, 225–230.
(239) B. Malézieux, R. Andrés, M. Brissard, M. Gruselle, C. Train, P. Herson, L. L Troitskaya, V. I. Sokolov, S. T. Ovseenko, T. V. Demeschik, N. S. Ovanesyan, I. A. Mamed'yarova, *J. Organomet. Chem*., **2001**, *637–639*, 182–190.
(240) S. Bénard, P. Yu, T. Coradin, E. Rivière, K. Nakatani, R. Clément, *Adv. Mater.*, **1997**, *9*, 981–984.
(241) S. Bénard, P. Yu, J. P. Audière, E. Rivière, R. Clément, J. Guilhem, L. Tchertanov, K. Nakatani, *J. Am. Chem. Soc*., **2000**, *122*, 9444–9454.
(242) J. S. O. Evans, S. Bénard, P. Yu, R. Clément, *Chem. Mater*., **2001**, *13*, 3813–3816.
(243) S. Bénard, P. Yu, *Adv. Mater.*, **2000**, *12*, 48–50.
(244) S. Bénard, E. Rivière, P. Yu, K. Nakatani, J. F. Delouis, *Chem. Mater*., **2001**, *13*, 159–162.

anfitriona $\{[M_1M_2(ox)_3]^{x-}\}_n$, que actúa como aceptor, o viceversa. Adicionalmente, como se han mostrado fenómenos de transferencia de energía entre cromóforos idénticos,[211,219] que se han confirmado en varios sistemas poliméricas ($\{[Ru(bpy)_3][NaAl(ox)_3]\}_n$, $\{[Ru_{1-x}Os_x(bpy)_3][NaAl(ox)_3]\}_n$, $\{[Ru(bpy)_3][NaCr(ox)_3]\}_n$ y $\{[Rh(bpy)_3][ClO_4][NaCr(ox)_3]\}_n$)[209,221] de excepcional interés debido al potencial de este tipo de las redes metal-orgánicas como catalizadores fotoactivos.

Capítulo II

Objetivos y Planteamiento de la Tesis

2.1. Objetivos de la Tesis

La química de los polímeros de coordinación (CP) y de las redes metal-orgánicas (MOF) se ha desarrollado enormemente en las últimas décadas debido a que esta nueva clase de materiales aportan algunas funcionalidades dinámicas y versátiles, que pueden ser diseñadas racionalmente mediante el establecimiento de enlaces de coordinación entre unidades de construcción orgánicas e inorgánicas, revelándose dichos materiales como firmes candidatos a ser usados en aplicaciones diversas, entre las que cabe destacar el almacenamiento de gases, los procesos de separación y la catálisis heterogénea.

Entre los diversos tipos de redes poliméricas descritas en la bibliografía, raramente se encuentran compuestos metal-orgánicos de estructura extendida conteniendo rutenio. Sin embargo, son bien conocidas las propiedades catalíticas, algunas excepcionales, de algunos compuestos de rutenio en fase homogénea, por lo que una investigación enfocada al diseño de polímeros de coordinación de este metal es previsible que conduzca a la síntesis de nuevos materiales susceptibles de ser usados como catalizadores heterogéneos. Por ello, el **objetivo general** de esta Tesis Doctoral se focaliza en la obtención de nuevos polímeros de coordinación basados en carboxilatos de rutenio y en la evaluación de sus propiedades, especialmente las magnéticas, ópticas y catalíticas. Para alcanzar dicho objetivo general, se han planteado varios objetivos específicos:

- Evaluar distintas estrategias sintéticas, que permitan obtener polímeros de coordinación basados en carboxilatos de rutenio de diferente dimensionalidad.

- Optimizar las metodologías evaluadas y estudiar las condiciones de síntesis con el fin de conocer su influencia en las características el producto final de la reacción.

- Seleccionar adecuadamente los bloques moleculares (unidades de construcción) que permitan dirigir el diseño hacia redes poliméricas (bi- o tri-dimensionales) con propiedades funcionales prestablecidas.

- Conocer la influencia de las unidades químicas integrantes de los nuevos polímeros de coordinación en sus propiedades.

- Caracterizar los nuevos materiales utilizando datos químicos y espectroscópicos, con especial atención a la determinación estructural mediante difracción de rayos X de muestras mono- o poli-cristalinas, incluyendo si fuese necesario técnicas de crecimiento cristalino. Adicionalmente, utilizar técnicas de análisis térmico para determinar la termo-estabilidad (incluyendo la detección de cambios estructurales) de los compuestos obtenidos, determinante para su uso en reacciones catalíticas en condiciones no ambientales.

- Evaluar las aplicaciones potenciales de los nuevos materiales, con especial atención hacia el uso de polímeros de coordinación basados en carboxilatos de rutenio(III) como catalizadores heterogéneos.

2.2. Planteamiento de la Tesis

En coherencia con los objetivos expuestos anteriormente, esta Tesis Doctoral abarca la síntesis y caracterización de nuevos polímeros de coordinación, basados en unidades constructivas de rutenio, con el fin último de conseguir redes extendidas metal-orgánicas que, con buenas propiedades estructurales, puedan ser utilizadas como catalizadores heterogéneos en una amplia variedad de reacciones orgánicas, incluyendo procesos fotocatalíticos, así como la preparación y caracterización de sistemas con propiedades magnéticas (véase el Esquema 2.2, donde se intenta visualizar de forma sistemática el trabajo realizado).

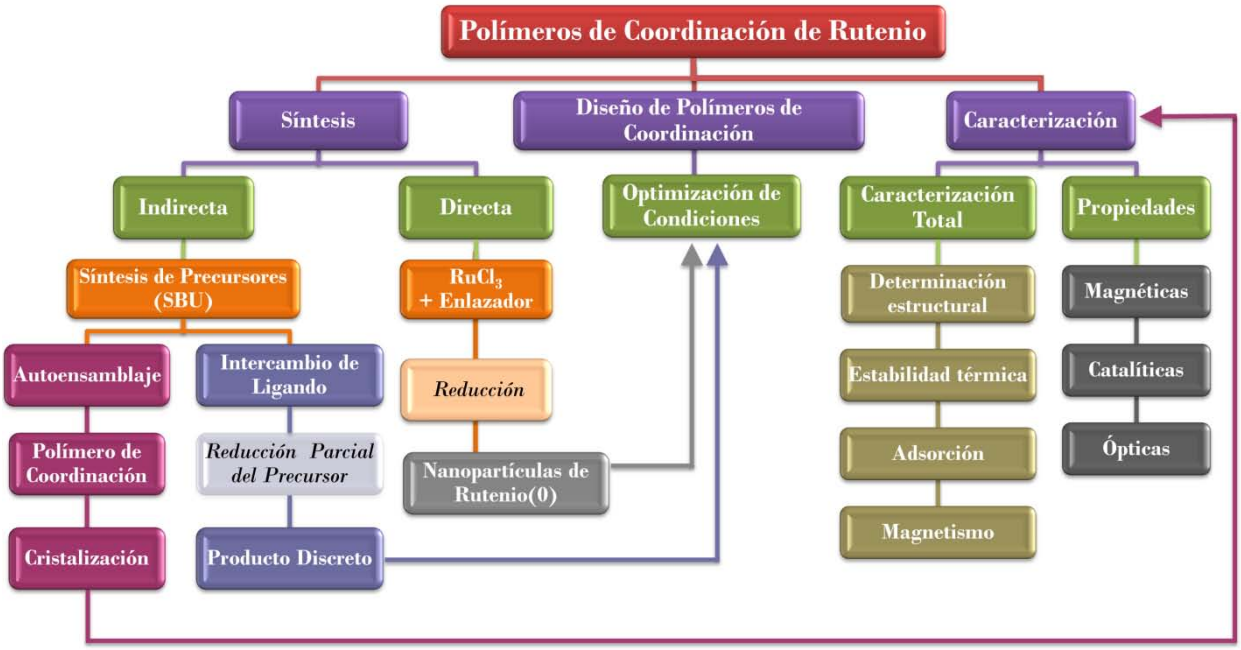

Esquema 2.2 *Representación esquemática del planteamiento de la Tesis y de los procesos experimentales realizados durante su desarrollo.*

Como se ha detallado en la Introducción de la presente Memoria, los métodos y estrategias preparativas tienen un gran impacto en la formación de redes poliméricas con funcionalidades deseadas. Como consecuencia, en este trabajo, para la obtención de polímeros de coordinación basados en carboxilatos de rutenio, se evaluaron dos tipos de estrategias de síntesis:

- Directas, en las que se utiliza tricloruro de rutenio como fuente del metal y un ligando carboxílico como enlazador orgánico.

- Indirectas, mediante la obtención previa de un compuesto precursor del material final.

En primer lugar, se exploraron los métodos de síntesis directa (el procedimiento más clásico en la construcción de estructuras tipo MOF). Los resultados obtenidos, que se detallan en *Capítulo V*, muestran la imposibilidad de obtener polímeros de coordinación de rutenio mediante esta vía, al menos en las condiciones experimentales estudiadas, como consecuencia de procesos de reducción Ru^{3+}–Ru^{0} provocados por todos y cada uno de los ácidos carboxílicos empleados (pretendidamente como enlazadores) en todos los rangos de pH y relaciones molares estudiados.

Sin embargo, la síntesis de partículas de Ru^0 de tamaño nanométrico, y los estudios llevados a cabo para determinar la relación entre el tamaño de las nanopartículas, el pH del medio de reacción y el agente reductor utilizado llevó a datos interesantes, que se reflejan en las *Publicaciones II* y *III*, recogidas esta Memoria.

Después de los resultados anteriores, se exploró la síntesis indirecta mediante el uso de unidades constructivas prediseñadas. Así, se utilizó el $[Ru^{III}_3O(CH_3CO_2)_6(CH_3OH)_3]CH_3CO_2$ como compuesto de partida con la intención de obtener, mediante procedimientos hidrotermales, redes poliméricas análogas al MIL-101. Nuevamente, se estableció la imposibilidad de sintetizar redes metal-orgánicas basadas en rutenio(III) mediante la ruta elegida, ya que la capacidad reductora de los enlazadores carboxílicos altera el estado de oxidación del centro metálico. Sin embargo, se pudo aislar un complejo trinuclear de acetato de rutenio de valencia mixta, $[Ru_2^{III}Ru^{II}O(CH_3CO_2)_6(H_2O)_3]\cdot 2H_2O$, estableciendo una nueva ruta para su síntesis, y determinando por primera vez su estructura cristalina. Estos resultados se detallan en el *Capítulo VI* (*Publicación IV*) de esta Memoria.

Como consecuencia de la experiencia acumulada durante la experimentación resumida en los párrafos anteriores, se exploró una estrategia de síntesis indirecta usando metaloligandos. Así, se prepararon nuevos polímeros de coordinación donde el metaloligando $[Ru(C_2O_4)_3]^{3-}$ actúa como unidad de construcción, conectando tres centros metálicos M^{II} (M^{II} = Fe, Co, Mn, Cu, Zn) a través del grupo carboxílico del anión oxalato, originando una red bidimensional tipo "panal de abeja". Estos polímeros de coordinación bidimensionales, de esqueleto aniónico y fórmula general $\{[K(18\text{-crown-6})]_3[M^{II}_3(H_2O)_4[Ru(C_2O_4)_3]_3]\}_n$, presentan sus espacios interlaminares ocupados por complejos catiónicos $[K(18\text{-crown-6})]^+$. Junto a la caracterización estructural de esta nueva familia de compuestos, su interesante comportamiento magnético y su actividad catalítica constituyen el *Capítulo VII* (*Publicación V*) de esta Memoria.

Posteriormente, explorando una estrategia sintética indirecta, usando el metaloligando $[Ru(C_2O_4)_3]^{3-}$ y plantillas moleculares monoquirales, se logró aislar una familia de polímeros de coordinación tridimensionales basados en rutenio(III) de fórmula general $\{[M^{II}(bpy)_3][M^{I}Ru(C_2O_4)_3]\}_n$ (bpy = 2,2´-bipiridina; M^{II} = Fe, Co, Ni; M^{I} = Na^+ o Li^+). Estos resultados se recogen en el *Capítulo VIII* de esta Memoria, que se focaliza en la síntesis y caracterización estructural y óptica de estos materiales, con especial atención a la actividad fotocatalítica de la nueva familia en la fotoreducción de CO_2 (*Publicaciones VI* y *VII*).

Relacionados con los compuestos comentados en el parágrafo anterior, se intentó ampliar la familia de polímeros de coordinación basados en oxalato de rutenio con estructuras tridimensionales "anfitrión-huésped", logrando obtener mediante autoensamblaje de $[Ru(C_2O_4)_3]^{3-}$, $[Z^{II}(bpy)_3]^{2+}$ y un catión alcalino (Na^+ o Li^+) las redes poliméricas de fórmula $\{[Z^{II}(bpy)_3][M^{I}Ru(C_2O_4)_3]\}_n$ y $\{[Zn(bpy)_3](H_2O)[LiRu(C_2O_4)_3]\}_n$ (donde bpy = 2,2´-bipyridyl; Z^{II} = Zn, Cu, Ru, Os; M^{I} = Na, Li). La caracterización estructural, las propiedades ópticas, y la actividad catalítica de estos nuevos materiales en la fotolisis del agua se detallan en el *Capítulo IX* (*Publicación VIII*) de esta Memoria.

Finalmente señalar que, durante el proceso de preparación de las plantillas moleculares utilizadas como compuestos de partida, se obtuvo un nuevo compuesto molecular, $[Rh(2,2´\text{-}bpy)_2Cl_2]ClO_4$, cuya caracterización estructural se recoge en la *Publicación I*, como una parte del *Capítulo IV* de esta Memoria.

Capítulo III

Técnicas Experimentales

En esta sección se describirán los procedimientos de caracterización estructural, incluyendo técnicas espectroscópicas, magnéticas y térmicas, en adición a la difracción de rayos X, utilizados en el estudio pormenorizado tanto de los compuestos cuya síntesis se describe en esta Memoria como de algunos de los materiales utilizados como compuestos de partida en su preparación. Además, se describirán también las técnicas instrumentales utilizadas en la evaluación de la actividad catalítica de los nuevos materiales, tanto en procesos de acetalización de aldehídos como en reacciones foto-catalizadas.

3.1. Difracción de Rayos X

Las técnicas de difracción, en particular aquellas que usan irradiación de rayos X, ocupan una posición apical entre los métodos más eficaces para la determinación estructural de la mayoría de los compuestos químicos, tanto orgánicos como inorgánicos y organometálicos. El resultado final de la experimentación permite conocer las posiciones relativas de los átomos e iones en los sólidos cristalinos y, por tanto, puede llegar a proporcionar una descripción estructural completa en términos de longitudes y ángulos de enlace. Esta información estructural puede ser interpretada en relación a las dimensiones atómicas e iónicas de sus componentes individuales, procurando caminos para la predicción estructural de nuevos compuestos y la comprensión de tendencias en muchas de sus propiedades. Además, los métodos difractométricos son no destructivos, lo que proporciona la posibilidad de que la misma muestra pueda ser analizada mediante técnicas experimentales complementarias.

El fenómeno de difracción es consecuencia de la interferencia que se produce entre las ondas radiantes como resultado de su interacción con la materia. Los rayos X son dispersados elásticamente por los electrones de los átomos, detectándose el fenómeno de difracción cuando existe una matriz periódica de estos centros de dispersión que se encuentran separados por una distancia *d* (Fig. 3.1.1a), generándose una interferencia constructiva (que producirá un máximo de intensidad de difracción) cuando la radiación, de longitud de onda λ, incide sobre la muestra con un ángulo θ, de acuerdo con la ecuación de Bragg:

$$n\lambda = 2d \cdot sin\theta$$

siendo *n* un número entero.

Así, un haz de rayos X incidiendo sobre un compuesto cristalino constituido por una matriz ordenada de átomos producirá un conjunto de máximos de difracción que constituirá su patrón característico, donde cada máximo, o reflexión, caracterizado por un ángulo θ, corresponderá a una determinada distancia *d* entre planos de átomos equivalentes en el empaquetamiento cristalino. Los rayos X serán dispersados por los átomos en proporción al número de electrones que poseen, siendo las intensidades de los picos de difracción una función del cuadrado de ese número. Así, el patrón de difracción obtenido estará condicionado por las posiciones y los tipos de átomos presentes en la muestra cristalina (en términos de su número de los electrones), por lo que el tratamiento adecuado de los datos experimentales proporcionará una potente vía para acceder a la información estructural contenida en ellos.

3.1.1. Difracción de Rayos X de Monocristal

El análisis de los datos de difracción obtenidos mediante la medida de una muestra monocristalina es el uno de los métodos más eficientes en la determinación estructural de sólidos metalorgánicos. El compuesto debe ser crecido como un cristal único con el suficiente tamaño y calidad para poder proporcionar información definitiva sobre su estructura molecular y su empaquetamiento cristalino. La simetría presente en un monocristal hace que pueda considerarse, a nivel microscópico, como una red de átomos y moléculas capaz de difractar un haz de rayos X. El patrón de difracción obtenido contiene toda información necesaria para la determinación estructural.

El proceso de caracterización estructural aplicando la técnica de difracción de rayos X de monocristal comienza con la selección de un monocristal adecuado para realizar las medidas y que cumpla, preferentemente, las siguientes condiciones:

- Sus dimensiones deben ser iguales o superiores a 50×50×50 μm^3, pero sin superar los 0.5 mm de longitud. El uso de cristales de pequeñas dimensiones evita los problemas asociados a los efectos de adsorción y al solapamiento entre picos de difracción, dado que el tamaño del cristal está relacionado directamente con el tamaño de spot (superficie de las intensidades difractadas).
- Debe poseer forma regular, con aproximadamente las mismas dimensiones en las tres direcciones. Así, se consigue que el cristal se comporte de forma aproximadamente isotrópica, evitando los problemas asociados a la absorción anisotrópica.
- Es deseable que contenga el menor número de defectos posibles. Para ello, se suelen observar los cristales al microscopio óptico bajo la acción de luz polarizada, que ayuda a descartar la presencia de cristales maclados, detectar fisuras o encontrar defectos de consideración. Los cristales, por poseer una estructura regular, al interactuar con la luz, ésta lo hace en determinados planos vibratorios que pueden ser observados cuando entre el observador y la muestra se ubica un polarizador, dejando pasar únicamente la luz que atraviesa un único plano, distinguiéndose en el cristal zonas o líneas brillantes, contra el fondo oscuro, cuando hay presencia de defectos en el cristal.

Tras seleccionar el cristal más apropiado, éste se fija en un extremo de un capilar de vidrio con resina amorfa. El capilar de vidrio debe haber sido previamente incrustado en una base metálica adaptada para ser montada sobre una cabeza goniométrica (en el caso de realizar la medida a baja temperatura, los cristales suelen situarse en micromonturas de poliimida). Una vez montado, se centra el cristal de forma que quede envuelto en su totalidad por el haz de rayos X. Hecho esto, puede comenzar el proceso de medida. La recogida de los datos de difracción se realiza por un difractómetro de rayos X de monocristal constituido por tres partes fundamentales: *i*) la fuente de rayos X, es el dispositivo encargado de generar el haz de rayos X que incide sobre el cristal; *ii*) el goniómetro, es el sistema de ejes sobre el que se monta el cristal, que permite el centrado del mismo y su giro en tres direcciones diferentes haciendo posible la orientación del mismo en cualquier dirección del espacio; *iii*) el detector, es el dispositivo encargado de registrar las intensidades difractados por el cristal.

En el presente trabajo, las medidas de difracción de rayos X sobre las muestras monocristalinas fueron realizadas en un difractometro Oxford Diffraction Gemini equipado con dos tubos de rayos X independientes, que emiten radiación CuKα (λ = 1.5418Å) y MoKα (λ =

0.71073Å), operados a alto voltaje, un goniómetro de cuatro círculos con geometría kappa, y un detector de área CCD (Figura 3.1.1c). Además, el difractómetro está equipado con un dispositivo Cryojet™ que permite la realización de medidas a temperaturas subambiente (90–300 K) mediante un flujo de nitrógeno líquido.

Esquemáticamente, el funcionamiento del goniómetro de geometría kappa se representa en la Figura 3.1.1b, estando formado por tres bloques sobre los cuales se definen tres ejes, entorno a los que puede girar el cristal.

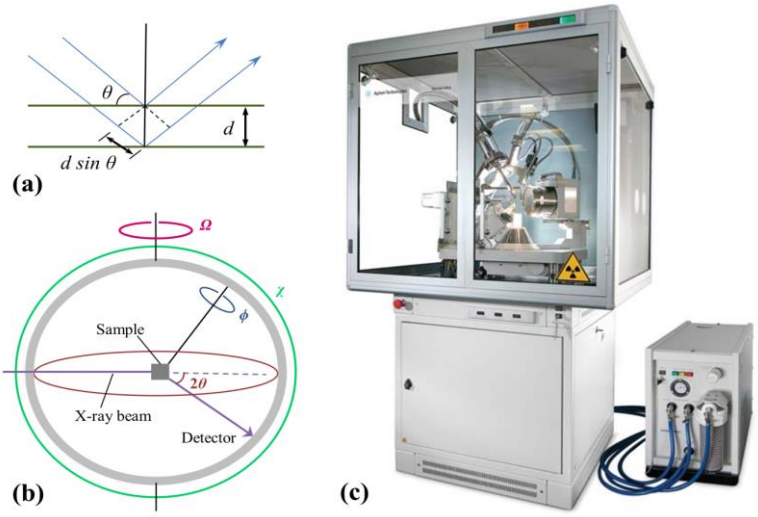

Figura 3.1.1 *(a) Representación esquemática de la ley de Bragg basada en la difracción de rayos X sobre planos atómicos. (b) Esquema del funcionamiento de un difractometro de cuatro círculos. (c) El equipo Oxford Diffraction Gemini utilizado en el presente trabajo.*

La cabeza goniométrica, en la que se encuentra montado el cristal, está situada sobre el bloque del eje phi (φ), que permite el giro del cristal sobre sí mismo. Este bloque se encuentra montado, a su vez, sobre el bloque kappa (χ) que permite la rotación del cristal en torno al eje kappa. Por su parte, este bloque se encuentra montado sobre el bloque omega (Ω) que hace posible el giro del cristal en dicho eje y que se encuentra montado sobre la plataforma del difractómetro. Además, el difractómetro posee un eje adicional, *2θ*, que permite el desplazamiento del detector a lo largo del plano horizontal. Los giros combinados en todos estos ejes de rotación permiten que el haz de rayos X incida sobre el cristal desde todos los ángulos posibles, pudiendo orientarse el detector de la forma adecuada para captar la totalidad de los haces difractados, que se recogen mediante un detector de área tipo CCD. La recogida de datos se lleva a cabo utilizando varias combinaciones de los ejes Ω, χ y *2θ*. Para cada una de estas combinaciones se toman varias imágenes del cristal a incrementos angulares del giro φ. Habrá tantos conjuntos de imágenes como posiciones del goniómetro sean necesarias para conseguir con éxito la resolución y el refinamiento de la estructura.

El tratamiento de los datos de difracción es el proceso a través del cual, a partir de las imágenes de difracción, obtendremos una lista completa de reflexiones, cada una con sus intensidades y desviaciones estándar. Fundamentalmente, este proceso de integración y reducción de los datos[1] se puede dividir en tres etapas. En la primera, se determinará la orientación del cristal, los parámetros de la celdilla unidad y su grupo espacial. En la segunda, se generará la lista de reflexiones y se integrarán todas las imágenes; es decir, a cada *spot* de cada

(1) W. Kabsch, *J. Appl. Cryst.*, **1988**, *21*, 916–924.

una de las imágenes se le asignará un índice de Miller (*hkl*), una intensidad y una desviación estándar. En los resultados que se presentan en esta Memoria, este proceso se llevó a cabo utilizando el programa CrysAlis PRO.[2]

El proceso de resolución estructural consiste en la búsqueda de una distribución atómica que se ajuste adecuadamente al conjunto de datos integrados y reducidos previamente. En la lista previamente obtenida, cada reflexión está determinada por los índices *hkl*, cada uno con sus respectivas intensidades de reflexión, que debe recordarse son proporcionales al cuadrado de la amplitud (factor de estructura $|F_{hkl}|$) que es un valor escalar. La relación entre la estructura de una molécula y los factores de estructura (magnitud de las intensidades medidas) hace posible construir de forma sistemática un modelo para la estructura estudiada. Los factores de estructura y las intensidades de cada reflexión se relacionan con la densidad electrónica de cada átomo presente en cristal. Por tanto, la función densidad electrónica, que se presenta como la transformada de Fourier entre el espacio real, ρ(xyz), y el reciproco, F(*hkl*), viene definida por:

$$\boldsymbol{\rho}(xyz) = \frac{1}{V}\sum_{h}\sum_{k}\sum_{l}|F(hkl)|\cos 2\pi(hx + ky + lz - \varphi(hkl)$$

donde V es volumen de la celdilla, $|F_{hkl}|$ es el módulo del factor de estructura de la reflexión *hkl*, y φ(*hkl*) su fase. Los módulos de los factores de estructura, que representan las amplitudes de los haces difractados, se obtienen a partir de las intensidades medidas experimentalmente. En cambio, las fases no se pueden obtener experimentalmente, por lo que hay que recurrir a distintos métodos para resolver lo que se ha denominado el problema de la fase. Los programas de resolución estructural utilizan dos aproximaciones matemáticas para solucionar dicho problema: el método de Patterson y los métodos directos. Programas como SHELXS, SIR, etc., permiten la resolución estructural mediante la aplicación de dichos métodos que, haciendo uso de funciones invariantes estructurales y de la normalización de los factores de estructura, recuperan los valores de la fase.

En la presente Memoria, la determinación estructural se llevó a cabo utilizando el paquete WinGX,[3] que incluye los programas SHELXS,[4] DIRDIF,[5] SUPERFLIP[6] y SIR[7,8,9,10,11] para resolución y SHELXL[12,13] para refinamiento estructural.

(2) Agilent 2011, *CrysAlis PRO*, Agilent Technologies, Yarnton, UK.
(3) L. J. Farrugia, *J. Appl. Cryst*., **1999**, *32*, 837–838.
(4) G. M. Sheldrick, *Acta Cryst*., **2008**, *A64*, 112–122.
(5) P. T. Beurskens, G. Beurskens, R. de Gelder, S. García-Granda, R. O. Gould, J. M. M. Smits. *The DIRDIF2008 program system*, Crystallography Laboratory, **2008**, University of Nijmegen, The Netherlands.
(6) L. Palatinus, G. Chapuis, *J Appl. Cryst*., **2007**, *40*, 786–790.
(7) M. C. Burla, R. Caliandro, M. Camalli, B. Carrozzini, G. L. Cascarano, C. Giacovazzo, M. Mallamo, A. Mazzone, G. Polidori, R. Spagna, *J. Appl. Cryst*., **2012**, *45*, 357–361.
(8) M. C. Burla, R. Caliandro, M. Camalli, B. Carrozzini, G. L. Cascarano, L. De Caro, C. Giacovazzo, G. Polidori, R. Spagna, *J. Appl. Cryst*., **2005**, *38*, 381–388.
(9) M. C. Burla, M. Camalli, B. Carrozzini, G. L. Cascarano, C. Giacovazzo, G. Polidori, R. Spagna. *J. Appl. Cryst*., **2003**, *36*, 1103.
(10) A. Altomare, M. C. Burla, M. Camalli, G. L. Cascarano, C. Giacovazzo, A. Guagliardi, A. G. G. Moliterni, G. Polidori, R. Spagna, *J. Appl. Cryst*., **1999**, *32*, 115–119.
(11) A. Altomare, G. Cascarano, C. Giacovazzo, A. Guagliardi, M. C. Burla, M. Camalli, *J. Appl. Cryst*., **1994**, *27*, 435.
(12) G. M. Sheldrick, *Acta. Cryst*., **1990**, *A46*, 467–473.
(13) G. M. Sheldrick, T. R. Chneider, *Methods Enzymol*., **1997**, *277*, 319–343.

3.1.2. Difracción de Rayos X de los Sólidos Policristalinos

La difracción de rayos X de polvo cristalino es una técnica no destructiva profusamente utilizada en la identificación de sólidos policristalinos que, además, permite realizar análisis semicuantitativos de materiales polifásicos y llevar a cabo resoluciones estructurales en sistemas monofásicos. Esta técnica se basa en el principio de que las muestras policristalinas constituidas por un enorme número de microcristales con tamaños de 0.1–10 μm, orientados caóticamente, actúan como una región de difracción siguiendo la ley de Bragg. Como resultado, cada conjunto de planos atómicos con idéntica separación (d) dará lugar a una señal cónica, que se recogerá en un espacio bidimensional en forma de un anillo de difracción. La multitud de espaciados interplanares diferentes, característicos de cada sólido cristalino, originará un número equivalente de anillos, cuyas intensidades estarán condicionadas por su composición, constituyendo un patrón de difracción propio para cada sólido cristalino. El difractómetro de sólidos policristalinos utiliza un detector electrónico para determinar los ángulos de incidencia de los diferentes rayos difractados. La muestra difracta la radiación que proviene del tubo generador de rayos X y ésta es recogida por el detector. El sólido problema rota a una velocidad angular constante, variándose el ángulo de incidencia del rayo primario, mientras el detector rota a una velocidad angular doble. De esta manera, se consigue que el ángulo de difracción sea igual al doble de ángulo de giro (θ) de la muestra, por lo que el detector escanea la muestra en un movimiento círcular recogiendo las intensidades de los máximos difractados como una función del ángulo del detector.

Cada compuesto cristalino exhibe un patrón de difracción característico, en el cual las posiciones 2θ de los máximos de difracción dependen de los parámetros de celdilla y del grupo espacial, y las intensidades relativas están directamente relacionadas con la composición de la muestra y sus posiciones atómicas. De este modo, cuando se conoce la estructura de un compuesto, es posible simular su patrón de difracción teórico y, posteriormente, compararlo con los datos experimentales para determinar, por ejemplo, el grado de pureza de una material.
Cuando nuevos compuestos, presuntamente isoestructurales con fases de estructura conocida, se obtienen en forma de polvo policristalino, sus detalles estructurales pueden ser accesibles a partir de datos de difracción de rayos X obtenidos de muestras pulverulentas. A partir de la información obtenida de los datos de fases isotípicas previamente descritas es posible realizar el cálculo y refinamiento de los parámetros de celdilla de las nuevas fases. Esta metodología se denomina *whole-powder pattern decomposition* o concordancia entre patrones de difracción (*pattern matching*). En esta misma dirección, es posible realizar los cálculos necesarios para generar un grupo de intensidades adecuadas para obtener datos estructurales precisos: es el método de Rietveld.

En esta Memoria, el refinamiento se realizó utilizando la aplicación WinPLOTR[14,15] del paquete de programas FULLPROF suite.[16] Para generar el perfil de forma de los picos de difracción se utilizó una función tipo pseudo-Voigt, y los parámetros refinados durante este proceso fueron: los coeficientes del fondo, el error en el punto cero y los parámetros de celdilla.

Los patrones de difracción de las muestras policristalinas fueron obtenidos a temperatura ambiente en un difractometro X´Pert Pro PANanalytical con geometría Bragg-Brentano

(14) T. Roisnel, J. Rodríguez-Carvajal, *Materials Science Forum*, **2001**, *378–381*, 118–123.
(15) J. Rodríguez-Carvajal, T. Roisnel, *Commission for Powder Diffraction, International Union of Crystallography, Newsletter*, **1998**, *20*, 35–36.
(16) J. Rodríguez-Carvajal, *Physica B: Condensed Matter.*, **1993**, *192*, 55–69.

equipado con un detector multicanal X´Celetor, utilizando radiación CuKα (λ = 1.5418 Å), operando a un voltaje de 45 kV y una intensidad de 40 mA (Figura 3.1.2c). Los datos utilizados para comprobar la pureza de las muestras masivas de los materiales sintetizados fueron recogidos en el rango de 2θ = 5–45° en pasos de 0.01° y tiempo de exposición de 0.5 s. Para el refinamiento de parámetros por el método Rietveld el rango angular recogido fue 2θ = 3–124° en pasos de 0.01° con un tiempo de exposición de 3.0 s.

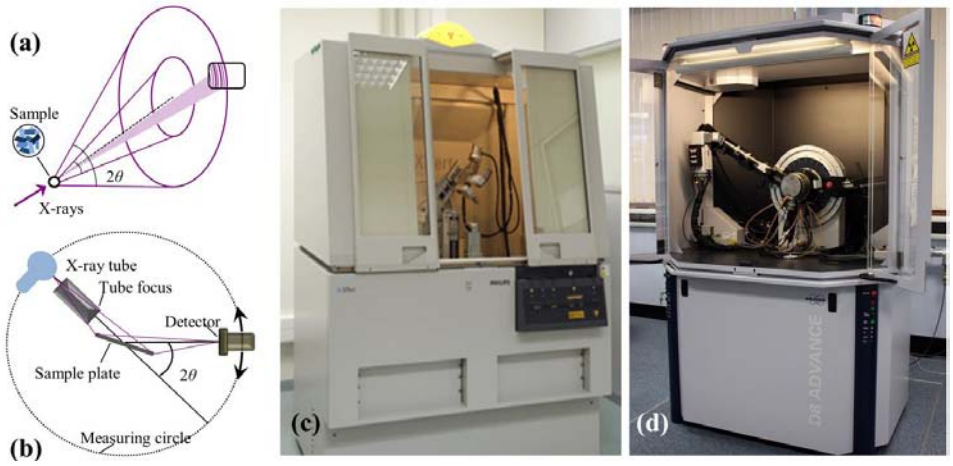

Figura 3.1.2 *(a) Cono producido como resultado de la difracción de los rayos X por una muestra policristalina. (b) Representación esquemática de un difractómetro de polvo cristalino. Los equipos (c) PHILIPS X´Pert Pro PANanalytical y (d) Bruker D8 Advance utilizados en este trabajo.*

Los procesos de deshidratación/rehidratación observables por efecto de la temperatura en algunos de los compuestos estudiados en este trabajo, fueron monitorizados mediante termodifracción de rayos X de polvo cristalino. Para ello, se utilizó un difractometro Bruker D8 Advance (geometría Bragg-Brentano), radiación CuKα (λ = 1.5418 Å), y un detector LynxEye de alta precisión, con una amplitud de 0.0001° y una máxima velocidad de giro de 20°/s (Figura 3.1.2d). A este equipo se le acopló una cámara de alta temperatura Anton Paar XRK900, que permite realizar medidas in situ de difracción de rayos X en muestras tratadas térmicamente desde temperatura ambiente hasta 900 °C en diferentes atmósferas de reacción (vacío, nitrógeno, aire). En los compuestos estudiados en esta Memoria, se efectuaron medidas al aire desde temperatura ambiente hasta 200 ºC. La medida a "temperatura ambiente" se realizó a 30 ºC. Después, se obtuvieron in situ patrones de difracción a intervalos constantes de 10 ºC (entre dos temperaturas consecutivas se utilizó una rampa de calentamiento de 10 °C/min y un periodo de estabilización de 5 min previo a la toma de datos). Las difractogramas obtenidos fueron tratados utilizando el programa Bruker AXS DIFFRAC.EVA. Con el fin a determinar el grupo especial y los parámetros de celdilla de los compuestos producto de la deshidratación, se ha realizado el indexe de los termodifractogramas utilizando la aplicación DICVOL06[17] del paquete de programas de refinamiento FULLPROF suite.

La identificación difractométrica de las fases policristalinas resultantes de los ciclos catalíticos, así como las obtenidas después de los estudios de descomposición mediante técnicas termoanalíticas (TG-DTA-DSC), no puede ser abordada mediante técnicas convencionales de difracción como las descritas en este apartado, dada la pequeña cantidad de muestra disponible (solamente unos pocos miligramos). Sin embargo, estos datos son accesibles mediante el uso de

(17) A. Boultif, D. Louer, *J. Appl. Cryst.*, **2004**, *37*, 724–731.

un difractómetro de monocristal operando en modo polvo. Para obtener los resultados descritos en esta Memoria, se utilizó un difractometro Gemini de la casa Oxford Diffraction, equipado con el tubo de grafito, utilizando radiación CuKα (λ = 1.5418 Å). Las muestras, finamente molidas, fueron montadas en un bucle del nylon. El reducido número de cristalitos expuestos a la radiación hace que la estadística de los datos obtenidos sea insuficiente para llevar a cabo refinamientos estructurales. Sin embargo, sí es posible obtener patrones de difracción adecuados para la identificación de fases cristalinas.

3.2. Microscopia Electrónica de Barrido (SEM)

Los microscopios electrónicos permiten obtener imágenes con una resolución varios órdenes de magnitud superior a la accesible mediante microscopia óptica. Este hecho se debe a que la fuente de iluminación utilizada es un haz de electrones, en lugar de la luz visible propia de la microscopia óptica, y que las lentes son campos magnéticos capaces de desviar la trayectoria de las partículas cargadas eléctricamente. Por lo tanto, la microscopia electrónica es capaz de proporcionar resultados de mayor amplitud, con una gran profundidad de campo, versatilidad y gran resolución, siendo posible examinar la estructura tridimensional y la morfología de los microcristales de los polímeros metal-orgánicos objeto de este trabajo. Esta técnica constituye una herramienta imprescindible para conocer la morfología, el tamaño de los cristales y el hábito cristalino de los sólidos objeto de estudio.

En la microscopia electrónica un haz de electrones incide sobre la muestra y, como consecuencia de la interacción entre esos electrones y la materia, surgen señales que son captadas por un detector o proyectadas directamente sobre una pantalla.

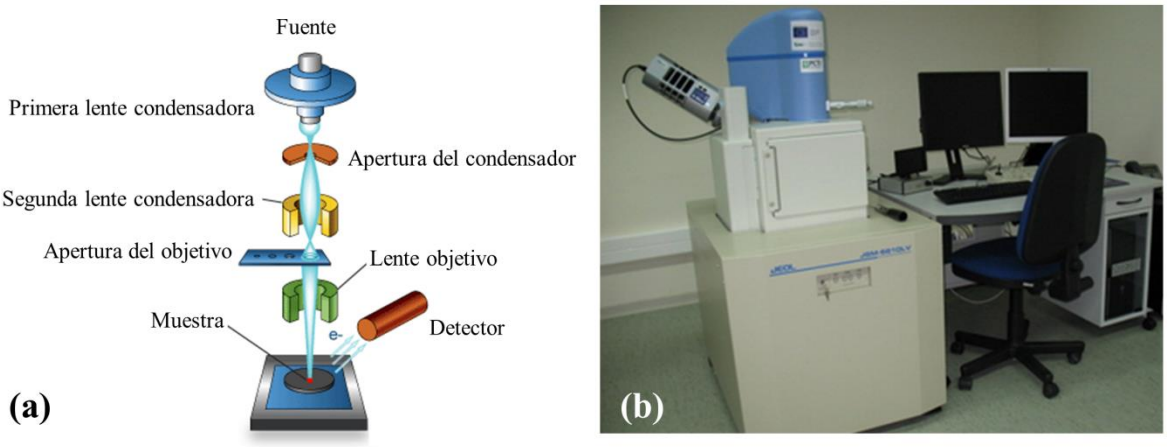

Figura 3.2 *Esquema de un (a) microscopio electrónico de barrido y (b) el equipo SEM utilizado en este trabajo.*

A continuación, se presenta una descripción sucinta (el recorrido que efectúa el haz de electrones viene recogido en el esquema que aparece en la Figura 3.2a) de un microscopio electrónico de barrido:

- La fuente representa el cañón de electrones, que produce el haz monocromático de electrones.

- El haz es focalizado por la primera lente condensadora que trabaja conjuntamente con la apertura del condensador para eliminar los electrones cuya trayectoria presenta un elevado ángulo.

- La segunda lente condensadora proporciona un haz delgado y coherente.

- Una apertura de objetivo (seleccionable) contribuye a colimar el haz de electrones.

- Finalmente, la lente objetivo focaliza el haz de electrones en la zona deseada de la muestra.

- Cuando el haz de electrones impacta con la muestra tienen lugar varios fenómenos. Parte de electrones (dependiendo del espesor y la composición de la muestra) son transmitidos o dispersados elásticamente. Otra parte produce interacciones inelásticas con los átomos de la muestra. Si la energía de estos electrones es suficiente para superar la función de trabajo del sólido, se emiten electrones secundarios y, también, radiación X. El número de electrones secundarios que escapan de la muestra depende del ángulo de incidencia del haz y de la morfología de la superficie del sólido. Por tanto, recogiendo los electrones secundarios es posible obtener una imagen de la superficie con notable profundidad de campo.

El microscopio electrónico de barrido (SEM) utilizado en este trabajo fue el modelo MEB JEOL-6610LV (Figura 3.2b) equipado con un cañón de electrones con filamento de wolframio, capaz de proporcionar desde 5 hasta 50000 aumentos y generar imágenes de electrones secundarios y de electrones retrodispersados acelerados en tensiones de 0.5 a 30 kV. Permite observaciones de hasta 3.0 nm de resolución y trabajar en modos de alto o bajo vacío. Las muestras, depositadas sobre una membrana, son previamente recubiertas de una delgada capa de oro para mejorar el contraste, utilizado para ello una unidad de recubrimiento por evaporación en alto vacío.

3.3. Microanálisis por Rayos X (EDX)

Esta técnica está implementada en el equipo de microscopia electrónica de barrido descrito en el apartado anterior. El microanálisis EDX utiliza la emisión de rayos X característicos producidos por el bombardeo de electrones de alta energía para el análisis cualitativo y semicuantitativo de muestras sólidas, siendo una herramienta extraordinariamente valiosa para el estudio de la composición química de materiales tanto mono- como polifásicos. En esta Memoria, esta técnica se ha utilizado para determinar la cantidad relativa de rutenio, otros metales de transición (Co, Ni, Fe, Zn, Cu, Mn, Os) y metales alcalinos (Na y K) en los materiales sintetizados, lo que permite obtener datos de la homogeneidad de las muestras, su pureza y la correlación entre morfología y composición.

El equipo de microanálisis utilizado en el presente trabajo, integrado en el microscopio MEB JEOL-6610LV, consta de un detector SDD modelo Xmax 50 con resolución de energías inferiores a 5.9 keV y 20000 cps, y un área activa de 50 mm^2, equipado con ventana ultra fina que permite la detección y el análisis de átomos ligeros (C, N, O).

3.4. Microscopia Electrónica de Transmisión (TEM)

La microscopia electrónica de transmisión permite obtener imágenes de elevada resolución a partir del análisis de electrones de alta energía que atraviesan la muestra objeto de estudio (Figura 3.4a). Ésta deberá ser lo suficiente delgada como para ser transparente a los electrones por lo que, en muchos casos, requerirá una preparación especial a fin de conseguir un espesor máximo aproximado de sólo unos miles de angstroms. Una de las principales ventajas de esta técnica consiste en la posibilidad de obtener información del espacio real, mediante las imágenes generadas por los electrones transmitidos, a la vez que permite el estudio en el espacio reciproco, a partir de los datos de difracción de electrones. Además, proporciona información relacionada con los posibles defectos presentes en el material, tales como dislocaciones, faltas de apilamiento, fronteras policristalinas o de multifase e, incluso, cambios composicionales, con una resolución que dependerá del tipo de defecto y del material analizado.

La microscopia electrónica de transmisión de alta resolución (HRTEM) es una variante de esta técnica. En este caso, la imagen se genera mediante la interferencia de más de un haz difractado, de manera que aparece un contraste de fase con el que analizar la muestra con una resolución estructural inferior a los 0.2 nm. En las imágenes de contraste de amplitud se obtienen imágenes de campo claro o campo oscuro seleccionando, mediante diafragmas o aperturas, el haz directo o los haces dispersados, respectivamente. Dentro del contraste de amplitud existen dos tipos principales: contraste debido al grosor o masa de la muestra y el contraste debido a la difracción de los electrones. En el primer caso, el contraste se produce debido a la dispersión incoherente y elástica de los electrones al atravesar la muestra y depende fuertemente del número atómico de sus componentes y del grosor de la misma. Este contraste es el más importante en el caso de muestras no cristalinas. El contraste de difracción se produce debido a la dispersión coherente y elástica de los electrones al atravesar la muestra y está controlado por la estructura cristalina y la orientación de la misma. Se da cuando la dispersión de los electrones se produce a un ángulo de Bragg determinado y, por tanto, sólo aparece en muestras cristalinas.

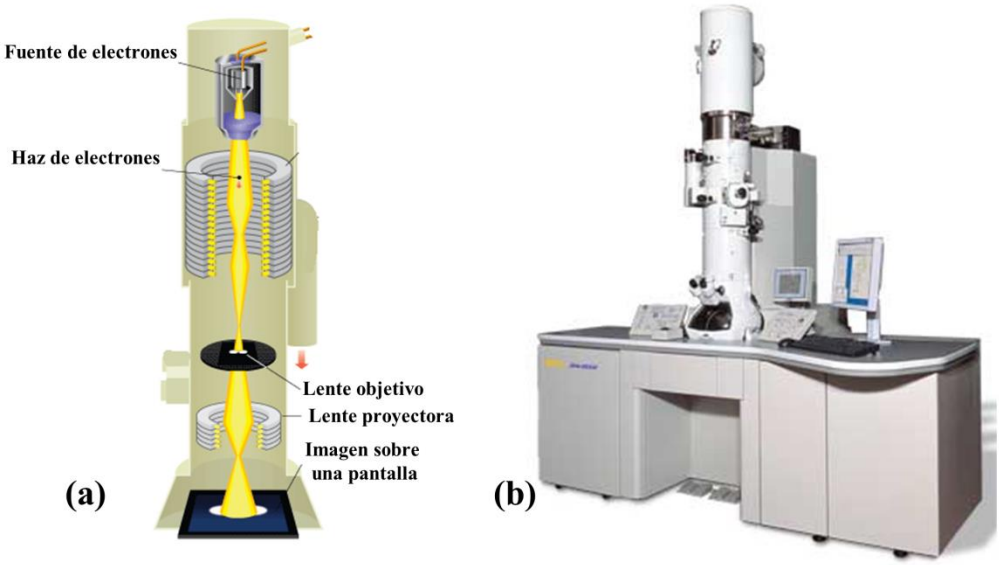

Figura 3.4 *(a) Esquema de un microscopio electrónico de transmisión y (b) imagen del equipo* JEOL JEM-2100 *utilizado en este trabajo.*

En la caracterización de las muestras estudiadas en esta tesis, se ha trabajado con los microscopios JEOL-2000 EX-II y JEOL JEM-2100 (Figure 3.4b), ubicados en la Unidad de Microscopia Electrónica de los Servicios Científico-Técnicos de la Universidad de Oviedo.

3.5. Análisis Elemental C-H-N-S

La técnica de análisis elemental descrita en este apartado se utiliza para determinar el contenido en carbono, hidrógeno, nitrógeno y azufre de un amplio abanico de muestras de naturaleza orgánica e inorgánica, tanto solidos como líquidos. En la Figura 3.4a se muestra un esquema de un analizador C-H-N-S. La técnica de análisis se basa en la combustión completa de una muestra que se somete a un tratamiento térmico a alta temperatura, aproximadamente 1000 °C, y bajo una atmosfera de oxígeno puro. Con ello, se consigue la conversión total de los elementos mencionados previamente en especies gaseosas oxidadas (CO_2, H_2O, SO_2 y NO_x, que posteriormente es reducido a N_2 mediante Cu). Los productos de la combustión son separados de forma secuencial y cuantificados mediante un detector de conductividad térmica, obteniéndose finalmente el contenido porcentual de cada elemento en la muestra analizada.

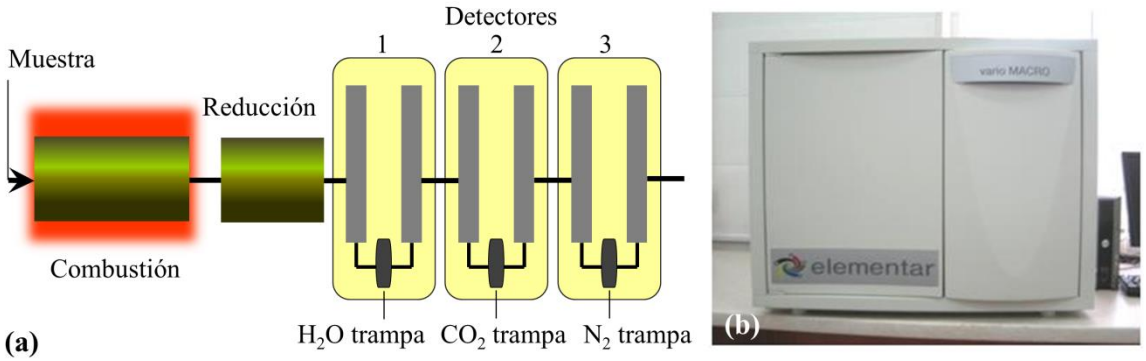

Figura 3.5 *Esquema de un analizador C-H-N-S (a) y el equipo ELEMENTAR VARIO MACRO utilizado (b) en este trabajo.*

En este trabajo, las determinaciones del contenido en carbono, hidrógeno y nitrógeno de los nuevos polímeros de coordinación y de sus precursores, en el caso de haber sido sintetizados en nuestro laboratorio, se realizaron en un equipo de la casa comercial ELEMENTAR modelo VARIO MACRO (Figura 3.5b).

3.6. Espectroscopia Infrarroja (IR)

La radiación infrarroja es aquella a la que le corresponden longitudes de onda comprendidas en el rango que va de 0.78 a 1000 µm; es decir, con números de onda de 12800 a 10 cm^{-1}. La región infrarroja del espectro (Figura 3.6a) se subdivide en tres zonas denominadas infrarrojo cercano (12800–4000 cm^{-1}), medio (4000–200 cm^{-1}) y lejano (200–10 cm^{-1}). La mayoría de las aplicaciones analíticas se restringen al uso de una parte del infrarrojo medio comprendido entre 4000 y 400 cm^{-1}.

La base del fundamento de esta técnica se encuentra en la vibración continua de los átomos de una molécula o celdilla unidad en torno a sus posiciones de equilibrio, algunas de las cuáles pueden ir asociadas a cambios en el momento dipolar. Cuando la frecuencia de alguna de estas vibraciones que transcurren con cambio del momento dipolar es aproximadamente igual a la frecuencia de la radiación incidente, se produce un fenómeno de resonancia con absorción de

energía por parte de sólido. La frecuencia de estas vibraciones está en el rango de la radiación infrarroja y es característica de los diferentes grupos funcionales que presenta la molécula o la red sólida en cuestión.

Si las muestras se encuentran en estado sólido, a no ser que estén compuestas por partículas extremadamente pequeñas (< 5 μm), se producen indeseables pérdidas de energía debidas a la difusión de la radiación. Este efecto puede minimizarse dispersándolas en medios con un índice de refracción semejante, por lo que las muestras sólidas suelen prepararse como disoluciones, pastas o dispersiones sólidas en KBr.

En esta memoria se ha utilizado la espectroscopia infrarroja con transformada de Fourier para identificar los diversos grupos funcionales orgánicos presentes en los polímeros de coordinación sintetizados, así como en los compuestos de partida preparados en nuestro laboratorio.

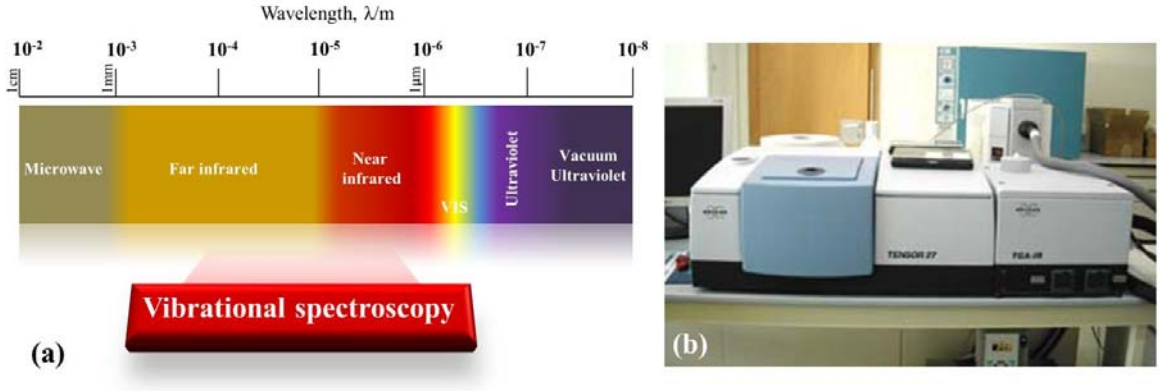

Figura 3.6 *Región espectral de las ondas electromagnéticas utilizadas en espectroscopia infrarroja (a) y el equipo FTIR Bruker Tesor 27 utilizado (b) en este trabajo.*

El equipo utilizado fue un espectrofotómetro FTIR Bruker Tesor 27, que permite trabajar en un rango de número de ondas de 7800 a 370 cm^{-1}, con una capacidad de resolución espectral estándar de 1 cm^{-1} (Figura 3.6b). Las muestras se prepararon en forma de pastillas de KBr con una proporción (en peso) muestra : KBr de 1:1000.

3.7. Espectroscopia Ultravioleta/Visible (UV-VIS)

Las medidas de absorción de radiación ultravioleta y visible encuentran gran aplicación en la identificación y determinación de una enorme cantidad de especies inorgánicas, orgánicas, y organometálicas. Los métodos espectroscópicos se basan en la capacidad de las moléculas o materiales para absorber la radiación electromagnética de frecuencia correspondiente a las energías de transición entre niveles energéticos relevantes. La espectroscopia ultravioleta-visible (UV-VIS), basada en los fenómenos relacionados con la absorción de ondas electromagnéticas correspondientes a la región espectral ultravioleta-visible (Figura 3.7a), se usa en la determinación de estructuras electrónicas de moléculas cromóforas. Esta técnica también se conoce como espectroscopia electrónica debido a que la energía absorbida origina cambios en la estructura electrónica del compuesto.

En esta Tesis se utilizó la espectroscopia de reflectancia difusa como forma eficaz de obtener los espectros directamente sobre muestras pulverulentas con un mínimo de preparación de las mismas y con gran rapidez. Las medidas se efectuaron, en condiciones ambientales, en los laboratorios de Física del Estado Solido de la Universidad de Cantabria (Santander), utilizando un espectrofotómetro Cary 6000i (Varian), equipado

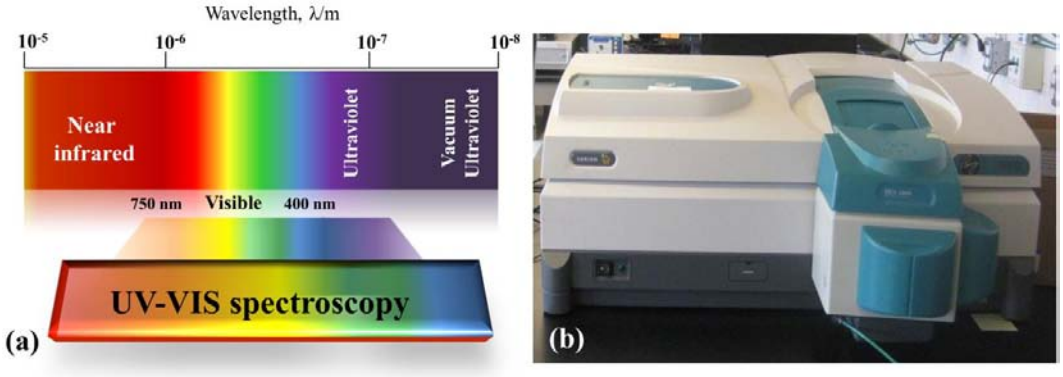

Figura 3.7 *Región espectral de las ondas electromagnéticas utilizadas en espectroscopia UV-VIS (a) y el equipo Cary 6000i (Varian) utilizado (b) en este trabajo.*

con una esfera integradora para la obtención de espectros de reflectancia difusa en el intervalo de 200 a 1800 nm de longitud de onda (Figura 3.7b).

3.8. Técnicas de Análisis Térmico

Las técnicas de análisis térmico son aquellas que estudian el comportamiento de una determinada propiedad física o química de la muestra en función de la temperatura o el tiempo. Cuando se calienta una sustancia se producen cambios físicos o químicos que a veces son observables a simple vista, pero que otras veces son casi imperceptibles. Pueden producirse procesos físicos como cambios de fase en estado sólido, fusión o ebullición; o cambios químicos como consecuencia de la descomposición o reacción de la sustancia. Todos estos procesos son características de cada sustancia, por lo que midiendo la temperatura a la que ocurren dichos cambios y cuantificado alguna propiedad relacionada con ellos, pueden caracterizarse los compuestos presentes en un determinado material.

3.8.1. Análisis Termogravimétrico (TG) y Termogravimetría Derivada (dTA)

El análisis termogravimétrico (TG) se basa en la determinación de manera continua de la variación de masa de una muestra sometida a tratamiento térmico (Figura 3.8.1a). Entre los diferentes tipos de experimentación termogravimétrica, la más utilizada es la dinámica. Esta técnica se basa en el tratamiento de la muestra en un determinado rango de temperaturas con una velocidad de calentamiento constante. La representación gráfica de la pérdida de masa de la muestra, en porcentaje, se denomina curva termogravimétrica. La información que se puede obtener de esta curva es muy variada: estabilidad térmica, composición de la muestra, determinación de volátiles y cenizas, destilación y evaporación de líquidos, grado de evaporación y sublimación, etc.

La termogravimetría derivada (dTG) es una técnica que se relaciona directamente con la anterior, en la cual se representa la variación de masa respeto al tiempo (dm/dt) frente a la temperatura o el tiempo. Es decir, una curva dTG es la primera derivada de una curva TG, de modo que los puntos de inflexión de las curvas TG se corresponden con mínimos en la curva dTG. Estos mínimos indican la temperatura a la cual la velocidad de pérdida de masa es máxima en cada etapa. La información obtenida de una curva dTG es visualmente más accesible que la

obtenida de una curva TG y, además, distingue mejor los procesos solapados. Las curvas dTG proporcionan la siguiente información:

- El mínimo de las bandas permite identificar la temperatura a la cual la velocidad de pérdida de masa es máxima.
- La altura del pico a cada temperatura está relacionada con la velocidad de pérdida de masa a esa temperatura, por lo que contiene información cinética del proceso.
- El área del pico es directamente proporcional al cambio de masa sufrido en el proceso.

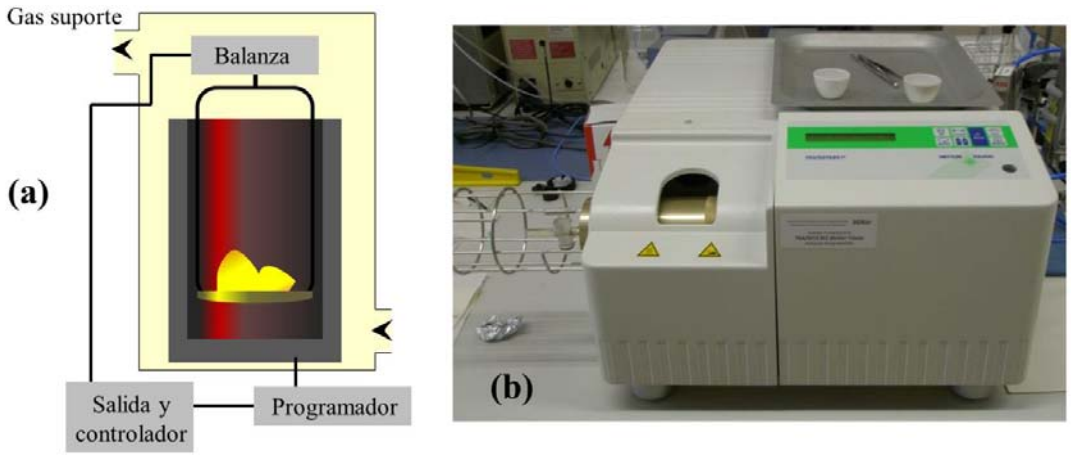

Figura 3.8.1 *Esquema de un termoanalizador vertical (a) y el equipo horizontal Mettler Toledo TG/SDTA 851 utilizado en este trabajo (b).*

En la presente Memoria los experimentos se realizaron en el equipo TG/SDTA 851 de la casa Mettler Toledo, que permite trabajar desde temperatura ambiente hasta 1300 °C con una precisión de 0.25 °C (Figura 3.8.1b).

3.8.2. Análisis Térmico Diferencial (DTA)

Las técnicas de análisis térmico diferencial proporcionan información cualitativa sobre los procesos de transformación térmica de una muestra, incluyendo aquellos que transcurren con constancia en el peso del material. Una curva típica de DTA presentan una serie de picos hacia arriba o hacia abajo (según sean exo- o endotérmicos), que dan información de cualquier proceso que tenga lugar, siempre que vaya acompañado de una variación entálpica. Los procesos que transcurren sin variación de calor también pueden ser detectados por esta técnica, ya que originan cambios en la línea de base del experimento.

En el análisis térmico diferencial se mide la diferencia de la temperatura entre una muestra y otra de referencia cuando a ambas se les aporta calor a velocidad constante. En esta técnica, tanto la muestra problema como la referencia son calentadas por una sola fuente de calor. Las temperaturas son medidas por sensores dispuestos junto a los crisoles que contienen los materiales. Se obtiene así una representación gráfica de la diferencia de temperatura entre muestra y referencia frente a la temperatura del sistema. Cuando la temperatura del sistema aumenta de forma lineal de acuerdo con el programa de temperatura previamente establecido, los procesos que tiene lugar en la muestra aparecen como cambios entálpicos. Si es proceso es exotérmico, la temperatura de la muestra es superior a la de referencia, ocurriendo lo contrario en reacciones endotérmicas. Esta técnica no implica una relación directa entre las áreas integradas

de cada pico y el calor de reacción. Esto hace del DTA una técnica cualitativa o, a lo sumo, semicuantitativa.

Los estudios realizados aplicando esta técnica a la caracterización de los compuestos objeto de esta Tesis se llevaron a cabo en el mismo equipo descrito para el análisis termogravimétrico. Dado que el registro de las curvas TG y DTA tiene lugar de forma simultánea, esta técnica suele denominarse TG-SDTA.

3.8.3. Análisis de los Gases Evacuados en el Análisis Térmico: Espectrometría de Masas

El análisis de los gases producidos durante el calentamiento en cualquiera de las técnicas anteriores es deseable para poder comprender el mecanismo de los procesos de descomposición térmica. Cuando se trata de compuestos metalorgánicos, la técnica más apropiada para realizar estos análisis es la espectroscopia de masas dado que, con un tiempo de respuesta muy bajo, permite detectar eficientemente especies gaseosas con límites de detección adecuados (≤ 1 ppm).

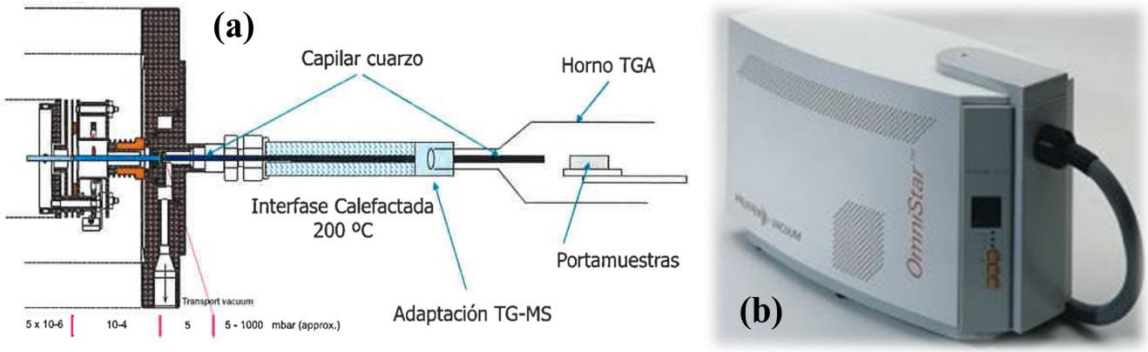

Figura 3.8.3 *Esquema de la conexión TG-MS (a) y el espectrómetro de masas MFeiffer Thermostar GSD301T utilizado en este trabajo (b).*

En este caso, se utilizó un espectrómetro de masas Thermostar GSD301T de la casa MFeiffer que permite detectar masas comprendidas entre 1 y 300 uma. El equipo se encuentra acoplado a la termobalanza mediante un tubo capilar de cuarzo termostatizado a 200 °C para evitar condensaciones (Figura 3.8.3a-b). Los gases de la salida del horno atraviesan la interface y penetran en el equipo de masas donde son ionizados, fragmentados, acelerados y separados de acuerdo a su relación masa/carga (m/z). Cada uno de los fragmentos elegidos es identificado mediante un detector SEM/Channelton (operando a 1000 V) en tiempo real, de manera que puede monitorizarse su abundancia en función de la temperatura de descomposición a la que se ha originado.

3.8.4. Calorimetría Diferencial de Barrido (DSC)

La calorimetría diferencial del barrido (DSC) se puede definir como la técnica cuantitativa que determina la potencia calorífica directamente asociada con el evento térmico que experimenta la muestra en estudio. En este tipo de experimento, la muestra problema se compara con una muestra de referencia (normalmente alúmina calcinada y seca), calentándose o enfriándose a una velocidad constante. La magnitud a determinar es el flujo de calor que es necesario suministrar para que la temperatura de ambas (muestra y referencia) sea la misma en todo momento. Dado que la referencia es inerte, las fluctuaciones de temperatura serán debidas a los procesos entálpicos sufridos por la muestra. La cantidad de muestra debe ser pequeña con el

fin de conseguir la mínima inercia térmica. Al igual que en las curvas DTA, el típico DSC presentará una serie de picos hacia arriba y hacia abajo (según sean los procesos exo- o endotérmicos, respectivamente) que dan información de cualquier proceso ocurrido, siempre que lleve asociado una variación entálpica. Las reacciones que transcurren sin variación del calor (transiciones de segundo orden), también pueden ser detectadas por esta técnica ya que, como consecuencia de la variación experimentada por la capacidad calorífica del material, originan cambios en la línea de base del experimento.

El equipo utilizado en esta Memoria fue un Mettler-Toledo DSC 822, que permite trabajar en un rango de temperaturas comprendiendo entre -65 y 650 °C con una reproducibilidad de 0.2 °C.

3.9. Isotermas de Adsorción/Desorción de Nitrógeno

Para determinar las propiedades texturales de materiales porosos se emplea la técnica de adsorción/desorción de nitrógeno a su temperatura de ebullición (77 K). La representación del volumen de gas adsorbido en el equilibrio por la muestra problema (previamente desgasificada) frente a presiones relativas crecientes conduce a la isoterma de adsorción. Alcanzada la saturación, se emprende el camino inverso, obteniendo la isoterma de desorción. Una simple inspección visual de las curvas de adsorción-desorción de un material proporciona una gran cantidad de información sobre sus características texturales, que puede ser cuantificada mediante el tratamiento matemático adecuado de los datos experimentales, pudiendo obtenerse parámetros tan relevantes como el área superficial específica o la distribución estadística del diámetro de sus poros.

El equipo que se ha utilizado ha sido un Micromeritics ASAP 2020, que se muestra en la Figura 3.9, el cual posee dos puertos de desgasificación y un puerto de análisis de la muestra. Está dotado de dos bombas de membrana y dos turbomoleculares. Consta de un sistema interno de válvulas para regular los procesos de desgasificación y análisis, y está conectado a un ordenador para controlar este sistema de válvulas y registrar los datos experimentales.

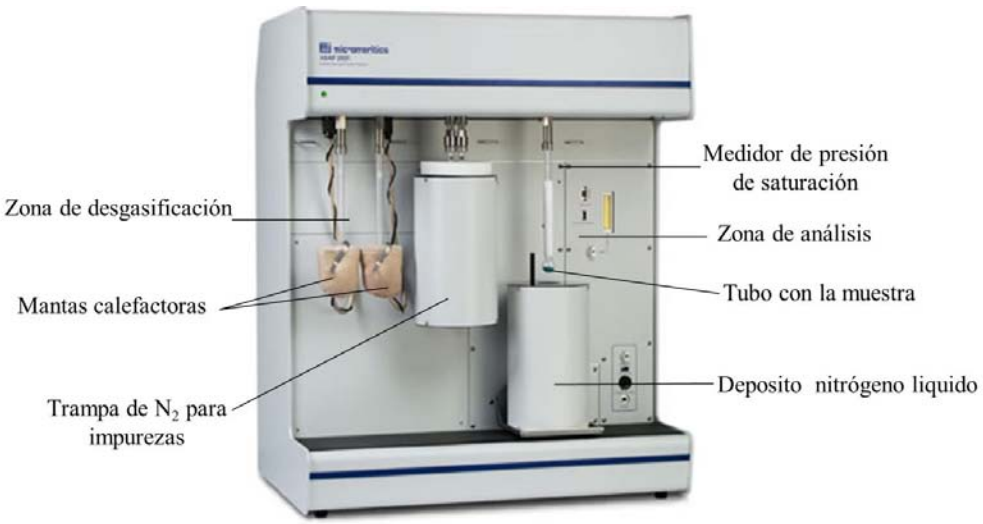

Figura 3.9 *Equipo Micromeritics ASAP 2020 utilizado para las medidas de adsorción/desorción N_2.*

La fase de desgasificación previa a la medida consta de dos partes. Primero, se evacua la muestra calentándola hasta 100 °C a vacío y, después, se mantiene el vacío aumentado la temperatura de tratamiento hasta alcanzar la elegida para cada muestra.

3.10. Medidas de Imanación y Susceptibilidad Magnética

La forma clásica de caracterizar las propiedades magnéticas de un compuesto pasa por determinar la atracción o repulsión que manifiesta al interaccionar con un campo magnético no homogéneo mediante la medida de la masa aparente de la muestra al aplicar sobre ella campos magnéticos de intensidad conocida. Siguiendo esta técnica, la muestra se pesa secuencialmente en una balanza Gouy (Figura 3.10a) con el campo

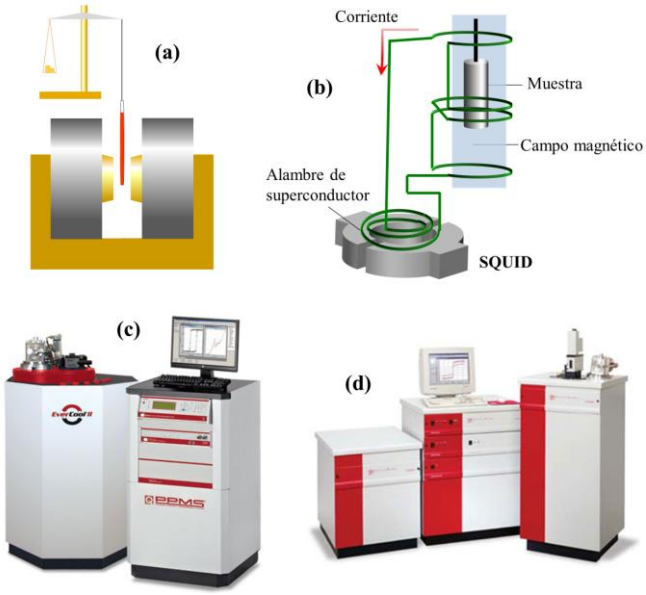

Figura 3.10 *Representación esquemática de la balanza de Gouy (a) y un equipo tipo SQUID (b). Los sistemas que se han utilizado: (c) sistema PPMS y (d) sistema MPMS-XL de Quantum Design.*

electromagnético activo y anulado, respectivamente. La diferencia entre ambas medidas es la fuerza que actúa sobre la muestra como resultado de la aplicación del campo. La susceptibilidad molar puede ser determinada si se conoce la masa de la muestra y su peso molecular. El momento magnético efectivo de los iones de los metales de transición presentes en el material puede deducirse de las medidas de susceptibilidad magnética y ser usado para inferir el número de sus electrones desapareados y, como consecuencia, su estado de espín. En términos técnicos, actualmente las medidas se realizan en dispositivos superconductores de interferencia cuántica (Superconducting Quantum Interference Device, SQUID), como el que se muestra esquemáticamente en Figura 3.10b. El SQUID permite cuantificar el flujo magnético en el bucle superconductor que constituye una parte del circuito, que está directamente relacionado con la susceptibilidad magnética de la muestra.

Las medidas de imanación y susceptibilidad magnética se han realizado en dos equipos instalados en los laboratorios de Física del Estado Solido de la Universidad de Cantabria (Santander):

- Un sistema PPMS de Quantum Design (Figura 3.10c), equipado con un criostato que permite variar la temperatura entre 1.9 K y 350 K, con una estabilidad de 0.01 K, y una bobina superconductora que permite alcanzar campos magnéticos de 90 kOe. Este equipo mide la imanación por el método de extracción y tiene una sensibilidad de 10^{-5} emu. También permite la medida de la susceptibilidad AC con un campo de excitación H_{ac}

entre -10 Oe y +10 Oe y una frecuencia entre 10 Hz y 10 kHz, con una sensibilidad de 10^{-8} emu.

- Un sistema MPMS-XL de Quantum Design (Figura 3.10d) que integra un magnetómetro SQUID que alcanza campos de 50 kOe y permite medir la imanación DC con una sensibilidad de 10^{-8} emu a 2500 Oe; y un criostato que permite variar la temperatura entre 1.8 K y 350 K. La susceptibilidad AC se puede medir aplicando un campo de excitación de ± 0.05 Oe y con una frecuencia entre 0.01 Hz y 1 kHz, alcanzando una sensibilidad de $2 \cdot 10^{-8}$ emu a 0 Oe.

3.11. Resonancia Paramagnética Electrónica (EPR)

La técnica de resonancia paramagnética electrónica se usa para el estudio de los materiales paramagnéticos, generalmente basados en los metales del bloque d, que poseen electrones desapareados. Al aplicar un campo magnético, los niveles energéticos degenerados se desdoblan, manifestándose el bien conocido efecto Zeeman (Figura 3.11a). El caso más simple se da cuando la especie presenta un solo electrón desapareado (s = 1/2). Entonces, en presencia de en campo externo, B0, se produce la diferenciación entre sus estados energéticos, ms = + 1/2 y ms = - 1/2, de acuerdo con la ecuación:

$$\Delta E = g\mu_B B_0$$

donde μB es una constante denominada "magnetón de Bohr" (9.274·10-24 J/T).

En los espectrómetros actuales se trabaja a campo magnético variable y frecuencia de radiación microondas constante. La frecuencia resonante aplicada en la mayoría de equipos EPR es próxima a 9 GHz, y se corresponde con una frecuencia de aproximadamente 0.3 cm^{-1}.

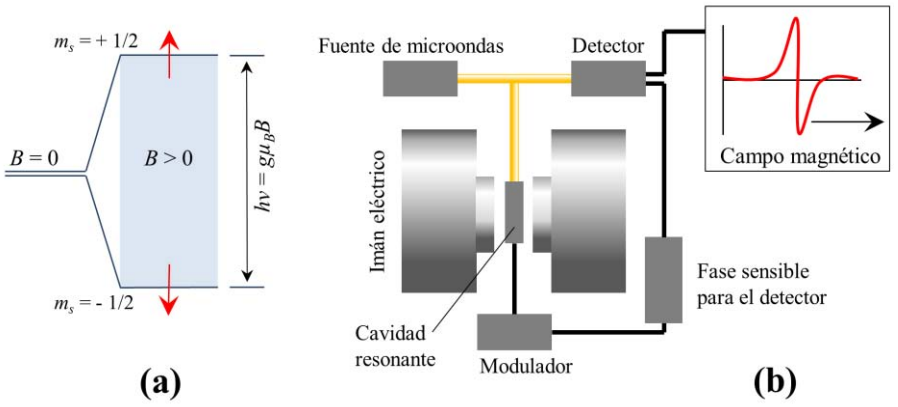

Figura 3.11 *(a) Efecto Zeeman electrónico como fundamento de la técnica EPR. (b)Representación esquemática de un espectrómetro EPR convencional.*

La radiación de microondas, producida en un dispositivo Klinstron, alcanza la cavidad resonante mediante una guía metálica (Figura 3.11b). La frecuencia de microondas se modula para que se produzca resonancia en la cavidad y, de esta forma, se amplifica la densidad de la energía del resonador. El campo magnético que actúa sobre la muestra colocada en la cavidad resonante debe ser homogéneo para proporcionar buena resolución a los espectros resultantes. Finalmente, la onda perturbada por la muestra se mide en un detector sensible a las microondas. Los espectros se registran como picos de absorción y se presentan como su primera derivada,

que es más sensible a los cambios de entorno. Los estudios realizados aplicando esta técnica se realizaron en un espectrómetro de resonancia paramagnética electrónica ADANI CMS-8400 instalado en la Facultad de Química de la Universidad Nacional de Kiev *Taras Shevchenko* (Kiev, Ucrania). El equipo utilizado alcanza un campo magnético de hasta 0.7 T, con una resolución de 0.006 mT y una sensibilidad de $5 \cdot 10^{15}$ spins/T.

3.12. Cromatografía de Gases

La cromatografía de gases es una técnica de separación que se basa en la inyección de una pequeña cantidad de la muestra a separar en una corriente de gas inerte a elevada temperatura; esta corriente gaseosa atraviesa una columna cromatográfica que separa los componentes de la mezcla por un mecanismo de partición (cromatografía gas-líquido), de absorción (gas-sólido) o, en algunos casos, por medio de una mezcla de ambos. Los componentes de la mezcla salen de la columna en intervalos discretos de tiempo, dependiendo de la afinidad de cada componente hacia el relleno de la columna utilizada, donde finalmente son detectados.

Los análisis por cromatografía de gases se han realizado en un equipo Agilent Hewlett Packard HP6890 equipado de un detector de ionización de llama (FID) utilizando una columna capilar Supelco Beta-Dex™ 120 de 30 m de longitud y 0.25 mm de diámetro

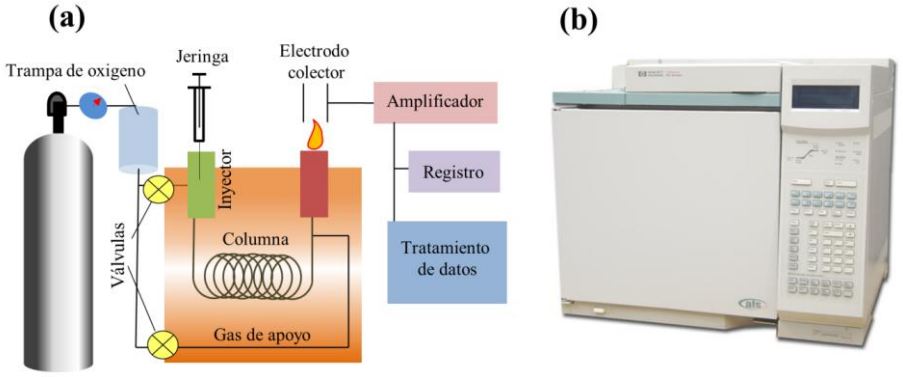

Figura 3.12 *(a) Esquema de un cromatógrafo de gases. (b) El equipo Agilent Hewlett Packard HP6890 utilizado en este trabajo.*

interno. Los análisis de cromatografía con detector de masas acoplado se han realizado en un aparato Agilent HP6890 equipado de un detector de masas Agilent5973 de ionización por impacto electrónico (70 eV) y de una columna capilar HP-1MS de 30 m de longitud y 0.25 mm de diámetro interno.

3.13. Foto-reactor con Radiación Ultravioleta

Las reacciones fotocatalitizadas por algunos de los polímeros de coordinación preparados en la presente Memoria requirió la instalación de un foto-reactor ultravioleta, que consta de tres bloques diferenciados: el bloque regulador/transformador, la lámpara UV (modelo GRE500W de la casa HELIOS ITALQUARTZ®) y el reactor (Figura 3.13).

El bloque del regulador/transformador incorpora la salida del conector eléctrico a una lámpara UV de mercurio a alta presión que, refrigerada por agua, opera a una potencia de 500 W, generando emisiones electromagnéticas que cubren toda la gama de la región ultravioleta con un pico de máxima intensidad a 366 nm.

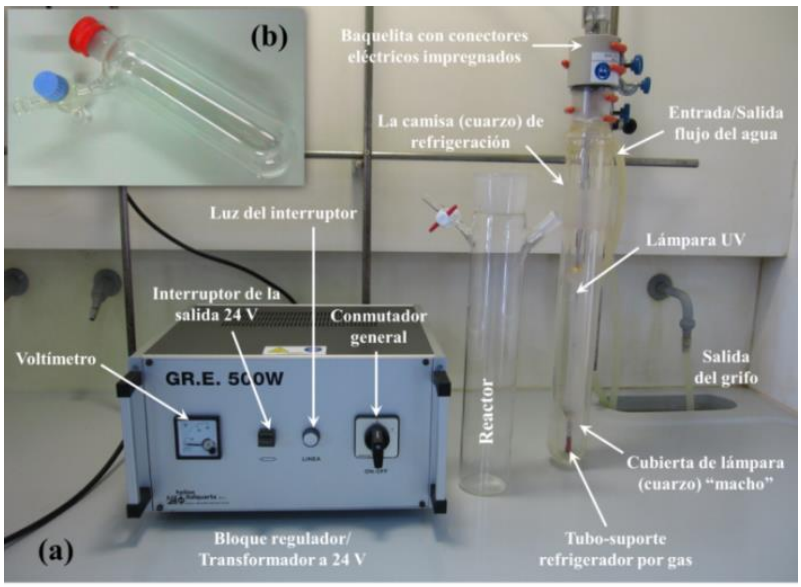

Figura 3.13 *(a) Instalación del foto-reactor con lámpara UV. (b) El tubo Schlenk de cuarzo con el tapón-septum SUBA-SEAL.*

El reactor, de fondo plano, es de vidrio Pyrex® con una capacidad de 100 mL, poseyendo una boca esmerilada de tipo "hembra" ajustable a la camisa de la lámpara UV. Las reacciones de las fases gaseosas se llevaron a cabo utilizando un tubo *Schlenk* de cuarzo con una capacidad de 100 mL, equipado con una llave del paso 2.5 cm, boca esmerilada de tipo "hembra" y tapón-*septum* SUBA-SEAL.

3.14. Detección de Gases Mediante Espectrometría de Masas usando un Equipo de Quimisorción como Sistema de Traspaso

Los productos gaseosos formados en las reacciones fotoasistidas se han determinado cualitativa y cuantitativamente mediante espectrometría de masas, utilizando el equipo Thermostar GSD301T de la casa MFeiffer descrito en el apartado 3.8.3, acoplado a un equipo de quimisorción Micromeritics AutoChem II 2920, que se ha utilizado como sistema de traspaso de los gases hacia el espectrómetro de masas. El equipo de quimisorción (Figura 3.14a-b) consta de cinco zonas generales: válvulas de gas de bucle, válvulas de gas de soporte, válvulas de gas de referencia, reactor y trampa fría, entrada *septum* para inyecciones manuales y, finalmente, detector de conductividad térmica.

El análisis del gas problema ha sido realizado mediante inyecciones manuales a través del *septum* del equipo AutoChem II 2920. Las porciones de la muestra gaseosa inyectadas al sistema se recogen con un flujo constante de gas soporte que las hace llegar al detector de masas Thermostar GSD301T. En nuestro caso, se han utilizado helio o argón como gases soporte (flujo = 10 mL/min). La inyección de la muestra se realizó mediante una jeringa de gases Gamilton® (volumen total 10 µL). Durante el análisis, las válvulas de los bloques de los gases de preparación y de bucle permanecieron cerradas, manteniendo estas zonas a una temperatura de 30 °C. El detector de conductividad térmica, que forma parte del sistema de traspaso, permaneció a 50 °C para evitar condensaciones indeseables.

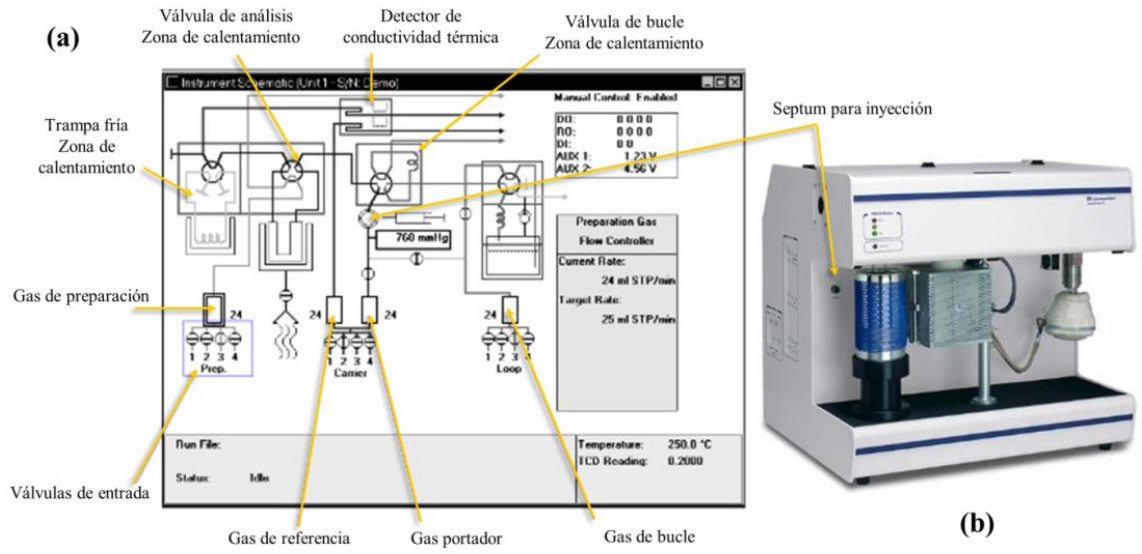

Figura 3.14 *Esquema (a) del equipo de quimisorción Micromeritics AutoChem II 2920 utilizado en este trabajo (b).*

El módulo de masas se utilizó en modo de trabajo MID (Detección de Iones Múltiples) con parámetros *m/z* prefijados a los valores adecuados para detectar las especies que se pretenden monitorizar.

3.15. Reducción a Temperatura Programada (TPR)

La técnica de reducción a temperatura programada permite la identificación de las diferentes especies presentes en la muestra a través de la facilidad con la cual dichas especies pueden ser reducidas. No se trata de una técnica superficial, sino que la reducción que tiene lugar involucra a la totalidad de las especies reducibles del catalizador. En este tipo de ensayos, una corriente de gas inerte, conteniendo una pequeña concentración del gas reductor (usualmente H_2), atraviesa la muestra. La concentración del agente reductor es monitorizada en el efluente del reactor y representada como una función de la temperatura de la muestra. La práctica usual es someter a la muestra a una rampa lineal y creciente de temperatura que, comenzando a temperatura ambiente, asciende a una velocidad de 10 °C/min. El monitoreo del consumo de H_2 a la salida del reactor se realiza empleando un detector de conductividad térmica.

Los análisis TPR realizados en el presente trabajo consistieron en someter una muestra de 100 mg del catalizador a una corriente del gas reductor (10% H_2 en Ar) aumentando la temperatura del lecho desde temperatura ambiente hasta 800 °C con una velocidad de calentamiento de 10 °C/min, bajo un flujo de 50 mL/min. A la salida del reactor se utiliza una trampa-desecadora de sílice a fin de retener el agua producida durante la reducción con el fin de no enmascarar las señales.

Para la realización de los experimentos de TPR se utilizó un analizador automático Micromeritics AutoChem II 2920 acoplado a un espectrómetro de masas Thermostar GSD301T (Figura 3.14a-b).

3.16. Espectroscopia de Absorción de Rayos X (XANES)

La espectroscopia de absorción de rayos X en borde de absorción (*X-ray Absorption Near Edge Spectroscopy*, *XANES*) es una técnica basada en el efecto fotoeléctrico, donde los electrones fuertemente ligados al núcleo absorben rayos X. Las medidas de XANES son muy

sensibles a los estados de oxidación y al entorno de coordinación del átomo estudiado por lo que en esta Tesis la dicha técnica fui utilizada para determinación de estado de oxidación del ion de rutenio en diversos estados.

Los experimentos de absorción de rayos X en las proximidades del umbral *K* del Ru, se realizaron en línea española BM25 de las instalaciones del sincrotrón de radiación europeo (ESRF, Grenoble) en modo de transmitancia. El monocromador estaba equipado con dos cristales planos de Si (111). Para medir la haz incidente y transmitido se utilizaron dos cámaras de ionización cargadas con nitrógeno y argón, respectivamente. Las muestras estudiadas se colocaron entre la cinta de kapton y se midieron a temperatura ambiente. Como patrones de referencia se utilizaron una lámina de rutenio metálico, muestra comercial de $RuCl_3$ y $[Ru(bpy)_3]Cl_2$, $K_3[Ru(C_2O_4)_3]$ obtenidas experimentalmente. El tratamiento de los datos se realizó con el programa ATHENA del paquete IFFEFIT.[18,19]

3.17. Espectroscopia Fotoelectrónica de Rayos X (XPS)

La espectroscopia fotoelectrónica de rayos X es una técnica habitual en la caracterización superficial de materiales como consecuencia de que los fotones tienen un poder penetrante limitado que, en un sólido, va de 1 a 10 µm. Esta técnica se basa en la determinación de la energía cinética de los electrones emitidos desde los niveles internos de los átomos que han sido excitados mediante la aplicación a la superficie del material de un haz de rayos X monoenergético (Figura 3.17a).

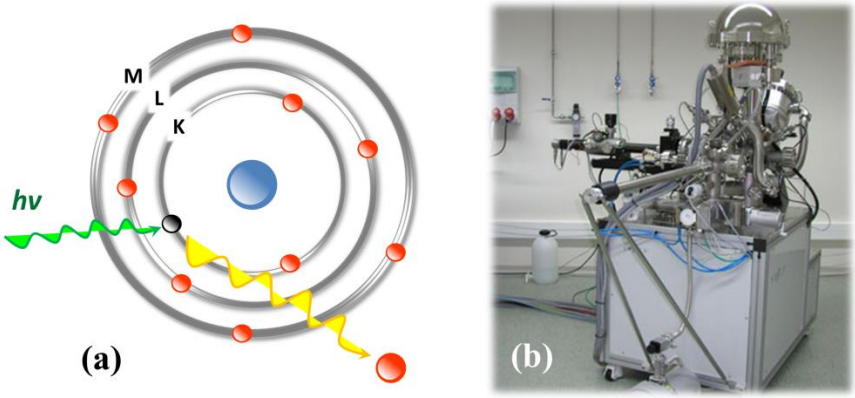

Figura 3.17 *Representación esquemática (a) del proceso de excitación de un electrón en capas energéticos superficiales de un átomo. (b) El sistema de espectroscopia fotoelectrónica de rayos X: SPECS Phoibos HSA3500-100*

Asumiendo que la emisión del electrón es elástica, su energía cinética puede expresarse del siguiente modo:

$$E_k = hv - E_l - \Phi$$

donde E_k es la energía cinética medida del electrón emitido, hv es la energía de la fuente de excitación de rayos X utilizada, y E_l es la energía de ligadura o potencial de ionización del átomo (como esta energía suele estar referida al nivel de Fermi, se introduce la función trabajo, Φ, como término corrector resultante de la combinación de factores instrumentales e intrínsecos a la muestra). Los valores de energía de ligadura o potencial de ionización van a ser los indicadores

(18) M. Newville, *J. Synchrotron Rad*., **2001**, *8*, 322–324.
(19) B. Ravel, M. Newville, *J. Synchrotron Rad*., **2005**, *12*, 537–541

que permitan identificar el átomo del cual procede el electrón y el estado de oxidación en el que se encuentre (como norma general la energía de ligadura aumenta al aumentar el estado de oxidación del átomo).

El perfil de la señal asociada a la energía del electrón emitido estará determinada por diversos factores. El tiempo de vida del hueco electrónico, que puede determinarse usando el principio de incertidumbre de Heisenberg, aumenta con la energía de enlace y el número atómico del átomo del que se extrae el electrón, debiendo originar una curva Lorentziana. Sin embargo, los factores instrumentales (la fuente de rayos X y el analizador) contribuyen a la forma del pico con una curva Gaussiana. Por este motivo, las señales XPS tienen forma Lorentziana-Gaussiana. Hasta aquí, se ha asumido que la emisión del electrón siempre es elástica; sin embargo, el electrón puede perder energía por choques inelásticos durante su salida del átomo, provocando la aparición de una cola en el pico principal en la región de alta energía de ligadura o baja energía cinética.

Mediante espectroscopia fotoelectrónica de rayos X se estimó la concentración superficial de los diferentes componentes de la muestra, obtenida mediante el espectro general, y los estados energéticos de alta resolución de los átomos constituyentes (carbono, oxígeno, nitrógeno, etc.). Se utilizó un espectrómetro SPECS Phoibos HS3500-100 (Figura 3.17b) con una fuente de rayos X (MgKα, 1253.6 eV, 175 W) trabajando a una presión de 10^{-7} Pa, ubicado en la Unidad de Espectroscopia Fotoelectrónica, UV-visible e IR de los Servicios Científico-Técnicos de la Universidad de Oviedo. Los electrones foto-excitados se analizaron en el modo de energía de paso constante, usando una energía de paso de 80 eV para el espectro general y 10 eV para los espectros de alta resolución. Se utilizó el software CasaXPS para el procesamiento de los datos. Todos los espectros analizados fueron sometidos a deconvoluciones de tipo mixto Gaussiana-Lorentziana, mediante minimización del error cuadrático medio y ajuste tipo Shirley de la línea base.

Capitulo IV

Síntesis y Caracterización de los Compuestos de Partida

En este Capítulo, se describe la síntesis y caracterización de los compuestos utilizados como precursores en la preparación de nuevos polímeros de coordinación, así como los que no han llevado a la formación de los polímeros de coordinación inicialmente esperados, incluyendo los protocolos de síntesis utilizados para cada compuesto, tanto los desarrollados por primera vez en este trabajo como aquellos que ya habían sido descritos en la bibliografía, habiendo considerado de interés, a efectos de referencia para la identificación de los precursores, incluir datos de los análisis espectroscópicos y estructurales, tales como IR, Vis-UV, difracción de rayos X de polvo cristalino y análisis térmico. La estructura cristalina de uno de los precursores, desconocida en la bibliografía, ha sido determinada mediante difracción de rayos X de monocristal y publicada en *Acta Crystallographica: Section E* (***2012***), *E68, m713–m714*.

4.1. $K_3[Ru(C_2O_4)_3]\cdot 4.5H_2O$

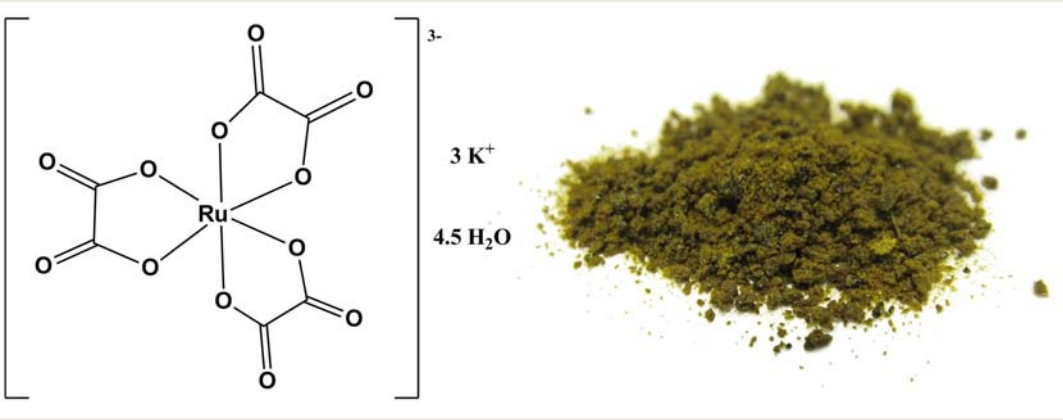

Systematic name	Potassium Tris(Oxalato)Ruthenate(III) Hydrate		
Molecular Formula	$C_6H_9K_3RuO_{16.5}$		
Molecular Weight	563.32 g/mol	**Appearance**	Olive green solid
CAS №	29475-51-2	**Boiling point**	365.1 ºC (atm)
Solubility	water, methanol	**Flash Point**	188.8 ºC

4.1.1. Synthesis

Materials: Commercial $RuCl_3\cdot xH_2O$ was obtained from Johnson Matthey; Oxalic acid dihydrate ($H_2C_2O_4\cdot 2H_2O$) 99.9% reagent grade from Sigma-Aldrich; Potassium hydroxide (KOH) pellets from Sigma-Aldrich; Silver nitrate ($AgNO_3$) 99% reagent grade from Sigma-Aldrich; Ethanol (C_2H_5OH) 96% v/v analytical grade from VWR International S.A.S.
Commercial $RuCl_3\cdot xH_2O$ is dried in an oven at 120°C for 3 hours. It is then finely ground in a mortar and returned to the oven for the further 1 hour prior to use.
The potassium oxalate salt ($K_2C_2O_4$) is prepared by addition of sodium hydroxide pellets (13.5 g, 0.24 mol) to about 50 mL aqueous solution of oxalic acid (15.2 g, 0.12 mol) and stirred until a potassium hydroxide was completely dissolves and neutralization has been completed. The resulted solution was carefully evaporated to dryness and the crude product was dried in an oven at 110°C for 6 hours prior to use.

Synthetic procedure. Compound $K_3[Ru(C_2O_4)_3]\cdot 4.5H_2O$ has been synthetized following the procedure described previously.[1–3] A solution of dried ruthenium trichloride (5.0 g, 24.1

(1) J. K. Witschy, J. K. Beattie, *Inorg. Nucl. Chem. Letters*, **1969**, *5*, 969–972.
(2) D. W. Raichart, H. Taube, *Inorg. Chem.*, **1972**, *11*, 999–1002.
(3) R. Kaziro, T. W. Hambley, R. A. Bistead, J. K. Beattie. *Inorg. Chim. Acta*, **1989**, *164*, 85−91.

mmol) and potassium oxalate (11.8 g) in water (100 mL) was refluxed with rapid agitation for 7 h. During this time the solution changed in color from black to olive-green. Olive-green oil like-precipitate was obtained by the addition of the hot solution to ethanol (250 mL). The mixture was filtered warm. The crude product was dissolved in water (10 mL) and the solution poured into ethanol (100 mL). The precipitated product was collected by filtration and the filtrate tested with aqueous solution of $AgNO_3$ on the presence of chloride ions. Recrystallization of the residue from water, by slow evaporation of the solvent over silica gel in a desiccator, gave olive-green needles and plates. Product was removed and dried on air. Yield of the product was 9.3 g (68%).

Elemental analysis. Anal. Calculated for $C_6H_9K_3O_{16.5}Ru$: C, 12.79%; H, 1.61%. Found: C, 12.3%; H, 1.4%.

4.1.2. Identification Procedures

4.1.2.1. Powder X-ray Diffraction

The crystal structure of $K_3[Ru(C_2O_4)_3]\cdot 4.5H_2O$ was reported previously,[1,4] the compound is isostructural to the rhodium analog,[5] and crystallizes in triclinic *P*-1 space group with a unit cell parameters: a = 6.813(5) Å, b = 10.519(1) Å, c = 12.470(2) Å, α = 76.28(1)°, β = 84.26(1)°, γ = 85.60(1)°, V = 862.5 Å^3, Z = 2. The published crystallographic parameters[1] are summarized in Table 4.1.2.1.

Table 4.1.2.1 *Crystallographic parameters for $K_3[Ru(C_2O_4)_3]\cdot 4.5H_2O$.* [1,4]

Molecular formula	$C_6H_9K_3RuO_{16.5}$
Formula Weight, g·mol^{-1}	563.3
Crystal system	Triclinic
Space group	*P*-1
Cell dimensions	
a, Å	6.813(5)
b, Å	10.519(1)
c, Å	12.470(2)
α, ^{0}	76.28(1)
β, ^{0}	84.26(1)
γ, ^{0}	85.60(1)
V, Å^3	862.5
Z	2
Density, g·cm^{-3}	2.170
Absorption coefficient, mm^{-1}	16.62
Radiation	Mo Kα, λ = 0.71069 Å

The structure consists of the $[Ru(C_2O_4)_3]^{3-}$ anions, potassium cations and water molecules with bonds connecting the potassium atoms with the oxalate oxygen atoms and with water oxygen atoms. All of the potassium cations are seven coordinated. The complex anion is formulated as $[Ru(C_2O_4)_3]^{3-}$, with all oxalate groups acting as bidentate chelating ligands. The coordination environment of ruthenium is octahedraly distorted, what is caused by a small bite angle of the oxalate ligand. The Ru−O bond lengths is averaged to 2.028(7) Å.

(4) P. R. Faure, G. Duc, J.-P. Deloume, *Acta Cryst*., **1986**, *C42*, 982−984.
(5) B. C. Dalzell, K. Eriks, *J. Am. Chem. Soc*., **1971**, *93*, 4298−4300.

In order to confirm the structural consistency between the synthesized precursor compound and the expected complex $K_3[Ru(C_2O_4)_3]\cdot 4.5H_2O$, an experimental powder pattern of obtained olive-green solid was compared with a simulated powder pattern from reported single crystal data. The *Crystallographic Information File* (CIF)[6] of $K_3[Ru(C_2O_4)_3]\cdot 4.5H_2O$ has been requested with the depositional number of IUCr 25932 from the *Cambridge Structural Database* (CSD)[7,8] which belongs to the *Cambridge Crystallographic Data Centre* (CCDC).[9]

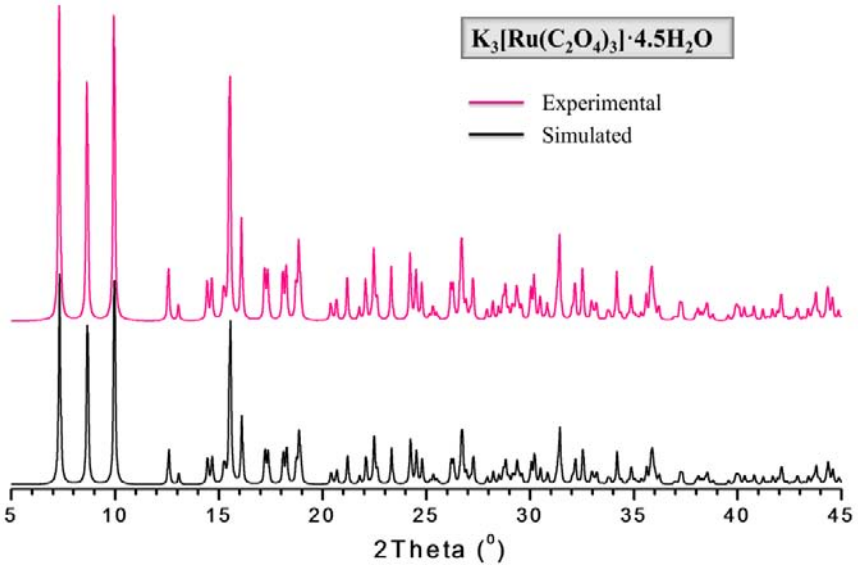

Figure 4.1.2.1 *Powder X-ray diffraction patterns of $K_3[Ru(C_2O_4)_3]\cdot 4.5H_2O$: experimental (red) and simulated (black).*

Figure 4.1.2.1 shows the experimental and simulated powder X-ray diffraction patterns for as-synthesized and reported compound $K_3[Ru(C_2O_4)_3]\cdot 4.5H_2O$, revealing a good accordance in Bragg reflections positions and their relative intensities, which subsequently indicates the phase purity and relates the pattern to the expected precursor compound.

4.1.2.2. Infrared Spectroscopy

The infrared spectrum of synthesized olive-green solid in the region 4000–400 cm^{-1} is shown in Figure 4.1.2.2. The bands assignments summarized in the Table 4.1.2.2 are in a good agreement with bibliographic data.[10–12] The spectrum of $K_3[Ru(C_2O_4)_3]\cdot 4.5H_2O$ consists of a relatively small number of absorption bands which may be assigned to the following motions: the strong broad absorption band between 3700 and 3100 cm^{-1} is attributed to O−H symmetric and asymmetric vibrations of crystallization water molecules; the strong band around 1700 cm^{-1} can be assigned to an asymmetric C=O stretch of a carboxylic group in the $C_2O_4^{2-}$ ligand;

(6) S. R. Hall, F. H. Allen, I. D. Brown, *Acta Cryst*., **1991**, *A47*, 655−685.
(7) F. H. Allen, *Acta Cryst.*, **2002**, *B58*, 380−388.
(8) R. Thomas, I. J. Bruno, J. C. Cole, C. F. Macrae, E. Pidcock, P. A. Wood, *J. Appl. Cryst*., **2010**, *43*, 362−366; http://www.ccdc.cam.ac.uk/Solutions/CSDSystem/Pages/CSD.aspx
(9) C. R. Groom, F. H. Allen, *Angew. Chem. Int. Ed*., **2014**, *53*, 662–671. http://www.ccdc.cam.ac.uk/pages/Home.aspx
(10) J. Gouteron, *J. Inorg. Nucl. Chem*., **1976**, *38*, 55−61.
(11) J. T. Wrobleski, D. B. Brown, *Inorg. Chem*., **1979**, *18*, 2738−2749.
(12) K. Nakamoto, In *Infrared and Raman Spectra of Inorganic and Coordination Compounds*; Part B: Applications in Coordination, Organometallic, and Bioinorganic Chemistry, John Wiley & Sons, LTD, 2009.

Table 4.1.2.2 *Selected bands in the IR spectrum of compound $K_3[Ru(C_2O_4)_3]\cdot 4.5H_2O$.*

Spectral Region / Band Maximum	Band assignments
3700−3100 *bs*	ν_{sy} (O−H) + ν_{asy} (O−H) or hydrogen bonding
1710−1480 *s*	ν_{asy} (C=O)
1660 *s*	δ_{sy} (O−H−O)
1370 *ms*	ν_{sy} (C−O) and/or ν_{sy} (C−C)
1280 *ms*	ν_{sy} (C−O) and/or δ (O−C=O)
910 *s*	δ (O−C=O) and/or deformation vibrations
820 *s*	ν (M−O) and/or δ (O−C=O)
560 *ms*	Crystal water
520 *vw*	ν (M−O) and/or ν (C−C)
470 *s*	δ (O−C=O) or ν (M−O) and/or ring deformation

b broad; ***s*** strong; ***w*** weak; ***vw*** very weak and ***m*** medium

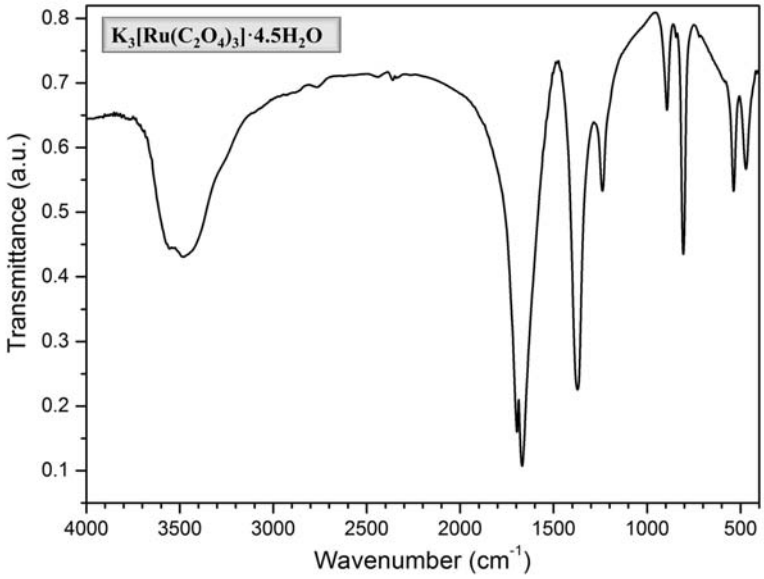

Figure 4.1.2.2 *Infrared spectrum of $K_3[Ru(C_2O_4)_3]\cdot 4.5H_2O$.*

a symmetric C−O stretch appears as the medium strong band around 1370 cm^{-1} with a partial contribution of a C−C stretching to the peak's intensity; the medium strong band at 1280 cm^{-1} relates to O−C=O deformation; the absorption bands at 910 and 820 cm^{-1} are attributed to O–C=O stretch/bending and deformation vibrations; the two peaks at 520 and 470 cm^{-1} are caused by a Ru−O stretch and a O−C=O bending, respectively. The assignments of different bands for various normal modes of vibration of $C_2O_4^{2-}$ groups are indicative of a proper chelation of the ligands which act as bidentate chelates.

4.1.2.3. Thermogravimetric Analysis

The thermogravimetric (TG) and corresponding derivative (dTG) curves, along with the mass spectra of evacuated vapors, of the precursor $K_3[Ru(C_2O_4)_3]\cdot 4.5H_2O$ are shown in Figure 4.1.2.3., and are in good accordance with bibliographic data.[13–18]

(13) N. Rajic, D. Stojakovic, R. Gabrovšek, *J. Therm. Anal. Cal*., **2001**, *63*, 191−195.
(14) N. Deb, *J. Therm. Anal. Calorim*., **2012**, *107*, 561−571.
(15) K. Nagase, K. Sato, N. Tanaka, *Bull. Chem. Soc. Japan*, **1975**, *48*, 868−873.
(16) D. Dollimore, *Thermochim. Acta*, **1987**, *117*, 331−363.
(17) K. Nagase, *Bull. Chem. Soc. Japan*, **1973**, *46*, 144−146.
(18) W. W. Wendlandt, T. D. George, K. V. Krishnamuty, *J. Inorg. Nucl. Chem.*, **1961**, *21*, 69–76.

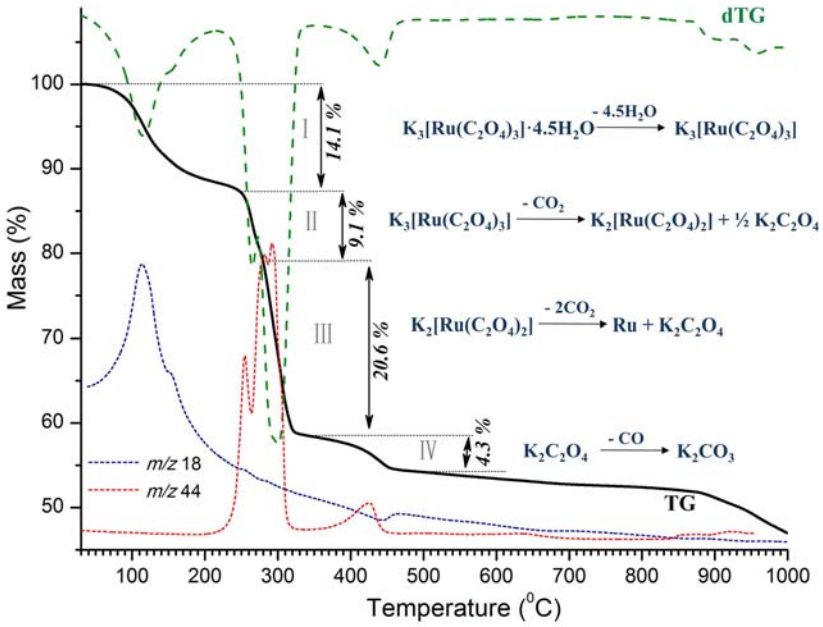

Figure 4.1.2.3 *TG, dTG profiles for thermal decomposition of $K_3[Ru(C_2O_4)_3]\cdot 4.5H_2O$ under a nitrogen atmosphere and mass spectroscopy curves of evacuated vapors*.

The TG-dTG curves exhibit several steps. Dehydration of the complex occurs up to 200 °C and proceeds in one single step (I). The most intense dTG maximum for this process is at about 115 °C corresponds to 14.1% mass loss (*calc*. 14.83%) and belongs to losing of 4.5 moles of crystallization water. The dehydration process was confirmed by mass spectroscopy detecting evacuation gas with *m/z* 18 for this process. The dehydration of the $K_3[Ru(C_2O_4)_3]\cdot 4.5H_2O$ precursor is immediately followed by a decomposition of the resulting anhydrous form and proceeds in three stages: the (II) with a mass loss of 9.1% (*calc*. 9.12%) reaches the maximum velocity at 270 °C; the (III) takes place in the range 280-310 °C with a mass loss of 20.6% (*calc*. 20.01%); the (IV) with a mass loss of 4.3% (*calc*. 4.02%) exhibits maximum velocity at 430 °C; the resulted carbonate decomposes up to 1100 °C.

4.1.2.4. Solid State UV-VIS Spectroscopy

The ground state in this complex has only one unpaired spin corresponding to the low-spin electron configuration d^5 with $^2T_2$ term.

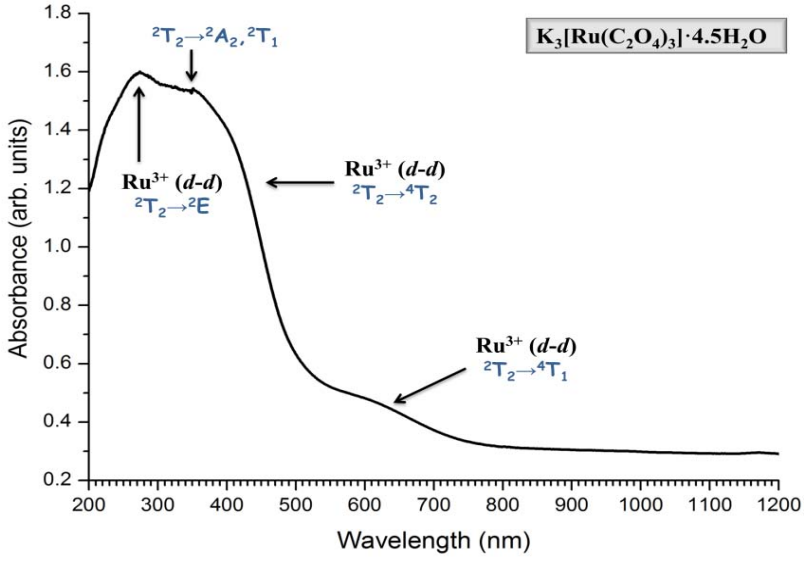

Figure 4.1.2.4 *The room temperature diffuse reflectance UV-VIS spectrum of $K_3[Ru(C_2O_4)_3]\cdot 4.5H_2O$.*

The experimental room temperature diffuse reflectance spectrum of compound $K_3[Ru(C_2O_4)_3]\cdot 4.5H_2O$ was recorded in the range from 200 nm to 1200 nm, and depicted in Figure 4.1.2.4. As expected, the electronic spectra is characterized by a strong absorption band at 285 nm and a shoulder at 376 nm which can be interpreted in terms of superimposition of spin-allowed bands corresponding to $^2T_2 \rightarrow {}^2E$ and $^2T_2 \rightarrow {}^2A_2, {}^2T_1$ transitions, respectively. In visible region the spectrum displays two as spin-forbidden bands attributed to $^2T_2 \rightarrow {}^4T_2$ and $^2T_2 \rightarrow {}^4T_1$ which appear as a broad shoulder at about 480 nm and a week intense band at 631 nm, respectively. These features are qualitatively similar and in good agreement with those reported in bibliography.[1,19,20]

4.2. $[Ru(2,2´\text{-bpy})_3](ClO_4)_2$

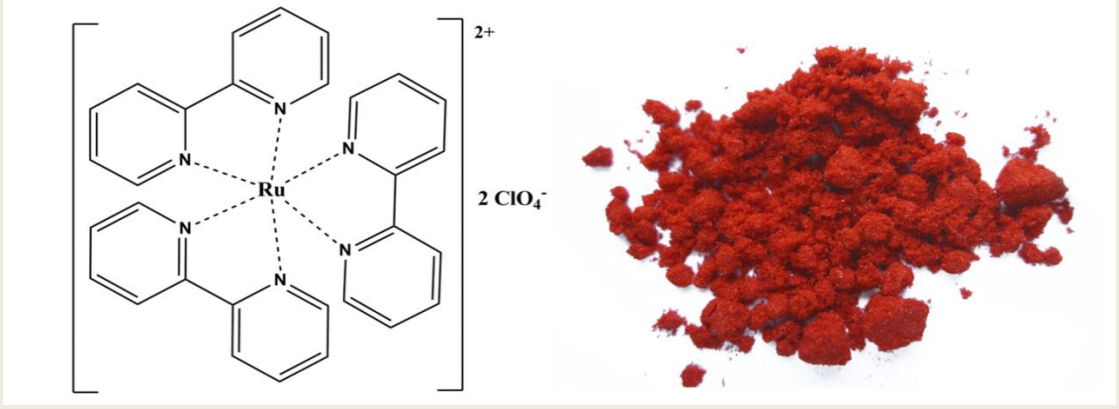

Systematic name	Tris(2,2´-Bipyridine)Ruthenium(II) Perchlorate		
Molecular Formula	$C_{30}H_{24}Cl_2N_6O_8Ru$		
Molecular Weight	768.52 g/mol	**Appearance**	Red solid
CAS №	15635-95-7	**Boiling point**	365.1 ºC (atm)
Solubility	water, acetone, ethanol	**Flash Point**	164.8 ºC

4.2.1. Synthesis

Materials: Commercial $RuCl_3\cdot xH_2O$ was obtained from Johnson Matthey; 2,2´-bipyridine ($C_{10}H_8N_2$) 99% reagent grade from Sigma-Aldrich; 50% aqueous solution of hypophosphorous acid (H_3PO_2) from Sigma-Aldrich; Potassium perchlorate ($KClO_4$) 99% reagent grade from Sigma-Aldrich; Potassium hydroxide (KOH) pellets from Sigma-Aldrich; Acetone (C_3H_6O) 99.9% analytical grade from VWR International S.A.S.

Commercial $RuCl_3\cdot xH_2O$ was dried in an oven at 120 °C for 3 hours. It was then finely ground in a mortar and returned to the oven for the further 1 hour prior to use.

The sodium hypophosphite solution was prepared by careful addition of potassium hydroxide pellets to about 10 mL 50% hypophosphorous acid until a slight cloudy precipitate was obtained. Hypophosphorous acid was then added dropwise until the precipitate has been dissolved.

Synthetic procedure. Compound $[Ru(2,2´\text{-bpy})_3](ClO_4)_2$ has been synthetized following bibliographic procedure described previously.[21] "Dried" $RuCl_3$ (0.8 g, 3.84 mmol), 2,2´-bipyridine (1.8 g, 11.52 mmol), and water (80 mL) were placed in a 100 mL flask fitted with a reflux condenser. Freshly prepared potassium hypophosphite solution (4 mL)was added and the

(19) R. W. Olliff, A. L. Odell, *J. Chem. Soc.*, **1964**, 2417–2421.
(20) Chr. K. Jørgensen, In *Advance in Chemical Physics*; Vol. 5: Spectroscopy of Transition-Group Complexes, John Wiley & Sons, LTD, 1963.
(21) J. A. Broomhead, C. G. Young, *Inorganic Synthesis*, **1982**, *21*, 127−128.

mixture was heated to its boil point and left for 30 min. During reflux, the initial green solution changed to brown in color and then to orange. It was filtered to remove traces of undissolved material and excess of potassium perchlorate (14.3 g) was added to the filtrate to precipitate the crude product. The solution and solid were then heated to boiling to give a deep-red solution in which on a cooling to room temperature, a precipitation of red needle-like crystals was occurred. They were filtered off, washed with ice-cold 10% aqueous acetone (25 mL), pure acetone (30 mL), and dried on air. The yield was 2.95 g (95 %). The crude product might be recrystallized from boiling water (~ 2.8 mL/g) and then air dried.

Elemental analysis. Anal. Calculated for $C_{30}Cl_2H_{24}N_6O_8Ru$: C, 46.88%; H, 3.15%; N, 10.93%. Found: C, 46.6%; H, 3.1%; N, 10.7%.

4.2.2. Identification Procedures

4.2.2.1. Powder X-ray Diffraction

The crystal structure of $[Ru(2,2´\text{-bpy})_3](ClO_4)_2$ was reported previously.[22,23] The compound crystallizes in the monoclinic *C*2/*c* space group with a unit cell parameters: a = 17.633(4) Å, b = 10.761(2) Å, c = 15.924(4) Å, α = γ = 90°, β = 90.77(2)°, V = 3021.3(12) Å^3, Z = 4. The published crystallographic parameters are summarized in Table 4.2.2.1.

Table 4.2.2.1 *Crystallographic parameters for $[Ru(2,2´\text{-bpy})_3](ClO_4)_2$.* [22]

Molecular formula	$C_{30}H_{24}Cl_2N_6O_8Ru$
Formula Weight, g·mol^{-1}	768.52
Crystal system	monoclinic
Space group	*C*2/*c*
Cell dimensions	
a, Å	17.633(4)
b, Å	10.761(2)
c, Å	15.924(4)
α, ^{0}	90
β, ^{0}	90.77(2)
γ, ^{0}	90
V, Å^3	3021.3(12)
Z	4
Density, g·cm^{-3}	1.690
Absorption coefficient, mm^{-1}	0.759
Radiation	Mo Kα, λ = 0.71073 Å

The crystal structure of $[Ru(2,2´\text{-bpy})_3](ClO_4)_2$ is composed of monomeric $[Ru(2,2´\text{-bpy})_3]^{2+}$ cations and perchlorate anions. The Ru(II) atom is surrounded by six N atoms from three chelating bpy ligands in a highly distorted octahedral arrangement with Ru–N bond lengths ranging from 2.059(2) Å to 2.060(3) Å with the average value of 2.059(5) Å, which are consistent with those in the other compounds[23–28] and are slightly greater than for [Ru(2,2´-

(22) J. M. Harrowfield, A. N. Sobolev, *Aust. J. Chem*., **1994**, *47*, 763–767.
(23) E. Krausz, H. Riesen, A. D. Rae, *Aust. J. Chem*., **1995**, *48*, 929−954.
(24) J. Breu, H. Domel, A. Stoll, *Eur. J. Inorg. Chem*., **2000**, 2401–2408.
(25) K. A. McGee, D. J. Veltkamp, B. J. Marquardt, K. R. Mann, *J. Am. Chem. Soc*., **2007**, *129*, 15092–15093.
(26) M. Biner, H.-B. Burgi, A. Ludi, C. Rohr, *J. Am. Chem. Soc*., **1992**, *114*, 5197–5203.

bpy)$_3$]^0 unit (mean of 2.051 Å).[29] The N–Ru^{II}–N bond angles in the precursor compound are in the 78.5–97.9° range. In order to confirm the structural consistency between the synthesized precursor compound and the expected complex [Ru(2,2´-bpy)$_3$](ClO$_4$)$_2$, the experimental powder pattern of obtained red solid was compared with the simulated powder pattern from reported single crystal data.[22] The CIF of [Ru(2,2´-bpy)$_3$](ClO$_4$)$_2$ has been requested with the depositional number of CSD HEGMIP, CSD HEGMIP01 from the CSD of Cambridge Crystallographic Data Centre (CCDC).

Figure 4.2.2.1 shows the experimental and simulated powder X-ray diffraction patterns for as-synthesized and reported compound [Ru(2,2´-bpy)$_3$](ClO$_4$)$_2$, which are in a good agreement

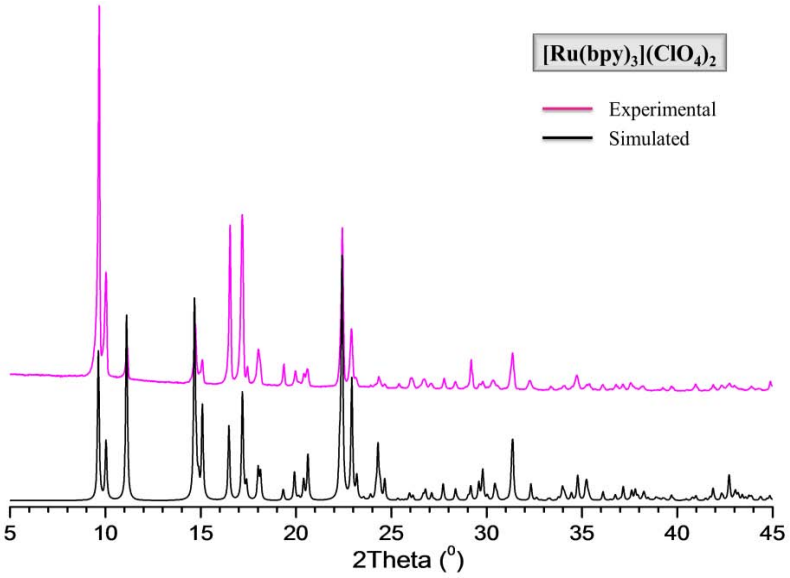

Figure 4.2.2.1 *Powder X-ray diffraction patterns of [Ru(2,2´-bpy)$_3$](ClO$_4$)$_2$: experimental (red) and simulated (black).*

between them in Bragg reflections positions and their relative intensities, which subsequently indicates the phase purity and relates the pattern to the expected precursor compound.

4.2.2.2. Infrared Spectroscopy

A solid state infrared spectrum of [Ru(2,2´-bpy)$_3$](ClO$_4$)$_2$ in the region 4000–400 cm^{-1} is shown in Figure 4.2.2.2. The bands assignments summarized in the Table 4.2.2.2 are in a good agreement with bibliographic data.[12,30–32] The observed bands are characteristic for tris-bipyridine complexes of transition metals in low oxidation state. The spectrum of [Ru(2,2´-bpy)$_3$](ClO$_4$)$_2$ consists of a relatively small number of absorption bands which might be assigned as follows: the broad absorption band in the region 3650–3250 cm^{-1} due to asymmetric and symmetric H–O–H stretching vibrations is assigned to physically adsorbed water molecules; an aromatic C–H stretching vibration of 2,2´-bpy ligands gives rise to a band at 3125−2880 cm^{-1} with weak-to-medium intensity and consists of a number of peaks. Interactions between rings C═C and C═N stretching vibrations result in two medium-to-strong absorptions.

(27) D. P. Rillema, D. S. Jones, H. A. Levy, *Chem. Comm.*, **1979**, 849–851.
(28) D. P. Rillema, D. S. Jones, C. Woods, H. A. Levy, *Inorg. Chem.*, **1992**, *31*, 2935–2938.
(29) E. E. Perez-Cordero, C. Campana, L. Echegoyen, *Angew. Chem., Int. Ed.*, **1997**, *36*, 137–140.
(30) G. Socrates, In *Infrared and Raman Characteristic Group Frequencies*, John Wiley & Sons, LTD, 2001.
(31) Y. Saito, J. Takemoto, B. Hutchinson, K. Nakamoto, *Inorg. Chem.*, **1972**, *11*, 2003−2011.
(32) G. C. Percy, D. A. Thornton, *J. Mol. Struct*., **1971**, *10*, 39–48.

Table 4.2.2.2 *Selected bands in the IR spectrum of compound [Ru(2,2´-bpy)$_3$](ClO$_4$)$_2$.*

Spectral Region / Band Maximum	Band assignments
3650−3250 *bvw*	ν_{sy} (O−H) + ν_{asy} (O−H) or hydrogen bonding
3125−2880 *w*	ν_{asy} (C−H) stretching
1660 *s*	δ_{sy} (O−H−O)
1650-1550*ms*	
1590−1555*m*	ν_{sy} (C═C) and/or ν_{sy} (C═N)
1510−1450*ms*	ring str. Vibration
1450−1410*m*	
1098−1090*s*	ν(Cl−O) and/or δ (Cl−O) of ClO_4^- uncoordinated
1350−1150*m*	δ (C−H) and/or C−H in-plane
1000−850*m*	deformation vibrations.
780−650*ms*	δ (C−H) and/or C−H out-of-plane deformation vibrations

b broad; ***s*** strong; ***w*** weak; ***vw*** very weak and ***m*** medium

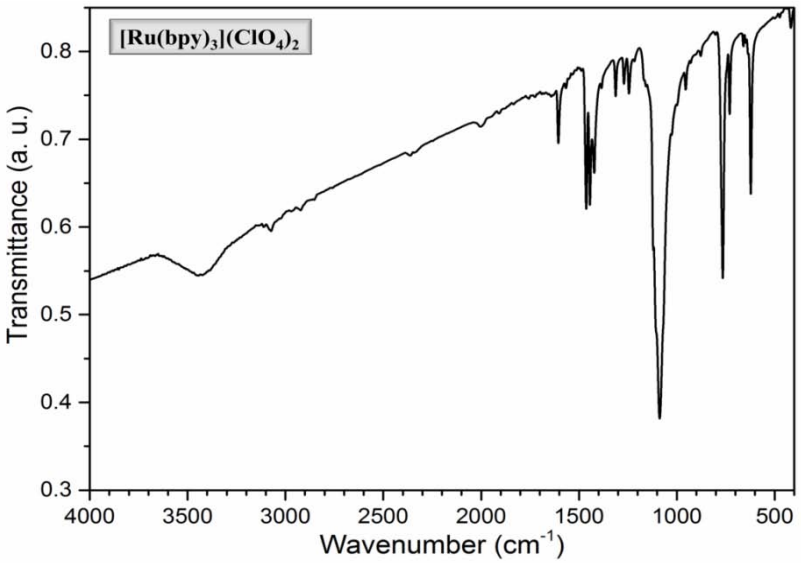

Figure 4.2.2.2 *Solid State Infrared Spectrum of [Ru(2,2´-bpy)$_3$](ClO$_4$)$_2$.*

These absorptions occur at 1650–1550 cm^{-1} and 1510–1450 cm^{-1}, the higher frequency band which often has another medium-intensity band on its low-frequency site is found to be at 1590–1555 cm^{-1}. Bands of variable intensities are observed in the regions 1350–1150 cm^{-1} and 1000–850 cm^{-1} where C−H ring deformation modes of the 2,2´-bpy ligand are expected. The 2,2´-bpy ligand strong adsorption bands at 780 and 650 cm^{-1} are assigned to aromatic out-of-plane hydrogen deformation modes. Furthermore, the spectra exhibit very strong single absorption bands associated with uncoordinated ClO_4^- anion at 1098 cm^{-1} and 1095−1090 cm^{-1}, respectively.

4.2.2.3. Thermogravimetric Analysis

The thermogravimetric analysis (TGA) has been carried out under an air atmosphere for the synthesized [Ru(2,2´-bpy)$_3$](ClO$_4$)$_2$ with the objectives to determine the level of dryness of the compound and confirm the sample purity. The thermogravimetric and corresponding derivative

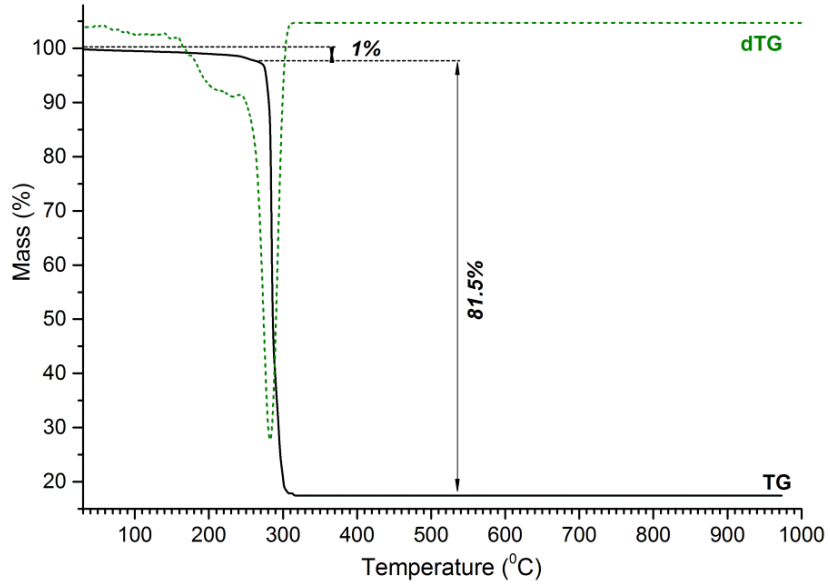

Figure 4.2.2.3 *TG, dTG profiles for thermal decomposition of [Ru(2,2´-bpy)$_3$](ClO$_4$)$_2$ under an air atmosphere*.

(dTG) curves for precursor [Ru(2,2´-bpy)$_3$](ClO$_4$)$_2$ are shown in Figure 4.2.2.3, and are in a good agreement with bibliographic data.[33] Thermal investigation along with X-ray diffraction data indicated that complex [Ru(2,2´-bpy)$_3$](ClO$_4$)$_2$ are anhydrous with some amount of absorbed humidity. According to TG data the weight percent of adsorbed humidity is ~ 1%. The TG and dTG profiles of thermal decomposition of [Ru(2,2´-bpy)$_3$](ClO$_4$)$_2$ are characterized by explosive combustion at 285 ºC with a total mass loss of 81.5%. This phenomenon associated with a strong oxidizing property of a ClO_4^- anion. The solid residue formed at around 400 °C is suggested to be RuO_2 (remaining weight 17.5%, Calcd.: 17.3%).

4.2.2.4. Solid State UV-VIS Spectroscopy

The ruthenium(II) complex [Ru(2,2´-bpy)$_3$]$^{2+}$ is considered to be a typical low-spin complex possessing a $^1A_1$ ($t_{2g}^5e_g^1$) ground state with all six *d* electrons nicely paired up in the t_{2g} orbitals.[34] The room temperature diffuse-reflectance UV-Vis spectra of synthesized [Ru(2,2´-bpy)$_3$](ClO$_4$)$_2$ complex is illustrated in the Figure 4.2.2.4. The absorption bands intensity and their positions are quite similar to bibliographic values reported for [Ru(2,2´-bpy)$_3$]$^{2+}$ complex, [20,23,35–40] that indicate a phase purity and consistence of the synthesized product with the expected precursor.

The absorption spectrum of this complex is dominated by two groups of intense high-energy bands: (*i*) well defined bands in the region 200–280 nm appear to be π→π* intraligand transitions; (*ii*) the sharp peak ranging from 320 nm to 620 nm is basically charge a transfer band which partially masks the *d–d* transition.

(33) A. Bujewski, H. Warachim, K. Grzędzicki, J. Dobrowolski, *Thermochim. Acta*, **1985**, *95*, 779–782.
(34) A. B. P. Lever, In *Inorganic Electronic Spectroscopy, Studies in Physical and Theoretical Chemistry*, Amsterdam, Elsevier, 1984.
(35) J. E. Fergusson, G. M. Harris, *J. Chem. Soc. (A)*, **1966**, 1293−1296.
(36) H. Riesen, L Wallace, E. Krausz, *Chem. Phys*., **1995**, *198*, 269–280.
(37) R. A. Palmer, T. S. Piper, *Inorg. Chem.*, **1966**, *5*, 864−878.
(38) G. N. Bryant, J. E. Fergusson, H. K. J. Powell, *Aust. J. Chem*., **1971**, *24*, 257–273.
(39) H. Riesen, L. Wallace, E. Krausz, *Chem. Phys. Lett*., **1994**, *228*, 605–609.
(40) T. Otsuka, N. Takahashi, N. Fujigasaki, Y. Ohashi, Y. Kaizu, *Inorg. Chem.*, **1999**, *38*, 1340–1347.

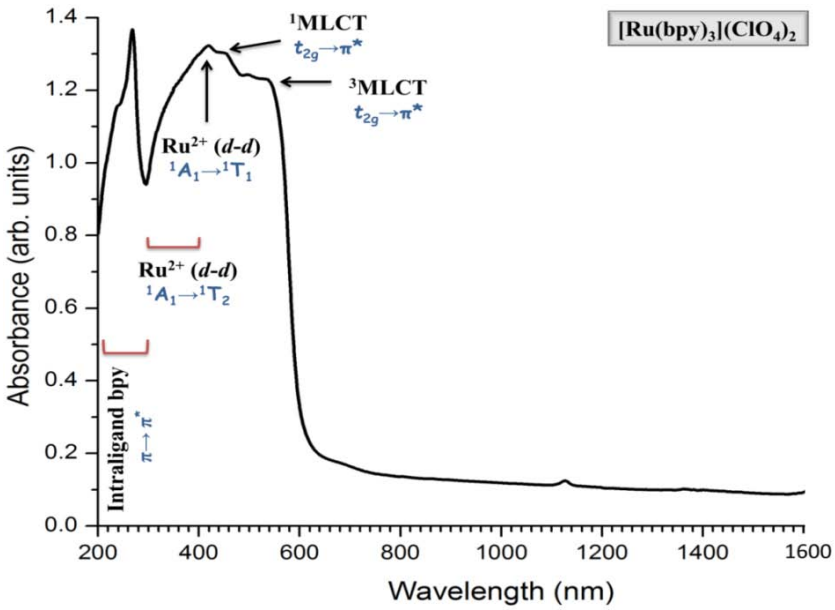

Figure 4.2.2.4 *The room temperature diffuse reflectance UV-VIS spectrum of [Ru(2,2´-bpy)$_3$](ClO$_4$)$_2$.*

There several components have been resolved: shoulder between 320–400 belongs to *d–d* transition $^1A_1 \rightarrow {}^1T_2$; the peak at 450 nm is attributed to $^1A_1 \rightarrow {}^1T_1$ transition. Moreover, the shoulder centered at 490 nm has been assigned to a $t_{2g} \rightarrow \pi^*$ metal-ligand charge transfer (MLCT) transition, while the broad shoulder observed at 560 nm belongs to a spin-forbidden third $t_{2g} \rightarrow \pi^*$ metal-ligand charge transfer (^{3}MLCT) transition. The last one has been observed and confirmed by several works.[39,40]

4.3. [Ru(2,2´-bpy)$_3$]Cl$_2$·6H$_2$O

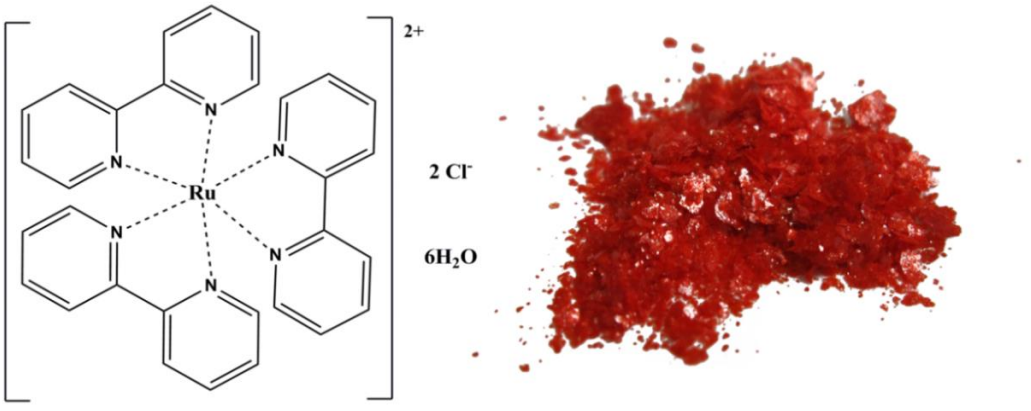

Systematic name	Tris(2,2´-Bipyridine)Ruthenium (II) Dichloride Hexahydrate		
Molecular Formula	$C_{30}H_{36}Cl_2N_6O_6Ru$		
Molecular Weight	748.62 g/mol	**Appearance**	Red solid
CAS №	50525-27-4	**Boiling point**	272.5 ºC (atm)
Solubility	Water, acetone, ethanol, methanol	**Flash Point**	107.2 ºC

4.3.1. Synthesis

Materials: Commercial $RuCl_3 \cdot xH_2O$ was obtained from Johnson Matthey; 2,2´-bipyridine ($C_{10}H_8N_2$) 99% reagent grade from Sigma-Aldrich; 50% aqueous solution of hypophosphorous acid (H_3PO_2) from Sigma-Aldrich; Potassium chloride (KCl) 99% reagent

grade from Sigma-Aldrich; Potassium hydroxide (KOH) pellets from Sigma-Aldrich; Acetone (C_3H_6O) 99.9% analytical grade from VWR International S.A.S.

Commercial $RuCl_3 \cdot xH_2O$ was dried in an oven at 120 °C for 3 hours. It was then finely ground in a mortar and returned to the oven for the further 1 hour prior to use.

The sodium hypophosphite solution was prepared by careful addition of potassium hydroxide pellets to about 10 mL 50% hypophosphorous acid until a slight cloudy precipitate was obtained. Then hypophosphorous acid was added dropwise until the precipitate was dissolved.

Synthetic procedure. Compound $[Ru(2,2´\text{-bpy})_3]Cl_2 \cdot 6H_2O$ has been synthesized following bibliographic procedure described previously.[21,41] "Dried" $RuCl_3$ (0.8 g, 3.84 mmol), 2,2´-bipyridine (1.8 g, 11.52 mmol), and water (80 mL) were placed in a 100 mL flask fitted with a reflux condenser. Freshly prepared sodium hypophosphite solution (4 mL) was added and the mixture heated at reflux for 30 min. During reflux, the initial green solution changed it color to brown and finally orange. It was filtered to remove traces of undissolved material and excess of potassium chloride (12.6 g) was added to the filtrate to precipitate the crude product. The solution and solid were then heated at reflux to give a deep-red solution which on a cooling to room temperature, red plate-like crystals appeared. These were filtered off, washed with ice-cold 10% aqueous acetone (2 × 5 mL), acetone (30 mL) and air dried. The yield was 2.15 g (90 %). The crude product might be recrystallized from boiling water (~ 2.8 mL/g) and then air dried.

Elemental analysis. Anal. Calculated for $C_{30}Cl_2H_{36}N_6O_6Ru$: C, 48.13%; H, 4.85%; N, 11.23%. Found: C, 47.9%; H, 5.1%; N, 11.4%.

4.3.2. Identification Procedures

4.3.2.1. Powder X-ray Diffraction

The crystal structure of $[Ru(2,2´\text{-bpy})_3]Cl_2 \cdot 6H_2O$ was reported previously.[42] The compound crystallizes in hexagonal *P*6/*mcc* space group with the unit cell parameters: a = 13.1383(12) Å, b = 13.1383(12) Å, c = 20.995(3) Å, α = β = 90°, γ = 120°, V = 3138.5(8) Å^3, Z = 4. The published crystallographic parameters are summarized in Table 4.3.2.1.

Table 4.3.2.1 *Crystallographic parameters for $[Ru(2,2´\text{-bpy})_3]Cl_2 \cdot 6H_2O$.* [42]

Molecular formula	$C_{30}H_{36}Cl_2N_6O_6Ru$
Formula Weight, g·mol^{-1}	748.62
Crystal system	hexagonal
Space group	*P*6/*mcc*
Cell dimensions	
a, Å	13.1383(12)
b, Å	13.1383(12)
c, Å	20.995(3)
α = β, ^{0}	90
γ, ^{0}	120
V, Å^3	3138.5(8)
Z	4
Density, g·cm^{-3}	1.206
Absorption coefficient, mm^{-1}	0.525
Radiation	Mo Kα, λ = 0.71073 Å

(41) S. Anderson, K. Seddon, *J. Chem. Research (S)*, **1979**, 74−75.

(42) K. S. Low, J. M. Cole, X. Zhou, N. Yufa, *Acta Cryst*., **2012**, *B68*, 137–149.

The crystal structure of $[Ru(2,2´\text{-}bpy)_3]Cl_2\cdot 6H_2O$ is composed of discrete $[Ru(2,2´\text{-}bpy)_3]^{2+}$ cations, chloride anions and water molecules. The Ru(II) atom is surrounded by six N atoms from three chelating bpy ligands on D_3 manner forming octahedral coordination environment with a Ru–N bond length of 2.065(3) Å, which are consistent with those in the in the other compounds.[22,23] The N–Ru^{II}–N bond angles in the precursor compound are in the 78.9–94.6° range. In order to confirm the structural consistency between the synthesized precursor compound and the expected complex $[Ru(2,2´\text{-}bpy)_3]Cl_2\cdot 6H_2O$, an experimental powder pattern of obtained red solid was compared to a simulated powder pattern from reported single crystal data.[42] The CIF of $[Ru(2,2´\text{-}bpy)_3]Cl_2\cdot 6H_2O$ has been requested from the CSD of Cambridge Crystallographic Data Centre (CCDC) as a supplementary information file of publication.[42]

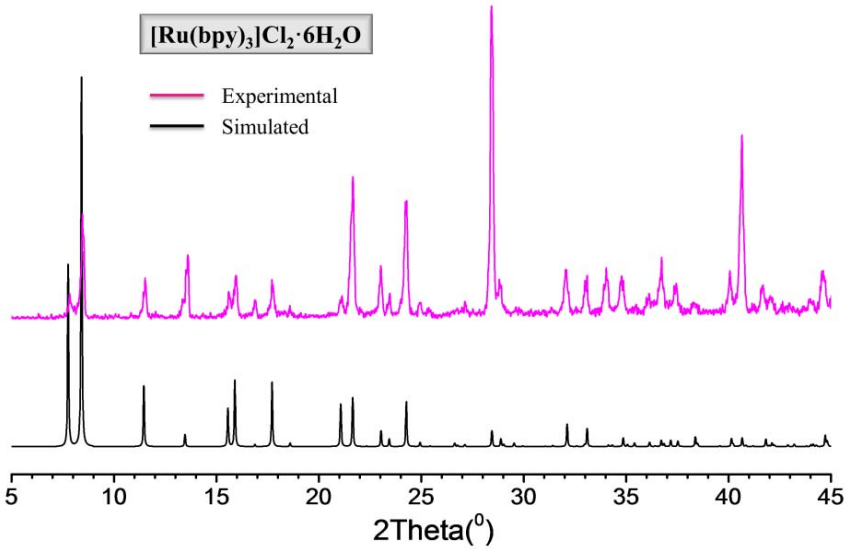

Figure 4.3.2.1 *Powder X-ray diffraction patterns of $[Ru(2,2´\text{-}bpy)_3]Cl_2\cdot 6H_2O$: experimental (red) and simulated (black).*

Figure 4.3.2.1 shows the experimental and simulated powder X-ray diffraction patterns for the as-synthesized and reported compound $[Ru(2,2´\text{-}bpy)_3]Cl_2\cdot 6H_2O$, and there are in a good agreement in Bragg reflections positions and their relative intensities, which subsequently indicates the phase purity and relates the pattern to the expected precursor compound. The slight difference in relative intensities of diffraction peaks is promoted by preferred orientation influence of plate-like crystals of the sample.

4.3.2.2. Infrared Spectroscopy

The solid state infrared spectrum of $[Ru(2,2´\text{-}bpy)_3]Cl_2\cdot 6H_2O$ (region 4000−400 cm^{-1}) is shown in Figure 4.3.2.2. The bands assignments summarized in the Table 4.3.2.2 are in a good agreement with bibliographic data.[12,30–32]

The observed bands are characteristic for tris-bipyridine complexes in low oxidation state. The strong broad absorption band between 3700 and 3100 cm^{-1} is attributed to the O−H symmetric and asymmetric vibrations of crystallization water molecules. An aromatic C–H stretching vibration of 2,2´-bpy ligands gives rise to a band at 3200–3000 cm^{-1} with weak-to-medium intensity and consists of a number of peaks. Interactions between rings C═C and C═N stretching vibrations result in two medium-to-strong absorptions.

Table 4.3.2.2 *Selected bands in the IR spectrum of compound [Ru(2,2´-bpy)$_3$]Cl$_2$·6H$_2$O.*

Spectral Region / Band Maximum	Band assignments
3700−3100 *bs*	ν_{sy} (O−H) + ν_{asy} (O−H) crystallization water
3200−3000 *w*	ν_{asy} (C−H) stretching
1660 *s*	δ_{sy} (O−H−O)
1615-1570*s* 1590−1575*m* 1520−1465*s* 1450−1410*m*	ν_{sy} (C═C) and/or ν_{sy} (C═N) ring str. vibration
1000−985*m*	δ (C−H) and/or C−H in-plane deformation vibrations.
780−750*ms*	δ (C−H) and/or C−H out-of-plane deformation vibrations

b broad; ***s*** strong; ***w*** weak; ***vw*** very weak and ***m*** medium

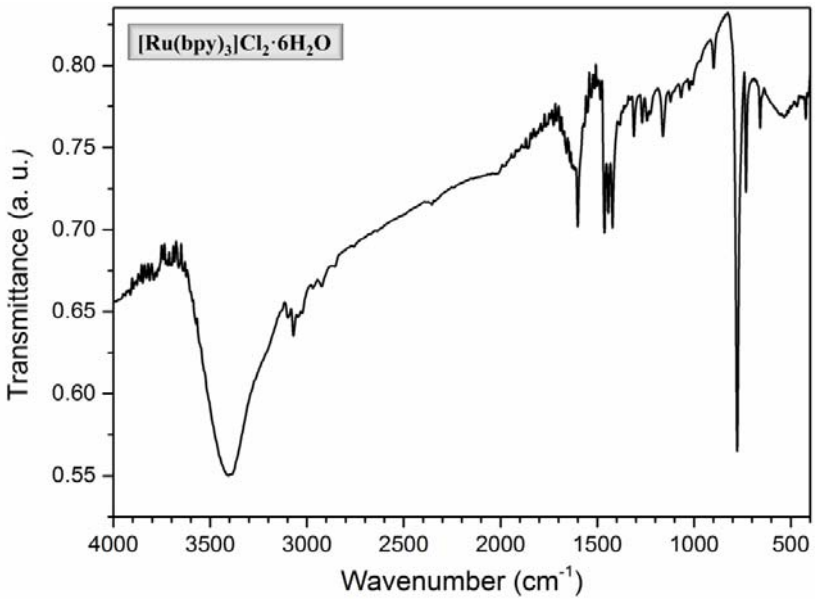

Figure 4.3.2.2 *Infrared spectrum of [Ru(2,2´-bpy)$_3$]Cl$_2$·6H$_2$O.*

These absorptions occur at 1750–1615 cm^{-1} and 1510–1365 cm^{-1}, a higher frequency band which often has another medium-intensity band on its low-frequency site is found at 1590–1555 cm^{-1}. Bands of variable intensities are observed in the regions 1300–1100 cm^{-1} and 1000–985 cm^{-1} where C–H ring deformation modes of the 2,2´-bpy ligand as expected. The 2,2´-bpy ligand strong adsorption bands at 780 and 750 cm^{-1}, are assigned to the aromatic out of plane hydrogen deformation modes.

4.3.2.3. Thermogravimetric Analysis

The thermogravimetric analysis (TGA) has been carried out for the synthesized [Ru(2,2´-bpy)$_3$]Cl$_2$·6H$_2$O with the objectives to determine amount of coordinated water molecules in the compound and confirm the sample purity. The thermogravimetric and corresponding derivative (dTG) curves of the precursor [Ru(2,2´-bpy)$_3$]Cl$_2$·6H$_2$O are shown in Figure 4.3.2.3. The data are in good agreement with the molecular formula and bibliographic data for analogous compounds.[33,43,44]

(43) A. Bujewski, M. Walewski, K. Grzędzicki, J. Dobrowolski, *Thermochim. Acta,* **1990**, *159*, 247–254.

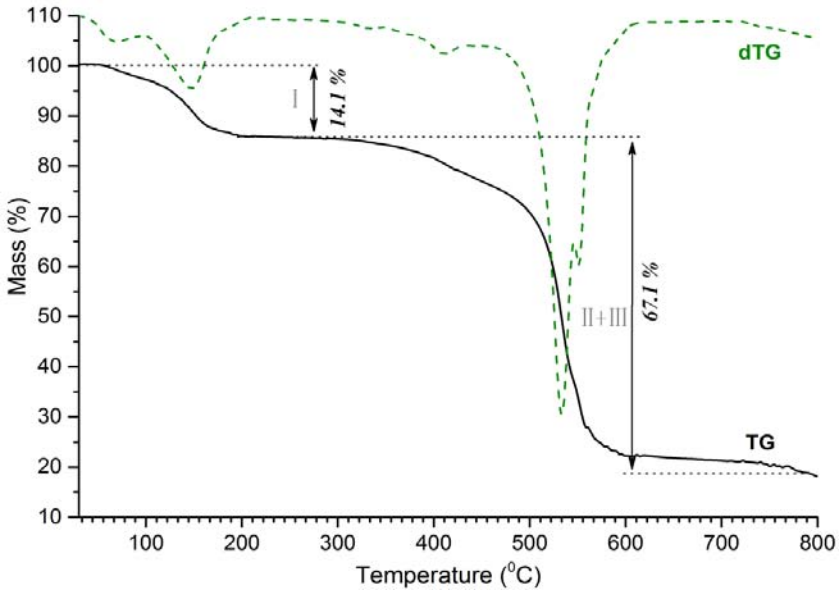

Figure 4.3.2.3 *TG, dTG profiles for thermal decomposition of [Ru(2,2´-bpy)$_3$]Cl$_2$·6H$_2$O under an air atmosphere*.

The TG-dTG curves exhibit several steps. Dehydration processes for the complex occurs in the region 30–200 °C and proceeds in two continuous steps (I). The most intense dTG maxima for these processes are at about 80 and 160 °C, and together correspond to a 14.1% mass loss (*calc*. 14.43%) and relate to losing of 6 molecules of crystallization water. The anhydrous compound [Ru(2,2´-bpy)$_3$]Cl$_2$ is stable up to 300 °C. Thermal decomposition of [Ru(2,2´-bpy)$_3$]Cl$_2$ begins above 300 °C and proceeds in two steps II and III, with the maximum of dTG peak at 400 °C. Rapid decomposition, associated with combustion of the sample, begins at 450 °C. Combustion of an organic product of decomposition proceeds to 600 °C and is accompanied by a total mass loss of 67.1% (*calc*. 67.8%) and reaches the maximum velocity at 530 °C.

Theoretical calculation based on the chemical formula match with the experimental losses during the steps (II) and (III) and might be attributed to the combustion of an organic part of molecule and a liberation of an oxidized gaseous form of chlorine. The final product of the decomposition of [Ru(2,2´-bpy)$_3$]Cl$_2$·6H$_2$O under an air atmosphere is RuO$_2$.

4.3.2.4. Solid State UV-VIS Spectroscopy

The ruthenium(II) complex [Ru(2,2´-bpy)$_3$]$^{2+}$ is considered to be a typical low-spin complex having a $^1A_1$ ($t_{2g}^5e_g^1$) ground state with all six *d* electrons paired up in the t_{2g} orbitals.[34] The room temperature diffuse-reflectance UV-Vis spectra of synthesized [Ru(2,2´-bpy)$_3$]Cl$_2$·6H$_2$O complex is illustrated in the Figure 4.3.2.4. The absorption bands intensity and their positions are quite similar with bibliographic values reported for [Ru(2,2´-bpy)$_3$]$^{2+}$ complex,[20,34,35,37,38,40,45–47] that indicate the phase purity and consistence of synthesized product with expected precursor.

The absorption spectrum of this complex is dominated by two groups of intense high-energy bands: (*i*) well defined bands in the region 200–280 nm appear to be π→π* intraligand transitions; (*ii*) the sharp peak ranging from 320 nm to 620 nm is basically a charge transfer band

(44) H. Warachim, A. Bujewski, *J. Therm. Anal*., **1984**, *29*, 1001–1004.
(45) S. Choudhury, A. K. Deb, S. Goswami, *J. Chem. Soc. Dalton. Trans.*, **1994**, 1305–1310.
(46) D. M. Klassen, G. A. Crosby, *J. Chem. Phys.*, **1968**, *48*, 1853–1858.
(47) B. Durham, J. V. Caspar, J. K. Nagle, T. J. Meyer, *J. Am. Chem. Soc*., **1982**, *104*, 4803–4810.

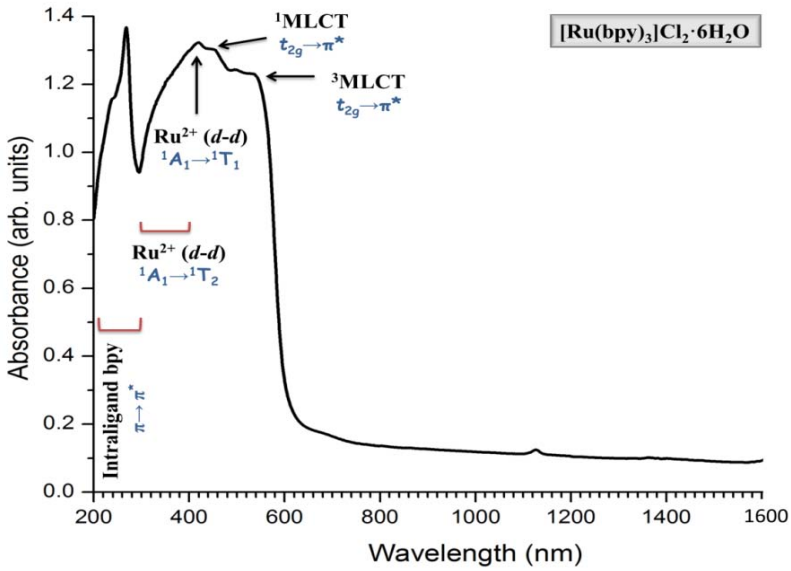

Figure 4.3.2.4 *The room temperature diffuse reflectance UV-VIS spectrum of [Ru(2,2´-bpy)$_3$]Cl$_2$·6H$_2$O.*

which partially masks the *d–d* transition. There several components have been resolved: the shoulder between 320–400 belongs to *d–d* transition $^1A_1 \rightarrow {}^1T_2$; the peak at 450 nm is attributed to $^1A_1 \rightarrow {}^1T_1$ transition. Moreover, the shoulder centered at 490 nm has been assigned to $t_{2g} \rightarrow \pi^*$ metal-ligand charge transfer (MLCT) transition, while the broad shoulder observed at 560 nm is belongs to the spin-forbidden third $t_{2g} \rightarrow \pi^*$ metal-ligand charge transfer (^{3}MLCT) transition. The last one has been observed and confirmed by several works.[39,40]

4.4. [Fe(2,2´-bpy)$_3$](ClO$_4$)$_2$

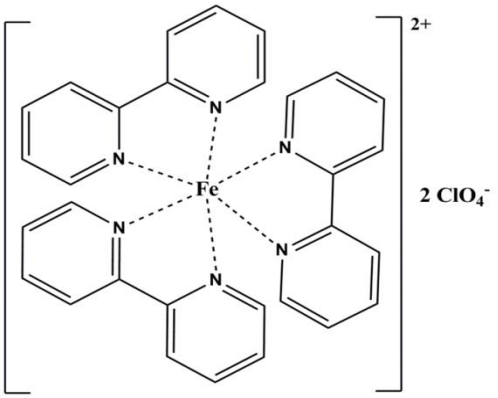

Systematic name	Tris(2,2´-Bipyridine)Iron(II) Perchlorate		
Molecular Formula	$C_{30}H_{24}Cl_2FeN_6O_8$		
Molecular Weight	723.38 g/mol	**Appearance**	Dark red solid
CAS №	15388-48-4	**Boiling point**	372.5 ºC (atm)
Solubility	water, acetone, ethanol, methanol	**Flash Point**	137.2 ºC

4.4.1. Synthesis

Materials: Commercial Iron sulfate heptahydrate ($FeSO_4 \cdot 7H_2O$) 98% reagent grade was obtained from VWR International S.A.S; 2,2´-bipyridine ($C_{10}H_8N_2$) 99% reagent grade from Sigma-Aldrich; Potassium perchlorate ($KClO_4$) 99% reagent grade from Sigma-Aldrich.

Synthetic procedure. Compound $[Fe(2,2´\text{-bpy})_3](ClO_4)_2$ has been synthetized following procedure described previously.[48,49] The 2,2´-bipyridine (2.32 g, 14.88 mmol), dissolved in hot distillated water (50 mL), was treated with excess of $FeSO_4 \cdot 7H_2O$ (4.17 g, 15.0 mmol) and potassium perchlorate $KClO_4$ (12.1 g, 87.3 mmol). The red solution was heated on the water-bath for one hour and then left cooling to room temperature, and, after on the ice-bath several hours until precipitation of plate-like red crystals of the complex. The red crystalline perchlorate was separated by filtration, well washed with ice cold distillated water, and dried in vacuum. The yield is 6.03 g (56%).

Elemental analysis. Anal. Calculated for $C_{30}Cl_2H_{24}FeN_6O_8$: C, 49.81%; H, 3.34%; N, 11.61%. Found: C, 49.4%; H, 3.4%; N, 11.6%.

4.4.2. Identification Procedures

4.4.2.1. Powder X-ray Diffraction

The crystal structure of $[Fe(2,2´\text{-bpy})_3](ClO_4)_2$ was reported previously.[50] The compound crystallizes in monoclinic *C*2/*c* space group with a unit cell parameters: a = 17.0545(10) Å, b = 10.5812(6) Å, c = 15.9456(7) Å, $\alpha = \gamma = 90°$, β = 91.332(6)°, V = 2876.7(3) Å^3, Z = 4. The published crystallographic parameters[50] are summarized in Table 4.4.2.1.

Table 4.4.2.1 *Crystallographic parameters for $[Fe(2,2´\text{-bpy})_3](ClO_4)_2$.*[50]

Molecular formula	$C_{30}H_{24}Cl_2FeN_6O_8$
Formula Weight, g·mol^{-1}	723.30
Crystal system	monoclinic
Space group	*C*2/*c*
Cell dimensions	
a, Å	17.0545(10)
b, Å	10.5812(6)
c, Å	15.9456(7)
α, ^{0}	90
β, ^{0}	91.332(6)
γ, ^{0}	90
V, Å^3	2876.7(3)
Z	4
Density, g·cm^{-3}	1.670
Absorption coefficient, mm^{-1}	0.776
Radiation	Mo Kα, λ = 0.71069 Å

The molecular structure of $[Fe(2,2´\text{-bpy})_3](ClO_4)_2$ is made of $[Fe(2,2´\text{-bpy})_3]^{2+}$ cationic units and perchlorate anions. The $[Fe(2,2´\text{-bpy})_3]^{2+}$ entities exhibit a quasi D_3 symmetry. The six-coordinated nitrogen atoms of three bpy ligands form a distorted octahedron around the Fe(II) center. The Fe^{II}–N bonds length are in the range of 1.953(3)–1.972(3) Å with the average value of 1.965 Å, which are consistent with those in the other compounds[42,51] and significantly longer

(48) F. H. Burstall, R. S. Nyholm, *J. Chem. Soc*., **1952**, 3570−3579.
(49) D. A. Thornton, G. M. Watkins, *J. Coord. Chem*., **1992**, *25*, 299−315.
(50) K. R. Batten, K. S. Murray, N. J. Sinclair, *Acta Crystallogr.*, **2000**, *C56*, e320−e320.
(51) P. C. Healy, B. W. Skelton, A. H. White, *Aust. J. Chem*., **1983**, *36*, 2057–2064.

than those found for $[Fe(2,2´\text{-bpy})_3]^{3+}$.[52] The N–$Fe^{II}$–N bond angles in the precursor compound are in the 81.2–96.1° range.

In order to confirm the structural consistency between the synthesized precursor compound and the expected complex $[Fe(2,2´\text{-bpy})_3](ClO_4)_2$, the experimental powder pattern of obtained deep red solid was compared with the simulated powder pattern from reported single crystal data.[50] The CIF of $[Fe(2,2´\text{-bpy})_3](ClO_4)_2$ has been requested with the depositional number of IUC0000176 from the CSD of Cambridge Crystallographic Data Centre (CCDC).

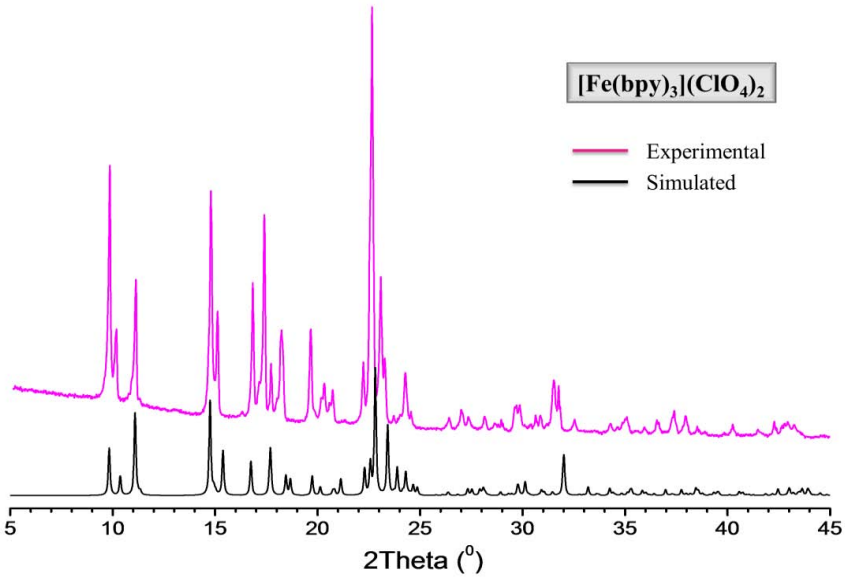

Figure 4.4.2.1 *Powder X-ray diffraction patterns of $[Fe(2,2´\text{-bpy})_3](ClO_4)_2$: experimental (red) and simulated (black).*

Figure 4.4.2.1 shows the experimental and simulated powder X-ray diffraction patterns for as-synthesized and reported compound $[Fe(2,2´\text{-bpy})_3](ClO_4)_2$, which are in a good agreement to each other exhibiting very similar sequences of Bragg reflections along with their relative intensities, indicate the phase purity and consistence with the expected precursor compound.

4.4.2.2. Infrared Spectroscopy

The solid state infrared spectrum of $[Fe(2,2´\text{-bpy})_3](ClO_4)_2$ in the region 4000−400 cm^{-1} is shown in Figure 4.4.2.2. The bands assignments summarized in the Table 4.4.2.2 are in good agreement with bibliographic data.[12,30–32,49,53,54]

The observed bands are characteristic for tris-bipyridine complexes of transition metals in low oxidation state. The spectrum of $[Fe(2,2´\text{-bpy})_3](ClO_4)_2$ consists of a relatively small number of absorption bands which may be assigned as follows: the broad absorption band in the region 3650–3200 cm^{-1} caused by asymmetric and symmetric H–O–H stretching vibrations is assigned to physically adsorbed water molecules; the aromatic C–H stretching vibration of 2,2´-bpy ligands gives rise to a band at 3150−2830 cm^{-1} with weak-to-medium intensity and consists of a few peaks. Interactions between rings C═C and C═N stretching vibrations result in two medium-to-strong absorptions.

(52) B. N. Figgis, B. V. Skelton, A. H. White, *Aust. J. Chem.*, **1978**, *31*, 57–64.
(53) R. G. Inskeep, *J. Inorg. Nucl. Chem.*, **1962**, *24*, 763–776.
(54) D. H. Busch, J. C. Bailar, *J. Am. Chem. Soc.*, **1956**, *78*, 1137–1142.

Table 4.4.2.2 *Selected bands in the IR spectrum of compound* $[Fe(bpy)_3](ClO_4)_2$.

Spectral Region / Band Maximum	Band assignments
3650−3200 *bvw*	ν_{sy} (O−H) + ν_{asy} (O−H) or hydrogen bonding
3150−2830 *w*	ν_{asy} (C−H) stretching
1660 *s*	δ_{sy} (O−H−O)
1645-1550*ms*	
1590−1575*m*	ν_{sy} (C═C) and/or ν_{sy} (C═N)
1500−1450*ms*	ring str. vibration
1450−1410*m*	
1100−1090*s*	ν(Cl−O) and/or δ (Cl−O) of ClO_4^- uncoordinated
1000−985*m*	δ (C−H) and/or C−H in-plane deformation vibrations.
780−750*ms*	δ (C−H) and/or C−H out-of-plane deformation vibrations

b broad; ***s*** strong; ***w*** weak; ***vw*** very weak and ***m*** medium

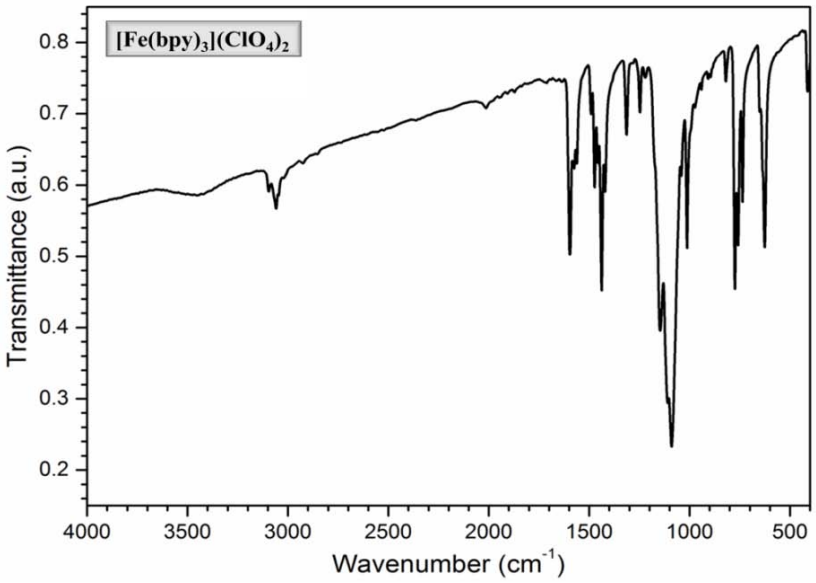

Figure 4.4.2.2 *Infrared spectrum of* $[Fe(2,2´\text{-}bpy)_3](ClO_4)_2$.

These absorptions occur at 1645–1550 cm^{-1} and 1500–1450 cm^{-1}, the higher frequency band which often has another medium-intensity band on its low-frequency site is found at 1590–1555 cm^{-1}. A bands of variable intensities are observed in the regions 1350–1200 cm^{-1} and 1000–885 cm^{-1} where C−H ring deformation modes of the 2,2´-bpy ligand are expected. The 2,2´-bpy ligand strong adsorption bands at 780 and 750 cm^{-1} were assigned to the aromatic out of plane hydrogen deformation modes. Furthermore, the spectra exhibit very strong single absorption bands associated with uncoordinated ClO_4^- anion at 1098 cm^{-1} and 1100−1090 cm^{-1}, respectively.

4.4.2.3. Thermogravimetric Analysis

The thermogravimetric analysis (TGA) has been carried out under an air atmosphere for the synthesized $[Fe(2,2´\text{-}bpy)_3](ClO_4)_2$ with the objectives to confirm the sample purity. The thermogravimetric and corresponding derivative (dTG) curves of the precursor $[Fe(2,2´\text{-}bpy)_3](ClO_4)_2$ are shown in Figure 4.4.2.3. Due to high explosive nature of perchlorate salts, its thermal decomposition data are rarely reported in bibliography. The thermal decomposition behavior of $[Fe(2,2´\text{-}bpy)_3](ClO_4)_2$ was investigated.

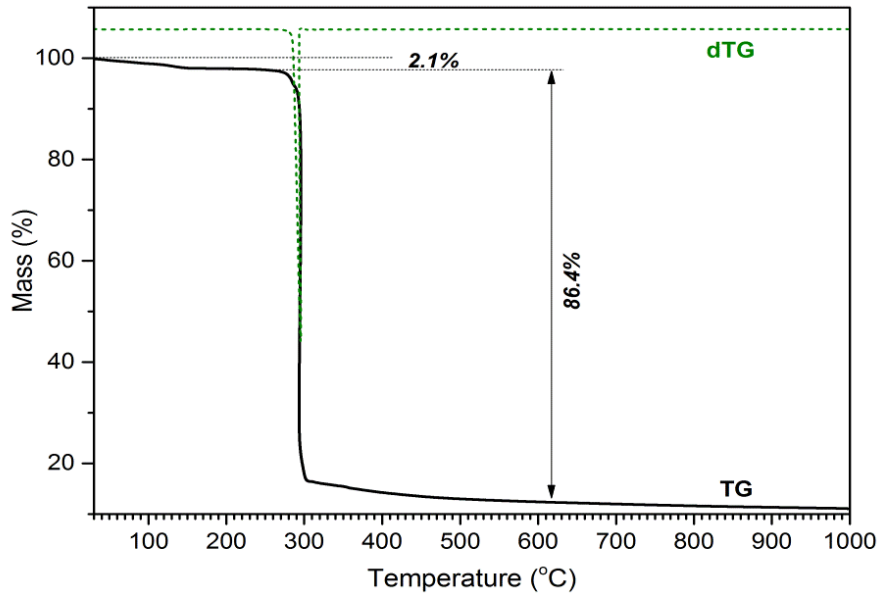

Figure 4.4.2.3 *TG, dTG profiles for thermal decomposition of [Fe(2,2´-bpy)$_3$](ClO$_4$)$_2$ under an air atmosphere*.

Thermal investigation along with X-ray diffraction data indicate that complex [Fe(2,2´-bpy)$_3$](ClO$_4$)$_2$ is anhydrous with some amount of absorbed humidity. According to TG data the weight percent of adsorbed humidity is ~ 2%. The TG and dTG profiles of thermal decomposition of [Fe(2,2´-bpy)$_3$](ClO$_4$)$_2$ are characterized by explosive combustion at 300 ºC with total mass loss of 86.4%. This phenomenon was caused by the strong oxidizing property of ClO_4^- anion. The solid residue formed at around 500 °C is suggested to be Fe_2O_3 (remaining weight 11.1%, Calcd.: 11.05%).

4.4.2.4. Solid State UV-VIS Spectroscopy

The iron(II) complex [Fe(2,2´-bpy)$_3$]$^{2+}$ is considered to be a typical low-spin complex having a $^1A_1$ ($t_{2g}^5e_g^1$) ground state with all six *d* electrons paired up in the t_{2g} orbitals.[20,34] The room temperature diffuse-reflectance UV-VIS spectra of synthesized [Fe(2,2´-bpy)$_3$](ClO$_4$)$_2$ complex are illustrated in the Figure 4.4.2.4., and the band maxima assignments are summarized in the Table 4.4.2.4. The absorption bands intensity and their positions are quite similar to bibliographic values reported for [Fe(2,2´-bpy)$_3$]$^{2+}$ complex,[35,37,54–58] and indicates the phase purity and consistence of the synthesized product with the expected precursor.

The absorption spectrum of this complex is dominated by three intense high-energy bands in the region 200−300 nm appear to be π→π* intraligand transitions. The sharp band that in fact is aggrupation of three π→e_g* ligand-metal charge transfer (LTMC) bands were observed in the region 310−450 nm. The strong band centered at 530 nm has been assigned to t_{2g}→π* metal-ligand charge transfer (MLCT) transition. This band has a characteristic shape, a sharp maximum and a prominent shoulder to lower wavelengths. The ligand-field strength for [Fe(2,2´-bpy)$_3$]$^{2+}$ complex is not far from the spin- crossover region, and ligand-field theory predicts a number of low-lying ligand-field states in addition to the MLCT state.

(55) R. R. Ruminski, J. D. Petersen, *Inorg. Chim. Acta*, **1984**, *88*, 63−66.
(56) R. R. Ruminski, J. D. Petersen, *Inorg. Chim. Acta*, **1985**, *97*, 129–134.
(57) A. Hauser, N. Amstutz, S. Delahaye, A. Sadki, S. Schenker, R. Sieber, M. Zerara, In *Optical Spectra and Chemical Bonding in Inorganic Compounds*; Vol.106: Structure and Bonding, Springer, Berlin, **2004**, 81–96.
(58) R. J. P. Williams, *J. Chem. Soc.*, **1955**, 137–145.

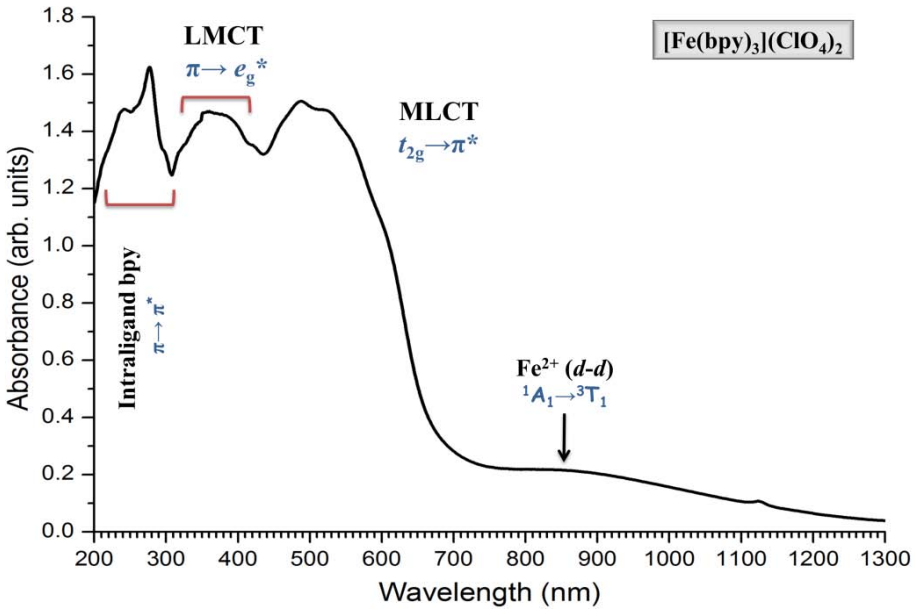

Figure 4.4.2.4 *The room temperature diffuse reflectance UV-VIS spectrum of [Fe(2,2´-bpy)$_3$](ClO$_4$)$_2$.*

The octahedral field *d*−*d* transitions are grouped in order of increasing energy: $^1A_1 \rightarrow {}^3T_1$, $^1A_1 \rightarrow {}^3T_2$, $^1A_1 \rightarrow {}^1T_1$ and $^1A_1 \rightarrow {}^1T_2$. The corresponding *d*−*d* transitions are not directly observable in the absorption spectrum as their intensities are too low relative to the intense MLCT band. Hence, in visible region of the spectra the low energy broad band at 869 nm which is related to $^1A_1 \rightarrow {}^3T_1$ transition, is observed.

Table 4.4.2.4 *Electronic Absorption Spectra Band Assignment for Low Spin and High Spin [Fe(2,2´-bpy)$_3$](ClO$_4$)$_2$ Complexes.*

Spin state / Complex	λ_{max}, nm	ε_{max}, mol^{-1}·cm^{-1}	Assignment [b]
Low Spin / $[Fe(bpy)_3]^{2+}$	246 (*sh*)	$46.5\cdot10^3$	Intraligand (π→π*)
	280	$77.1\cdot10^3$	Intraligand (π→π*)
	299	$66.2\cdot10^3$	Intraligand (π→π*)
	350(*sh*)	$36.0\cdot10^3$	LMCT (π→ e_g*)
	385	$37.0\cdot10^3$	LMCT (π→ e_g*)
	414(*sh*)	$35.6\cdot10^3$	LMCT (π→ e_g*)
	497	$27.0\cdot10^3$	MLCT (t_{2g}→ π*)
	521 (sh)	$25.0\cdot10^3$	MLCT (t_{2g}→ π*)
	869	4.2	$^1A_1 \rightarrow {}^3T_1$
High Spin / $[Fe(bpy)_3]^{2+}$	260 (*sh*)	$30.4\cdot10^3$	Intraligand (π→ π*)
	306	$37.1\cdot10^3$	Intraligand (π→ π*)
	317	$33.7\cdot10^3$	Intraligand (π→ π*)
	350−415	~$37.0\cdot10^3$	LMCT (π→ e_g*)
	490−530	~$27.0\cdot10^3$	MLCT (t_{2g}→ π*)
	917	$2.3\cdot10^3$	$^5T_{2g} \rightarrow {}^5E_g$

sh: shoulder band; [b] The bands assignment following the bibliographic data [35,37,57,59]

However, the $[Fe(2,2´\text{-}bpy)_3]^{2+}$ complex have been found in high spin state. The absorption spectra of high spin form exhibit significant differences compared to low spin form. The high spin complex in octahedral environment has $^5T_{2g}$ ($t_{2g}^4e_g^2$) ground sate, and for it was predicted

(59) R. D. Hancock, G. J. McDougall. *J. Chem. Soc., Dalton*, **1977**, 67−70.

singlet-singlet transition to ^5E_g state that usually separated as a result of Jahn–Teller distortion. The absorption spectrum of high spin $[Fe(2,2´\text{-bpy})_3]^{2+}$ complex exhibit one broad characteristical band at 917 nm corresponding to spin allowed $^5T_{2g} \rightarrow {}^5E_g$ transition.
The band maxima assignments basing on bibliographic data for high spin complex are summarized in the Table 4.4.2.4. From our results and basing on data from Table 4.4.2.4 it is reasonable to conclude that synthetized precursor belongs to low spin $[Fe(2,2´\text{-bpy})_3](ClO_4)_2$ complex.

4.5. $[Os(2,2´\text{-bpy})_3](PF_6)_2$

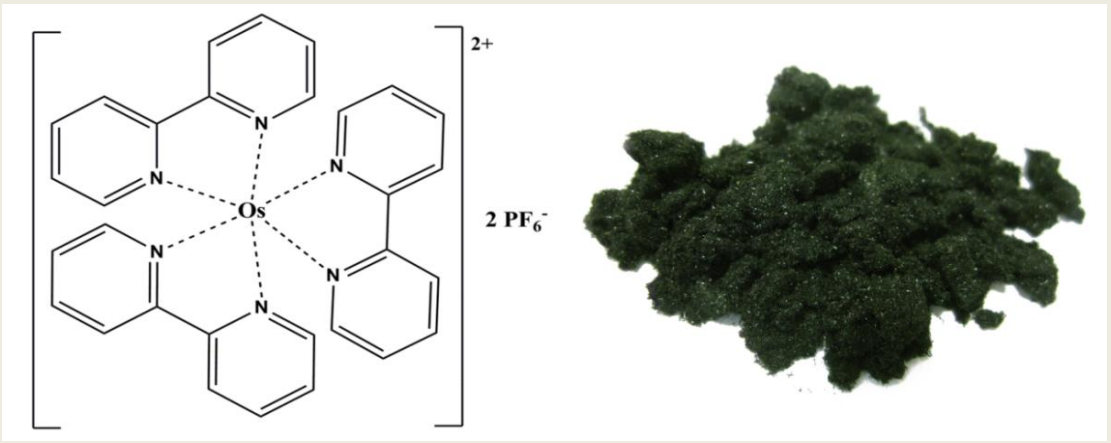

Systematic name	Tris(2,2´-Bipyridine)Osmium (II) Bis(Hexafluorophosphate)		
Molecular Formula	$C_{30}F_{12}H_{24}N_6OsP_2$		
Molecular Weight	948.66 g/mol	**Appearance**	Dark green solid
CAS №	75441-79-1	**Boiling point**	284.3 ºC (atm)
Solubility	acetone, ethanol, methanol	**Flash Point**	117.2 ºC

4.5.1. Synthesis

Materials: Commercial $OsCl_3 \cdot xH_2O$ was obtained from Johnson Matthey; 2,2´-bipyridine ($C_{10}H_8N_2$) 99% reagent grade from Sigma-Aldrich; Ethylene glycol ($C_2H_6O_2$) 99.8% chemical grade from VWR International S.A.S; Ammonium hexafluorophosphate (NH_4PF_6) 99.99 % trace metals basis from Sigma-Aldrich; Acetone (C_3H_6O) 99.9% analytical grade from VWR International S.A.S.; Diethyl ether ($(CH_3CH_2)_2O$) 98.0% reagent grade from VWR International S.A.S.
Commercial $OsCl_3 \cdot xH_2O$ is dried in an oven at 120 °C for 4 hours. It is then finely ground in a mortar and returned to the oven for the further 1 hour prior to use.

Synthetic procedure. Compound $[Os(2,2´\text{-bpy})_3](PF_6)_2$ has been synthetized following procedure described previously.[60,61] "Dried" $OsCl_3$ (1.0 g, 3.35 mmol) and 2,2´-bipyridine (1.57 g, 10.05 mmol) were added to 50 mL of ethylene glycol and refluxed under nitrogen flow for 48 h. 50 mL of NH_4PF_6 aqueous solution was added to resulted cold dark solution to precipitate the PF_6^- salt. Immediately, the dark green precipitate started to appear, and the solution was reposed into ice-cold bath for 1 h. The resulting dark green fine needle-like crystals were firstly filtered, washed with small portions of ace-cold water, and after, recrystallized three times from acetone/ether mixture, washed with ether and air-dried. The yield was 2.98 g (94%).

(60) J. G. Gaudiello, P. G. Bradley, K. A. Norton, W. H. Woodruf, A. J. Bard, *Inorg.Chem.*,**1984**, *23*, 3–10.
(61) F. H. Burstall, F. P. Dwyer, E. C. Gyarfas, *J. Chem. Soc*., **1950**, 953−955.

Elemental analysis. Anal. Calculated for $C_{30}F_{12}H_{24}N_6OsP_2$: C, 37.98%; H, 2.55%; N, 8.86%. Found: C, 38.0%; H, 2.4%; N, 8.9%.

4.5.2. Identification Procedures

4.5.2.1. Powder X-ray Diffraction

The crystal structure of $[Os(2,2´\text{-bpy})_3](PF_6)_2$ was reported previously.[62,63] The compound crystallize in hexagonal *P*-3*c* space group with a unit cell parameters: a = 10.790(3) Å, b = 10.790(3) Å, c = 16.365(4) Å, α = β = 90°, γ = 120°, V = 1650.0(12) Å^3, Z = 2. The published crystallographic parameters are summarized in Table 4.5.2.1.

Table 4.5.2.1 *Crystallographic parameters for $[Os(2,2´\text{-bpy})_3](PF_6)_2$.* [62,63]

Molecular formula	$C_{30}H_{24}F_{12}N_6OsP_2$
Formula Weight, g·mol^{-1}	948.72
Crystal system	hexagonal
Space group	*P*-3*c*
Cell dimensions	
a, Å	10.790(3)
b, Å	10.790(3)
c, Å	16.365(4)
α, ^{0}	90
β, ^{0}	90
γ, ^{0}	120
V, Å^3	1650.0(12)
Z	2
Density, g·cm^{-3}	1.910
Absorption coefficient, mm^{-1}	4.062
Radiation	Mo Kα, λ = 0.71073 Å

The crystal structure of $[Os(2,2´\text{-bpy})_3](PF_6)_2$ is composed of discrete $[Os(2,2´\text{-bpy})_3]^{2+}$ cations and hexafluorophosphate anions. The Os(II) atom is surrounded by six N atoms from three chelating bpy ligands on D_3 manner forming octahedral coordination environment with Os–N bond length of 2.062(4) Å, which are consistent with those in the other compounds,[64,65] a slightly shorter than in $[Os(2,2´\text{-bpy})_3]^{+}$ unit (mean 2.079(1) Å)[66] and $[Os(2,2´\text{-bpy})_3]^{3+}$ unit (mean 2.078(1) Å).[64] The N–Os^{II}–N *trans* bond angle in the precursor compound is 172.4(2)°, the N–Os^{II}–N bite angles of 77.9(2)°, and remained N–Os^{II}–N angles ranging from 89.3(2)° to 96.6(2)°. The ordered PF_6^- anions locate on sites of three fold (C_3) symmetry with average bond distances of 1.566(8) Å. In the crystal packing are no significant intermolecular contacts between the $[Os(2,2´\text{-bpy})_3]^{2+}$ cations and PF_6 anions. In order to confirm the structural consistency between the synthesized precursor compound and the expected complex $[Os(2,2´\text{-bpy})_3](PF_6)_2$, the experimental powder pattern of obtained dark green solid was compared with the simulated

(62) E. C. Constable, P. R. Raithby, D. N. Smit, *Polyhedron,* **1989**, *8*, 367–369.
(63) M. M. Richter, B. Scott, K. J. Brewer, R. D. Willett, *Acta Cryst*., **1991**, *C47*, 2443–2444.
(64) K. D. Demadis, D. M. Dattelbaum, E. M. Kober, J. J .Concepcion, J. J. Paul, T. J. Meyer, P. S. White, *Inorg. Chim. Acta,* **2007**, *360*, 1143–1153.
(65) J. Breu, C. Kratzer, H. Yersin, *J. Am. Chem. Soc.*, **2000**, *122*, 2548–2555.
(66) R. Ceron-Camacho, S. Hernandez, R. Le Lagadec, A. D. Ryabov, *Chem. Commun*., **2011**, *47*, 2823–2825.

powder pattern from reported single crystal data.[62,63] The CIF of $[Os(2,2´\text{-bpy})_3](PF_6)_2$ has been requested with the depositional codes of CSD KUFDOE, CSD KAZXUE01 from the CSD of Cambridge Crystallographic Data Centre (CCDC).

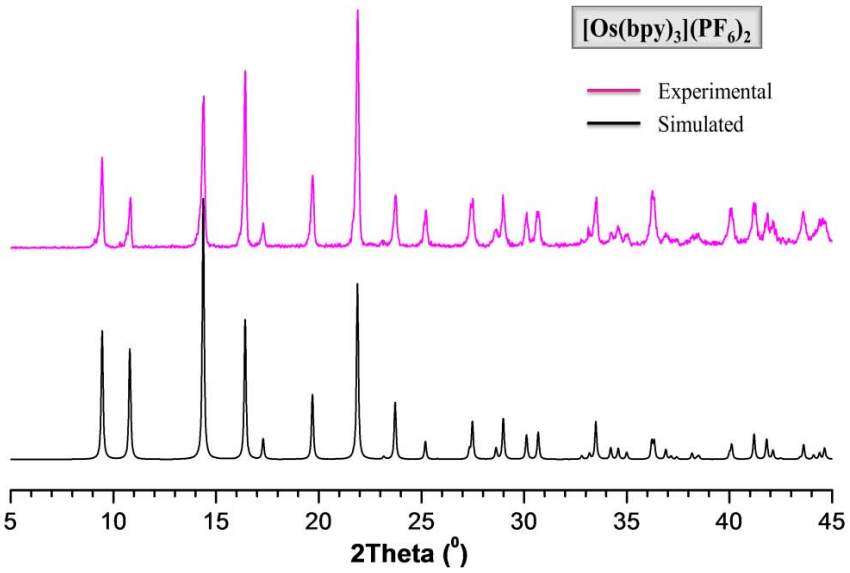

Figure 4.5.2.1 *Powder X-ray diffraction patterns of $[Os(2,2´\text{-bpy})_3](PF_6)_2$: experimental (red) and simulated (black).*

Figure 4.5.2.1 shows the experimental and simulated powder X-ray diffraction patterns for as-synthesized and reported compound $[Os(2,2´\text{-bpy})_3](PF_6)_2$, which are in a good agreement with each other exhibiting very similar sequences of Bragg reflections along with their relative intensities, indicate the phase purity and consistence with the expected precursor compound.

4.5.2.2. Infrared Spectroscopy

The solid state infrared spectrum of $[Os(2,2´\text{-bpy})_3](PF_6)_2$ in the region 4000−400 cm^{-1} is shown in Figure 4.5.2.2. The bands assignments summarized in the Table 4.5.2.2 are in a good agreement with bibliographic data.[12,30,31] The observed bands are characteristic for tris-bipyridine complexes of transition metals in low oxidation state.

Table 4.5.2.2 *Selected bands in the IR spectrum of compound $[Os(2,2´\text{-bpy})_3](PF_6)_2$.*

Spectral Region / Band Maximum	Band assignments
3600−3350 *bvw*	ν_{sy} (O−H) + ν_{asy} (O−H) or hydrogen bonding
3110−2980 *w*	ν_{asy} (C−H) stretching
1660 *s*	δ_{sy} (O−H−O)
1650-1550*ms* 1590−1555*m* 1510−1450*ms* 1450−1410*m*	ν_{sy} (C═C) and/or ν_{sy} (C═N) ring str. Vibration
1350−1150*m* 1000−850*m* 915*m*	δ (C−H) and/or C−H in-plane deformation vibrations.
850−840*vs* 750−745*m* 580−555*m*	ν(P−F) and/or δ (P−F) of PF_6^- uncoordinated
780−650*ms*	δ (C−H) and/or C−H out-of-plane deformation vibrations

b broad; ***s*** strong; ***w*** weak; ***vw*** very weak and ***m*** medium

The spectrum of $[Os(2,2´\text{-bpy})_3](PF_6)_2$ consists of a relatively small number of absorption bands which may be assigned as follows: the broad absorption band in the region 3600–3350 cm^{-1} caused by asymmetric and symmetric H–O–H stretching vibrations is assigned to physically adsorbed water molecules; the aromatic C–H stretching vibration of 2,2´-bpy ligands gives rise to a band at 3110−2980 cm^{-1} with weak-to-medium intensity and consists of a number of peaks.

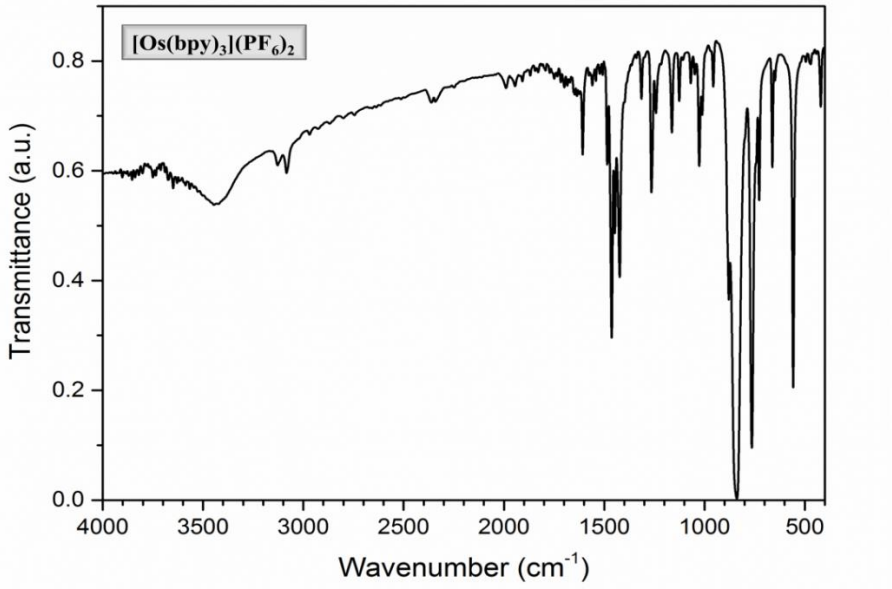

Figure 4.5.2.2 *Solid State Infrared Spectrum of $[Os(2,2´\text{-bpy})_3](PF_6)_2$.*

Interactions between rings C═C and C═N stretching vibrations results in two medium-to-strong absorptions. These absorptions occur at 1650–1550 cm^{-1} and 1510–1450 cm^{-1}, the higher frequency band which often has another medium-intensity band on its low-frequency site is found at 1590–1555 cm^{-1}. A bands of variable intensities are observed in the regions 1350–1150 cm^{-1} and 1000–850 cm^{-1} where C−H ring deformation modes of the 2,2´-bpy ligand were expected. The 2,2´-bpy ligand strong adsorption bands at 780 and 650 cm^{-1}, assigned to the aromatic out of plane hydrogen deformation modes. Furthermore, the spectra exhibit several very strong series of absorption bands associated with uncoordinated PF_6^- anion at 915 cm^{-1}, 850−840 cm^{-1}, 750−745 cm^{-1} and 580−555 cm^{-1}, respectively.

4.5.2.3. Thermogravimetric Analysis

The thermogravimetric analysis (TGA) has been carried out under an air atmosphere for the synthesized $[Os(2,2´\text{-bpy})_3](PF_6)_2$ with objectives to confirm the sample purity. The thermogravimetric and corresponding derivative (dTG) curves of the precursor $[Os(2,2´\text{-bpy})_3](PF_6)_2$ are shown in Figure 4.5.2.3. The data are in a good agreement with molecular formula. Thermal investigation along with X-ray diffraction data indicated that complex $[Os(2,2´\text{-bpy})_3](PF_6)_2$ is anhydrous with some amount of absorbed humidity. According to TG data the weight percent of adsorbed humidity is ~ 3%. The precursor compound is stable up to 380 °C, after that temperature decomposes gradually.

The decomposition profile of $[Os(2,2´\text{-bpy})_3](PF_6)_2$ shows the three continuous overplayed stages occurring during heating from 30 °C to 1000 °C. The continuous first, second and third stages take place in the range 390–600 °C with total mass loss of 77.4% reaching the maxima velocity at 420, 462 and 531 °C, respectively. The experimental mass loss of 77.4% is consistent with the calculated value 77.6% and attributed to the stepwise removing three 2,2´-bpy and two

hexafluorophosphine molecules. The solid residue formed at around 700 °C is suggested to be OsO_2 (remaining weight 21.4%, Calcd.: 23.3%).

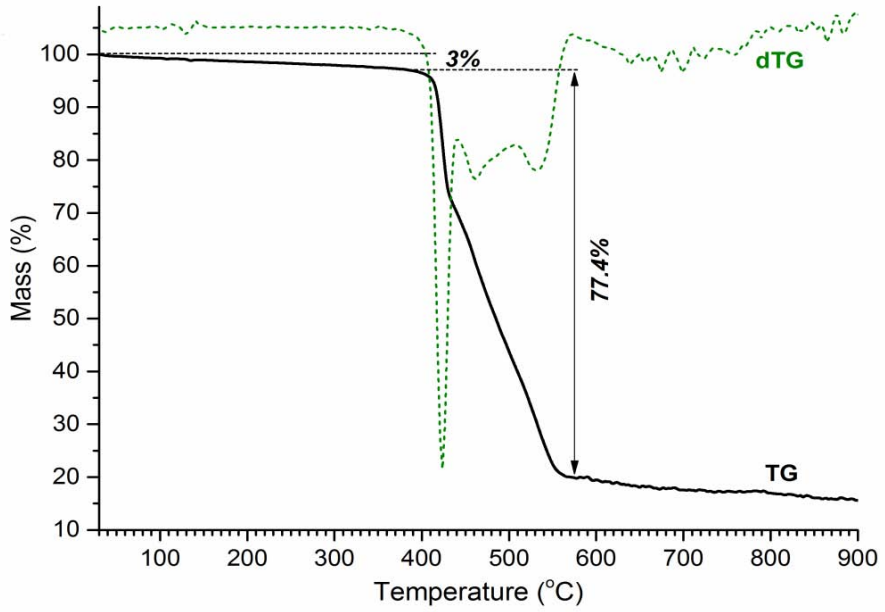

Figure 4.5.2.3 *TG, dTG profiles for thermal decomposition of [Os(2,2´-bpy)$_3$](PF$_6$)$_2$ under an air atmosphere.*

4.5.2.4. Solid State UV-VIS Spectroscopy

The osmium(II) complex $[Os(2,2´\text{-bpy})_3]^{2+}$ is considered a typical low-spin complex having a $^1A_1$ ($t_{2g}^5e_g^1$) ground state with all six *d* electrons paired up in the t_{2g} orbitals.[34] The room temperature diffuse-reflectance UV-Vis spectra of synthesized $[Os(2,2´\text{-bpy})_3](PF_6)_2$ complex are illustrated in the Figure 4.5.2.4.

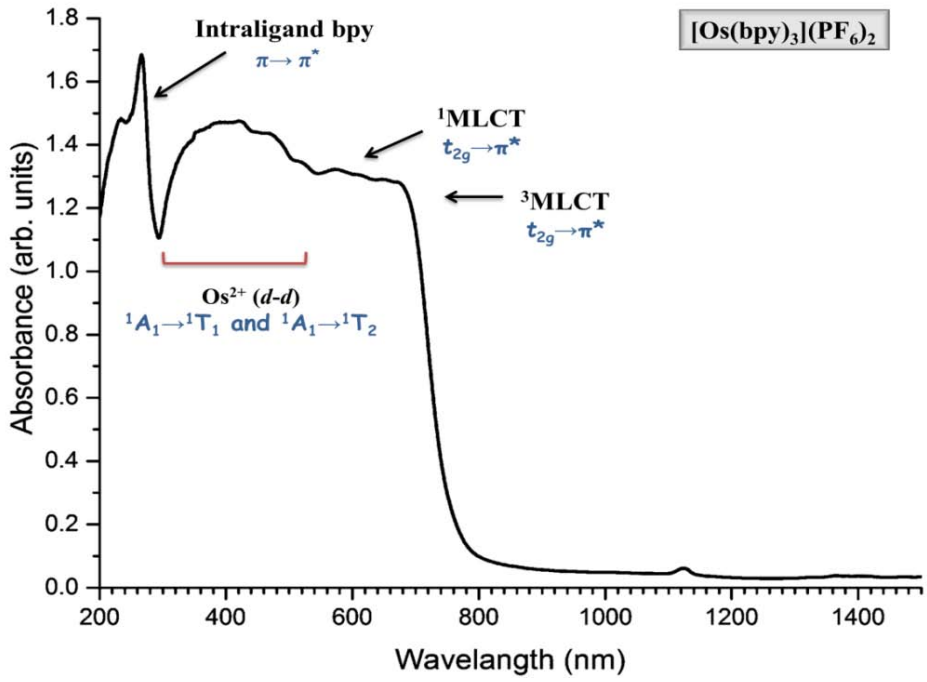

Figure 4.5.2.4 *The room temperature diffuse reflectance UV-VIS spectrum of [Os(2,2´-bpy)$_3$](PF$_6$)$_2$.*

reported for $[Os(2,2´\text{-bpy})_3]^{2+}$ complex,[20,34,35,38,40,61,67,68] that indicates the phase purity and consistence of the synthesized product with the expected precursor.

The absorption spectrum of this complex is dominated by three groups of bands: (*i*) well defined bands in the region 200–300 nm appear to be π→π* intraligand transitions; (*ii*) the sharp peak in the visible region that located from 300 nm to 560 nm and consists of $^1A_1 \rightarrow {}^1T_2$ and $^1A_1 \rightarrow {}^1T_1$ *d–d* transition; the broad shoulder centered from 560 nm to 800 nm has been assigned to $t_{2g} \rightarrow \pi^*$ metal-ligand charge transfer (MLCT) transition along with the spin-forbidden third $t_{2g} \rightarrow \pi^*$ metal-ligand charge transfer (^{3}MLCT) transition observed by several authors.[40,68]
It is reasonable to conclude that the bands are at lower energy for $[Os(2,2´\text{-bpy})_3]^{2+}$ complex compared to related $[Ru(2,2´\text{-bpy})_3]^{2+}$ complex, what's caused by being of the t_2 orbitals of osmium(II) at higher energies than those of ruthenium(II).

4.6. $[Co(2,2´\text{-bpy})_3](ClO_4)_2$

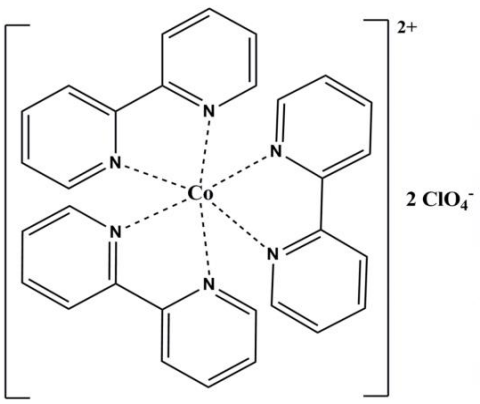

Systematic name	**Tris(2,2´-Bipyridine)Cobalt(II) Perchlorate**		
Molecular Formula	**$C_{30}H_{24}Cl_2CoN_6O_8$**		
Molecular Weight	**726.39 g/mol**	**Appearance**	**Dark yellow solid**
CAS №	**21349-81-5**	**Boiling point**	**272.5 ºC (atm)**
Solubility	**water, acetone, ethanol**	**Flash Point**	**107.2 ºC**

4.6.1. Synthesis

Materials: Commercial cobalt chloride hexahydrate ($CoCl_2 \cdot 6H_2O$) 98% reagent grade was obtained from VWR International S.A.S; 2,2´-bipyridine ($C_{10}H_8N_2$) 99% reagent grade from Sigma-Aldrich; potassium perchlorate ($KClO_4$) 99% reagent grade from Sigma-Aldrich; Ethanol (C_2H_5OH) 96% v/v analytical grade from VWR International S.A.S.

Synthetic procedure: Compound $[Co(2,2´\text{-bpy})_3](ClO_4)_2$ has been synthetized following procedure described previously.[48,49] The filtered solution of cobalt chloride hexahydrate (3.0 g, 0.013 mol) in ethanol (10 mL) was, boiled to remove air, and treated with 2,2´-bipyridine (6.1 g, 0.039 mol) in hot ethanol (20 mL), the solution became brown. Carbon dioxide was passed into the mixture, which was then diluted with air-free distillated water (10 mL), and excess of potassium perchlorate was added. After 15 minutes in ace, the plate-like yellow-brown crystals

(67) E. M. Kober, B. P. Sullivan, W. J. Dressick, J. V. Caspar, T. J. Meyer, *J. Am. Chem. Soc.*, **1980**, *102*, 7385–7387.
(68) F. Barigelletti, L. De Cola, V. Balzani, R. Hage, J. G. Haasnoot, J. Reedijk, J. G. Vos, *Inorg. Chem.*, **1991**, *30*, 641–645.

of the salt was filtered off, well washed with distilled water and dried in vacuum. The yield is 8.7 g (92%).

Elemental analysis. Anal. Calculated for $C_{30}Cl_2CoH_{24}N_6O_8$: C, 49.60%; H, 3.33%; N, 11.57%. Found: C, 49.5%; H, 3.8%; N, 11.4%.

4.6.2. Identification Procedures

4.6.2.1. Powder X-ray Diffraction

The crystal structure of $[Co(2,2´\text{-bpy})_3](ClO_4)_2$ was reported previously,[69] the compound crystallize in monoclinic *C*2/*c* space group with a unit cell parameters: a = 17.538(4) Å, b = 10.897(2) Å, c = 16.078(2) Å, $\alpha = \gamma = 90°$, β = 91.01(3)°, V = 3072.2(11) Å^3, Z = 4. The published crystallographic parameters[69] are summarized in Table 4.6.2.1.

Table 4.6.2.1 *Crystallographic parameters for $[Co(2,2´\text{-bpy})_3](ClO_4)_2$.*[69]

Molecular formula	$C_{30}H_{24}Cl_2CoN_6O_8$
Formula Weight, g·mol^{-1}	726.38
Crystal system	monoclinic
Space group	*C*2/*c*
Cell dimensions	
a, Å	17.538(4)
b, Å	10.897(2)
c, Å	16.078(3)
α, ^{0}	90
β, ^{0}	91.01(3)
γ, ^{0}	90
V, Å^3	3072.2(11)
Z	4
Density, g·cm^{-3}	1.571
Absorption coefficient, mm^{-1}	0.795
Radiation	Mo Kα, λ = 0.71069 Å

The structure of precursor compound is composed of discrete $[Co(2,2´\text{-bpy})_3]^{2+}$ cations and perchlorate anions. The central Co(II) ion is six coordinated by the nitrogen donor atoms from three bidentate bipyridine ligands, forming three five-membered chelated rings. The six Co^{II}–N bonds lengths are in the range of 2.119–2.136 Å with the average value of 2.129 Å, which are comparable to those in other $[Co(2,2´\text{-bpy})_3]^{2+}$ structure (mean value of 2.128 Å),[70] and significantly longer than the Co^{III}–N distances in $[Co(2,2´\text{-bpy})_3]^{3+}$ subunits (mean value of 1.931 Å).[71,72] The N–Co^{II}–N bond angles in the precursor compound are in the 77.0–98.3° range. Thus, the coordination polyhedron around Co^{II} center could be described as distorted octahedron. The crystal packing is completed with the partially disordered perchlorate anions surrounding the cationic complex.

In order to confirm the structural consistency between the synthesized precursor compound and the expected complex $[Co(2,2´\text{-bpy})_3](ClO_4)_2$, the experimental powder pattern of obtained yellow-brown solid was compared with the simulated powder pattern from reported

(69) J.-C. Yao, L.-F. Ma, F.-J. Yao, *Z. Kristallogr. – New Cryst. Struct.*, **2005**, *220*, 483−484.
(70) D. J. Szalda, C. Creutz, D. Mahajan, N. Sutin, *Inorg. Chem.*, **1983**, *22*, 2372–2379.
(71) M. Du, X.-J. Zhao, H. Cai, *Z. Kristallogr. – New Cryst. Struct.*, **2004**, *219*, 463–464.
(72) W. Liu, W. Xu, J.-L. Lin, H.-Z. Xie, *Acta Cryst.*, **2008**, *E64*, m1586–m1586.

single crystal data.[69] The CIF of $[Co(2,2´\text{-bpy})_3](ClO_4)_2$ has been requested with the depositional number of CCDC 240261 from the CSD of Cambridge Crystallographic Data Centre (CCDC). Figure 4.6.2.1 shows the experimental and simulated powder X-ray diffraction patterns for as-synthesized and reported compound $[Co(2,2´\text{-bpy})_3](ClO_4)_2$, which are in a good agreement to each other, exhibiting very similar sequences of Bragg reflections along with their relative

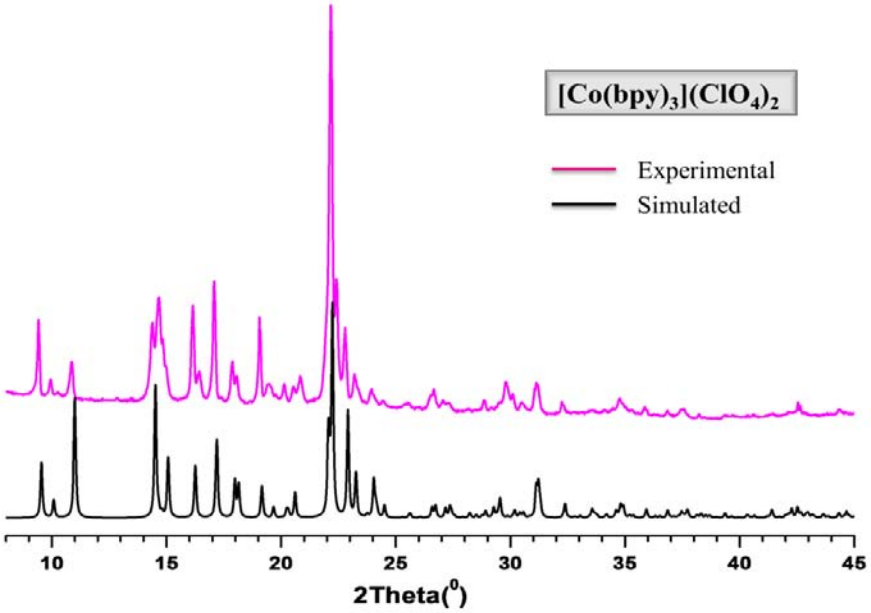

Figure 4.6.2.1 *Powder X-ray diffraction patterns of $[Co(2,2´\text{-bpy})_3](ClO_4)_2$: experimental (red) and simulated (black).*

intensities, indicate the phase purity and consistence with the expected precursor compound. Notably that the slight differences in the relative intensities of the peaks at 11° and 15° observed caused by a preferential orientation of the plate-like crystals of the sample.

4.6.2.2. Infrared Spectroscopy

The solid state infrared spectrum of $[Co(2,2´\text{-bpy})_3](ClO_4)_2$ in the region 4000−400 cm^{-1} is shown in Figure 4.6.2.2. The bands assignments summarized in the Table 4.6.2.2 are in a good agreement with bibliographic data.[30–32,49,53,73] The observed bands are characteristic for tris-bipyridine complexes of transition metals in low oxidation state.

The spectrum of $[Co(2,2´\text{-bpy})_3](ClO_4)_2$ consists of a relatively small number of absorption bands which may be assigned as follows: the broad absorption band in the region 3600−3300 cm^{-1} caused by asymmetric and symmetric H−O−H stretching vibrations is assigned to physically adsorbed water molecules; the aromatic C−H stretching vibration of 2,2´-bpy ligands gives rise to a band at 3200−2880 cm^{-1} with weak-to-medium intensity and consists of a number of peaks.

Interactions between rings C═C and C═N stretching vibrations result in two medium-to-strong absorptions. These absorptions occur at 1615−1575 cm^{-1} and 1520−1465 cm^{-1}, the higher frequency band with a medium-intensity satellite on its low-frequency site was found at 1590−1555 cm^{-1}. A bands of variable intensities are observed in the regions 1300−1180 cm^{-1} and 1000−985 cm^{-1} where C−H ring deformation modes of the 2,2´-bpy ligand were expected.

(73) K. Winkler, M. E. Płońska, K. Rećko, L. Dobrzyński. *Electrochim. Acta,* **2006**, *51*, 4544−4553.

Table 4.6.2.2 *Selected bands in the IR spectrum of compound [Co(2,2´-bpy)$_3$](ClO$_4$)$_2$.*

Spectral Region / Band Maximum	Band assignments
3600−3300 *bw*	ν_{sy} (O−H) + ν_{asy} (O−H) or hydrogen bonding
3200−2880 *w*	ν_{asy} (C−H) stretching
1660 *s*	δ_{sy} (O−H−O)
1615-1575*ms*	
1590−1575*m*	ν_{sy} (C═C) and/or ν_{sy} (C═N)
1520−1465*ms*	ring str. vibration
1450−1410*m*	
1097−1090 *ms*	ν(Cl−O) and/or δ (Cl−O) of ClO_4^- uncoordinated
1000−985*m*	δ (C−H) and/or C−H in-plane deformation vibrations.
780−750*ms*	δ (C−H) and/or C−H out-of-plane deformation vibrations

b broad; ***s*** strong; ***w*** weak; ***vw*** very weak and ***m*** medium

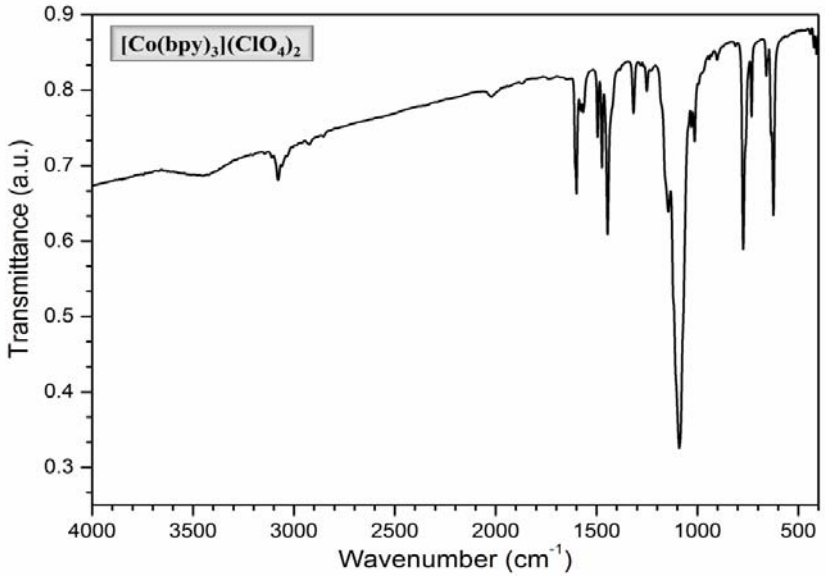

Figure 4.6.2.2 *Infrared spectrum of [Co(2,2´-bpy)$_3$](ClO$_4$)$_2$.*

The 2,2´-bpy ligand strong adsorption bands at 780 and 750 cm^{-1}, assigned to the aromatic out-of-plane hydrogen deformation modes. Furthermore, the spectra exhibit very strong single absorption bands associated with uncoordinated ClO_4^- anion at 1097 cm^{-1} and 1090−1092 cm^{-1}, respectively.

4.6.2.3. Thermogravimetric Analysis

The thermogravimetric analysis (TGA) has been carried out under air atmosphere for the synthesized [Co(2,2´-bpy)$_3$](ClO$_4$)$_2$ with the objectives to confirm the sample purity. The thermogravimetric and corresponding derivative (dTG) curves of the precursor [Co(2,2´-bpy)$_3$](ClO$_4$)$_2$ are shown in Figure 4.6.2.3. Due to high explosive nature of perchlorate salts, its thermal decomposition data are rarely reported in bibliography. The thermal decomposition behavior of [Co(2,2´-bpy)$_3$](ClO$_4$)$_2$ was investigated and compared with the similar compounds.[74]

(74) Z. Li, Z. Zhou, T. Zhang, Z. Tang, L. Yang, J. Zhang, *Polyhedron*, **2012**, *44*, 59–65.

The TG-dTG curves show five well defined decomposition stages. The first stage takes place in the range of 46–143 °C with the mass loss of 8.9% reaching the maximum velocity at 117 °C. The experimental mass loss of 8.9% is consistent with the calculated value 8.8% and may be attributed to the partial conversion of one perchlorate anion into the chlorate. The second stage observed in the range of 143–219 °C with maximum velocity at 201 °C, amounting to total mass loss of 13.8%, consistent with the calculated value of 13.7% for the elimination of four oxygen and one chlorine atoms from one perchlorate anion.

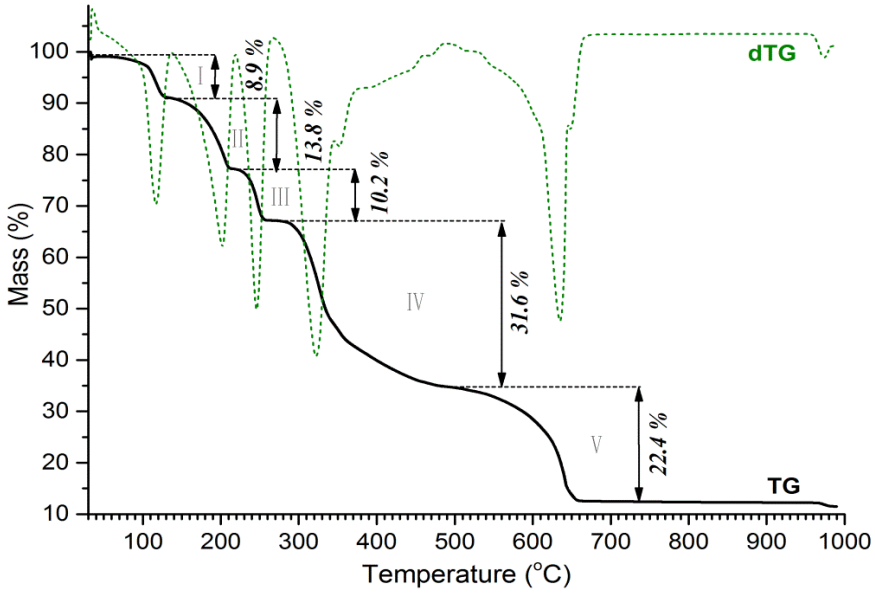

Figure 4.6.2.3 *TG, dTG profiles for thermal decomposition of [Co(2,2´-bpy)$_3$](ClO$_4$)$_2$ under an air atmosphere.*

The third decomposition stage belongs to removal of 0.5 mole of 2,2´-bpy and take place in the range of 220–269 °C with the maxima of dTG at 246 °C. The experimental mass loss of 10.2% is consistent with the calculated value 10.5% for the elimination of 0.5 moles of 2,2´-bpy molecule. The weight loss of 31.6% observed in the range of 269–489 °C (fourth stage, dTG maxima at 324 °C) is equivalent to the loss of 1.5 moles of 2,2´-bpy molecule (Calcd.: 32.2 %). The final, broad fifth stage, ranging from 490 °C to 667 °C with the maxima velocity at 637 °C, corresponds to the experimental mass loss of 22.4%. The experimental mass loss of 22.4% is consistent with the calculated value of 22.6% and corresponds to the loss of one 2,2´-bpy molecule along with removing two chloride molecules in form of gaseous products. The solid residue formed at around 700 °C is suggested to be Co_2O_3 (remaining weight 12.3%, Calcd.: 12.4%).

4.6.2.4. Solid State UV-VIS Spectroscopy

The $[Co(bpy)_3]^{2+}$ complex generally is a typical d^7 high-spin complex with a $^4T_1$ ($t_{2g}^5e_g^2$) ground state.[34] The UV-VIS diffuse-reflectance spectra of synthesized [Co(2,2´-bpy)$_3$](ClO$_4$)$_2$ complex is illustrated in the Figure 4.6.2.4, and the band maxima assignments are summarized in the Table 4.6.2.4.

The absorption bands intensity and their positions are quite similar to bibliographic values reported for $[Co(2,2´\text{-}bpy)_3]^{2+}$ complex and related compounds,[20,37,55,59,75] and indicate the phase

(75) E. C. Constable, In *Advances In Inorganic Chemistry*; Vol. 34: Homoleptic Complexes of 2,2´-Bipyridine, Academic Press Inc., University of Cambridge, England, 1989.

purity and consistence of the synthesized product with the expected precursor. The electronic absorption spectra of $[Co(2,2´\text{-bpy})_3](ClO_4)_2$ complex consist of two group of bands: (*i*) three strong well defined bands in UV region; (*ii*) several medium strong bands in visible region. The three high-energy bands in UV-region at 243, 294 and 395 appear to be intraligand transition and have been assigned to a $\pi \rightarrow \pi^*$ transition.

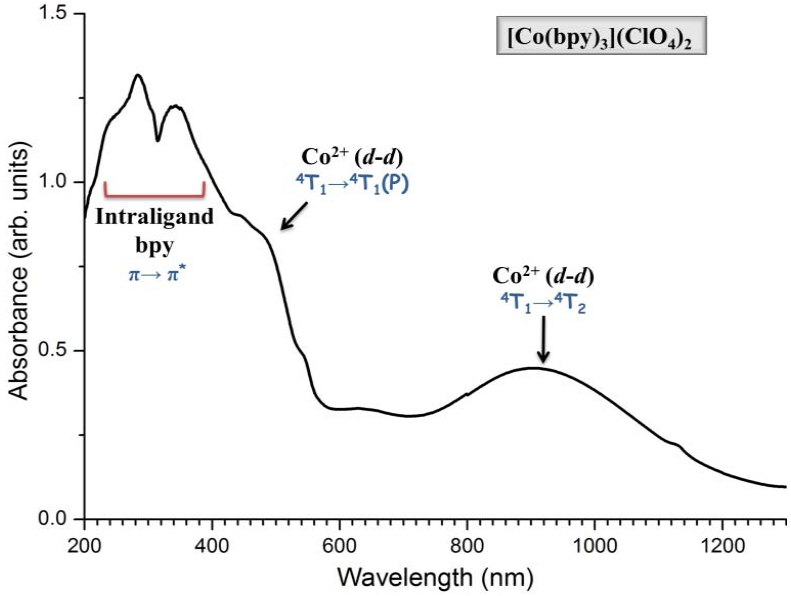

Figure 4.6.2.4 *The room temperature diffuse reflectance UV-VIS spectrum of $[Co(2,2´\text{-bpy})_3](ClO_4)_2$.*

In the visible region, the electronic absorption spectrum of precursor has a broad, low energy band at 910 nm assigned to the $^4T_1(F) \rightarrow {}^4T_2(P)$ transition characteristic for a high spin complex. The higher energy absorption at 440 nm appeared as a shoulder belongs to $^4T_1(F) \rightarrow {}^4T_1(P)$ transition. However, its mergence with the charge-transfer spectrum makes assessment of its energy and intensity uncertain. Hence, the $[Co(2,2´\text{-bpy})_3]^{2+}$ complex has been found to be in a low spin state. The absorption spectra of the low spin form exhibit significant differences in

Table 4.6.2.4. *Electronic Absorption Spectra Band Assignment for High Spin and Low Spin $[Co(2,2´\text{-bpy})_3](ClO_4)_2$ Complexes.*

Spin state / Complex	λ_{max}, nm	ε_{max}, $mol^{-1}\cdot cm^{-1}$	Assignment [b]
High Spin / $[Co(2,2´\text{-bpy})_3]^{2+}$	243 (*sh*)	$30.4\cdot10^3$	Intraligand ($\pi \rightarrow \pi^*$)
	294	$37.1\cdot10^3$	Intraligand ($\pi \rightarrow \pi^*$)
	395	$33.7\cdot10^3$	Intraligand ($\pi \rightarrow \pi^*$)
	440 (*sh*)	94	$^4T_1(F) \rightarrow {}^4T_1(P)$
	910	6	$^4T_1(F) \rightarrow {}^4T_2(F)$
Low Spin / $[Co(2,2´\text{-bpy})_3]^{2+}$	260 (*sh*)	$30.4\cdot10^3$	Intraligand ($\pi \rightarrow \pi^*$)
	306	$37.1\cdot10^3$	Intraligand ($\pi \rightarrow \pi^*$)
	317	$33.7\cdot10^3$	Intraligand ($\pi \rightarrow \pi^*$)
	540 (*sh*)	0.5-1.5	$^2E \rightarrow {}^2T_1(P,H)$
	714	11.36	$^2E \rightarrow {}^2T_1, {}^2T_2$

sh: shoulder band; [b] The bands assignment following the bibliographic data [34,37,59,75]

comparison with the high spin form. The low spin complex has electronic configuration $^2A_1$ ($t_{2g}^6 e_g^1$) and undergoes Jahn–Teller distortion. The absorption spectrum of low spin $[Co(2,2´\text{-}$

$bpy)_3]^{2+}$ complex exhibits two characteristic band at 714 nm and a high energy shoulder at 540 nm which corresponds to spin allowed and overlapped *d-d* $^2E \rightarrow {}^2T_1$, $^2E \rightarrow {}^2T_2$ transitions and second spin-allowed $^2E \rightarrow {}^2T_1$ transition, respectively. The band maxima assignments basing on bibliographic data for low spin complex are summarized in the Table 4.6.2.4. From our results and data in Table 4.6.2.4 it is reasonable to conclude that synthetized precursor belongs to the high spin $[Co(2,2´\text{-bpy})_3](ClO_4)_2$ complex.

4.7. *cis*-$[Rh(2,2´\text{-bpy})_2Cl_2]ClO_4$

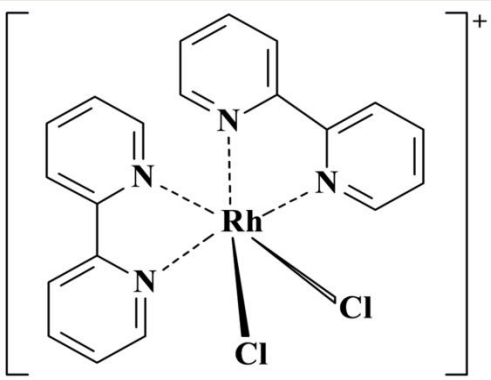

ClO_4^-

Systematic name	**Bis(2,2´-Bipyridyl-κ² N,N´)dichlorido Rhodium (III) Perchlorate**		
Molecular Formula	$C_{20}H_{16}Cl_3N_4O_4Rh$		
Molecular Weight	585.63 g/mol	**Appearance**	Yellow solid
CAS №	49727-33-5	**Boiling point**	272.5 ºC (atm)
Solubility	acetone, ethanol, methanol	**Flash Point**	107.2 ºC

4.7.1. Synthesis

Materials: Commercial $RhCl_3 \cdot xH_2O$ was obtained from Johnson Matthey; 2,2´-bipyridine ($C_{10}H_8N_2$) 99% reagent grade from Sigma-Aldrich; Potassium perchlorate ($KClO_4$) 99% reagent grade from Sigma-Aldrich.

Commercial $RhCl_3 \cdot xH_2O$ is dried in an oven at 120 °C for 4 hours. It is then finely ground in a mortar and returned to the oven for the further 1 hour prior to use.

Synthetic procedure. *cis*-$[Rh(2,2´\text{-bpy})_2Cl_2]ClO_4$ has been synthetized following the published procedures.[76–80] "Dried" $RhCl_3$ (0.2 g, 0.95 mmol) and 2,2´-bipyridine (0.267 g, 2.01 mmol) were fused in a test-tube. After expulsion of water the temperature was allowed to rise to the boiling point of 2,2´-bipyridine (272-273 °C) and kept thereat for 20 min, during which the reddish-black color of the rhodium trichloride disappeared leaving a part green, part orange, residue. The test tube was cooled; the solid was dissolved in 75 mL of boiling water, and filtered hot. The filtrate was treated with potassium perchlorate and cooled. The first yellow precipitate of the $[Rh(2,2´\text{-bpy})_2Cl_2]ClO_4$ was separated as a pure form from the second pink precipitate $[Rh(2,2´\text{-bpy})_3](ClO_4)_3$ by repeated fractional crystallization. The yield is 0.3 g (60%)

Elemental analysis. Anal. Calculated for $C_{20}Cl_4H_{16}N_4O_4Rh$: C, 40.98%; H, 2.73%;N, 9.56%. Found: C, 39.1%; H, 2.5%; N, 9.3%.

(76) B. Martin, G. M. Waind, *J. Chem. Soc*., **1958**, 4284–4288.
(77) R. D. Gillard, J. A. Osborn, G. Wilkinson, *J. Chem. Soc*., **1965**, 1951–1965.
(78) B. Martin, G. M. Waind, *Proc. Chem. Soc.*, **1958**, 169–169.
(79) P. Andersen, J. Josephsen, G. N. Waind, C. E. Schäffer, R. L. Tranter, *J. Chem. Soc. D*, **1969**, *8*, 408–409.
(80) R. D. Gillard, B. T. Heaton, *J. Chem. Soc. A*, **1969**, *3*, 451–454.

4.7.2. Identification Procedures

4.7.2.1. Single Crystal X-Ray Diffraction Study

The single crystal X-ray diffraction analysis of isolated compound through method described above indicates the precipitation of compound with the formulation $[Rh(2,2´\text{-}bpy)_2Cl_2]ClO_4$ which crystal structure has not been reported previously. Considering the unknown crystallographic parameters for precursor compound, we reported our results regarded to crystal structure determination in the following *Publication I*. The manuscript is a complement part for the characterization of compound $[Rh(2,2´\text{-}bpy)_2Cl_2]ClO_4$.

Publication I

"Bis(2,2´-bipyridine)dichloridorhodium(III) perchlorate"

Acta Crystallographica Section E: Structure Reports

E68 (m713–m714)

Year ***2012***

DOI: *10.1107/S1600536812018685*

Impact Index: 0.347

metal-organic compounds

Acta Crystallographica Section E
Structure Reports Online
ISSN 1600-5368

Bis(2,2′-bipyridyl-κ^2N,N')dichloridorhodium(III) perchlorate

Alla Dikhtiarenko,[a] Laura Torre-Fernández,[b] Santiago García-Granda,[b]* José R. García[a] and José Gimeno[a]

[a]Departamento Química Orgánica e Inorgánica, Universidad de Oviedo, 33006 Oviedo, Spain, and [b]Departamento de Química Física y Analítica, Facultad de Química, Universidad de Oviedo–CINN, C/ Julián Clavería, 8, 33006 Oviedo, Asturias, Spain
Correspondence e-mail: sgg@uniovi.es

Received 3 April 2012; accepted 25 April 2012

Key indicators: single-crystal X-ray study; T = 293 K; mean σ(C–C) = 0.005 Å; disorder in solvent or counterion; R factor = 0.042; wR factor = 0.081; data-to-parameter ratio = 23.5.

The asymmetric unit of the title compound, $[RhCl_2(C_{10}H_8N_2)_2]ClO_4$, consists of one unit of the cationic complex $[RhCl_2(bipy)_2]^+$ and one uncoordinated perchlorate anion. The Rh^{III} atom is coordinated by four N atoms from two bipyridyl ligands and two Cl atoms, forming a distorted octahedral environment. The Cl ligands are *cis*. Two intramolecular C—H···Cl hydrogen bonds occur in the cationic complex . In the crystal, molecules are linked together by a hydrogen-bond network involving the H atoms of bipyridyl rings and perchlorate anions. An O atom of the perchlorate anion is disordered over two sites, with an occupancy-factor ratio of 0.78 (3):0.22 (3).

Related literature

For potential applications of noble metal complexes of pyridyl ligands in biochemistry, catalysis and anticancer activity, see: Chifotides *et al.* (2004); Mbaye *et al.* (2003); Karidi *et al.* (2005); Tan *et al.* (2005). For their photochemical and photophysical properties, see: Forster & Rund (2003); Arachchige *et al.* (2008) and for their electrochemical properties, see: Rasmussen *et al.* (1990). For related structures, see: Al-Noaimi & Haddad (2007); Andansen & Josephsen (1971); Choudhury *et al.* (2006); De Munno *et al.* (1993); Figgis *et al.* (1985); Fontaine (2001); Gao & Ng (2010); Kramer & Straehle (1986); Sofetis *et al.* (2006); Strenger *et al.* (2000). For similar structures with platinum group metals, see: Lahuerta *et al.* (1991); Kim *et al.* (2009); Helberg *et al.* (1996); Prajapati *et al.* (2008); Eggleston *et al.* (1985).

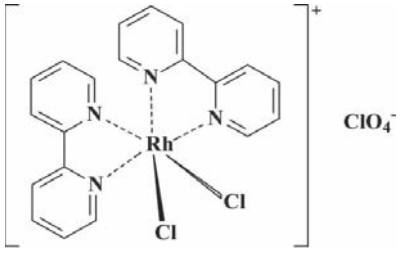

Experimental

Crystal data

$[RhCl_2(C_{10}H_8N_2)_2]ClO_4$
M_r = 585.63
Orthorhombic, $P2_12_12_1$
a = 11.0344 (2) Å
b = 11.6796 (2) Å
c = 17.0884 (3) Å
V = 2202.33 (8) Å^3
Z = 4
Mo $K\alpha$ radiation
μ = 1.18 mm^{-1}
T = 293 K
0.19 × 0.16 × 0.12 mm

Data collection

Agilent Xcalibur Ruby Gemini diffractometer
Absorption correction: multi-scan (*CrysAlis PRO*; Agilent, 2011)
T_{min} = 0.973, T_{max} = 1
12115 measured reflections
6922 independent reflections
5569 reflections with $I > 2\sigma(I)$
R_{int} = 0.026

Refinement

$R[F^2 > 2\sigma(F^2)]$ = 0.042
$wR(F^2)$ = 0.081
S = 1.02
6922 reflections
294 parameters
H-atom parameters constrained
$\Delta\rho_{max}$ = 0.75 e Å^{-3}
$\Delta\rho_{min}$ = −0.25 e Å^{-3}
Absolute structure: Flack (1983), 2630 Friedel pairs
Flack parameter: 0.47 (3)

Table 1
Selected geometric parameters (Å, °).

Rh1—N2	2.019 (2)	Rh1—N4	2.038 (3)
Rh1—N1	2.023 (2)	Rh1—Cl3	2.3291 (9)
Rh1—N3	2.037 (2)	Rh1—Cl2	2.3344 (9)
N1—Rh1—N3	174.22 (10)	Cl3—Rh1—Cl2	91.18 (4)

Table 2
Hydrogen-bond geometry (Å, °).

D—H···A	D—H	H···A	D···A	D—H···A
C1—H1···Cl2	0.93	2.70	3.301 (4)	123
C11—H11···Cl3	0.93	2.76	3.358 (4)	123
C3—H3···O1^{i}	0.93	2.29	3.192 (5)	164
C8—H8···O1^{ii}	0.93	2.56	3.142 (6)	121
C9—H9···O1^{ii}	0.93	2.58	3.154 (6)	120
C13—H13···O4^{iii}	0.93	2.56	3.427 (6)	155

Symmetry codes: (i) $-x+2, y+\frac{1}{2}, -z+\frac{3}{2}$; (ii) $x-\frac{1}{2}, -y-\frac{1}{2}, -z+1$; (iii) $-x+2, y+\frac{1}{2}, -z+\frac{1}{2}$.

Data collection: *CrysAlis PRO* (Agilent, 2011); cell refinement: *CrysAlis PRO*; data reduction: *CrysAlis PRO*; program(s) used to solve structure: *SIR92* (Altomare *et al.*, 1994); program(s) used to refine structure: *SHELXL97* (Sheldrick, 2008); molecular graphics: *Mercury* (Macrae *et al.*, 2006); software used to prepare material for publication: *WinGX* (Farrugia, 1999) and *enCIFer* (Allen *et al.*, 2004).

metal-organic compounds

This work was supported by the Spanish MICINN (projects MAT2006–01997, FC-08-IB08–036 and MAT2010–15094) and FEDER. AD also thanks MICINN for their pre-doctoral FPU grant (AP2008–03942).

Supplementary data and figures for this paper are available from the IUCr electronic archives (Reference: LR2059).

References

Agilent (2011). *CrysAlis PRO*. Agilent Technologies, Yarnton, England.
Allen, F. H., Johnson, O., Shields, G. P., Smith, B. R. & Towler, M. (2004). *J. Appl. Cryst.* **37**, 335–338.
Al-Noaimi, M. & Haddad, S. F. (2007). *Acta Cryst.* E**63**, m2332.
Altomare, A., Cascarano, G., Giacovazzo, C., Guagliardi, A., Burla, M. C., Polidori, G. & Camalli, M. (1994). *J. Appl. Cryst.* **27**, 435.
Andansen, P. & Josephsen, J. (1971). *Acta Chem. Scand.* **25**, 3255–3260.
Arachchige, S. M., Brown, J. & Brewe, K. J. (2008). *J. Photochem. Photobiol. A*, **197**, 13–17.
Chifotides, H. T., Fu, P. K. L., Dunbar, K. R. & Turro, C. (2004). *Inorg. Chem.* **43**, 1175–1183.
Choudhury, S. R., Dutta, A., Mukhopadhyay, S., Lu, L.-P. & Zhu, M.-L. (2006). *Acta Cryst.* E**62**, m1489–m1491.
De Munno, G., Nicolò, F. & Julve, M. (1993). *Acta Cryst.* C**49**, 1049–1052.
Eggleston, D. S., Goldsby, K. A., Hodgson, D. J. & Meyer, T. J. (1985). *Inorg. Chem.* **24**, 4573–4580.
Farrugia, L. J. (1999). *J. Appl. Cryst.* **32**, 837–838.
Figgis, B. N., Reynolds, P. A. & White, A. H. (1985). *Inorg. Chem.* **24**, 3762–3770.
Flack, H. D. (1983). *Acta Cryst.* A**39**, 876–881.
Fontaine, F. G. (2001). *Acta Cryst.* E**57**, m270–m271.
Forster, L. C. & Rund, J. V. (2003). *Inorg. Chem. Commun.* **6**, 78–81.
Gao, S. & Ng, S. W. (2010). *Acta Cryst.* E**66**, m1692.
Helberg, L. E., Orth, S. D., Sabat, M. & Harman, W. D. (1996). *Inorg. Chem.* **35**, 5584–5594.
Karidi, K., Garoufis, A., Tsipis, A., Hadjiliadis, N., Dulk, H. & Reedijk, J. (2005). *Dalton Trans.* pp. 1176–1187.
Kim, N.-H., Hwang, I.-C. & Ha, K. (2009). *Acta Cryst.* E**65**, m180.
Kramer, T. & Straehle, J. (1986). *Z. Naturforsch. Teil B*, **41**, 692–696.
Lahuerta, P., Latorre, J., Martínez-Máñez, R., García-Granda, S. & Gómez-Beltrán, F. (1991). *Acta Cryst.* C**47**, 519–522.
Macrae, C. F., Edgington, P. R., McCabe, P., Pidcock, E., Shields, G. P., Taylor, R., Towler, M. & van de Streek, J. (2006). *J. Appl. Cryst.* **39**, 453–457.
Mbaye, M. D., Demersement, B., Reneaud, J.-L., Toupet, L. & Bruneau, C. (2003). *Angew. Chem. Int. Ed.* **42**, 5066–5068.
Prajapati, R., Yadan, V. K., Dubey, S. K., Durham, B. & Mishra, L. (2008). *Indian J. Chem. Sect. A*, **47**, 1780–1787.
Rasmussen, S. C., Richter, M. M., Yi, E., Place, H. & Brewer, K. J. (1990). *Inorg. Chem.* **29**, 3926–3932.
Sheldrick, G. M. (2008). *Acta Cryst.* A**64**, 112–122.
Sofetis, A., Raptopoulou, C. P., Terzis, A. & Zafiropoulos, T. F. (2006). *Inorg. Chim. Acta*, **359**, 3389–3395.
Strenger, I., Rosu, T. & Negoiu, M. (2000). *Z. Kristallogr. New Cryst. Struct.* **215**, 489–490.
Tan, L. F., Chao, H., Li, H., Liu, Y. J., Sun, B., Wei, W. & Ji, L. N. (2005). *J. Inorg. Biochem.* **99**, 513–520.

supplementary materials

supplementary materials

Acta Cryst. (2012). E**68**, m713–m714 [doi:10.1107/S1600536812018685]

Bis(2,2′-bipyridyl-κ^2N,N')dichloridorhodium(III) perchlorate

Alla Dikhtiarenko, Laura Torre-Fernández, Santiago García-Granda, José R. García and José Gimeno

Comment

In recent years, noble metal complexes of pyridyl ligands have received much attention because of their rich electrochemical (Rasmussen *et al.*, 1990, photophysical (Forster & Rund, 2003) and photochemical (Arachchige *et al.*, 2008) properties, and their potential applications in catalysis (Mbaye *et al.*, 2003), biochemistry (Tan *et al.*, 2005; Chifotides *et al.*, 2004) and anticancer activity (Karidi *et al.*, 2005). Bipyridine (bipy) is one of the most commonly used bidentate ligand of this type in the formation of wide variety of transition metal complexes with a general formula of $[M^{II}(bipy)_2X_2]$ (*M* = Co, Ni, Mn, Fe) in which *X* is an coordinated anionic ligand such as CN, SCN and chloride (De Munno *et al.*, 1993; Eggleston *et al.*, 1985; Kramer & Straehle, 1986; Al-Noaimi and Haddad, 2007; Fontaine, 2001; Choudhury *et al.*, 2006; Gao & Ng, 2010) and complexes with cationic part $[M^{III}Cl_2(bipy)_2]^+$ (*M* = Re, Ru, Co, Ga) and any counter anion like Cl^-, PF_6^- (Figgis *et al.*, 1985; Sofetis *et al.*, 2006; Andansen & Josephsen, 1971; Strenger *et al.*, 2000; Kim *et al.*, 2009; Prajapati *et al.*, 2008; Helberg *et al.*, 1996). The complex $[RhCl_2(bipy)_2]Cl.2H_2O$ has also been obtained and crystallographycaly determined by Lahuerta *et al.*, 1991. Yet, no crystal structure has been reported for the cationic complex *cis*-$[Rh(bipy)_2Cl_2]^+$ in its perchlorate form as counter anion, therefore, we report the crystal structure of compound (**I**).

Complex (**I**) crystallizes in the orthorhombic space group $P2_12_12_1$. The molecular structure of **(I)** depicted in Figure 1. It has a distorted octahedral geometry with the two chloride ions in *cis* positions. Selected bond lengths for the complex are given in Table 1. The Rh–N axial bond distance (2.038 (3) Å) is slightly longer than Rh–N equatorial bonds (average 2.026 (5) Å). Its may be well compared with the negligible difference between equatorial and axial M–N bonds distances seen in the analogous complexes of platinum metal group (Lahuerta *et al.*, 1991; Kim *et al.*, 2009; Helberg *et al.*, 1996; Prajapati *et al.*, 2008; Eggleston *et al.*, 1985), but greater distortion observed in majority of transition metal complexes (Strenger *et al.*, 2000; Fontaine, 2001; Kramer & Straehle, 1986; Sofetis *et al.*, 2006; Figgis *et al.*, 1985; Choudhury *et al.*, 2006; Gao & Ng, 2010). The Rh–Cl bond distances in (**I**) are 2.3291 (9) (equatorial) and 2.3344 (9) Å (axial). The N_{eq}–Rh–N_{eq} angle is 174.22 (10)° and its distorted from linearity by approximately 6 °. Also Cl_{eq}–Rh–Cl_{ax} angle (91.18 (4) °) is nearly octahedral. The *cis* isomerization of cationic complex $[RhCl_2(bipy)_2]^+$ is stabilized by short contacts. Coordinated chlorides which situated in *cis* position to respect to each other make up short contact Cl2···H1 and Cl3···H11 with distances 2.7 and 2.76 Å, respectively (Tabl. 2). The crystal lattice of (**I**) is made up of well separated ClO_4^- anions and $[RhCl_2(bipy)_2]^+$ cations. The perchlorate anion contribute to forming extensive hydrogen bonding net linked together cationic and anionic parts of the structure. The interactions involve the hydrogen bonding between H atoms of bipy ring with oxygen atoms uncoordinated perchlorate anion. Each oxygen atoms participates in four hydrogen bonds to H atoms of aryl groups (Tabl. 2). The atom O2 of the perchlorate anion is disordered and splited over two sites with refined occupancy ratio of 0.78 (3):0.22 (3).

Experimental

To a solution of $RhCl_3.xH_2O$ (0.05 g, 0.231 mmol) and $KClO_4$ (0.09 g, 0.693 mmol) in H_2O (10 ml) was added 2,2′-bipyridine (0.04 g, 0.462 mmol) in CH_3OH (10 ml), and was stirred for 2 h to yellow solution resulted. Yellowish rhombohedral crystals suitable for X-ray analysis were obtained by slow evaporation during two weeks. $RhCl_3.xH_2O$ purchased from Johnson Matthey, all other reagents was obtained commercially from Sigma-Aldrich and used without futher purification.

Refinement

H atoms were positioned geometrically and allowed to ride on their respective parent atoms [C—H = 0.93 Å and U_{iso}(H) = 1.2U_{eq}(C)]. The value of the Flack parameter, 0.47 (3) suggests that the crystal is a racemic twin.

Computing details

Data collection: *CrysAlis PRO* (Agilent, 2011); cell refinement: *CrysAlis PRO* (Agilent, 2011); data reduction: *CrysAlis PRO* (Agilent, 2011); program(s) used to solve structure: *SIR92* (Altomare *et al.*, 1994); program(s) used to refine structure: *SHELXL97* (Sheldrick, 2008); molecular graphics: Mercury (Macrae *et al.*, 2006); software used to prepare material for publication: *WinGX* (Farrugia, 1999) and *enCIFer* (Allen *et al.*, 2004).

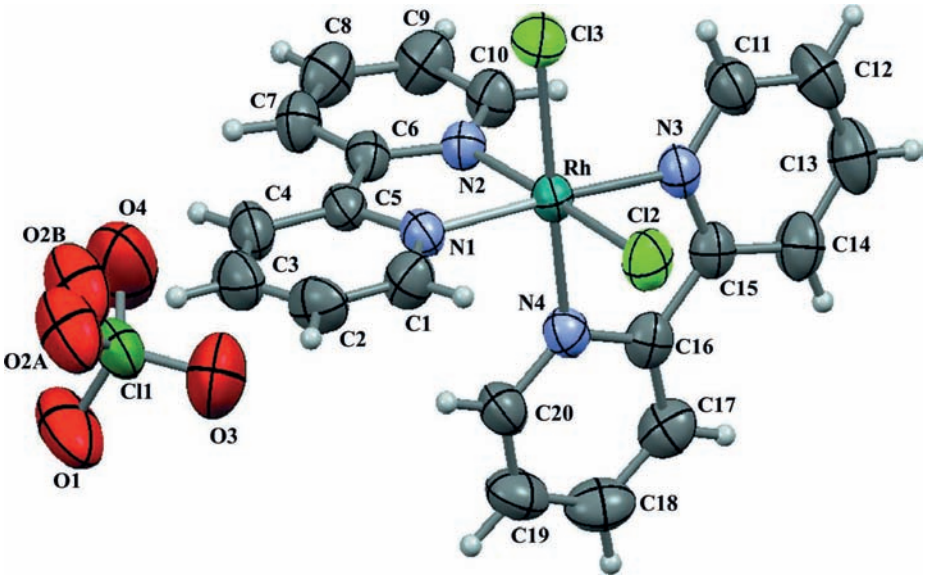

Figure 1

A view of $[RhCl_2(C_{10}H_8N_2)_2]ClO_4$ asymmetric unit. Displacement ellipsoids are drawn at the 50% probability level.

Bis(2,2′-bipyridyl-κ^2N,N')dichloridorhodium(III) perchlorate

Crystal data

$[RhCl_2(C_{10}H_8N_2)_2]ClO_4$
M_r = 585.63
Orthorhombic, $P2_12_12_1$
Hall symbol: P 2ac 2ab
a = 11.0344 (2) Å
b = 11.6796 (2) Å
c = 17.0884 (3) Å
V = 2202.33 (8) Å^3
Z = 4
F(000) = 1168
D_x = 1.766 Mg m^{-3}
Mo $K\alpha$ radiation, λ = 0.7107 Å
Cell parameters from 4926 reflections
θ = 3.5–32.1°
μ = 1.18 mm^{-1}
T = 293 K
Rhombohedron, yellow
0.19 × 0.16 × 0.12 mm

supplementary materials

Data collection

Agilent Xcalibur Ruby Gemini diffractometer
Radiation source: Enhance (Mo) X-ray Source
Graphite monochromator
Detector resolution: 10.2673 pixels mm^{-1}
ω scans
Absorption correction: multi-scan (*CrysAlis PRO*; Agilent, 2011)
T_{min} = 0.973, T_{max} = 1

12115 measured reflections
6922 independent reflections
5569 reflections with $I > 2\sigma(I)$
R_{int} = 0.026
θ_{max} = 32.1°, θ_{min} = 3.5°
h = −8→16
k = −17→10
l = −22→25

Refinement

Refinement on F^2
Least-squares matrix: full
$R[F^2 > 2\sigma(F^2)]$ = 0.042
$wR(F^2)$ = 0.081
S = 1.02
6922 reflections
294 parameters
0 restraints
H-atom parameters constrained

$w = 1/[\sigma^2(F_o^2) + (0.0292P)^2 + 0.1669P]$ where $P = (F_o^2 + 2F_c^2)/3$
$(\Delta/\sigma)_{max}$ = 0.001
$\Delta\rho_{max}$ = 0.75 e Å^{-3}
$\Delta\rho_{min}$ = −0.25 e Å^{-3}
Absolute structure: Flack (1983), 2630 Friedel pairs
Flack parameter: 0.47 (3)

Special details

Geometry. All e.s.d.'s (except the e.s.d. in the dihedral angle between two l.s. planes) are estimated using the full covariance matrix. The cell e.s.d.'s are taken into account individually in the estimation of e.s.d.'s in distances, angles and torsion angles; correlations between e.s.d.'s in cell parameters are only used when they are defined by crystal symmetry. An approximate (isotropic) treatment of cell e.s.d.'s is used for estimating e.s.d.'s involving l.s. planes.

Refinement. Refinement of F^2 against ALL reflections. The weighted R-factor wR and goodness of fit S are based on F^2, conventional R-factors R are based on F, with F set to zero for negative F^2. The threshold expression of $F^2 > \sigma(F^2)$ is used only for calculating R-factors(gt) *etc*. and is not relevant to the choice of reflections for refinement. R-factors based on F^2 are statistically about twice as large as those based on F, and R- factors based on ALL data will be even larger.

Fractional atomic coordinates and isotropic or equivalent isotropic displacement parameters (Å²)

	x	*y*	*z*	U_{iso}*/U_{eq}	Occ. (<1)
Rh1	0.98325 (2)	0.241474 (19)	0.367163 (12)	0.04095 (7)	
Cl1	0.97063 (10)	−0.18258 (8)	0.63515 (5)	0.0629 (2)	
Cl2	1.10302 (9)	0.40548 (7)	0.35644 (6)	0.0609 (2)	
Cl3	0.80775 (9)	0.35183 (8)	0.37395 (6)	0.0603 (2)	
N1	0.9798 (2)	0.2369 (2)	0.48547 (13)	0.0439 (5)	
N2	0.8794 (2)	0.1010 (2)	0.38286 (14)	0.0426 (6)	
N3	0.9942 (3)	0.2300 (2)	0.24844 (13)	0.0467 (6)	
N4	1.1338 (3)	0.1414 (2)	0.35733 (15)	0.0455 (6)	
O1	1.0370 (4)	−0.2722 (3)	0.6687 (2)	0.1228 (15)	
O2A	0.9396 (14)	−0.1068 (7)	0.6981 (7)	0.102 (3)	0.78 (3)
O2B	0.891 (4)	−0.123 (3)	0.6744 (18)	0.102 (3)	0.22 (3)
O3	1.0402 (4)	−0.1234 (3)	0.57914 (19)	0.1075 (12)	
O4	0.8704 (4)	−0.2320 (5)	0.5957 (2)	0.1495 (17)	
C1	1.0374 (3)	0.3097 (3)	0.5332 (2)	0.0557 (9)	
H1	1.0805	0.3705	0.5117	0.067*	
C2	1.0344 (4)	0.2968 (4)	0.6128 (2)	0.0654 (11)	
H2	1.0755	0.3481	0.6448	0.078*	
C3	0.9706 (4)	0.2082 (4)	0.6450 (2)	0.0672 (11)	

H3	0.968	0.1985	0.699	0.081*
C4	0.9098 (4)	0.1331 (3)	0.59588 (19)	0.0586 (9)
H4	0.8657	0.0725	0.6166	0.07*
C5	0.9153 (3)	0.1492 (3)	0.51615 (17)	0.0446 (7)
C6	0.8570 (3)	0.0741 (2)	0.45826 (17)	0.0442 (7)
C7	0.7849 (4)	−0.0179 (3)	0.4774 (2)	0.0546 (9)
H7	0.7708	−0.036	0.5297	0.065*
C8	0.7341 (4)	−0.0825 (3)	0.4193 (2)	0.0665 (11)
H8	0.6858	−0.1452	0.4316	0.08*
C9	0.7550 (4)	−0.0539 (3)	0.3429 (2)	0.0637 (10)
H9	0.72	−0.0963	0.3028	0.076*
C10	0.8279 (3)	0.0380 (3)	0.3260 (2)	0.0535 (9)
H10	0.8421	0.0572	0.274	0.064*
C11	0.9169 (4)	0.2771 (3)	0.1977 (2)	0.0629 (10)
H11	0.8496	0.3163	0.2166	0.075*
C12	0.9344 (4)	0.2689 (4)	0.1183 (2)	0.0719 (11)
H12	0.8797	0.3022	0.0837	0.086*
C13	1.0325 (5)	0.2118 (3)	0.0909 (2)	0.0726 (13)
H13	1.0453	0.2058	0.0373	0.087*
C14	1.1141 (4)	0.1621 (3)	0.1429 (2)	0.0632 (10)
H14	1.182	0.1231	0.1249	0.076*
C15	1.0912 (3)	0.1724 (3)	0.22194 (18)	0.0461 (8)
C16	1.1686 (3)	0.1207 (3)	0.28234 (18)	0.0464 (8)
C17	1.2693 (4)	0.0539 (3)	0.2680 (2)	0.0595 (9)
H17	1.2956	0.0422	0.2169	0.071*
C18	1.3302 (4)	0.0049 (3)	0.3289 (3)	0.0698 (12)
H18	1.3968	−0.042	0.3196	0.084*
C19	1.2925 (4)	0.0256 (3)	0.4035 (3)	0.0686 (11)
H19	1.3331	−0.0074	0.4455	0.082*
C20	1.1956 (4)	0.0945 (3)	0.4161 (2)	0.0563 (9)
H20	1.1715	0.1094	0.4673	0.068*

Atomic displacement parameters (Å²)

	U^{11}	U^{22}	U^{33}	U^{12}	U^{13}	U^{23}
Rh1	0.04542 (12)	0.04254 (12)	0.03489 (10)	−0.00107 (11)	−0.00011 (10)	0.00272 (10)
Cl1	0.0798 (6)	0.0651 (5)	0.0438 (4)	0.0109 (5)	−0.0048 (5)	0.0050 (4)
Cl2	0.0664 (6)	0.0557 (5)	0.0606 (5)	−0.0147 (4)	0.0015 (5)	0.0072 (4)
Cl3	0.0580 (5)	0.0612 (5)	0.0618 (5)	0.0098 (4)	0.0026 (5)	0.0058 (5)
N1	0.0474 (14)	0.0471 (13)	0.0370 (11)	0.0040 (18)	−0.0028 (10)	0.0026 (10)
N2	0.0443 (15)	0.0422 (13)	0.0414 (15)	−0.0005 (11)	0.0015 (12)	0.0017 (11)
N3	0.0537 (16)	0.0491 (14)	0.0375 (12)	−0.0050 (17)	−0.0008 (11)	0.0049 (11)
N4	0.0483 (16)	0.0430 (13)	0.0451 (15)	−0.0016 (12)	−0.0021 (13)	0.0042 (12)
O1	0.157 (4)	0.120 (3)	0.091 (2)	0.073 (3)	0.009 (2)	0.032 (2)
O2A	0.160 (8)	0.084 (3)	0.063 (4)	0.040 (4)	0.005 (4)	−0.011 (3)
O2B	0.160 (8)	0.084 (3)	0.063 (4)	0.040 (4)	0.005 (4)	−0.011 (3)
O3	0.123 (3)	0.108 (3)	0.092 (2)	−0.013 (2)	0.025 (2)	0.0163 (19)
O4	0.137 (4)	0.207 (5)	0.104 (3)	−0.053 (4)	−0.027 (3)	0.028 (3)
C1	0.057 (2)	0.062 (2)	0.0480 (18)	−0.0090 (18)	0.0027 (17)	−0.0091 (15)
C2	0.063 (3)	0.085 (3)	0.048 (2)	0.002 (2)	−0.0115 (18)	−0.0183 (19)

C3	0.070 (3)	0.090 (3)	0.0414 (18)	0.009 (2)	−0.0019 (19)	−0.0028 (17)
C4	0.069 (3)	0.065 (2)	0.0419 (18)	0.008 (2)	0.0038 (18)	0.0098 (17)
C5	0.0456 (19)	0.0481 (17)	0.0401 (16)	0.0076 (15)	0.0025 (14)	0.0040 (14)
C6	0.051 (2)	0.0390 (16)	0.0432 (16)	0.0056 (15)	0.0066 (15)	0.0031 (13)
C7	0.067 (3)	0.0458 (19)	0.0512 (18)	−0.0012 (17)	0.0086 (18)	0.0064 (16)
C8	0.071 (3)	0.049 (2)	0.079 (3)	−0.0105 (19)	0.011 (2)	0.0006 (19)
C9	0.069 (3)	0.058 (2)	0.063 (2)	−0.009 (2)	0.0035 (19)	−0.0161 (19)
C10	0.060 (2)	0.056 (2)	0.0453 (18)	−0.0061 (18)	0.0009 (17)	−0.0073 (16)
C11	0.071 (3)	0.069 (2)	0.0481 (19)	0.004 (2)	−0.0041 (18)	0.0063 (17)
C12	0.090 (3)	0.079 (3)	0.046 (2)	0.004 (2)	−0.0136 (19)	0.007 (2)
C13	0.108 (4)	0.070 (2)	0.0402 (19)	−0.006 (2)	0.002 (2)	−0.0029 (17)
C14	0.081 (3)	0.062 (2)	0.047 (2)	−0.004 (2)	0.011 (2)	−0.0068 (17)
C15	0.056 (2)	0.0385 (16)	0.0441 (17)	−0.0077 (15)	0.0018 (16)	−0.0020 (13)
C16	0.054 (2)	0.0384 (16)	0.0467 (18)	−0.0089 (15)	0.0023 (15)	−0.0056 (13)
C17	0.060 (2)	0.055 (2)	0.063 (2)	−0.0002 (19)	0.0051 (19)	−0.0151 (18)
C18	0.057 (3)	0.054 (2)	0.098 (3)	0.0120 (19)	−0.003 (2)	−0.013 (2)
C19	0.061 (3)	0.061 (2)	0.084 (3)	0.012 (2)	−0.014 (2)	0.011 (2)
C20	0.060 (2)	0.059 (2)	0.050 (2)	0.0023 (18)	−0.0066 (18)	0.0101 (17)

Geometric parameters (Å, º)

Rh1—N2	2.019 (2)	C4—H4	0.93
Rh1—N1	2.023 (2)	C5—C6	1.470 (4)
Rh1—N3	2.037 (2)	C6—C7	1.377 (5)
Rh1—N4	2.038 (3)	C7—C8	1.369 (5)
Rh1—Cl3	2.3291 (9)	C7—H7	0.93
Rh1—Cl3	2.3291 (9)	C8—C9	1.366 (5)
Rh1—Cl2	2.3344 (9)	C8—H8	0.93
Rh1—Cl2	2.3344 (9)	C9—C10	1.373 (5)
Cl1—O2B	1.31 (3)	C9—H9	0.93
Cl1—O1	1.401 (3)	C10—H10	0.93
Cl1—O3	1.408 (3)	C11—C12	1.375 (5)
Cl1—O4	1.418 (4)	C11—H11	0.93
Cl1—O2A	1.434 (9)	C12—C13	1.354 (6)
N1—C1	1.338 (4)	C12—H12	0.93
N1—C5	1.353 (4)	C13—C14	1.392 (6)
N2—C10	1.344 (4)	C13—H13	0.93
N2—C6	1.349 (4)	C14—C15	1.379 (5)
N3—C11	1.335 (4)	C14—H14	0.93
N3—C15	1.343 (4)	C15—C16	1.469 (5)
N4—C20	1.332 (4)	C16—C17	1.380 (5)
N4—C16	1.359 (4)	C17—C18	1.365 (5)
C1—C2	1.369 (5)	C17—H17	0.93
C1—H1	0.93	C18—C19	1.362 (6)
C2—C3	1.367 (6)	C18—H18	0.93
C2—H2	0.93	C19—C20	1.356 (5)
C3—C4	1.387 (5)	C19—H19	0.93
C3—H3	0.93	C20—H20	0.93
C4—C5	1.377 (4)		

N2—Rh1—N1	80.50 (10)	C2—C3—C4	118.9 (3)
N2—Rh1—N3	96.45 (10)	C2—C3—H3	120.5
N1—Rh1—N3	174.22 (10)	C4—C3—H3	120.5
N2—Rh1—N4	90.41 (11)	C5—C4—C3	119.5 (4)
N1—Rh1—N4	94.74 (10)	C5—C4—H4	120.3
N3—Rh1—N4	80.32 (11)	C3—C4—H4	120.3
N2—Rh1—Cl3	88.36 (8)	N1—C5—C4	120.6 (3)
N1—Rh1—Cl3	87.08 (7)	N1—C5—C6	114.9 (3)
N3—Rh1—Cl3	97.78 (8)	C4—C5—C6	124.4 (3)
N4—Rh1—Cl3	177.61 (8)	N2—C6—C7	121.0 (3)
N2—Rh1—Cl3	88.36 (8)	N2—C6—C5	115.1 (3)
N1—Rh1—Cl3	87.08 (7)	C7—C6—C5	123.9 (3)
N3—Rh1—Cl3	97.78 (8)	C8—C7—C6	119.6 (3)
N4—Rh1—Cl3	177.61 (8)	C8—C7—H7	120.2
Cl3—Rh1—Cl3	0.00 (5)	C6—C7—H7	120.2
N2—Rh1—Cl2	176.85 (7)	C9—C8—C7	119.3 (4)
N1—Rh1—Cl2	96.36 (8)	C9—C8—H8	120.3
N3—Rh1—Cl2	86.69 (7)	C7—C8—H8	120.3
N4—Rh1—Cl2	90.16 (8)	C8—C9—C10	119.4 (4)
Cl3—Rh1—Cl2	91.18 (4)	C8—C9—H9	120.3
Cl3—Rh1—Cl2	91.18 (4)	C10—C9—H9	120.3
N2—Rh1—Cl2	176.85 (7)	N2—C10—C9	121.5 (3)
N1—Rh1—Cl2	96.36 (8)	N2—C10—H10	119.2
N3—Rh1—Cl2	86.69 (7)	C9—C10—H10	119.2
N4—Rh1—Cl2	90.16 (8)	N3—C11—C12	121.5 (4)
Cl3—Rh1—Cl2	91.18 (4)	N3—C11—H11	119.2
Cl3—Rh1—Cl2	91.18 (4)	C12—C11—H11	119.2
Cl2—Rh1—Cl2	0.00 (5)	C13—C12—C11	119.2 (4)
O2B—Cl1—O1	122.6 (14)	C13—C12—H12	120.4
O2B—Cl1—O3	117.0 (14)	C11—C12—H12	120.4
O1—Cl1—O3	111.1 (2)	C12—C13—C14	120.1 (3)
O2B—Cl1—O4	86 (2)	C12—C13—H13	119.9
O1—Cl1—O4	107.4 (3)	C14—C13—H13	119.9
O3—Cl1—O4	107.5 (2)	C15—C14—C13	118.1 (4)
O1—Cl1—O2A	106.2 (5)	C15—C14—H14	121
O3—Cl1—O2A	109.7 (4)	C13—C14—H14	121
O4—Cl1—O2A	115.0 (7)	N3—C15—C14	121.3 (3)
C1—N1—C5	119.7 (3)	N3—C15—C16	115.6 (3)
C1—N1—Rh1	125.7 (2)	C14—C15—C16	123.1 (3)
C5—N1—Rh1	114.7 (2)	N4—C16—C17	119.7 (3)
C10—N2—C6	119.1 (3)	N4—C16—C15	115.2 (3)
C10—N2—Rh1	126.0 (2)	C17—C16—C15	125.1 (3)
C6—N2—Rh1	114.8 (2)	C18—C17—C16	119.9 (4)
C11—N3—C15	119.8 (3)	C18—C17—H17	120.1
C11—N3—Rh1	125.6 (2)	C16—C17—H17	120.1
C15—N3—Rh1	114.6 (2)	C19—C18—C17	119.3 (4)
C20—N4—C16	119.6 (3)	C19—C18—H18	120.4
C20—N4—Rh1	126.2 (2)	C17—C18—H18	120.4
C16—N4—Rh1	114.2 (2)	C20—C19—C18	119.7 (4)

N1—C1—C2	121.6 (3)	C20—C19—H19	120.1
N1—C1—H1	119.2	C18—C19—H19	120.1
C2—C1—H1	119.2	N4—C20—C19	121.8 (4)
C3—C2—C1	119.8 (4)	N4—C20—H20	119.1
C3—C2—H2	120.1	C19—C20—H20	119.1
C1—C2—H2	120.1		

N1—Rh1—Cl2—Cl2	0E1 (8)	Cl2—Rh1—N4—C16	−84.4 (2)
N3—Rh1—Cl2—Cl2	0.00 (2)	C5—N1—C1—C2	1.0 (5)
N4—Rh1—Cl2—Cl2	0.00 (2)	Rh1—N1—C1—C2	−176.9 (3)
Cl3—Rh1—Cl2—Cl2	0.00 (2)	N1—C1—C2—C3	−0.4 (6)
Cl3—Rh1—Cl2—Cl2	0.00 (2)	C1—C2—C3—C4	−0.1 (6)
N2—Rh1—Cl3—Cl3	0.00 (3)	C2—C3—C4—C5	0.2 (6)
N1—Rh1—Cl3—Cl3	0.00 (3)	C1—N1—C5—C4	−0.9 (5)
N3—Rh1—Cl3—Cl3	0.00 (3)	Rh1—N1—C5—C4	177.2 (3)
Cl2—Rh1—Cl3—Cl3	0.00 (3)	C1—N1—C5—C6	−179.4 (3)
Cl2—Rh1—Cl3—Cl3	0.00 (3)	Rh1—N1—C5—C6	−1.3 (3)
N2—Rh1—N1—C1	178.2 (3)	C3—C4—C5—N1	0.3 (5)
N4—Rh1—N1—C1	88.5 (3)	C3—C4—C5—C6	178.7 (3)
Cl3—Rh1—N1—C1	−93.0 (3)	C10—N2—C6—C7	1.5 (5)
Cl3—Rh1—N1—C1	−93.0 (3)	Rh1—N2—C6—C7	178.3 (3)
Cl2—Rh1—N1—C1	−2.2 (3)	C10—N2—C6—C5	−178.8 (3)
Cl2—Rh1—N1—C1	−2.2 (3)	Rh1—N2—C6—C5	−2.0 (4)
N2—Rh1—N1—C5	0.2 (2)	N1—C5—C6—N2	2.2 (4)
N4—Rh1—N1—C5	−89.4 (2)	C4—C5—C6—N2	−176.2 (3)
Cl3—Rh1—N1—C5	89.0 (2)	N1—C5—C6—C7	−178.2 (3)
Cl3—Rh1—N1—C5	89.0 (2)	C4—C5—C6—C7	3.4 (5)
Cl2—Rh1—N1—C5	179.9 (2)	N2—C6—C7—C8	−0.7 (6)
Cl2—Rh1—N1—C5	179.9 (2)	C5—C6—C7—C8	179.7 (3)
N1—Rh1—N2—C10	177.6 (3)	C6—C7—C8—C9	−0.6 (6)
N3—Rh1—N2—C10	−7.4 (3)	C7—C8—C9—C10	1.0 (6)
N4—Rh1—N2—C10	−87.7 (3)	C6—N2—C10—C9	−1.1 (5)
Cl3—Rh1—N2—C10	90.3 (3)	Rh1—N2—C10—C9	−177.5 (3)
Cl3—Rh1—N2—C10	90.3 (3)	C8—C9—C10—N2	−0.1 (6)
N1—Rh1—N2—C6	1.1 (2)	C15—N3—C11—C12	−0.5 (5)
N3—Rh1—N2—C6	176.1 (2)	Rh1—N3—C11—C12	177.1 (3)
N4—Rh1—N2—C6	95.8 (2)	N3—C11—C12—C13	0.0 (6)
Cl3—Rh1—N2—C6	−86.3 (2)	C11—C12—C13—C14	0.0 (6)
Cl3—Rh1—N2—C6	−86.3 (2)	C12—C13—C14—C15	0.5 (6)
N2—Rh1—N3—C11	89.5 (3)	C11—N3—C15—C14	1.0 (5)
N4—Rh1—N3—C11	178.8 (3)	Rh1—N3—C15—C14	−176.9 (3)
Cl3—Rh1—N3—C11	0.3 (3)	C11—N3—C15—C16	−178.1 (3)
Cl3—Rh1—N3—C11	0.3 (3)	Rh1—N3—C15—C16	4.0 (3)
Cl2—Rh1—N3—C11	−90.4 (3)	C13—C14—C15—N3	−1.0 (5)
Cl2—Rh1—N3—C11	−90.4 (3)	C13—C14—C15—C16	178.1 (3)
N2—Rh1—N3—C15	−92.7 (2)	C20—N4—C16—C17	−1.7 (5)
N4—Rh1—N3—C15	−3.4 (2)	Rh1—N4—C16—C17	−179.9 (2)
Cl3—Rh1—N3—C15	178.0 (2)	C20—N4—C16—C15	177.4 (3)
Cl3—Rh1—N3—C15	178.0 (2)	Rh1—N4—C16—C15	−0.8 (3)

Cl2—Rh1—N3—C15	87.3 (2)	N3—C15—C16—N4	−2.1 (4)
Cl2—Rh1—N3—C15	87.3 (2)	C14—C15—C16—N4	178.8 (3)
N2—Rh1—N4—C20	−79.4 (3)	N3—C15—C16—C17	177.0 (3)
N1—Rh1—N4—C20	1.1 (3)	C14—C15—C16—C17	−2.2 (5)
N3—Rh1—N4—C20	−175.9 (3)	N4—C16—C17—C18	2.8 (5)
Cl2—Rh1—N4—C20	97.5 (3)	C15—C16—C17—C18	−176.2 (3)
Cl2—Rh1—N4—C20	97.5 (3)	C16—C17—C18—C19	−1.8 (6)
N2—Rh1—N4—C16	98.7 (2)	C17—C18—C19—C20	−0.2 (7)
N1—Rh1—N4—C16	179.2 (2)	C16—N4—C20—C19	−0.4 (5)
N3—Rh1—N4—C16	2.3 (2)	Rh1—N4—C20—C19	177.6 (3)
Cl2—Rh1—N4—C16	−84.4 (2)	C18—C19—C20—N4	1.4 (6)

Hydrogen-bond geometry (Å, º)

D—H···*A*	*D*—H	H···*A*	*D*···*A*	*D*—H···*A*
C1—H1···Cl2	0.93	2.7	3.301 (4)	123
C11—H11···Cl3	0.93	2.76	3.358 (4)	123
C3—H3···O1^{i}	0.93	2.29	3.192 (5)	164
C8—H8···O1^{ii}	0.93	2.56	3.142 (6)	121
C9—H9···O1^{ii}	0.93	2.58	3.154 (6)	120
C13—H13···O4^{iii}	0.93	2.56	3.427 (6)	155

Symmetry codes: (i) −*x*+2, *y*+1/2, −*z*+3/2; (ii) *x*−1/2, −*y*−1/2, −*z*+1; (iii) −*x*+2, *y*+1/2, −*z*+1/2.

4.8. $[Ni(2,2´\text{-bpy})_3]Cl_2\cdot 6H_2O$

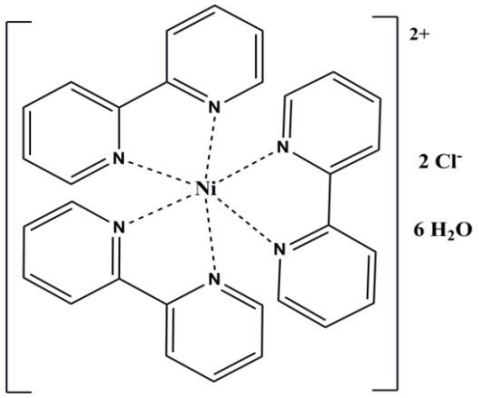

Systematic name	**Tris(2,2´-Bipyridine)Nickel(II) Dichloride Hexahydrate**		
Molecular Formula	$C_{30}H_{36}Cl_2N_6NiO_6$		
Molecular Weight	706.23 g/mol	**Appearance**	Pink solid
CAS №	15554-91-3	**Boiling point**	279.5 °C (atm)
Solubility	water, acetone, ethanol, methanol	**Flash Point**	147.9 °C

4.8.1. Synthesis

Materials: Commercial nickel chloride hexahydrate ($NiCl_2\cdot 6H_2O$) 98% reagent grade was obtained from VWR International S.A.S; 2,2´-bipyridine ($C_{10}H_8N_2$) 99% reagent grade from Sigma-Aldrich; Potassium chloride (KCl) 99% reagent grade from VWR International S.A.S; Acetone (C_3H_6O) 99.9% analytical grade from VWR International S.A.S.

Synthetic procedure. Compound $[Ni(2,2´\text{-bpy})_3]Cl_2\cdot 6H_2O$ has been synthetized following procedure described previously.[48,81,82] Nickel chloride hexahydrate $NiCl_2\cdot 6H_2O$ (1.18 g, 4.96 mmol) and 2,2´-bipyridine (2.32 g, 14.88 mmol) were dissolved in water (10 mL) and vigorously stirred. During mixing the color of solution became pink. Posterior, to the resulted pink solution the excess of potassium chloride was added, the mixture heated to let evaporate approximately half of it volume and cooled down to room temperature, the pink solid started to appear. To complete precipitation, the pink solution was being cooled in ice-bath for 3 h and plate-like pink crystals were filtered, washed several times with small amount of ice-cold water, and air dried. The yield is 3.26 g (93%). The crude solid was recrystallized two times from the minimum amount of hot acetone and air dried.

Elemental analysis. Anal. Calculated for $C_{30}Cl_2H_{36}N_6NiO_6$: C, 51.02%; H, 5.14%; N, 11.89%. Found: C, 49.9%; H, 4.8%; N, 11.7%.

4.8.2. Identification Procedures

4.8.2.1. Powder X-ray Diffraction

The crystal structure of $[Ni(2,2´\text{-bpy})_3]Cl_2\cdot 6H_2O$ was reported previously,[83] the compound crystallize in monoclinic *C*2/*c* space group with a unit cell parameters: a = 13.410(2) Å, b = 22.509(4) Å, c = 23.781(4) Å, $\alpha = \gamma = 90°$, β = 105.39(2)°, V = 6921(2) Å^3, Z = 8. The published crystallographic parameters[83] are summarized in Table 4.8.2.1.

(81) V. F. M. Jaeger, J. A. van Dijk, *Z. Anorg. Allg. Chem.*, **1936**, *227*, 273−327.
(82) G. T. Morgan, F. H. Burstall, *J. Chem. Soc. (R)*, **1931**, 2213−2218.

Table 4.8.2.1 *Crystallographic parameters for* $[Ni(2,2´\text{-bpy})_3]Cl_2 \cdot 6H_2O$.[83]

Molecular formula	$C_{30}H_{36}Cl_2N_6NiO_6$
Formula Weight, g·mol^{-1}	793.11
Crystal system	Monoclinic
Space group	*C*2/*c*
Cell dimensions	
a, Å	13.410(2)
b, Å	22.509(4)
c, Å	23.781(4)
α, ^{0}	90
β, ^{0}	105.39(2)
γ, ^{0}	90
V, Å^3	6921(2)
Z	8
Density, g·cm^{-3}	1.522
Absorption coefficient, mm^{-1}	1.171
Radiation	Mo Kα, λ = 0.71073 Å

The molecular structure of $[Ni(2,2´\text{-bpy})_3]Cl_2 \cdot 6H_2O$ is made of $[Ni(2,2´\text{-bpy})_3]^{2+}$ cationic units, coordinated chloride anions and water molecules of crystallization which are linked through ionic and hydrogen-bonding interactions. The $[Ni(2,2´\text{-bpy})_3]^{2+}$ entities exhibit a quasi D_3 symmetry. The six-coordinated nitrogen atoms of three bpy ligands form a distorted octahedron around the Ni(II) ions. The Ni^{II}–N bonds length are in the range of 2.086 Å –2.101 Å with the average value of 2.094 Å, which are consistent with those in the other compounds.[84–87] The N–Ni^{II}–N bond angles in the precursor compound are within a 78.4–93.9° range.

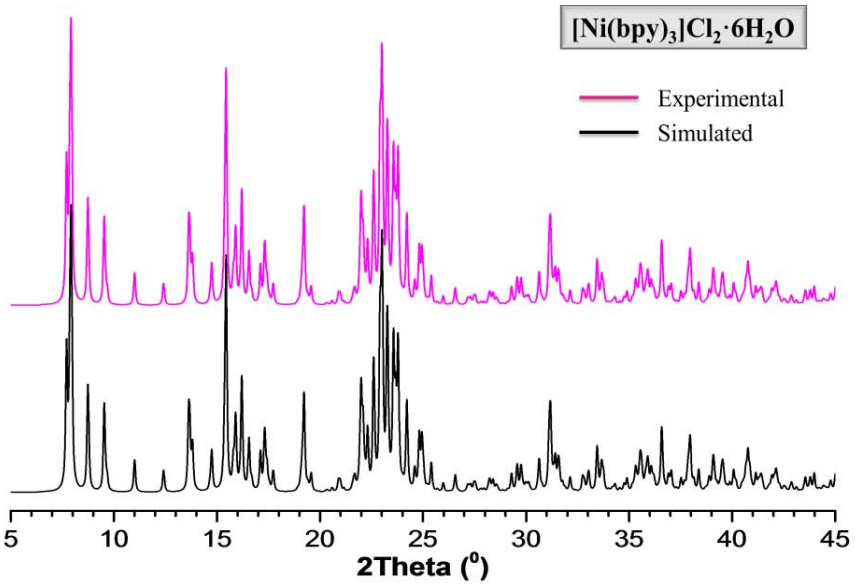

Figure 4.8.2.1 *Powder X-ray diffraction patterns of* $[Ni(2,2´\text{-bpy})_3]Cl_2 \cdot 6H_2O$*: experimental (red) and simulated (black).*

(83) C. Ruiz-Perez, P. A. L. Luis, F. Lloret, M. Julve, *Inorg. Chim. Acta*, **2002**, *336*, 131−136.
(84) Y. Zhou, X. Li, Y. Xu, R. Cao, M. Hong, *Acta Cryst*., **2003**, *E59*, m300– m302.
(85) A. Wada, C. Katayama, J. Tanaka, *Acta Cryst*., **1976**, *B32*, 3194–3199.
(86) J. Cernák, M. Kanuchová, J. Chomic, I. Potocnák, J. Kamenícek, Z. Zák, *Acta Cryst*., **1994**, *C50*, 1563–1566.
(87) A. Wada, N. Sakabe, J. Tanaka, *Acta Cryst*., **1976**, *B32*, 1121–1127.

The overall crystal packing is constructed by three kinds of layers: (*i*) the layer of the Λ-$[Ni(2,2´\text{-bpy})_3]^{2+}$cations; (*ii*) the layer of water/chloride molecules; (*iii*) the layer of Δ-$[Ni(2,2´\text{-bpy})_3]^{2+}$cations and a chloride anions. In order to confirm the structural consistency between the synthesized precursor compound and the expected complex $[Ni(2,2´\text{-bpy})_3]Cl_2\cdot 6H_2O$, the experimental powder pattern of obtained pink solid was compared with the simulated powder pattern from reported single crystal data.[83] The CIF of $[Ni(2,2´\text{-bpy})_3]Cl_2\cdot 6H_2O$ has been requested along with the depositional number of CCDC 116427 from the CSD of Cambridge Crystallographic Data Centre (CCDC).

Figure 4.8.2.1 shows the experimental and simulated powder X-ray diffraction patterns for as-synthesized and reported compound $[Ni(2,2´\text{-bpy})_3]Cl_2\cdot 6H_2O$, which are in a good agreement to each other, exhibiting very similar sequences of Bragg reflections along with their relative intensities and indicate the phase purity and consistence with the expected precursor compound.

4.8.2.2. Infrared Spectroscopy

The solid state infrared spectrum of $[Ni(2,2´\text{-bpy})_3]Cl_2\cdot 6H_2O$ in the region 4000−400 cm^{-1} is shown in Figure 4.8.2.2. The bands assignments summarized in the Table 4.8.2.2 are in a good agreement with bibliographic data.[12,30–32,53] The observed bands are characteristic for tris-bipyridine complexes in low oxidation state.

Table 4.8.2.2 *Selected bands in the IR spectrum of compound $[Ni(2,2´\text{-bpy})_3]Cl_2\cdot 6H_2O$.*

Spectral Region / Band Maximum	Band assignments
3700−3100 *bs*	ν_{sy} (O−H) + ν_{asy} (O−H) crystallization water
3200−3000 *w*	ν_{asy} (C−H) stretching
1660*s*, 1615-1570*s*	δ_{sy} (O−H−O)
1590−1575*m*	
1520−1465*s*	ν_{sy} (C═C) and/or ν_{sy} (C═N) ring str. vibration
1450−1410*m*	
1000−985*m*	δ (C−H) and/or C−H in-plane deformation vibrations.
780−750*ms*	δ (C−H) and/or C−H out-of-plane deformation vibrations

b broad; ***s*** strong; ***w*** weak; ***vw*** very weak and ***m*** medium

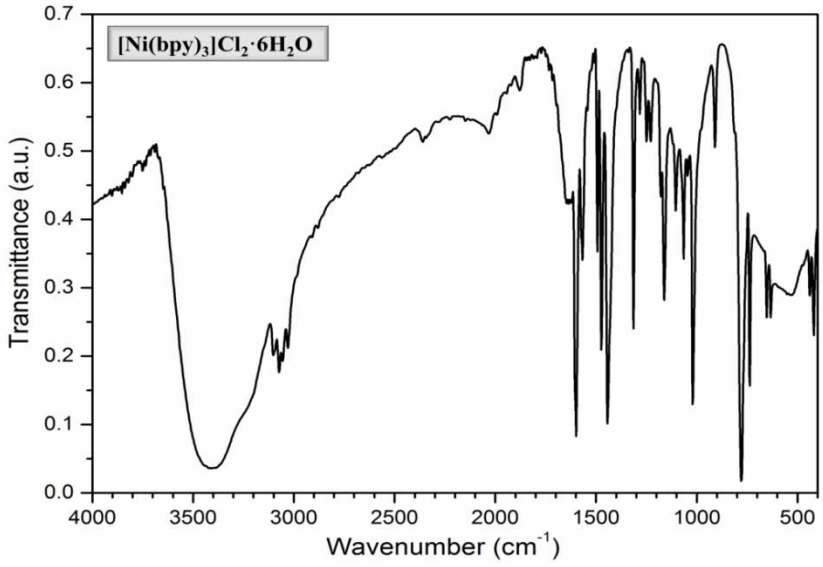

Figure 4.8.2.2 *Infrared spectrum of $[Ni(2,2´\text{-bpy})_3]Cl_2\cdot 6H_2O$.*

The strong broad absorption band between 3700 and 3100 cm^{-1} is attributed to the O−H symmetric and asymmetric vibrations of crystallization water molecules. The aromatic C–H stretching vibration of 2,2´-bpy ligands gives rise to a band at 3200–3000 cm^{-1} with weak-to-medium intensity and consists of a number of peaks. Interactions between rings C═C and C═N stretching vibrations results in two medium-to-strong absorptions. These absorptions occur at 1750–1615 cm^{-1} and 1510–1365 cm^{-1}, the higher frequency band which often possess medium-intensity satellite on its low-frequency site was found at 1590–1555 cm^{-1}. A bands of variable intensities are observed in the regions 1300–1100 cm^{-1} and 1000–985 cm^{-1} where C–H ring deformation modes of the 2,2´-bpy ligand were expected. The 2,2´-bpy ligand strong adsorption bands at 780 and 750 cm^{-1} were assigned to the aromatic out of plane hydrogen deformation modes.

4.8.2.3. Thermogravimetric Analysis

The thermogravimetric analysis (TGA) has been carried out under a nitrogen atmosphere for the synthesized $[Ni(2,2´\text{-bpy})_3]Cl_2\cdot 6H_2O$ with the objectives to determine amount of coordinated water molecules in the compound and confirm the sample purity. The thermogravimetric and corresponding derivative (dTG) curves of the precursor $[Ni(2,2´\text{-bpy})_3]Cl_2\cdot 6H_2O$ are shown in Figure 4.8.2.3., and are in a good agreement with molecular formula and bibliographic data for analogous compounds.[83–91]

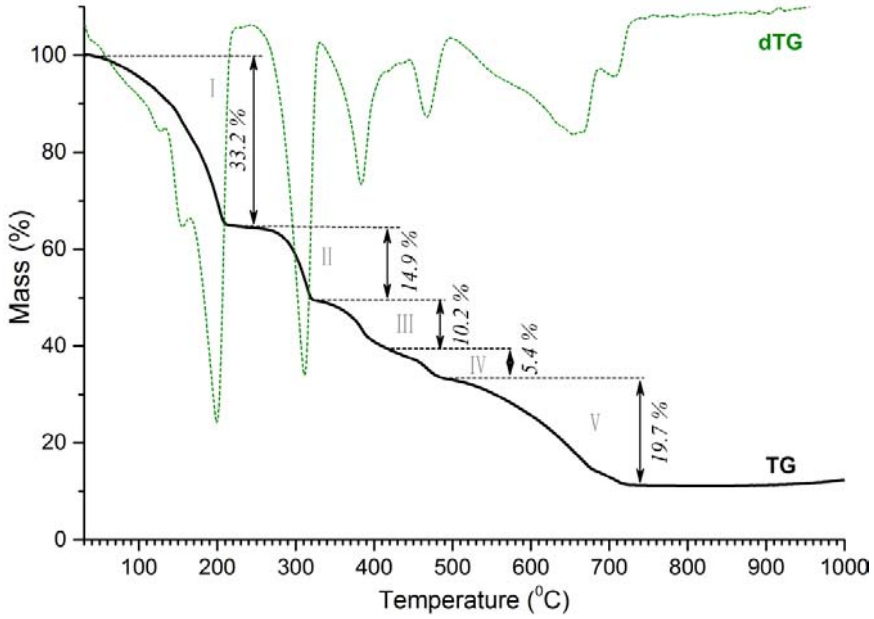

Figure 4.8.2.3 *TG, dTG profiles for thermal decomposition of* $[Ni(2,2´\text{-bpy})_3]Cl_2\cdot 6H_2O$ *under a nitrogen atmosphere*.

The TG-dTG curves exhibit several steps. Dehydration processes along with the loss of one molecule of bipyridine for the complex occur in the region 30–200 °C and proceed in one continuous step (I). The most intense dTG maximum for this process is at about 200 °C, and corresponds to 33.2% total mass loss (*calc*. 33.29%). The resulted compound $[Ni(2,2´\text{-bpy})_2]Cl_2$

(88) R. H. Lee, E. Griswold, J. Kleinberg, *Inorg. Chem*., **1964**, *3*, 1278–1283.
(89) S. K. Dhar, F. Basolo, *J. Inorg. Nucl. Chem*., **1963**, *25*, 37–44.
(90) G. N. Natu, S. B. Kulkarni, P. S. Dhar, *J. Therm. Anal*., **1982**, *23*, 101–109.
(91) N. Parveen, R. Nazir, M. Mazhar, *J. Therm. Anal. Calorim*., **2013**, *111*, 93–99.

was kept stable up to 250 °C, after decomposition step II occurred with a total mass loss of 14.9% (*calc*. 14.31%) reaching the maximum velocity at 320 °C which corresponds to releasing of 0.5 molecule of 2,2´-bpy and one chlorine molecule. The decomposition step (III) with10.2% mass loss belongs to the decomposition of 0.5 remained 2,2´-bpy molecule and shows the maximum velocity at 380 °C. The step (IV) with the 5.4% (*calc*. 4.47%) mass losing and maxima at 470 °C was caused by the liberation of one chlorine molecule. The decomposition of last remaining 2,2´-bpy molecule is observed at the stage (V) with a mass loss of 19.7% (*calc*. 21.0%) and reaches the maximum velocity at 650 °C. According to the calculation based on total experimental and theoretical losses, the final decomposition product of $[Ni(2,2´\text{-bpy})_3]Cl_2\cdot 6H_2O$ under a nitrogen atmospheres is NiO.

4.8.2.4. Solid State UV-VIS Spectroscopy

The electronic configuration of Ni^{2+} in $[Ni(2,2´\text{-bpy})_3]^{2+}$complex is d^8 and the octahedral ground state is $^3A_2$.[20,34,92,93] The room temperature diffuse-reflectance UV-VIS spectrum of synthesized $[Ni(2,2´\text{-bpy})_3]Cl_2\cdot 6H_2O$ complex is illustrated in the Figure 4.8.2.4. The absorption bands intensity and their positions are quite similar to bibliographic values reported for $[Ni(2,2´\text{-bpy})_3]^{2+}$ complex,[37,56,59,94] that indicates the phase purity and consistence of the synthesized product with the expected precursor.

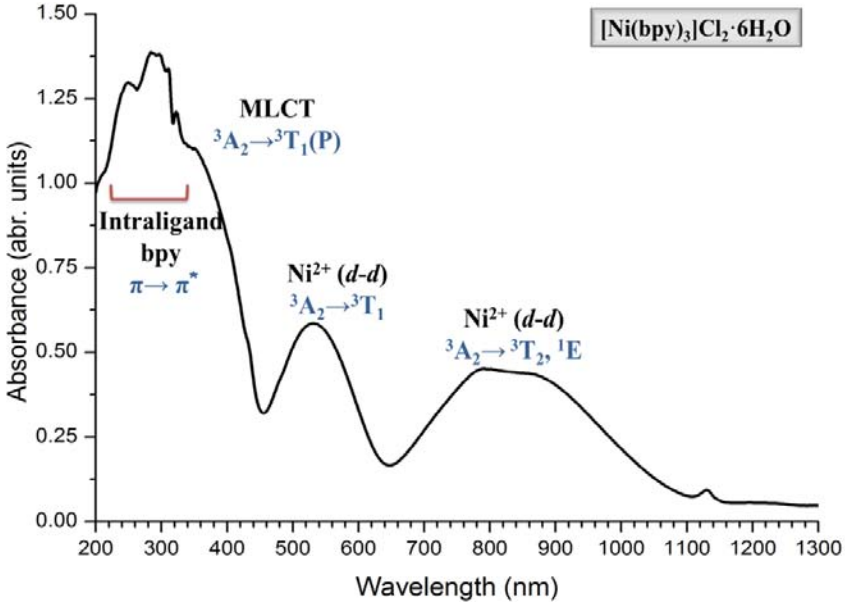

Figure 4.8.2.4 *The room temperature diffuse reflectance UV-VIS spectrum of $Ni(2,2´\text{-bpy})_3]Cl_2\cdot 6H_2O$.*

The high energy bands observed in the range 200−340 nm are caused by π→π* transition within 2,2´-bpy ligand. The octahedral field spin-allowed *d-d* transition can be arranged in order of increasing energy as $^3A_2\rightarrow{}^3T_2(F)$, $^3A_2\rightarrow{}^3T_1(F)$ and $^3A_2\rightarrow{}^3T_1(P)$. The transition $^3A_2\rightarrow{}^3T_1(P)$, which can be seen as a shoulder at *ca*. 365 nm, is partially obscured in the absorption spectra of $[Ni(2,2´\text{-bpy})_3]Cl_2\cdot 6H_2O$ complex by the intense broad shoulder on the ultraviolet 2,2´-bpy bands. The spin-allowed transition $^3A_2\rightarrow{}^3T_1(F)$ is observed at 521 nm. The broad double peak in the region 660−1000 nm is basically two partially overlapped absorption maxima attributed to

(92) Y. Sasaki, *Bull. Inst. Chem. Res. Kyoto Univ*., **1980**, *58*, 187–192.
(93) M. J. Harding, S. F. Mason, B. J. Peart, *J. Chem. Soc. Dalton*, **1973**, 955–960.
(94) C. M. Harris, E. D. McKenzie, *J. Inorg. Nucl. Chem.*, **1967**, *29*, 1047–1068.

the spin-allowed $^3A_2 \rightarrow {}^3T_2(F)$ (*ca.* 890 nm) and the spin-forbidden $^3A_2 \rightarrow {}^1E$ (*ca.* 787 nm) transitions. The resulting doublet corresponds to the crossover point of the $^3T_{1g}$ and ^1E_g energy levels. At the same time, the spin-forbidden transition to the ^1E_g level "borrows" intensity from the spin-allowed transition to the $^3T_{1g}$ level. Both energy levels are actually mixed, and neither of two peaks can be considered to correspond to a pure transition to any of them.

4.9. $[Cu(2,2´\text{-bpy})_3](ClO_4)_2$

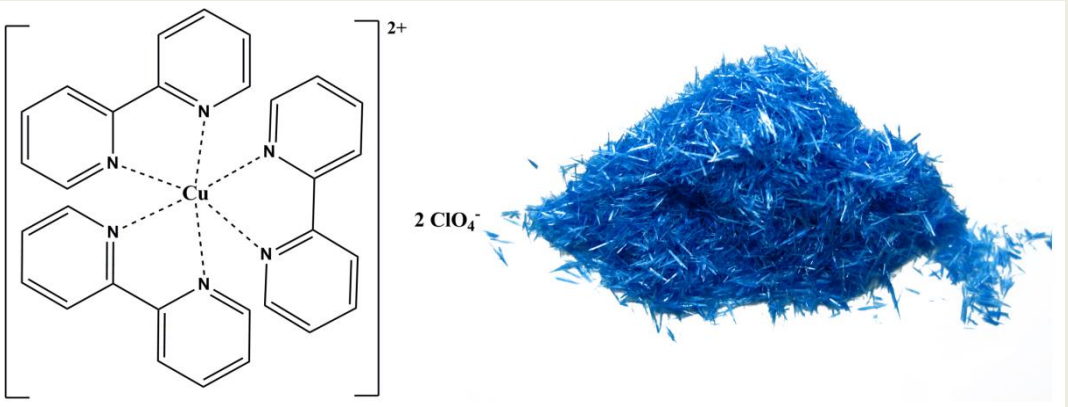

Systematic name	Tris(2,2´-Bipyridine)Copper(II) Perchlorate		
Molecular Formula	$C_{30}H_{24}CuCl_2N_6O_8$		
Molecular Weight	731.08 g/mol	**Appearance**	Blue solid
CAS №	14375-99-6	**Boiling point**	311.4 ºC (atm)
Solubility	water, acetone, ethanol, methanol	**Flash Point**	189.6 ºC

4.9.1. Synthesis

Materials: Commercial copper chloride ($CuCl_2$) 97% reagent grade was obtained from VWR International S.A.S; 2,2´-bipyridine ($C_{10}H_8N_2$) 99% reagent grade from Sigma-Aldrich; Potassium perchlorate ($KClO_4$) 99% reagent grade from Sigma-Aldrich; Ethanol (C_2H_5OH) 96% v/v analytical grade from VWR International S.A.S; Acetone (C_3H_6O) 99.9% analytical grade from VWR International S.A.S.

Synthetic procedure. Compound $[Cu(2,2´\text{-bpy})_3](ClO_4)_2$ has been synthetized following procedure described previously.[49,81,95,96] A 10 mL hot aqueous solution of copper chloride $CuCl_2$ (1.00 g, 7.44 mmol) was added to 10 mL hot ethanol solution of 2,2´-bipyridine (3.49 g, 22.32 mmol), with stirring. The solution of complex was heated 10-15 min over; posterior, excess of potassium perchlorate was added to precipitate the crude product. As a result, the blue precipitate started to appear, and the cooling was being continued in an ice-bath to complete the precipitation. The resulted blue needle-like crystals have been filtered, washed several times with ice-cold water and air dried. The yield is 5.16 g (95%). The crude solid was recrystallized two times from the minimum amount of hot acetone and air dried.

Elemental analysis. Anal. Calculated for $C_{30}Cl_2CuH_{24}N_6O_8$: C, 49.28%; H, 3.31%; N, 11.49%. Found: C, 49.0%; H, 3.5%; N, 11.3%.

(95) M. P. Taboada Sotomayor, A. A. Tanaka, L. T. Kubota, *Electrochim. Acta*, **2003**, *48*, 855−865.
(96) P. Majumdar, A. K. Ghosh, L. R. Falvello, S. M. Peng, S. Goswami, *Inorg. Chem.*, **1998**, *37*, 1651−1654.

4.9.2. Identification Procedures

4.9.2.1. Powder X-ray Diffraction

The crystal structure of $[Cu(2,2´\text{-bpy})_3](ClO_4)_2$ was reported previously.[96–98] The compound crystallize in triclinic *P*-1 space group with a unit cell parameters: a = 12.673(17) Å, b = 18.44(2) Å, c = 7.937(7) Å, α = 90.37(14)°, β = 120.56(13)°, γ = 98.80(11)°, V = 1571(4) Å^3, Z = 2. The published crystallographic parameters are summarized in Table 4.9.2.1.

Table 4.9.2.1 Crystallographic parameters for *$[Cu(2,2´\text{-bpy})_3](ClO_4)_2$*.[96]

Molecular formula	$C_{30}H_{24}Cl_2CuN_6O_8$
Formula Weight, g·mol^{-1}	754.81
Crystal system	triclinic
Space group	*P*-1
Cell dimensions	
a, Å	12.673(17)
b, Å	18.44(2)
c, Å	7.937(7)
α, ^{0}	90.37(14)
β, ^{0}	120.56(13)
γ, ^{0}	98.80(11)
V, Å^3	1571(4)
Z	2
Density, g·cm^{-3}	1.393
Absorption coefficient, mm^{-1}	0.912
Radiation	Mo Kα, λ = 0.71073 Å

The crystal structure of $[Cu(2,2´\text{-bpy})_3](ClO_4)_2$ is composed of monomeric $[Cu(2,2´\text{-bpy})_3]^{2+}$ cations and uncoordinated perchlorate anions. The Cu(II) atom is surrounded by six N atoms from three chelating bpy ligands showing a considerable deviation from the D_3 symmetry. The four Cu^{II}–N bonds of equal lengths, mean 2.031 Å. The remaining two Cu^{II}–N bonds are unequal lengths of 2.450 Å and 2.226 Å. The significant elongation of two Cu^{II}–N bonds in relative trans-position indicates the Jahn-Teller effect which is in a good agreement with analogous compound.[99] The second main distortion of the coordination shell around the Cu(II) atom is the contraction of three N–Cu^{II}–N angles from the ideal octahedral values, caused by three chelate ligands. The chelate angles for bpy ligand, N–Cu^{II}–N, vary from 73.9(2)° to 101.6(2)°. In order to confirm the structural consistency between the synthesized precursor compound and the expected complex $[Cu(2,2´\text{-bpy})_3](ClO_4)_2$, the experimental powder pattern of obtained blue solid was compared with the simulated powder pattern from the reported single crystal data.[96–98] The CIF of $[Cu(2,2´\text{-bpy})_3](ClO_4)_2$ has been requested with the depositional number of CSD TBPYCU01, CSD TBPYCU02, CSD TBPYCU03 from the CSD of Cambridge Crystallographic Data Centre (CCDC).

Figure 4.9.2.1 shows the experimental and simulated powder X-ray diffraction patterns for as-synthesized and reported compound $[Cu(2,2´\text{-bpy})_3](ClO_4)_2$, which are in a good

(97) Z. M. Liu, Z. H. Jiang, D. Z. Liao, G. L. Wang, X. K. Yao, H. G. Wang, *Polyhedron*, **1991**, *10*, 101–102.
(98) O. P. Anderson, *J. Chem. Soc. Dalton Trans*., **1972**, 2597–2601.
(99) G. A. van Albada, S. Nur, I. Mutikainen, U. Turpeinen, J. Reedijk, *J. Mol. Struct*., **2008**, 875, 91–95.

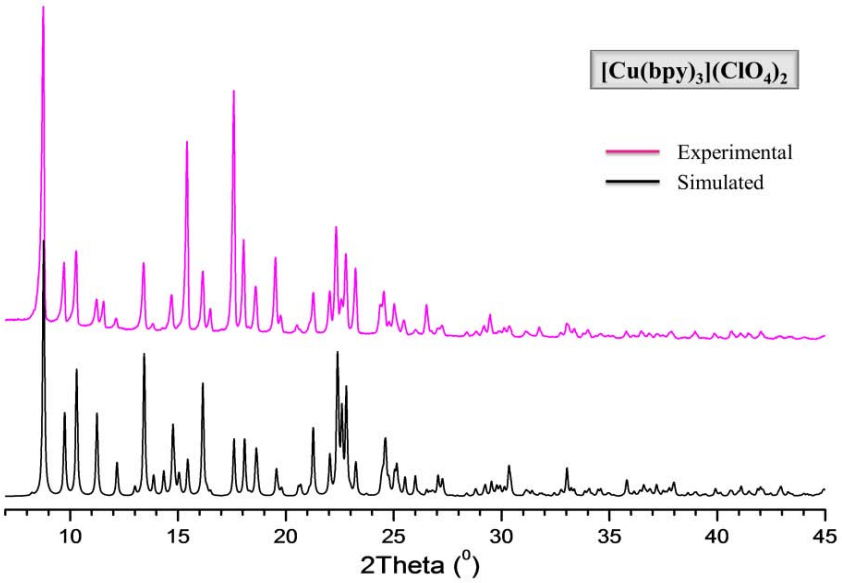

Figure 4.9.2.1 *Powder X-ray diffraction patterns of [Cu(2,2´-bpy)$_3$](ClO$_4$)$_2$: experimental (red) and simulated (black).*

agreement to each other exhibiting very similar sequences of Bragg reflections and indicate to the phase purity and consistence with the expected precursor compound. The slight difference in the relative intensities of diffraction peaks is promoted by a preferred orientation as an influence of needle-like crystals of the sample.

4.9.2.2. Infrared Spectroscopy

The solid state infrared spectrum of [Cu(2,2´-bpy)$_3$](ClO$_4$)$_2$ in the region 4000−400 cm^{-1} is shown in Figure 4.9.2.2. The bands assignments summarized in the Table 4.9.2.2 are in good agreement with bibliographic data.[12,30–32,49,53,100] The observed bands are characteristic for tris-bipyridine complexes of transition metals in a low oxidation state.

Table 4.9.2.2 *Selected bands in the IR spectrum of compound [Cu(2,2´-bpy)$_3$](ClO$_4$)$_2$.*

Spectral Region / Band Maximum	Band assignments
3650−3250 *bvw*	ν_{sy} (O−H) + ν_{asy} (O−H) or hydrogen bonding
3125−2880 *w*	ν_{asy} (C−H) stretching
1660 *s*	δ_{sy} (O−H−O)
1650-1550*ms* 1590−1555*m* 1510−1450*ms* 1450−1410*m*	ν_{sy} (C═C) and/or ν_{sy} (C═N) ring str. vibration
1098−1090*s*	ν(Cl−O) and/or δ (Cl−O) of ClO_4^- uncoordinated
1350−1150*m* 1000−850*m*	δ (C−H) and/or C−H in-plane deformation vibrations.
780−650*ms*	δ (C−H) and/or C−H out-of-plane deformation vibrations

b broad; ***s*** strong; ***w*** weak; ***vw*** very weak and ***m*** medium

(100) G. C. Percy, *J. Mol. Struct*., **1972**, *14*, 313–319.

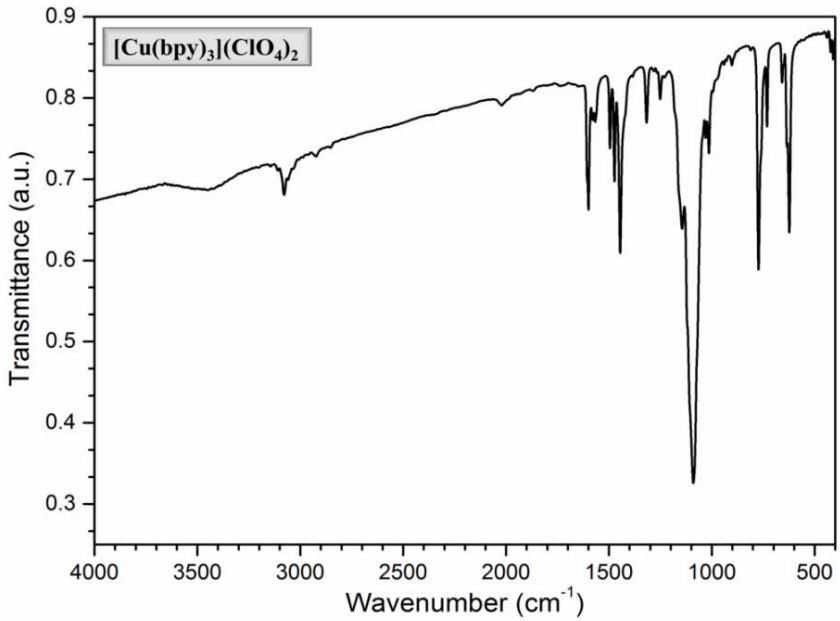

Figure 4.9.2.2 *Infrared spectrum of [Cu(2,2´-bpy)$_3$](ClO$_4$)$_2$.*

The spectrum of [Cu(2,2´-bpy)$_3$](ClO$_4$)$_2$ consists of a relatively small number of absorption bands which may be assigned as follows: the broad absorption band in the region 3650–3250 cm^{-1} due to asymmetric and symmetric H–O–H stretching vibrations is assigned to physically adsorbed water molecules; the aromatic C–H stretching vibration of 2,2´-bpy ligands gives rise to a band at 3125−2880 cm^{-1} with weak-to-medium intensity and consists of a few peaks. Interactions between rings C═C and C═N stretching vibrations result in two medium-to-strong absorptions. These absorptions occur at 1650–1550 cm^{-1} and 1510–1450 cm^{-1}, the higher frequency band which often has a medium-intensity satellite on its low-frequency site is found at 1590–1555 cm^{-1}. A bands of variable intensities are observed in the regions 1350–1150 cm^{-1} and 1000–850 cm^{-1} where C−H ring deformation modes of the 2,2´-bpy ligand were expected. The 2,2´-bpy ligand strong adsorption bands at 780 and 650 cm^{-1}, are assigned to the aromatic out-of-plane hydrogen deformation modes. Furthermore, the spectra exhibit very strong single absorption bands associated with uncoordinated ClO_4^- anion at 1098 cm^{-1} and 1095−1090 cm^{-1}, respectively.

4.9.2.3. Thermogravimetric Analysis

The thermogravimetric analysis (TGA) has been carried out under an air atmosphere for the synthesized [Cu(2,2´-bpy)$_3$](ClO$_4$)$_2$ with the objectives to confirm the sample purity. The thermogravimetric and corresponding derivative (dTG) curves of the precursor [Cu(2,2´-bpy)$_3$](ClO$_4$)$_2$ are shown in Figure 4.9.2.3. Due to high explosive nature of perchlorate salts, its thermal decomposition data are rarely reported in bibliography. The thermal decomposition behavior of [Cu(2,2´-bpy)$_3$](ClO$_4$)$_2$ was investigated and compared with the similar compounds.[74,101–104]

(101) G. Singh, I. P. Singh Kapoor, D. Kumar, U. P. Singh, N. Goel, *Inorg. Chim. Acta*, **2009**, *362*, 4091–4098.
(102) G. Singh, A. K. Shrimal, I. P. Singh Kapoor, C. Prakash Singh, D. Kumar, S. Mudi Manan, *J. Therm. Anal. Calorim*., **2011**, *103*, 149–155.
(103) G. Singh, C. Prakash Singh, S. M. Mannan, *Thermochim. Acta*, **2005**, *437*, 21–25.
(104) S. Cudziło, M. Nita, *J. Hazard. Mater*., **2010**, *177*, 146–149.

The TG-dTG curves show two well defined decomposition stages. The first stage takes place in the range of 190–250 °C with a mass loss of 21.4% reaching the maximum velocity at 240 °C.

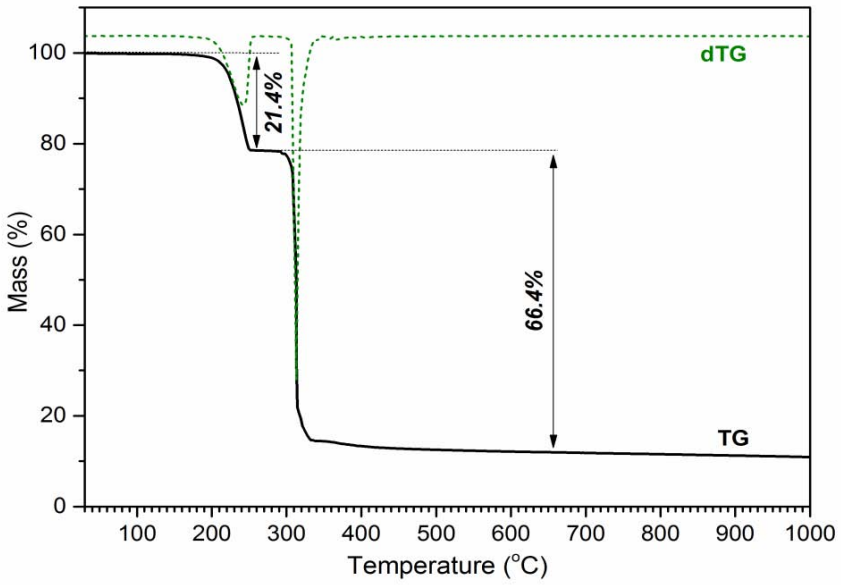

Figure 4.9.2.3 *TG, dTG profiles for thermal decomposition of [Cu(2,2´-bpy)$_3$](ClO$_4$)$_2$ under an air atmosphere*.

The experimental mass loss of 21.4% is consistent with the calculated value of 21.36% and may be attributed to the removal of one 2,2´-bpy molecule. The second stage observed in the range of 260–350 °C with the mass loss of 66.4% and reaching the maximum velocity at 320 °C, corresponds to explosive combustion of the resulted compound. The solid residue formed at around 600 °C is suggested to be CuO (remaining weight 11.3%, Calcd.: 10.8%).

4.9.2.4. Solid State UV-VIS Spectroscopy

The electronic configuration of Cu^{2+} in $[Cu(2,2´\text{-bpy})_3]^{2+}$complex is d^9 and the octahedral ground state is ^2E_g ($t_{2g}^6e_g^3$).[34] The room temperature diffuse-reflectance UV-Vis spectra of synthesized $[Cu(2,2´\text{-bpy})_3](ClO_4)_2$ complex is illustrated in the Figure 4.9.2.4.

The absorption bands intensity and their positions are quite similar with bibliographic values reported for $[Cu(2,2´\text{-bpy})_3]^{2+}$ complex,[20,37,96,105,106] that indicate the phase purity and consistence of the synthesized product with the expected precursor.

The electronic absorption spectrum of $[Cu(2,2´\text{-bpy})_3](ClO_4)_2$ complex consists of three group of bands: (*i*) two strong well-defined bands at the UV region; (*ii*) the shoulder at the near-UV region; (*iii*) two medium strong bands in the visible region. The two high-energy bands in UV-region at 240, 280 appear to be intraligand transitions and have been assigned to a $\pi\rightarrow\pi^*$ transition. In the near-UV region, the electronic absorption spectrum of precursor has a shoulder which can be assigned to MLCT. The MLCT energy is slightly higher than for analogous $[M(2,2´\text{-bpy})_3]^{2+}$ complexes, and the higher energy transition may be understood as an increase of $d\sigma^*\rightarrow p\pi^*$ gap as metal *d* orbitals are stabilized across the periodic table, while ligand $p\sigma$ and $p\pi$ remain unchanged. In octahedral crystal field for Cu^{2+} ion with the excited electronic state $t_{2g}^5e_g^4$ ($^2T_{2g}$), only one single electron transition $^2E_g \rightarrow {}^2T_{2g}$ is expected.

(105) E. Prenesti, P. G. Daniele, S. Berto, S. Toso, *Polyhedron*, **2006**, *25*, 2815–2823.
(106) R. R. Ruminski, *Inorg. Chim. Acta*, **1985**, *103*, 159–161.

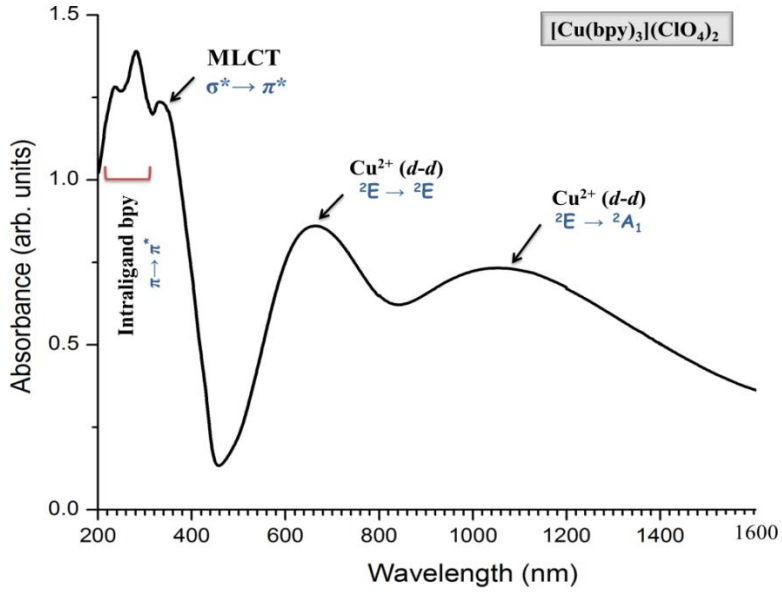

Figure 4.9.2.4 *The room temperature diffuse reflectance UV-VIS spectrum of [Cu(2,2´-bpy)$_3$](ClO$_4$)$_2$.*

Normally, the octahedral coordination of Cu^{2+} ions undergoes Jahn-Teller distortion leading to the trigonally distorted pseudo D_3 symmetry. In case of $[Cu(2,2´\text{-bpy})_3]^{2+}$ complex, it is proposed that 2,2´-bpy ligand rigidly restricts Jahn-Teller distortion and the observed *d–d* transitions should be treated as in trigonal field. Basing on this consideration, the *d–d* transitions observed in visible and near infrared regions can be assigned as follows: the band at 680 nm to $^2E \rightarrow {}^2E$ transition, and sharp band at 1100 nm to $^2E \rightarrow {}^2A_1$ transition.

From these results it is reasonable to conclude that synthetized precursor can be formulated as $[Cu(2,2´\text{-bpy})_3](ClO_4)_2$ complex.

4.10. $[Zn(2,2´\text{-bpy})_3](ClO_4)_2$

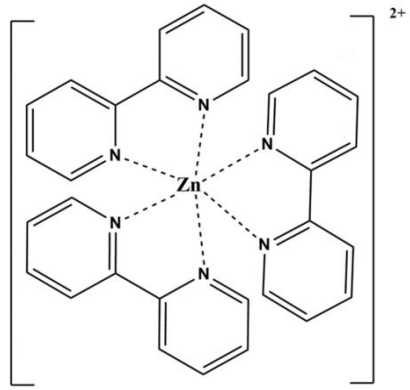

Systematic name	Tris(2,2´-Bipyridine)Zinc(II) Perchlorate		
Molecular Formula	$C_{30}H_{24}Cl_2N_6O_8Zn$		
Molecular Weight	732.93 g/mol	**Appearance**	Pale pink solid
CAS №	36578-63-9	**Boiling point**	365.1 ºC (atm)
Solubility	water, acetone, ethanol, methanol	**Flash Point**	164.8 ºC

4.10.1. Synthesis

Materials: Commercial zinc chloride ($ZnCl_2$) 98% reagent grade was obtained from Sigma-Aldrich; 2,2´-bipyridine ($C_{10}H_8N_2$) 99% reagent grade from Sigma-Aldrich; Potassium perchlorate ($KClO_4$) 99% reagent grade from Sigma-Aldrich; Methanol (CH_3OH) 98% v/v

analytical grade from VWR International S.A.S; Acetone (C_3H_6O) 99.9% analytical grade from VWR International S.A.S.

Synthetic procedure. Compound $[Zn(2,2´\text{-bpy})_3](ClO_4)_2$ has been synthetized following procedure described previously.[49,81,107] The zinc chloride $ZnCl_2$ (1.03 g, 7.56 mmol) was dissolved in 10 mL H_2O and added with vigorous stirring to hot methanol solution contained 2,2´-bipyridine (3.54 g, 22.67 mmol). The resulted solution was being heated for 15-20 min with stirring, treated with an excess of potassium perchlorate and the heating was being continued until half of its volume is evaporated. The colorless solution was cooled down to room temperature until the pink solid started to appear. To completing precipitation, the solution was being cooled in an ice-bath for 3 h. The resulted plate-like pink crystals were filtered, washed several times with small amount of ice-cold water, and air dried. The complex was recrystallized two times from the minimum amount of hot acetone and air dried. The yield is 4.76 g (86%).

Elemental analysis. Anal. Calculated for $C_{30}Cl_2H_{24}N_6O_8Zn$: C, 49.16%; H, 3.30%; N, 11.47%. Found: C, 49.1%; H, 3.1%; N, 11.3%

4.10.2. Identification Procedures

4.10.2.1. Powder X-ray Diffraction

The crystal structure of $[Zn(2,2´\text{-bpy})_3](ClO_4)_2$ was reported previously,[23,107–109] the compound crystallize in monoclinic *C*2/*c* space group with a unit cell parameters: *a* = 17.473(3) Å, *b* = 10.926(2) Å, *c* = 16.163(3) Å, α = γ = 90°, β = 91.17(3)°, V = 3085.0(10) Å^3, Z = 4. The published crystallographic parameters are summarized in Table 4.10.2.1.

Table 4.10.2.1 *Crystallographic parameters for $[Zn(2,2´\text{-bpy})_3](ClO_4)_2$.* [23,107–109]

Molecular formula	$C_{30}H_{24}Cl_2N_6O_8Zn$
Formula Weight, g·mol^{-1}	732.84
Crystal system	monoclinic
Space group	*C*2/*c*
Cell dimensions	
a, Å	17.473(3)
b, Å	10.926(2)
c, Å	16.163(3)
α, ^{0}	90
β, ^{0}	91.17(3)
γ, ^{0}	90
V, Å^3	3085.0(10)
Z	4
Density, g·cm^{-3}	1.578
Absorption coefficient, mm^{-1}	1.031
Radiation	Mo Kα, λ = 0.71073 Å

The crystal structure of $[Zn(2,2´\text{-bpy})_3](ClO_4)_2$ is composed of monomeric $[Zn(2,2´\text{-bpy})_3]^{2+}$ cations and perchlorate anions. The Zn(II) atom is surrounded by six N atoms from three

(107) G. H. Eom, H. M. Park, M. Y. Hyun, S. P. Jang, C. Kim, J. H. Lee, S. J. Lee, S.-J. Kim, Y. Kim, *Polyhedron*, **2011**, *30*, 1555−1564.
(108) X.-M. Chen, R.-Q. Wang, X.-L. Yu, *Acta Cryst.*, **1995**, *51*, 1545−1547.
(109) U. Klement, D. Trumbach, H. Yersin, *Z. Kristallogr. – New Cryst. Struct.*, **1995**, *210*, 228−228.

chelating bpy ligands arranged in a highly distorted octahedral with Zn–N bond lengths ranging from 2.135(2) Å to 2.172(3) Å with the average value of 2.157 Å, which are consistent with those in the other compounds.[24] The N–Zn^{II}–N bond angles in the precursor compound are in the 75.8–98.1° range. In order to confirm the structural consistency between the synthesized precursor compound and the expected complex $[Zn(2,2´\text{-bpy})_3](ClO_4)_2$, the experimental powder pattern of obtained light pink solid was compared with the simulated powder pattern from the reported single crystal data.[23,107–109] The CIF of $[Zn(2,2´\text{-bpy})_3](ClO_4)_2$ has been requested with the depositional number of IUCr JZ1001, CSD 400893 and CCDC 802854 from the CSD of Cambridge Crystallographic Data Centre (CCDC).

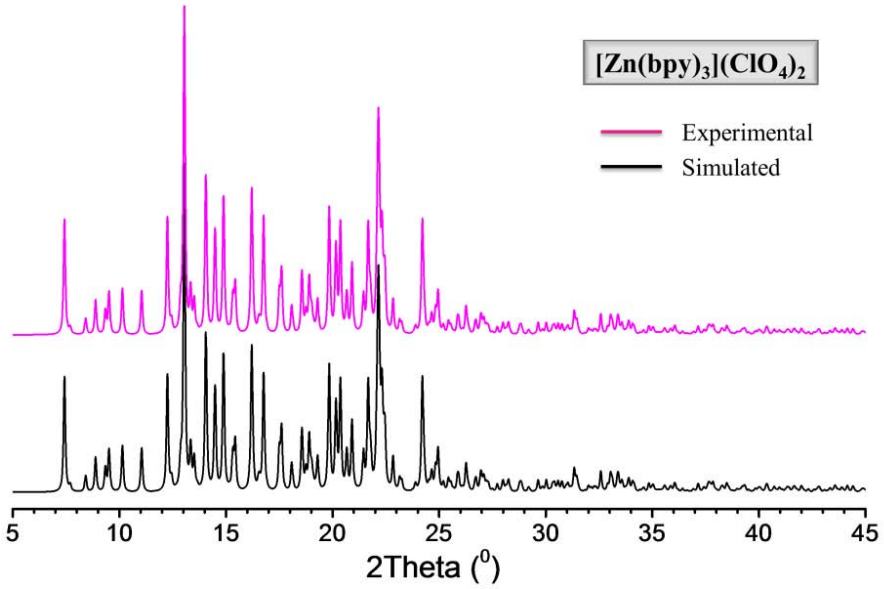

Figure 4.10.2.1 *Powder X-ray diffraction patterns of $[Zn(2,2´\text{-bpy})_3](ClO_4)_2$: experimental (red) and simulated (black).*

Figure 4.10.2.1 shows the experimental and simulated powder X-ray diffraction patterns for the as-synthesized and the reported compound $[Zn(2,2´\text{-bpy})_3](ClO_4)_2$, which are in a good agreement to each other, exhibiting very similar sequences of Bragg reflections along with their relative intensities, indicate the phase purity and consistence with the expected precursor compound.

4.10.2.2. Infrared Spectroscopy

The solid state infrared spectrum of $[Zn(2,2´\text{-bpy})_3](ClO_4)_2$ in the region 4000−400 cm^{-1} is shown in Figure 4.10.2.2. The bands assignments summarized in the Table 4.10.2.2 are in good agreement with bibliographic data.[12,30–32,49,53] The observed bands are characteristic for tris-bipyridine complexes of transition metals in a low oxidation state. The spectrum of $[Zn(2,2´\text{-bpy})_3](ClO_4)_2$ consists of a relatively small number of absorption bands which may be assigned as follows: the broad absorption band in the region 3650–3350 cm^{-1} caused by asymmetric and symmetric H–O–H stretching vibrations is assigned to physically adsorbed water molecules; the aromatic C–H stretching vibration of 2,2´-bpy ligands gives rise to a band at 3200−2880 cm^{-1} with weak-to-medium intensity and consists of a few peaks. Interactions between rings C═C and C═N stretching vibrations result in two medium-to-strong absorptions. These absorptions occur at 1650–1550 cm^{-1} and 1510–1450 cm^{-1}, the higher frequency band which often has a medium-intensity satellite on its low-frequency site is found at 1590–1555 cm^{-1}. The bands of variable

intensities are observed in the regions 1350–1150 cm^{-1} and 1000–850 cm^{-1} where C−H ring deformation modes of the 2,2´-bpy ligand were expected.

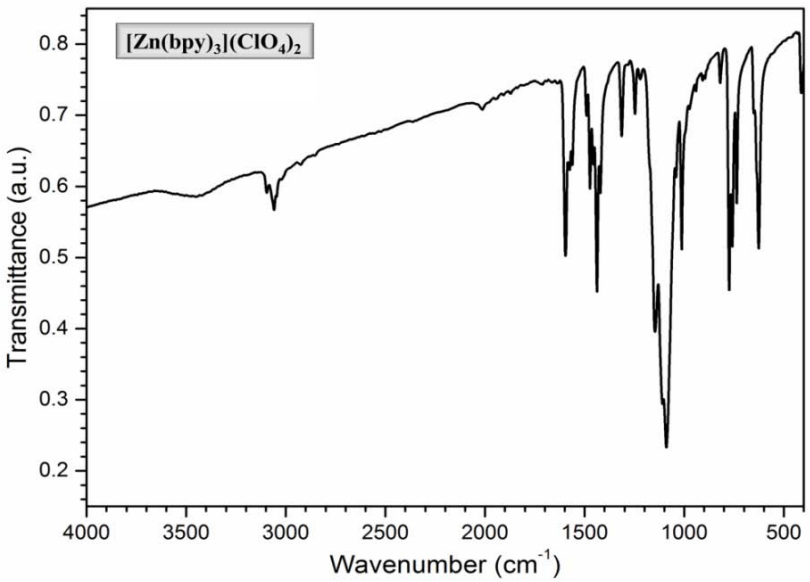

Figure 4.10.2.2 *Infrared spectrum of [Zn(2,2´-bpy)$_3$](ClO$_4$)$_2$.*

Table 4.10.2.2 *Selected bands in the IR spectrum of compound [Zn(2,2´-bpy)$_3$](ClO$_4$)$_2$.*

Spectral Region / Band Maximum	Band assignments
3650−3350 *bvw*	ν_{sy} (O−H) + ν_{asy} (O−H) or hydrogen bonding
3200−2880 *w*	ν_{asy} (C−H) stretching
1660 *s*	δ_{sy} (O−H−O)
1650-1550*ms*	
1590−1555*m*	ν_{sy} (C═C) and/or ν_{sy} (C═N)
1510−1450*ms*	ring str. vibration
1450−1410*m*	
1098−1090*s*	ν(Cl−O) and/or δ (Cl−O) of ClO_4^- uncoordinated
1350−1150*m*	δ (C−H) and/or C−H in-plane deformation
1000−850*m*	vibrations.
780−650*ms*	δ (C−H) and/or C−H out-of-plane deformation vibrations

b broad; ***s*** strong; ***w*** weak; ***vw*** very weak and ***m*** medium

The 2,2´-bpy ligand strong adsorption bands at 780 and 650 cm^{-1} are assigned to the aromatic out-of-plane hydrogen deformation modes. Furthermore, the spectrum exhibits very strong single absorption bands associated with uncoordinated ClO_4^- anion at 1098 cm^{-1} and 1095−1090 cm^{-1}, respectively.

4.10.2.3. Thermogravimetric Analysis

The thermogravimetric analysis (TGA) has been carried out under a nitrogen atmosphere for the synthesized [Zn(2,2´-bpy)$_3$](ClO$_4$)$_2$ with the objectives to confirm the sample purity. The thermogravimetric and corresponding derivative (dTG) curves of the precursor [Zn(2,2´-bpy)$_3$](ClO$_4$)$_2$ are shown in Figure 4.10.2.3. Due to high explosive nature of perchlorate salts, its thermal decomposition data are rarely reported in bibliography. The thermal decomposition

behavior of $[Zn(2,2´\text{-bpy})_3](ClO_4)_2$ was investigated and compared with the similar compounds.[74,101–103]

The decomposition profile of $[Zn(2,2´\text{-bpy})_3](ClO_4)_2$ shows three well defined stages occurring during heating from 25 °C to 1000 °C. The first stage takes place in the range of 30–208 °C with the mass loss of 21.3% reaching the maximum velocity at 190 °C.

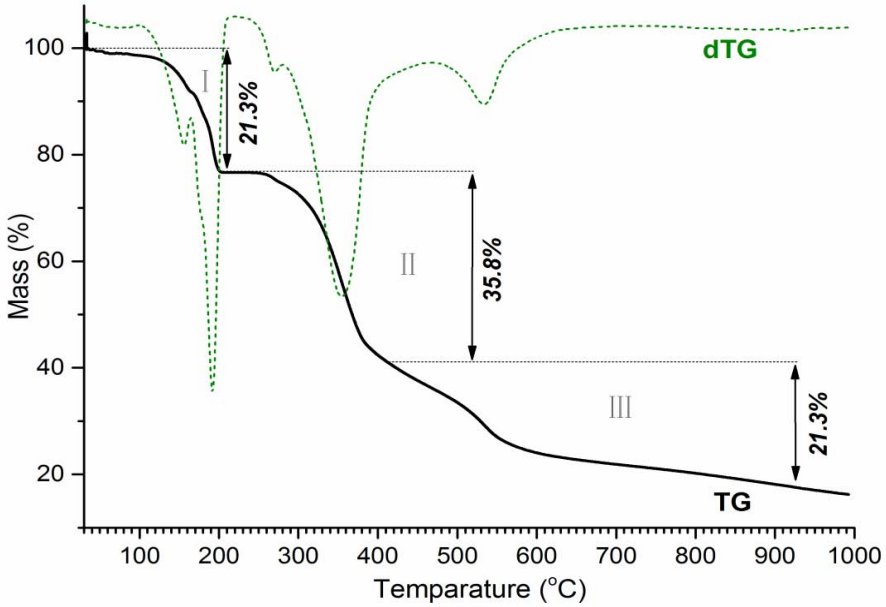

Figure 4.10.2.3 *TG, dTG profiles for thermal decomposition of $[Zn(2,2´\text{-bpy})_3](ClO_4)_2$ under a nitrogen atmosphere.*

The experimental mass loss of 21.3% is consistent with the calculated value 21.3% and attributes to the stepwise removing of one 2,2´-bpy molecule. The second stage observed in wide range of 213–422 °C with maximum velocity at 355 °C, amounting to total mass loss of 35.8%, is consistent with the calculated value of 35.7% for the decomposition of one 2,2´-bpy molecule and elimination of four oxygen atoms from two perchlorate anion. Finally, broad third stage, ranging from 415 °C to 998 °C with the maximum velocity at 534 °C, corresponds to the experimental mass loss of 21.3%. The experimental mass loss of 21.3% is consistent with the calculated value of 23.3% and corresponds to the loss of one 2,2´-bpy molecule along with removing two chloride molecules as gaseous products. The solid residue formed at around 700 °C is suggested to be Zn with the residual carbon residues.

4.10.2.4. Solid State UV-VIS Spectroscopy

The zinc(II) cationic complex $[Zn(2,2´\text{-bpy})_3]^{2+}$ is considered be a typical close shell complex having a $^1A_{1g}$ ($t_{2g}^6e_g^4$) ground state with all ten *d* electrons nicely paired up on the t_{2g} orbitals. The room temperature diffuse-reflectance UV-Vis spectra of synthesized $[Zn(2,2´\text{-bpy})_3](ClO_4)_2$ complex is illustrated in the Figure 4.10.2.4. The absorption bands intensity and their positions are quite similar to bibliographic data[20,23,34,36,110] reported for $[Zn(2,2´\text{-bpy})_3]^{2+}$ complex that indicates the phase purity and consistence of the synthesized product with the expected precursor.

(110) H. Riesen, A. D. Rae, E. Krausz, *J. Luminescence*, **1994**, *62*, 123–137.

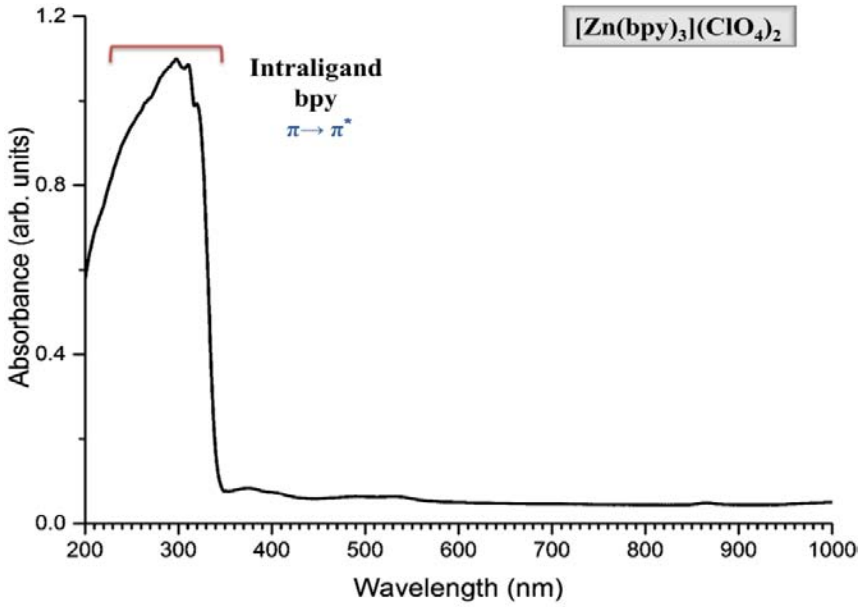

Figure 4.10.2.4 *The room temperature diffuse reflectance UV-VIS spectrum of [Zn(2,2´-bpy)$_3$](ClO$_4$)$_2$.*

The absorption spectrum of this complex is dominated by one intense high-energy bands in the region 200−300 nm, which appear to be π→π* intraligand transitions. Due to the close shell configuration for d^{10} Zn^{2+} ion, as expected, no *d-d* transitions are observed in the diffuse-reflectance UV-Vis spectra. With these results it is reasonable to conclude that the synthetized precursor can be formulated as [Zn(2,2´-bpy)$_3$](ClO$_4$)$_2$ complex.

Capítulo V

Preparación de Nanopartículas de Rutenio(0) *vía* Síntesis Hidrotermal

El *Capítulo V* se dedica a la preparación de nanopartículas de rutenio(0) aplicando procedimientos de síntesis hidrotermal. Los resultados descritos en esta sección tuvieron su origen en el desarrollo sistemático de la parte experimental diseñada para la síntesis directa de polímeros de coordinación basados en carboxilatos de rutenio. En ciertas condiciones experimentales, puede alcanzarse la formación del polímero de coordinación termodinámicamente estable mediante reacción directa entre la sal metálica y el enlazador orgánico (frecuentemente, ácidos carboxílicos multidentados). Sin embargo, en las condiciones hidrotermales utilizadas, los ácidos carboxílicos empleados *(cítrico, ascórbico o succínico)* actúan como agentes reductores de las especies de Ru^{III} conduciendo a la formación de nanopartículas. Con objeto de sistematizar la síntesis de nanopartículas de rutenio decidimos explorar el sistema $RuCl_3 \cdot xH_2O$ – ácido carboxílico, siendo ambos componentes comercialmente accesibles. Esta metodología no es nueva, ya que varios ácidos carboxílicos han sido utilizados previamente como reductores suaves en la preparación de nanopartículas de metales nobles, tales como Ag, Au, Pt o Pd.[1,2]

En los últimos años, la preparación de nanopartículas de metales nobles utilizando procedimientos de química verde ha propiciado el interés en el desarrollo de nuevos métodos, más ecológicos, para la síntesis de nanopartículas. Con el objetivo de encontrar rutas de síntesis sencillas, de bajo coste, y compatibles con el escalado para su uso comercial, ha sido habitual la descripción de métodos de preparación de partículas con tamaño nanométrico, en medio acuoso, utilizando compuestos carboxílicos como agentes reductores. Al mismo tiempo, este tipo de reductores pueden actuar como estabilizantes de la superficie de las nanopartículas generadas, promoviendo su crecimiento preferente en direcciones determinadas. El escaso número de publicaciones que describen la preparación de nanopartículas de rutenio(0) por métodos ecológicos, unido al aparente interés práctico del establecimiento de una vía verde para su síntesis eficiente, hizo que el proceso de reducción de cloruro de rutenio(III) mediante compuestos carboxílicos en medio acuoso, promovido en condiciones hidrotermales, fuese investigado profundamente y, finalmente, expuesto en el presente capítulo de esta Tesis.

Con el objeto de establecer las condiciones experimentales (reductor, concentración del reductor, relación molar Ru^{3+}: reductor, pH del medio de reacción) más adecuadas para la preparación de nanopartículas de rutenio(0) con morfologías y tamaños determinados, se llevó a cabo un estudio sistemático para determinar el efecto de distintas variables de síntesis sobre el tamaño y la forma de las partículas resultantes. Por ello, la *Publicación II*, que se presenta como parte del contenido de esta Tesis, describe la influencia de varios compuestos carboxílicos y del pH del medio de reacción en el tamaño y en la forma de las nanopartículas de rutenio(0) obtenidas. En primer lugar, el foco de la investigación se centró en la influencia de la concentración del agente reductor en el tamaño de las nanopartículas de rutenio(0). Usando citrato de sodio como reductor (180 °C, condiciones hidrotermales) el tamaño de las nanopartículas *quasi*-esféricas disminuye desde 3.3 nm hasta 2.8 nm cuando aumenta la concentración del agente reductor. Esta misma tendencia se observa cuando es el ácido ascórbico el que actúa como reductor (el tamaño de las nanopartículas disminuye de 4.9 nm a 3.0 nm), siendo mayor la diferencia en el tamaño de las nanopartículas formadas cuando disminuye la concentración del ácido succínico (de 5.9 nm a 3.1 nm). Los datos experimentales indican que el pH del medio de reacción es un factor

(1) S. Panigrahi, S. Kundu, S. K. Ghosh, S. Nath, T. Pal, *Colloids Surf. A: Physicochem. Eng. Asp*., **2005**, *264*, 133–138.

(2) N. N. Mallikarjuna, R. S. Varma, *Cryst.Growth Des*., **2007**, *7*, 686–690.

determinante en el tamaño de los nanocristales resultantes. Cuando los agentes reductores son citrato de sodio y ácido ascórbico, como tendencia general, se observa la formación de partículas más grandes a pHs más bajos. Además, el citrato de sodio favorece la formación de nanopartículas de forma hexagonal en el rango de pH 1.1–3.3, mientras a pH 4 origina nanopartículas rectangulares, que pasan a ser esféricas en medios neutros y básicos. Sin embargo, cuando se utiliza ácido succínico, no se observa una disminución gradual en el tamaño de las nanopartículas con el aumento del pH del medio de reacción, pudiendo describirse mejor el comportamiento experimental mediante una función gaussiana. Así, a pH 1.1 predominan partículas esféricas con un diámetro próximo a 1.5 nm, que va aumentando hasta llegar a 120 nm a pH 4.1 (el posterior incremento del pH de la reacción produce una disminución del tamaño de las nanopartículas hasta valores cercanos a 2.5 nm).

Un estudio posterior, detallado en la *Publicación III*, está enfocado a la determinación de las especies existentes en cada etapa de reducción y su influencia en la morfología de las nanopartículas de rutenio(0) obtenidas. En concreto, se ha establecido que la forma pentagonal de los nanocristales de rutenio(0) es promovida por la presencia de especies acuosas Ru(III)-hidroxo-cloruro, mientras las especies $[Ru(H_2O)_6]^{2+}$ (predominantes a pH 3–4) son responsables de la formación de partículas rectangulares. Los análisis mediante microscopia electrónica de transmisión de alta resolución, junto con la simulación de las superficies en las partículas con morfología hexagonal y rectangular, permiten determinar las direcciones de crecimiento preferente. Así, en el caso de las partículas rectangulares, el crecimiento está favorecido en la dirección (110) con respecto a la (1-10), mientras son las direcciones (002) y (100) las más favorecidas en el crecimiento de nanopartículas pentagonales en medios muy ácidos.

El ácido ascórbico, que es un reductor más potente que el citrato de sodio y el ácido succínico, conduce a la formación de partículas esféricas desagrupadas. El proceso de reducción transcurre con la formación de especies ascorbato, $[RuCl_2(H_2O)_2]Asc$, en un amplio rango de pH (2–12) que, durante el tratamiento hidrotermal, derivan en clústeres de Ru(0), que actúan como núcleos de crecimiento de las nanopartículas metálicas.

Finalmente, en función de su tamaño, se han estudiado las propiedades redox de las nanopartículas obtenidas, estableciéndose que la temperatura de reducción de las nanopartículas de rutenio(0), previamente oxidadas, es función de sus dimensiones. El hecho de que el tamaño de las partículas influya en su temperatura de reducción hace que este factor deba ser considerado como determinante en la optimización del rendimiento de catalizadores de rutenio(0).

Publication II

"Hydrothermal Synthesis and Physicochemical Properties of Ruthenium(0) Nanoparticles"

Journal of Alloys and Compounds

536 (S437–S440)

Year ***2012***

DOI: *10.1016/j.jallcom.2011.12.148*

Impact Factor: 2.999

Journal of Alloys and Compounds 536S (2012) S437–S440

Contents lists available at SciVerse ScienceDirect

Journal of Alloys and Compounds

journal homepage: www.elsevier.com/locate/jallcom

Hydrothermal synthesis and physicochemical properties of ruthenium(0) nanoparticles

A. Dikhtiarenko[a,*], S.A. Khainakov[a], J.R. García[a], J. Gimeno[a], I. de Pedro[b], J. Rodríguez Fernández[b], J.A. Blanco[c]

[a] *Departamento de Química Orgánica e Inorgánica, Universidad de Oviedo – CINN, 33006 Oviedo, Spain*
[b] *CITIMAC, Facultad de Ciencias, Universidad de Cantabria, 39005 Santander, Spain*
[c] *Departamento de Física, Universidad de Oviedo, 33007 Oviedo, Spain*

ARTICLE INFO

Article history:
Received 26 June 2011
Received in revised form
14 December 2011
Accepted 29 December 2011
Available online 8 January 2012

PACS:
81.07.Wx, 75.75.Fk

Keywords:
Ru-nanoparticles
Hydrothermal synthesis
Magnetic susceptibility

ABSTRACT

The synthesis of ruthenium nanoparticles in hydrothermal conditions using mild reducing agents (succinic acid, ascorbic acid and sodium citrate) is reported. The shape of the nanoparticles depends on the type of the reducing agent, while the size is more influenced by the pH of the medium. The magnetic response seems to be dominated by a paramagnetic contribution characteristic of the band electronic magnetism of the nanoparticles.

1. Introduction

Metal nanoparticles have been extensively studied owing to their unique physical properties, and potential applications in electronics [1], biochemistry [2–5] and catalysis [6–13]. In the synthesis of metal nanoparticles the control over the shape and size has been one of the important and challenging tasks, as a consequence of that the shape and crystallographic features are the principal factors that determine the surface activity and the catalytic behavior [14]. Apart from that in the last years, dilute magnetic systems have attracted much attention in solid state physics and chemistry since the discovery of additional fascinating magnetic phenomena such magnetic properties in gold nanoparticles [15].

Chemical reduction of ruthenium salts is still a general approach, although it is well-known that nanoparticles prepared tend to be in narrow range of sizes due to common strategy of the fast reduction [16,17]. In this way, the reduction in aqueous medium of a noble metal precursor using carboxylic compounds as reducing agents lead to good control of particle size, size distribution and morphological variety [18–21]. Although the mechanisms of particle formation have yet to be determined, the combination of mild reducing agents and hydrothermal procedures offers a relatively simple route to make metal nanoparticles with the additional advantage that this method is environmentally benign and amenable to scale-up [22].

In this work, we present the synthesis of ruthenium nanoparticles using carboxylate derivatives as reducing agents, i.e., sodium citrate, succinic and ascorbic acids. We will show that it is possible to synthesize nanoparticles (size 1–100 nm) using hydrothermal conditions.

2. Experimental procedures

At room temperature, ruthenium chloride hydrate (Johnson Matthey – 40.1% Ru), reducing agent (trisodium citrate, ascorbic acid or succinic acid, all Sigma–Aldrich – 99%) and water were mixed at a molar ratio of 1:*x*:50 (*x* = 1–4). Later, the mixture was adjusted at pH = 6 by addition 0.1 M NaOH and stirred, previously to be placed and sealed in a Teflon-lined digestion bomb. After a reaction time of 3 days ($T = 180\,^{\circ}C$), the mixture was cooled and after centrifugation, the resulting solid was washed several times with water, and then dried in air. pH influence on the size nanoparticles, the procedure is similar to described previously: ruthenium chloride, reducing agent and water were mixed at a molar ratio of 1:1:50 and, after, the pH of the mixture was adjusted to the preset value (1–12) with 0.1 M NaOH or 0.1 M HCl.

The size of ruthenium nanoparticles was determined by transmission electron microscopy (JEOL 2000 EX-II). The samples were prepared in a dispersion of 0.1 M CTAB (cetyl trimethylammonium bromide, Sigma–Aldrich, 99%) methanolic solution. For each sample, the average size is obtained by measuring a minimal quantity

* Corresponding author. Tel.: +34 985105753.
E-mail address: dikhtiarenkoalla@uniovi.es (A. Dikhtiarenko).

0925-8388/$ – see front matter © 2012 Elsevier B.V. All rights reserved.
doi:10.1016/j.jallcom.2011.12.148

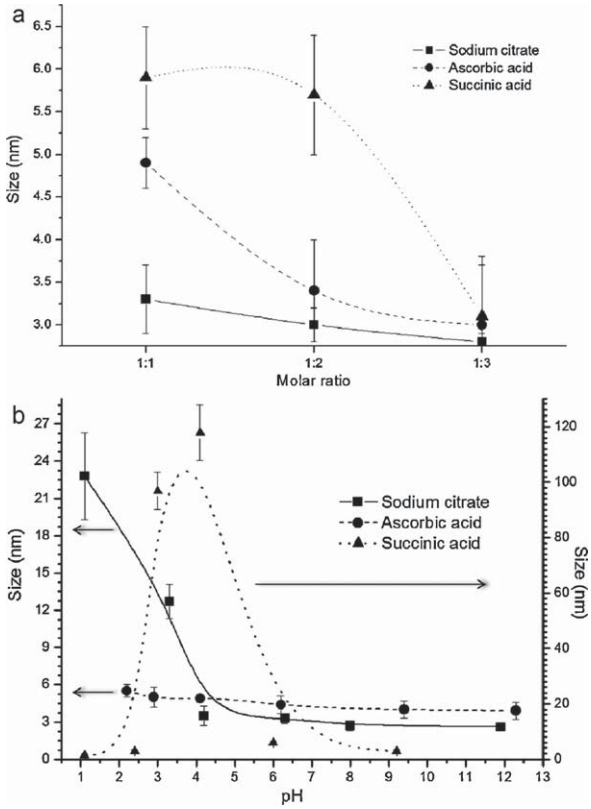

Fig. 1. Effect of the reducing agent concentration (a) and pH (b) on the diameter of ruthenium(0) nanoparticles. It is worth noting that the right *Y*-axis is only for the black triangles, succinic acid.

of a hundred nanoparticles. Powder X-ray diffraction (XRD) measurements were performed on an Oxford-Gemini X-ray diffractometer using CuKα radiation. The samples for XRD analysis were prepared by supporting the powder on nylon CryoLoop.

DC magnetic susceptibility measurements were performed using a Quantum Design SQUID magnetometer while heating from 2 to 300 K at 10 and 1 kOe, after cooling in either the presence (field cooling, FC) or the absence (zero field cooling, ZFC) of the applied magnetic field. Due to the low magnetic signal, the analysis of the magnetic data of ruthenium nanoparticles is experimentally difficult and therefore has been performed subtracting the sample holder background from the samples signals. Thus, initially all magnetic curves have been performed with the empty (diamagnetic) sample holder. Next, the same measurement procedure has been repeated with the sample and the holder. And then the two magnetic signals have been subtracted from each other, yielding to the magnetization due only to the ruthenium nanoparticle sample.

3. Results and discussion

We have synthesized ruthenium(0) nanoparticles by hydrothermal procedures, using several carboxylates as reducing agents. The influence of the reducing concentration on the particle size was evaluated comparing samples obtained with 1:1, 1:2, and 1:3 molar ratios of [Ru]:[Red].

Aggregates of non-spherical nanoparticles were obtained using sodium citrate. Their diameters decrease slightly (from 3.3 to 2.8 nm) when decreasing the [Ru]:[Red] molar ratio. In the case of a reduction with ascorbic acid, the particles also have a small size, but in range from 4.9 to 3.0 nm. When succinic acid was used as reducing agent, average size of nanoparticles moves from 5.9 to 3.1 nm. The comparative results are displayed in Fig. 1(a), while Fig. 1(b) shows the great pH influence on the size of ruthenium(0) nanoparticles.

Is noticeable the great influence that, in the size of ruthenium(0) nanoparticles, exerts the precursor solution pH values (see Fig. 1(b)). In the samples obtained from sodium citrate at pH 1.1

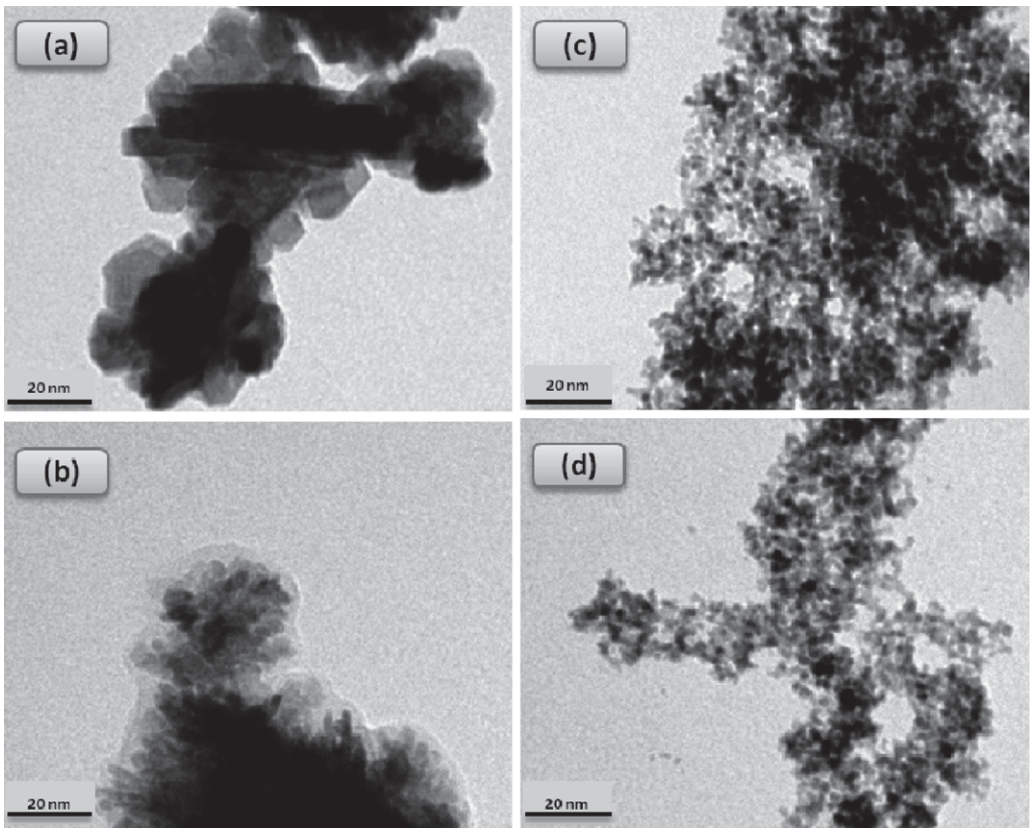

Fig. 2. TEM images of ruthenium(0) nanoparticles by reduction with sodium citrate at pH 3.3 (a), 4.2 (b), 6.3 (c) and 8.0 (d).

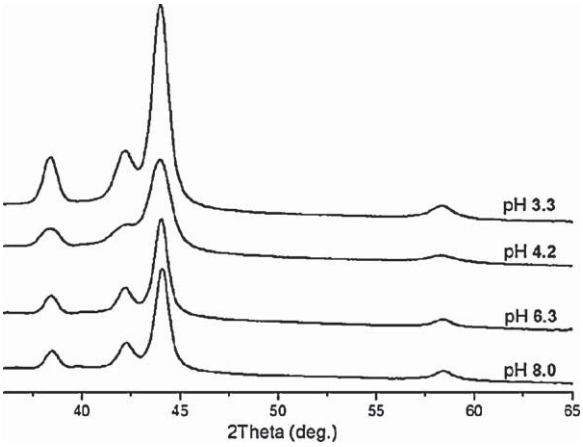

Fig. 3. Powder XRD patterns of ruthenium(0) nanoparticles obtained by reduction with sodium citrate at different pHs.

is observed the formation of nanoparticles with hexagonal shape characterized by up to 22.8 ± 3.5 nm. At pH 3.3, most of the particles maintains the hexagonal shape, but begin to appear some particles with elongated rectangular shape, where their average sizes decrease to 12.3 ± 1.4 nm (Fig. 2(a)). By raising the pH to 4.2, the hexagonal morphology disappears, enhancing the rectangular shape, while the average size lowers to 3.5 ± 0.8 nm (Fig. 2(b)). A new increasing of pH produces the formation of spherical disaggregated particles, with average diameter, which decreases with increasing pH (3.3 ± 0.4 nm at pH 6.3; 2.7 ± 0.4 nm at pH 8.0) (see Fig. 2(c) and (d)).

In all cases, the solid phase obtained after hydrothermal treatment has been identified by reflections of hexagonal close-packed (hcp) ruthenium (see Fig. 3).

A similar situation is observed when ascorbic acid is used as reducing agent. As in the previous case, the size of nanoparticles of ruthenium(0) decreases with increasing the pH of synthesis, although the sizes of nanoparticles obtained at pHs lower than 3 by reduction with ascorbic acid are much smaller than those

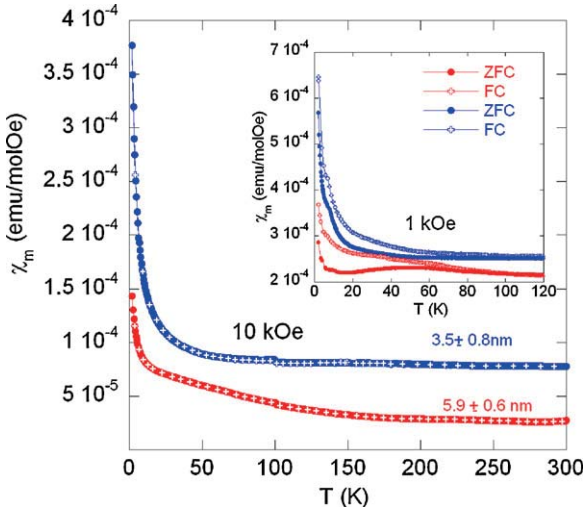

Fig. 4. Temperature dependence of the magnetic susceptibility χ_m for ruthenium nanoparticles of sizes 3.5 ± 0.8 and 5.9 ± 0.6 nm measured under an external magnetic field of 10 kOe. The inset shows low temperature ZFC-FC magnetic susceptibility when measured under 1 kOe.

synthesized in presence of sodium citrate. When succinic acid is used as the reducing agent, the product is characterized by isolated spherical particles. The changes of diameter of the nanoparticles are related to the pH of the precursor solution. In solutions of pH = 4.1, the average particle diameter is greater than 100 nm. However, in neutral medium such as basic and strongly acid, the average diameter is decreased in two orders of magnitude (see Fig. 1(b)).

The temperature dependence of the magnetic susceptibility at 10 kOe (see Fig. 4) for two powdered ruthenium nanoparticles samples evidences an almost constant behavior in the interval 100–300 K, with a magnetic signal of magnitude around 7.9×10^{-5} and 3.2×10^{-5} emu/Oe mol for ruthenium(0) nanoparticle samples of average size of 3.5 ± 0.8 and 5.9 ± 0.6 nm, respectively. This behavior is found to be observed in non-magnetic metals [23]. At lower temperatures, the magnetic susceptibility has a tendency to increase. Taking account these results, we have performed low temperature ZFC-FC (1 kOe) magnetic measurements (see inset of Fig. 4). The curves show the existence of a small irreversibility below 60 K in all the studied samples. Nevertheless, due to the experimental difficulties commented in the experimental section, further experiments are needed to investigate the origin of this unexpected behavior.

4. Conclusions

Under hydrothermal conditions, ruthenium nanoparticles were synthesized by reduction of ruthenium trichloride with sodium citrate, ascorbic acid or succinic acid. The average size of the ruthenium(0) nanoparticles are in the range of 1–20 nm, 3–5 nm, or 1–120 nm when sodium citrate, ascorbic acid or succinic acid are used, respectively. Magnetic measurements down to 2 K indicate that the magnetic response seems to be dominated by an electronic band paramagnetic-like contribution with some enhancement of the magnetic signal at low temperatures.

Acknowledgements

The authors thank FEDER and Spanish MICINN for financial support under projects MAT2008-06542-C04, MAT2010-15094, MAT2006-01997, FC-08-IB08-036, and MAT2010-01997 and *Factoría de Cristalización – Consolider Ingenio 2010*. A.D. also thanks to MICINN by their pre-doctoral FPU grant (AP2008-03942).

References

[1] E.H. Sargent, Adv. Mater. 17 (2005) 515.
[2] N.L. Rosi, C.A. Mirkin, Chem. Rev. 105 (2005) 1547.
[3] M.C. Daniel, D. Astruc, Chem. Rev. 104 (2004) 293.
[4] C.J. Murphy, A.M. Gole, S.E. Hunyadi, J.W. Stone, P.N. Sisco, A. Alkilany, B.E. Kinard, P. Hankins, Chem. Commun. (2008) 544.
[5] N.J. Durr, T. Larson, D.K. Smith, B.A. Korgel, K. Sokolov, A. Ben-Yakar, Nano Lett. 7 (2007) 941.
[6] R. Bernini, S. Cacchi, G. Fabrizi, G. Forte, S. Niembro, F. Petrucci, R. Pleixats, A. Prastaro, R.M. Sebastián, R. Soler, M. Tristany, A. Vallribera, Org. Lett. 10 (2008) 561.
[7] S. Niembro, A. Shafir, A. Vallribera, R. Alibés, Org. Lett. 10 (2008) 3215.
[8] M.V. Escárcega-Bobadilla, C. Tortosa, E. Teuma, C. Pradel, A. Orejón, M. Gómez, A.M. Masdeu-Bultó, Catal. Today 148 (2009) 398.
[9] M. Liu, J. Zhang, J. Liu, W.W. Yu, J. Catal. 278 (2011) 1.
[10] A. Roucoux, J. Schulz, H. Patin, Chem. Rev. 102 (2002) 3757.
[11] P.S. Campbell, C.C. Santini, F. Bayard, Y. Chauvin, V. Collière, A. Podgoršek, M.F. Costa-Gomes, J. Sá, J. Catal. 275 (2010) 99.
[12] C. Evangelisti, N. Panziera, A. D'Alessio, L. Bertinetti, M. Botavina, G. Vitulli, J. Catal. 272 (2010) 246.
[13] M.I. Burguete, E. García-Verdugo, I. García-Villar, F. Gelat, P. Licence, S.V. Luis, V. Sanz, J. Catal. 269 (2010) 150.
[14] J. Gavnholt, J. Schiøtz, Phys. Rev. B77 (2008) 035404.

[15] P. Crespo, R. Litrán, T.C. Rojas, M. Multigner, J.M. de la Fuente, J.C. Sánchez-López, M.A. García, A. Hernando, S. Penadés, A. Fernández, Phys. Rev. Lett. 93 (2004) 087204.
[16] J. Yang, T.C. Deivaraj, H.P. Too, J.Y. Lee, Langmuir 20 (2004) 4241.
[17] X. Zhang, K.Y. Chan, Chem. Mater. 15 (2003) 451.
[18] E. Filippo, A. Serra, A. Buccolieri, D. Manno, J. Non-Crystalline Solids 356 (2010) 344.
[19] V.K. Sharma, R.A. Yngard, Y. Lin, Adv. Colloid Interf. Sci. 145 (2009) 83.
[20] N.N. Mallikarjuna, R.S. Varma, Crystal Growth Des. 7 (2007) 686.
[21] B.L. Cushing, V.L. Kolesnichenko, C.J. O'Connor, Chem. Rev. 104 (2004) 3893–3946.
[22] C. Xu, A.S. Teja, J. Supercrit. Fluids 44 (2008) 85.
[23] M.T. Béal-Monod, T.M. Lawrence, Phys. Rev. B21 (1980) 5400.

Publication III

"High-yielding Green Hydrothermal Synthesis of Ruthenium Nanoparticles and their Characterization"

Journal of Nanoscience and Nanotechnology

(in press)

Year ***2015***

DOI: *10.1166/jnn.2015.10862*

Impact Factor: 1.556

Article

Journal of Nanoscience and Nanotechnology
Vol. 15, 1–10, 2015
www.aspbs.com/jnn

High-Yielding Green Hydrothermal Synthesis of Ruthenium Nanoparticles and Their Characterization

Alla Dikhtiarenko*, Sergei A. Khainakov, Olena Khaynakova, José R. García, and José Gimeno

Departamento de Química Orgánica e Inorgánica, Universidad de Oviedo–CINN, 33006 Oviedo, Spain

Using hydrothermal techniques, a novel synthetic approach to prepare ruthenium nanoparticles has been developed. At 180 °C and under autogenous pressure, starting from an aqueous solution of ruthenium trichloride, the method yielded nanoparticles whose form and size both depended on the reducing agent: sodium citrate (hexagonal shaped nanocrystals, 1–20 nm), ascorbic acid (spherical nanoparticles, 3–5 nm) and succinic acid (spherical nanoparticles, 1–120 nm). Depending on the reaction variables, the nature and concentration of partially reduced species determines the characteristics of the final products. HRTEM image analysis along with the simulation techniques were stabilized preferential growth of nanoparticles on specific directions. Ruthenium samples have been investigated by Temperature-Programmed Reduction (TPR) showing that the reduction temperature of nanoparticles is correlated to their nanocrystalline size.

Keywords: Ruthenium Nanoparticles, Hydrothermal Synthesis, Redox Properties, Transmission Electron Microscopy.

1. INTRODUCTION

The preparation of nanoparticles has received considerable attention in the past few years because they possess unique physical and chemical properties.[1–3] Furthermore, nanosized materials have also found promising technological application in many different areas such as nanoelectronics,[4] photocatalysis,[5] electrocatalysis,[6,7] biomedical application,[8,9] and chemical processes.[10–13] Ruthenium nanoparticles, in particular, are renowned for their catalytic activity.[13–20]

The large number of methods has been developed to prepare ruthenium nanoparticles using stabilizers such as polymers,[21] ligands,[22] organosilane fragments,[23] and cellulose derivatives.[24] Most of these preparations are carried out in organic medium and using organometallic precursors. Recently, Chaudret and co-workers have published two excellent works dedicated to the synthesis of fine dispersed ruthenium nanoparticles (1.2 nm) by decomposition, under H_2, of [Ru(COD)(COT)] (COD = 1,5-cyclooctadiene; COT = 1,3,5-cyclooctatriene), in various imidazolium derived ionic liquids.[25,26] Similarly, Debouttière et al. reported the synthesis of ruthenium nanoparticles by decomposition of a THF solution of the organometallic precursor [Ru(COD)(COT)] under dihydrogen.[27] Also, THF-based route to reduce ruthenium organometallic precursors are realized by Favier et al.[28]

Increasing awareness regarding green chemistry has led to a desire to develop an eco-friendly approach for the synthesis of nanoparticles which has several advantages, such as simplicity, cost effectiveness, and compatibility, as well as for their large-scale commercial production. The choice of an environmentally compatible solvent system, an eco-friendly reducing agent, and a nonhazardous capping agent for stabilizing the nanoparticles are three main criteria for a 'green' nanoparticle synthesis.[29–31] Many interesting methods have been applied in recent years to the "green" preparation of noble metal nanoparticles such as control shape synthesis using carboxylic compounds as reducing agents in aqueous medium.[32]

In particular, Panigrahi et al. used fructose, glucose and sucrose as reducing and capping agents for the preparation of Au, Ag, Pd, Pt and Au–Ag nanoparticles, heating the solutions for 2 h in a hot water bath to dryness.[33] A simple method for the shape-controlled synthesis of nanostructures (size 2–15 nm) of noble metals such as Au, Ag, Pd and Pt by reduction of noble metal salts using α-D-glucose, sucrose and maltose in aqueous solution has also been reported by Mallikarjuna et al.[34] This production route of nanoparticles attribute to co-precipitation

*Author to whom correspondence should be addressed.

technique. In these cases the reduction of metal salts led to a several problems because of the composition control in addition to size, size distribution, morphology and nanoparticles yield. An alternative method which has evolved as one of the most efficient methods of soft chemistry in processing the nanoparticles with a controlled size and shape are hydrothermal method. The hydrothermal technique has been widely used to prepare inorganic nanoparticles.[35–39] Moreover, the hydrothermal technique has been characterized very well for the processing of nanoparticles having narrow particle size distribution, controlled morphology, high purity, yield and crystallinity, and therewith excellent reproducibility.[40] Herein, we present extended study on a simple "green" approach to the synthesis and stabilization of ruthenium nanoparticles (different sizes in the range 1–100 nm) obtained with high yields under hydrothermal conditions, using commonly available carboxylate derivatives as reducing and capping agents. The influence of partially reducing species on morphology and growth process of ruthenium nanoparticles and their size-depending oxidative-reductive properties also has been discussed.

2. EXPERIMENTAL DETAILS

2.1. Preparation of Ruthenium Nanoparticles

Ruthenium(III) chloride hydrate (Johnson Matthey, 40.1% Ru), sodium hydroxide (pellet Prolabo, 98%), hydrochloric acid (Prolabo, 37%), trisodium citrate (Sigma-Aldrich, 99%), ascorbic acid (Sigma-Aldrich, 99%) and succinic acid (Sigma-Aldrich, 99%) were obtained commercially. Deionized water, prepared using a Milli-Q water purification system, was used throughout the experiments. All glassware, autoclave and Teflon-coated magnetic stir bars were cleaned with *aqua regia*, followed by copious rinsing with distilled water before drying in an oven.

To study the effect of the concentration of reducing agent on nanoparticle size at room temperature, ruthenium chloride {Ru}, the reducing agent (trisodium citrate, ascorbic acid or succinic acid) and water were mixed at a molar ratio of 1:x:50 ($x = 1$–4). The mixture was then adjusted to pH = 6 by addition of 0.1 M NaOH and stirred for 30 min to obtain a homogenously mixed solution, prior to being placed and sealed inside a Teflon-lined digestion bomb. After a reaction time of one day ($T = 180$ °C), the resulting mixture was cooled to room temperature. Following centrifugation, the resulting solid was separated, washed several times with water, and then dried in air. The mass yield of nanoparticles using succinic acid as the reduction agent was about 75%, sodium citrate–56%, and ascorbic acid–42%.

A similar procedure to that described above was employed to study the influence of pH on both the size and shape of the nanoparticles. Ruthenium chloride, the reducing agent and water were mixed at a molar ratio of 1:1:50, subsequently adjusting the pH of the mixture to the preset value (1–12) with 0.1 M NaOH or 0.1 M HCl.

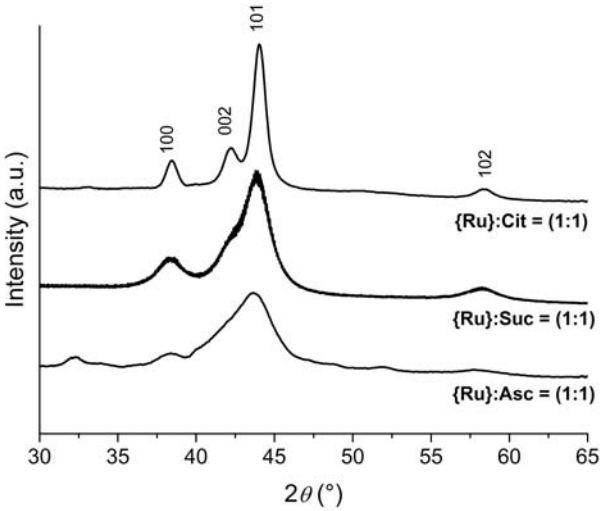

Figure 1. Powder X-ray diffraction patterns of ruthenium nanoparticles obtained at pH = 6 as a function of the reducing agent.

2.2. Materials and Instrumentation

The morphology and the mean size of the ruthenium nanoparticles were characterized by transmission electron microscopy (JEOL 2000 EX-II). TEM samples were obtained by placing 10 drops of suspension onto a carbon-coated copper TEM grid, which was left to dry in a desiccator. For each sample, the size of a large number of particles was measured to obtain their average size and size distribution. High resolution TEM images were obtained using JEOL JEM-2100. HRTEM image simulations were made with the help of the QSTEM software package.[41]

X-ray diffraction (XRD) measurements were performed on an Oxford-Gemini X-ray diffractometer using CuKα radiation. The samples for XRD analysis were prepared by supporting the powder on nylon CryoLoops. The surface of the samples was analyzed by X-ray photoelectron spectroscopy (XPS) with a SPECS Phoibos 100 MCD5 system equipped with a hemispherical electron analyzer operating in a constant pass energy, using monochromatic MgKα radiation (1253.6 eV). High-resolution scan were

Table I. Average diameter (determined by TEM) of ruthenium nanoparticles, obtained at pH = 6, as a function of type and concentration of reducing agent.

Reducing agent	{Ru}:{Red}	d^{av}, nm
Sodium citrate	1:1	3.3 ± 0.4
	1:2	3.0 ± 0.2
	1.3	2.8 ± 0.1
Ascorbic acid	1:1	4.9 ± 0.3
	1:2	3.4 ± 0.6
	1.3	3.0 ± 0.7
Succinic acid	1:1	5.9 ± 0.6
	1:2	5.7 ± 0.7
	1.3	3.1 ± 0.7

recorded with pass energy of 30 eV. UV-visible spectra were collected using a Perkin-Elmer Lambda-20 Scan UV-visible spectrometer over the 300 to 1100 nm range (all samples were prepared with deionized water and loaded into a quartz cell, $l = 1$ cm, for analysis).

Temperature-programmed reduction (TPR) experiments were carried out on a flow system using a Micrometrics AutoChem™ II 2920 Automated Catalyst Characterization System equipped with thermal conductivity detectors (TCD), using *ca*. 0.1 g of solid sample in contact with a hydrogen gas flow (10 mL · min^{-1}, 10% H_2 in Ar) at a heating rate of 10 °C · min^{-1}. The samples had been previously annealed at 400 °C (12 h) in an oxidizing atmosphere (50 mL · min^{-1}, 10% O_2 in He). A silica gel water trap was interposed between the analyzed sample and the TCD detector in order to ensure the good stability and sensitivity of the detection system.

3. RESULTS AND DISCUSSION

3.1. Effect of Precursor Concentration on Particle Size

In the course of this work, we synthesized ruthenium nanoparticles by hydrothermal procedures using several carboxylates as reducing agents. The influence of the concentration of the reducing agent on particle size was evaluated by comparing samples obtained with 1:1, 1:2, and 1:3 molar ratios of {Ru}:{reducing agent}.

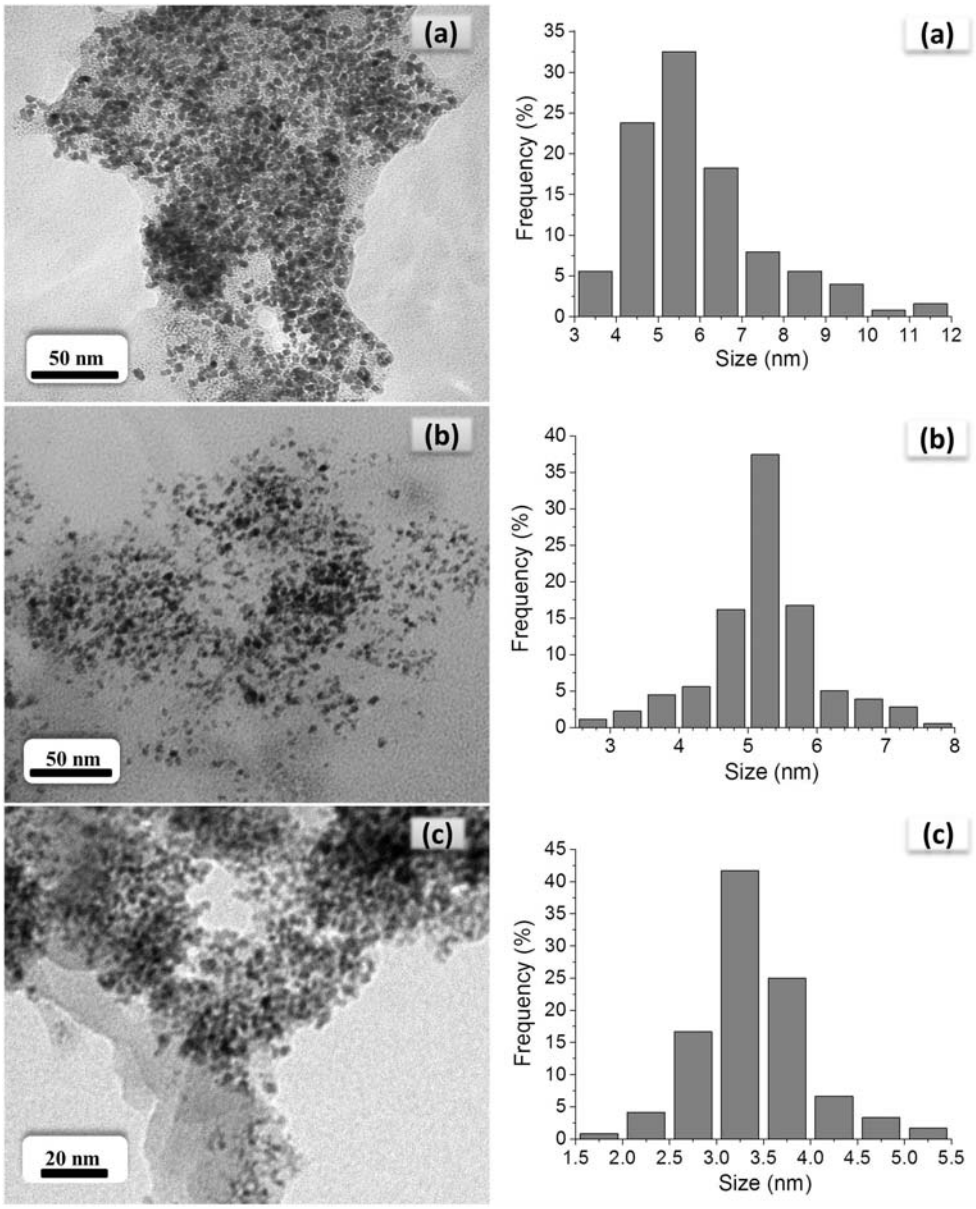

Figure 2. TEM images and size distribution diagrams of ruthenium nanoparticles obtained by reduction with succinic acid. Molar ratio {Ru}:{Suc} equal to 1:1 (a), 1:2 (b), and 1:3 (c).

The solid phase obtained after hydrothermal treatment was analyzed by powder X-ray diffraction. The results are shown in Figure 1, where reflections (100), (002), (101) and (102) of hexagonal close-packed (*hcp*) ruthenium are observed.[42]

The narrow diffraction peaks in the samples prepared with sodium citrate indicate larger particle sizes to those obtained when using ascorbic or succinic acid.

TEM images provide direct information on the morphological characteristics of nanoparticles. The numerical data gathered from the TEM images (average diameter of particles) are given in Table I.

Aggregates of non-spherical nanoparticles were obtained using sodium citrate (Fig. S1). The distribution diagrams show a wide range of particle sizes, although the particle diameter decreases slightly (from 3.3 ± 0.4 to 2.8 ± 0.1 nm) when decreasing the {Ru}: {reducing agent} molar ratio.

When ruthenium trichloride is reduced with ascorbic acid, the effect of agglomeration described in the previous case is not observed (Fig. S2). The diagrams of particle-size distribution are narrow, indicating the formation of relatively uniform-size nanoparticles. The particles also show a decrease in size (from 4.9 ± 0.3 to 3.0 ± 0.7 nm) when decreasing the {Ru}: {reducing agent} molar ratio, though the decrease is more pronounced in this case.

Figure 2 shows representative TEM images of the nanoparticles obtained by reduction with succinic acid. They comprise non-aggregated spherical particles with a Gaussian size distribution and restricted in diameter. The results in Table I show that, as in the previous cases, an increase in reducing agent concentration leads to a decrease in the average size of ruthenium nanoparticles, which in this system changes from 5.9 ± 0.6 to 3.1 ± 0.7 nm when varying the {Ru}: {reducing agent} molar ratio from 1:1 to 1:3.

As already mentioned when analyzing the results individually, the particle size diminishes with decreasing {Ru}: {reducing agent} molar ratio, probably as a result of blocking on the particle surface due to absorption of the reducing agent. This leads to a higher concentration of crystallization nuclei and hence a greater number of smaller particles.

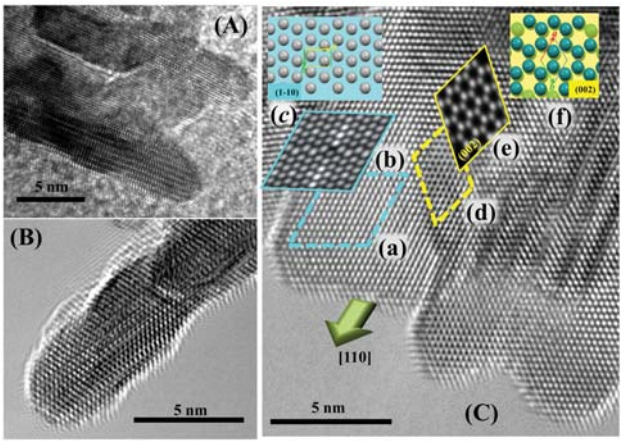

Figure 4. (A,B) HRTEM image of the elongated Ru nanoparticle formed through reduction with sodium citrate at pH 4.2, (C) surface analysis of elongated particle and comparison of facets regions with theoretically simulated ones corresponding to different crystallographic directions: facets face of Ru nanoparticle (a), corresponding to (1–10) plane theoretical simulation (b), and theoretical model used (c); lateral region of Ru nanoparticle (d), corresponding to (002) plane theoretical simulation (e) and theoretical model used (f).

3.2. Effect of pH on Particle Size and Morphology

The influence of pH on the size of ruthenium nanoparticles was determined in reducible solutions with a {Ru}: {reducing agent} molar ratio equal to 1:1. The powder XRD data are shown in Figure S3. Samples obtained by reduction with both ascorbic and succinic acid are characterized by peaks of variable width. This peak width increases with increasing pH, thus indicating the formation of larger particles in the region of higher acidity. When reduction is achieved using sodium citrate, the diffraction peaks are narrower, indicating the formation of larger particles. TEM images of samples obtained from sodium citrate show that the nanoparticles differ both in shape and size (Fig. S4). The formation of pentagonal nanoparticles is observed at pH 1.1 which present by Gaussian distribution and are quite large in size, characterized by up to 22.8 ± 3.5 nm.

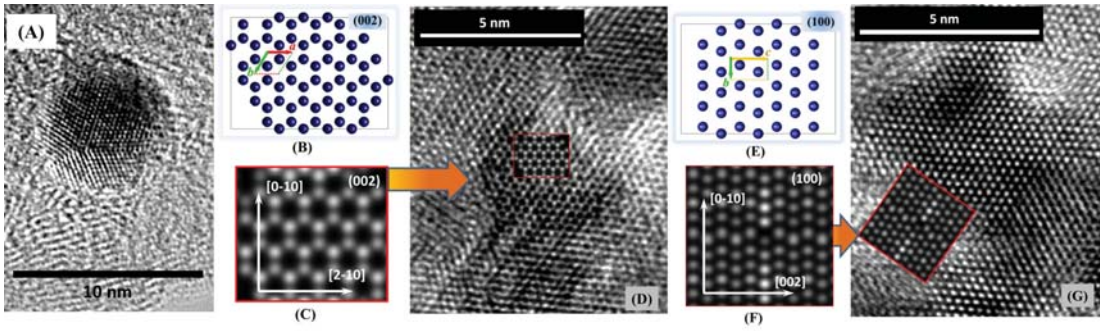

Figure 3. (A) HRTEM image of a decahedral Ru nanoparticle with pentagonal shape obtained through reduction with sodium citrate at pH 3.3, (B) the ruthenium hexagonal (*hcp*) packing viewed along *c* crystallographic direction, and (C) theoretically simulated TEM image. (D) HRTEM image of surface decahedral Ru nanoparticle comparing with simulated one (insertion). (E) The Ru packing viewed along *a* direction, and (F) corresponding theoretically simulated TEM image. (G) HRTEM image of decahedral Ru nanoparticle comparing with simulated one (insertion).

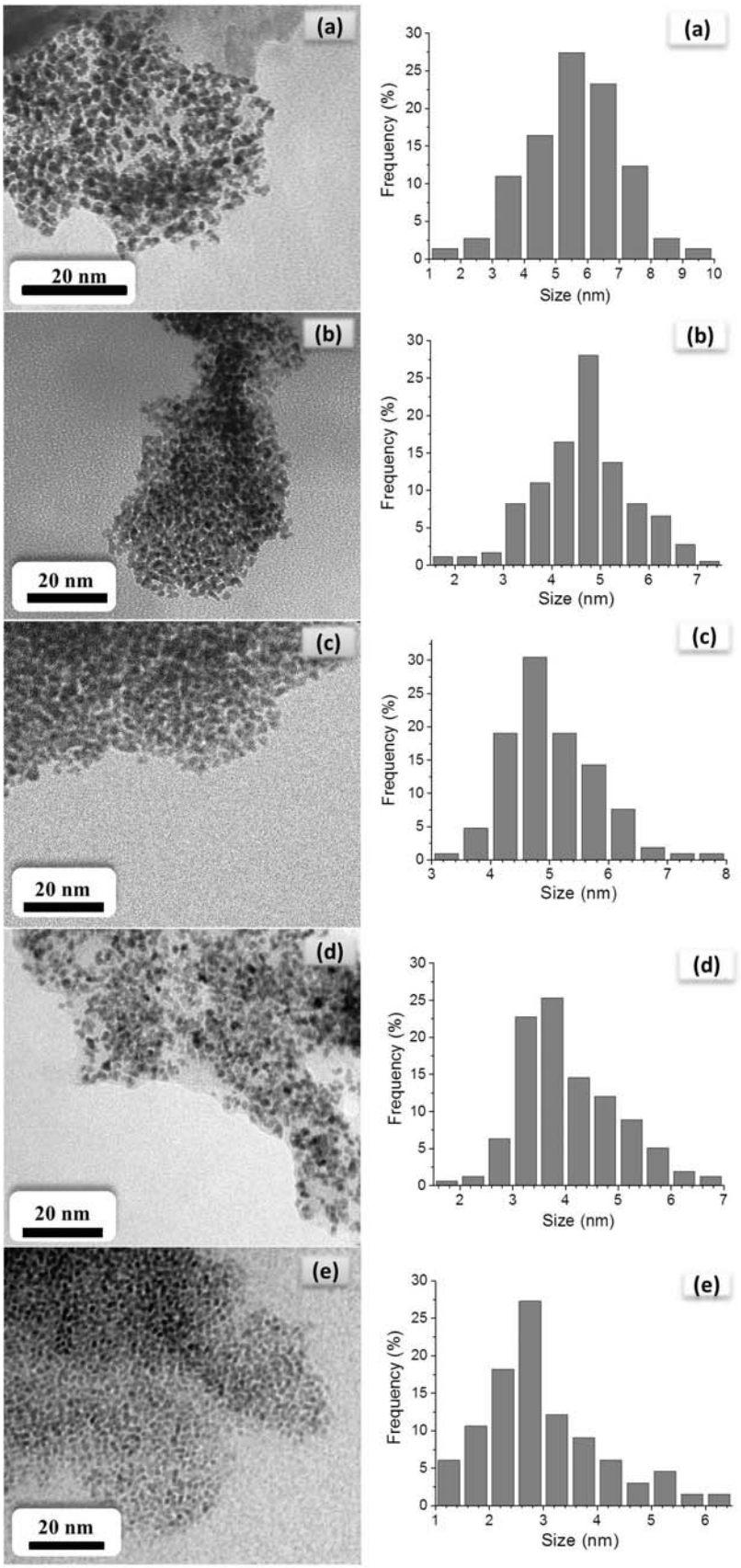

Figure 5. TEM images and size distribution diagrams of ruthenium nanoparticles obtained by reduction with ascorbic acid (molar ratio {Ru}:{AA} = 1:1) as a function of pH: 2.2 (a), 3.1 (b), 4.1 (c), 9.4 (d), and 12.3 (e).

At pH 3.3, the majority of particles maintain the pentagonal shape, but some particles with elongated rectangular shape begin to appear, whose average size decreases to 12.3 ± 1.4 nm, presenting a narrower Gaussian distribution than in the previous case. On raising the pH to 4.2, the decahedral morphology disappears, enhancing the rectangular shape, while the average size decreases to 3.5 ± 0.8 nm. A new increase in pH leads to the formation of disaggregated spherical particles, with an average diameter that decreases with increasing pH (3.3 ± 0.4 nm at pH 6.3; 2.7 ± 0.4 nm at pH 8.0; 2.6 ± 0.3 nm at pH 11.9). In both cases, the Gaussian distribution is narrow, indicating that the nanoparticles are quite uniform in size. In this study, simulated HRTEM images were used to compare with the experimental images for understanding the nanoparticle growth process. As shown in Figure 3(A), the Ru nanoparticle obtained through reduction with sodium citrate at pH 3.3 has decahedral shape. The simulated HRTEM images (Figs. 3(B)–(C), (E)–(F)) basing on the crystal packing of ruthenium atoms, in hexagonal (*hcp*) phase, along *c* and *a* crystallographic direction, show good arrangement with experimental data. As shown in Figures 3(D) and (G), the surface of nanoparticle presents two simultaneously growing regions which correspond to (002) and (100) crystallographic planes, respectively. In case of nanoparticles formed at pH 4.2, the decahedral shape of nanoparticles is disappeared and resulting in formation of elongated particles with rectangular shape (Figs. 4(A), (B)). The surficial analysis along with HRTEM simulations suggests that preferential growing take place. As shown in Figure 4(C), the facet faces of the particle are reproducible by simulation of (1–10) plane (see inserts (a)–(c) in Fig. 4(C)). Furthermore, the regions reproducible by simulation of (002) plane are rare (inserts (d)–(f) in Fig. 4(C)), indicating that this crystallographic direction are favorable for growing in the conditions offered at pH 4.2. Along with discussions above it is reasonable to conclude that the (1–10) crystallographic direction is blocked by soluble species predominated at pH 4.2, whereas the [110] directions became suitable for growing and leading the elongated shape of the resulted nanoparticles.

As observed, when ascorbic acid is used as reducing agent (Fig. 5), most of the samples consist of non-agglomerated particles possessing a well-defined spherical shape, whose size depends on the conditions of synthesis. The size distribution diagrams have narrow ranges, indicating the homogeneity of the analyzed particles. As in the previous case, the size of the ruthenium nanoparticles decreases when increasing the pH of synthesis, although the sizes of the nanoparticles obtained at acid pH by reduction with ascorbic acid are much lower than those synthesized in the presence of sodium citrate. This fact can be explained by the higher reducing power of ascorbic acid, which is manifested in the first phase of the reduction at room temperature with the formation of more crystallization nuclei, leading concomitantly to less favorable growth of large nanoparticles under hydrothermal conditions.

When succinic acid is used as the reducing agent, the product is characterized by isolated spherical particles (Figs. S5–S6). The Gaussian distribution of their average diameters is quite narrow, indicating the homogeneity of samples, and changes in the diameter of the nanoparticles due to the pH of the precursor solution. In solutions of $pH = 4.1$, the average particle diameter is greater than 100 nm. However, in basic and strongly acid medium, the average diameter decreases in two orders of magnitude.

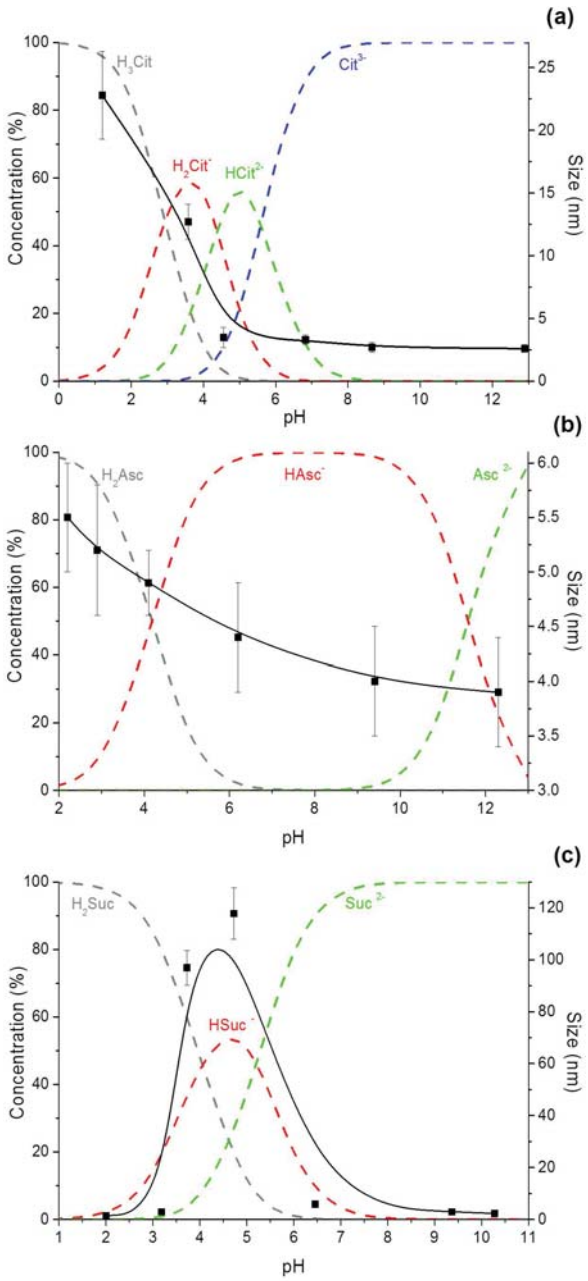

Figure 6. Effect of pH on the diameter of ruthenium nanoparticles as a function of the reducing agent: sodium citrate (a), ascorbic acid (b) or succinic acid (c).

The results discussed in this section show that a regular variation in particle size was only obtained through the use of sodium citrate and ascorbic acid as reducing agents, which is not observed when using succinic acid.

Figures 6(a)–(b) show the relationship between particle size and pH on sodium citrate and ascorbic acid systems, in addition to including the speciation curves of these species as a function of pH. It should be noted that, in both cases, the particle size curve is a delayed reflection of the curve of disappearance of the protonated species of the corresponding acids. Returning to the dependence of particle size and the percentage of species derived from the corresponding acids of the reducing agent, the behavior in the case of succinic acid is seen to be different to that for sodium citrate and ascorbic acid. As shown in Figure 6(c), the resulting nanoparticle size increases with increasing pH of the precursor solution and then decreases with it, describing a curve which roughly coincides with the one that defines the abundance of the ionic form generated in the first step of acid dissociation. Figures 7(a)–(b) shows the UV-VIS spectra of the precursor solutions of ruthenium nanoparticles using sodium citrate as reduction agent, determined just after mixing (a) and at the instant before the beginning of hydrothermal treatment (b). The spectra of solutions recorded in the initial time period indicate that the type and relative concentration of species in solution is related to pH. At pH = 1.1, the presence of an absorption maximum around 550 nm may be associated with the presence of ruthenium(III)-hydroxo-chloride aqueous species,[43,44] while the band at 475 nm is caused by complex species containing $RuCit^{2+}$.[45] When increasing pH values to 3.3 and 4.2, the band related to the metal hydroxo-chloride aqueous complex disappears, while the absorption of the complex form in the solution still exists for further increasing the pH. At pH values of 8.0 and 11.9, the solution already contains reduced $[Ru(H_2O)_6]^{2+}$ species characterized by an absorption band at 420 nm.[46] In addition, the background increase indicates the formation of ruthenium(0) clusters.[47] Noticeable changes are detected in the first step of the reduction process, at room temperature, reached after mixing solutions for 30 min (Fig. 7(b)). At pH 1.1, only species of $RuCit^{2+}$ (~475 nm) are observed. The remaining solutions also contain $[Ru(H_2O)_6]^{2+}$ species, which manifest with an absorption maximum at 420 nm. In addition, the baseline rises with increasing pH, indicating the formation of an increasing number of ruthenium(0) clusters.

When ascorbic acid is used as the reducing agent, the UV-VIS spectra behave differently (Figs. 7(c)–(d)). When solutions are freshly prepared, the absorption maximum at 510 nm indicates the existence of mixed $[RuCl_2(H_2O)_2]$Asc the ascorbato-chloride-aqua complex[48] and mixed hydroxo-chloride aqueous species of ruthenium(III).[49] After 30 min of mixing, these species still exist, while an increase in the concentration of clusters is detected, which is related to the rise of the baseline, especially evident at pH 12.3 (Fig. 7(d)). In the second step of reduction, which occurs under hydrothermal conditions, different soluble forms of complexes in the reaction medium affect the size of the generated nanoparticles. The wide variation in concentrations and existing forms in the solution when using sodium citrate as the reducing agent produce a very broad range of nanoparticle size. In the case of ascorbic acid, however, only one complex

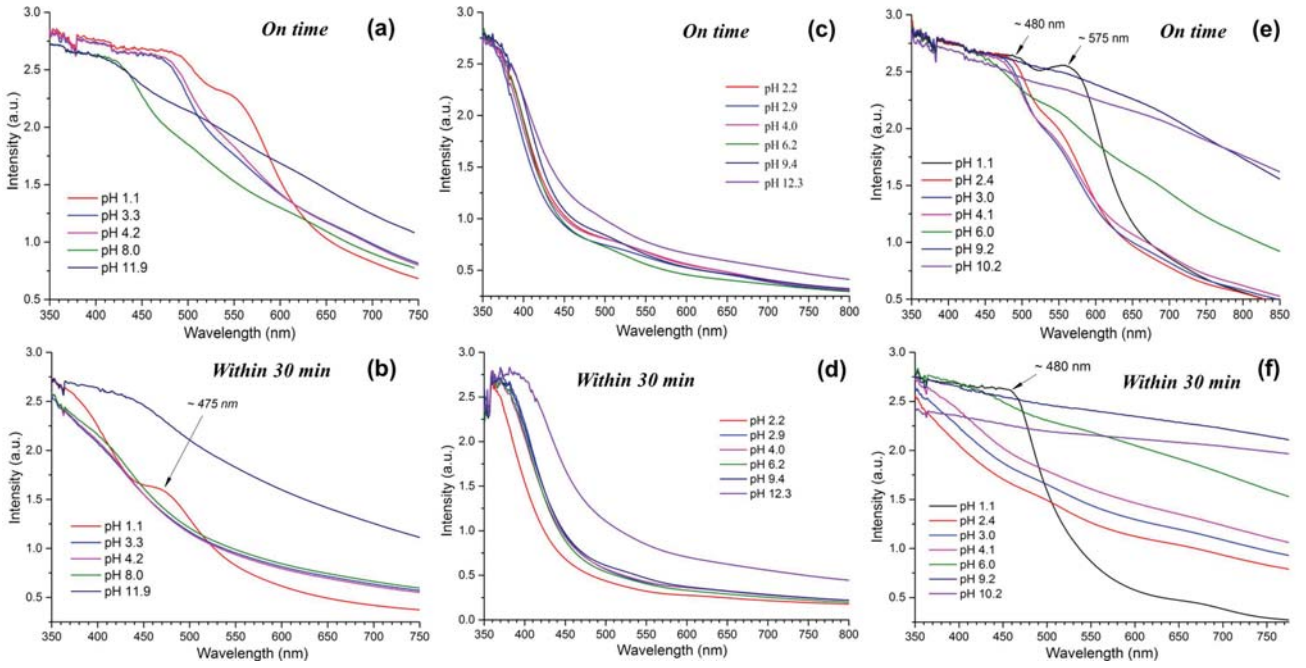

Figure 7. UV-VIS spectra of freshly prepared solutions (on time) and after 30 min of mixing (delayed), contained ruthenium trichloride and sodium citrate (a, b), ascorbic acid (c, d) or succinic acid (e, f) at different pHs.

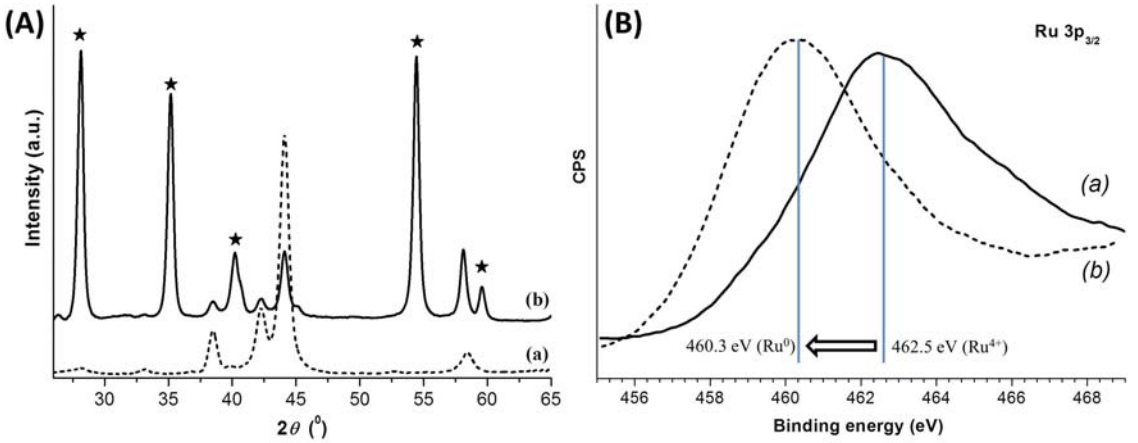

Figure 8. (A) Powder X-ray diffraction patterns of ruthenium nanoparticles (average size 5.9 ± 0.6 nm) before (a) and after (b) the temperature programmed oxidation cycle (*corresponds to RuO_2). (B) XPS surface survey of the oxidized ruthenium nanoparticles (average size 5.9 ± 0.6 nm) before (a) and after (b) sputtering with Ar^+.

is present in solution, leading to very narrow ranges in nanoparticle size. It should also be noted that the high concentration of primary clusters in the solutions obtained at high pH results in the production of nanoparticles of a smaller size due to the abundance of crystallization centers at the beginning of the hydrothermal process.

In case of succinic acid, the UV-VIS spectra indicate that the freshly prepared solutions contain two soluble forms of ruthenium at pH 1.1 (Fig. 7(e)): the ruthenium(III)-hydroxo-chloride aqueous species characterized by the absorption maximum at 575 nm and the $RuSuc^{2+}$ species manifested by the absorption maximum at 480 nm (the assignments can be compared to the case of citrate system). In neutral and basic pH regions, the increased absorption background indicates the presence of clusters of ruthenium(0) in solution, at a high concentration. Significant changes are detected after 30 min of mixing. As shown in Figure 7(f), at pH = 1.1, $RuSuc^{2+}$ continues to exist. However, at higher pHs (2.4, 3.0 and 4.1) most of the metal is in a form of $[Ru(H_2O)_6]^{2+}$ with an absorption shoulder at 400 nm. The solutions of higher pH (6.0, 9.2 and 10.2) are characterized by an elevated baseline, associated with increasing concentrations of ruthenium(0) clusters. In the second step of reduction under hydrothermal conditions, the different existing forms in solution determine the size of the resulting nanoparticles. The broad variation in concentrations and different existing forms in the succinic acid solutions produced nanoparticles with a wide variety of sizes. It is also worth noting that the homogeneity of the solution in terms of the concentration of complex forms affects the appearance of nanoparticles with a specific morphology.

3.3. Reductive-Oxidative Properties

Five samples with very different average particle sizes (*ca.* 1 to 100 nm) were selected to investigate the relationship between nanoparticle dimensions and their reduction temperature. Previously, all the samples had been annealed at 400 °C in an O_2/He gas mixture. Comparative powder X-ray diffraction patterns of nanoparticles before and after oxidizing (Fig. 8(A)) reveal that after oxidizing by thermal treatment, the sample shows well-defined RuO_2

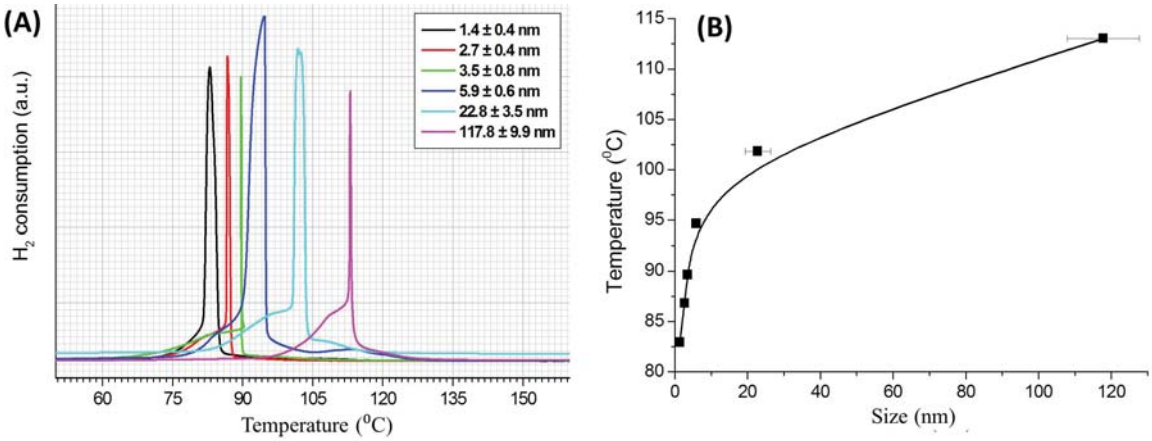

Figure 9. (A) Temperature-Programmed Reduction (TPR) curves for RuO_2 nanoparticles with different average sizes. (B) Comparative diagram of reduction temperature as function of RuO_2 nanoparticle size.

reflections. This fact is confirmed by X-ray photoelectron spectroscopy (XPS). Figure 8(B) show the Ru-$3p_{2/3}$ region for the oxidized nanoparticles, where the maximum at 462.5 eV should be assigned to the ruthenium(IV) as RuO_2.[50] This specie completely disappear after the argon sputtering (see peak at 460.3 eV, characteristic of ruthenium(0)).[51]

The comparative TPR data of the ruthenium nanoparticles obtained from samples oxidized at 400 °C are shown in Figure 9(A). The H_2 consumption in TPR runs was ascribed to the reduction of RuO_2 (confirmed by powder X-ray diffraction). Experimental data indicate that the reduction temperature is a size-dependent parameter (Fig. 9(B)).

4. CONCLUSIONS

Herein, we present a green synthesis of ruthenium nanoparticles under hydrothermal conditions using mild reducing agents (succinic acid, ascorbic acid and sodium citrate). The nanoparticles have been characterized by transmission electron microscopy, powder X-ray diffraction, and X-ray photoelectron and UV-VIS spectroscopies. The reaction begins with the slow reduction of ruthenium(III) trichloride at room temperature, which is completed under hydrothermal conditions ($T = 180$ °C). UV-Vis spectroscopic studies of reaction solutions (ruthenium trichloride, succinic acid, ascorbic acid or sodium citrate) at beginning of hydrothermal treatment suggest the existence of different partially reduced species which have influence on the nanoparticles size and shape. In case of reduction with sodium citrate, the preferential growth of ruthenium particles on specific directions were observed by HRTEM imaging and confirmed by HRTEM simulation technique. Furthermore, the size parameter of nanoparticles is influenced by the pH of the reacting medium and depends of nucleation rate, concentration of partially reduced species and reduction power of reduction agent used. The reductive-oxidative properties of ruthenium nanoparticles are related to their size, and our experimental results indicate that the effect of particle size on the reduction temperature can greatly assist in the performance optimization of the ruthenium catalysts.

Acknowledgments: The authors thank FEDER and Spanish MINECO for financial support under project MAT2010-15094, the International Project FP7-PEOPLE-2012-IRSES and Consolider ORFEO (CSD2007-00006). Alla Dikhtiarenko also thanks to Spanish *Ministerio de Educación, Cultura y Deporte* (grant AP2008-03942).

References and Notes

1. T. K. Sau, A. L. Rogach, F. Jäckel, T. A. Klar, and J. Feldman, *Adv. Mater.* 22, 1805 (**2010**).
2. I. Tokarev, I. Tokaeva, V. Gopishetty, E. Katz, and S. Minko, *Adv. Mater.* 22, 1412 (**2010**).
3. N. M. A. Hadia, S. García-Granda, and J. R. García, *J. Nanosci. Nanotechnol.* 14, 5443 (**2014**).
4. G. Schmid, Nanoparticles from Theory to Applications, VCH, Weinheim (**2004**).
5. N. Sakamoto, H. Ohtsuka, T. Ikeda, K. Maeda, D. Lu, M. Kanehara, K. Teramura, T. Teranishi, and K. Domen, *Nanoscale* 1, 106 (**2009**).
6. H. Chu, Y. Shen, L. Lin, X. Qin, G. Feng, Z. Lin, J. Wang, H. Liu, and Y. Li, *Adv. Func. Mater.* 20, 3747 (**2010**).
7. B. Wu, Y. Kuang, X. Zhang, and J. Chen, *Nanotoday* 6, 75 (**2011**).
8. X. Huang and M. A. El-Sayed, *J. Adv. Res.* 1, 13 (**2010**).
9. R. Bardhan, S. Lal, A. Joshi, and N. J. Halas, *Acc. Chem. Res.* 44, 936 (**2011**).
10. R. Bernini, S. Cacchi, G. Fabrizi, G. Forte, S. Niembro, F. Petrucci, R. Pleixats, A. Prastaro, R. M. Sebastián, R. Soler, M. Tristany, and A. Vallribera, *Org. Lett.* 10, 561 (**2008**).
11. S. Niembro, A. Shafir, A. Vallribera, and R. Alibés, *Org. Lett.* 10, 3215 (**2008**).
12. C. Evangelisti, N. Panziera, A. D'Alessio, L. Bertinetti, M. Botavina, and G. Vitulli, *J. Catal.* 272, 246 (**2010**).
13. M. I. Burguete, E. García-Verdugo, I. García-Villar, F. Gelat, P. Licence, S. V. Luis, and V. Sanz, *J. Catal.* 269, 150 (**2010**).
14. R. H. Grubbs and S. Chang, *Tetrahedron* 54, 4413 (**1998**).
15. H. Bielawa, O. Hinrichsen, A. Birkner, and M. Muhler, *Angew. Chem. Int. Ed.* 40, 1061 (**2001**).
16. B. Z. Zhan, A. M. White, T. K. Sham, J. A. Pincock, R. J. Doucet, K. V. R. Rao, K. N. Robertson, and T. S. Cameron, *J. Am. Chem. Soc.* 125, 2195 (**2003**).
17. Y. H. Kim, E. D. Park, H. C. Lee, D. Lee, and K. H. Lee, *Catal. Today* 146, 253 (**2009**).
18. J. Assmann, V. Narkhede, N. A. Breuer, M. Muhler, A. P. Seitsonen, M. Knapp, D. Crihan, A. Farkas, G. Mellau, and H. Over, *J. Phys. Condens. Matter* 20, 184017/1 (**2008**).
19. I. Balint, A. Miyazaki, and K. Aika, *J. Catal.* 220, 74 (**2003**).
20. S. Miao, Z. Liu, B. Han, J. Huang, Z. Sun, J. Zhang, and T. Jiang, *Angew. Chem. Int. Ed.* 45, 266 (**2006**).
21. C. Pan, K. Pelzer, K. Philippot, B. Chaudret, F. Dassenoy, P. Lecante, and M.-J. Casanove, *J. Am. Chem. Soc.* 123, 7584 (**2001**).
22. S. Jansat, D. Picurelli, K. Pelzer, K. Philippot, M. Gomez, G. Muller, P. Lecantec, and B. Chaudret, *New J. Chem.* 30, 115 (**2006**).
23. K. Pelzer, B. Laleu, F. Lefebvre, K. Philippot, B. Chaudret, J. P. Candy, and J. M. Basset, *Chem. Mater.* 16, 4937 (**2004**).
24. A. Duteil, R. Queau, B. Chaudret, R. Mazel, C. Roucau, and J. S. Bradley, *Chem. Mater.* 5, 341 (**1993**).
25. G. Salas, C. C. Santini, K. Philippot, V. Colliere, B. Chaudret, B. Fenetd, and P. F. Fazzinie, *Dalton Trans.* 40, 4660 (**2011**).
26. G. Salas, A. Podgoršek, P. S. Campbell, C. C. Santini, A. A. H. Pádua, M. F. Costa Gomes, K. Philippot, B. Chaudret, and M. Turminee, *Phys. Chem. Chem. Phys.* 13, 13527 (**2011**).
27. P.-J. Debouttière, V. Martinez, K. Philippot, and B. Chaudret, *Dalton Trans.* 46, 10172 (**2009**).
28. I. Favier, S. Massou, E. Teuma, K. Philippot, B. Chaudret, and M. Gómez, *Chem. Commun.* 3296 (**2008**).
29. R. S. Varma, *Curr. Opin. Chem. Eng.* 1, 123 (**2012**).
30. J. A. Dahl, B. L. S. Maddux, and J. E. Hutchison, *Chem. Rev.* 107, 2228 (**2007**).
31. N. Roy, A. Gaur, A. Jain, S. Bhattacharya, and V. Rani, *Environ. Toxicol. Pharmacol.* 36, 807 (**2013**).
32. E. Filippo, A. Serra, A. Buccolieri, and D. Manno, *J. Non-Cryst. Sol.* 356, 344 (**2010**).
33. S. Panigrahi, S. Kundu, S. K. Ghosh, S. Nath, and T. Pal, *Colloids Surf. A: Physicochem. Eng. Asp.* 264, 133 (**2005**).
34. N. N. Mallikarjuna and R. S. Varma, *Cryst. Growth Des.* 7, 686 (**2007**).
35. N. M. A. Hadia, S. García-Granda, and J. R. García, *J. Nanosci. Nanotechnol.* 14, 5449 (**2014**).
36. K. Sue, T. Sato, S. Kawasaki, Y. Takebayashi, S. Yoda, T. Furuya, and T. Hiaki, *Ind. Eng. Chem. Res.* 49, 8841 (**2010**).

37. M. Miyauchi, Z. Liu, Z. G. Zhao, S. Anandan, and K. Hara, *Chem. Commun.* 46, 1529 (**2010**).
38. M. Taguchi, S. Takami, T. Adschiri, T. Nakane, K. Sato, and T. Naka, *Cryst. Eng. Comm.* 13, 2841 (**2011**).
39. J. Lian, Z. Ding, F. Kwong, and D. H. L. Ng, *Cryst. Eng. Comm.* 13, 4820 (**2011**).
40. B. L. Cushing, V. L. Kolesnichenko, and C. J. O'Connor, *Chem. Rev.* 104, 3893 (**2004**).
41. C. Koch, Determination of Core Structure Periodicity, and Point Defect Density Along Dislocations, Tesis, Arizona State University (**2002**).
42. R. H. Schroeder, N. Schmitz-Pranghe, and R. Kohlhaas, *Z. Metallkd.* 63, 12 (**1972**).
43. N. C. Antonels and R. Meijbom, *Langmuir* 23, 13433 (**2013**).
44. X. Yan, H. Liu, and K. Y. Liew, *J. Chem. Mater.* 11, 3387 (**2001**).
45. R. Bittel, C. Bremard, G. Nowogrocki, and G. Tridot, *Bull. Soc. Chem. Fr.* 11, 3824 (**1969**).
46. E. E. Mercer and R. R. Buckley, *Inorg. Chem.* 4, 1692 (**1965**).
47. Y. Zhang, J. Yu, H. Niu, and H. Liu, *J. Colloid. Interface Sci.* 313, 503 (**2007**).
48. M. M. Taqui Khan and R. S. Shukla, *Polyhedron* 10, 2711 (**1991**).
49. M. Zawadzki and J. Okal, *Mater. Res. Bull.* 43, 3111 (**2008**).
50. M. A. Ernst and W. G. Sloof, *Surf. Interface Anal.* 40, 334 (**2008**).
51. M. Zahmakiran, Y. Tonbul, and S. Ozkar, *J. Am. Chem. Soc.* 132, 6541 (**2010**).

Received: 18 July 2014. Accepted: 2 February 2015.

Capítulo VI

$[Ru_3^{(II,III,III)}O(CH_3CO_2)_6(H_2O)_3]\cdot 2H_2O$, un Acetato Trinuclear de Rutenio de Valencia Mixta: Síntesis, Estructura y Actividad Catalítica

El *Capítulo VI* describe la preparación de un clúster trinuclear de rutenio con valencia mixta, $[Ru_3^{(II,III,III)}O(CH_3CO_2)_6(H_2O)_3]\cdot 2H_2O$, así como su caracterización estructural y la descripción de su comportamiento como catalizador homogéneo en transformaciones orgánicas. Los resultados descritos en esta sección tuvieron su origen en el desarrollo sistemático de la parte experimental diseñada para la síntesis de polímeros de coordinación basados en carboxilatos de rutenio mediante el uso de estrategias sintéticas que emplean compuestos precursores (*Precursor Approach*) ya que, como se ha detallado en el *Capítulo I* (sección 1.6.2.1.), dicha metodología de síntesis de polímeros de coordinación y redes metal-orgánicas implica la utilización de complejos de coordinación polinucleares prediseñados, de forma que éstos presenten en su entorno de coordinación ligandos lábiles capaces de ser sustituidos por los grupos coordinativos de enlazadores multidentados, dando lugar a la formación de redes de coordinación extendidas.[1] Actualmente, esta ruta sintética ha sido explorada con éxito en la formación de algunas redes poliméricas imposibles de obtener mediante vías sintéticas convencionales.[2] Por ejemplo, la red metal-orgánica con topología UiO-66(Zr) ha sido obtenida mediante una reacción de intercambio de los ligandos metacrilato en el oxo-clúster $[Zr_6O_4(OH)_4(OMc)_{12}]$ (donde OMc es CH_2=CH(CH_3)COO, metacrilato) por aniones de ácidos carboxílicos (i.e.: *trans*-mucónico, tereftálico).[3] Utilizando una estrategia semejante, también fue preparada la red polimérica MIL-127, basada en unidades polinucleares con cetros metálicos mixtos (Fe^{III}/M^{II}, M = Ni, Co, Mg)[4], así como una serie de MOFs isoreticulares (IRMOFs) que contienen un oxo-clúster de zinc prediseñado.[5]

Considerando las ventajas que se derivan de utilizar complejos precursores, pero haciendo uso de la experiencia adquirida en el trabajo detallado en el *Capítulo V* de esta Tesis, donde se describe la reducción de compuestos de rutenio(III) y la generación de partículas de Ru^0 de tamaño nanométrico, se decidió explorar el uso de un acetato trinuclear de rutenio como precursor en la formación de redes poliméricas. Con este fin, siguiendo el método propuesto por Spencer y Wilkinson,[6] se sintetizó el compuesto $[Ru_3O(CH_3CO_2)_6(CH_3OH)_3]\cdot CH_3CO_2$, donde los tres átomos de rutenio(III) se disponen alrededor de un átomo de oxígeno central, completando su coordinación con ligandos acetato (véase la Figura 6.1).

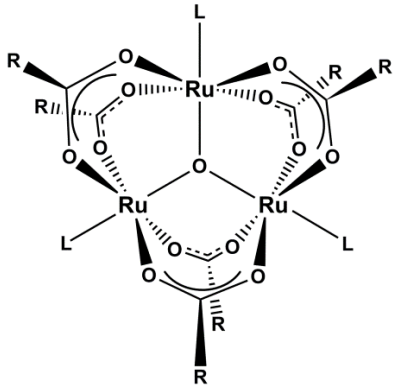

Figura 6.1. *Clúster trinuclear de rutenio $[Ru_3O(RCO_2)_6(L)_3]^n$ (donde R = H, CH_3, C_2H_5, C_3H_7, etc.; L = H_2O, CH_3OH, etc.; n = 0, +1, +2, etc.).*

(1) J.-R. Li, H.-C. Zhou, *Nat. Chem.*, **2010**, *2*, 893–898.
(2) U. Schubert, *Chem. Soc. Rev*., **2011**, *40*, 575–582.
(3) V. Guillerm, S. Gross, C. Serre, T. Devic, M. Bauer, G. Férey, *Chem. Commun.*, **2010**, *46*, 767–769.
(4) S. Wongsakulphasatch, F. Nouar, J. Rodriguez, L. Scott, C. Le Guillouzer, T. Devic, P. Horcajada, J.-M. Grenèche, P. L. Llewellyn, A. Vimont, G. Clet, M. Daturid, C. Serre, *Chem. Commun*., **2015**, *51*, 10194–10197.
(5) D. Prochowicz, K. Sokołowski, I. Justyniak, A. Kornowicz, D. Fairen-Jimenez, T. Friščićd, J. Lewiński, *Chem. Commun*., **2015**, *51*, 4032–4035.
(6) A. Spencer, G. Wilkinson, *J. Chem. Soc., Dalton Trans*., **1972**, *14*, 1570–1577.

Posteriormente, con la intención de sustituir estos ligandos acetato por enlazadores multidentados, el oxo-clúster se hizo reaccionar con varios ácidos carboxílicos seleccionados (ácido tartárico, múcico, málico, glutárico, 2,6-pyridindicarboxilico y 1,2,3,5-benzenotetracarboxilico) en medio hidrotermal. En las condiciones experimentales empleadas, los ácidos carboxílicos actuaron únicamente como agentes reductores del complejo de partida dando lugar, en todos los casos, a la formación de un oxo-clúster de rutenio de valencia mixta, $[Ru_3^{(II,III,III)}O(CH_3CO_2)_6(H_2O)_3]\cdot 2H_2O$, observándose que el rendimiento de esta reacción es función del ácido carboxílico utilizado (véase la Figura 6.2). Dado a que la metodología clásica, propuesta por Spencer y Wilkinson,[6] para la síntesis de oxo-clústeres de rutenio de valencia mixta es de alto costo (catalizador de óxido de platino) e implica condiciones experimentales especiales (corriente de hidrógeno), el método descrito aquí debe considerarse una vía alternativa adecuada para la preparación de este tipo de complejos.

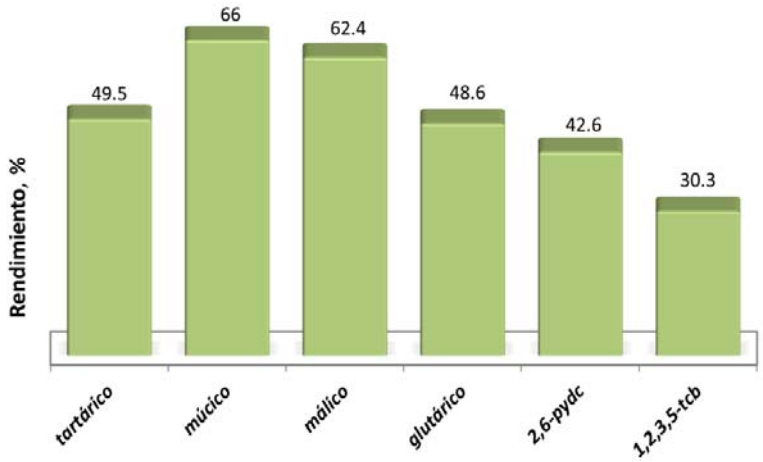

Figura 6.2. *Rendimientos en la síntesis de* $[Ru_3^{(II,III,III)}O(CH_3CO_2)_6(H_2O)_3]\cdot 2H_2O$ *en función del ácido carboxílico utilizado (ácido tartárico, múcico, málico, glutárico, 2,6-pydc = 2,6-pyridindicarboxílico, y 1,2,3,5-tcb = 1,2,3,5-benzenotetracarboxílico).*

Además, en condiciones hidrotermales, fue posible obtener mono-cristales de $[Ru_3^{(II,III,III)}O(CH_3CO_2)_6(H_2O)_3]\cdot 2H_2O$ de tamaño y calidad adecuados para su resolución estructural, lo que no había sido conseguido hasta el momento por otros autores. Por ello, la *Publicación IV*, que se presenta como parte del contenido de esta Tesis, describe la caracterización estructural del compuesto $[Ru_3^{(II,III,III)}O(CH_3CO_2)_6(H_2O)_3]\cdot 2H_2O$, utilizando datos de difracción de rayos X. Este complejo trinuclear de valencia mixta cristaliza en el grupo espacial *C*2/*c* del sistema cristalino monoclínico, con los siguientes parámetros de celdilla a = 27.032(6) Å, b = 13.832(3) Å, c = 15.257(4) Å, β = 123.62(3)° a 293 K; y a = 26.923(9) Å, b = 13.841(3) Å, c = 15.165(6) Å, β = 123.13(5)° a 100 K. Su estructura está basada en un triángulo μ_3-oxo-centrado, con los tres átomos de rutenio en los vértices, presentando una deslocalización electrónica asimétrica en los átomos de Ru a temperatura ambiente. El análisis de los datos de difracción de rayos X adquiridos a 100 K revela que el grado de deslocalización entre los átomos de rutenio disminuye significativamente, estableciéndose Ru^{II} y Ru_2^{III} como estados de oxidación formales. Análisis experimentales adicionales (XANES y EPR) confirman la valencia mixta de la unidad $Ru^{II}Ru_2^{III}$, al tiempo que el análisis termogravimétrico del complejo $[Ru_3^{(II,III,III)}O(CH_3CO_2)_6(H_2O)_3]\cdot 2H_2O$ revela su estabilidad hasta 250 °C.

El comportamiento catalítico de $[Ru_3^{(II,III,III)}O(CH_3CO_2)_6(H_2O)_3]\cdot 2H_2O$ ha sido examinado experimentalmente en la hidratación de nitrilos y en reacciones de isomerización de alcoholes alílicos, revelando ser activo en ambas transformaciones orgánicas. Las pruebas

catalíticas realizadas en la hidratación de los nitrilos en medio acuoso muestran conversiones de hasta el 99% (los rendimientos más altos se obtuvieron mediante calentamiento asistido por microondas). La evaluación de la actividad de los distintos sustratos sugiere que la reacción de hidratación de nitrilos es bifásica, con el orden benzonitrilo > 3-nitrobenzonitrilo > fenoxiacetonitrilo > 3-clorbenzonitrilo > hexanenitrilo > 3-metilbenzonitrilo. Además, tanto la naturaleza del grupo electro-aceptor como su posición en el sustrato afecta a la eficiencia de la reacción y a la actividad catalítica de loa nitrilos, disminuyendo en el orden Cl > NO_2 > CH_3 > OCH_3 y en la secuencia de posición *para* > *meta* > *ortho*. Por otra parte, las pruebas de reciclaje del catalizador revelan actividad catalítica constante, al menos, durante tres ciclos catalíticos consecutivos. Además del comportamiento notable del $[Ru_3^{(II,III,III)}O(CH_3CO_2)_6(H_2O)_3]\cdot 2H_2O$ en la reacción de la hidratación de nitrilos, se comprobó que este oxo-clúster también es activo en la reacción de isomerización de alcoholes alílicos en derivados carbonílicos y en presencia de $NaHCO_3$.

Publication IV

"Mixed-Valence μ-Oxo-Bridged Triruthenium Acetate Cluster $[Ru_3^{(II,III,III)}O(CH_3CO_2)_6(H_2O)_3]\cdot 2H_2O$: Synthesis, Structure, Characterization, Valence-State Delocalization and Catalytic Behaviour"

Inorganica Chimica Acta

(in preparation)

*Year **2015***

Mixed-Valence μ-Oxo-Bridged Triruthenium Acetate Cluster $[Ru_3^{(II,III,III)}O(CH_3CO_2)_6(H_2O)_3]\cdot 2H_2O$: Synthesis, Structure, Characterization, Valence-State Delocalization and Catalytic Behavior

Alla Dikhtiarenko, Sergei Khainakov, José R. García and José Gimeno

Departamento de Química Orgánica e Inorgánica, Universidad de Oviedo – CINN, 33006 Oviedo, Spain

Abstract

The oxo-centered, trinuclear, mixed valence $[Ru_3^{(II,III,III)}O(CH_3CO_2)_6(H_2O)_3]\cdot 2H_2O$ (**2**) acetate complex has been prepared with high yield through reduction of $[Ru_3^{(III,III,III)}O(CH_3CO_2)_6(CH_3OH)_3]\cdot CH_3CO_2$ precursor compound in presence of carboxylic acid under hydrothermal conditions (180 °C). The crystalline trinuclear oxo-cluster has been obtained as crystalline powder and characterized by single-crystal and powder X-ray diffraction, elemental analysis, electronic microscopy, thermogravimetric analysis, infrared spectroscopy. The single-crystal X-ray analysis reveals that complex **2** crystallizes in monoclinic space group *C*2/*c* with unit cell dimensions a = 27.032(6), b = 13.832(3), c = 15.257(4) Å, $\alpha = \gamma = 90°$, β = 123.62(3)° at 293 K, and a = 26.923(9), b = 13.841(3), c = 15.165(6) Å, $\alpha = \gamma = 90°$, β = 123.13(5)° at 100 K. Compound **2** composes of μ_3-oxocentered trinuclear ruthenium array and present mixed valence type structure where oxidation state delocalization between three Ru atoms take place at 293 K. Accurate single-crystal analysis along with valence bond calculations reveal trapped-valence state delocalization at room temperature, while three-site relaxation occurs at 100 K leading to Ru(II) and Ru_2(III) formal states. Moreover, the mixed valence of $Ru^{II}Ru_2^{III}$ unit in compound **2** has been confirmed by XANES and EPR spectroscopies. The crystal packing of **2** formed through hydrogen bonding displays 2D honeycombed network. The catalytic behavior of oxo-centered triruthenium complex **2** has been examined in hydration of nitriles and isomerization of allylic alcohols reactions both realized in aqueous media. The catalytic performances were discussed in light of variable reaction conditions and substrates' activities.

Keywords: Triruthenium oxo-cluster, mixed-valence delocalization, synthesis, hydration of nitriles, isomerization of allylic alcohols, catalysis.

1. Introduction

Triangular μ-oxo-centered ruthenium-carboxylate clusters of general formula $[Ru_3O(RCO_2)_6L_3]^n$ (R = H, CH_3, C_2H_5, C_3H_7, C_3F_7, C_6H_5, C_7H_{15}, C_8H_{16}; L = H_2O, PPh_3, CO, CH_3OH, *N*-heterocycles, $OS(CH_3)_2$, etc.),[1–7] where three ruthenium atoms are bridged by the oxygen atom located at the center of an ruthenium triangle and also by the six carboxylate ligands in the circumference (Scheme 1), show multiple redox behavior, intriguing mixed-valence chemistry, and versatile catalytic properties.[8–11]

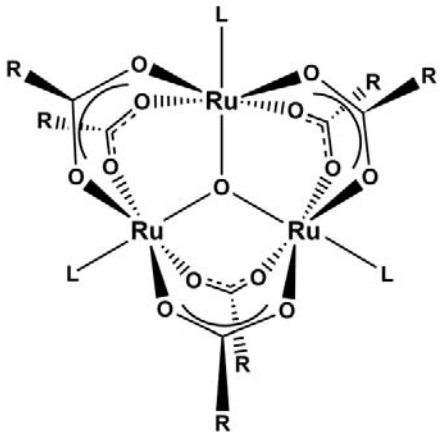

Scheme 1. Molecular structure of trinuclear ruthenium cluster $[Ru_3O(RCO_2)_6L_3]^n$ (R = H, CH_3, C_2H_5, C_3H_7, C_3F_7, C_6H_5, C_7H_{15}, C_8H_{16}; L = H_2O, PPh_3, CO, CH_3OH, *N*-heterocycles, $OS(CH_3)_2$, etc.)

The axial ligands L are comparatively labile and can readily be substituted, thus enhancing significantly the richness of triruthenium chemistry. Moreover, along axial ligand substitution, the bridging carboxylates of oxo-centered triruthenium core $[Ru_3(\mu_3\text{-}O)(\mu\text{-}RCO_2)_6]^n$ can be replaced affording an excellent means to control the chemical and electronic properties by introducing proper organic ligands.[3,12,13] Nowadays, metal-oxo clusters gained particular interest as class of compounds that can be used as predesigned building blocks to elaborate functional hybrid materials such as metal-organic frameworks (MOFs).[14–18]

Among the variety of $[Ru_3O(RCO_2)_6L_3]^n$ clusters, considerable attention has been paid to those that has a mixed-valence state of ruthenium atoms, e.g. $[Ru_3^{II,III,III}O(RCO_2)_6L_3]^0$, because their original spectral and catalytic behavior.[19–21] Classical method for preparation of $[Ru_3^{II,III,III}O(RCO_2)_6L_3]^0$-type complexes firstly has been described by Spencer and Wilkinson.[6] According to this method, the $[Ru_3^{II,III,III}O(CH_3CO_2)_6(H_2O)_3]^0$ complex can be prepared through the reduction of $Ru_3^{(III,III,III)}O(CH_3CO_2)_6(CH_3OH)_3]\cdot CH_3CO_2$ precursor in stream of hydrogen at 2 atm pressure, in aqueous solution, in presence of platinum oxide catalyst. Beside high cost and rigorous conditions of the method, the oxo-centered triruthenium (II,III,III) cluster core is frequently undergo second step reduction leading to binuclear μ-tetraacetate $Ru^{II}Ru^{III}$ product with loss of the central μ-oxo ion.[6,22] Although the synthesis procedure for neutral $[Ru_3^{II,III,III}O(CH_3CO_2)_6(H_2O)_3]^0$ complex has been reported, no evidence of its detailed crystal structure has been shown so far.

Herein, we report a first detailed crystal structure of trinuclear ruthenium oxo-cluster $[Ru_3^{(II,III,III)}O(CH_3CO_2)_6(H_2O)_3]\cdot 2H_2O$ (**2**) which was prepared as crystalline powder in high yield by reduction with muccic acid under hydrothermal conditions. To the best of our knowledge, using the carboxylic acid as a mild reduction agent for the controlled one-electron reduction of $[Ru_3^{(III,III,III)}O(CH_3CO_2)_6(CH_3OH)_3]\cdot CH_3CO_2$ precursor is reported for the first time. Furthermore, the proposed synthetic approach can be viewed as easy-feasible alternative method for preparation of mixed-valence clusters. In addition, mixed-valence delocalization taking place in the $[Ru_3^{(II,III,III)}O(CH_3CO_2)_6(H_2O)_3]$ complex at room temperature along with catalytic properties of the cluster have been discussed in details here.

2. Experimental Section

2.1. Materials

The compound $[Ru_3^{(III,III,III)}O(CH_3CO_2)_6(CH_3OH)_3]\cdot CH_3CO_2$ (**1**) was used as starting material for the preparation of **2** and was obtained by modifying the synthesis method reported by Spencer and Wilkinson.[6] Muccic acid and other chemicals are commercially available and were used as purchased.

2.2. Synthesis of $[Ru_3^{(III,III,III)}O(CH_3CO_2)_6(CH_3OH)_3]\cdot CH_3CO_2$ (1)

Following the modified procedure described by Baumann *et al.*,[7] 3.0 g (12 mmol) of $RuCl_3\cdot 3H_2O$ and 6.0 g (44 mmol) of sodium acetate were dissolved in mixture of 75 mL of ethanol and 75 mL of glacial acetic acid. After being heated at reflux for 4 h or more, the solution was cooled. In order to separate the product from excess of non-reacted impurities, resulted solution was centrifuged for about 20 min at a medium speed and filtered. The resulting filtrate was reduced to green oil by removing the volatiles on a rotary evaporator. A total of 150 mL of CH_3OH was added to the oil substance, stirred and then filtered. The filtrate was cooled at - 40 °C for 4 h, and the precipitate of sodium chloride and sodium acetate was removed by filtration. Again, the resulting filtrate was evaporated on rotary evaporator, dissolved in methanol, filtered and evaporated. The pure acetate **1** was obtained by two recrystallizations from methanol-acetone, and subsequently dried in vacuum giving a 46% yield (basing on Ru).

Anal. Calcd. for $C_{17}H_{30}O_{18}Ru_3$: C, 24.64%; H, 3.62%. Found: C, 24.5%; H, 3.6%. IR (KBr disks): 1594s, 1511w, 1423s, 1373w, 1332w, 1297m, 1222w, 1045w, 929w, 784m, 767m, 727w, 526m cm^{-1}.

2.3. Synthesis of $[Ru_3^{(II,III,III)}O(CH_3CO_2)_6(H_2O)_3]\cdot 2H_2O$ (2)

For the preparation, 0.83 g (1 mmol) of **1** and 0.02 g (0.1 mmol) of muccic acid ($C_6H_{10}O_8$) were mixed in 10 mL of distilled water. Then the reaction mixture was stirred at room temperature to complete dissolving of chemicals, transferred in a Teflon-lined stainless vessel (40 mL) and heated at 180 °C for 72 h under autogenous pressure. After, the reaction was cooled down to room temperature, and resulted solid was filtered, washed several times with ice-cold distillated water and air-dried. The yield of dark green solid lustrous solid was 0.144 g (66%).

Anal. Calcd. for $C_{12}H_{28}O_{18}Ru_3$: C, 18.87 %; H, 3.67%. Found: C, 18.9%; H, 3.7%.

2.4. Single-crystal X-ray diffraction and structure determination of 2

Single-crystal X-ray diffraction data collection was performed at 293 K and 100 K on Oxford-Diffraction-Gemini diffractometer with a monochromatic CuKα radiation source (λ = 1.5418 Å). The CrysAlisPro program was used for cell refinement and data reduction. Images were collected at a 55 mm fixed crystal-detector distance, using the oscillation method, with 1° oscillation and variable exposure time per image. The structures were solved by direct methods using the SIR92 program.[23] The refinement was performed by SHELX-97[24] using full-matrix least squares on F^2. All non-H atoms were anisotropically refined except two crystallization water molecules which were treated isotopically. Position of the H atoms were calculated based on geometric criteria (C-H = 0.96 Å for methyl groups) than have been placed in their calculated position and refined isotropically using a rider model with $U_{iso}(H) = 1.5\ U_{eq}(C)$ for methyl group. An absorption correction was performed using XABS2 program.[25] All intra- and inter-molecular interactions were found by PARST[26] and PLATON[27] program packages. Crystallographic data for **2** have been deposited to Cambridge Crystallographic Data Center with CCDC# 813218–813219 and can be obtained free of charge upon request at www.ccdc.cam.ac.uk/data_request/cif. Crystal data and structure refinement details for **2** at 293 K and 100 K are presented in Table 1.

Table 1. Crystallographic data and structure refinement for $[Ru_3(CH_3CO_2)_6(H_2O)_3]\cdot 2H_2O$ (**2**)

Temperature	**293 K**	**100 K**
Formula	$C_{12}H_{28}O_{18}Ru_3$	$C_{12}H_{28}O_{18}Ru_3$
Formula weight / g·mol^{-1}	763.55	763.55
Wavelength	CuKα (1.54184 Å)	CuKα (1.54184 Å)
Crystal system	monoclinic	monoclinic
Space group	*C2/c*	*C2/c*
Unit cell dimensions		
a / Å	27.032(6)	26.923(9)
b / Å	13.832(3)	13.841(3)
c / Å	15.257(4)	15.165(6)
α / °	90	90
β / °	123.62(3)	123.13(5)
γ / °	90	90
Cell volume / Å^3	4751(3)	4732(4)
Z	8	8
Calc. Density / mg·m^{-3}	1.135	1.072
Absorption coefficient / mm^{-1}	16.01	16.07
F(000)	3008	2928
Crystal size / mm^3	0.03 × 0.06 × 0.08	0.03 × 0.06 × 0.08
Theta range for data collection / °	3.8 to 71	3.5 to 71.9
Index ranges	$-32\leq h\leq 33$, $-16\leq k\leq 14$, $-18\leq l\leq 18$	$-30\leq h\leq 33$,$-17\leq k\leq 14$,$-18\leq l\leq 15$
Reflection collected	19481	8935
Independent reflections	4541 [R_{int} = 0.04]	4405[R_{int} = 0.121]
Completeness to θ=70°	99 %	99 %
Absorption corrections	Empirical	Empirical
Max. and min. transmission	0.590 and 0.350	0.373 and 0.852
Refinement method	Full-matrix least-squares on F^2	Full-matrix least-squares on F^2
Data/restraints/parameters	4541/0/308	4405/0/288
Goodness-of-fit on F^2	0.901	0.972
Final R indices [$I>2\sigma(I)$]	R_1 = 0.049, wR_2 = 0.117	R_1 = 0.088, wR_2 = 0.203
R indices (all data)	R_1 = 0.084, wR_2 = 0.130	R_1 = 0.204, wR_2 = 0.293
Largest diff. peak and hole	1.35 and -0.72 e·Å^{-3}	1.17 and -1.05 e·Å^{-3}

$R_1 = \Sigma \, ||F_0| - |F_c|| \, / \, \Sigma \, |F_0|$ for observed data ($I > 2\sigma(I)$); number in parentheses is for all data.
$wR_2 = \{\Sigma \, [w(F_0^2 - Fc^2)^2] / \Sigma \, [w(F_0^2)^2]\}^{1/2}$ for observed data ($I > 2\sigma(I)$); number in parentheses is for all data.

2.5. Characterization methods

Microanalyses were carried out using a Perkin-Elmer model 2400B elemental analyzer. The IR spectra were recorded on a Bruker Tensor-27 spectrophotometer as KBr pellets in the 4000–400 cm^{-1} region. A Mettler-ToledoTGA/SDTA851 were used for the thermal analyses in nitrogen dynamic atmosphere (50 mL/min) at a heating rate of 10 °C/min. Approximately 10 mg of powder sample was thermally treated, and blank runs were performed.

X-ray microanalysis (SEM/EDX) confirmed composition of $[Ru_3^{(II,III,III)}O(CH_3CO_2)_6(H_2O)_3]\cdot 2H_2O$, by using JEOL JSM-6100 scanning microscopy (SEM) coupled with an INCA Energy-200 dispersive X-ray microanalysis system (EDX) with a PentaFET ultrathin window detector. As show Figure S1 (Supporting Information), the lustrous dark green powder of **2** consists of macro-sized crystals exhibiting prismatic habit.

X-Ray powder diffraction patterns were collected with a X´Pert Philips X-ray diffractometer (CuK_α radiation, λ = 1.5418 Å) at room temperature. The powder diffraction analysis indicate that synthesized compound **2** show analogous pattern as for simulated from the atomic coordinates of **2** determined by single-crystal X-ray diffraction (Fig. S3, Supporting Information). X-ray near-edge absorption spectra (XANES) at Ru *K*-edge were recorded in transmittance mode at European Synchrotron Radiation Facility (ESRF, Grenoble) in Beamline BM25.The excitation energy was selected using a Si(111) double-crystal monochromator. The beam size of 1 mm (horizontal) × 1 mm (vertical) was controlled with a slit. The XANES spectra

were measured on pallets containing approximately 40 mg of solid compound **2** in 200 mg of boron nitride. Each spectrum was recorded with 0.25 eV step size. All spectra processing procedures (i.e., normalization, smoothing, background subtraction and windowing) including linear combination calculations were done in the IFEFFIT software package.[28,29] X-band EPR measurement was performed with ADANI CMS-8400 spectrometer at room temperature.

2.6. Catalytic experiments

Hydration reactions were carried out in Schlenk tube under N_2 atmosphere. The reaction mixture was prepared dissolving 5 mg (6.5 μmol) of catalyst **2** in 3 mL of H_2O. The mixture was degassed and 1.5 mmol of corresponding acetonitrile substrate was added with micropipette to stirred solution. The reaction was allowed for heating at 110 °C using oil bath or microwave-assisted heating. The isomerization reactions of allylic alcohols were conducted Schlenk tube under N_2 atmosphere. The reaction mixture was prepared dissolving 3 mg (3.9 μmol) of catalyst **2** in 2 mL of appropriate solvent (DMF, EtOH or H_2O). The mixture was degassed and 1 mmol of corresponding allylic alcohol substrate was added with micropipette to stirred solution. The reaction was allowed for heating using oil bath

The reaction solutions were analyzed by regular sampling using GC/FID (Hewlett Packard) equipped with Beta DEX 120 (30 m × 0.25 mm × 0.25 μm) 30 m long column. The degrees of conversion were calculated on the basis of the ratio of areas of the substrate material and the products determined from corresponding chromatograms. The optimization of chromatographic methods and the calibration procedures for detection of products as well as substrates were realized by injection of authentic commercial samples.

3. Results and Discussion

3.1. Crystal structure of $[Ru_3O(CH_3CO_2)_6(H_2O)_3]\cdot 2H_2O$ (2)

The single-crystal X-ray diffraction analysis reveals that compound **2** crystalizes in monoclinic space group *C*2/*c* with unit cell parameters listed in Table 1. The molecular structure of the acetate complex **2** is depicted in Figure 1. The asymmetric unit of 2 contains three crystallographically independent ruthenium atoms, one μ_3-oxygen, six acetate ligands, three coordinated and two lattice water molecules.

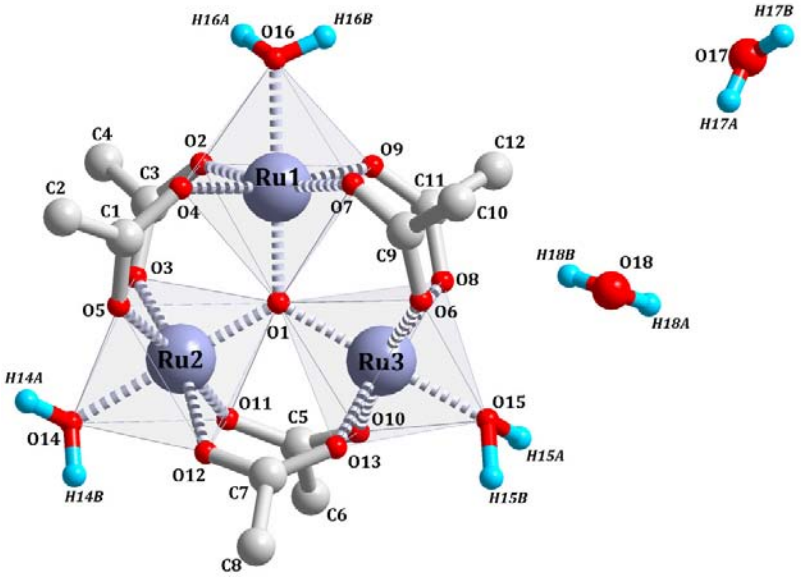

Figure 1. Molecular structure of complex **2** represented with corresponding atom labeling scheme. H atoms from the methyl groups were omitted for clarity.

As shown in Figure 1, the three ruthenium atoms form a near to the equilateral triangle where pseudo-C_3 axis pass through μ_3-O perpendicular to the Ru–Ru plane with Ru···Ru separation distances of 3.322 and 3.274 Å. In similar way, three coordinated water molecules are located in the same plane that defines for Ru atoms. The central μ_3-O1 atom is located in the Ru_3 triangular plane near to the center of the triangle. The acetate ligands deviate from Ru_3 triangular plane on the angle of 45.2°. Furthermore, each ruthenium atom is in distorted octahedral coordination geometry formed by four carboxyl oxygen atoms originated from four different acetate ligands, one μ_3-O and one oxygen atom coming from coordinated water molecule. The average bond length of Ru-O is varied from 1.875(6) Å to 2.128(7) Å and depends from the temperature of measurement. Selected bond distances for ruthenium coordination environments in **2** at 100 K and 293 K are summarized in Table S1 (Supporting Information).

The crystal packing of **2** stabilized through multiple hydrogen bonds involving the coordinated water in $[Ru_3O(CH_3CO_2)_6(H_2O)_3]$ complex and two crystallization water molecules. There obviously exists strong intermolecular interaction in the hydrogen-bonding network associated with the valence state conversion. In the complex **2**, a calculation of intermolecular contacts suggests five hydrogen bonds listed in Table 2.

Table 2. Hydrogen bonds geometry* in structure of **2**

D*–H···*A	**d (*D*–H), Å**	**d (H···*A*), Å**	**d (*D*···*A*), Å**	**∠(*D*–H···*A*), °**
O14–H14A···O13	0.90	2.09	2.996(12)	179
O15–H15B···O5	0.90	2.09	3.145(17)	168
O16–H16B···O9	0.89	2.23	3.044(13)	152
O18–H18A···O17	0.89	1.93	2.69(4)	148
O18–H18B···O8	0.89	2.57	3.39(3)	161

*The hydrogen bonds were considered according to [30,31]

The O18–H18B···O8 hydrogen bond holds one crystalized water molecule near to Ru3 site, while intermolecular O14–H14A···O13, O15–H15B···O5 and O16–H16B···O9 contacts contribute to the strengthen of cluster molecules packing (Fig. S4). Moreover, the hydrogen bonds between individual cluster molecules connect the neighboring $[Ru_3O(CH_3CO_2)_6(H_2O)_3]$ complexes to construct a 2D framework. Better insight of resulted packing network can be achieved by topological analysis using TOPOS4.0 program package.[32] As shown in Figure S5, each ruthenium oxo-cluster is linked to six equivalent neighbors *via* hydrogen bonds and represents a 6-connected node. The resulted non-interpenetrating 6-connected unimodal net is simplified as well-known Shubnikov hexagonal plane net topology (***hcb***) with the Schläfli symbol of (6,3) and the 6.6.6. vertex symbol.

3.2. Ruthenium mixed valence delocalization in $[Ru_3^{(II,III,III)}O(CH_3CO_2)_6(H_2O)_3]\cdot 2H_2O$

The formulation of $[Ru_3O(CH_3CO_2)_6(H_2O)_3]\cdot 2H_2O$ determined by single-crystal X-ray study implies that the ruthenium atoms in complex **2** are in mixed oxidation state with Ru^{II}:Ru^{III} ratio equal to 1:2. As have been observed in similar trinuclear-oxo compounds, where transition metal centers are found in mixed oxidation states, the resonant mixed valence delocalization between those three centers is usually occurred at room temperature.[33–35] The geometry of the coordination sphere around the transition metal centers atoms provides much more information about the oxidation state of these atoms and the degree of valence delocalization in the M_3O core.[36–38] In particular, the Ru–μ_3O distance and angles analysis are expected to be useful for determination of formal valences at each ruthenium center in $[Ru_3O(CH_3CO_2)_6(H_2O)_3]\cdot 2H_2O$ complex. Thus, the Ru–μ_3O distance and angles in Ru_3O triangular core were analyzed using single-crystal X-ray diffraction data measured at 293 K and 100 K. As shown in Figure 2a, the Ru2–μ_3O bond length (1.875 Å) is significantly shorter than Ru1–μ_3O (1.905 Å) and Ru3–μ_3O (1.9931 Å), suggesting that Ru2 center is likely exhibit 3+ oxidation state.

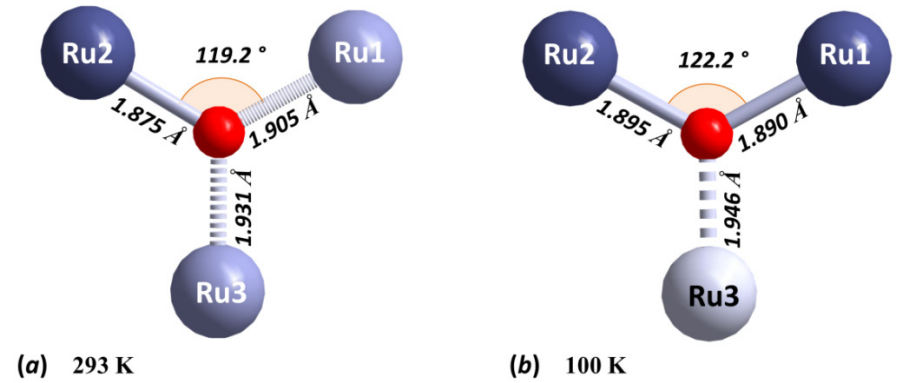

Figure 2. The Ru–μ_3O bond lengths and Ru2–O–Ru1 angle in triangular Ru_3O core of 2 as determined from single-crystal X-ray diffraction data at (a) 295 K and (b) 100K.

Furthermore, the Ru3–μ_3O appears to be longer than Ru1–μ_3O that is within the range as expected for an Ru(2+) atom. Meanwhile, intermediate position of Ru1–μ_3O bond points to the valence delocalization at Ru1 center. To support this, charge ordering calculation performed using VaList program,[39] suggest that Ru2 atom site is mainly Ru(3+) while the Ru1 and Ru3 centers exhibit mixed valence state resembling charges of 2.3+ and 2.7+, respectively. This result indicate that the mixed oxidation delocalization take place between Ru1 and Ru3 at room temperature, where Ru1 atom site trend to Ru(2+) approximation. In contrast, as shown in Figure 2b, at lower temperature Ru2–μ_3O and Ru1–μ_3O bond are close to be equal with lengths of 1.895 Å and 1.890 Å, respectively, while Ru3–μ_3O bond become larger (1.946 Å). Moreover, the Ru2–μ_3O–Ru1 is also depended on the valence state and, as shown in Figure 2, upon temperature decreasing became larger on 3°. These observations indicate that oxidation state trapping (3+) on Ru1 center occurs at lower temperatures. As supported by valence bond calculation at 100 K, the ruthenium site oxidation for Ru1 and Ru2 metal centers are 3+ whereas for Ru3 center calculated value became Ru(2+).

In order to confirm the mixed oxidation states of ruthenium atoms in oxo-cluster **2**, the XANES technique was applied. The normalized XANES spectra for solid samples of **2** and reference compounds measured on Ru K adsorption edge are shown in Figure 3a.

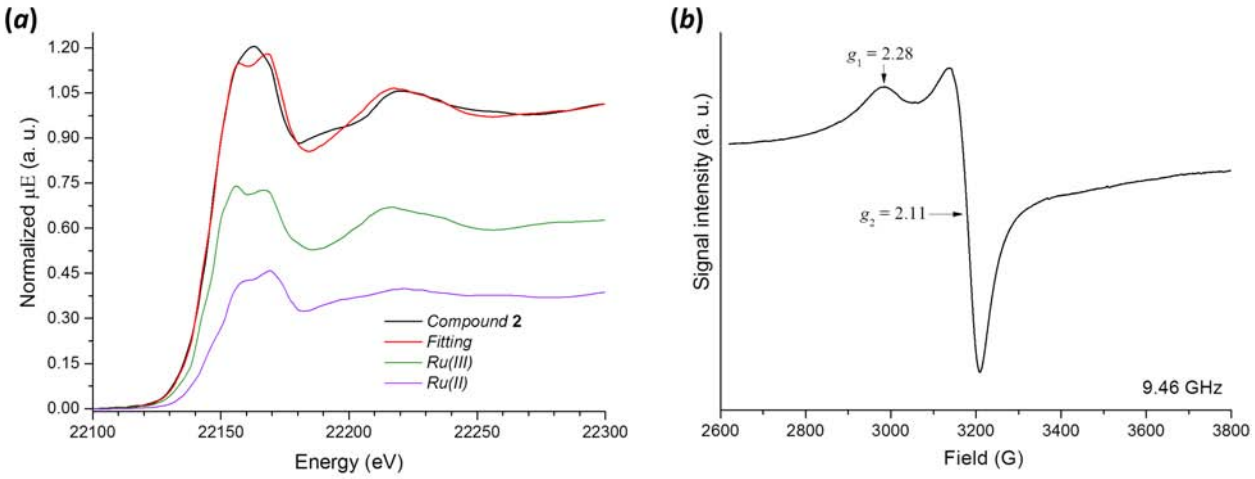

Figure 3. (a) XANES part of the Ru K-edge X-ray absorption spectra of compound **2** with corresponding fitting plot realized using the absorption edges positions of reference compounds Ru(III) and Ru(II) as a calibration data for determination of Ru formal oxidation states in oxo-cluster **2**. (b) EPR spectrum of polycrystalline sample of complex **2** at 293 K.

The adsorption edges (determined from the derivatives of normalized spectra) were used to estimate the formal oxidation state of ruthenium atoms in triruthenium oxo-cluster **2**. As follows

from fitting data represented in Figure 3a, the $[Ru_3^{(II,III,III)}O(CH_3CO_2)_6(H_2O)_3]\cdot 2H_2O$ complex have the position of the Ru absorption K-edge E_o close to 22142 eV. A combination fit of the experimental data using the E_o values of corresponding Ru(III) and Ru(II) reference compounds suggests that the ruthenium centers in complex **2** exhibit II-III mixed valance state. The Ru^{II}:Ru^{III} ratio of formal oxidation states for three ruthenium centers is found to be 0.38:0.62 (calc. 0.33:0.67) which is consistent with expected for $Ru^{II}Ru_2^{III}$ core.

EPR spectroscopy has been very useful for characterizing the electronic and magnetic properties of diruthenium(II,III) centers in the dinuclear metal complexes.[40–42] When the high-spin Ru^{II} (S = 2) and Ru^{III} (S = 5/2) centers are antiferromagnetically coupled they exhibit characteristic signals at $g_{av} \geq 2$ resulting from a ground state (S_{total} = 1/2). For example, $Ru_2^{II,III}(O_2CC_3H_7)_4Cl$ complexes exhibit signals near $g_{\perp}$ = 2.1 and $g_{\parallel}$ = 2.18 due to the antiferromagnetic coupling between the two ruthenium centers.[43] In turn, complex **2** exhibits the intense EPR signals at g_1 = 2.11 and g_2 = 2.28 (Fig. 3b). These signals are originated from high-spin Ru^{III} (S = 5/2) and Ru^{II} (S = 2) centers with axial symmetry ($g_1 > g_2$) occurred as a result of elongation of octahedral coordination environment due to the valence delocalization. Since the octahedral coordination each ruthenium center is axially distorted, the g_1 = 2.11 and g_2 = 2.28 values correspond to *g*-factors for perpendicular and parallel orientations, respectively. Thus, these results reveal that complex **2** has a strong antiferromagnetic coupling between the Ru^{II} and Ru^{III} centers with axially distorted octahedral geometry.

3.3. Thermogravimetric analysis

The thermal stability of **2** in nitrogen atmosphere was investigated. As shown in Figure 4, where corresponding TG/DTG curves are presented, decomposition of ruthenium oxo-cluster proceeds through three steps with total mass loss of 58.4%. The first step, which take place in temperature range of 60–200 °C with maximum velocity at 130 °C and has endothermic effect in SDTA curve, reveals mass loss of 9.4 % and corresponds evacuation of 4 moles (calc. 9.43%) of water molecules (two crystallization and two coordinated water).

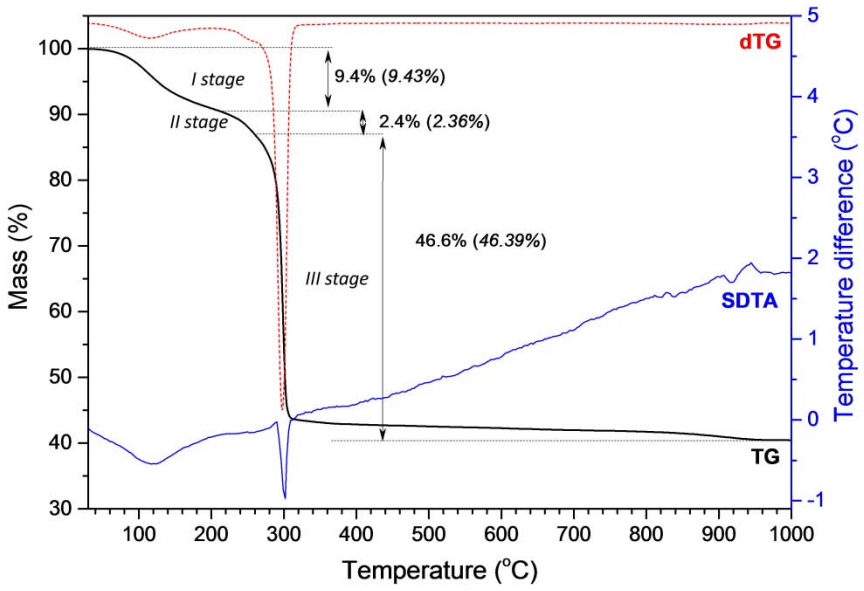

Figure 4. Thermogravimetric (TG), derivative (dTG) and simultaneous differential thermal analysis (SDTA) curves corresponding to decomposition profile of **2** in nitrogen atmosphere.

The second mass loss step is partially overlapped with third stage and occurred between 240 and 280 °C reaching maximum velocity at 260 °C. The mass loss corresponding to this stage is 2.4% followed by endothermic peak in SDTA graph and attributed to the loss of one remaining coordinated water molecule (calc. 2.36 %). The third step occurred in the range of temperatures 290–400 °C with maximum velocity at 300 °C and the mass loss of 46.6% is

associated with decomposition of acetate ligands in resulted anhydrous acetate oxo-cluster (calc. 46.39%). Assuming that decomposition of **2** take place in inert nitrogen atmosphere, metallic ruthenium is expected as final product of pyrolysis that leads to the residue mass of 41.6 % (calc. 41.07%).

3.4. Infrared spectroscopic characterization

The infrared spectrum of complex **2** acquired from 4000 cm^{-1} to 400 cm^{-1} is dominated by vibrational modes involving the bridging acetate group (Fig. S6a). The high-energy, relatively weak bands observed ~ 2925 cm^{-1} are attributed to C–H stretching of acetate ligands, while the methyl bending mode is represented by peak centered at 1354 cm^{-1}. Other bands occurred at 948 cm^{-1} and 686 cm^{-1} apparently attribute to acetate ligands.[44] The intense peaks located at 1630 cm^{-1} and 1572 cm^{-1} are associated to asymmetric carboxylate stretching frequencies, whereas the lower energy band ~1429 cm^{-1} is due to symmetric stretching of carboxylic group.[45] Furthermore, the bands observed at 1039 cm^{-1} and 619 cm^{-1} were assigned to (μ_3-O)–Ru bridging vibrations in complex **2**.[46]

Vibration modes of coordinated water molecules occur in the region 3600–3300 cm^{-1}, among the peak centered at 3550 cm^{-1} corresponds to crystallized water molecules.[45] Interestingly, when the complex **2** was heated at 140 °C under vacuum during 3 hours, the dehydration of ruthenium oxo-cluster is occurred as was evidenced by disappearance of the broad peak in the region of 3600–3300 cm^{-1} (Fig. S6b). Moreover, the bands attributed to variations of carboxyl groups are slightly shifted to 1537 cm^{-1} and 1410 cm^{-1} indicating that the polarity of Ru–$O_{carboxyl}$ bond increase as a result of releasing coordinated water molecules out of ruthenium coordination sphere.

*3.5. Catalytic activity of **2** in hydration of nitriles to amides in aqueous medium*

Hydration of nitriles is one of the most important reaction applied for industrial purposes since its form inherent link in the large-scale production of amines, which are synthetic intermediates used in manufacture of pharmacological products, polymers, detergents, etc.[47] To this regard, a variety of ruthenium-based complexes able to selectively and efficiently catalyze hydration of nitriles to amides in aqueous media have been reported.[48−50] Basing on these precedents, the trinuclear oxo-cluster **2** was examined in nitrile hydration reaction. In a typical experiment, 1.5 mmol% of **2** was dissolved in 3 mL of H_2O and 1.5 mmol of corresponding acetonitrile substrate was added. The reaction mixtures were allowed for heating at 110 °C using oil bath or microwave-assisted heating.

As shown in Table 3, the triruthenium oxo-cluster **2** was found to be active catalyst, reaching amides formation with yields up to TOF of 248 h^{-1}. It worth to noting that the activity of complex **2** is higher and more pronounced when reaction was assisted by microwave heating. Comparing to the nitriles conversions obtained using conventional heating, which are usually occurred from 5 to 50 h, the microwave-assisted transformation was much faster reaching high conversion percentage in less than two hours.

In order to explore the effect of hydrophobicity of the substrate on the course of hydration of nitriles in aqueous media, we focused on the wide array of aliphatic nitriles with different chain lengths. Thus, as observed in entries 1a-d, the TOF values corresponding to conversions of different substrates increases as the aliphatic chain length increases. Since the solubility of those aliphatic nitriles in aqueous media drastically decreases as the aliphatic chain growth, it is reasonable to conclude that the hydration reaction is favorable biphasic.

As expected, the hydration reaction course should vary somewhat depending on the reactivity of the nitrile. Using the same reaction conditions a wide range of nitriles substrates was examined, i.e.: benzonitrile, hexanenitrile, phenoxyacetonitrile, 3-chlorbenzonitrile, methylbenzonitrile and 3-nitrobenzonitrile.

Table 3. Hydration of nitriles in aqueous mediuam catalyzed by triruthenium oxo-cluster **2** at 110 °C

Entry	Substrate	Product	Conventional heating [a]			Microwave-assisted heating [b]		
			time, h	yield, %	TOF, h^{-1}	time, h	yield, %	TOF, h^{-1}
1a	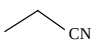	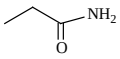	47	59	3.1	2	28	35
1b	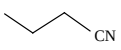	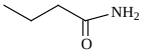	13	45	8.6	2	65	81
1c	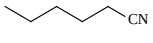	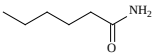	14	87	15.5	2	92	115
1d	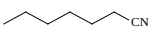	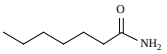	7	92	32.9	1	78	195
2a		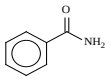	6.5	97	37.3	1	97	242
2b		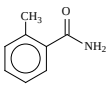	27	64	5.9	2	41	51
2c	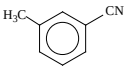	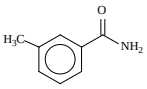	11	57	12.9	2	76	95
2d	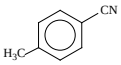	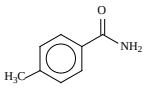	17	92	13.5	1.5	94	156.7
3a	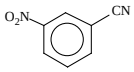	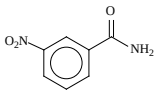	9	94	26.1	1	92	230
4a		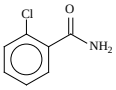	18	85	23.6	1	86	215
4b	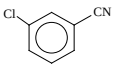	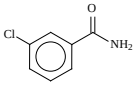	7	87	31.1	1	99	247.5
4c	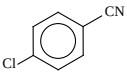	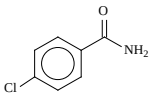	6	97	40.4	1	99	247.5
5a	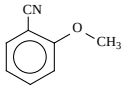	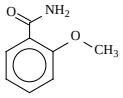	50	51	2.6	4	61	38.1
5b	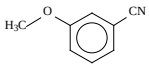	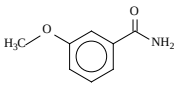	40	72	4.5	2	88	110
5c	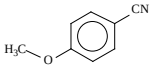	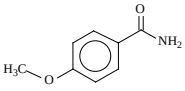	13	99	19	1	93	232.5
6a	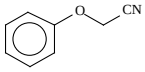	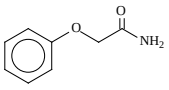	12	92	19.2	1	82	205
6b	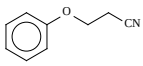	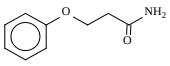	9	98	27.2	1	99	247.5
			Recycling tests					
7a	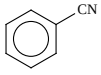	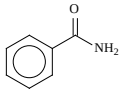	–	–	–	1	96	222
7b	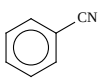	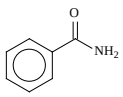	–	–	–	1	96	222

[a] Reaction performed under N_2 atmosphere at 110 °C in Schlenk tube using 1.3 mmol% (Ru) of catalyst, 1.5 mmol of substrate and 3 mL H_2O.
[b] Reaction performed under N_2 atmosphere at 110 °C in microwave autoclave using the same conditions as for ***a***.
TOF = mmol of product / mmol of catalyst (basing on Ru) / hours.

As shown in Figure S7, the kinetic plots for the studied substrates exhibit different slopes featuring variable reactivity. Summarizing, the order of reactivity of nitriles is benzonitrile > 3-nitrobenzonitrile > phenoxyacetonitrile > 3-chlorbenzonitrile > hexanenitrile > 3-methylbenzonitrile. The same order of reactivity is observed upon microwave-assisted heating, as shown in and Table 3 (entries 1d, 2a, 2c, 3a, 4b and 6a-b).

Also, the reactivity of benzonitrile as a function of electron-withdrawing groups was studied. Thus, comparing the conversion rates for methyl-, nitro-, chlor- and methoxy-substituted in ortho-position benzonitriles (entries 2c, 3a, 4b and 5b), the reactivity of the substrates fall in order of Cl > NO_2 > CH_3 > OCH_3 that is also confirmed by results obtained in microwave-assisted experiments. In other hand, beside to consequence of electron-withdrawing power of the substituents, the position of these groups is also expected to affect the reactivity of the substrates. As resulted from the data in Table 3 corresponding to entries 2c-d (for methyl-group), 4a-c (for chlor-group) and 5a-c (for methoxy-group), ortho-substituted substrates showed a lower reactivity compared to their meta- or para-substituted counterparts (entry 2b *vs* 2b-c, entry 4a *vs* 4b-c, 5a *vs* 5b-c) which is likely due to steric factors.

In overall, the reactivity of the substrates follows the order of para > meta > ortho perceiving particular electron-withdrawing effects of each sort of substituent group.

The recyclability tests for complex **2** have been performed using benzonitrile as a model substrate. The catalytic system contained **2** was allowed to react with benzonitrile for 1 h under microwave heating at 110 °C, then reaction mixture was cooled to 10°C for quantitative separation of crystalline benzamide product. After, the aqueous solution contained dissolved oxo-cluster **2** was removed by decantation and reused for next catalytic run through adding a new portion of benzonitrile (Fig. S8). As shown in Table 3 (entries 2a, 7a-b), the catalytic activities of **2** along three consecutive cycles (2a: 1st, 7a: 2nd, 7b: 3rd run) is remain almost constant leading to conversions of 96% in 1 h (TOF = 222 h^{-1}). These observations suggest that acetate triruthenium oxo-cluster **2** remain catalytic activity upon at least three consecutive cycles.

*3.6. Catalytic activity of **2** in isomerization of allylic alcohols*

The high catalytic activities of rhodium oxo-complex selective isomerization of allylic alcohols early reported by Morrill and Grubbs,[51] and similarity in the catalytic behavior of ruthenium-based compounds,[52−54] motivated us for realizing the catalytic tests of ruthenium oxo-cluster **2** in this organic transformation. In typical experiment, the ruthenium complex **2** (1.2 mmol% Ru) was dissolved in appropriate solvent and 1 mmol of allylic alcohol substrate was added. The results of catalytic tests performed with ruthenium complex **2** are summarized in Table 4. A set of variables were examined in order to optimize reaction conditions. The first variable was a temperature (Table 4, entries 1b, 4a-c). The 1-penten-3-ol was chosen as a model substrate. It was observed that the catalytic activity of **2** decreases as the temperature increases, and the higher performance with TOF of 1.7 h^{-1} is stabilized at 80 °C. Therefore, this temperature was used as an optimal for the next set of experiments.

The earliest study of Peterson and Larock,[55] focused on the isomerization of primary and secondary allylic alcohols, demonstrates considerable improvement of catalytic activities upon addition of base, i.e. $NaHCO_3$. Thus, in order to evaluate the effect base, the corresponding tests were conducted with $NaHCO_3$, KOH and without additive (Table 4: entry 1e, 5a and 5b, respectively). Unsatisfactory conversion was obtained in experiment 5b, where the isomerization reaction was realized at 80 °C without the base. Meanwhile, the addition of KOH improves isomerization of 1-octen-3-ol to 3-octanone reaching TOF of 0.01 h^{-1}. The best catalytic performance of **2** has been obtained with addition of $NaHCO_3$ (TOF 1.7 h^{-1}).

Using the optimized catalytic conditions, the next task was to determinate the effect of solvent. A series of substrates (i.e.: 3-buten-2-ol, 1-penten-3-ol, 1-hexen-3-ol, 1-hepten-3-ol and 1-octen-3-ol) was examined with three commonly employed solvents (Table 4: entries 1a-e, 2a-e, 3a-e).

Table 4. Isomerization of allylic alcohols catalyzed by triruthenium oxo-cluster **2**

Entry	Substrate	Product	Solvent	Base	T, °C	*t*, h	yield, %	TOF, h^{-1}
1a						45	97	1.8
1b	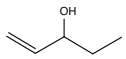	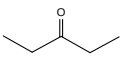				47	95	1.7
1c	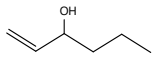	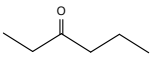	DMF	$NaHCO_3$	80	41	86	1.7
1d	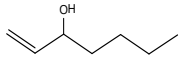	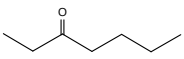				41	96	1.9
1e	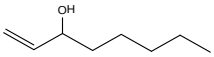	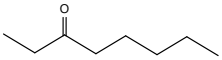				65	67	0.9
2a						23	94	3.4
2b	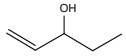	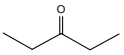				23	96	3.5
2c	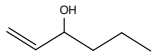	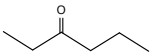	EtOH	$NaHCO_3$	80	30	74	2.1
2d	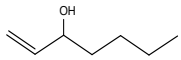	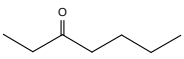				71	38	0.4
2e	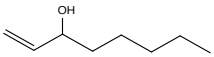	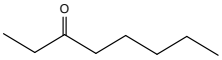				60	95	1.3
3a						48	5	0.1
3b	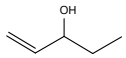	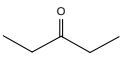				24	2	0.1
3c	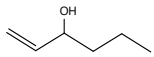	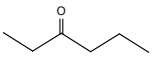	H_2O	$NaHCO_3$	80	12	1.5	0.1
3d	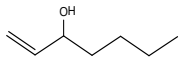	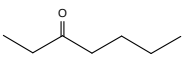				24	0	0
3e	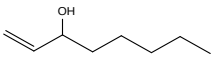	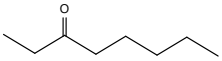				24	1	0.03
4a	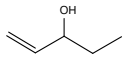	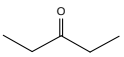			RT	48	0.6	0.01
4b	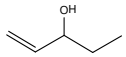	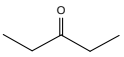	DMF	$NaHCO_3$	65	71	6.5	0.01
4c	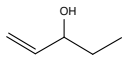	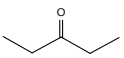			100	26	51	1.6
5a	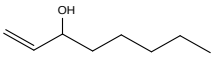	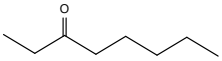	DMF	KOH	80	24	1	0.03
5b	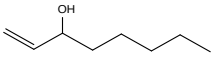	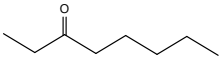		–	80	72	0	0

Reaction performed under N_2 atmosphere in Schlenk tube using 1.2 mmol% (Ru) of catalyst and 1 mmol of substrate. TOF = mmol of product / mmol of catalyst (basing on Ru) / hours.

A survey of the results show that the use of water as reaction medium don't favor the isomerization reaction and the catalytic activity decreases as the length of aliphatic chain of the substrate increases. As expected, the hydrophobicity of substrate alcohols increase in order 3-buten-2-ol > 1-penten-3-ol > 1-hexen-3-ol > 1-hepten-3-ol > 1-octen-3-ol, that stimulate the aqueous reaction solution to became a inhomogeneous biphasic mixture and lead to worsening of interactions between substrate and dissolved homogeneous catalyst. In contrast, the use of DMF as the solvent led to almost complete conversion of the started alcohol and afforded desired ketone with yields up to 97% (TOF of 1.8 h^{-1}). Notably, that effect of reactivity of alcohol

substrate as a function of length of aliphatic chain is not observed with DMF solution, which is reasonable considering that the DMF is one of the best solvents for variety of chemical substances. Finally, as expected the highest catalytic performances of **2** were obtained with ethanol as reaction solvent reaching TOF values up to 3.5 h^{-1} (Table 4: entries 2a-e).

4. Conclusions

The trinuclear ruthenium-oxo cluster $[Ru_3^{(II,III,III)}O(CH_3CO_2)_6(H_2O)_3]\cdot 2H_2O$ (**2**) firstly has been prepared with high yield by one-electron reduction of $[Ru_3^{(III,III,III)}O(CH_3CO_2)_6(CH_3OH)_3]\cdot CH_3CO_2$ precursor **1** using muccic acid as redactor under hydrothermal conditions at 180 °C. Single-crystal X-ray analysis reveals that synthesized compound **2** is mixed-valence oxo-centered trinuclear ruthenium acetate complex where oxidation state delocalization at room temperature between one Ru^{III} and one Ru^{II} sites are postulated basing on the precise analysis of crystallographic data and valence bond calculations. Furthermore, the mixed-valence states in Ru^{II}–μ_3O–Ru_2^{III} structural unit have been confirmed basing on the XANES spectral analysis of $[Ru_3^{(II,III,III)}O(CH_3CO_2)_6(H_2O)_3]\cdot 2H_2O$. The paramagnetic complex displays a rhombic EPR spectrum ($g_\perp$= 2.11 $g_\parallel$ = 2.28) arising from Ru^{III} (S = 5/2) and Ru^{II} (S = 2) centers with a ground state of S = ½ high-spin system in axially elongated octahedral environment.

The crystal structure of **2** displays 2D supramolecular networks extended through multiple hydrogen bonds which can be simplified to hexagonal plane (***hcb***) topological net. Moreover, triruthenium oxo-cluster **2** is thermally stable up to 250 °C, and its molecular structure remains unchanged upon dehydration.

The catalytic tests performed for hydration of nitriles in water medium reveal that oxo-cluster **2** shows to be active homogeneous catalyst in this transformation reaching conversions up to 99%. Notably, the highest catalytic performances were obtained under experimental sets where heating have been assisted by microwaves. The evaluation of activity of various nitrile substrates suggests that hydration of nitriles is likely biphasic and follow the order of benzonitrile > 3-nitrobenzonitrile > phenoxyacetonitrile > 3-chlorbenzonitrile > hexanenitrile > 3-methylbenzonitrile. In addition, the nature of electron-withdrawing group as well as its position also shows to affect the reaction efficiency, and the catalytic activity was decreasing in order Cl > NO_2 > CH_3 > OCH_3 and in sequence para > meta > ortho positions. Moreover, the recyclability tests for catalyst **2** reveal constant catalytic activity up to three consecutive runs.

Beside remarkable behavior of **2** in hydration of nitriles reaction, the triruthenium oxo-cluster shows to be active in isomerization of allylic alcohols reaction in presence of $NaHCO_3$. Under evaluation of reaction conditions we determine that optimal temperature for this organic transformation is 80 °C. The set of experiments suggest that the best conversions of variety of substrates were achieved using DMF as a solvent which is expected due to the miscibility effects. Furthermore, the substrate activity evaluations define order of 3-buten-2-ol > 1-penten-3-ol > 1-hexen-3-ol > 1-hepten-3-ol > 1-octen-3-ol.

Acknowledgements. The authors thank FEDER and Spanish MINECO for financial support under projects MAT2013-40950-R, Consolider ORFEO. A.D. also thanks to Spanish *Ministerio de Educación, Cultura y Deporte* by their pre-doctoral FPU grant (AP2008-03942). The synchrotron measurement time was provided by ESRF (Grenoble, France) within the research project No. CH-3428. The authors thank staff members of BM25 (SpLine): Dr. Germán R. Castro, Dr. Iván Da Silva González and Dr. Pilar Ferrer Escorihuela for the technical support, guidance and useful suggestions on XANES data collection at the synchrotron facility.

Supporting Information containes digital micrographas of **1**–**8** crystal habits, SEM images, observed and calculated X-ray powder diffraction patterns, IR spectra, additional structure plots, kinetic plots for nydtation of nintriles reaction and imeges of recyclability tests.

References

(1) O. Almog, A. Bino, D. Garfinkel-Shweky, *Inorg. Chim. Acta*, **1993**, *213*, 99–102.
(2) H. E. Toma, C. J. Cunha, C. Cipriano, *Inorg. Chim. Acta*, **1988**, *154*, 63–66.
(3) S. Davis, R. S. Drago, *Inorg. Chem*., **1988**, *27*, 4759–4760.
(4) M. Abe, Y. Sasaki, T. Yamaguchi, T. Ito, *Bull. Chem. Soc. Jpn*., **1992**, *65*, 1585–1590.
(5) A. Ohto, A. Tokiwa-Yamamoto, M. Abe, T. Ito, Y. Sasaki, K. Umakoshi, R. D. Cannon, *Chem. Lett.*, **1995**, 97–98.
(6) A. Spencer, G. Wilkinson, *J. Chem. Soc., Dalton Trans*., **1972**, *14*, 1570–1577.
(7) J. A. Baumann, D. J. Salmon, S. T. Wilson, T. J. Meyer, W. E. Hatfield, *Inorg.Chem*., **1978**, *17*, 3342–3350.
(8) H. E. Toma, K. Araki, A. D. P. Alexiou, S. Nikolaou, S. Dovidauskas, *Coord. Chem. Rev*., **2001**, *219–221*, 187–234.
(9) S. A. Fouda, G. L. Rempel, *Inorg. Chem*., **1979**, *18*, 1–8.
(10) H. E. Toma, K. Araki, A. L. Barboza Formiga, A. D. P. Alexiou, G. S. Nunes, *Quim. Nova*, **2010**, *33*, 2046–2050.
(11) C. Bilgrien, S. Davis, R. S. Drago, *J. Am. Chem. Soc.*, **1987**, *109*, 3786–3787.
(12) J.-L. Chen, X.-D. Zhang, L.-Y. Zhang, L.-X. Shi, Z.-N. Chen, *Inorg. Chem*., **2005**, *44*, 1037–1043.
(13) Z.-N. Chen, F.-R. Dai, *Struct. Bond.*, **2009**, *133*, 93–120.
(14) V. Guillerm, S. Gross, C. Serre, T. Devic, M. Bauer, G. Férey, *Chem. Commun*., **2010**, *46*, 767–769.
(15) U. Schubert, *Chem. Soc. Rev*., **2011**, *40*, 575–582.
(16) M. Eddaoudi, D. B. Moler, H. Li, B. Chen, T. M. Reineke, M. O'Keeffe, O. M. Yaghi, *Acc. Chem. Res.*, **2001**, *34*, 319–330.
(17) D. J. Tranchemontagne, J. L. Mendoza-Cortés, M. O'Keeffe, O. M. Yaghi, *Chem. Soc. Rev*., **2009**, *38*, 1257–1283.
(18) A. Schoedela, M. J. Zaworotko, *Chem. Sci.*, **2014**, *5*, 1269−1282.
(19) Y. Sasson, G. L. Rempel, *Can. J. Chem*., **1974**, *52*, 3825–3827.
(20) H. E. Toma, A. D. P. Alexiou, S. Dovidauskas, *Eur. J. Inorg. Chem.*, **2002**, 3010–3017.
(21) C. Bilgrien, S. Davis, R. S. Drago, *J. Am. Chem. Soc*., 1987, 109, 3786–3787.
(22) S. A. Fouda, B. C. Y. Hui, G. L. Rempel, *Inorg. Chem*., **1978**, *17*, 3213–3220.
(23) A. Altomare, G. Cascarano, C. Giacovazzo, A. Guagliardi, M. C. Burla, G. Polidori, M. Camalli, *J. Appl. Cryst.*, **1994**, *27*, 435.
(24) G. M. Sheldrick, *Acta. Cryst*., **1990**, *A46*, 467–473.
(25) S. Parkin, B. Moezzi, H. Hope, *J. Appl. Cryst*., **1995**, *28*, 53−56.
(26) M. Nardelli, *J. Appl. Cryst*., **1995**, *28*, 659.
(27) A. L. Spek, *Acta Cryst*., **2009**, *D65*, 148−155.
(28) M. Newville, *J. Synchrotron Rad*., **2001**, *8*, 322–324.
(29) B. Ravel, M. Newville, *J. Synchrotron Rad*., **2005**, *12*, 537–541.
(30) G. R. Desiraju, *Acc. Chem. Res*., **1991**, *24*, 290–296.
(31) G. R. Desiraju, *Acc. Chem. Res*., **1996**, *29*, 441–449.
(32) V. A. Blatov, A. P. Shevchenko, D. M. Proserpio, *Cryst. Growth Des*., **2014**, *14*, 3576−3586.
(33) T. Sato, F. Ambe, *Acta Cryst*., **1996**, *C52*, 3005−3007.
(34) T. Sato, F. Ambe, K. Endo, M. Katada, H. Maeda, T. Nakamoto, H. Sano, *J. Am. Chem. Soc*., **1996**, *118*, 3450–3458.
(35) Y.-K. Lv, Y.-L. Feng, L.-H. Gan, M.-X. Liu, L. Xu, H.-W. Zheng, J. Li, *J. Solid State Chem*., **2012**, *185*, 198–205.
(36) J. Overgaard, F. K. Larsen, B. Schiøtt, B. B. Iversen, *J. Am. Chem. Soc*., **2003**, *125*, 11088–11099.
(37) A. E. Tapper, J. R. Long, R. J. Staples, P. Stavropoulos, *Angew. Chem., Int. Ed*., **2000**, *39*, 2343–2346.
(38) M. Manago, S. Hayami, Y. Yano, K. Inoue, R. Nakata, A. Ishida, Y. Maeda, *Bull. Chem. Soc, Jpn*., **1999**, *72*, 2229–2234.
(39) A. S. Wills, *VaList*, Program available from www.ccp14.ac.uk
(40) B. C. Bunker, R. S. Drago, D. N. Hendrickson, R. M. Richman, S. L. Kessell, *J. Am. Chem. Soc*., **1978**, *100*, 3805–3814.
(41) R. Lomoth, A. Magnuson, Y. Xu, L. Sun, *J. Phys. Chem. A*, **2003**, *107*, 4373–4380.
(42) D. Kumbhakar, B. Sarkar, F. A. Urbanos, S. Maji, R. Jiménez-Aparicio, S. M. Mobin, W. Kaim, G. K. Lahiri, *J. Am. Chem. Soc*., **2008**, *130*, 17575–17583.

(43) J. G. Norman, G. E. Renzoni, D. A. Case, *J. Am. Chem. Soc*., **1979**, *101*, 5256–5267.
(44) J. A. Baumann, D. J. Salmon, S. T. Wilson, T. J. Meyer, W. E. Hatfield, *Inorg. Chem*., **1978**, *17*, 3342−3350.
(45) G. Socrates, In *Infrared and Raman Characteristic Group Frequencies*, John Wiley & Sons, LTD, 2001.
(46) K. Nakamoto, In *Infrared and Raman Spectra of Inorganic and Coordination Compounds*; Part B: Applications in Coordination, Organometallic, and Bioinorganic Chemistry, John Wiley & Sons, LTD, 2009.
(47) T. J. Ahmed, S. M. M. Knapp, D.R. Tyler, *Coord. Chem. Rev*., **2011**, *255*, 949–974.
(48) R. García-Álvarez, J. Díez, P. Crochet, V. Cadierno, *Organometallics*, **2010**, *29*, 3955–3965.
(49) R. García-Álvarez, J. Díez, P. Crochet, V. Cadierno, *Organometallics*, **2011**, *30*, 5442–5451.
(50) R. García-Álvarez, P. Crochet, V. Cadierno, *Green Chem*., **2013**, *15*, 46−66.
(51) C. Morrill, R. H. Grubbs, *J. Am. Chem. Soc*., **2005**, *127*, 2842–2843.
(52) B. M. Trost, R. J. Kulawiec, *J. Am. Chem. Soc*., **1993**, *115*, 2027–2036.
(53) V. Cadierno, P. Crochet, J. Gimeno, *Synlett*, **2008**, *8*, 1105−1124.
(54) P. Lorenzo-Luis, A. Romerosa, M. Serrano-Ruiz, *ACS Catal.*, **2012**, *2*, 1079–1086.
(55) K. P. Peterson, R. C. Larock, *J. Org. Chem*., **1998**, *63*, 3185–3189.

SUPPORTING INFORMATION

Mixed-Valence μ-Oxo-Bridged Triruthenium Acetate Cluster $[Ru_3^{(II,III,III)}O(CH_3CO_2)_6(H_2O)_3]\cdot 2H_2O$: Synthesis, Structure, Characterization, Valence-State Delocalization and Catalytic Behavior

Alla Dikhtiarenko, Sergei Khainakov, José R. García and José Gimeno

Departamento de Química Orgánica e Inorgánica, Universidad de Oviedo – CINN, 33006 Oviedo, Spain

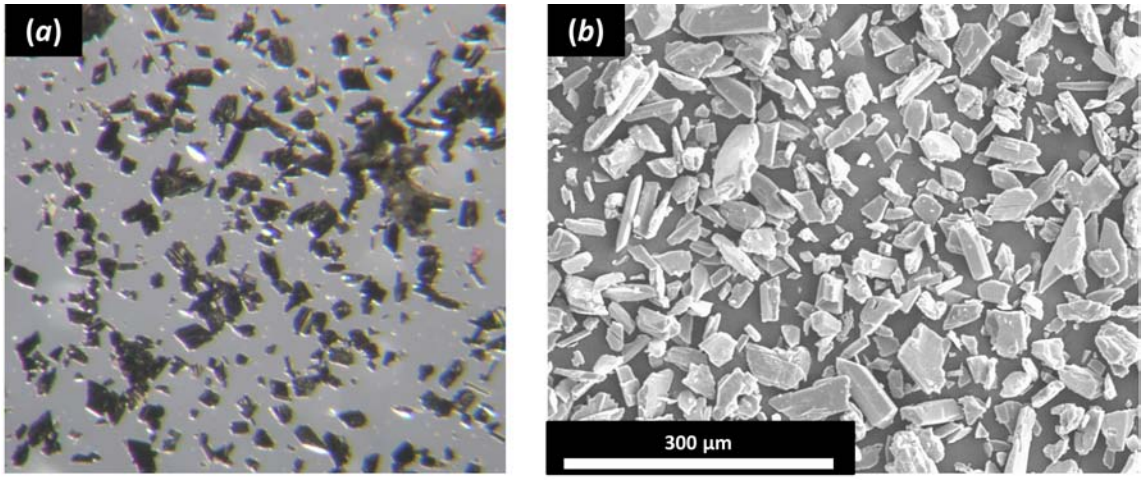

Figure S1. (a) Digital photographs and (b) SEM image showing the crystal habits of **2**.

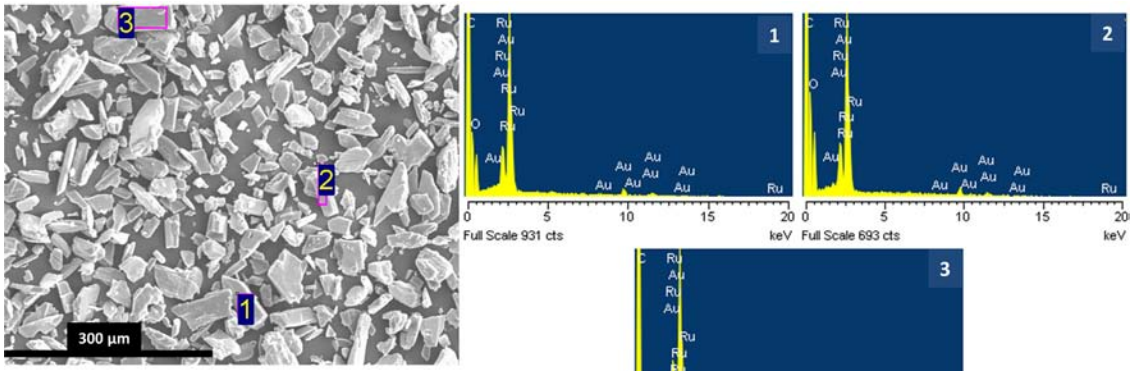

Elemental analysis based on atomic %

Spectrum	C	O	Ru
1	23.86	54.41	8.11
2	28.38	54.51	9.05
3	23.42	57.50	10.08

Figure S2. Results of elemental analysis of **2** performed using INCA Energy-200 dispersive X-ray microanalysis system (EDX) coupled with JEOL JSM-6100 scanning microscope (SEM).

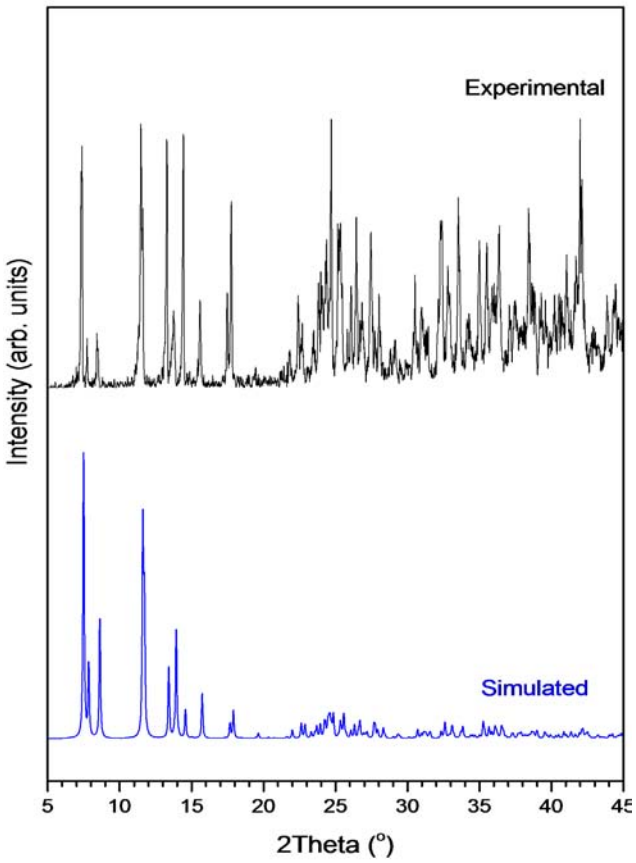

Figure S3. Experimental (black) and theoretical (blue) powder X-Ray diffraction patterns for acetate oxo-cluster **2**. The differences of relative intensities at higher 2θ attributed to the sample's packing effects and diffractometer scan mode.

Table S1. Selected Ru–O bond lengths for ruthenium coordination environments in compound **2** at 100 and 293 K

Bonds	**293 K**	**100 K**
Ru1—O1	1.905 (6)	1.890 (16)
Ru1—O7	2.025 (7)	1.99 (2)
Ru1—O2	2.027 (8)	2.03 (2)
Ru1—O4	2.053 (7)	2.014 (17)
Ru1—O9	2.054 (8)	2.076 (18)
Ru1—O16	2.125 (6)	2.120 (15)
Ru1—O(*carbox*) average	**2.013(6)**	**2.008(5)**
Ru2—O1	1.875 (6)	1.894 (15)
Ru2—O12	2.021 (9)	2.03 (2)
Ru2—O3	2.033 (8)	2.05 (2)
Ru2—O5	2.042 (7)	1.989 (18)
Ru2—O11	2.048 (7)	2.04 (2)
Ru2—O14	2.128 (7)	2.110 (17)
Ru2—O(*carbox*) average	**2.004 (7)**	**2.000(6)**
Ru3—O1	1.931 (15)	1.946 (6)
Ru3—O15	1.999 (8)	2.05 (2)
Ru3—O13	2.027 (8)	2.038 (18)
Ru3—O6	2.033 (8)	2.06 (2)
Ru3—O10	2.044 (7)	2.011 (19)
Ru3—O8	2.048 (8)	2.034 (17)
Ru3—O(*carbox*) average	**2.020(4)**	**2.007(7)**

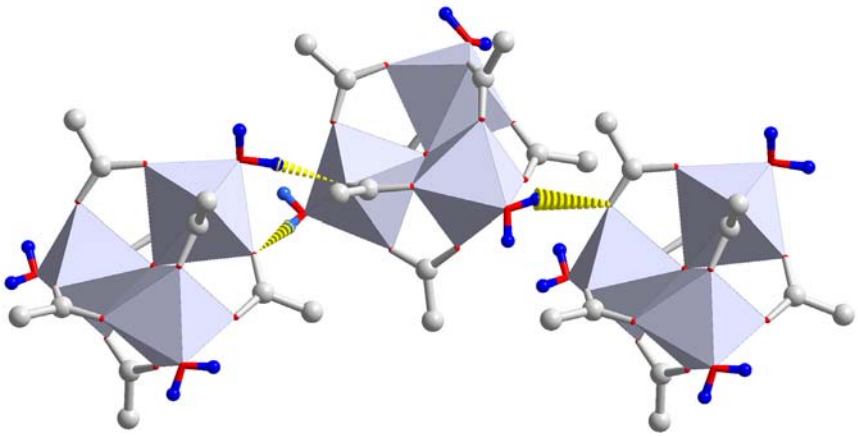

Figure S4. The hydrogen bonding interactions formed between coordinated water molecules of three adjecent cluster of 2. Hydrogen bonds are depicted as yellow doted line. C atoms are grey, H of coordinated water are blue. The methyl hydrogens were omitted.

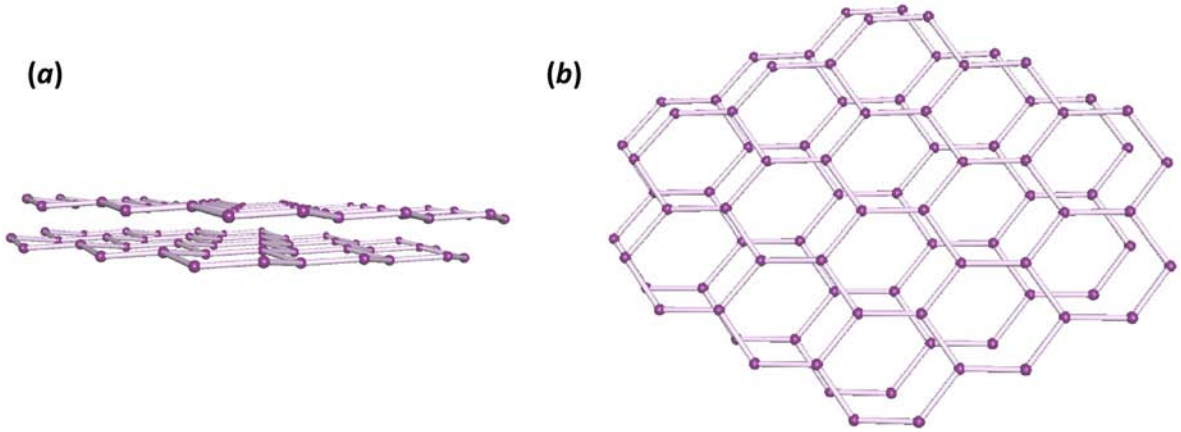

Figure S5. Simplified topological representation of crystal packing in **2** stabilizad througth hydrogen bonds between individual $[Ru_3O(CH_3CO_2)_6(H_2O)_3]$ complexes. (a) View of 2D layer staking and (b) ***hcb***-layer topology. Circles represent $[Ru_3O(CH_3CO_2)_6(H_2O)_3]$ individual complex and stiks are hydrogen bonds.

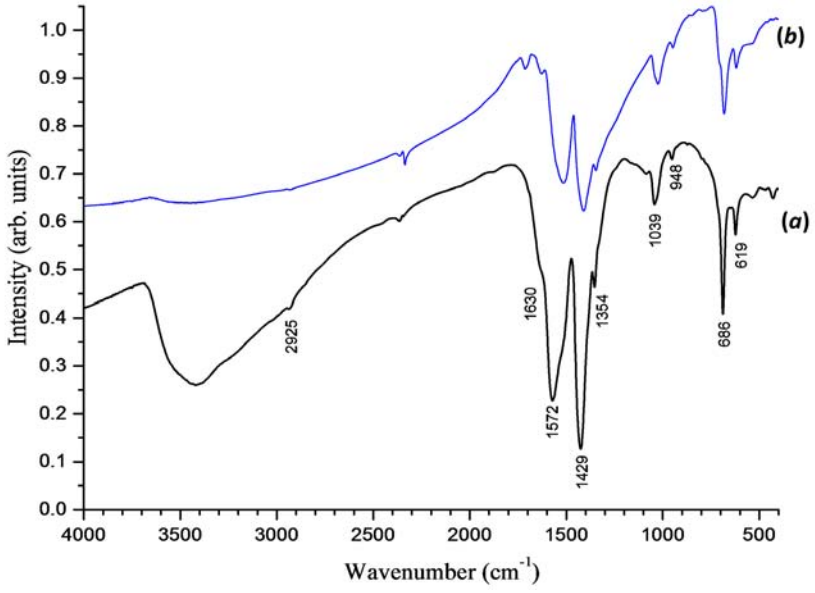

Figure S6. Infrered spectra of ruthenium oxo-cluster **2** before (a) and after (b) heating at 140 °C under vacuum during 3 hours.

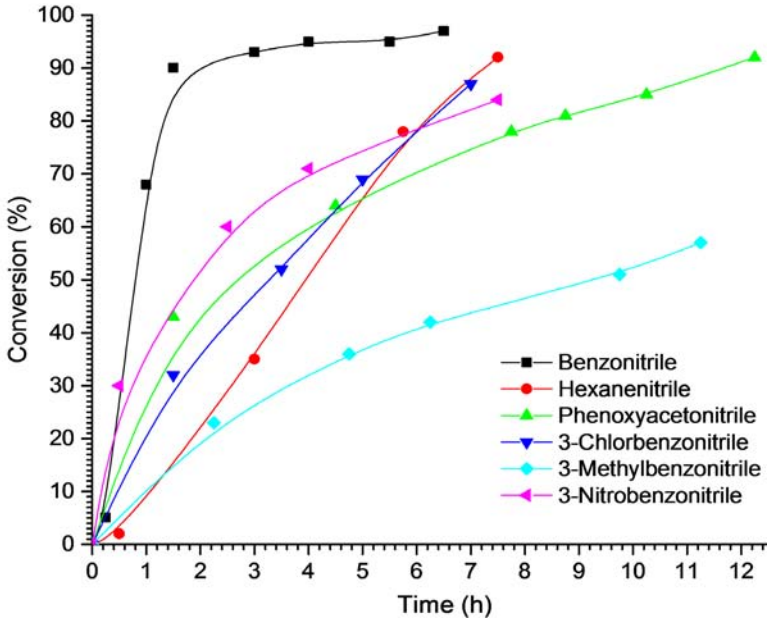

Figure S7. Kinetic plots of catalytic performance of complex 2 in hydration of nitriles with substituents of different nature: benzonitrile (black), hexanenitrile (red), phenoxyacetonitrile (green), 3-chlorobenzonitrile (blue), 3-methylbenzonitrile (light blue) and 3-nitrobenzonitrile (pink).

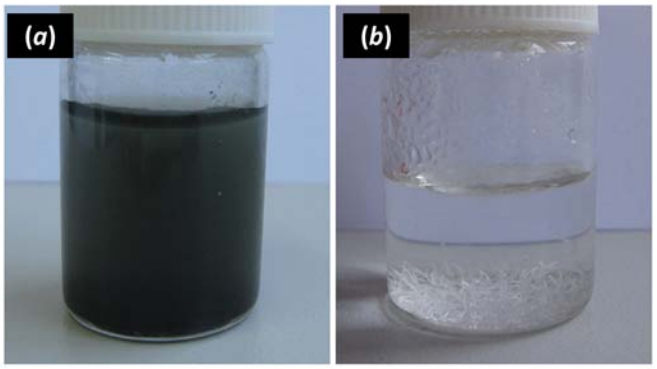

Figure S8. Hydration of benzonitrile to benzamide using trinuclear ruthenium-oxo complex **2**: (a) homogeneous catalyst solution before the reaction; (b) benzamide crystals separated after cooling and decanting the aqueous reaction solution containing **2**.

Capítulo VII

Polímeros de Coordinación Heterometálicos 2D Basados en Unidades $[Ru(C_2O_4)_3]^{3-}$ como Catalizadores Heterogéneos

El *Capítulo VII* se dedica a la preparación y caracterización estructural de polímeros de coordinación bidimensional de formula general $\{[K(18\text{-crown-}6)]_3[M^{II}_3(H_2O)_4[Ru(ox)_3]_3]\}_n$ (donde M^{II} = Mn, Fe, Co, Cu y Zn; ox = $C_2O_4^{2-}$), así como a sus propiedades catalíticas y magnéticas.

La química de los polímeros de coordinación (*PCs*) se ha desarrollado enormemente en las últimas décadas debido especialmente a las numerosas aplicaciones de estos nuevos materiales, incluyendo almacenamiento de gases y procesos de separación,[1] sensores,[2] catalizadores heterogéneos,[3] etc. La presencia potencial de enlaces de coordinación muy diversos y una amplia variedad de metales ha conducido a la preparación de múltiples y versátiles carcasas poliméricas. Un especial interés se ha focalizado en la síntesis de polímeros de coordinación heterometálicos a través de la utilización de metaloligandos que, actuando como enlazadores entre metales diferentes, llevan a la preparación de materiales con múltiples y diferentes centros de coordinación. La posibilidad de utilizar ligandos estructuralmente flexibles amplia el interés en este campo, puesto que se pueden generar redes poliméricas con geometrías diversas conduciendo al diseño de redes heterometálicas de propiedades únicas.

Un ejemplo particularmente bien descrito en la bibliografía, es el uso de metaloligandos del tipo $[M^{III}(ox)_3]^{3-}$ en la preparación de familias de polímeros de coordinación de fórmula general $\{[A][M^{II}M^{III}(ox)_3]\}_n$ (M^{II} = Mn, Fe, Co, Ni, Cu, Zn; M^{III} = Cr, Fe, V; A = XR_4^+; X = N, P, As, y R = *n*-C_2H_5, *n*-C_4H_9, *n*-C_3H_7, *n*-C_5H_{11}, C_6H_5, $C_6H_5CH_2$, $[(C_6H_5)_3PNP(C_6H_5)_3)]_{0.25}$ o $[K(18\text{-crown-}6)]^+$).[4–18] La red polimérica resultante es bidimensional, consecuencia de la coordinación de los cationes divalentes (M^{II}) por metaloligandos $[M^{III}(ox)_3]^{3-}$, mientras los monocationes orgánicos garantizan la neutralidad de la estructura polimérica global. Además de la función huésped, las plantillas catiónicas moleculares actúan como agentes directores estructurales, siendo determinantes en la formación de redes bidimensionales, como en este caso, o de dimensionalidad superior. Los compuestos basados en unidades poliméricas $\{[A][M^{II}M^{III}(ox)_3]\}_n$ han sido objeto de gran interés como sistemas magnéticos, ya que sus propiedades pueden ser moduladas en función de su composición, a causa de la variedad de metales de transición que pueden ser incorporados a su red cristalina.

(1) M. P. Suh, H. J. Park, T. K. Prasad, D.-W. Lim, *Chem. Rev*., **2012**, *112*, 782−835.
(2) Z. Hu, B. J. Deiberta, J. Li, *Chem. Soc. Rev*., **2014**, *43*, 5815–5840.
(3) A. Corma, H. García, F. X. Llabrés i Xamena, *Chem. Rev*., **2010**, *110*, 4606–4655.
(4) E. Coronado, J. R. Galán-Mascarós, C. Martí-Gastaldo, J. C. Waerenborgh, P. Gaczyński, *Inorg. Chem*., **2008**, *47*, 6829−6839.
(5) E. Coronado, J. R. Galán-Mascarós, C. Martí-Gastaldo, *Inorg. Chem*., **2006**, *45*, 1882−1884.
(6) R. Andrés, M. Gruselle, B Malézieux, M. Verdaguer, J. Vaissermann, *Inorg. Chem*., **1999**, *38*, 4637−4646.
(7) E. Coronado, J. R. Galán-Mascarós, C. Martí-Gastaldo, *J. Am. Chem. Soc*., **2010**, *132*, 5456−5468.
(8) E. Coronado, J. R. Galán-Mascarós, C. Martí-Gastaldo, *J. Am. Chem. Soc*., **2008**, *130*, 14987−14989.
(9) E. Coronado, J. R. Galán-Mascarós, C. J. Gómez-García, C. Martí-Gastaldo, *Inorg. Chem.*, **2005**, *44*, 6197−6202.
(10) Coronado, J. R. Galán-Mascarós, C. Martí-Gastaldo, *Inorg. Chem*., **2007**, *46*, 8108−8110.
(11) E. Coronado, J. R. Galán-Mascarós, C. Martí-Gastaldo, *Inorg. Chim. Acta*, **2008**, *361*, 4017−4023.
(12) E. Coronado, J. R. Galán-Mascarós, C. Martí-Gastaldo, *Polyhedron*, **2007**, *26*, 2101−2104.
(13) E. Coronado, J. R. Galán-Mascarós, C. Martí-Gastaldo, *J. Mater. Chem*., **2006**, *16*, 2685−2689.
(14) C. Mathonière, K. J. Nuttall, S. G. Carling, P. Day, *Inorg. Chem*., **1996**, *35*, 1201−1206.
(15) H. Tamaki, Z. J. Zhong, N. Matsumoto, S. Kida, M. Koikawa, N. Achiwa, Y. Hashimoto, H. Okawa, *J. Am. Chem. Soc.*, **1992**, *114*, 6974−6979.
(16) K. S. Min, A. L. Rhinegold, J. S. Miller, *Inorg. Chem*. **2005**, *44*, 8433−8441.
(17) N. S. Ovenesyan, V. D. Makhaev, S. M. Aldoshin, P. Gredin, K. Boubekeur, C. Train, M. Gruselle, *Dalton Trans*., **2005**, 3101−3107.
(18) S. Decurtins, H. W. Schmalle, H. R. Oswald, A. Linden, J. Ensling, P. Gutlich, A. Hauser, *Inorg. Chim. Acta*, **1994**, *216*, 65–73.

La química versátil, la actividad catalítica, y las propiedades magnéticas, características de los compuestos de rutenio, unido al hecho de que solamente había sido descrita una familia de polímeros de coordinación heterometálicos de este metal, $\{[M^{III}Cp_2][M^{II}Ru^{III}(ox)_3]\}_n$ (M^{III} = Co, Fe; M^{II} = Mn, Fe, Co, Cu, Zn; Cp = C_5Me_5) y $\{[NBu_4][M^{II}Ru^{III}(ox)_3]\}_n$ (M^{II} = Mn, Fe, Cu),[19,20] hizo que se planificase la síntesis de los compuestos de fórmula $\{[K(18\text{-crown-}6)]_3[M^{II}_3(H_2O)_4[Ru(ox)_3]_3]\}_n$ (M^{II} = Mn, Fe, Co, Cu, Zn; ox = $C_2O_4^{2-}$). Así, la *Publicación V*, que se presenta como parte del contenido de esta Tesis, describe la síntesis, caracterización y las propiedades magnéticas y catalíticas de esta nueva serie de polímeros de coordinación bidimensionales basados en unidades de complejos octaédricos $[Ru^{III}(ox)_3]^{3-}$.

La síntesis de estos *PCs* se llevó a cabo mediante auto-ensamblaje del metaloligando $[Ru(ox)_3]^{3-}$ y la sal inorgánica del metal de transición divalente en medio acuoso a temperatura ambiente. Todos los compuestos de la serie fueron aislados como muestras microcristalinas y su estructura cristalina fue refinada aplicando el método Rietveld presentando, sin excepción, simetría monoclínica (grupo espacial *C*2/c) con valores de parámetros de celda que varían ligeramente como una función del metal de transición incorporado en la red polimérica. La estructura cristalina de cada miembro de esta serie puede describirse partiendo de la plantilla molecular catiónica, $[K(18\text{-crown-}6)]^+$, que se localiza en el espacio interlaminar de la red polimérica aniónica, $\{[M^{II}_3(H_2O)_4[Ru(ox)_3]_3]^-\}_n$, que se construye alternando poliedros octaédricos, $\{M^{II}O_6\}$ y $\{RuO_6\}$, enlazados mediante ligandos oxalato con tres modos de coordinación diferentes, dos de los cuales aparecen en el entorno del metal divalente (M^{II}). Considerando la existencia en la red polimérica tanto de enlaces covalentes como de enlaces de hidrógeno, y dado que cada centro metálico muestra una conectividad similar, la lámina bidimensional aniónica, $\{[M^{II}_3(H_2O)_4[Ru(ox)_3]_3]^-\}_n$, presenta una topología tipo "panal de abeja", caracterizada por el símbolo 6^3 de Schläfli.

Todos los compuestos que forman parte de la familia descrita en este Capítulo, presentan alta estabilidad térmica tanto en atmósfera reactiva (aire) como inerte (nitrógeno). En general, los datos de análisis termogravimétrico indican que la degradación térmica de cada miembro de la serie procede en tres etapas diferenciadas. Previamente a su degradación, los compuestos de esta serie sufren dos cambios estructurales que acompañan al proceso de deshidratación. Mediante estudios de termodifracción de rayos-X de muestras policristalinas, fue posible identificar la transición del compuesto $\{[K(18\text{-crown-}6)]_3[Mn_3(H_2O)_4[Ru(ox)_3]_3]\}_n$ hacia una fase parcialmente hidratada, $\{[K(18\text{-crown-}6)]_3[Mn_3(H_2O)_2[Ru(ox)_3]_3]\}_n$, previamente a la formación de la fase anhidra $\{[K(18\text{-crown-}6)]_3[Mn_3[Ru(ox)_3]_3]\}_n$.

El conocimiento de los cambios estructurales relacionados con procesos de deshidratación puede ser relevante en la comprensión del comportamiento catalítico de estos materiales ya que, en polímeros de coordinación, la liberación de las moléculas de disolvente coordinadas al centro metálico, con generación de vacantes de coordinación en el metal, será determinante para su capacidad de interacción con el substrato. Un camino para alcanzar este objetivo es la activación térmica. Un ejemplo relevante de esta estrategia corresponde al polímero de coordinación $Cu_3(BTC)_2$ (BTC = ácido 1,3,5-benzenetricarboxílico), conocido como HKUST-1, que se consigue por tratamiento térmico al expulsar, reversiblemente, moléculas de

(19) E. Coronado, R. J. Galán-Mascarós, C. J. Gómez-García, J. M. Martínez-Agudo, E. Martínez-Ferrero, J. C. Waerenborgh, M. Almeida, *J. Solid State Chem.*, **2001**, *159*, 391−402.

(20) J. Larionova, B. Mombelli, J. Sanchiz, O. Kahn, *Inorg. Chem.*, **1998**, *37*, 679−684.

agua de coordinación, originando sitios vacantes en el centro metálico[21,22] que, actuando como ácidos de Lewis, catalizan la cianosililación del benzaldehído a acetona.[23] Algo semejante sucede en el MIL-101, $[Cr_3F(H_2O)_2O(BDC)_3]$, donde la activación térmica consigue que los sitios de Cr(III) sean aún más activos en la reacción de la cianosililación del benzaldehído que los del HKUST-1.[24] Otro ejemplo es la reacción de cianosililación de aldehídos aromáticos catalizada por centros ácidos de Lewis, utilizando $Mn_3[(Mn_4Cl)_3BTT_8(CH_3OH)_{10}]_2$ (BTT=1,3,5-benzenetris(tetrazol-5-il)) como catalizador heterogéneo, cuya estructura porosa tridimensional, con dos sitios Mn(II) activos en zonas estructuralmente bien diferenciadas, hace que este material presente actividad catalítica selectiva en función del tamaño y la forma del substrato.[25]

Las fases hidratada, parcialmente hidratada y anhidra se evaluaron como catalizadores heterogéneos en la reacción de acetalización del benzaldehído Las fases hidratadas mostraron altos rendimientos con actividades diferentes en función del metal divalente (M^{II}) que las constituye. La actividad más elevada correspondió al compuesto $\{[K(18\text{-crown-}6)]_3[Cu_3(H_2O)_4[Ru(ox)_3]_3]\}_n$, donde se observó una conversión del 96% después de 24 h de reacción. Cabe resaltar que la actividad catalítica es mayor que las descritas en la bibliografía para polímeros de coordinación 2D y 3D, con la posibilidad de ser recuperados y reusados en posteriores transformaciones En la serie de compuestos anhidros, $\{[K(18\text{-crown-}6)]_3[M^{II}_3[Ru(ox)_3]_3]\}_n$, la actividad catalítica aumenta, alcanzando un máximo de conversión del 98% en 24 h para el compuesto $\{[K(18\text{-crown-}6)]_3[Cu_3[Ru(ox)_3]_3]\}_n$. La compilación de todos los datos experimentales indica que la actividad catalítica de esta familia de compuestos, tanto hidratados como anhidros, es una función del catión metálico divalente contenido en la estructura cristalina de la fase catalítica, actuando como ácido de Lewis y siguiendo el orden $Mn^{2+} < Fe^{2+} < Co^{2+} < Ni^{2+} < Cu^{2+} > Zn^{2+}$ en una secuencia similar a la serie de Irving-Williams de estabilidad de compuestos de coordinación.

(21) L. Alaerts, E. Seguin, H. Poelman, F. Thibault-Starzyk, P. A. Jacobs, D. E. De Vos, *Chem.-Eur. J.*, **2006**, *12*, 7353–7363.
(22) C. Prestipino, L. Regli, J. G. Vitillo, F. Bonino, A. Damin, C. Lamberti, A. Zecchina, P. L. Solari, K. O. Kongshaug, S. Bordiga, *Chem. Mater.*, **2006**, *18*, 1337–1346.
(23) K. Schlichte, T. Kratzke, S. Kaskel, *Microporous Mesoporous Mater.*, **2004**, *73*, 81–88.
(24) A. Henschel, K. Gedrich, R. Kraehnert, S. Kaskel, *Chem. Commun.*, **2008**, 4192–4194.
(25) S. Horike, M. Dinca, K. Tamaki, J. R. Long, *J. Am. Chem. Soc.*, **2008**, *130*, 5854–5855.

Publication V

"Series of 2D Heterometallic Coordination Polymers Based on Ruthenium(III) Oxalate Building Units: Synthesis, Structure, and Catalytic and Magnetic Properties"

Inorganic Chemistry

52 (3933–3941)

Year ***2013***

DOI: *dx.doi.org/10.1021/ic302725v*

Impact Factor: 4.794

Inorganic Chemistry

Article

pubs.acs.org/IC

Series of 2D Heterometallic Coordination Polymers Based on Ruthenium(III) Oxalate Building Units: Synthesis, Structure, and Catalytic and Magnetic Properties

Alla Dikhtiarenko,[†] Sergei A. Khainakov,[†] Imanol de Pedro,[‡] Jesús A. Blanco,[§] José R. García,*[,†] and José Gimeno[†]

[†]Departamento de Química Orgánica e Inorgánica, Universidad de Oviedo—CINN, 33006 Oviedo, Spain

[‡]CITIMAC, Facultad de Ciencias, Universidad de Cantabria, Avenida de los Castros 39005 Santander, Spain

[§]Departamento de Física, Universidad de Oviedo—CINN, 33007 Oviedo, Spain

Supporting Information

ABSTRACT: A series of 2D ruthenium-based coordination polymers with hcb-hexagonal topology, $\{[K(18\text{-crown-}6)]_3[M^{II}_3(H_2O)_4\{Ru(ox)_3\}_3]\}_n$ (M^{II} = Mn (**1**), Fe (**2**), Co (**3**), Cu (**4**), Zn (**5**)), has been synthesized through self-assembly reaction. All compounds are isostructural frameworks that crystallize in the monoclinic space group *C*2/*c*. The crystal packing consists of a 2D honeycomb-like anionic mixed-metal framework intercalated by $[K(18\text{-crown-}6)]^+$ cationic template. Dehydration processes take place in the range 40−200 °C exhibiting two phase transitions. However, the spontaneous rehydration occurs at room temperature. Both hydrated and dehydrated compounds were tested as Lewis acids heterogeneous catalysts in the acetalyzation of benzaldehyde achieving high yields with the possibility to be recovered and reused. All the investigated materials do not show any long-range magnetic ordering down to 2 K. However, the Fe-based compound **2** presents a magnetic irreversibility in the ZFC-FC magnetization data below 5 K, which suggest a spin-glass-like behavior, characterized also by short-range ferromagnetic correlations. The coercive field increases as the temperature is lowered below 5 K, reaching a value of 1 kOe at 2 K. Alternating current measurements obtained at different frequencies confirm the freezing process that shows weak frequency dependence, being characteristic of a system exhibiting competing magnetic interactions.

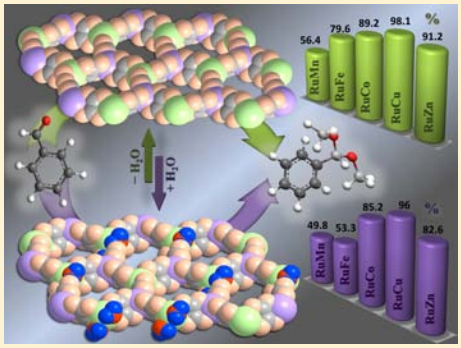

INTRODUCTION

During the past decade, synthesis and studies of coordination polymers (CPs) have received considerable attention[1] because of their widely functional properties including catalysis,[2] ion-exchange,[3] gas storage and separation,[4] luminescence,[5] and magnetic behaviors.[6] Among them, heterometallic coordination polymers (HCPs) formed by building blocks with different chemical nature are particularly interesting due to their diverse functionality. The building blocks used in the synthesis of heterometallic polymers are known as metalloligands. Contrary to organic ligands, metalloligands act as bridging ligands incorporating several advantages: multicoordination sites, flexible geometric control, and the ability to assemble a discrete unit into a polymeric frame giving rise to polymeric heterometallic frameworks with appealing structural and/or physicochemical properties.[1a]

One of the most successful strategies for preparing functional heterometallic coordination polymers is the self-assembly of polyhedral coordination-donor building blocks with a second metal center/metalloligand unit which provides additional coordination sites. Most of the reported investigations have been devoted to HCPs containing d−f[7] or d−d[8] metal centers. The d−d polynuclear compounds have been found to exhibit interesting magnetic properties varying from paramagnetic to ferromagnetic or antiferromagnetic behaviors. The most striking examples belong to the family of oxalate (ox) bridged mixed-metal coordination polymers of general formula $A[M^{II}M^{III}(ox)_3]_n$ [M^{II} = Mn, Fe, Co, Ni, Cu, Zn; M^{III} = Cr, Fe, V, Mn; A = XR_4 (X = N, P, As; R = *n*-C_2H_5, *n*-C_4H_9, *n*-C_3H_7, *n*-C_5H_{11}, C_6H_5, $C_6H_5CH_2$, $[(C_6H_5)_3PNP(C_6H_5)_3)]_{0.25}$ or $[K(18\text{-crown-}6)]^+$ cationic metal-complex)][9,10] in which the oxalate dianion acts as a bridging ligand forming extended networks of either 2D or 3D dimensionalities.[11] In these compounds, the extended anionic bimetallic network $[M^{II}M^{III}(ox)_3]_n$ combined with a molecular bulky cation (A) which acts as a sort of template controlling the type of the resulting structure. In particular, the 2D network series displays honeycomb-like layer topology built by octahedral M^{II} and M^{III} geometries and tris-chelate oxalate sites in which the oxalate ligand is shown to be a useful tool in the spatial arrangement of spin-carrying metal ions.[12] These layered structures may provide structural and chemical versatility as can be shown by magnetic properties which are tuned by changing the electronic nature of interlayer

Received: December 11, 2012
Published: March 11, 2013

Table 1. Crystallographic Data for Compounds 1−5

	1	2	3	4	5
empirical formula	$C_{54}H_{80}K_3Mn_3O_{58}Ru_3$	$C_{54}Fe_3H_{80}K_3O_{58}Ru_3$	$C_{54}Co_3H_{80}K_3O_{58}Ru_3$	$C_{54}Cu_3H_{80}K_3O_{58}Ru_3$	$C_{54}H_{80}K_3O_{58}Ru_3Zn_3$
fw	2242.51	2244.33	2254.48	2268.34	2273.86
cryst syst	monoclinic	monoclinic	monoclinic	monoclinic	monoclinic
space group	*C*2/*c*	*C*2/*c*	*C*2/*c*	*C*2/*c*	*C*2/*c*
a, Å	26.896(4)	26.620(3)	26.539(9)	26.547(5)	26.593(7)
b, Å	19.840(3)	19.908(3)	20.025(7)	19.279(4)	19.230(7)
c, Å	18.129(2)	18.009(2)	18.036(6)	17.995(3)	18.192(5)
β, deg	115.8(6)	115.3(5)	115.3(1)	113.8(1)	114.1(1)
V, Å^3	8710(2)	8625(2)	8664(5)	8425(3)	8495(4)
Z	4	4	4	4	4
ρ_{calcd}, g cm^{-3}	1.710	1.728	1.728	1.788	1.778
T, K	298	298	298	298	298
R_p, R_{wp}	4.56, 5.97	3.25, 4.30	2.66, 3.65	4.12, 5.25	6.32, 8.03
R_B	7.65	10.2	8.81	8.12	7.86

and network components. On the basis of this particular behavior, this family of compounds may be taken as illustrative examples to attain desirable functional properties. In spite of the versatile coordination chemistry, catalytic properties, and magnetic behavior of ruthenium complexes,[13] to date only two examples of oxalate bridged HCPs of general formula $[M^{III}Cp_2][M^{II}Ru^{III}(ox)_3]_n$ (M^{III} = Co, Fe; M^{II} = Mn, Fe, Co, Cu, Zn; Cp = pantamethylcyclopentadienyl) and $[NBu_4]$-$[M^{II}Ru^{III}(ox)_3]_n$ (M^{II} = Mn, Fe, Cu) containing $[Ru(ox)_3]^{3-}$ building units have been reported.[14] Therefore, inspired by potential magnetic properties of $[M^{II}Ru^{III}(ox)_3]_n$ mixed-metal frameworks and attractive catalytic features of ruthenium complexes,[15] our investigation has been focused on the rational structural and functional design of $Ru(ox)_3$-based heterometallic coordination polymers.

Herein, we report the synthesis and structural characterization of the 2D series of $\{[(K\text{-}18\text{-}crown\text{-}6)_3][M_3^{II}(H_2O)_4(Ru(ox)_3)_3]\}_n$ (M^{II} = Fe, Co, Cu, Mn, Zn; ox = C_2O_4) heterometallic coordination polymers resulting from self-assembling reaction of the $[Ru(ox)_3]^{3-}$ salt, acting as metalloligand, with corresponding transition metal ions. Also, their thermal, catalytic, and magnetic behaviors have been discussed. The dehydrated compounds $\{[(K\text{-}18\text{-}crown\text{-}6)][M^{II}(Ru(ox)_3]\}_n$ (M^{II} = Fe, Co, Cu, Mn, Zn) have been isolated and characterized exhibiting reversible rehydration process and high catalytic activity in Lewis acid promoted reaction.

EXPERIMENTAL SECTION

Materials and Methods. All reagents and solvents used were of commercially available grade and were used without any previous purification. $K_3[Ru(ox)_3]\cdot 4.5H_2O$ was prepared according to a previously described method.[16]

The IR spectra were recorded on a Bruker Tensor-27 spectrophotometer as KBr pellets in the 4000−400 cm^{-1} region. Microanalyses (C, H, N) were completed by the use of a Perkin-Elmer model 2400B elemental analyzer. The microcrystalline texture of samples and metal contents were confirmed by using a JEOL JSM-6100 scanning microscopy (SEM) coupled with an INCA Energy-200 dispersive X-ray microanalysis system (EDX), and a PentaFET ultrathin window detector. Mettler-Toledo TGA/SDTA851 and DSC822 were used for the thermal analyses in nitrogen (or air) dynamic atmosphere (50 mL/min) at a heating rate of 10 °C/min (approximately 10 mg of powder sample was thermally treated, and blank runs were performed). A Pfeiffer Vacuum TermoStar GSD301T mass spectrometer was used to determine the evacuated vapors. The masses 18 (H_2O) and 44 (CO_2) were tested by using a detector C-SEM, operating at 1200 V, with a time constant of 1 s.

Magnetic susceptibility measurements were performed in PPMS (QD-PPMS) and SQUID (QD-PMPMS-5T) magnetometers in the temperature range 2−250 K. For measurements of the magnetization in a zero-field cooled (ZFC) state, the sample was cooled from the paramagnetic state in a zero applied field, and the magnetization was measured while warming the sample. The magnetization data in the field cooled (FC) state were collected while cooling the sample. Several magnetization versus field ($M(H)$) isotherms in fields up to 85 kOe were measured at different temperatures, cooling the sample every time from the paramagnetic state to the temperature of the measurement. Alternating curent magnetic susceptibility measurements were made using the SQUID device, with an alternating excitation field (h) of 3 Oe. Data were recorded from 2 to 10 K as a function of frequency, between 10 and 10^3 Hz, in the absence of a dc applied field.

Synthesis of $\{[K(18\text{-}crown\text{-}6)]_3[M^{II}_3(H_2O)_4\{Ru(ox)_3\}_3]\}_n$ (M^{II} = Mn (1), Fe (2), Co (3), Cu (4), Zn (5)). The synthesis process was performed in accordance with a previously published procedure[10a,b] for the $\{[(K\text{-}18\text{-}crown\text{-}6)_3][M_3^{II}(H_2O)_4(M^{III}(ox)_3)_3]\}_n$ (M^{III} = Cr, Fe; M^{II} = Mn, Fe, Ni, Co, Cu; ox = C_2O_4) series of compounds introducing $[Ru(ox)_3]^{3-}$ moiety instead of $[Cr(ox)_3]^{3-}$ or $[Fe(ox)_3]^{3-}$. In a typical synthesis, 124 mg (0.25 mmol) of $K_3[Ru(ox)_3]\cdot 4.5H_2O$ and 198 mg (0.75 mmol) of 18-crown-6 ether were dissolved in 10 mL of methanol, and 0.25 mmol of the transition metal salt ($MnCl_2\cdot 4H_2O$, 50 mg; $FeCl_2\cdot 4H_2O$, 49 mg; $CoCl_2\cdot 6H_2O$, 54 mg; $CuCl_2$, 34 mg; $ZnCl_2$, 34 mg) dissolved in 5 mL of methanol was added dropwise, immediately a precipitates appeared, and the mixture was stirred for 30 min. The methanolic solutions were filtered in vacuum, and the precipitates were washed with methanol and air-dried. Yellow precipitate of **1** yields 77%. Anal. for $C_{54}H_{80}K_3Mn_3O_{58}Ru_3$ (**1**): C, 28.92%; H, 3.57%. Found: C, 28.91%; H, 3.54%. Green precipitate of **2** yields 79%. Anal. for $C_{54}Fe_3H_{80}K_3O_{58}Ru_3$ (**2**): C, 28.89%; H, 3.56%. Found: C, 28.93%; H, 3.78%. Brown precipitate of **3** yields 74%. Anal. for $C_{54}Co_3H_{80}K_3O_{58}Ru_3$ (**3**): C, 28.13%; H, 3.47%. Found: C, 27.53%; H, 3.61%. Orange precipitate of **4** yields 81%. Anal. for $C_{54}Cu_3H_{80}K_3O_{58}Ru_3$ (**4**): C, 27.99%; H, 3.47%. Found: C, 25.38%; H, 3.72%. Yellow precipitate of **5** yields 70%. Anal. for $C_{54}H_{80}K_3O_{58}Ru_3Zn_3$ (**5**): C, 27.93%; H, 3.45%. Found: C, 26.91%; H, 3.62%.

X-ray Diffraction Characterization. Powder X-ray diffraction patterns were recorded on X'pert Philips diffractometer with Cu K*α* radiation. The samples were gently ground in an agate mortar. All data were collected at room temperature over the angular 2*θ* range 5−142° with a step of 0.013° and a counting time of 0.424 s/channel. The initial structure model was constructed from unit cell parameters and fractional atomic coordinates taken from previous reported analogous Cr-based compound.[10a,b] Rietveld refinement was performed in the range 2*θ* = 7−50° using Reflex module of Materials Studio,[17] applying Motion Group sets. As the rigid groups of atoms have been composed, there are Ru, M^{II}, K atoms, 18-crown-6, and oxalate ligand fragments.

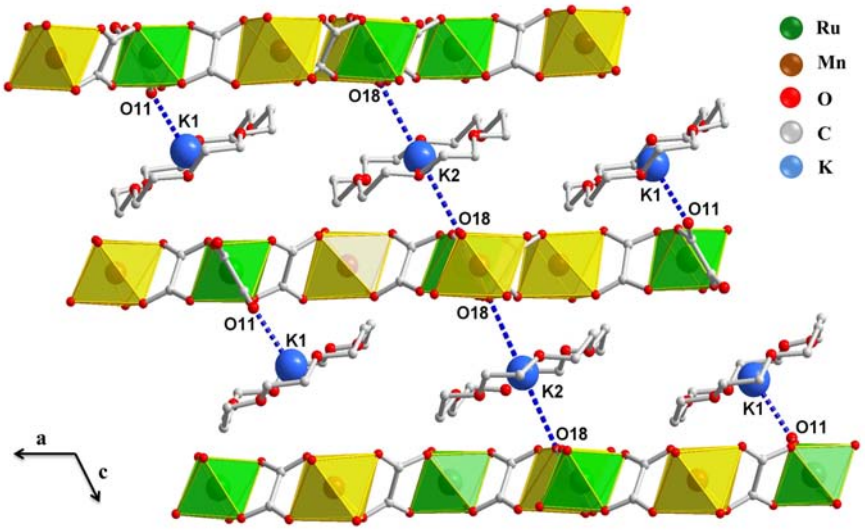

Figure 1. Perspective view along *b*-axis of heterometallic 2D layers and intercalated between them K(18-crown-6)$^+$ cations.

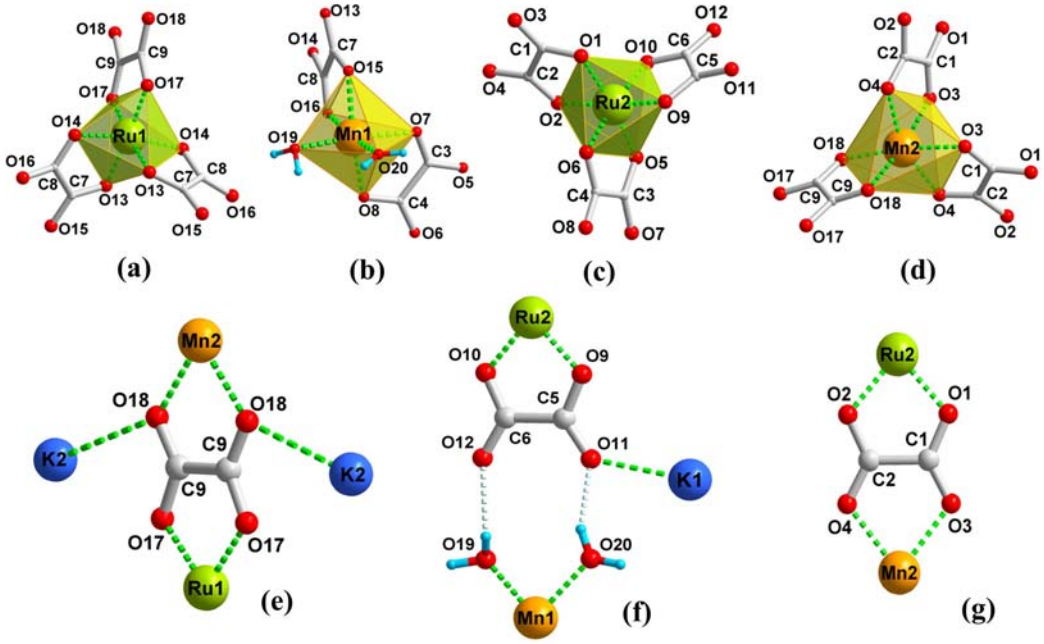

Figure 2. Coordination environments of Ru^{III} (a, c), Mn^{II} (b, d), and coordination modes of the oxalate ligand $\mu_4 = (\eta_2{:}\,\eta_1{:}\,\eta_2{:}\,\eta_1)$ (e), $\mu = (\eta_2{:}\,\eta_1)$ (f), and $\mu = (\eta_2{:}\,\eta_2)$ (g).

First, the zero offset, the scale factor, background terms, profile parameters, and the unit cell were refined. The profiles have been modeled as a pseudo-Voigt function. After that the atomic positions and global isotropic parameter were refined. In the final refinement the water molecules have been placed geometrically and fixed in this position. The unit cell parameters and the final values of figures of merit are listed in Table 1.

Powder X-ray thermodiffraction studies were performed in air with the sample placed in an Anton Paar XRK 900 reactor chamber on a Bruker D8 Advance diffractometer with DAVINCI design, using Cu Kα radiation, equipped with LynxEye detector. Each powder pattern was recorded in the 4−110° range of 2θ at intervals of 25 °C up to 195 °C and cooling down to 25 °C with a step of 0.015° and a counting time of 0.424 s/channel. The temperature ramp between two consecutive temperatures was 10 °C/min. The PXRD data acquisition and analysis in this work were carried out using Bruker AXS DIFFRAC.EVA software. The dehydrated **1a** and dehydrated **1b** compounds was indexed using DICVOL06 program.[18]

Catalytic Procedure of Benzaldehyde Acetalyzation with Trimethylorthoformate (TMOF). Under nitrogen atmosphere a benzaldehyde substrate (0.05 mL, 0.5 mmol) and TMOF (0.5 mL, 5 mmol) were added to a suspension of the corresponding catalyst (1 mol %) in 3 mL of tetrachloromethane used as a solvent. The reaction mixture was stirred in a 25 mL Schlenk tube at 70 °C in oil bath. The course of the reaction was monitored by regular sampling and analysis by GC-FID. After 24 h, the catalyst was isolated by centrifugation, washed, and reused on subsequent runs.

■ RESULTS AND DISCUSSION

The family of coordination polymers **1**−**5** has been isolated as microcrystalline powders with plate-like habits, as is shown from the micrograph analysis (Supporting Information, Figure

dx.doi.org/10.1021/ic302725v | *Inorg. Chem.* 2013, 52, 3933−3941

S1). Rietveld refinement shows the isostructurality of our synthesized materials between them and with the Cr- and Fe-based analogous series of compounds ($\{[K(18\text{-crown-}6)]_3[M^{II}_3(H_2O)_4\{M^{III}(ox)_3\}_3]\}_n$, where M^{III} = Cr, Fe; M^{II} = Mn, Fe, Ni, Co, and Cu) which was reported previously[10a,b] (see Figure S2). The layered heterometallic polymers with the general formula $\{[K(18\text{-crown-}6)]_3[M^{II}_3(H_2O)_4\{Ru(ox)_3\}_3]\}_n$, where M^{II} = Mn(**1**), Fe(**2**), Co(**3**), Cu(**4**), and Zn(**5**), crystallize in monoclinic space group $C2/c$. Details of crystallographic data are summarized in Table 1. The crystal cell parameters are slightly changed as function of M^{II} transition ion incorporated in coordination network. The remarkable aspect of these structures is the packing arrangement where the positive potassium complex $[K(18\text{-crown-}6)]^+$ is intercalated between the negative 2D sheets (see Figure 1). Herein, only the structure of compound **1** is described in detail. The asymmetric unit of **1** contains three pairs of crystallographically independent metal centers (Mn1 and Mn2, Ru1 and Ru2, K1 and K2): (i) Ru1 and Ru2 are six coordinated, in a octahedral geometry, by oxygen atoms from the oxalate ligands (Figure 2a,c); (ii) the six-coordinated Mn1 exhibits octahedral coordination environment with six oxygen atoms, four of them belonging to oxalate anion and other two from coordinated water molecules (Figure 2b); (iii) Mn2 is bonded to six oxygen atoms coming from these oxalate ligands in octahedral coordination environment; (iv) two crystallographically nonequivelent K1 and K2 ions incorporated in crown ring form a planar coordination environment with six oxygen atoms of ether; additionally, K1 coordinates to one oxygen atom of terminal oxalate ligand, and K2 is involved in strong electrostatic interaction with two oxygen atoms of two different oxalate ligands which belong to two adjacent layers (above and below), contributing to effective 3D packing (Figure 1). In this structure, the oxalate ligand exhibits three kinds of coordination modes (Figure 2e–g): mode e, oxalate exhibits μ_4-(η_2: η_1: η_2: η_1)-bridging mode where two oxygen atoms (O18) coordinate two K2 and chelate one Mn2, and the other two chelate the Ru1; mode f, the terminal oxalate ligand is coordinate to one K1 and chelate Ru2 in μ-(η_1: η_2)-bridging mode; mode g, oxalate ligand chelates Ru2 and Mn2 exhibiting μ-(η_2: η_2)-bridging mode. The oxalate dianion, which behaves as a μ-(η_2: η_2) bridge, connects one by one [Ru1O_6], [Mn1O_6], [Ru2O_6], and [Mn2O_6] polyhedra (primary building units) to form a motif (secondary building unit) (Figure 3a) running along *a*-direction, resulting in zigzag-like 1D chains (Figure 3b). These chains are further extended along *b*-axis by μ_4-(η_2: η_1: η_2: η_1) oxalate, which bridges [Mn2O_6] and [Ru1O_6] polyhedra, to result in a 2D honeycombed layer structure which consists of a large 14-member ring based on three 6-member rings. Inside of large rings, [Ru2O_6] and [Mn1O_6] polyhedra are hold together by hydrogen bonds coming from μ-(η_1: η_2) oxalate ligand chelated to Ru2 and coordinated water molecules to Mn1; these hydrogen bonds define three smaller 6-membered rings. That is, two of them are regular with dimensions *ca.* 8.9 Å × 9.5 Å and one is elongated with dimensions *ca.* 6.8 Å × 11.4 Å (Figure S3). From the topological point of view, the metal centers can be reduced to three connected nodes and the oxalate ligands can be considered as ditopic linker. Therefore, the 2D layer is represented as 2D heterometallic uninodal three-connected net of hcb hexagonal plane network type (Figure S4) with Schläfli symbol 6^3, which agrees with TOPOS analysis.[19]

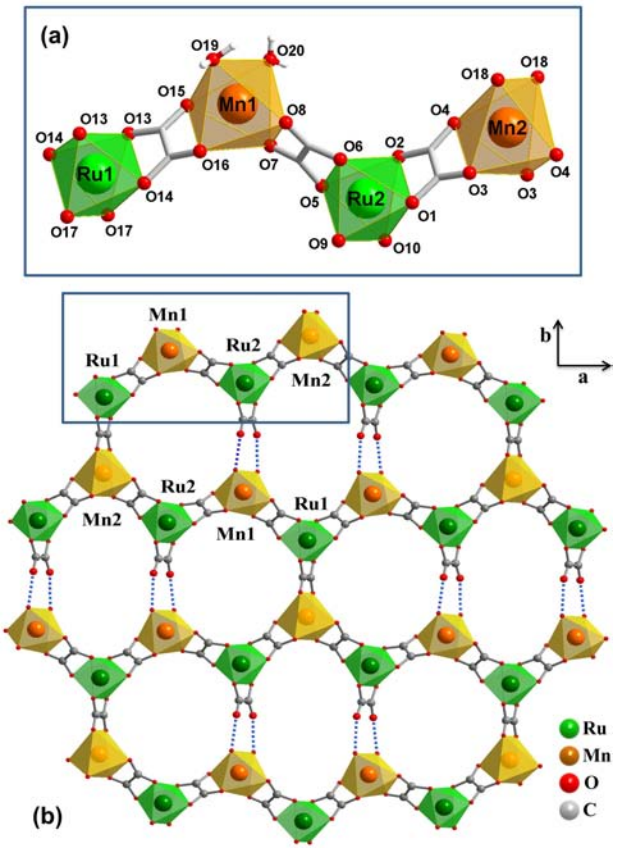

Figure 3. Representation of 2D honeycomb-like (6,3)-network, view along *c*-axis (b) and secondary building unit (a) (zigzag-like motif in applied zone) of compound **1**.

In the infrared spectra (see Figure S5) of compounds **1**–**5**, broad absorption bands at 1715–1713 and 1696–1679 cm^{-1} could be assigned to the symmetric and asymmetric contribution of chelated oxalate C═O bonds (ν_sC═O and ν_{as}C═O), respectively. Two other strong peaks at 1424–1412 cm^{-1} (ν_sC–O + ν_sC–C) and 1279–1264 cm^{-1} (ν_{as}C–O + ν_{as}C–C) are assigned to symmetric and asymmetric vibrations of oxalate C–O and C–C bonds. The absorption bands between 400 and 615 cm^{-1} show the presence of $\nu_{M\text{-}O}$ bonds, while absorptions at 825, 992, and 1106 cm^{-1} are due to C–C stretching vibrations.[20] The presence of coordinated water molecules is confirmed by the presence of a broad band in the region 3500–3200 cm^{-1}, which is due to O–H stretching vibrations. The incorporation of $[K(18\text{-crown-}6)]^+$ complex in the structures **1**–**5** is confirmed by the presence of bands between 2955 and 2920 cm^{-1}, which are associated with C–H stretching frequencies of the crown ring.[21]

Thermal stability in nitrogen and air atmosphere of compounds **1**–**5** was investigated. Thermal decomposition profiles, as shown in Figure S6, are similar for all title materials. For each compound the thermal analysis data are summarized in Table S1. Degradation process in nitrogen atmosphere of compound **1** has been taken as representative example. As shown in Figure S7, the thermal decomposition process proceeds in three stages. The first mass loss between 40 and 110 °C with the total mass loss of 1.5% (calcd 1.6%), corresponds to the gradual loss of the two water molecules coordinated to Mn1 atoms, which is accompanied by an

dx.doi.org/10.1021/ic302725v | *Inorg. Chem.* 2013, 52, 3933–3941

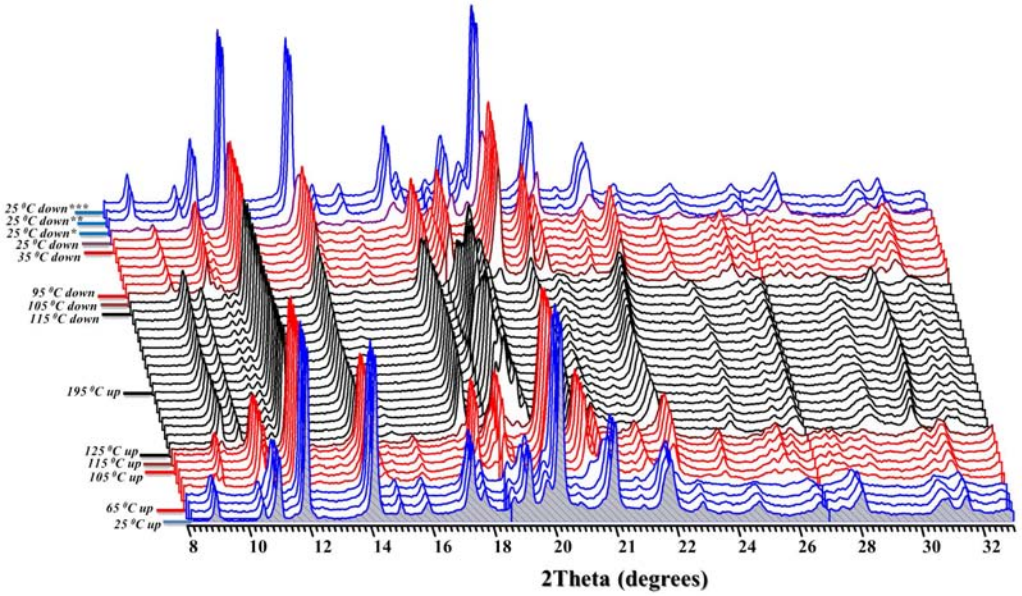

Figure 4. Powder X-ray thermodiffractograms of compound **1** recorded in air heating up from 25 to 195 °C and cooling down to 25 °C. Color code corresponding to the structural changes: blue, compound **1**; red, partially dehydrated compound **1a**; black, dehydrated compound **1b**. Asterisk marked pattern are recorded at 25 °C after half (*), one (**), and three (***) hour after experiment.

endothermic peak in the SDTA and DSC curves. The second step observed in the range 110−160 °C (endothermic process), with the total mass loss of 1.5% (calcd 1.6%), corresponds to loss of the last two water molecules coordinated to Mn1 atoms. These two steps of losing water molecules, confirmed by additional experiments in air atmosphere (see Figure S8), have been observed as endothermic peaks in the range 40−160 °C in SDTA and DSC curves. Up to 270 °C the compound remains stable until the third stage, which takes place in the range 270−350 °C (continuous process) with the total mass loss of *ca.* 64.3%, and corresponds to the progressive decomposition of the crown fragment and oxalate ligand, associated with endothermic and exothermic peaks in nitrogen and air atmospheres, respectively. The associated mass spectrometry m/z 18 (H_2O), and m/z 44 (CO_2) curves are in a good agreement with TG/DTG curves and show that the first and the second stages are purely attributed to water mass loss. In contrast, the third stage is accompanied with mass losses of m/z 18 (H_2O) and m/z 44 (CO_2) due to decomposition of crown and oxalate ligands. The residual solids resulting after total decomposition of compounds **1**−**5** were investigated by PXRD, which have been identified as mixture of Ru metal, K_2O, and MO in nitrogen atmosphere and as mixtures of RuO_2, K_2O, and M_2O_3 (**2**, **4**, and **5**), MO_2 (**1**), or MO (**3**) in the thermal oxidative degradation process in air atmosphere.

The powder X-ray thermodiffraction analysis carried out under air atmosphere by heating from 25 to 195 °C and cooling down to 25 °C was performed for **1** (see Figure 4) as a representative example of the series. The results confirm that compound **1** exhibits two phase transformation corresponding to two dehydration processes. This first one is produced by losing two water molecules coordinated to Mn1 atom, and the second one is due to the loss of last two bonded water molecules remaining in the partially dehydrated phase. Both partially and dehydrated phases exhibit a spontaneous rehydration processes after cooling down to room temperature (deep blue powder patterns at 25 °C down). For compound **1** no structural changes occur below 45 °C. The first phase transformation which leads to partially dehydrated compound **1a** begins at 55 °C, and the total transformation is reached at 75 °C and maintained until 105 °C, which is consistent with the TG analysis. The second phase transformation begins at 115 °C, and the total transformation to the anhydrous phase **1b** is reached at 125 °C and maintained until 195 °C. During the temperature decrease the anhydrous phase is preserved, and the first rehydration step begins at 95 °C and continues until room temperature giving the phase **1a**. In contrast, the second rehydration step is not achieved at the end of the experiment and requires a few additional hours in air, indicating the slow reversibility of this process compared with the previous one. It is worth mentioning that the peak at 2θ = ∼11° (at 25 °C), corresponding to interlayer distance in **1** (8.16 Å), is shifted to 10.6° (at 85 °C) and 10.3° (at 185 °C) due to increasing of interlayer spacing to *ca.* 8.4 Å and 8.6 Å for **1a** and **1b**, respectively. Powder X-ray diffraction patterns of partially dehydrated **1a** (at 65 °C) and anhydrous **1b** (at 185 °C) phases have been indexed in the monoclinic crystal system with the following unit cell dimensions: a = 19.33(1) Å, b = 11.46(1) Å, c = 14.46(1) Å, V = 3181.1(3) Å^3, for **1a**; a = 18.52(1) Å, b = 8.58(1) Å, c = 16.00(6) Å, V = 2543.7(2) Å^3, for **1b**. The results reveal that the unit cell contracts after dehydration processes maintaining the monoclinic crystal symmetry.

The catalytic activities of compounds **1**−**5** have been evaluated to behave as Lewis acid catalysts in the acetalyzation reaction of benzaldehyde with trimethylorthoformate (Scheme 1). In model experiments, the reaction was catalyzed in CCl_4 by using 1 mol % of catalyst affording phenyldimethylacetal in moderate to good yields: 49.8% for **1** (MnRu); 53.3% for **2** (FeRu); 85.2% for **3** (CoRu); 96.0% for **4** (CuRu); 82.6% for **5** (ZnRu) after 24 h at 70 °C (Figure 5). The TOF values (min^{-1}) obtained (124 (**1**); 133 (**2**); 213 (**3**); 240 (**4**); 206 (**5**)) indicate that the catalytic activity is higher than the reported previously for 2D and 3D coordination polymers.[22,23] In addition, the catalysts are easily separated from the resulting

Scheme 1. Acetalyzation of Benzaldehyde with Trimethyl Orthoformate

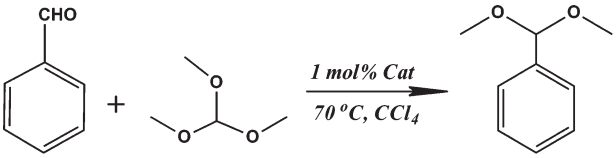

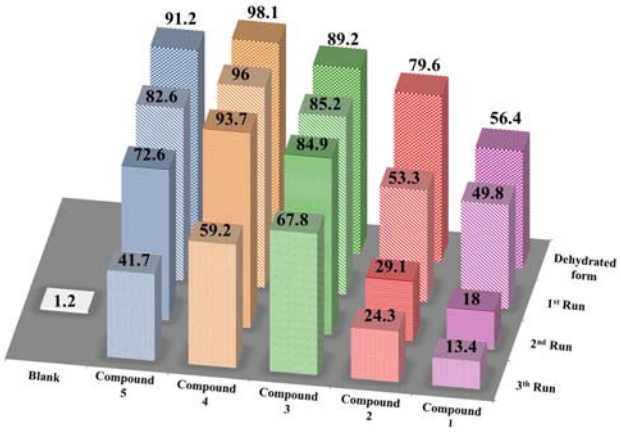

Figure 5. Catalytic properties of compounds **1**−**5** and their dehydrated forms **1b**−**5b** in reaction of benzaldehyde acetalyzation with TMOF at different catalytic runs. Reaction conditions: benzaldehyde (0.05 mL, 0.5 mmol), TMOF (0.5 mL, 5 mmol), CCl_4 (3 mL), heterogeneous catalyst (1 mol %), temperature 70 °C, under N_2 atmosphere. Conversion yields were determined by GC-FID. Blank run was carried out without heterogeneous catalyst.

solution by simple sedimentation (Figure S10). After the first catalytic run, catalysts **1**−**5** have been recovered by filtration, washed, and reused in two further consecutive runs. As expected, the resulting yields decrease (2nd run, 18 − 93.7%; third run, 13.4 − 41.7%) due to the partial mass loss of the catalyst. For comparison, a blank experiment without catalyst was carried out under the same reaction conditions obtaining a thermal conversion of only 1.2%. In addition, it is interesting to mention that when the catalyst **1** is removed by centrifugation after 5 h of reaction (23%), no significant transformation is observed (see Figure S9). This indicates that the catalytic activity is originated by active sites of the heterogeneous catalyst, rather than the molecular species contained in the filtrate which can be generated from the leaching of the solid catalyst. Also, after three catalytic runs catalyst **1** has been isolated and characterized by PXRD proving its thermal stability (Figure S11). As it was indicated above, coordinated water molecules in compounds **1**−**5** can be easily removed by heating under vacuum generating free coordination sites at the metal M^{II} center. In order to test the catalytic activity of the dehydrated solids, compounds **1**−**5** were totally dehydrated before their use as catalysts. Under the same reaction conditions, i.e., 1 mol % of catalyst loading, using CCl_4 as a solvent, and heating at 70 °C during 24 h, the phenyldimethylacetal is obtained in higher yields (56.4% vs 49.8% (**1**); 79.6% vs 53.3% (**2**); 89.2% vs 85.2% (**3**); 98.1% vs 96% (**4**); 91.2% vs 82.6% (**5**)), as compared with those obtained using hydrated forms (Figure 5). It is obvious that the dehydration gives rise to Lewis acid centers with an enhanced strength toward benzaldehyde and hence improved catalytic performance. The generation of Lewis acid centers in metal−organic frameworks $[Cu_3(BTC)_2(H_2O)_3]\cdot xH_2O$ (BTC = benzene 1,3,5-tricarboxylate) by removal of the copper(II) bonded water molecules is also known.[22] The higher catalytic activity observed for the dehydrated MOF $[Cu_3(BTC)_2]$ is reasoned on the basis of the easier access to the copper(II) sites. It is worth mentioning that the catalytic activity for hydrated and anhydrous compounds **1**−**5** follows the sequence **1** < **2** < **3** < **4** > **5** in a similar way as the Irving−Williams series for the formation constants of divalent metal ions $Mn^{2+} < Fe^{2+} < Co^{2+} < Ni^{2+} < Cu^{2+} > Zn^{2+}$. As it is well-known, this sequence results from the decrease of the ionic radii as well as the ligand field stabilization energies.[24] The exceptional Cu(II) position, in spite of its d^9 electronic configuration, arises from the additional stabilization energy due to the Jahn−Teller distortion which leads to a tetragonal distorted coordination environment. The highest catalytic activity shown by compound **4** is probably reflecting the enhanced binding energy of benzaldehyde which is coordinated in the equatorial plane and therefore is undergoing the strongest Lewis acid interaction. Finally, it is worth noting that a much lower catalytic performance is found when the salt $Cu(NO_3)_2\cdot 4H_2O$ is used as catalyst (1.8% yield of diphenylmethylacetal after heating in CCl_4 for 24 h) which means that the Lewis acid sites incorporated into the coordination polymers play a key catalytic role. In summary, these results show further examples of the utility of 2D coordination polymers as efficient heterogeneous catalysts which also can be easily recovered by filtration and reused in three cycles.

Variable temperature magnetic susceptibility measurements of compound **1**−**5** have been carried out on powdered samples in the 2−250 K temperature range. The temperature dependence of the molar magnetic susceptibilities, χ_m, and the reciprocal, χ_m^{-1}, is represented in Figure 6. The linear

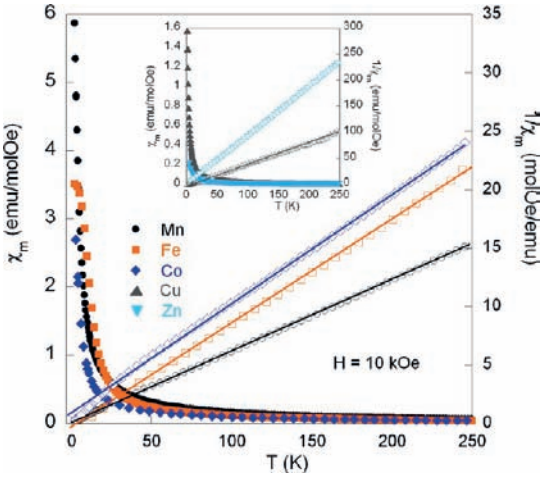

Figure 6. Temperature dependence of molar magnetic susceptibilities, χ_m, and reciprocal, χ_m^{-1}, for compounds **1**−**3** (M^{II} = Mn (**1**), Fe (**2**), Co (**3**)). The inset shows the variations corresponding to the compounds **4** and **5** (M^{II} = Cu (**4**), Zn (**5**)).

behavior of χ_m^{-1} at high temperatures can be fitted to a Curie−Weiss law for all investigated compounds. The experimental and calculated values of the effective paramagnetic moments and the paramagnetic Curie temperatures are gathered in Table 2. The values of the paramagnetic Curie−Weiss temperatures, θ, do not show any clear trend, with positive and negative

dx.doi.org/10.1021/ic302725v | *Inorg. Chem.* 2013, 52, 3933−3941

Table 2. Main Magnetic Data for Compounds 1−5 (M^{II} = Mn (1), Fe (2), Co (3), Cu (4), and Zn (5))[a]

compd/ M^{II}	μ_{eff} (μ_B/molecule)	μ_{eff} (μ_B/M^{II})	μ^{teo}_{eff} (μ_B/M^{II})	θ (K)	M (μ_B/molecule), T = 2K, H = 85 kOe
1/Mn	11.43(1)	6.37	5.90	−0.91(1)	16.05(1)
2/Fe	9.40(1)	5.16	5.40	6.84(1)	8.81(1)
3/Co	9.16(1)	5.01	4.80	−3.73(1)	7.76(1)
4/Cu	4.42(1)	1.92	1.90	1.33(1)	4.98(1)
5/Zn	2.91(1)	0.00	0.00	2.16(1)	2.72(1)

[a]Paramagnetic moments (for the molecule, for the M^{2+} magnetic moments and the theoretical expected ones) extracted from the high temperature behavior of the magnetic susceptibility, paramagnetic Curie temperature, and maximum magnetic moment measured under 85 kOe at 2 K (see text).

values, such that $|\theta| < 7$ K. This feature indicates that these compounds are characterized by the existence of competing magnetic interactions, which are too weak (except for those of the compound **2**, the Fe-based one) to establish magnetic ordering. This situation is not surprising because, in other related Ru^{III}-transition metal systems mediated through the oxalate bridge, ferromagnetic[14a] or antiferromagnetic[14b] states have been reported. The fact that compound **5** has a totally filled 3d shell means that the paramagnetic value of 2.91 μ_B could be associated with the paramagnetic moment of the Ru^{3+} ions. Taking into account this, the values of the paramagnetic moments of **1**−**4** can be extracted (see Table 2). The comparison of the experimental paramagnetic moments with the theoretical expected values obtained from the quenching of the orbital magnetic moment is in good agreement (see Table 2). No magnetic ordering has been detected in all the investigated compounds, except for the compound **2**, where the results of the magnetization at different magnetic fields, measured warming under a certain magnetic field after cooling down at zero field from room temperature first, without applied magnetic field (ZFC) and subsequently under applied magnetic field (FC), are shown in Figure 7. The low-temperature behavior is characterized by a sharp maximum in the ZFC-FC

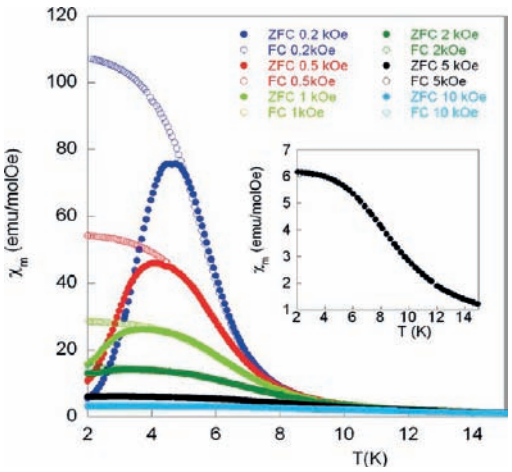

Figure 7. Low-temperature dependence of molar magnetic susceptibility, χ_m, for compound **2** (M^{II} = Fe), under ZFC and FC conditions. The inset shows the detail of the low-temperature behavior of χ_m under 10 kOe.

signals at temperature near T_f = 5 K under 0.2 kOe that shifts to low temperature as the intensity of the applied magnetic field increases, and disappearing under 5 kOe, where no maximum and irreversibility is observed in the ZFC-FC measurements (see inset of Figure 7). This effect of irreversibility observed in the magnetization curves is characteristic of a spin-glass-like behavior, which is suppressed using low magnetic fields. Magnetization data for all the investigated compounds have been measured as a function of field at 2 K under magnetic fields up to 85 kOe (Figure 8). The saturation magnetization

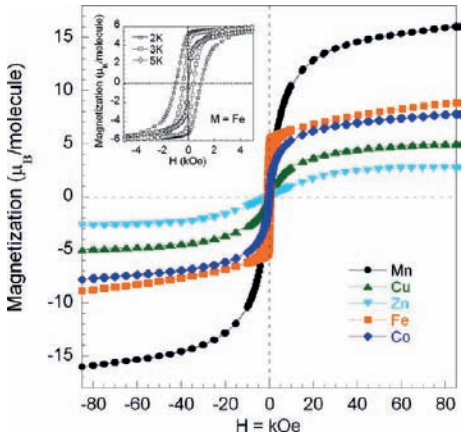

Figure 8. Magnetic hysteresis loops, $M(H)$, for **1**−**5** (M^{II} = Mn (**1**), Fe (**2**), Co (**3**), Cu (**4**), Zn (**5**)) collected at 2 K. The inset shows the detail of the loops around H = 0 for the investigated temperatures below T_f = 5 K for compound **2** (M^{II} = Fe).

values at 2 K are gathered in Table 2. These values are smaller than the theoretical saturation magnetization moments for the transition M^{II} metals. All of them have neither coercivity or remanence, except the case of compound **2** (M^{II} = Fe), where the coercive field reaches a value close to 1 kOe at 2 K. For this last compound magnetization has been also measured at 3, 4, and 5 K. Whereas the saturation magnetization is nearly constant, the coercive field decreases from 930 to 640, 410 Oe for 3 and 4 K, respectively, disappearing for 5 K, in good agreement with magnetic susceptibility data.

In order to study a possible dynamical response in compound **2**, ac measurements were carried out with an alternating excitation field of 3 Oe at different frequencies from 0.01 to 10^3 Hz. The real (M′) and out-of phase (M″) components of the susceptibility are shown in Figure 9. In a first view, the existence of a sharp peak around 5 K in both M′ and M″ parts could be indicative of the possible presence of a spin-glass state. The M′ values present a slight shift with the frequency whereas the peak height is almost constant. The more significant feature is that the position of the maximum shifts to higher temperatures with increasing frequency, which is usually considered as fingerprint of the spin-glass transition.[25] The freezing temperature T_f, associated with the spin-glass state, corresponds to the maximum in real part, M′. Depending on the interactions between the magnetic moments, T_f can be weakly (strong interactions) or strongly (weak interactions) dependent on the frequency (see Figure 9). In compound **2**, the frequency shifts the freezing temperature, within experimental errors, 0.015 (see inset of Figure 9a). Following Mydosh analysis,[26] the frequency dependence of the maximum agrees with the empirical Vogel−Fulcher law

dx.doi.org/10.1021/ic302725v | *Inorg. Chem.* 2013, 52, 3933−3941

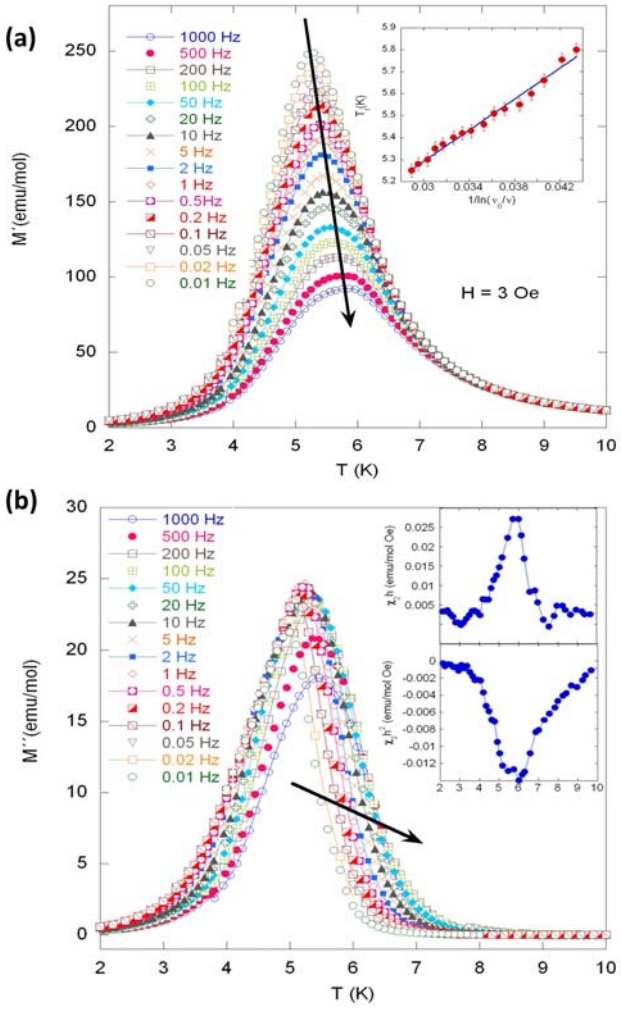

Figure 9. In-phase (M′) and out-of-phase (M″) ac magnetization for compound **2** (M^{II} = Fe) measured under different excitation frequencies from 1000 to 0.01 Hz. The inset on part b shows the temperature variations of the nonlinear susceptibilities χ_2 and χ_3, when the static applied magnetic field H = 0, and the alternating excitation field h = 3 Oe, and the frequency = 1 kHz.

$$\tau_m = \tau_o \exp\left[\frac{E_a}{k_B(T_f - T_o)}\right]$$

with the relaxation time τ_o characteristic of strong interactions and weak frequency dependence of the freezing temperature. Assuming the variation of M′ to a Gaussian function around T_f and taking $\nu_o = \tau_o^{-1} = 10^{13}$ Hz,[27] we obtain reasonable fitting parameters of the activation energy E_a and the Vogel−Fulcher temperature T_o with E_a = 35.5 K and T_o = 4.2 K. These values are similar to those observed for other iron insulator spin-glasses previously reported.[28]

A combined investigation of both odd and even harmonics of the ac magnetic response enables one to distinguish between a canonical and a cluster spin glass.[29] While the odd harmonics yield true asymptotic values of the critical exponents of the spin glasses, the even harmonics can confirm the presence or absence of correlated spin regions (spin clusters). In this sense, the even harmonics of the nonlinear susceptibilities χ_2 and χ_4 are zero[30] for an ideal SG at temperatures $T \sim T_f$. By contrast, for a ferromagnet, χ_2 and χ_4 are finite.[31] On the basis of these considerations, the $\chi_2(T)$ and $\chi_3(T)$ data, presented in the inset of Figure 9, provide direct evidence for the existence of two different time (and hence length) scales for the SG and FM order in compound **2**. A global SG order and a small contribution of short-range FM order (it is likely due to the existence of cluster Fe rich domains) are observed at the experimental time scales.

CONCLUSIONS

A series of isostructural coordination polymers based on a ruthenium trioxalate building unit and several transition metals $\{[K(18\text{-crown-}6)]_3[M^{II}_3(H_2O)_4\{Ru(ox)_3\}_3]\}_n$ (M^{II} = Mn (**1**), Fe (**2**), Co (**3**), Cu (**4**), Zn (**5**)) have been synthetized and structurally characterized. Topological simplification of isostructural 2D frameworks gives rise to a uninodal three-connected net with hcb hexagonal plane type. This series of compounds have been obtained as a microcrystalline powders and exhibit high thermal stability. Also, the compounds **1**−**5** exhibit two phase transformations characterized by spontaneous rehydration processes with different kinetics. All the coordination polymers **1**−**5** behave as highly active Lewis acid catalysts in the acetalyzation reaction of benzaldehyde with trimethylorthoformate exhibiting an increased activity in the sequence $Mn^{2+} < Fe^{2+} < Co^{2+} < Ni^{2+} < Cu^{2+} > Zn^{2+}$, and can be reused in three consecutive runs preserving a considerable catalytic activities. The dehydrated coordination polymers **1b**−**5b** show higher catalytic performances due to the creation of active-accessible Lewis acid centers. The magnetic susceptibility shows that all the investigated compounds do not present any long-range magnetic order down to 2 K. The Fe-based compound **2** shows the existence of a cluster spin-glass-like state below 5 K, characterized by the presence of a magnetic irreversibility in the ZFC-FC magnetization data. Alternating current magnetic susceptibility shows the presence of a maximum at 5 K that shifts to higher temperatures with increasing frequency. The coercive field increases as the temperature is lowered below 5 K, reaching a value of 1 kOe at 2 K.

ASSOCIATED CONTENT

Supporting Information

SEM images, IR spectra, thermoanalytical data, and X-ray crystallographic information (CIF data) for compounds **1**−**5**. This material is available free of charge via the Internet at http://pubs.acs.org.

AUTHOR INFORMATION

Corresponding Author

*E-mail: jrgm@uniovi.es.

Notes

The authors declare no competing financial interest.

ACKNOWLEDGMENTS

The authors thank FEDER and Spanish MINECO for financial support under projects MAT2010-15094, MAT2008-06542-C04-03, MAT2011-27573-C04-02, and FC-08-IB08-036. A.D. also thanks the Spanish Ministerio de Educación, Cultura y Deporte for the predoctoral FPU grant (AP2008-03942).

REFERENCES

(1) (a) Batten, S. R.; Neville, S. M.; Turner, D. R. *Coordination Polymers. Design, Analysis and Applications*; RSC Publishing Cambridge: Cambridge, U.K., 2009. (b) Long, J. R.; Yaghi, O. M. *Chem. Soc. Rev.* **2009**, *38*, 1213−1214. (c) Zhou, H.-C.; Long, J. R.; Yaghi, O. M. *Chem. Rev.* **2012**, *112*, 673−674.

(2) (a) Corma, A.; García, H.; Llabrés-Xamena, F. X. *Chem. Rev.* **2010**, *110*, 4606−4655. (b) Yoon, M.; Srirambalaji, R.; Kim, K. *Chem. Rev.* **2012**, *112*, 1196−1231. (c) Ma, L.; Abney, C.; Lin, W. *Chem. Soc. Rev.* **2009**, *38*, 1248−1256. (d) Lee, J. Y.; Farha, O. K.; Roberts, J.; Scheidt, K. A.; Nguyen, S.-B. T.; Hupp, J. T. *Chem. Soc. Rev.* **2009**, *38*, 1450−1459. (e) Farrusseng, D.; Aguado, S.; Pinel, C. *Angew. Chem., Int. Ed.* **2009**, *48*, 7502−7513.

(3) Fei, H.; Rogow, D. L.; Oliver, S. R. J. *J. Am. Chem. Soc.* **2010**, *132*, 7202−7209.

(4) (a) Suh, M. P.; Park, H. J.; Prasad, T. K.; Lim, D.-W. *Chem. Rev.* **2012**, *112*, 782−835. (b) Murray, L. J.; Dincă, M.; Long, J. R. *Chem. Soc. Rev.* **2009**, *38*, 1294−1314. (c) Li, J.-R.; Kuppler, R. J.; Zhou, H.-C. *Chem. Soc. Rev.* **2009**, *38*, 1477−1504. (d) Sumida, K.; Rogow, D. L.; Mason, J. A.; McDonald, T. M.; Bloch, E. D.; Herm, Z. R.; Bae, T.-H.; Long, J. R. *Chem. Rev.* **2012**, *112*, 724−781.

(5) (a) Cui, Y.; Yue, Y.; Qian, G.; Chen, B. *Chem. Rev.* **2012**, *112*, 1126−1162. (b) Kreno, L. E.; Leong, K.; Farha, O. K.; Allendorf, M.; Van Duyne, R. P.; Hupp, J. T. *Chem. Rev.* **2012**, *112*, 1105−1125. (c) Allendorf, M. D.; Bauer, C. A.; Bhakta, R. K.; Houk, R. J. T. *Chem. Soc. Rev.* **2009**, *38*, 1330−1352.

(6) (a) Kurmoo, M. *Chem. Soc. Rev.* **2009**, *38*, 1353−1379. (b) Zhang, W.; Xiong, R.-G. *Chem. Rev.* **2012**, *112*, 1163−1195.

(7) (a) Liang, L.; Peng, G.; Ma, L.; Sun, L.; Deng, H.; Li, H.; Li, W. *Cryst. Growth Des.* **2012**, *12*, 1151−1158. (b) Feng, R.; Chen, L.; Chen, Q.-H.; Shan, X.-C.; Gai, Y.-L.; Jiang, F.-L.; Hong, M.-C. *Cryst. Growth Des.* **2011**, *11*, 1705−1712. (c) Zhao, X.-Q.; Zhao, B.; Wei, S.; Cheng, P. *Inorg. Chem.* **2009**, *48*, 11048−11057.

(8) (a) Su, Z.; Fan, J.; Okamura, T.-A.; Sun, W.-Y.; Ueyama, N. *Cryst. Growth Des.* **2010**, *10*, 3515−3521. (b) Li, L.; Niu, S.-Y.; Jin, J.; Meng, Q.; Chi, Y.-X.; Xing, Y.-H.; Zhang, G.-N. *J. Solid State Chem.* **2011**, *184*, 1279−1285. (c) Sun, D.; Wang, D.-F.; Han, X.-G.; Zhang, N.; Huang, R.-B.; Zhenga, L.-S. *Chem. Commun.* **2011**, *47*, 746−748.

(9) (a) Coronado, E.; Galán-Mascarós, J. R.; Martí-Gastaldo, C. *J. Mater. Chem.* **2006**, *16*, 2685−2689. (b) Mathonière, C.; Nuttall, K. J.; Carling, S. G.; Day, P. *Inorg. Chem.* **1996**, *35*, 1201−1206. (c) Tamaki, H.; Zhong, Z. J.; Matsumoto, N.; Kida, S.; Koikawa, M.; Achiwa, N.; Hashimoto, Y.; Okawa, H. *J. Am. Chem. Soc.* **1992**, *114*, 6974−6979. (d) Min, K. S.; Rhinegold, A. L.; Miller, J. S. *Inorg. Chem.* **2005**, *44*, 8433−8441. (e) Ovenesyan, N. S.; Makhaev, V. D.; Aldoshin, S. M.; Gredin, P.; Boubekeur, K.; Train, C.; Gruselle, M. *Dalton Trans.* **2005**, 3101−3107. (f) Decurtins, S.; Schmalle, H. W.; Osward, H. R.; Linden, A.; Ensling, J.; Gütlich, P.; Hauser, A. *Inorg. Chim. Acta* **1994**, *216*, 65−73.

(10) (a) Coronado, E.; Galán-Mascarós, J. R.; Martí-Gastaldo, C.; Waerenborgh, J. C.; Gaczyński, P. *Inorg. Chem.* **2008**, *47*, 6829−6839. (b) Coronado, E.; Galán-Mascarós, J. R.; Martí-Gastaldo, C. *Inorg. Chem.* **2006**, *45*, 1882−1884. (c) Andrés, R.; Gruselle, M.; Malézieux, B.; Verdaguer, M.; Vaissermann, J. *Inorg. Chem.* **1999**, *38*, 4637−4646. (d) Coronado, E.; Galán-Mascarós, J. R.; Martí-Gastaldo, C. *J. Am. Chem. Soc.* **2010**, *132*, 5456−5468. (e) Coronado, E.; Galán-Mascarós, J. R.; Martí-Gastaldo, C. *J. Am. Chem. Soc.* **2008**, *130*, 14987−14989. (f) Coronado, E.; Galán-Mascarós, J. R.; Gómez-García, C. J.; Martí-Gastaldo, C. *Inorg. Chem.* **2005**, *44*, 6197−6202. (g) Coronado, E.; Galán-Mascarós, J. R.; Martí-Gastaldo, C. *Inorg. Chem.* **2007**, *46*, 8108−8110. (h) Coronado, E.; Galán-Mascarós, J. R.; Martí-Gastaldo, C. *Inorg. Chim. Acta* **2008**, *361*, 4017−4023. (i) Coronado, E.; Galán-Mascarós, J. R.; Martí-Gastaldo, C. *Polyhedron* **2007**, *26*, 2101−2104.

(11) (a) Rao, C. N. R.; Natarajan, S.; Vaidhyanathan, R. *Angew. Chem., Int. Ed.* **2004**, *43*, 1466−1496. (b) Coronado, E.; Clemente-León, M.; Galán-Mascarós, J. R.; Giménez-Saiz, C.; Gómez-García, C. J.; Martínez-Ferrero, E. *J. Chem. Soc., Dalton Trans.* **2000**, 3955−3961. (c) Cheetham, A. K.; Rao, C. N. R.; Feller, R. K. *Chem. Commun.* **2006**, 4780−4795.

(12) Coronado, E.; Galán-Mascarós, J. R.; Gómez-García, C. J.; Laukhin, V. *Nature* **2000**, *408*, 447−449.

(13) (a) McClaverty, J. A.; Mayer, T. J. *Comprehensive Coordination Chemistry II. From Biology to Nanotechnology. Transition Metal Groups 7 and 8*; Elsevier Ltd.: Oxford, U.K., 2004; Vol. 5. (b) Seddon, E. A.; Seddon, K. R. *Ruthenium Chemistry*; Elsevier Science Publishers B. V.: Amsterdam, The Netherlands, 1984.

(14) (a) Coronado, E.; Galán-Mascarós, J. R.; Gómez-García, C. J.; Martínez-Agudo, J. M.; Martínez-Ferrero, E.; Waerenborgh, J. C.; Almeida, M. *J. Solid State Chem.* **2001**, *159*, 391−402. (b) Larionova, J.; Mombelli, B.; Sanchiz, J.; Kahn, O. *Inorg. Chem.* **1998**, *37*, 679−684.

(15) (a) Murahashi, S.-I. *Ruthenium in Organic Synthesis*; Wiley-VCH: New York, 2004. (b) Bruneau, C.; Dixneuf, P. H. *Ruthenium Catalysts and Fine Chemistry (Topics in Organometallic Chemistry)*; Springer-Verlag: New York, 2004.

(16) Kaziro, R.; Hambley, T. W.; Bistead, R. A.; Beattie, J. K. *Inorg. Chim. Acta* **1989**, *164*, 85−91.

(17) http://accelrys.com/products/materials-studio/

(18) Boultif, A.; Louer, D. *J. Appl. Crystallogr.* **2004**, *37*, 724−731.

(19) Blatov, V. A.; Shevchenko, A. P. *TOPOS-Version 4.0 Professional (beta evaluation)*; Samara State University: Samara, Russia, 2006.

(20) Nakamoto, K. *Infrared and Raman Spectra of Inorganic and Coordination Compounds, Part B.*; John Wiley & Sons Inc.: New York, 2009.

(21) Socrates, G. *Infrared and Raman Characteristic Group Frequencies*; John Wiley & Sons Ltd: London, U.K., 2001.

(22) (a) Amghouz, Z.; Roces, L.; García-Granda, S.; García, J. R.; Souhail, B.; Mafra, L.; Shi, F.; Rocha, J. *Inorg. Chem.* **2010**, *49*, 7917−7926. (b) Amghouz, Z.; García-Granda, S.; García, J. R.; Ferreira, R. A. S.; Mafra, L.; Carlos, L. D.; Rocha, J. *Inorg. Chem.* **2012**, *51*, 1703−1716. (c) Gándara, F.; Gomez-Lor, B.; Gutiérrez-Puebla, E.; Iglesias, M.; Monge, M. A.; Proserpio, D. M.; Snejko, N. *Chem. Mater.* **2008**, *20*, 72−76. (d) Perles, J.; Iglesias, M.; Ruiz-Valero, C.; Snejko, N. *Chem. Commun.* **2003**, 346−347. (e) Bernini, M. C.; Gándara, F.; Iglesias, M.; Snejko, N.; Gutiérrez-Puebla, E.; Brusau, E. V.; Narda, G. E.; Angeles Monge, M. *Chem.—Eur. J.* **2009**, *15*, 4896−4905. (f) Gomez-Lor, B.; Gutiérrez-Puebla, E.; Iglesias, M.; Monge, M. A.; Ruiz-Valero, C.; Snejko, N. *Inorg. Chem.* **2002**, *41*, 2429−2432. (g) Perles, J.; Iglesias, M.; Ruiz-Valero, C.; Snejko, N. *J. Mater. Chem.* **2004**, *14*, 2683−2689. (h) Gómez-Lor, B.; Gutiérrez-Puebla, E.; Iglesias, M.; Monge, M. A.; Ruiz-Valero, C.; Snejko, N. *Chem. Mater.* **2005**, *17*, 2568−2573.

(23) (a) Schlichte, K.; Kratzke, T.; Kaskel, S. *Microporous Mesoporous Mater.* **2004**, *73*, 81−88. (b) Dhakshinamoorthy, A.; Alvaro, M.; García, H. *Adv. Synth. Catal.* **2010**, *352*, 3022−3030. (c) Alaerts, L.; Séguin, E.; Poelman, H.; Thibault-Starzyk, F.; Jacobs, P. A.; De Vos, D. E. *Chem.—Eur. J.* **2006**, *12*, 7353−7363.

(24) Schriver, D.; Atkins, P. W. *Inorganic Chemistry*, 5th ed.; Oxford University Press: Oxford, U.K., 2010.

(25) Fischer, K. H.; Hertz, J. *Spin Glasses*; Cambridge University Press: Cambridge, U.K., 1991.

(26) Mydosh, J. A. *Spin Glasses: An Experimental Introduction*; Taylor & Francis: London, U.K., 1993.

(27) Tholence, J. L. *Solid State Commun.* **1980**, *35*, 113−117.

(28) Chan Chung, U.; Mesa, J. L.; Pizarro, J. L.; Meatza, I.; Bengoechea, M.; Rodríguez Fernández, J.; Arriortua, M. I.; Rojo, T. *Chem. Mater.* **2011**, *23*, 4317−4330.

(29) Bitla, Y.; Kaul, S. N.; Fernández-Barquín, L. *Phys. Rev. B* **2012**, *86*, 094405(1)−(9).

(30) (a) Suzuki, M. *Prog. Theor. Phys.* **1977**, *58*, 1151−1165. (b) Wada, K.; Takayama, H. *Prog. Theor. Phys.* **1980**, *64*, 327−329. (c) Fujiki, S.; Katsura, S. *Prog. Theor. Phys.* **1981**, *65*, 1130−1144.

(31) Bitla, Y.; Kaul, S. N. *Europhys. Lett.* **2011**, *96*, 37012(1)−(6).

2D Heterometallic Coordination Polymers Based on Ruthenium Oxalate Building Units: Synthesis, Structure, Catalytic and Magnetic Properties

Alla Dikhtiarenko[a], Sergei A. Khainakov[a], Imanol de Pedro[b], Jesús A. Blanco[c], José R. García[a], and José Gimeno[a]

[a] *Departamento de Química Orgánica e Inorgánica, Universidad de Oviedo – CINN, 33006 Oviedo, Spain*

[b] *CITIMAC, Facultad de Ciencias, Universidad de Cantabria, Avenida de los Castros 39005 Santander, Spain*

[c] *Departamento de Física, Universidad de Oviedo - CINN, 33007 Oviedo, Spain*

Supplementary Information

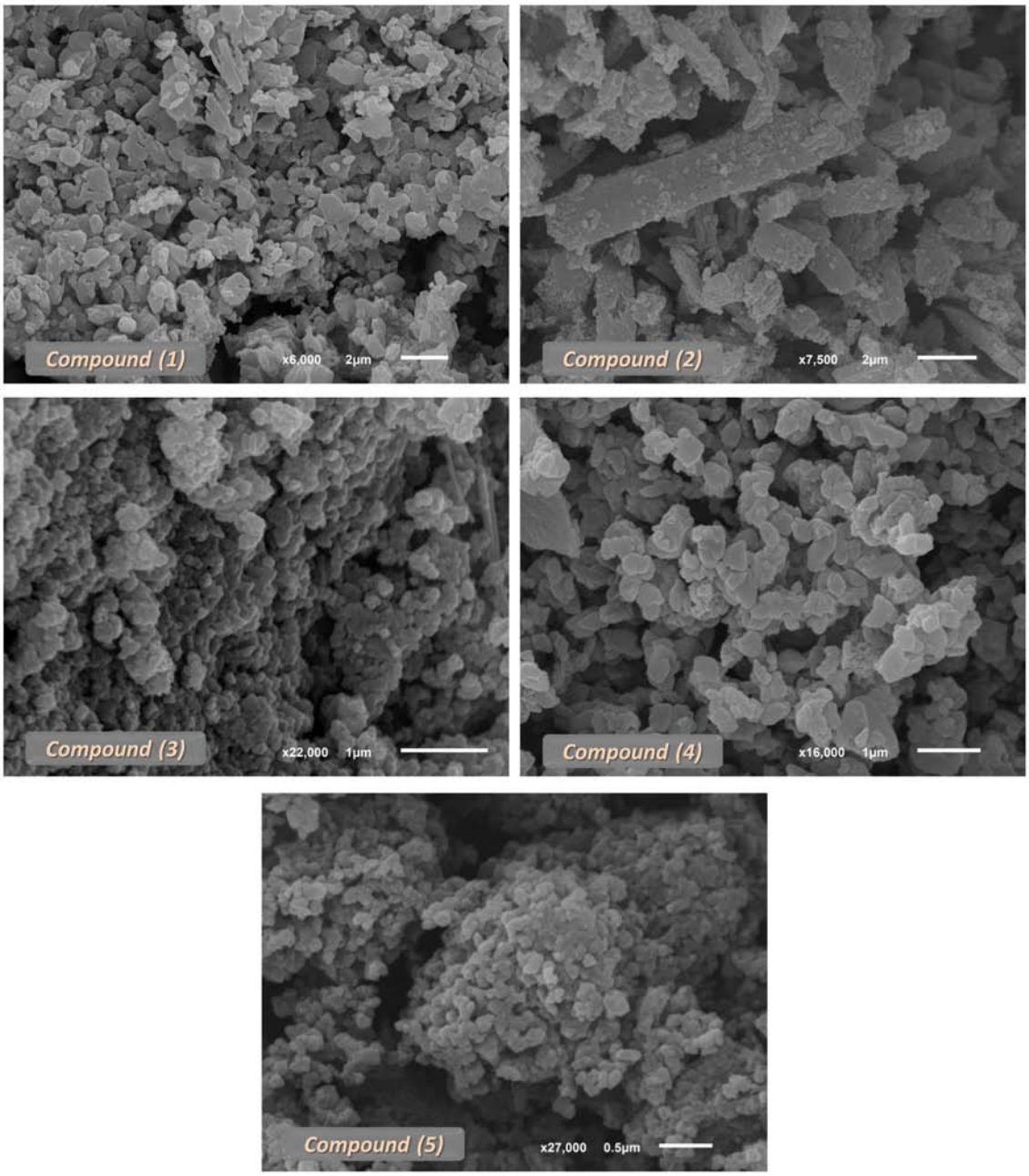

Figure S1. SEM images of compound **1-5**.

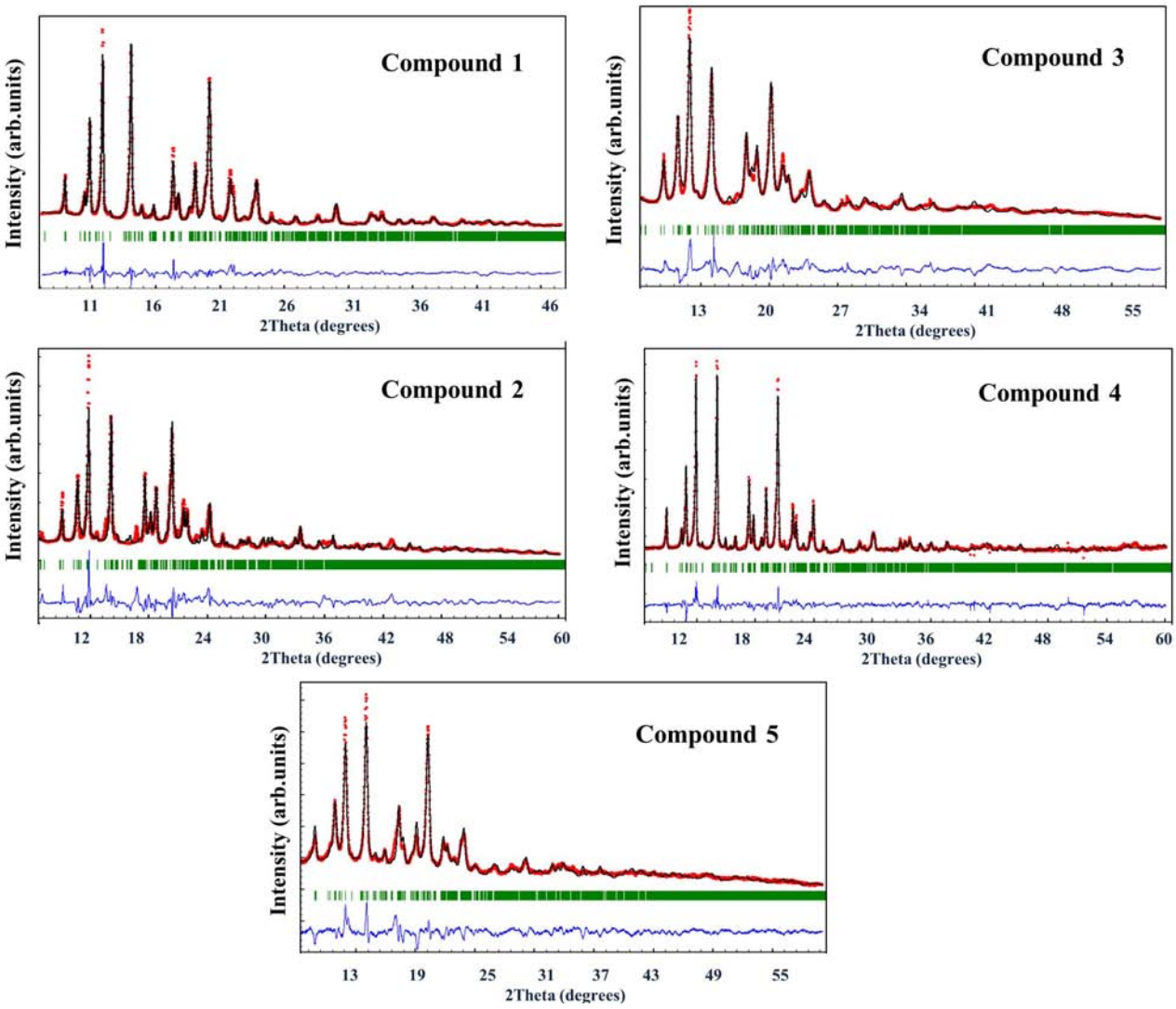

Figure S2. Observed (red solid points) and calculated (black solid line) profiles for the final Rietveld refinement of compound **1-5**. The difference plot (blue solid line) is on the same intensity scale.

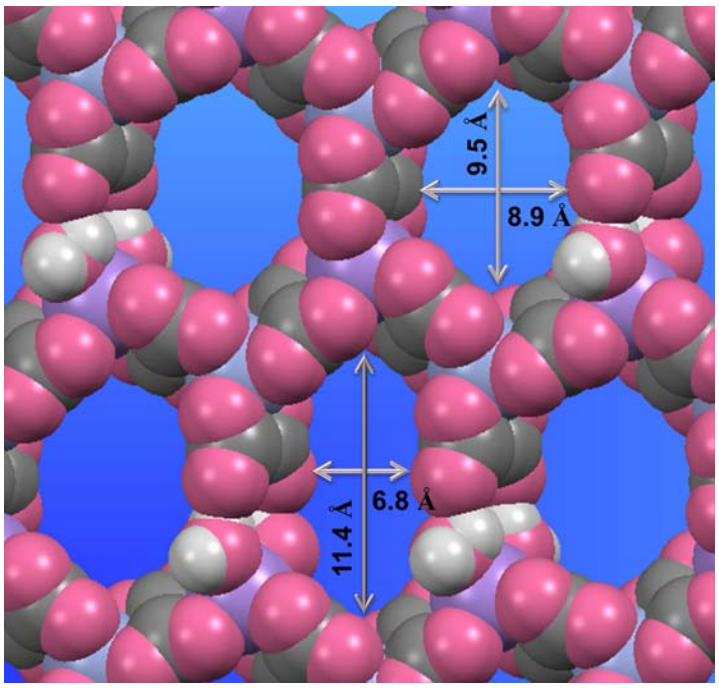

Figure S3. Space filling view of 2D layer along *c*-axis, showing two porous types. The Ru atoms are purple, Mn are blue, O are pink and C are gray.

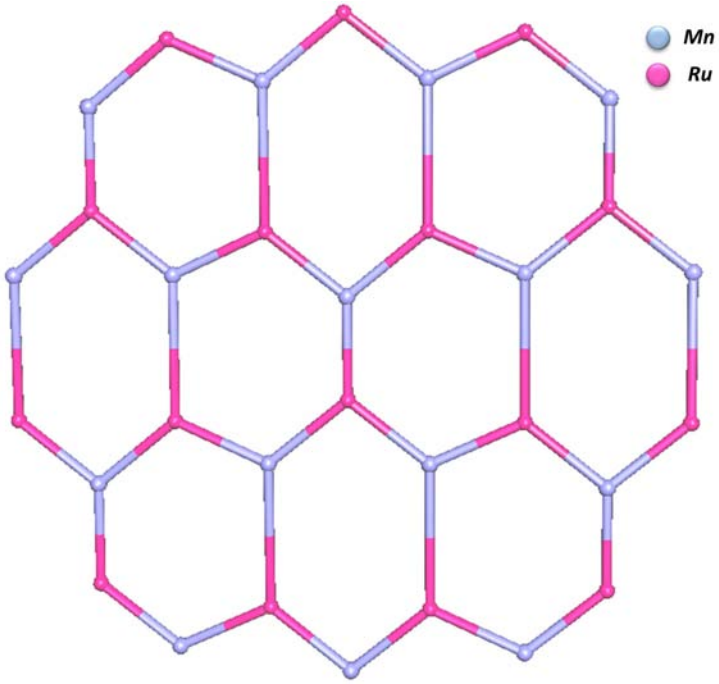

Figure S4. Simplified planar honeycombed (6,3) network with each oxalate anion shown as a single rod connecting the two metal centers.

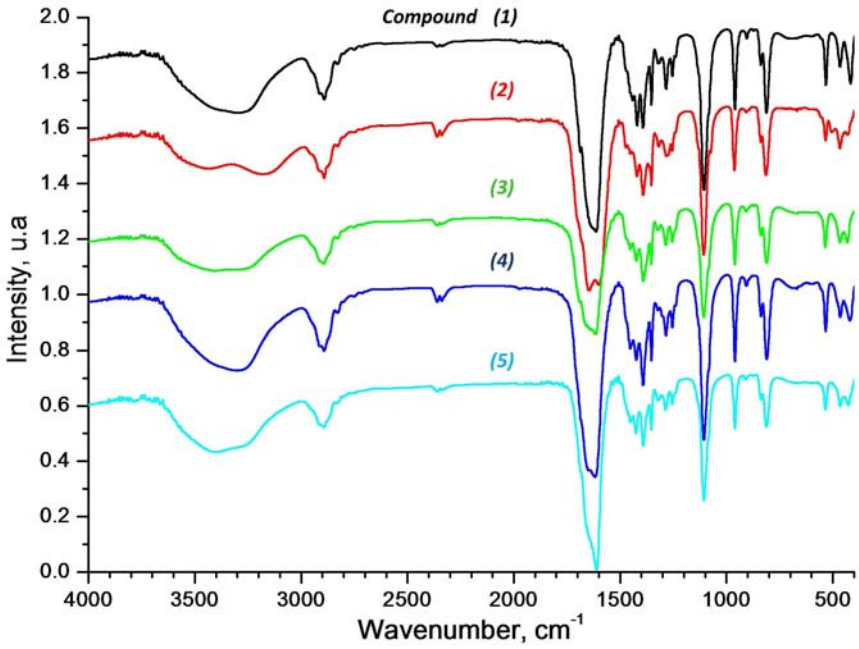

Figure S5. Infrared spectra of compounds **1**-**5**.

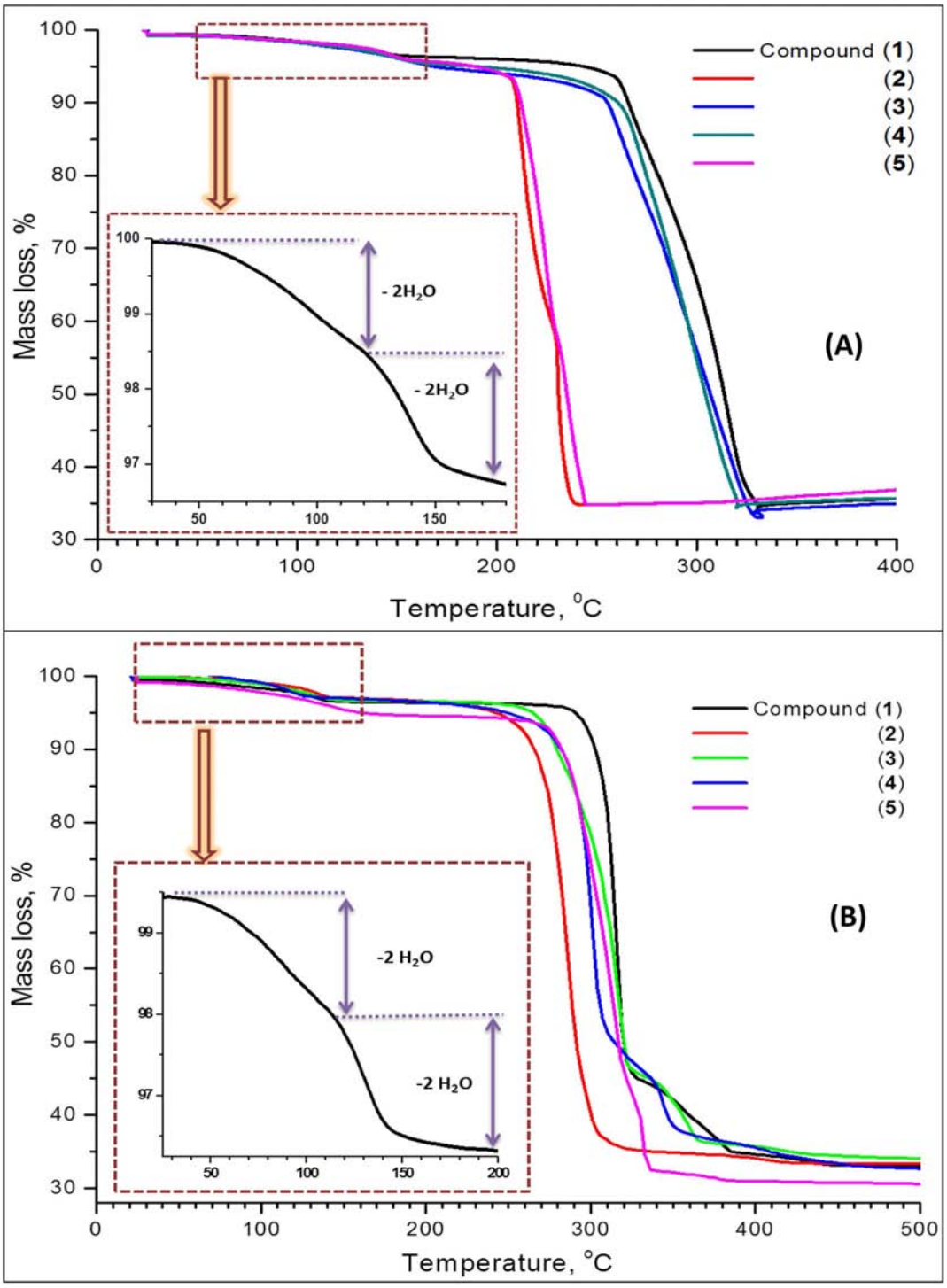

Figure S6. Thermogravimetric curves for compounds **1-5** in air **(A)** and nitrogen **(B)** atmospheres. In multiplied regions shows two steps corresponds to gradual water loss for compound **1**.

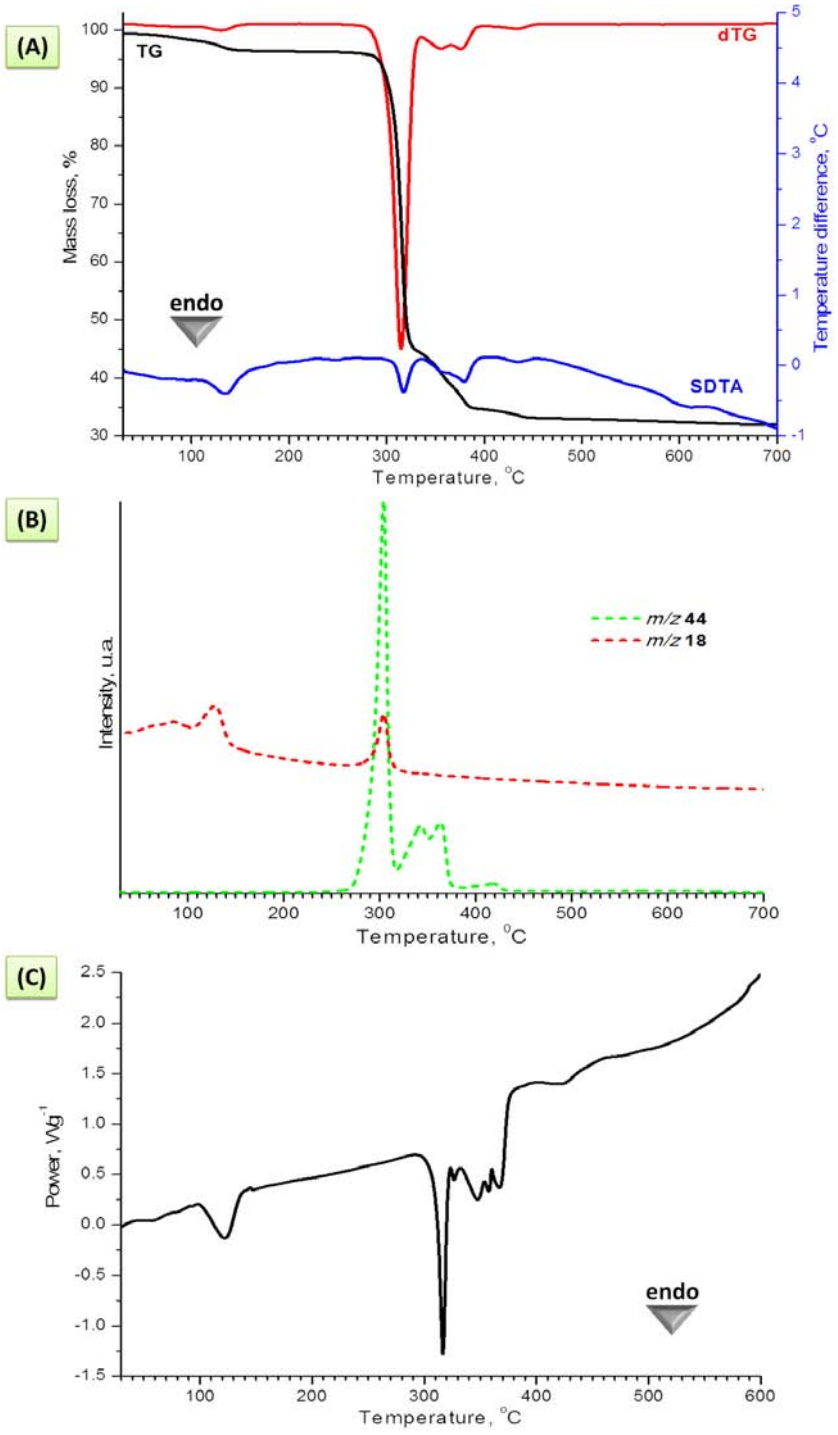

Figure S7. TG, DTG and SDTA curves (A), mass spectrometry of evacuated vapors (B), and DSC curve (C), for compound **1** in nitrogen atmosphere.

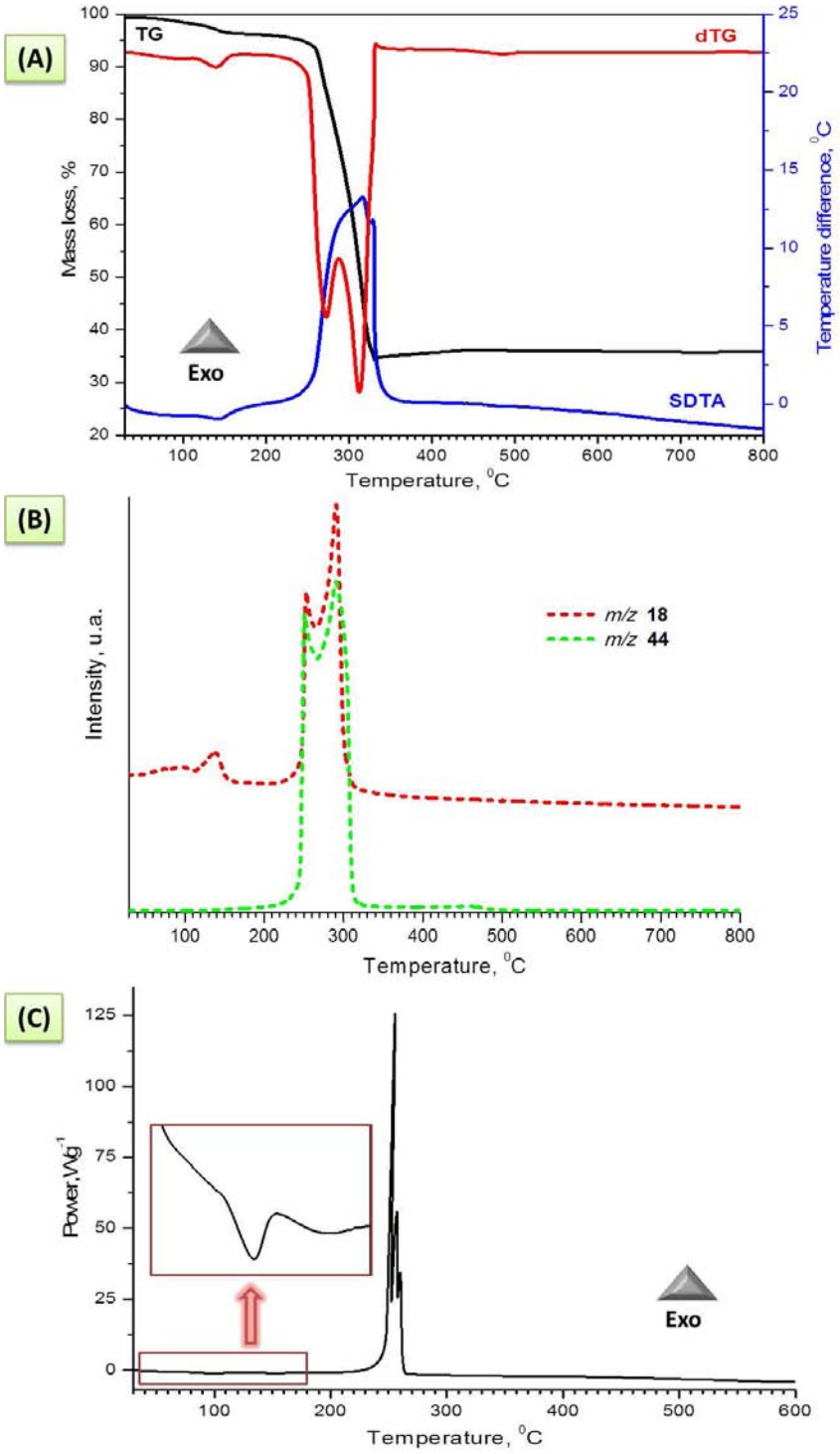

Figure S8. TG, DTG and SDTA curves (A), mass spectrometry of evacuated vapors (B), and DSC curve (C), for compound **1** in air atmosphere.

Table S1. Thermoanalytical data for compound **1–5** obtained in nitrogen or air atmospheres

Compound	**1**		**2**		**3**		**4**		**5**	
Atmosphere	***Nitrogen***	***Air***	***Nitrogen***	***Air***	***Nitrogen***	***Air***	***Nitrogen***	***Air***	***Nitrogen***	***Air***
1st weight loss step										
Reaction	$[KC_{12}H_{24}O_6]_3[M_3(H_2O)_4\{Ru(C_2O_4)_3\}_3] \rightarrow [KC_{12}H_{24}O_6]_3[M_3(H_2O)_2\{Ru(C_2O_4)_3\}_3] + 2\,H_2O\uparrow$									
T^{range} (°C)	40÷108	40÷110	36÷109	39÷111	43÷98	36÷108	43÷97	36÷110	42÷108	53÷114
T^{max} (°C)	90	96	82	84	83	83	74	83	91	97
Weight loss (%), obs./calc.	1.5/1.6	1.7/1.6	1.3/1.6	1.5/1.6	1.4/1.6	1.7/1.6	1.3/1.6	1.2/1.6	1.3/1.6	1.5/1.6
m/z	18 (H_2O)	18 (H_2O)	18 (H_2O)	18 (H_2O)	18 (H_2O)	18 (H_2O)	18 (H_2O)	18 (H_2O)	18 (H_2O)	18 (H_2O)
Enthalpy (J/g)	51.4	6.2	32.4	3.1	35.8	54.2	20.8	7.6	11.7	9.6
2nd weight loss step										
Reaction	$[KC_{12}H_{24}O_6]_3[M_3(H_2O)_2\{Ru(C_2O_4)_3\}_3] \rightarrow [KC_{12}H_{24}O_6]_3[M_3\{Ru(C_2O_4)_3\}_3] + 2\,H_2O\uparrow$									
T^{range} (°C)	108÷157	110÷163	109÷153	111÷166	98÷155	116÷171	97÷133	110÷150	108÷168	118÷178
T^{max} (°C)	130	139	132	146	129	147	118	118	142	155
Weight loss (%), obs./calc.	1.5/1.6	1.8/1.6	1.7/1.6	1.7/1.6	1.7/1.6	1.9/1.6	1.7/1.6	1.8/1.6	1.5/1.6	1.8/1.6
m/z	18 (H_2O)	18 (H_2O)	18 (H_2O)	18 (H_2O)	18 (H_2O)	18 (H_2O)	18 (H_2O)	18 (H_2O)	18 (H_2O)	18 (H_2O)
Enthalpy (J/g)	53.3	22.5	73.7	35.9	54.4	18.3	94.9	61.9	64.3	25.9
3rd weight loss step										
Reaction	$[KC_{12}H_{24}O_6]_3[M_3\{Ru(C_2O_4)_3\}_3] \rightarrow 3\,RuKMO_x + y(18\text{-}3x)CO_2\uparrow + z(18\text{-}3x)CO\uparrow + 36H_2O\uparrow$									
T^{range} (°C)	271÷380	241÷353	203÷455	184÷249	227÷485	188÷342	200÷495	160÷300	268÷342	196÷305
T^{max} (°C)	316	311	283	218	316	275	308	231	331	264
Weight loss (%), obs./calc.	66.2/64.3	62.2/61.1	67.1/66.7	64.6/64.6	65.2/66.4	63.7/63.4	64.7/65.4	59.6/60.8	67.3/67.1	62.8/61.8
m/z	44(CO_2)/ 18(H_2O)	44(CO_2)/ 18(H_2O)	44(CO_2)/ 18(H_2O)	44(CO_2)/ 18(H_2O)	44(CO_2)/ 18(H_2O)	44(CO_2)/ 18(H_2O)	44(CO_2)/ 18(H_2O)	44(CO_2)/ 18(H_2O)	44(CO_2)/ 18(H_2O)	44(CO_2)/ 18(H_2O)
Enthalpy (J/g)	324.9	- 4562.3	147.2	- 3623.3	286.7	- 5014.9	289.9	- 3515.1	284.5	- 4403.9
Total weight loss										
Formula weight (g/mol)	2242.51		2244.33		2254.48		2268.34		2273.86	
Weight loss (%), obs./calc.	69.2/67.5	66.7/64.3	69.9/69.9	69.2/67.8	70.0/69.6	68.9/66.6	69.7/68.6	62.6/64.0	71.7/70.3	68.1/65.0

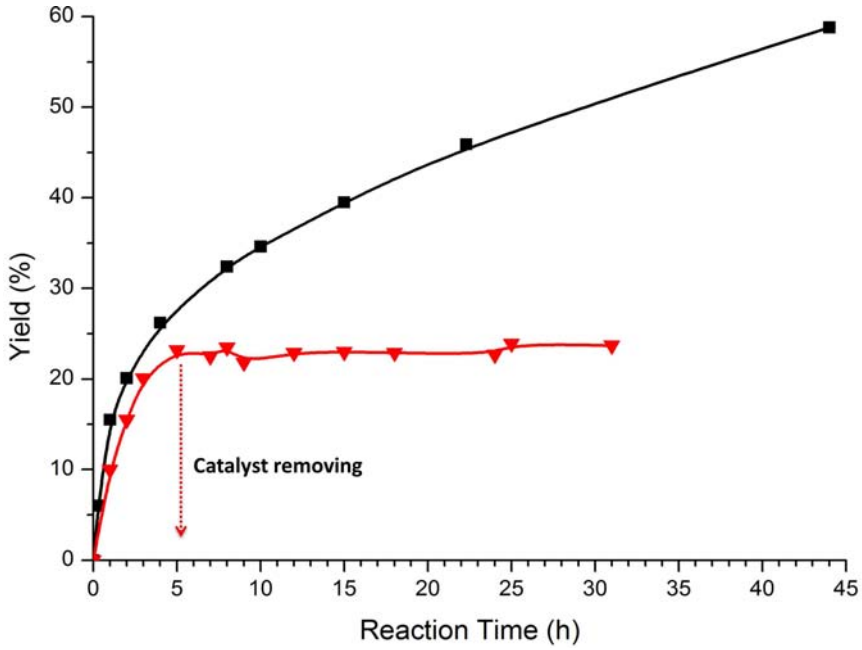

Figure S9. Kinetic profile for compound **1** catalyzed acetalization of benzaldehyde (black) and profile after removing of catalyst by filtration after 5 hours of reaction (red).

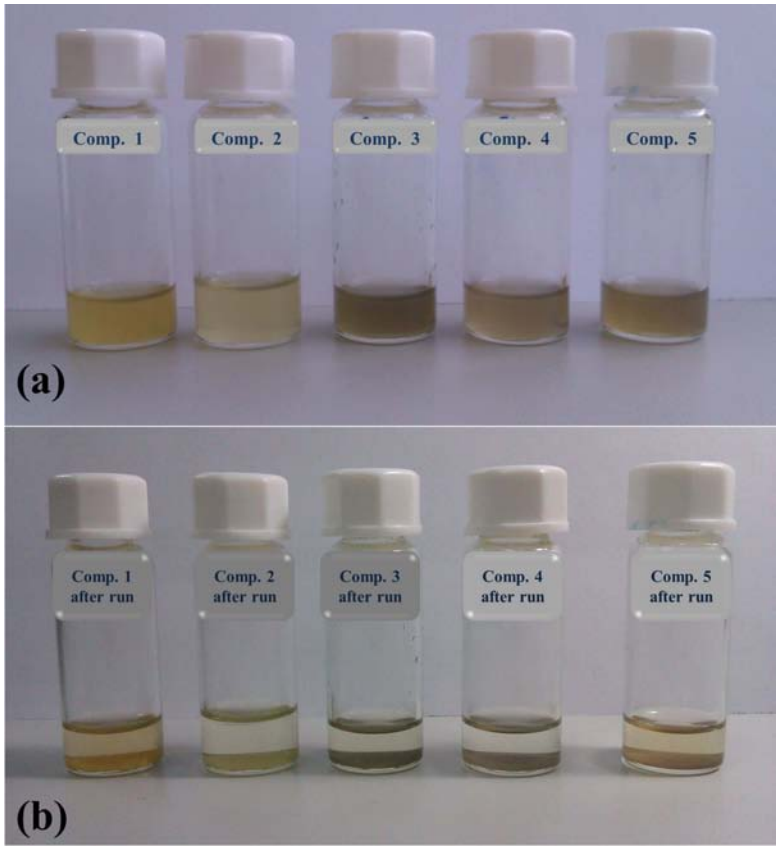

Figure S10. Digital photographs of heterogeneous **1-5** catalytic systems before (a) and after (b) catalytic runs. Figure show possibility of catalyst recycling from solution by simple sedimentation.

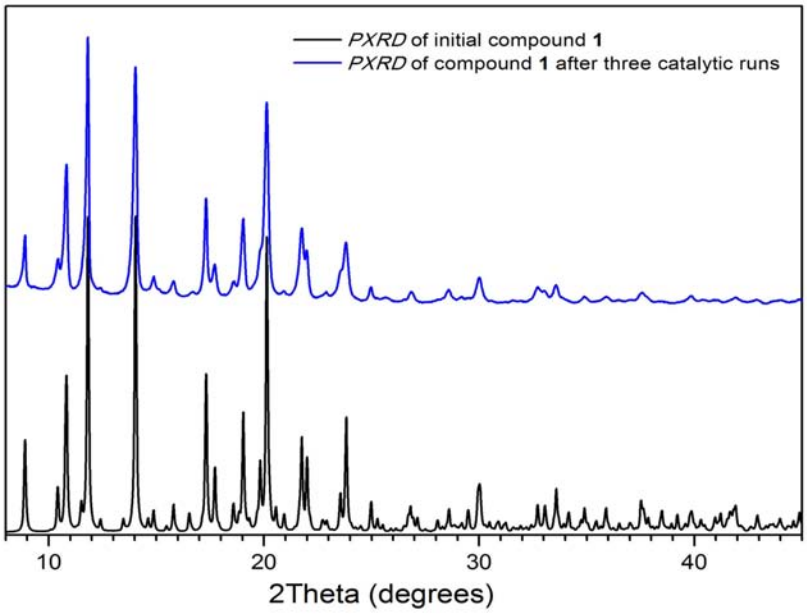

Figure S11. Comparison of PXRD patterns of compound **1** before (black line) and after three consecutive catalytic runs (blue line).

Capítulo VIII

Polímeros de Coordinación 3D Basados en Unidades Oxalato de Rutenio(III) $[Ru(C_2O_4)_3]^{3-}$ como Catalizadores Heterogéneos para la Fotoreducción de CO_2 a CO

El *Capítulo VIII* se dedica a la preparación de polímeros de coordinación tri-dimensionales de fórmula general $\{[M^{II}(bpy)_3][M^{I}Ru(C_2O_4)_3]\}_n$ (donde M^{II} = Fe, Ni, Co; bpy = 2,2´-bipiridina), así como a la caracterización estructural y a la determinación de su actividad como fotocatalizadores heterogéneos.

La utilización de la luz solar como fuente de energía alternativa para la industria de las transformaciones químicas es actualmente uno de los grandes desafíos de la humanidad. En particular, la reducción fotoquímica de dióxido de carbono por la luz solar es considerada como uno de los procesos más interesantes y deseados ya que no solo contribuirá a disminuir el calentamiento global, sino también permitirá el uso de CO_2 atmosférico como materia prima barata para la síntesis de productos químicos valiosos.[1–6] A día de hoy, se conocen un buen número de catalizadores homogéneos activos en la fotoreducción de CO_2, la mayoría de cuales son complejos de metales de transición mononucleares o polinucleares que contienen macrociclos o ligandos como bipiridina.[7–11]

Considerando las desventajas que poseen los sistemas homogéneos fotoactivos, básicamente relacionadas con dificultades de reciclabilidad (separación de los productos y el catalizador) y desactivación del catalizador, el diseño de fotocatalizadores heterogéneos es objeto actualmente de un interés especial. En este ámbito, las redes metal-orgánicas (MOFs) y los polímeros de coordinación (PCs) tienen potencial para combinar varias ventajas ya que, al tiempo que permiten su reciclaje, presentan una alta selectividad derivada de su capacidad de reconocer el tamaño del sustrato.[12–14] Además, las propiedades de los sistemas de este tipo, que incorporan componentes fotosensibles con capacidad para almacenar la luz, pueden ser modificadas drásticamente a través de la incorporación a sus canales o cajas de moléculas huésped ópticamente activas (en particular, varios polímeros de coordinación y redes metal-orgánicas desarrollados recientemente han demostrado una alta actividad catalítica en numerosas fotorreacciones, tales como oxidación del agua, evolución de hidrógeno, reducción de sales metálicas produciendo nanopartículas, y transformaciones orgánicas).[15–17]

En función de estos antecedentes, y considerando el hecho de que se conocen solamente unos pocos ejemplos de polímeros de coordinación activos en la fotoreducción de CO_2, las redes heterometálicas con estructuras tri-dimensionales formuladas como $\{[M^{II}(bpy)_3][M^{I}M^{III}(C_2O_4)_3]\}_n$ (M^{II} = Co, Ni, Fe, Ru; M^{I} = Na, Li; M^{III} = Cr, Fe; bpy = 2,2´-bipiridina) son firmes candidatas a ser utilizadas como fotocatalizadores. Estos materiales son

(1) A. J. Morris, G. J. Meyer, E. Fujita, *Acc. Chem. Res*., **2009**, *42*, 1983.
(2) M. D. Doherty, D. C. Grills, J. T. Muckerman, D. E. Polyansky, E. Fujita, *Coord. Chem. Rev.*, **2010**, *54*, 2472.
(3) H. Takeda, O. Ishitani, *Coord. Chem. Rev*., **2010**, *254*, 346.
(4) J. Schneider, H. Jia, J. T. Muckerman, E. Fujita, *Chem. Soc. Rev*., **2012**, *41*, 2036.
(5) C. D. Windle, R. N. Perutz, *Coord. Chem. Rev*., **2012**, *256*, 2562.
(6) B. Kumar, M. Llorente, T. D. Froehlich, A. Sathrum, C. P. Kubiak, *Annu. Rev. Phys. Chem*., **2012**, *63*, 541
(7) K. Kiyosawa, N. Shiraishi, T. Shimada, D. Masui, H. Tachibana, S. Takagi, O. Ishitani, D. A. Tryk, H. Inoue, *J. Phys. Chem. C*, **2009**, *113*, 11667.
(8) S. Sato, K. Koike, H. Inoue, O. Ishitani, *Photochem. Photobiol. Sci*., **2007**, *6*, 454.
(9) J. Grodkowski, T. Dhanasekaran, P. Neta, P. Hambright, B. S. Brunschwig, K. Shinozaki, E. Fujita, *J. Phys. Chem. A*, **2000**, *104*, 11332.
(10) J. Grodkowski, P. Neta, E. Fujita, A. Mahammed, L. Simkhovich, Z. Gross, *J. Phys. Chem. A*, **2002**, *106*, 4772.
(11) S. L.-F. Chan, T. L. Lam, C. Yang, S.-C. Yan, N. M. Cheng, *Chem. Commun.*, **2015**, *51*, 7799−7801.
(12) A. Corma, H. García, F. X. Llabrés-Xamena, *Chem. Rev*., **2010**, *110*, 4606.
(13) P. García-García, M. Muller, A. Corma, *Chem. Sci*., **2014**, *5*, 2979.
(14) J. Gascon, A. Corma, F. Kapteijn, F. Llabrés i Xamena, *ACS Catalysis*, **2014**, 36.
(15) C. A. Kent, B. P. Mehl, L. Ma, J. M. Papanikolas, T. J. Meyer, W. Lin, *J. Am. Chem. Soc*., **2010**, *132*, 12767.
(16) J.-L. Wang, C. Wang, W. Lin, *ACS Catal*., **2012**, *2*, 2630.
(17) M. A. Nasalevich, M. van der Veen, F. Kapteijn, J. Gascon, *Cryst. Eng. Comm*., **2014**, *16*, 4919.

fácilmente accesibles mediante autoensamblaje del metaloligando, $[M^{III}(C_2O_4)_3]^{3-}$, un centro metálico monovalente y una plantilla catiónica, $[M^{II}(bpy)_3]^{2+}$.[18–21] El hecho de que estas estructuras aniónicas tridimensionales sean capaces de incorporar homogénea y selectivamente complejos catiónicos $[M^{II}(bpy)_3]^{2+}$ garantiza la neutralidad de la estructura polimérica global, proporcionando además a la red polimérica una capacidad de funcionalización que puede ser explorada en aplicaciones fotocatalíticas.

El *Capítulo* VIII se dedica a la síntesis y caracterización de una serie de nuevos polímeros de coordinación de fórmula $\{[M^{II}(bpy)_3][M^{I}Ru(C_2O_4)_3]\}_n$ (M^{II} = Ni, Fe, Co; M^{I} = Na, Li; bpy = 2,2´-bipiridina) y, en particular, al estudio de su actividad catalítica en la foto-reducción de CO_2. Los resultados desarrollados en este campo son reflejados en las *Publicaciones VI* y *VII*, que se presentan como parte del contenido de esta Tesis.

La *Publicación VI*, se dedica a la preparación y caracterización de dos polímeros de coordinación formulados como $\{[Co(bpy)_3][NaRu(C_2O_4)_3]\}_n$ y $\{[Co(bpy)_3][LiRu(C_2O_4)_3]\}_n$, que se originan mediante auto-ensamblaje del metaloligando $[Ru(C_2O_4)_3]^{3-}$ en medio acuoso a temperatura ambiente y en presencia del cloruro de un metal alcalino (Na o Li). Estos polímeros de coordinación fueron aislados como muestras monofásicas y su estructura cristalina fue determinada a partir de datos de difracción de rayos X de monocristal, revelando simetría cúbica (grupo espacial $P4_13$). Ambos compuestos son isoestructurales, pudiendo describirse sus estructuras cristalinas a partir de la plantilla molecular catiónica, $[Co(bpy)_3]^{2+}$, que reside en las cajas de la red aniónica, $\{[Na/LiRu(C_2O_4)_3]^{2-}\}_n$, construida alternando poliedros octaédricos, $\{Na/LiO_6\}$ y $\{RuO_6\}$, enlazados mediante ligandos oxalato. Considerando los enlaces covalentes en la red polimérica, y dado que cada centro metálico muestra una conectividad similar, la estructura tridimensional aniónica, $\{[Na/LiRu(C_2O_4)_3]^{2-}\}_n$, presenta una topología tipo "panal de abeja", caracterizada por el símbolo 10^3 de Schläfli. El hecho de que sus arquitecturas poliméricas no dispongan de espacios vacíos accesibles, hace que estos compuestos sean no porosos. Además, $\{[Co(bpy)_3][NaRu(C_2O_4)_3]\}_n$ y $\{[Co(bpy)_3][LiRu(C_2O_4)_3]\}_n$ exhiben propiedades magnéticas interesantes ya que la plantilla catiónica molecular incorporada en la red aniónica, $[Co(bpy)_3]^{2+}$, muestra un equilibrio entre los estados de alto y bajo espín. En función de la composición de la red polimérica (es decir, dependiendo de la presencia de Na o Li), el complejo-plantilla, $[Co(bpy)_3]^{2+}$, exhibe diferente grado de población de estados del espín (*spin-crossover*) en función de la temperatura. Así, la plantilla catiónica incorporada en la red $\{[LiRu(C_2O_4)_3]^{2-}\}_n$ se encuentra en estado de bajo espín a 10 K mientras que, a esa temperatura, presenta espín mixto cuando forma parte de la red $\{[LiRu(C_2O_4)_3]^{2-}\}_n$. Este hecho indica que el estado electrónico de la especie $[Co(bpy)_3]^{2+}$ se encuentra afectado por la red polimérica en la que reside.

Las propiedades catalíticas de $\{[Co(bpy)_3][NaRu(C_2O_4)_3]\}_n$ y $\{[Co(bpy)_3][LiRu(C_2O_4)_3]\}_n$ fueron evaluadas en la reacción de foto-reducción de CO_2, realizada en la mezcla trietilamina/acetonitrilo (10 mL, v/v = 1:5) con 10 μmol de catalizador y bajo luz ultravioleta incidente de $\lambda \leq 366$ nm. Los polímeros de coordinación estudiados demostraron capacidad para reducir selectivamente CO_2 a CO, alcanzando conversiones de 1.5 y 1.2 mmol en 10 h de irradiación para $\{[Co(bpy)_3][NaRu(C_2O_4)_3]\}_n$ y $\{[Co(bpy)_3][LiRu(C_2O_4)_3]\}_n$,

(18) S. Decurtins, H. W. Schmalle, P. Schneuwly, J. Ensling, P. Gütlich, *J. Am. Chem. Soc.*, **1994**, *116*, 9521.
(19) R. Andrés, M. Gruselle, B. Malézieux, M. Verdaguer, J. Vaissermann, *Inorg. Chem.*, **1999**, *38*, 4637.
(20) R. Sieber, S. Decurtins, H. Stoeckli-Evans, C. Wilson, D. Yufit, J. A. K. Howard, S. C. Capelli, A. Hauser, *Chem.-Eur. J.*, **2000**, *6*, 361.
(21) V. M. Russell, D. C. Craig, M. L. Scudder, I. G. Dance, *Cryst. Eng. Comm.*, **2000**, *2*, 16.

respectivamente. Como consecuencia de la conocida sinergia entre los componentes de estos polímeros de coordinación, el mecanismo de reacción foto-catalítica debe seguir los siguientes pasos: (*i*) la transferencia de electrones tiene lugar desde la especie rutenio(III) foto-excitada al complejo de cobalto(II), que actúa como catalizador; (*ii*) el intermedio resultante, $[(Co(bpy)_3]^+$, es capaz de coordinar y reducir CO_2 a CO, regenerándose a $[(Co(bpy)_3]^{2+}$; (*iii*) la transferencia electrónica desde la trietilamina (actuando como dador de electrones sacrificante) al centro de rutenio oxidado de la superficie de la red polimérica regenera el componente fotosensible del polímero de coordinación. En resumen, aparentemente, estos PC´s son materiales relevantes como fotocatalizadores y presentan potencialidad para ser estudiados en otros procesos fotoactivos.

La *Publicación VII* se dedica a la preparación de la familia compuestos $\{[M^{II}(bpy)_3][M^{I}Ru(C_2O_4)_3]\}_n$ (donde M^{II} = Fe, Ni; M^{I} = Na, Li; bpy = 2,2´-bipiridina). Además, la caracterización de los miembros de esta serie se discute de forma comparada con respecto a los compuestos $\{[Co(bpy)_3][NaRu(C_2O_4)_3]\}_n$ y $\{[Co(bpy)_3][LiRu(C_2O_4)_3]\}_n$, detallados en la *Publicación VI*. Los datos recogidos en este trabajo revelan que todos estos compuestos son isoestructurales, diferenciándose en la composición química de la plantilla catiónica, $[M^{II}(bpy)_3]^{2+}$ (M^{II} = Fe, Ni, Co; bpy = 2,2´-bipiridina), y en el catión alcalino que constituye la red polimérica. Las estructuras cristalinas de todos los compuestos de la serie fueron determinadas mediante datos de difracción de rayos X de monocristal, revelando simetría cúbica y naturaleza polimérica. Todos los polímeros de coordinación descritos en este Capítulo presentan relativamente alta estabilidad térmica, tanto en atmósfera reactiva (aire) como inerte (nitrógeno). La degradación térmica de cada miembro de la serie procede en única etapa, en rangos de temperaturas comprendidos entre 280 °C y 700 °C, sin revelar cambios estructurales previos al colapso irreversible de la red polimérica.

En este trabajo, se determinaron las propiedades ópticas de todos los compuestos mediante estudios espectroscópicos UV-VIS. El conocimiento de estos datos, junto con sus características estructurales, será relevante en el estudio teórico del comportamiento fotocatalítico de estos materiales ya que, en las reacciones promovidas por fotones, las absorciones de luz característica, relacionadas con transiciones electrónicas particulares, son importantes para la exploración eficiente de la actividad fotocatalítica de cada compuesto. Los polímeros de coordinación $\{[Fe(bpy)_3][NaRu(C_2O_4)_3]\}_n$, $\{[Fe(bpy)_3][LiRu(C_2O_4)_3]\}_n$, $\{[Ni(bpy)_3][NaRu(C_2O_4)_3]\}_n$ y $\{[Ni(bpy)_3][LiRu(C_2O_4)_3]\}_n$ preservan el estado electrónico de las plantillas catiónicas en contraposición a las dos redes poliméricas, $\{[Co(bpy)_3][NaRu(C_2O_4)_3]\}_n$ y $\{[Co(bpy)_3][LiRu(C_2O_4)_3]\}_n$, detalladas en *Publicación VI*. Sin excepción, todos los miembros de la serie exhiben bandas de absorción UV bien definidas, correspondientes a transferencias de carga de metal-ligando.

La actividad fotocatalítica de los nuevos miembros de la serie de polímeros de coordinación fue evaluada en la foto-reducción de CO_2 a CO, usando acetonitrilo como disolvente y trietilamina como dador de electrones, revelando una menor actividad que la observada para los compuestos $\{[Co(bpy)_3][NaRu(C_2O_4)_3]\}_n$ y $\{[Co(bpy)_3][LiRu(C_2O_4)_3]\}_n$. En todos los casos, el reciclaje del catalizador muestra una disminución irrelevante de su actividad catalítica intrínseca, ya que la menor eficiencia observada debe relacionarse con pérdidas del catalizador heterogéneo en los procesos de recuperación y lavado. Además, se confirmó que la actividad catalítica no es consecuencia de las especies solubles que puedan aparecer en procesos de descomposición del polímero de coordinación. La compilación de todos los datos experimentales indica que la actividad fotocatalítica de los polímeros de coordinación

$\{[M^{II}(bpy)]_3[M^{I}Ru(C_2O_4)_3]\}_n$ (donde M^{II} = Fe, Ni, Co; M^{I} = Na, Li; bpy = 2,2´-bipiridina) es función de la plantilla catiónica molecular, siguiendo el orden $Co^{2+} > Ni^{2+} > Fe^{2+}$ para redes $\{[NaRu(C_2O_4)_3]^{2-}\}_n$ y $Co^{2+} > Fe^{2+} > Ni^{2+}$ para $\{[LiRu(C_2O_4)_3]^{2-}\}_n$.

Publication VI

"Non-Porous 3D Oxalate Bridged Coordination Polymers $\{[M^IRu(C_2O_4)_3]^{2-}\}_n$ (M^I = Li, Na) Templated by $[Co(bpy)_3]^{2+}$: Efficient Catalysts for Selective Photoreduction of CO_2 to CO"

Chemical Communications

(submitted)

Year ***2015***

Impact Factor: 6.718

ChemComm

RSCPublishing

COMMUNICATION

Non-Porous 3D Oxalate Bridged Coordination Polymers $\{[M^IRu(C_2O_4)_3]^{2-}\}_n$ (M^I = Li, Na) Templated by $[Co(bpy)_3]^{2+}$: Efficient Catalysts for Selective Photoreduction of CO_2 to CO

Cite this: DOI: 10.1039/x0xx00000x

Received 00th October 2014,
Accepted 00th October 2014

DOI: 10.1039/x0xx00000x

www.rsc.org/

Alla Dikhtiarenko,[a] Rafael Valiente,[b] Jesús A. Blanco,[c] Jorge Gascon,[d] José R. García[a] and José Gimeno[a]

We present the synthesis, characterization and photocatalytic performance of two new 3D coordination polymers with molecular formula $\{[Co(bpy)_3][M^IRu(C_2O_4)_3]\}_n$ (M^I = Li, Na; bpy = 2,2´-bipyridine). These honeycomb-like anionic networks $\{[M^IRu(C_2O_4)_3]^{2-}\}_n$ hosting cationic $[Co(bpy)_3]^{2+}$ are efficient and recyclable heterogeneous catalysts for the photo-induced reduction of CO_2 to CO, displaying the highest TON (120 - 150) values reported to date.

The efficient utilization of sunlight as an energy source for chemical transformations is one of the grand challenges mankind faces nowadays. Although photosynthesis is a relatively well known process, the design and synthesis of artificial materials able to emulate this natural process has proved challenging.[1] Remarkably, the light-driven photochemical reduction of carbon dioxide is considered to be among the most interesting and desired processes since it would not only contribute to decreasing global warming, but would also allow the use of CO_2 as a cheap feedstock for the synthesis of chemicals.[2] A number of homogeneous catalysts active in photoinduced reduction of CO_2 has been reported,[3] most of which are mononuclear or polynuclear transition metal complexes containing either macrocyclic or bipyridine-type ligands. Considering the disadvantages of homogeneous systems, basically related to difficulties in recycling, catalysts/product separation and catalyst deactivation via dimerization, the design of heterogeneous photo-catalysts is at the forefront of research nowadays. On the basis of these requirements, Metal Organic Frameworks (MOFs) or more widely speaking coordination polymers (CPs), have the potential to combine the advantages of being high selective and recyclable catalysts, along with additional feature to show shape-selectivity. Indeed, during the last two decades CPs have shown to bridge homo- and heterogeneous catalysis for a wide range of reactions.[4] Moreover, in contrast to classical semiconductors such as TiO_2, CdS, and ZnO, CPs exhibit excellent optical tunability. The latter has obtained in the first applications of these materials as photocatalysts.[5] Indeed, light harvesting can be drastically improved through the functionalization of the skeletal framework by light-sensible moieties[5d] or by incorporation into the channels/cages of molecular photo-sensitizers. In particular, several photoactive CPs/MOFs recently developed, have demonstrated catalytic activity in water oxidation,[6a] hydrogen evolution,[7] nanoparticle production,[8] and organic transformations.[6a,9]

With these precedents in mind and motivated by the fact that, to the best of our knowledge, only few examples of CPs have been reported for the photocatalytic reduction of CO_2,[6] we envisioned the design of new materials bearing both ruthenium complexes as the photosensible component and $[Co(bpy)_3]^{2+}$ (bpy= 2,2′-bipyridine) as catalytic site for the photoreduction of CO_2.[10] In this spirit, herein we report the synthesis and characterization of 3D honeycomb-like coordination polymers $\{[Co^{II}(bpy)_3][M^IRu(C_2O_4)_3]\}_n$ (M^I = Na (**1**), Li (**2**)) and their catalytic activity in UV-driven ($\lambda \leq 366$ nm) CO_2 reduction. The following features are remarkable: (*i*) the CPs **1** and **2** (see below) are selective photoactive catalysts in the UV induced reduction of CO_2 to CO (H_2 is not detected); (*ii*) these catalysts can be easily recovered and remain catalytically active for several consecutive runs; (*iii*) the catalytic activity is outstanding with the highest TON values reported to date.

Novel compounds **1** and **2** were obtained through reactions between $K_3[Ru(C_2O_4)_3]$, $[Co(bpy)_3](ClO_4)_2$ and NaCl/LiCl salts in aqueous media. Single-crystal analysis reveals that both are isostructural with the series of coordination polymers $\{[M^{II}(bpy)_3][M^IM^{III}(C_2O_4)_3]\}_n$ (M^{II} = Co, Fe, Ru, Ni; M^I= Na, Li; M^{III} = Cr, Fe)[11] which crystallize in a chiral cubic space group $P2_13$ (see Supporting Information, Table S1). The crystal structure consists of a 3D anionic backbone formed by tetra-coordinate oxalate ligands bridging Ru and Na/Li ions, with the cationic $[Co(bpy)_3]^{2+}$ acting as template (Fig. 1; Figs. S1-S8; Tables S2-S3). The anionic framework is a three-connected uninodal (10^3) - net of ***srs*** - type with honeycomb like channels running along the {111} direction $[Co(bpy)_3]^{2+}$ resides in large cages in a specific and high symmetrical mode.[11] The agreement between the experimental and

simulated powder X-ray diffraction (PXRD) patterns (Fig. S9-S10), and elemental analyses indicate high purity of both compounds.

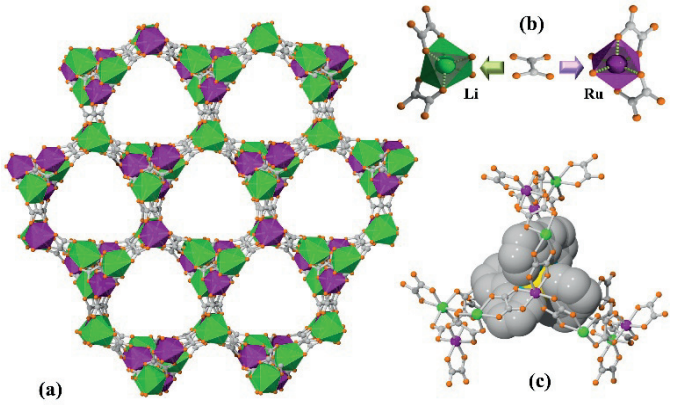

Fig.1 (a) 3D anionic network (left) of **2** with the honeycomb-like channels viewed along {111} direction (the template moieties were omitted for clarity). (b) The octahedral coordination environments of Li (green) and Ru (violet) atoms in **2**, and the oxalate linker exhibiting μ-tetracoordination mode. (c) The 3-fold anionic cage occupied by $[Co(bpy)_3]^{2+}$ guests.

The thermal stability of the synthesized compounds **1** and **2** was examined by thermal analysis, showing a relatively high thermal stability (up to 270 ºC) (Figs. S11-S12). On the other hand, adsorptive characterization performed using N_2 and CO_2 as probe molecules suggests that the CPs are non-porous (Fig. S14).

Significant features of **1** and **2**, derived from the structures in the solid state, are evidenced from their UV-Vis spectra and magnetic properties. The room temperature diffuse-reflectance UV-Vis-NIR spectra of **1** and **2** (Fig. 2a) are similar and consist of: (*i*) the strong absorptions in the UV region at 200-400 nm, associated with the π→π* transition of the bpy ligand and to the MLCT transition in the $[M^{I}Ru(C_2O_4)_3]^{2-}$ units and (*ii*) one weak absorption around 540 nm assigned to the $^4T_1 \rightarrow {}^4T_1(P)$ spin-allowed transition of d^7 (Co^{2+}) in $[Co(bpy)_3]^{2+}$ template, also appearing in the spectrum of $[Co(bpy)_3](ClO_4)_2$ high-spin (HS) complex.[12] However, the weaker and broad absorption band observed at *ca*. 910 nm (~ 5 L/mol·cm) in the spectrum of $[Co(bpy)_3](ClO_4)_2$, ascribed to the HS $^4T_1 \rightarrow {}^4T_1$ *d-d* transition, is absent in the spectra of **1** and **2** (probably lost in the background due to the lower concentration of the cobalt complex itself). This fact is consistent with very weak band observed in the spectrum of the analogous compound $\{[Co(bpy)_3][LiCr(C_2O_4)_3]\}_n$.[11c,13]

It is apparent from the electronic spectra that the photosensitizer ruthenium(III) oxalate framework $\{[M^{I}Ru(C_2O_4)_3]^{2-}\}_n$ does not affect the electronic configuration of the catalyst $[Co(bpy)_3]^{2+}$ remaining in the HS state. Magnetic properties of **1** and **2** are also informative about the properties of the pre-catalyst $[Co(bpy)_3]^{2+}$ located in the large cages of $\{[M^{I}Ru(C_2O_4)_3]^{2-}\}_n$ frameworks. Fig. S13a shows the magnetic susceptibilities (χT / $cm^3 \cdot mol^{-1} \cdot K$) as a function of the temperature for **1** and **2** resulting from subtracting the corresponding values of ruthenium(III) species in $\{[Zn(bpy)_3][M^{I}Ru(C_2O_4)_3]\}_n$ (M^{I}= Li, Na) which are the only spin carriers in this system (see Fig. S13b). Both χT curves indicate a strong temperature dependence arising from the typical magnetic behaviour of $[Co(bpy)_3]^{2+}$ in the $^4T_1$ HS state for which the orbital contribution to the magnetic moment is expected.

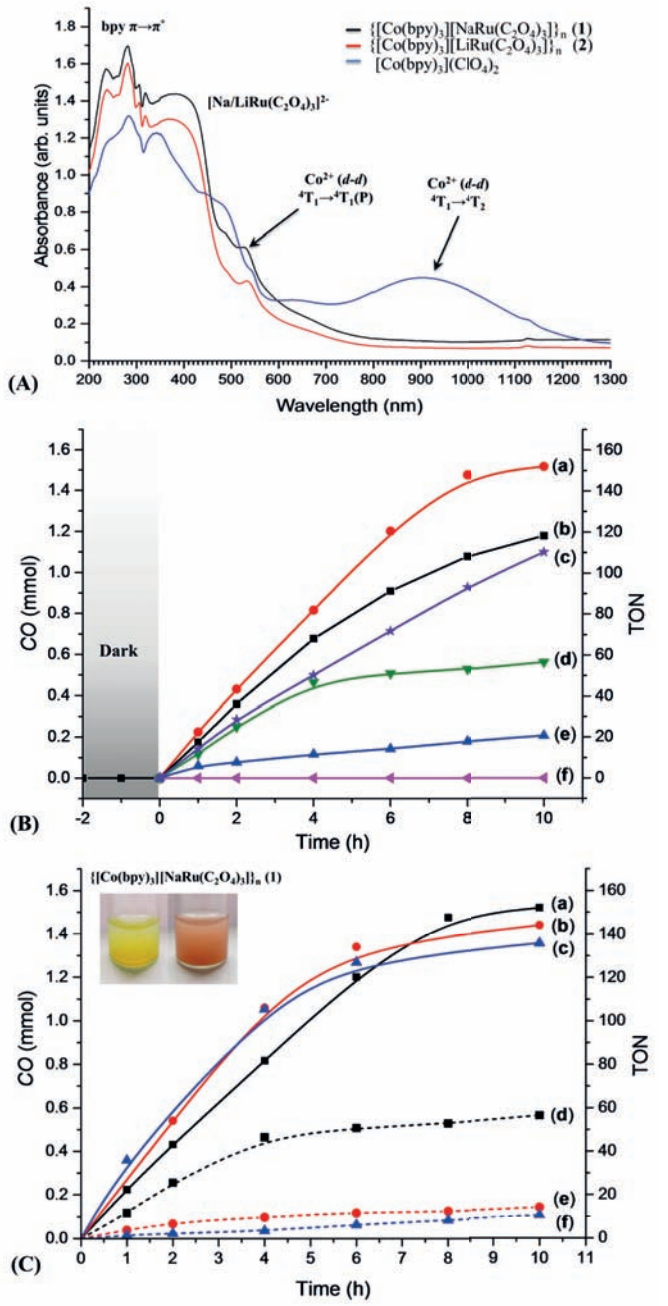

Fig.2 (*A*) Comparison of the room temperature UV-Vis-NIR diffuse reflectance spectrum for $\{[Co(bpy)_3][NaRu(C_2O_4)_3]\}_n$ (**1**), $\{[Co(bpy)_3][LiRu(C_2O_4)_3]\}_n$ (**2**) and HS $[Co(bpy)_3](ClO_4)_2$. (*B*) Evolution of CO as a function of the UV irradiation time over: (a) $\{[Co(bpy)_3][NaRu(C_2O_4)_3]\}_n$ (**1**) (red); (b) $[Co(bpy)_3][LiRu(C_2O_4)_3]$ (**2**) (black); (c) equivalent mixture of $[Co(bpy)_3](ClO_4)_2$ and $K_3[Ru(C_2O_4)_3]$ complexes (purple); (d) $[Co(bpy)_3](ClO_4)_2$ complex (green); (e) $K_3[Ru(C_2O_4)_3]$ complex (blue); and (f) UV light irradiation without a sample (pink). Photocatalytic conditions: 10 μmol photocatalysts, 10 mL of MeCN/TEA = 5:1 mixture. TON = CO mmol·10^3 /10 μmol of catalyst. (*C*) The kinetic plots of CO evolution over $\{[Co(bpy)_3][NaRu(C_2O_4)_3]\}_n$ (**1**) in 1st (a), 2nd (b), and 3rd (c) consecutive catalytic runs. The left insert illustrates the colour changes from yellow to reddish **1** catalyst.

At 300 K, the χT values of 2.95 $cm^3 \cdot mol^{-1} \cdot K$ (μ_{eff} = 4.87 μ_B) and 3.02 $cm^3 \cdot mol^{-1} \cdot K$ (μ_{eff} = 4.93 μ_B), much higher than that expected for a HS $t_{2g}^5 e_g^2$ electronic configuration, indicate a significant interaction in the $^4T_1$ states between the ground state ($t_{2g}^5 e_g^2$) and the excited state

($t_{2g}^4e_g^3$).[14] The χT temperature dependence curves are however different for both compounds. Significantly, at 10 K whilst for **1** χT value is 1.83 $cm^3 \cdot mol^{-1} \cdot K$ (μ_{eff} = 3.84 μ_B), in contrast for **2** lower value is found 0.91 $cm^3 \cdot mol^{-1} \cdot K$ (μ_{eff} = 2.7 μ_B). This fact points to $[Co(bpy)_3]^{2+}$ being in the ^2E_g low-spin (LS) state ($t_{2g}^6e_g^1$) and seems to indicate the existence of an equilibrium $^2E_1 \leftrightarrow {}^4T_1$ LS-HS states (spin crossover), with the HS species being preferred at higher temperatures. A similar behaviour has been found in the isostructural $\{[Co(bpy)_3][LiCr(C_2O_4)_3]\}_n$,[11c,13] and has been attributed to the *chemical pressure* of the metal oxalate framework towards the cationic hostages $[Co(bpy)_3]^{2+}$ destabilizing the $^4T_1$ ($t_{2g}^5e_g^2$) HS state of Co^{2+} ions to such an extent that they become in the $^2E_1$ ($t_{2g}^6e_g^1$) LS state. From these results, we conclude that the cobalt complexes encapsulated within the framework of the CP material are electronically activated with respect to the free cation $[Co(bpy)_3]^{2+}$ positively contribute to the energy transfer from the photosensitizer ruthenium framework.

The catalytic activity of **1** and **2** was examined in the photoreduction of CO_2 at mild reaction conditions (20 ºC, 1 atm CO_2) using triethylamine (TEA) as an electron donor. The reduction reactions were performed using a reactor equipped with a refrigerated 500 W Hg-lamp. As shown in Fig. 2b, the heterogeneous catalysts **1** and **2** selectively reduce CO_2 to CO (no traces of H_2, formic acid or methanol were detected), reaching 1.5 mmol (TON = 150) and 1.2 mmol (TON = 120) of CO, respectively, after 10 h of UV irradiation. Under the same reaction conditions, the precursor compounds $K_3[Ru(C_2O_4)_3]$ and $[Co(bpy)_3](ClO_4)_2$ as well as a mixture of $K_3[Ru(C_2O_4)_3]$ and $[Co(bpy)_3](ClO_4)_2$ also catalyse CO_2 reduction, *albeit* with lower yield (0.2 mmol, 0.6 mmol and 1.1 mmol, respectively) than that observed for the corresponding CPs. Indeed, Lehn and co-workers already demonstrated that mixtures of both components in the homogeneous phase are able to catalyse the selective photoreduction of CO_2 to CO.[10] Comparison between the catalytic performance of the CPs and their homogenous counterpart demonstrates that even a higher level of synergy between both species can be achieved when combined in a solid CP scaffold. Moreover, considering the non-porous nature of these CPs, one has to realize that the catalytic reaction would only take place at the catalyst surface, meaning that turnover frequency per exposed $[Co(bpy)_3]^{2+}$ site is several orders of magnitude higher in the CPs than in the homogenous system. In order to demonstrate that most reaction occurs at the external surface, we performed an additional catalytic test by crashing the CP **2** microcrystals, obtaining a 6% increment in catalytic activity (1.6 mmol, TON = 163).

On the other hand, no CO formation was observed when the reaction is performed in the dark or under UV light without heterogeneous catalyst, proving that the process is UV-induced and catalysed by **1** and **2** (Fig. 2b). Additional experiments performed in the absence of CO_2 demonstrate that CO formation is associated neither with the photodecomposition of the polymeric network nor with the photodegradation of TEA. Last but not least, when the supernatant solution, after removing the catalyst **1**, was again saturated with CO_2 and UV-irradiated for up to several hours, no catalysis was detected, demonstrating the absence of leaching and the full heterogeneous nature of the catalysts here presented.

Recyclability tests were performed with **1**, demonstrating that the heterogeneous catalyst remains active (Fig. 2c) over three consecutive runs. Remarkably, we observed a colour change in the solid from yellow to reddish during the first 8 h of the first photocatalytic run (Fig. 2c, right insert). PXRD patterns of the recovered solids demonstrate that this change in colour can be ascribed neither to a crystal-to-crystal transformation not to the amorphization of the framework (Fig. S16). This permanent colour change along with the higher initial activity observed after the first and second recycle indicate the formation of time-stable active species generated upon UV-irradiation.[15] Current work focuses on identifying the exact nature of these species.

In summary, we have reported the synthesis and characterization of two photoactive 3D coordination polymers $\{[Co(bpy)_3][M^IRu(C_2O_4)_3]\}_n$ (M^I = Li, Na) able to selectively photoreduce CO_2 to CO under UV-irradiation with circa 100 % selectivity. The new catalysts remains active for at least three consecutive runs reaching a total TON up to 150, the highest catalytic activity reported to date for this heterogeneous process.[16] This is an outstanding result considering the non-porous nature of these solids. Based on the well-known synergy between both components of the CPs,[10a] we propose the following reaction mechanism: *i*) electron transfer takes place from the photoexcited ruthenium complex to the cobalt catalyst; *ii*) the resulting intermediate $[Co(bpy)_3]^+$ is able to coordinate and reduce CO_2 to CO regenerating $[Co(bpy)_3]^{2+}$; *iii*) the sacrificial amine TEA donates the electron to the superficial oxidized ruthenium framework regenerating the sensitizer component of the CP. The high reduction potential of the couple $[Co(bpy)_3]^{2+}/[Co(bpy)_3]^+$,[17] along with the ability of cobalt(I) complexes for the activation of CO_2,[18] support the clean transformation of CO_2 into CO. This simple and potentially universal design strategy opens new opportunities for the catalytic photoreduction of CO_2. The ready accessibility and amenability of the $\{[Na/LiRu(C_2O_4)_3]^{2-}\}_n$ frameworks for functional tuning, makes them interesting heterogeneous catalysts for further applications as efficient photocatalysts and multifunctional photo - switchable materials. Studies directed to characterize the catalytic active species generated under reaction conditions are currently being carried out.

The authors thank FEDER and Spanish MINECO for financial support under projects MAT2010-15094, MAT2011-27573-CO4-02, MAT2013-40950-R, UCAN08-4E-008, MAT2012-38664-C02-1 and Consolider ORFEO. A.D. also thanks to Spanish *Ministerio de Educación, Cultura y Deporte* by the FPU grant (AP2008-03942).

Notes and references

[a] Departamento de Química Orgánica e Inorgánica, Universidad de Oviedo – CINN, 33006 Oviedo, Spain

[b] MALTA Consolider Team, Departamento de Física Aplicada, Universidad de Cantabria, 39005 Santander, Spain

[c] Departamento de Física, Universidad de Oviedo, 33007 Oviedo, Spain

[d] Catalysis Engineering, ChemE, Delft University of Technology, Julianalaan 136, 2628 BL Delft, The Netherlands

† Electronic Supplementary Information (ESI) available: Details about the samples preparation, thermal data (TG-DTA), powder XRD patterns, IR spectra, crystallographic information and additional figures. CCDC 892008 and 892009. See DOI: 10.1039/c000000x/

1 Y. Amao, *ChemCatChem*., 2011, **3**, 458.

2 (*a*) A. J. Morris, G. J. Meyer and E. Fujita, *Acc. Chem. Res.*, 2009, **42**, 1983; (*b*) M. D. Doherty, D. C. Grills, J. T. Muckerman, D. E. Polyansky and E. Fujita, *Coord. Chem. Rev.*, 2010, **254**, 2472; (*c*) H. Takeda and O. Ishitani, *Coord. Chem. Rev*., 2010, **254**, 346; (*d*) J. Schneider, H. Jia, J. T. Muckerman and E. Fujita, *Chem. Soc. Rev*., 2012, **41**, 2036; (*e*) C. D. Windle and R. N. Perutz, *Coord. Chem. Rev*., 2012, **256**, 2562; (*f*) B. Kumar, M. Llorente, T. D. Froehlich, A. Sathrum and C. P. Kubiak, *Annu. Rev. Phys. Chem*., 2012, **63**, 541.

3 (*a*) K. Kiyosawa, N. Shiraishi, T. Shimada, D. Masui, H. Tachibana, S. Takagi, O. Ishitani, D. A. Tryk and H. Inoue, *J. Phys. Chem. C*, 2009, **113**, 11667; (*b*) S. Sato, K. Koike, H. Inoue and O. Ishitani, *Photochem. Photobiol. Sci*., 2007, **6**, 454; (*c*) J. Grodkowski, T. Dhanasekaran, P. Neta, P. Hambright, B. S. Brunschwig, K. Shinozaki and E. Fujita, *J. Phys. Chem. A*, 2000, **104**, 11332; (*d*) J. Grodkowski and P. Neta, *J. Phys. Chem. A*, 2000, **104**, 1848; (*e*) J. Grodkowski, P. Neta, E. Fujita, A. Mahammed, L. Simkhovich and Z. Gross, *J. Phys. Chem. A*, 2002, **106**, 4772.

4 (*a*) A. Corma, H. García and F. X. Llabrés-Xamena, *Chem. Rev.,* 2010, **110**, 4606; (*b*) M. Yoon, R. Srirambalaji and K. Kim, *Chem. Rev.,* 2012, **112**,1196; (*c*) L. Ma, C. Abney and W. Lin, *Chem. Soc. Rev*., 2009, **38**, 1248; (*d*) J. Y. Lee, O. K. Farha, J. Roberts, K. A. Scheidt, S.-B. T. Nguyen and J. T. Hupp, *Chem. Soc. Rev*., 2009, **38**, 1450; (*e*) D. Farrusseng, S. Aguado and C. Pinel, *Angew. Chem., Int. Ed*., 2009, **48**, 7502; (*f*) A. Dhakshinamoorthy, A. M. Asiri and H. García, *Chem. Commun*., 2014, **50**, 12800; (*g*) Z. Wang, G. Chen and K. Ding, *Chem. Rev*., 2009, **109**, 322; (*h*) A. Dhakshinamoorthy and H. Garcia, *Chem. Soc. Rev.*, 2012, **41**, 5262; (*i*) P. Garcia-Garcia, M. Muller and A. Corma, *Chem. Sci*., 2014, **5**, 2979; (*j*) J. Gascon, A. Corma, F. Kapteijn and F. Llabrés i Xamena, *ACS Catalysis,* 2014, 361.

5 (*a*) C. A. Kent, B. P. Mehl, L. Ma, J. M. Papanikolas, T. J. Meyer and W. Lin, *J. Am. Chem. Soc*., 2010, **132**, 12767; (*b*) J.-L. Wang, C. Wang and W. Lin, *ACS Catal*., 2012, **2**, 2630; (*c*) M. A. Nasalevich, M. van der Veen, F. Kapteijn and J. Gascon, *CrystEngComm.,* 2014, **16**, 4919; (*d*) M. A. Nasalevich, M. G. Goesten, T. J. Savenije, F. Kapteijn and J. Gascon, *Chem. Commun.,* 2013, **49**, 10575.

6 (*a*) C. Wang, Z. Xie, K. E. deKrafft and W. Lin, *J. Am. Chem. Soc*., 2011, **133**, 13445; (*b*) Y. Fu, D. Sun, Y. Chen, R. Huang, Z. Ding, X. Fu and Z. Li, *Angew. Chem., Int. Ed*., 2012, **51**, 3364; (*c*) S. Wang, W. Yao, J. Lin, Z. Ding and X. Wang, *Angew. Chem., Int. Ed*., 2014, **53**, 1034; (*d*) L. Li, S. Zhang, L. Xu, J. Wang, L.-X. Shi, Z.-N. Chen, M. Hong and J. Luo, *Chem. Sci.*, 2014, **5**, 3808; (*e*) D. Sun, Y. Fu, W. Liu, L. Ye, D. Wang, L. Yang, X. Fu and Z. Li, *Chem. Eur. J*., 2013, **19**, 14279; (*f*) Y. Lee, S. Kim, J. K. Kang and S. M. Cohen, *Chem. Commun*., 2015, **51**, 5735.

7 (*a*) A. Fateeva, P. A. Chater, C. P. Ireland, A. A. Tahir, Y. Z. Khimyak, P. V. Wiper, J. R. Darwent and M. J. Rosseinsky, *Angew. Chem.,Int. Ed.*, 2012, **51**, 7440; (*b*) Y. Kataoka, K. Sato, Y. Miyazaki, K. Masuda, H. Tanaka, S. Naito and W. Mori, *Energy Environ. Sci*., 2009, **2**, 397; (*c*) C. Gomes Silva, I. Luz, F. Llabres i Xamena, A. Corma and H. García, *Chem.-Eur. J.*, 2010, **16**, 11133.

8 S. Han, Y. Wei and B. A. Grzybowski, *Chem.Eur. J*., 2013, **19**, 11194.

9 (*a*) C. Wang, K. E. deKrafft and W. Lin, *J. Am. Chem. Soc*., 2012, **134**, 7211; (*b*) P. Wu, C. He, J. Wang, X. Peng, X. Li, Y. An and C. Duan, *J. Am. Chem. Soc*., 2012, **134**, 14991.

10 Analogous homogeneous systems consisting of a mixture of ruthenium(II) and cobalt(II) complexes in the presence of donor reducing sacrificial amines, used by Lehn and co-workers in the pioneering studies, have shown to be active in the photo-catalytic reduction of CO_2: (*a*) J. M. Lehn and R. Ziessel, *Proc. Natl. Acad. Sci. USA*, 1982, **79**, 701. Hirose and co-workers have also reported the photo-catalytic activity of a partially heterogeneous catalytic system formed by a solution of $[Co(bpy)_3]^{2+}$ sensitized by $[Ru(bpy)_3]^{2+}$ fixed to cation exchange polymers: (*b*) T. Hirose, Y. Maeno and Y. Himeda, *J. Mol. Cat. A: Chem.*, 2003, **193**, 27; (*c*) An efficient cobalt molecular catalyst has been reported recently: S. L.-F. Chan, T. L. Lam, C. Yang, S.-C. Yan and N. M. Cheng, *Chem. Commun*., 2015, **51**, 7799.

11 (*a*) S. Decurtins, H. W. Schmalle, P. Schneuwly, J. Ensling and P. Gütlich, *J. Am. Chem. Soc*., 1994, **116**, 9521; (*b*) R. Andrés, M. Gruselle, B. Malézieux, M. Verdaguer and J. Vaissermann, *Inorg. Chem*., 1999, **38**, 4637; (*c*) R. Sieber, S. Decurtins, H. Stoeckli-Evans, C. Wilson, D. Yufit, J. A. K. Howard, S. C. Capelli and A. Hauser, *Chem.-Eur. J*., 2000, **6**, 361; (*d*) V. M. Russell, D. C. Craig, M. L. Scudder and I. G. Dance, *CrystEngComm*., 2000, **2**, 16.

12 R. A. Palmer and T. S. Piper, *Inorg. Chem*., 1966, **5**, 864.

13 A. Hauser, N. Amstutz, S. Delahaye, A. Sadki, S. Schenker, R. Sieber and M. Zerara, *Structure and Bonding Series 106: Optical Spectra and Chemical Bonding in Inorganic Compounds*, ed. D. M. P. Mingos, T. Schönherr, Springer, Berlin, 2004, vol. 1, p 81.

14 B. N. Figgis and J. Lewis, *Progress in Inorganic Chemistry: The magnetic properties of transition metal complexes*, ed. F. A. Cotton, John Wiley & Sons, New York, 1964, vol. 6, p 37.

15 Significantly, comparison of the XPS spectrum of this solid *vs* that shown for $\{[Co(bpy)_3][LiRu(C_2O_4)_3]\}_n$ (**2**) shows that the original binding energies peaks are shifted (see Fig. S15).

16 Other heterogeneous catalytic systems namely: (*a*) the cobalt containing imidazolate MOF (Co-ZIF-9) show much lower catalytic activity with simultaneous production of either H_2, $HCOO^-$ or MeOH (ref. 6c, TON = 89.6); (*b*) the catalyst $[Co(bpy)_3]^{2+}$ sensitized by $[Ru(bpy)_3]^{2+}$ fixed to cation exchange polymers (ref. 10b, TON = 125); (*c*) the doped MOF of $[Zr_6(\mu_3\text{-}O)_4(\mu_3\text{-}OH)_4(bpdc)_{6-x}(L)_x]$ (L = Re(I) complex) (ref. 6a, TON = 10.9); (*d*) $[TiO_8(OH)_4(bdc\text{-}NH_2)_6]$ (ref. 6b, TON = 162.8 μmol/g); (*e*) the coordination polymer $\{Y[Ir(ppy)_2(dcbpy)]_2[OH]\}$ reduces CO_2 to $HCOO^-$ under visible light (ref. 6d, TON = 708 μmol/g).

17 (*a*) J. Hawecker, J. M. Lehn and R. Ziessel, *J. Chem. Soc., Chem. Commun*., 1983, 536; (*b*) C. Creutz and N. Sutin, *Coord. Chem. Rev*., 1985, **64**, 321.

18 (a) E. Fujita, C. Creutz and D. J. Szalda, *J. Am. Chem. Soc.*, 1991, **113**, 343; (b) C. Creutz, H. A. Schwarzt, J. F. Wishart, E. Fujita and N. Sutin, *J. Am. Chem. Soc.*, 1991, **113**, 3361.

Supporting Information

3D Oxalate Bridged Coordination Polymers $\{[M^IRu(C_2O_4)_3]^{2-}\}_n$ (M^I = Li, Na) Templated by $[Co(bpy)_3]^{2+}$: Efficient Catalysts for Selective Photoreduction of CO_2 to CO

Alla Dikhtiarenko,[a] Rafael Valiente,[b] Jesús A. Blanco,[c] Jorge Gascon,[d] José R. García[a] and José Gimeno[a]

[a] *Departamento de Química Orgánica e Inorgánica, Universidad de Oviedo – CINN, 33006 Oviedo, Spain*
[b] *MALTA Consolider Team, Departamento de Física Aplicada, Universidad de Cantabria, 39005 Santander, Spain*
[c] *Departamento de Física, Universidad de Oviedo, 33007 Oviedo, Spain*
[d] *Catalysis Engineering, ChemE, Delft University of Technology, Julianalaan 136, 2628 BL Delft, The Netherlands*

This PDF file includes:

Section S1. Materials and Methods

Materials. The precursor complexes $[Co(bpy)_3](ClO_4)_2$ and $K_3[Ru(C_2O_4)_3]\cdot 4.5H_2O$ were prepared according to the literature methods previously reported for related compounds.[1-2]

Synthesis of $\{[Co(bpy)_3][NaRu(C_2O_4)_3]\}_n$ (1). An aqueous solution (5 mL) containing 0.2 g of $K_3[Ru(C_2O_4)_3]\cdot 4.5H_2O$ (0.25 mmol) and 0.02 g of NaCl (0.5 mmol) was added with stirring to a solution of $[Co(bpy)_3](ClO_4)_2$ (0.25 mmol) in 10 mL of water. A precipitate started to appear in a few minutes. After 1 h, the formed yellow solid was filtered off, washed with water and air dried to yield 0.31 g (72%)
Anal. Calc. for $C_{36}CoH_{24}N_6NaO_{12}Ru$: C, 47.18%; H, 2.62%; N, 9.17%.
Found: C, 47.1%; H, 2.7%; N, 9.2%.

Synthesis of $\{[Co(bpy)_3][LiRu(C_2O_4)_3]\}_n$ (2). Compound **2** was prepared by a similar procedure used for **1**, replacing NaCl by LiCl. The yield of yellow solid is 0.28 g (70%).
Anal. Calc. for $C_{36}CoH_{24}LiN_6O_{12}Ru$: C, 48.02%; H, 2.67%; N, 9.34%.
Found: C, 47.8%; H, 2.6%; N, 9.4%.

Single Crystal Growth. Single crystals of **1** and **2** were obtained by crystallization in a tetramethoxysilane gel containing $K_3[Ru(C_2O_4)_3]\cdot 4.5H_2O$ (0.01 M). When the gel is formed, a water solution containing a stoichiometric amount of $[Co(bpy)_3](ClO_4)_2$ and NaCl (**1**)/LiCl (**2**) were added. After one month, yellow tetrahedral shaped crystals are formed.

Structural Characterization. Tetrahedral shaped single crystals of **1** and **2** were collected and mounted on an Oxford-Gemini X-ray Diffractometer equipped with graphite-monochromated CuK_α radiation (λ = 1.5418 Å) and MoK_α radiation (λ = 0.7107 Å). X-Ray diffraction data were collected at 293 K. The CrysAlisPro program was used for cell refinement and data reduction. Images were collected at a 55 mm fixed crystal-detector distance, using the oscillation method, with 1° oscillation and variable exposure time per image. The structure solution was solved by direct methods using the SIR92 program.[3] Refinement was performed by SHELX-97[4] using full-matrix least squares on F^2. All non-H atoms were anisotropically refined. The Flack`s absolute parameter (x) was used to determine the space group of compounds.[5]
CCDC892008-892009 contains the supplementary crystallographic data for this paper. These data can be obtained free of charge from The Cambridge Crystallographic Data Centre via www.ccdc.cam.ac.uk/data_request/cif.
The topological analysis of **1** and **2** polymeric frameworks was performed using TOPOS4.0 software package.[6]

Characterization Methods. X-ray powder patterns were collected with a X´Pert Philips X-ray diffractometer (CuK_α radiation, λ = 1.5418 Å) at room temperature. The powder diffraction patterns

indicate that all compounds are isostructural and show analogous patterns to the simulated patterns from the atomic coordinates of the crystal structures of **1** and **2**.

A Mettler-Toledo TGA/SDTA851 was used for the thermal analyses air dynamic atmosphere (50 mL/min) at a heating rate of 10 °C/min. Approximately 10 mg of powder sample was thermally treated, and blank runs were performed.

Microanalyses (C, H, N) were carried out by the use of a Perkin-Elmer model 2400B elemental analyzer.

The N_2 and CO_2 adsorption measurements were performed on a Micromeritics ASAP 2020 surface-area and pore-size analyzer. The air dried sample was directly outgassed at 240 °C for 24 h under vacuum prior to measurements.

A Cary 6000i (Varian) spectrophotometer was used to measure diffuse reflectance spectra in the range 200-1800 nm using a polytetrauoroethylene (PTFE)-coated integrating sphere.

DC magnetic susceptibility measurements were performed using a Quantum Design SQUID magnetometer whilst heating from 2 to 300 K at 10 and 1 kOe, after cooling in either the presence (field cooling, FC) or the absence (zero field cooling, ZFC) of the applied magnetic field. Initially all magnetic curves have been performed with the empty (diamagnetic) sample holder. Next, the same measurement procedure was repeated with the sample. Then the two magnetic signals have been subtracted from each other, yielding to the magnetization due only to the sample.

Photochemical Experiments. Photocatalytic activities of compounds **1** and **2** were evaluated in the photoreduction of CO_2 to CO. Supercritical-fluid grade CO_2 was purchased from AirLiquid (Spain) to avoid any hydrocarbon contamination. It was certified maximum hydrocarbons less than 20 ppb. All experiments were conducted at room temperature. In each experiment, 10 mg (10 μmol) of heterogeneous catalyst **1** or 9 mg (10 μmol) of heterogeneous catalyst **2** was dispersed in 10 mL of CH3CN (MeCN) / Triethylamine (TEA) (5:1, v/v) mixed solvent. The experiments were carried out in a 100 mL gastight photolysis photoreaction cell that was custom-designed in order to allow purging and irradiation of the suspension. The gastight cell was a 100 mL two-necked, flat-bottomed flask equipped with a quartz window and water refrigerator.

The cell volume was 100 mL, of which 90 mL was occupied by gases. Prior to photolysis, CO_2 was bubbled through the reactor for at least 30 min to purge air and to saturate the solution. A magnetic stirrer agitated the catalyst suspended solution at the bottom to prevent sedimentation of the catalyst. The system was irradiated by UV light at room temperature with 500 W mercury lamp operated with maxima emission at 366 nm (HELIOS ITALQUARTZ Apparatus, model UV50F – 85P503I5) for 10 h. The evolution of CO during the reaction was monitored by regular gas sampling. Gas samples (0.5 mL) were taken from the cell through a septum using gastight syringe and analyzed by mass spectrometry. Mass spectrometry analyses were performed using an OmniStar™ (Pfeiffer Vacuum) gas analysis module connected to AutoChem II 2920 (Micromeritics) catalyst characterization system. A cold trap was used with He as the carrier gas. Each gas was identified and quantified using the working curve, which had been previously obtained using standard CO gas (AirLiquid). Blank reactions were conducted to ensure that CO production was due to the photoreduction of CO_2, and to

eliminate surrounding interference. One blank was UV-illuminated without the catalyst, and another was in the dark with the catalyst and CO_2 under the same experimental conditions. Negligible quantity of CO was detected in the above two blank tests. After the catalyst's sedimentation, the liquid phase was analyzed in GC/FID (Hewlett Packard) equipped with Beta DEX 120 30 m (30m x 0.25 mm x 0.25 μm) long column. Each analysis did not detect the formation of addition products such as CH_3OH, CH_2O or HCOOH. The repetitive photoreduction during three consecutive cycles was performed. After each cycle, the catalyst was washed with CH_3CN and reused in subsequent cycles.

The crystallinity of the powder solids after each catalytic runs was checked by powder X-ray diffraction. The samples have been mounted on nylon CryoLoop and measured on an Oxford-Gemini X-ray diffractometer equipped with graphite-monochromatic CuK_α radiation (λ = 1.5418 Å) at room temperature.

Section S2. Crystallographic data

Table S1. Crystallographic data for **1** and **2.**

Compound	1	2
Formula	$C_{36}H_{24}CoN_6NaO_{12}Ru$	$C_{36}H_{24}CoLiN_6O_{12}Ru$
M_r (g/mol)	915.6	899.55
Temperature (^{0}C)	293(2)	293(2)
Wavelength (Å)	0.7107	1.54184
Crystal system	cubic	cubic
Space group	$P2_13$	$P2_13$
Unit cell dimensions		
a (Å)	15.6996(3)	15.4877(1)
B (Å)	15.6996(3)	15.4877(1)
c (Å)	15.6996(3)	15.4877(1)
α (degree)	90.0	90.0
V (Å^3)	3869.6(1)	3715.02(4)
Z	4	4
D_{calcd} (g/cm^3)	1.572	1.608
F(000)	1840	1808
μ (mm^{-1})	0.90	7.413
Crystal size (mm^3)	0.2×0.1×0.1	0.3×0.2×0.2
Θ range for data (^{0})	3.6 to 30.9	4.0 to 70.2
Index ranges	-13 ≤ h ≤ 13 -3 ≤ k ≤ 20 -21 ≤ l ≤ 6	-10 ≤ h ≤ 14 -17 ≤ k ≤ 18 -11 ≤ l ≤ 14
Reflection collected	3743	4505
Independent reflections	3023[R(int) = 0.043]	2227[R(int) = 0.024]
Completeness to ϑ_{max}	99.5%	99.7%
Refinement method	Full-matrix least-squares on F^2	Full-matrix least-squares on F^2
Data/restraints/parameters	3743 / 0 / 172	2270 / 0 / 173
Final R indices [I>2σ(I)]	R1 = 0.055, wR2 = 0.112	R1 = 0.048, wR2 = 0.137
R indices (all data)	R1 = 0.073, wR2 = 0.119	R1 = 0.049, wR2 = 0.139
Largest diff. peak and hole (e.Å^{-3})	1.01 and -0.58	1.63 and -0.49
Flack parameter	-0.13(3)	0.48(1)
Goodness-of-fit on F^2	1.121	1.124

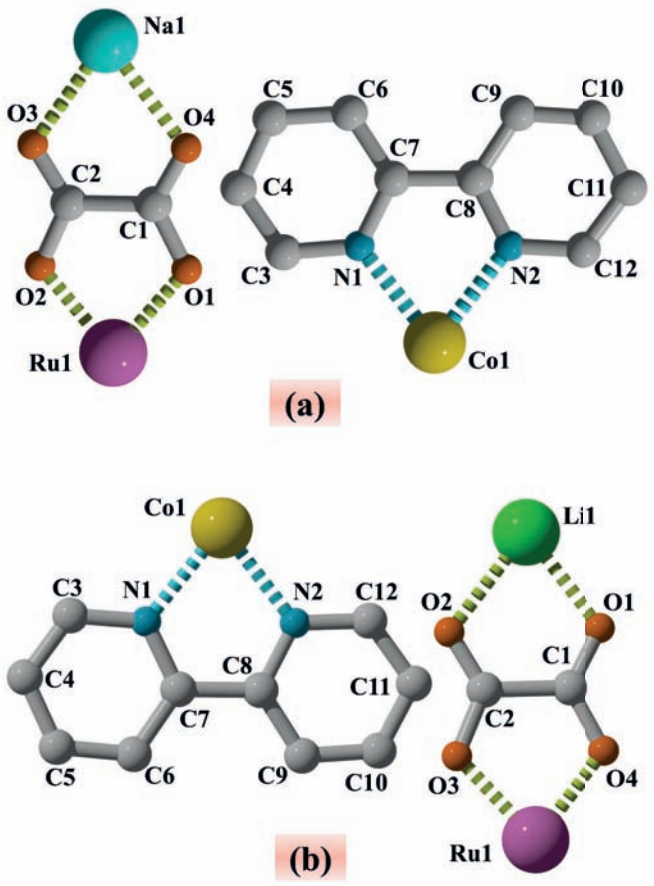

Figure S1. Asymmetric unit with atomic numbering of $\{[Co(bpy)_3][NaRu(C_2O_4)_3]\}_n$ **(1)** (a) and $\{[Co(bpy)_3][LiRu(C_2O_4)_3]\}_n$ **(2)** (b). H atoms were omitted for clarity.

Table S2. Selected Bond Distances (Å) and Angles (degree) for **1.**

Bond Length (Å)							
Ru1—O1^{i}	2.013 (3)	*Average*	*2.020(7)*	O1—C1	1.283 (5)	*Average*	*1.249(40)*
Ru1—O1	2.013 (3)			O2—C2	1.297 (5)		
Ru1—O1^{ii}	2.013 (3)			O3—C2	1.207 (5)		
Ru1—O2^{i}	2.027 (3)			O4—C1	1.212 (5)		
Ru1—O2	2.027 (3)			N1—C7	1.330 (5)	*Average*	*1.337(7)*
Ru1—O2^{ii}	2.027 (3)			N1—C3	1.349 (6)		
Co1—N1^{iii}	2.168 (3)	*Average*	*2.171(3)*	N2—C12	1.330 (6)		
Co1—N1	2.168 (3)			N2—C8	1.340 (6)		
Co1—N1^{iv}	2.168 (3)			C1—C2	1.547 (5)		
Co1—N2^{iii}	2.174 (3)			C3—C4	1.386 (7)	*Average*	*1.387(24)*
Co1—N2	2.174 (3)			C4—C5	1.360 (9)		
Co1—N2^{iv}	2.174 (3)			C5—C6	1.404 (8)		
Na1—O4^{v}	2.334 (4)	*Average*	*2.348(14)*	C6—C7	1.388 (7)		
Na1—O4^{vi}	2.334 (4)			C7—C8	1.473 (6)		
Na1—O4	2.334 (4)			C8—C9	1.386 (6)		
Na1—O3^{v}	2.363 (4)			C9—C10	1.339 (9)		
Na1—O3	2.363 (4)			C10—C11	1.394 (10)		
Na1—O3^{vi}	2.363 (4)			C11—C12	1.359 (8)		
Angles (^{0})							
O1^{i}—Ru1—O1	93.11 (12)			N1^{iv}—Co1—N2	165.90 (14)		
O1^{i}—Ru1—O1^{ii}	93.11 (12)			N2^{iii}—Co1—N2	94.16 (13)		
O1—Ru1—O1^{ii}	93.11 (12)			N1^{iii}—Co1—N2^{iv}	165.90 (14)		
O1^{i}—Ru1—O2^{i}	82.03 (12)			N1—Co1—N2^{iv}	96.37 (14)		
O1—Ru1—O2^{i}	88.57 (13)			N1^{iv}—Co1—N2^{iv}	75.78 (14)		
O1^{ii}—Ru1—O2^{i}	174.94 (13)			N2^{iii}—Co1—N2^{iv}	94.16 (13)		
O1^{i}—Ru1—O2	174.94 (13)			N2—Co1—N2^{iv}	94.16 (13)		
O1—Ru1—O2	82.03 (12)			O4^{v}—Na1—O4^{vi}	90.17 (16)		
O1^{ii}—Ru1—O2	88.57 (13)			O4^{v}—Na1—O4	90.17 (16)		
O2^{i}—Ru1—O2	96.39 (12)			O4^{vi}—Na1—O4	90.17 (16)		
O1^{i}—Ru1—O2^{ii}	88.57 (13)			O4^{v}—Na1—O3^{v}	72.69 (11)		
O1—Ru1—O2^{ii}	174.94 (13)			O4^{vi}—Na1—O3^{v}	93.85 (13)		
O1^{ii}—Ru1—O2^{ii}	82.03 (12)			O4—Na1—O3^{v}	162.39 (15)		
O2^{i}—Ru1—O2^{ii}	96.39 (12)			O4^{v}—Na1—O3	93.85 (13)		
O2—Ru1—O2^{ii}	96.39 (12)			O4^{vi}—Na1—O3	162.39 (15)		
N1^{iii}—Co1—N1	95.28 (13)			O4—Na1—O3	72.69 (11)		
N1^{iii}—Co1—N1^{iv}	95.28 (13)			O3^{v}—Na1—O3	103.73 (13)		
N1—Co1—N1^{iv}	95.28 (13)			O4^{v}—Na1—O3^{vi}	162.39 (15)		
N1^{iii}—Co1—N2^{iii}	75.78 (14)			O4^{vi}—Na1—O3^{vi}	72.69 (11)		
N1—Co1—N2^{iii}	165.90 (14)			O4—Na1—O3^{vi}	93.85 (13)		
N1^{iv}—Co1—N2^{iii}	96.37 (14)			O3^{v}—Na1—O3^{vi}	103.73 (13)		
N1^{iii}—Co1—N2	96.37 (14)			O3—Na1—O3^{vi}	103.73 (13)		
N1—Co1—N2	75.78 (14)						

Symmetry codes: (i) −*z*, *x*+1/2, −*y*+1/2; (ii) *y*−1/2, −*z*+1/2, −*x*; (iii) *y*, *z*, *x*; (iv) *z*, *x*, *y*; (v) *z*+1/2,−*x*+1/2, −*y*; (vi) −*y*+1/2, −*z*, *x*−1/2.

Table S3. Selected Bond Distances (Å) and Angles (degree) for **2.**

Bond Length (Å)							
Ru1—O4^{i}	2.033 (4)	*Average*	*2.039(6)*	N1—C7	1.340 (8)	*Average*	*1.342(7)*
Ru1—O4	2.033 (4)			N1—C3	1.355 (8)		
Ru1—O4^{ii}	2.033 (4)			N2—C12	1.328 (9)		
Ru1—O3	2.045 (4)			N2—C8	1.344 (9)		
Ru1—O3^{i}	2.045 (4)			O1—C1	1.217 (8)	*Average*	*1.25(4)*
Ru1—O3^{ii}	2.045 (4)			O2—C2	1.207 (8)		
Co1—N2^{iii}	2.145 (5)	*Average*	*2.148(3)*	O3—C2	1.303 (8)		
Co1—N2^{iv}	2.145 (5)			O4—C1	1.281 (7)		
Co1—N2	2.145 (5)			C1—C2	1.548 (8)		
Co1—N1^{iv}	2.151 (5)			C3—C4	1.365 (10)	*Average*	*1.38(2)*
Co1—N1	2.151 (5)			C4—C5	1.367 (14)		
Co1—N1^{iii}	2.151 (5)			C5—C6	1.382 (13)		
Li1—O1^{v}	2.162 (12)	*Average*	*2.22(6)*	C6—C7	1.404 (9)		
Li1—O1^{vi}	2.162 (12)			C7—C8	1.472 (9)		
Li1—O1	2.162 (12)			C8—C9	1.388 (9)		
Li1—O2	2.278 (10)			C9—C10	1.367 (14)		
Li1—O2^{vi}	2.278 (10)			C10—C11	1.354 (16)		
Li1—O2^{v}	2.278 (10)			C11—C12	1.372 (12)		
Angles (^{0})							
O4^{ii}—Ru1—O3	88.36 (19)			N2—Co1—N1	76.6 (2)		
O4^{i}—Ru1—O3^{i}	81.34 (17)			N1^{iv}—Co1—N1	94.69 (19)		
O4—Ru1—O3^{i}	88.36 (19)			N2^{iii}—Co1—N1^{iii}	76.6 (2)		
O4^{ii}—Ru1—O3^{i}	174.79 (19)			N2^{iv}—Co1—N1^{iii}	167.3 (2)		
O3—Ru1—O3^{i}	96.67 (17)			N2—Co1—N1^{iii}	95.2 (2)		
O4^{i}—Ru1—O3^{ii}	88.36 (19)			N1^{iv}—Co1—N1^{iii}	94.69 (19)		
O4—Ru1—O3^{ii}	174.79 (19)			N1—Co1—N1^{iii}	94.69 (19)		
O4^{ii}—Ru1—O3^{ii}	81.34 (17)			O1^{v}—Li1—O1^{vi}	91.0 (6)		
O3—Ru1—O3^{ii}	96.67 (17)			O1^{v}—Li1—O1	91.0 (6)		
O3^{i}—Ru1—O3^{ii}	96.67 (17)			O1^{vi}—Li1—O1	91.0 (6)		
N2^{iii}—Co1—N2^{iv}	94.9 (2)			O1^{v}—Li1—O2	93.6 (2)		
N2^{iii}—Co1—N2	94.9 (2)			O1^{vi}—Li1—O2	165.8 (4)		
N2^{iv}—Co1—N2	94.9 (2)			O1—Li1—O2	75.48 (17)		
N2^{iii}—Co1—N1^{iv}	95.2 (2)			O1^{v}—Li1—O2^{vi}	165.8 (4)		
N2^{iv}—Co1—N1^{iv}	76.6 (2)			O1^{vi}—Li1—O2^{vi}	75.48 (17)		
N2—Co1—N1^{iv}	167.3 (2)			O2—Li1—O2^{v}	100.6 (5)		
N2^{iii}—Co1—N1	167.3 (2)			O2^{vi}—Li1—O2^{v}	100.6 (5)		
N2^{iv}—Co1—N1	95.2 (2)						

Symmetry codes: (i) −y+1/2, −z+1, x+1/2; (ii) z−1/2, −x+1/2, −y+1; (iii) −z+1/2, −x+1, y−1/2; (iv)−y+1, z+1/2, −x+1/2; (v) y−1, z+1, x; (vi) z, x+1, y−1.

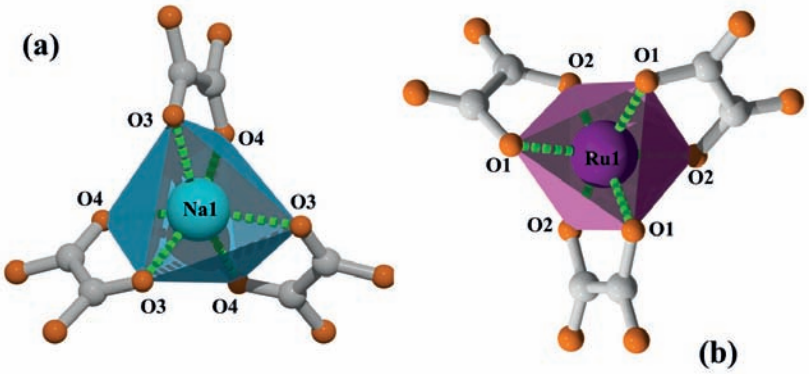

Figure S2. Coordination environments of Na (a) and Ru (b) atoms in anionic framework $\{[NaRu(C_2O_4)_3]^{2-}\}_n$ of **1**. The atoms: C is grey, O is red, Na is blue, Ru is violet.

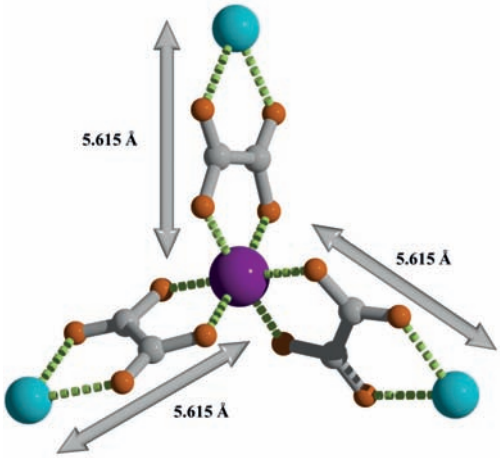

Figure S3. View of part of heterometallic anionic network $\{[NaRu(C_2O_4)_3]^{2-}\}_n$ of **1** showing equivalent distances between Ru and Na centers. The atoms: C is grey, O is red, Na is blue, Ru is violet.

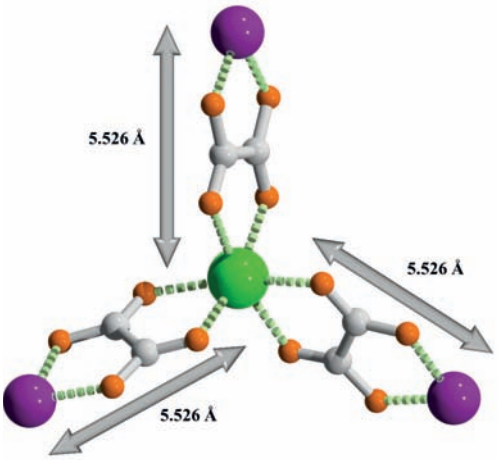

Figure S4. View of part of heterometallic anionic network $\{[LiRu(C_2O_4)_3]^{2-}\}_n$ of **2** showing equivalent distances between Ru and Li centers. The atoms: C is grey, O is red, Li is green, Ru is violet.

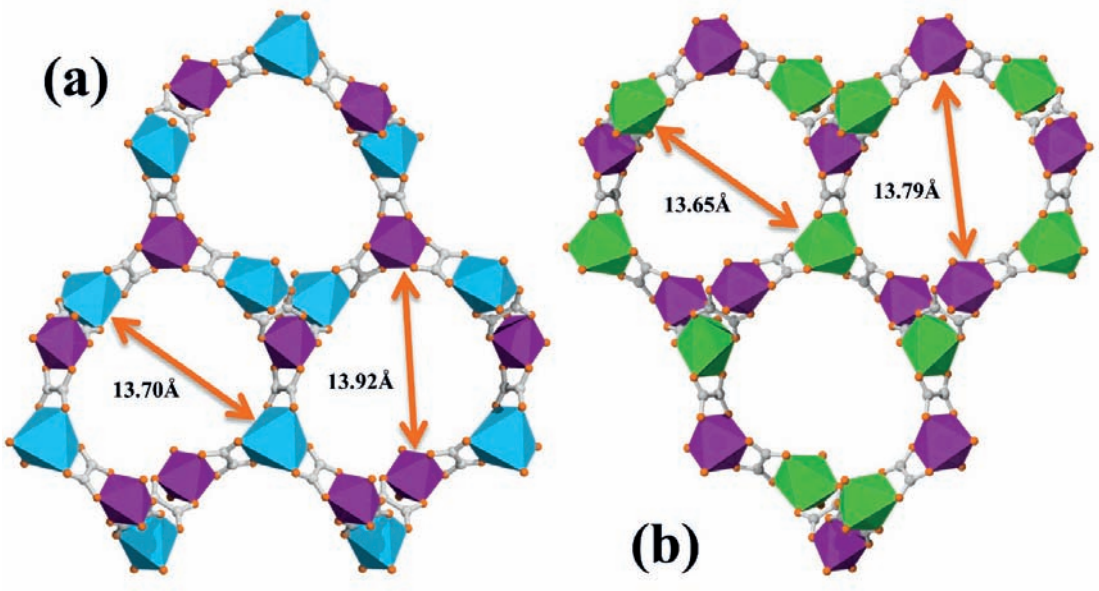

Figure S5. {111}-directed view of honeycombed channels of $\{[NaRu(C_2O_4)_3]^{2-}\}_n$ (**1**) (a) and $\{[LiRu(C_2O_4)_3]^{2-}\}_n$ (**2**) (b) anionic networks and their dimensions. The atoms: C is grey, O is red, Na is blue, Li is green, Ru is violet.

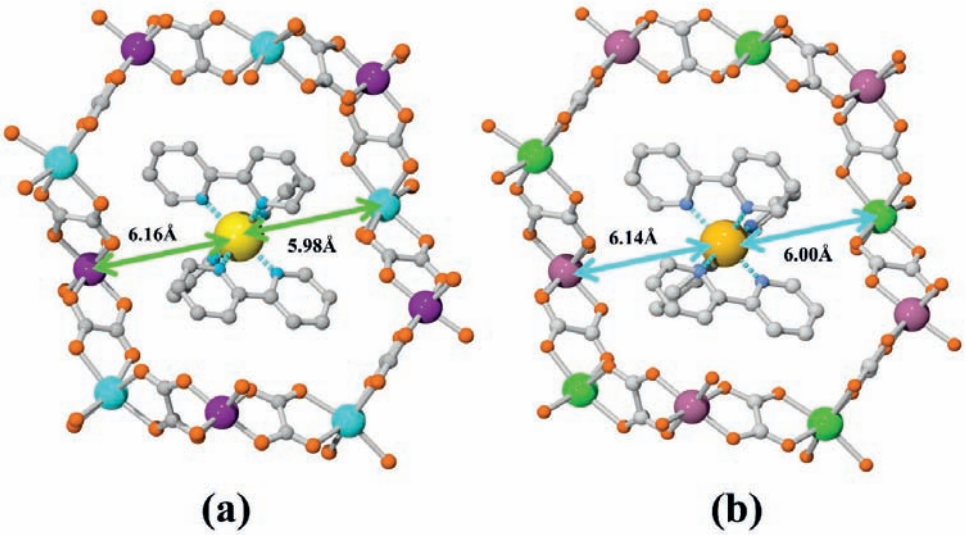

Figure S6. View of cationic $[Co(bpy)_3]^{2+}$ template residing in anionic channels of $\{[NaRu(C_2O_4)_3]^{2-}\}_n$ (**1**) (a) and $\{[LiRu(C_2O_4)_3]^{2-}\}_n$ (**2**) (b) anionic networks, shown the distances between Co atom to Ru and Na/Li centers. The atoms: C is grey, O is red, Na is blue, Li is green, Ru is violet.

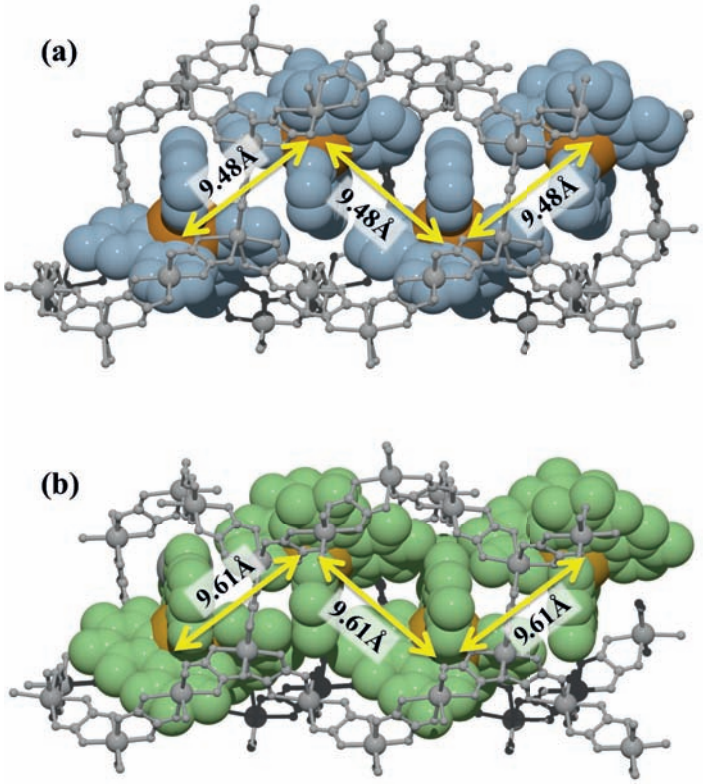

Figure S7. Space filling representation of the packing mode of the $[Co(bpy)_3]^{2+}$ cationic complexes in 3D anionic array of $\{[Co(bpy)_3][NaRu(C_2O_4)_3]\}_n$ (**1**) (a) and $\{[Co(bpy)_3][LiRu(C_2O_4)_3]\}_n$ (**2**) (b). The distances between Co – Co centers are shown as a numbers. The hydrogen atoms have been omitted for clarity.

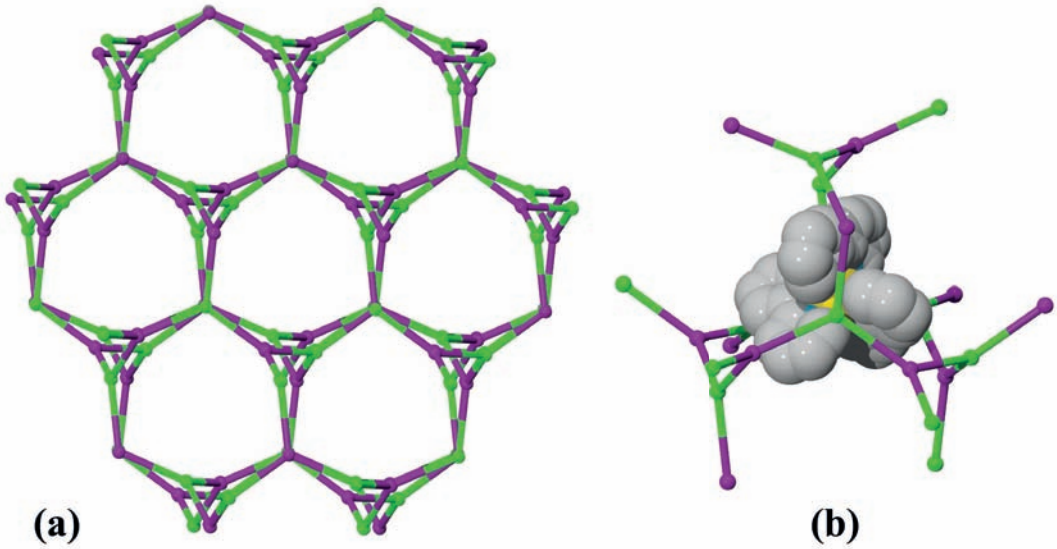

Figure S8. (a) Topological representation of 3D anionic network with the honeycomb-like channels viewed along {111} direction (the template moieties were omitted for clarity); (b) the topological representation of 3-fold anionic cage occupied by $[Co(bpy)_3]^{2+}$ guests.

Section S3. Characterization data

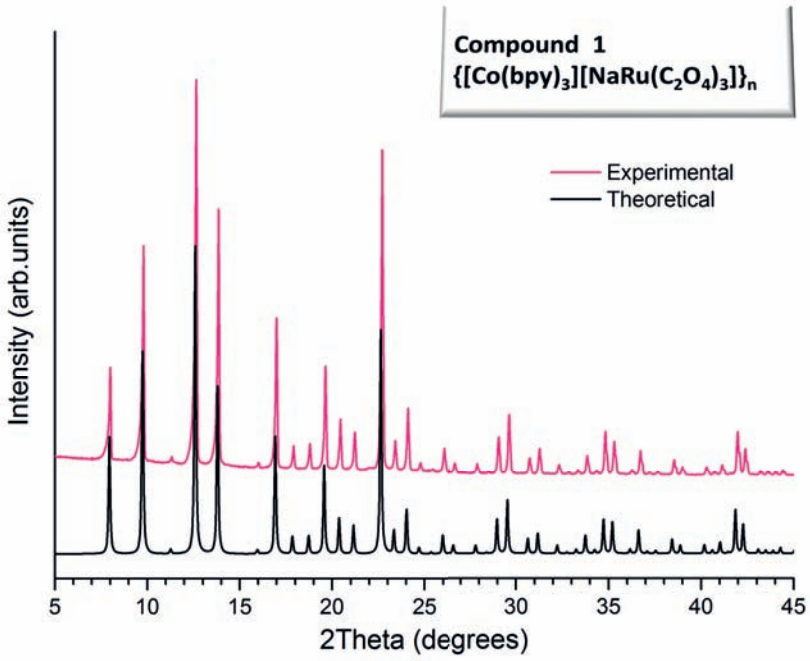

Figure S9. Experimental X-ray powder diffraction pattern of $\{[Co(bpy)_3][NaRu(C_2O_4)_3]\}_n$ **(1)** and simulated pattern calculated from single crystal data.

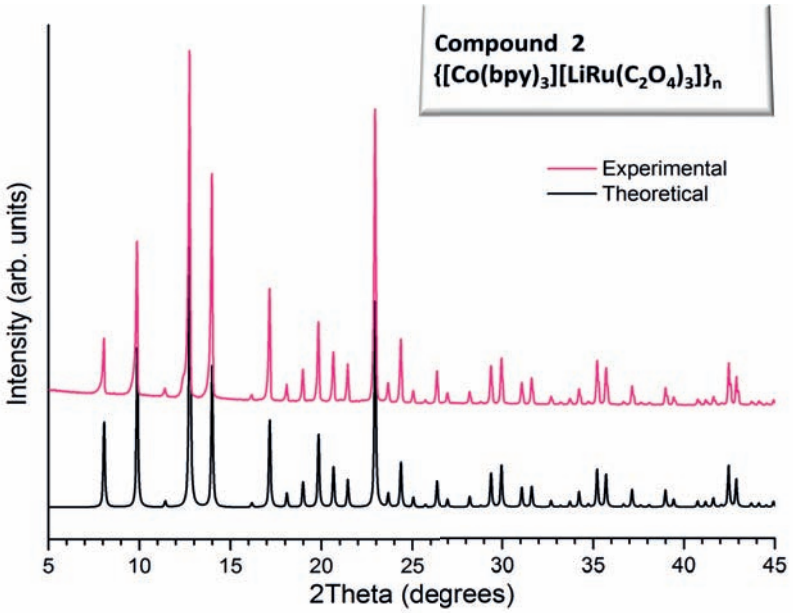

Figure S10. Experimental X-ray powder diffraction pattern of $\{[Co(bpy)_3][LiRu(C_2O_4)_3]\}_n$ **(2)** and simulated pattern calculated from single crystal data.

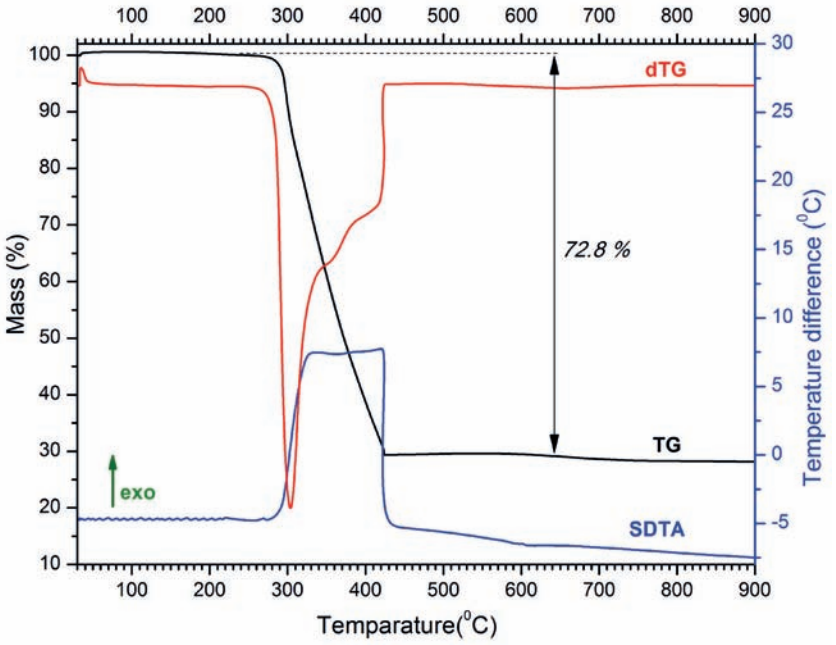

Figure S11. TG, dTG and SDTA curves of $\{[Co(bpy)_3][NaRu(C_2O_4)_3]\}_n$ (**1**) in air.

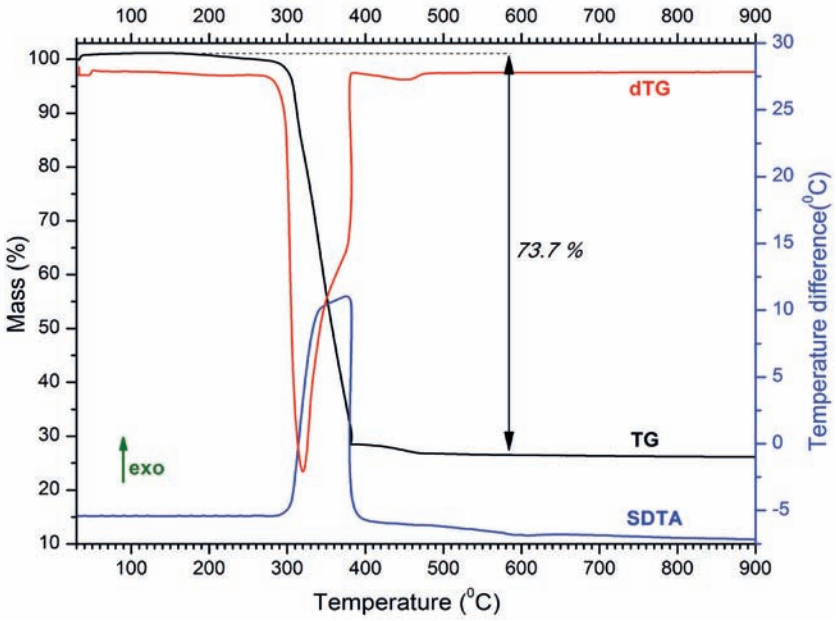

Figure S12. TG, dTG and SDTA curves of $\{[Co(bpy)_3][LiRu(C_2O_4)_3]\}_n$ (**2**) in air.

The results of thermogravimetric analysis (TGA) reveal that decomposition of coordination polymers **1** and **2** occurs on a single step in the range 270−440 ºC with the total mass losses of 72.8% (Calc. for **1**: 73.03%) and 73.7% (Calc. for **2**: 74.34%) which are associated with a broad exothermic bounds on the SDTA curves, corresponding to simultaneous degradation of organic matter and oxalate ligand.

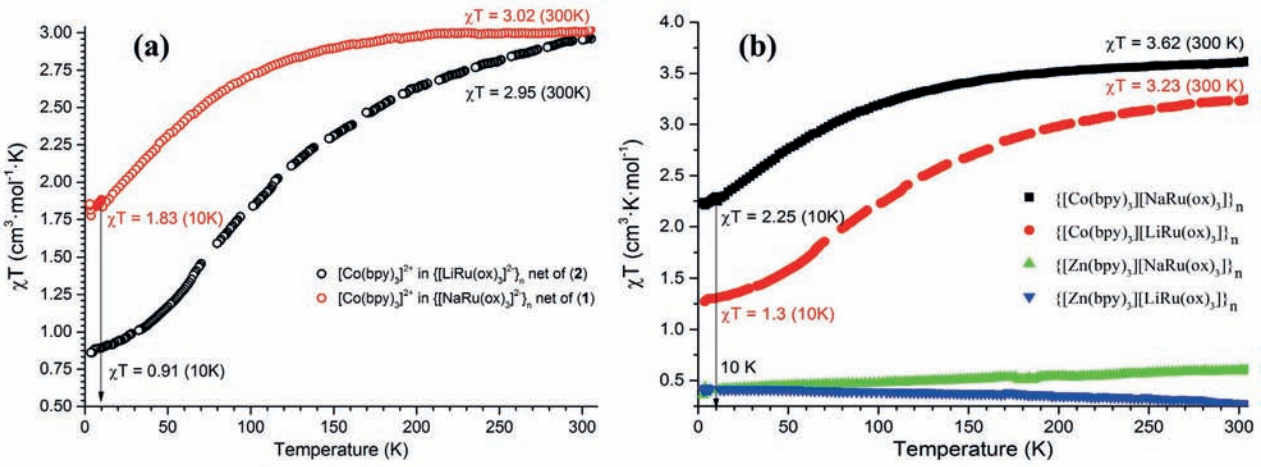

Figure S13. (a) Magnetic susceptibilities of $\{[Co(bpy)_3][NaRu(C_2O_4)_3]\}_n$ (**1**) and $\{[Co(bpy)_3][LiRu(C_2O_4)_3]\}_n$ (**2**) with extraction of $\{[Zn(bpy)_3][NaRu(C_2O_4)_3]\}_n$ and $\{[Zn(bpy)_3][LiRu(C_2O_4)_3]\}_n$ contribution*. (b) Magnetic susceptibilities of $\{[Co(bpy)_3][NaRu(C_2O_4)_3]\}_n$ (**1**), $\{[Co(bpy)_3][LiRu(C_2O_4)_3]\}_n$ (**2**), $\{[Zn(bpy)_3][NaRu(C_2O_4)_3]\}_n$ and $\{[Zn(bpy)_3][LiRu(C_2O_4)_3]\}_n$ plotted as χT *vs* temperature.

* The χT of the latter is almost temperature independent with values in the range of 0.1-0.5 $cm^3 \cdot mol^{-1} \cdot K$ (μ_{eff} ~ 0.89-1.9 μB) between 10 K and 300 K. These are the expected typical values for isolated $[Ru(C_2O_4)_3]^{3-}$ complex (according to Kotani calculations for a $^2T_{2g}$ ground state).[7]

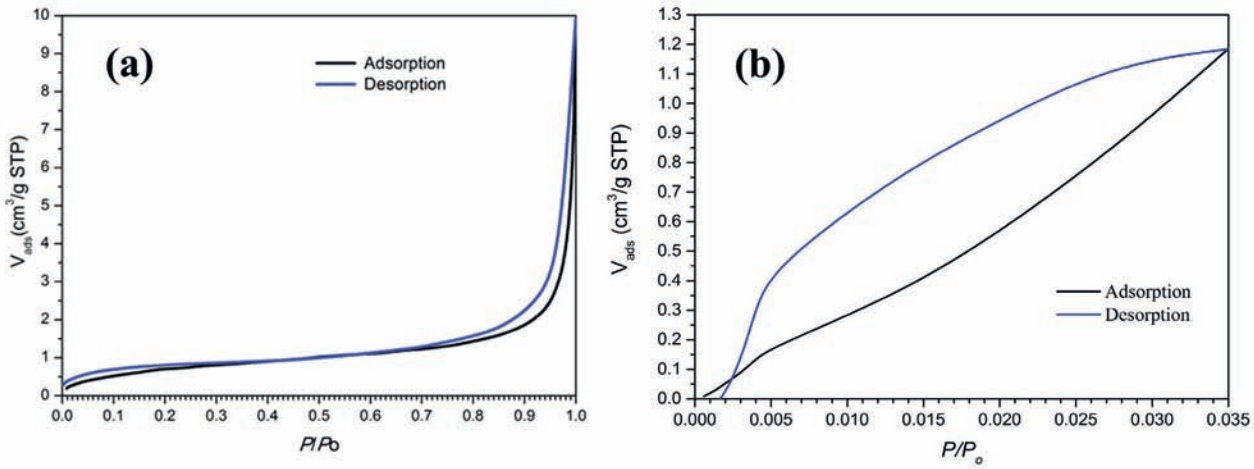

Figure S14. (a) N_2 adsorption (black solid line) and desorption (blue solid line) isotherms at 77 K on $\{[Co(bpy)_3][LiRu(C_2O_4)_3]\}_n$ (**2**). (b) CO_2 adsorption (black solid line) and desorption (blue solid line) isotherms at 273 K on $\{[Co(bpy)_3][LiRu(C_2O_4)_3]\}_n$ (**2**).

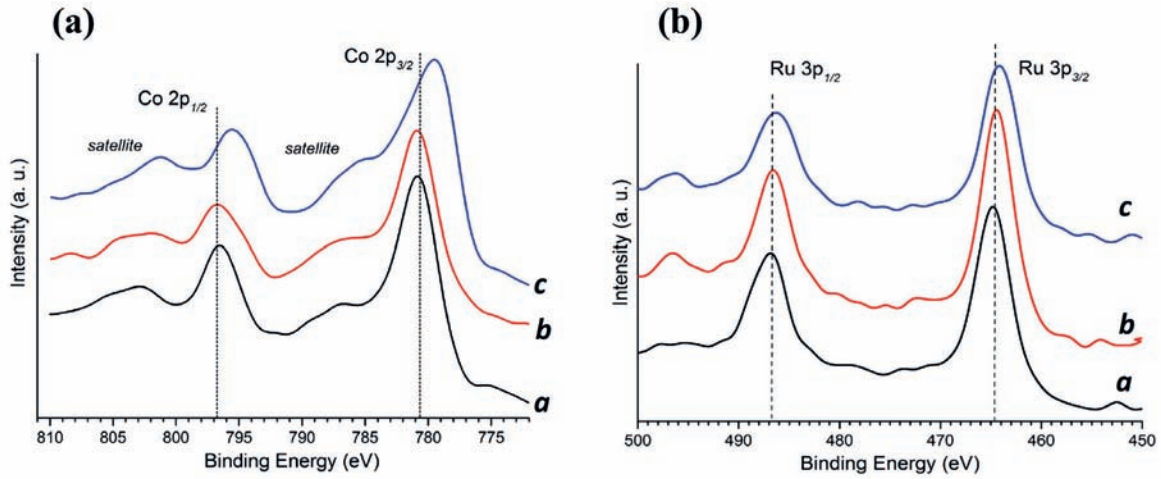

Figure S15. XPS spectrum of (a) Co $2p_{1/2}$ and $2p_{3/2}$ region and (b) Ru $3p_{1/2}$ and $3p_{3/2}$ region of fresh catalyst (*a-spectra*), after photocatalytic run (*b-spectra*) without CO_2 in inert argon atmosphere, and after photocatalytic run (*c-spectra*) in 1 atm. of CO_2.

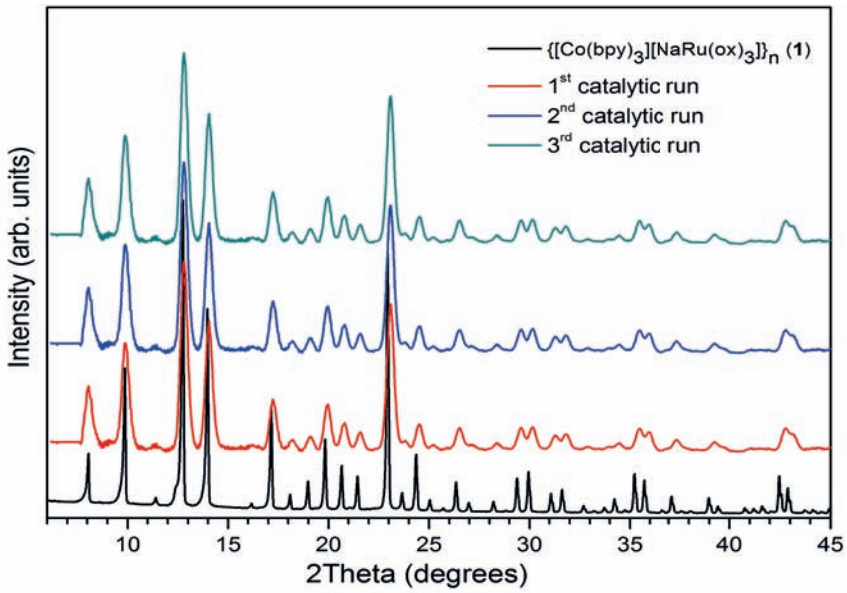

Figure S16. Comparison of PXRD patterns of **1** as-synthesized (black solid line), after 1st (red line), 2nd (blue line), and 3rd (green line) catalytic runs.

References

(1) F. H. Burstall and R. S. Nyholm, *J. Chem. Soc.*, 1952, 3570.
(2) R. Kaziro, T. W. Hambley, R. A. Bistead and J. K. Beattie, *Inorg. Chim. Acta,* 1989, **164**, 85.
(3) A. Altomare, G. Cascarano, C. Giacovazzo, M. C. Guagliardi, M. C. Burla, G. Polidori and M. Camalli, *J. Appl. Cryst.,* 1994, **27**, 435.
(4) G. M Sheldrick, SHELXL-97, *Program for refinement of crystal structures*, University of Göttingen, Germany, 1997.
(5) H. D. Flack and G. Bernardinelli, *J. Appl. Cryst.,* 2000, **33**, 1143.
(6) V. A. Blatov, A. P. Shevchenko and D. M. Proserpio, *Cryst. Growth Des*., 2014, **14**, 3576.
(7) B. N. Figgis and J. Lewis, *Progress in Inorganic Chemistry: The magnetic properties of transition metal complexes*, ed. F. A. Cotton, John Wiley & Sons, New York, 1964, vol. 6, 37

Publication VII

"Templating 3D Honeycomb-like Coordination Polymers Based on Ruthenium Oxalate Building Unit: Characterization and Catalytic Activity in Carbon Dioxide Photoreduction"

Dalton Transactions

(in preparation)

*Year **2015***

Templating 3D Honeycomb-like Coordination Polymers Based on Ruthenium Oxalate Building Unit: Characterization and Catalytic Activity in Carbon Dioxide Photoreduction

Alla Dikhtiarenko,[a] Rafael Valiente,[b] José R. García,[a] and José Gimeno[a]

[a] Departamento de Química Orgánica e Inorgánica, Universidad de Oviedo – CINN, 33006 Oviedo, Spain
[b] MALTA Consolider Team, Departamento de Física Aplicada, Universidad de Cantabria, 39005 Santander, Spain

Abstract

Family of heterometallic oxalate bridged ruthenium-based coordination polymers with the general formula of $\{[M^{II}(bpy)_3][M^{I}Ru(C_2O_4)_3]\}_n$ (M^{II} = Ni^{2+}, Fe^{2+}; M^{I} = Li^{+}, Na^{+}; bpy = 2,2´-bipyridine), have been successfully synthesized and characterized by microanalysis, IR spectroscopy, diffuse reflectance UV-VIS spectroscopy, thermogravimetric analysis (TGA), powder (PXRD) and single-crystal X-ray diffraction. Series of compounds crystallize in cubic chiral space group $P2_13$ and represent 3D three-connected decagon oxalate-bridged anionic networks with (10,3)-a array topology (***srs***-type net) which possess large honeycomb-like channels templated by $[M^{II}(bpy)_3]^{2+}$ counter cations. These templates locate in 3-fold cages which represent simple natural tiles as triangle vertex figures. The honeycomb-like 3D coordination polymers **1**−**4** containing encapsulated photosensitive $[M^{II}(bpy)_3]^{2+}$ tris-chelating bipyridine complexes can be used as self-supported photocatalysts. They were shown to be highly effective and recyclable heterogeneous catalysts for selective photoreduction of CO_2 to CO under UV-irradiation in CH_3CN/TEA media.

Keywords: Ruthenium oxalate, carbon dioxide photoreduction, coordination polymers

Introduction

Solar-based production of organic chemicals by the reduction of carbon dioxide is currently important area of research due to the increase of gas emissions that leads to global warming and, in other hand, fossil fuel shortages. Recently, CO_2 capture and subsequent reduction to valuable chemical products and liquid fuels gained interest as a potential technology to recycle atmospheric CO_2.[1]

The photocatalytic conversion of carbon dioxide into liquid fuels with homo- and heterogeneous systems[2–5] are needed to develop a sustainable infrastructure for solar fuels. One possible strategy to utilize CO_2 as a raw material for hydrocarbon products is reduce CO_2 to CO, a chemical feedstock for such industrial processes as hydroformylation[6] and the Fisher-Tropsch reaction.[7]

Transition metal complexes with N-contained chromophore ligands such as bipyridine (bpy), phenantroline are well-known photocatalysts for CO_2 reduction.[8,9] Their current efficiencies and product selectivity are quite high. The first published catalyst of this type was $Re(bpy)(CO)_3X$ (bpy = 2,2'-bipyridine, X = Cl, Br) as a simple molecular photocatalyst for reduction CO_2 to CO with UV light in DMF/TEOA (DMF = dimethylformamide; TEOA = triethanolamine) solution, with TEOA acting as a sacrificial electron donor.[10,11] Other homogeneous photocatalytic systems based on $[Ru(bpy)_3]^{2+}$ complex,[12] mixtures of $[Ru(bpy)_3]^{2+}$ and $[Co(bpy)_3]^{2+}$,[13] or $[Ru(bpy)_3]^{2+}$ and $[Ni(cyclam)]^{2+}$ (cyclam = 1,4,8,11-tetraazacyclotetradecane)[14] have been also developed. Although homogenous catalysts systems usually exhibit high activity, their practical applications remain limited because of catalyst instability and difficulty in catalyst/product separation. Immobilization of each photocatalysts systems can facilitate its' recovery and reuse. Recently, a number of approaches have been developed for this purpose, typically immobilizing the photocatalyst system on organic polymers,[15,16] metal oxides,[17] or complex/semiconducting polymers.[18,19] Example to immobilization of $[Ru(bpy)_3]^{2+}$ photosensitizer and $[Co(bpy)_3]^{2+}$ catalyst on cation exchange polymers for CO_2 reduction have been reported by Hirose *et al.*[15] It was demonstrated that resulted heterogeneous system allowed easy handling and recovery of catalyst including repeated cycles with CO turnover numbers (TNs) of 8.5.

Coordination polymers (CPs) with infinite network structures build from organic bridging ligands and inorganic connecting nodes have been emerged as very promising materials for gas storage, separation, heterogeneous catalysis, sensing and drug delivery.[20–29] A reasonable synthetic approach to build new transition metal coordination polymers with tailored-made architectures and specific chemical and physical properties consists of connecting transition metal ions through multidentate ligands to form multidimensional structures whose topologies can be controlled by a careful choice of coordination nature of metal nodes and the structural features of organic ligands. For instance, the oxalate ligand has appeared as a useful linker for the design of great diversity of homo- and hetero-metallic coordination compounds, which have played a key role in the theoretical and experimental development in areas of molecular-based magnetism.[30] The topology and dimensionality of polymeric networks based on the oxalate-bridged ligand essentially depend on the shape and charge of the templating counter ions.[31] Three dimensional oxalate networks with general composition of $\{[M^{II}(bpy)_3][M^{I}M^{III}(C_2O_4)_3]_n$, $\{[M^{III}(bpy)_3][M^{II}M^{III}(C_2O_4)_3]\}_n$, $\{[M^{III}(bpy)_3](ClO_4)[M^{I}M^{III}(C_2O_4)_3]\}_n$ (M^{I} = Li^+, Na^+; M^{II} = Zn^{2+}, Co^{2+}, Fe^{2+}, Mn^{2+}, etc.; M^{III} = Al^{3+}, Cr^{3+}, Rh^{3+}, Ru^{3+}; bpy = 2,2'-bipyridine) were first synthesized by Decurtins *et al.*[32–38] In this class of compounds, the tris-bipyridine cation tingly fit into the cavities provided by the three-dimensional polymeric anionic $\{[M^{I/II}M^{III}(C_2O_4)_3]\}_n^{2+/+}$ network. With respect to the research for an additional, synergistic property that could be combined with the molecular magnetic function, it is also aimed to exploit the photophysical behavior of these molecular frameworks. Thereby, chemical variation and combination of the metal ions of different valences in oxalate backbone as well as in tris-bipyridine cation offer unique opportunities for studying a large variety of photochemical and photophysical processes, such as light-induced electron transfer and excitation energy transfer in the solid state.[39–44] In

general, the sensitizer can be incorporated into the oxalate backbone, such as a $[M^{III}(C_2O_4)_3]^{3-}$ entity, or as a guest cation, in the form of ubiquitous photosensitizer $[M^{II}(bpy)_3]^{2+}$. This features makes the $\{[M^{II}(bpy)_3][M^{I}M^{III}(C_2O_4)_3]\}_n$ host-guest systems a very interesting and promising as self-supported photocatalysts.

Herein, we report family of 3D-dimensional ruthenium-based oxalate-bridged anionic networks of $\{[M^{I}Ru(C_2O_4)_3]^{2-}\}_n$ (M^{I} = Na^+, Li^+) in which large honeycombed channels occupied by $[M^{II}(bpy)_3]^{2+}$ (bpy = 2,2'-bipyridine, M^{II} = Ni^{2+}, Fe^{2+}) photosensitizers as template cations. The coordination polymers will be examined as self-supported catalysts for photoreduction of CO_2 to CO. Their thermal and photophysical behaviors will be also discussed.

Experimental Section

Materials. The complexes $[Fe(bpy)_3](ClO_4)_2$, $[Ni(bpy)_3]Cl_2\cdot 6H_2O$ and $K_3[Ru(C_2O_4)_3]\cdot 4.5H_2O$ were prepared according to the literature methods.[45,46] The other chemicals are commercially available and were used as purchased.

Synthesis of $\{[M^{II}(bpy)_3][NaRu(C_2O_4)_3]\}_n$ (M^{II} = Ni (1) and Fe (3)) and $\{[M^{II}(bpy)_3][LiRu(C_2O_4)_3]\}_n$ (M^{II} = Ni (2) and Fe (4)) series of compounds. The synthesis process was performed in accordance with a previously published procedure[32] for the $\{[Fe^{II}(bpy)_3][M^{I}Cr(ox)_3]\}$ (where M^{I} = Na^+, Li^+) compounds introducing $[Ru(ox)_3]^{3-}$ moiety instead of $[Cr(ox)_3]^{3-}$. In a typical synthesis, 200 mg (0.25 mmol) of $K_3[Ru(ox)_3]\cdot 4.5H_2O$ and 30 mg (0.5 mmol) of NaCl or 20 mg (0.5 mmol) of LiCl were dissolved in 5 mL of water, and 0.25 mmol of the $[M^{II}(bpy)_3]X_2$ salt ($[Ni(bpy)_3]\cdot 6H_2O$, 176 mg; $[Fe(bpy)_3](ClO_4)_2$, 180 mg) dissolved in water was added dropwise, after few minutes a precipitates appeared, and the suspensions was stirred for 1 h. The resulted precipitates were filtered, washed with ethanol and air-dried.

Yellow precipitates of **1** and **2** yield 67% and 68%, respectively. Anal. Calc. for (**1**) $C_{36}H_{24}N_6NaNiO_{12}Ru$: C, 47.19%; H, 2.62%; N, 9.18%. Found: C, 46.9%; H, 2.4%; N, 9.3%. Anal. Calc. for (**2**) $C_{36}H_{24}LiN_6NiO_{12}Ru$: C, 48.04%; H, 2.67%; N, 9.34%. Found: C, 47.6%; H, 2.4%; N, 9.5%.

Dip red precipitates of **3** and **4** yield 92% and 98%, respectively. Anal. Calc. for (**3**) $C_{36}H_{24}FeN_6NaO_{12}Ru$: C, 47.34%; H, 2.63%; N, 9.21%. Found: C, 48.1%; H, 2.4%; N, 9.2%. Anal. Calc. for (**4**) $C_{36}H_{24}FeLiN_6O_{12}Ru$: C, 48.19%; H, 2.68%; N, 9.37%. Found: C, 47.8%; H, 3.0%; N, 9.0%.

Crystal Growth. Single crystals of all compounds **1**−**4** were obtained by crystallization in a tetramethoxysilane gel containing $K_3[Ru(C_2O_4)_3]\cdot 4.5H_2O$ (0.01 M). When the gel is formed, the stoichiometric quantities of a water solution of $[M^{II}(bpy)_3]^{2+}$ and LiCl or NaCl were added. After one month, the color tetrahedral shaped crystals of **1**−**4** are formed in gel phase (see Fig. S1, Supporting Information).

Structural Characterization. Tetrahedral shaped single crystals of **1**−**4** were collected and mounted on an Oxford-Gemini X-ray diffractometer equipped with graphite-monochromatic Cu-Kα (λ = 1.5418 Å) and Mo-Kα (λ = 0.7107 Å) radiation. X-Ray diffraction data were collected at 293 K. The CrysAlisPro program was used for cell refinement and data reduction. Images were collected at a 55 mm fixed crystal-detector distance, using the oscillation method, with 1° oscillation and variable exposure time per image. The structure solution was solved by direct methods using the SIR92 program.[47] The refinement was performed by SHELX-97[48] using full-matrix least squares on F^2. All non-H atoms were anisotropically refined. The Flack`s absolute parameter (x) was used to determine the space group of four compounds.[49] Crystal data and structure refinement details for **1**−**4** are presented in Table 1.

X-Ray powder diffraction patterns were collected with a X´Pert Philips X-ray diffractometer (Cu-Kα radiation, λ_α = 1.5418 Å) at room temperature. The powder diffraction patterns indicate that all compounds are isostructural and show analogous patterns to the simulated patterns from the atomic coordinates of the crystal structures of **1**−**4** (Figs. S2–S3).

Powder X-ray thermodiffraction studies were performed in air with the sample placed in an Anton Paar XRK 900 Reactor Chamber on a Bruker D8 Advance diffractometer with DAVINCI design, using Cu-Kα radiation, equipped with LynxEye detector. Each powder pattern were recorded in the 5−70º range of 2θ with a step of 0.019º and a counting time of 0.2 s/step. Heating of the samples was realized applying two temperature intervals: from 30 ºC up to 350 ºC with temperature ramp between two consecutive temperatures was 50 ºC/min; from 350 ºC up to 625 ºC with temperature ramp of 25 ºC/min. The powder XRD data acquisition and analysis in this work were carried out using Bruker AXS DIFFRAC.EVA software.

Characterization Instruments. The inferred spectra for **1**−**4** were recorded on a Bruker Tensor-27 spectrophotometer as KBr pellets in the 4000−500 cm^{-1} region.

Microanalyses (C, H, N) were carried out by the use of a Perkin-Elmer model 2400B elemental analyzer.

X-ray microanalysis (SEM/EDX) confirmed the ratio $Ru:M^{II}$ to be 1:1 (M^{II} = Fe^{2+}, Ni^{2+}, Co^{2+}), by using JEOL JSM-6100 scanning microscopy (SEM) coupled with an INCA Energy-200 dispersive X-ray microanalysis system (EDX) with a PentaFET ultrathin window detector. As show Figure S4, the microcrystalline texture of the samples consists of microcrystals that repeat the same habit as those obtained single crystals, indicating that powder products have been obtained as pure phases.

A Mettler-ToledoTGA/SDTA851 were used for the thermal analyses in nitrogen and air dynamic atmosphere (50 mL/min) at a heating rate of 10°C/min. Approximately 10 mg of powder sample was thermally treated, and blank runs were performed. An Pfeiffer Vacuum TermoStar™ GSD301T mass spectrometer was used to determine the evacuated vapors. The masses *m/z* 15 (NH_3), 18 (H_2O), 44 (CO_2) and 46 (NO_2) were tested by using a detector C-SEM, operating at 1200 V, with a time constant of 1 s.

A Cary 6000i (Varian) spectrophotometer was used to measure UV-VIS-NIR diffuse reflectance spectra in the range 200−1800 nm using a polytetrauoroethylene (PTFE)-coated integrating sphere.

Photochemical Experiments. Photocatalytic activities of **1**−**4** were evaluated by the reduction CO_2 to CO. Supercritical-fluid grade CO_2 was purchased from AirLiquid (Spain) to avoid any hydrocarbon contamination. It was certified maximum hydrocarbons less than 20 ppb. All experiments were conducted at room temperature. In each experiments, 10 μmol of heterogeneous catalyst was dispersed in 10 mL of acetonitrile (CH_3CN)/triethylamine (TEA) (5:1, v/v) mixed solvent. The experiments were carried in a 100 mL gastight photolysis photoreaction cell that was custom-designed in order to allow purging and irradiation of the suspension. The gastight cell was a 100 mL two-necked, flat-bottomed flask equipped with a quartz window and water refrigerator. The cell volume was 100 mL, of which 90 mL was occupied by gases. Prior to photolysis, CO_2 was bubbled through the reactor for at least 30 min to purge air and to saturate the solution. A magnetic stirrer agitated the catalyst suspended solution at the bottom to prevent sedimentation of the catalyst. The system was irradiated by UV light at room temperature with 500 W mercury lamp (≤ 366 nm) (HELIOS ITALQUARTZ Apparatus, model UV50F – 85P503I5) for 10 h. The entire system was shielded by a metal case during the reaction to prevent interference from outside light. For experiments performed with visible light irradiation (≥ 417 nm) the xenon lamp (150 W) was used as light source. The evolution of CO during the reaction was monitored by regular gas sampling. Gas samples (0.5 mL) were taken from the cell through a septum using gastight syringe and analyzed by mass spectrometry. Mass spectrometry analyses were performed using an OmniStar™ (Pfeiffer Vacuum) gas analysis module connected to AutoChem II 2920 (Micromeritics) catalyst characterization system. A cold trap was used with He as the carrier gas. Each gas was identified and quantified using the working curve, which had been previously obtained using standard CO gas (AirLiquid). Blank reactions were conducted to ensure that CO production was due to the photoreduction of CO_2, and to eliminate surrounding interference. One blank was UV-

illuminated without the catalyst, and another was in the dark with the catalyst and CO_2 under the same experimental conditions. Negligible quantity of CO was detected in the above two blank tests. After the catalyst's sedimentation, the liquid phase was analyzed in GC/FID (Hewlett Packard) equipped with Beta DEX 120 (30 m × 0.25 mm × 0.25 μm) 30 m long column. Each analysis did not detect the formation of addition products such as CH_3OH, CH_2O or HCOOH. In some cases, repetitive photoreduction during three consecutive cycles was performed. After each cycle, the catalyst was washed with H_2O/CH_3CN mixture and reused in subsequent cycles.

Results and Discussion

The detailed crystal data and structure determination parameters of ruthenium based coordination polymers **1**–**4** are summarized in Table 1. The compounds present the 3D three-connected decagon oxalate-bridged anionic network $\{[M^{I}Ru(C_2O_4)_3]^{2-}\}_n$ ($M^{I} = Na^{+}$, Li^{+}), which selective templates $[M^{II}(bpy)_3]^{2+}$ (where $M^{II} = Fe^{2+}$, Ni^{2+}) cationic complex. The single-crystal X-ray analysis series of ruthenium based 3D oxalate bridged polymers revels that they are isomorphous with the series of $\{[M^{II}(bpy)_3][M^{I}M^{III}(C_2O_4)_3]^{2-}\}_n$ (M^{II} = Co, Fe, Ru, Ni; $M^{I} = Na^{+}$, Li^{+}; M^{III} =Cr, Fe, Ru) compounds[32–35] which crystallize in the cubic chiral space group $P2_13$.

Table 1. Crystallographic data and structure refinement parameters for compounds **1**–**4**.

Compound	**1**	**2**	**3**	**4**
Formula	$C_{36}H_{24}FeN_6NaO_{12}Ru$	$C_{36}H_{24}FeLiN_6O_{12}Ru$	$C_{36}H_{24}N_6NaNiO_{12}Ru$	$C_{36}H_{24}LiN_6NiO_{12}Ru$
M_r	912.52	896.47	915.36	899.31
Crystal system	cubic	Cubic	cubic	cubic
Space group	$P2_13$	$P2_13$	$P2_13$	$P2_13$
a (Å)	15.4771(2)	15.2099(1)	15.6016(1)	15.3586(4)
α (deg)	90.0	90.0	90.0	90.0
V (Å^3)	3707.4(1)	3518.72(8)	3797.58(4)	3622.9(3)
Z	4	4	4	4
D_{calcd} (g/cm^3)	1.635	1.692	1.601	1.649
F(000)	1836	1804	1844	1812
μ (mm^{-1})	7.183	7.44	4.56	1.01
Reflection collected	4738	5367	7245	5041
Independent reflections	2290[R_{int} = 0.072]	2133[R_{int} = 0.026]	2398[R_{int} = 0.026]	2381[R_{int} = 0.039]
Data/restraints/parameters	2290 / 0 / 172	2133 / 0 / 172	2398 / 0 / 173	3182 / 0 / 172
Final R indices [I>2σ(I)]	R_1 = 0.053, wR_2 = 0.131	R_1 = 0.041, wR_2 = 0.117	R_1 = 0.028, wR_2 = 0.084	R_1 = 0.032, wR_2 = 0.070
R indices (all data)	R_1 = 0.063, wR_2 = 0.139	R_1 = 0.042, wR_2 = 0.118	R_1 = 0.031, wR_2 = 0.085	R_1 = 0.046, wR_2 = 0.072
Flack parameter	-0.004(12)	0.024(9)	-0.027(11)	0.000(19)
Goodness-of-fit on F^2	1.029	1.083	1.075	0.934

As shown representative example of **1** depicted in the Figure 1a, the asymmetric unit contains a complete oxalate ligand, Ru^{3+} and Li^{+} ions of the anionic network, Fe^{2+} metal center and the complete bpy ligand of the cationic template. Each Ru^{3+} ion coordinates to six oxygen atoms of oxalate ligand and forms the octahedral coordination environment. The Li^{+}/Na^{+} centers are six-coordinated by oxygen atoms of oxalate ligand, where larger Na−O bond lengths indicate its' weaker covalent bonding character comparing to the shortest Li−O ones. For comparison, selected bond lengths of coordination environments of each metal center and corresponding distortion parameters in compounds **1**−**4** and in previously reported $\{[Co(bpy)_3][NaRu(C_2O_4)_3]\}_n$ and $\{[Co(bpy)_3][LiRu(C_2O_4)_3]\}_n$[50] are summarized in Table 2.

As expected from the different ionic radii of Li^{+} and Na^{+}, there is a large difference in M^{I}−O and Ru^{III}−O bond lengths between the compounds containing Na^{+} and Li^{+} but they are similar for the three Na^{+} compounds ($Na-O_{average}$= 2.3307(2) Å; $Ru-O_{average}$= 2.0205(3) Å) and the three Li^{+} compounds ($Li-O_{average}$ = 2.1876(7) Å; y $Ru-O_{average}$ = 2.0351(5) Å).

Table 2. Selected bond length (Å) for $\{[M^{II}(bpy)_3][M^{I}Ru(C_2O_4)_3]\}_n$ (M^{II} = Fe^{2+}, Ni^{2+}; M^{I} = Na^+, Li^+) coordination polymers and the structural distortion parameters of $[M^{II}(bpy)_3]^{2+}$ (M^{II} = Fe^{2+}, Ni^{2+}) guests compared with corresponding $[M^{II}(bpy)_3]^{2+}$ cation in salts.[a] Reported data for $\{[Co(bpy)_3][M^{I}Ru(C_2O_4)_3]\}$ (M^{I}= Na, Li) are also included.[50]

	$\{[Fe(bpy)_3][M^{I}Ru(C_2O_4)_3]\}_n$		$\{[Ni(bpy)_3][M^{I}Ru(C_2O_4)_3]\}_n$		$\{[Co(bpy)_3][M^{I}Ru(C_2O_4)_3]\}_n$	
	M^{I} = Na	M^{I} = Li	M^{I} = Na	M^{I} = Li	M^{I} = Na	M^{I} = Li
Ru–O1	2.017(5)	2.033(3)	2.017(2)	2.029(2)	2.013(3)	2.033(4)
Ru–O2	2.025(5)	2.034(3)	2.024(2)	2.037(2)	2.027(3)	2.045(4)
M^{I}–O3	2.304(6)	2.122(9)	2.329(3)	2.151(6)	2.334(4)	2.162(12)
M^{I}–O4	2.310(6)	2.176(7)	2.344(3)	2.235(5)	2.363(4)	2.278(10)
M^{II}–N1	1.977(4)	1.964(3)	2.086(3)	2.072(2)	2.168(3)	2.145(5)
M^{II}–N2	1.980(4)	1.967(4)	2.094(2)	2.074(2)	2.174(3)	2.151(5)
M^{II}–N $_{average}$	1.978(1)	1.965(1)	2.090(4)	2.073(1)	2.171(3)	2.148(3)
Σ, $^{\circ}$ [b]	27.9	28.8	48.9	49.2	78.6	69.1
Δ [c]	$5.7\cdot10^{-7}$	$5.8\cdot10^{-7}$	$36.6\cdot10^{-7}$	$2.3\cdot10^{-7}$	$19.1\cdot10^{-7}$	$19.5\cdot10^{-7}$

Bond length and distortion parameters of $[M^{II}(bpy)_3]^{2+}$ cation in salts [a]

	$[Fe(bpy)_3]^{2+}$	$[Ni(bpy)_3]^{2+}$	$[Co(bpy)_3]^{2+}$
M^{II}–N $_{range}$	1.953(5) –1.972(3)	2.091(7) –2.101(6)	2.119(2) –2.136(5)
M^{II}–N $_{average}$	1.965(8)	2.096(3)	2.129(7)
Σ, $^{\circ}$ [b]	32.9	50.5	69.1
Δ [c]	$188.2\cdot10^{-7}$	$21.1\cdot10^{-7}$	$121.1\cdot10^{-7}$

[a] The M^{II}-N bonds lengths for $[Fe(bpy)_3](ClO_4)_2$, $[Ni(bpy)_3]Cl_2\cdot6H_2O$ and $[Co(bpy)_3](ClO_4)_2$ salts ware taken from the published crystallographic data.[51–53]

[b] The bond angle variance: $\Sigma = \frac{1}{11}\sum_{n=1,12}(\theta_n - 90°)$, where θ_n is one of the twelve N-M^{II}-N angles in the coordination sphere.[54,55]

[c] The mean quadratic elongation: $\Delta = \frac{1}{6}\sum_{n=1,6}\left[\frac{(d_n-\langle d\rangle)}{\langle d\rangle}\right]$, where ‹*d*› and d_n are the mean M^{II}-N bond length and the six M^{II}-N bond lengths in coordination polyhedra, respectively.[54]

The unit cell volumes (Å^3) also reflect the larger size of sodium cation as followed: 3518.72(8) Å^3 *vs* 3707.4(1) Å^3 (M^{II}= Fe; M^{I}= Li *vs* Na); 3622.9(3) Å^3 *vs* 3797.58(4) Å^3 (M^{II}= Ni; M^{I}= Li *vs* Na); 3715.02(4) Å^3 *vs* 3869.6(1) Å^3 (M^{II}= Co; M^{I}= Li *vs* Na).

In the coordination frameworks of **1**–**4**, the oxalate ligand show μ-coordination mode (Fig. 1b) linking Ru^{3+} and Li^+/Na^+ ions, forming a dinuclear motif which connecting each other along the *b*-axis through planar oxalate ligands (Fig. 1b) result in a helical backbone chain (Fig. 1c).

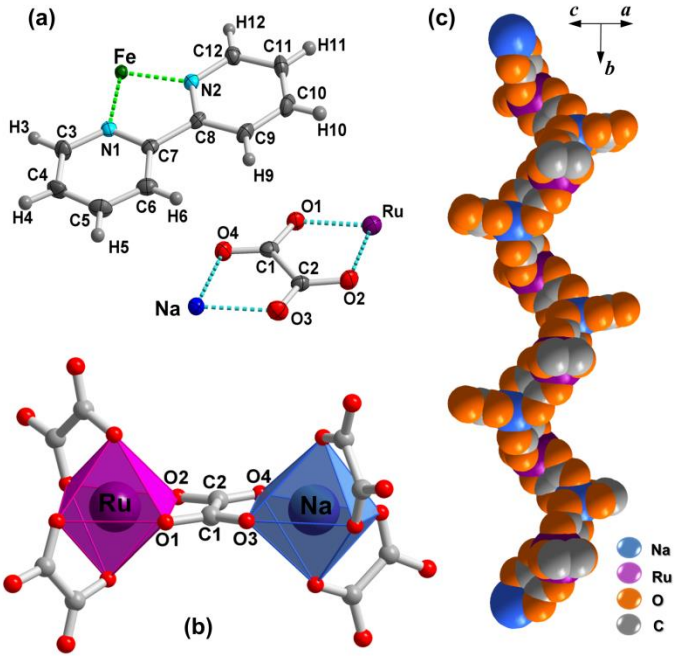

Figure 1. (a) View of the asymmetric unit drawn with ellipsoids at the 50% probability level. (b). The bridging mode of oxalate ligand, Ru(III) and Na(I) coordination environment in compound **1**. (c) Space-filling representation of helical chain in **1** running along *b*-axis.

These helices are chiral with 3-fold axis interpretation. Adjacent helices are reputedly connected through $\{Ru(C_2O_4)_3\}$ or $\{Li/Na(C_2O_4)_3\}$ coordination entities in all three dimensions to form a 3D porous anionic structure with large cubic channels along *c*-axis, as presented in Figure 2a. There are two kinds of the cubic cavities which are differentiated on the diameter (see Fig. S6). Simultaneously, if the anionic network can be viewed as projection on the [111] direction, the large cubic channels transform to the honeycombed cavities, as depicted in Figure 2c. To better understanding the structure of $\{[Li/NaRu(C_2O_4)_3]^{2-}\}_n$ anionic networks, the topological analysis approach using TOPOS 4.0 software has been employed.[56] As shown in Figure 2(b,d), this net contains one kind of nodes: Ru and Li/Na ions can be considered as three-connected nodes, while the oxalate ligands as linear rod which repeatedly connect both metal centers. Thus, this 3D network can be described as an three-connected uninodal net with (10,3)-a array topology (also denoted as ***srs***-type net).[57]

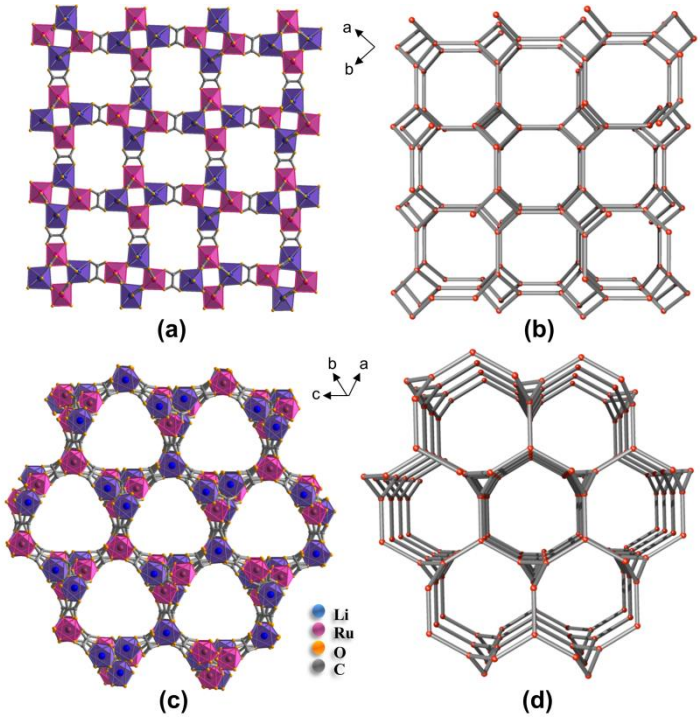

Figure 2. The 3D three-connected decagon anionic network $\{[NaRu(C_2O_4)_3]^{2-}\}_n$ in **1**: (a) view of cubic channels along the *c*-axis and (b) their simplified topological representation viewed from the same direction (the ruthenium and sodium nodes are shown as red spheres, the oxalate ligand are grey rods); (c) projection of honeycombed channels on the [111] direction and (d) their simplified topological representation.

To balance the negative charge of the 3D anionic network there are dipositive $[M^{II}(bpy)_3]^{2+}$ cations incorporated in the lattice of the framework. The arrays of cations in the cavities of these networks, such as that all $M^{II}\cdots M^{II}$ distances are equivalent (see Fig. S7, Supporting Information). The tris-chelating cationic template fit the large negative cavities in a specific and highly symmetrical manner. Additionaly, the cationic entity acts as a structural (appropriate size/shape), stoichiometric and chiral template. The role of bulky $[M(bpy)_3]^{2+}$ cations in oxalate-based anionic coordination arrays have been previously investigated and have a significant effect on the network structure formation.[33,58]

However, in actual case the tris-chelating complex selectively reside within 3-fold cage what formed as result of interconnection of tree adjacent chiral helices. An examination of the site symmetry for this cavities, and hence the site for the hosted cations, reveals that there is a crystallographically imposed symmetry in form of a 3-fold axis.

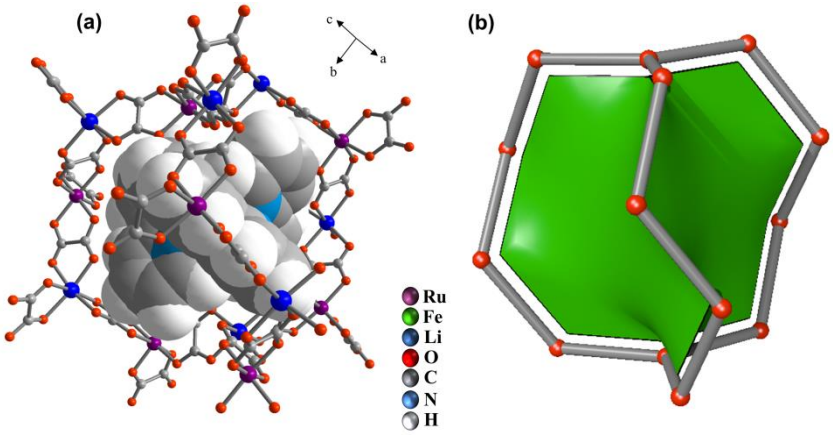

Figure 3. (a) Perspective view of $[Fe(bpy)_3]^{2+}$ complex hosted in the anionic 3-fold cage. (b) Simplified topological representation of cage (red nodes are Ru and Na metal centers, grey rods is oxalate ligand) with ***srs*** triangular tile.

Interestingly, during topological analysis those anionic boxes can be generalized as natural tiles for this type of network. As show in Figure 3b, the natural tile has been described as triangle vertex figure with 14 vertices and 3 faces. It is worth noting that our regular (10,3)-net is minimal periodic net with self-dual natural tilling. For this reason, the whole structure is constructed of two kinds of natural tiles with common formula of $[10^3]$ and stoichiometric ratio between them of 1:1. Both tiles connected by "kissing" mode give 3D honeycombed structure (see Figs. 4b,c).

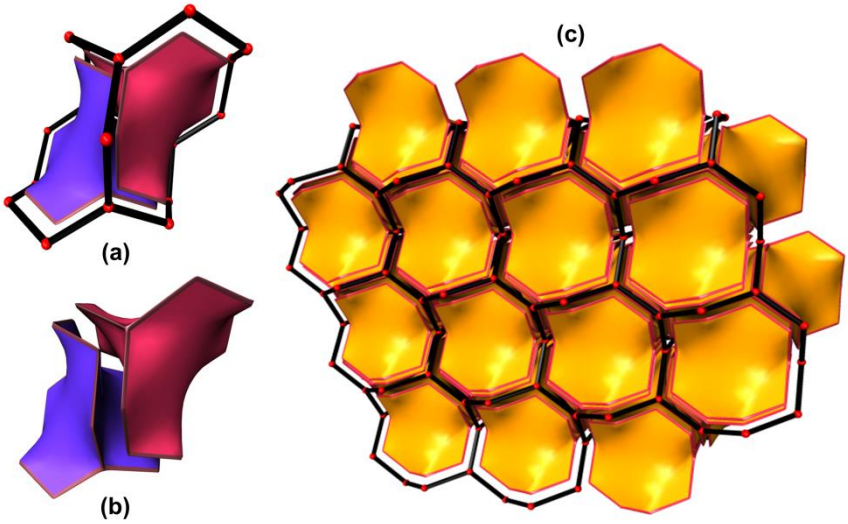

Figure 4. (a) Two kinds of natural tiles in (10,3) anionic net. (b) Two types of tiles connected by "kissing" mode, which (c) packed together generate the 3D honeycombed structure.

The most significant features of the crystal structures arise from the size of the 3-fold anionic cages $\{[M^{I}Ru(C_2O_4)_3]^{2-}\}_n$ (M^{I} = Na, Li) where the cationic species $[M^{II}(bpy)_3]^{2+}$ (M^{II} = Fe, Ni, Co) are incorporated within the networks. To this regard, the corresponding volumes for both anionic cages and cationic hostages in those polymeric networks were calculated, applying the models of Voronoi-Dirichlet polyhedra (Fig. 5).[59,60] The volumes of the cationic species in the free salts $[M^{II}(bpy)_3]^{2+}$ are also shown, fulfilling the sequence Fe (579 $Å^3$) < Ni (611 $Å^3$) < Co (619 $Å^3$) in accord with the corresponding electronic configuration of the metal ions $Fe^{2+}(t_{2g}^6)$, Ni^{2+} $(t_{2g}^6 e_g^2)$, Co^{2+} $(t_{2g}^5 e_g^2)$.[61]

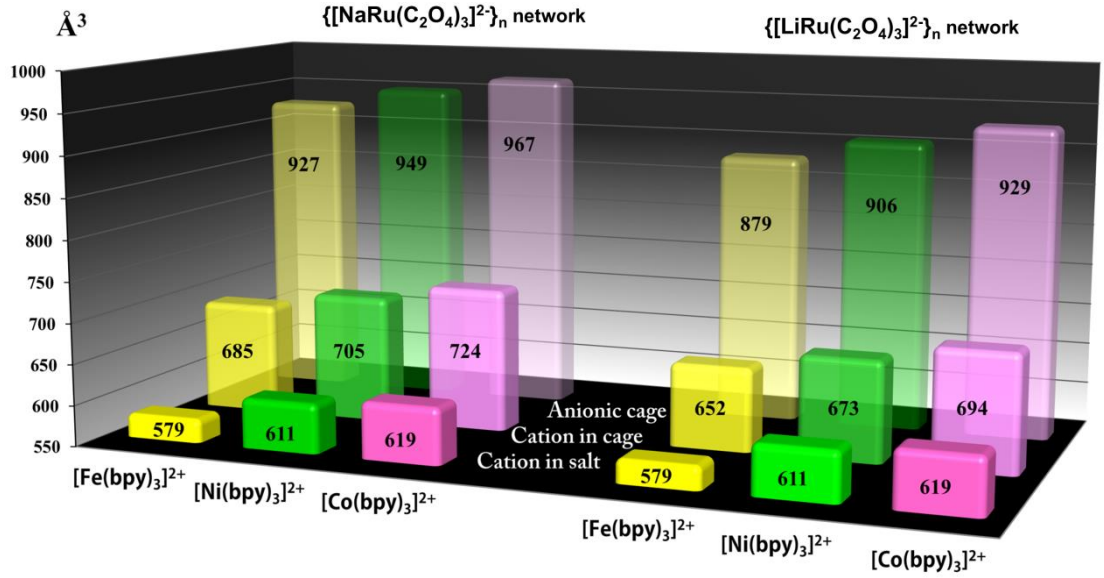

Figure 5. The accessible volumes of anionic cages in $\{[M^{I}Ru(C_2O_4)_3]^{2-}\}_n$ (M^{I} = Na^{+}, Li^{+}) networks, the volumes of $[M^{II}(bpy)_3]^{2+}$ (M^{II} = Fe^{2+}, Ni^{2+}, Co^{2+}) cations in salts and incorporated in corresponding polymeric nets. The volume calculation for $[Fe(bpy)_3](ClO_4)_2$, $[Ni(bpy)_3]Cl_2 \cdot 6H_2O$ and $[Co(bpy)_3](ClO_4)_2$ salts was performed using the published crystallographic data.[51–53]

Similar trends appear for the corresponding volumes of the anionic cages of $\{[M^{I}Ru(C_2O_4)_3]^{2-}\}_n$ (M^{I} = Na: 927 $Å^3$ (Fe) < 949 $Å^3$ (Ni) < 967 $Å^3$ (Co); M^{I} =Li: 879 $Å^3$ (Fe) < 906 $Å^3$ (Ni) < 929 $Å^3$ (Co)) also revealing not only the effect of the larger size of the sodium *vs* lithium partners but also the size of the cationic hostages. It is worth to note that the volumes found for the cationic species $[M^{II}(bpy)_3]^{2+}$ occupying the corresponding cages are larger than those of the free salts *i.e*. 685 *vs* 579 $Å^3$ (Fe), 705 *vs* 611 $Å^3$ (Ni), 724 *vs* 619 $Å^3$ (Co). Notably, the M^{II}–N bond lengths (Å) found for the cationic species $[M^{II}(bpy)_3]^{2+}$ occupying the corresponding cages increase with respect to those shown by the free salts *i.e*. M^{II} = Fe: $1.965(8)_{av.}$ *vs* 1.978(1) Å (M^{I} = Na); 1.965(1) Å (M^{I} = Li); M^{II} = Ni; $2.096(3)_{av.}$ *vs* M^{I} = 2.090(4) Å (M^{I} = Na); 2.073(1) Å (M^{I} = Li); M^{II} = Co; $2.129(7)_{av.}$ *vs* 2.171(3) Å (M^{I} = Na); 2.148(3) Å (M^{I} = Li).

These experimental facts seem to indicate that the anionic networks modify the structural parameters of the cationic hostages and, therefore, induce different electronic properties. This influence can be the key of the improved catalytic activity observed by these materials as heterogeneous catalysts as compared with that shown by mixtures of the starting free salts acting as homogeneous catalysts (see below).

The IR spectrums of **1**–**4** are very similar (Fig. S7) and show the characteristic absorption bands of the oxalate ligand in regions 1610−1625 cm^{-1} (ν_{as} O–C–O), 1305−1315 cm^{-1}, 1350−1365 cm^{-1} (ν_s O–C–O), and 795−805 cm^{-1} (δ O–C–O). The bands between 540 cm^{-1} and 490 cm^{-1} are assigned to Ru−O, Li−O and M^{II}–N stretching vibrations. The bands between 3100 cm^{-1} and 2800 cm^{-1} and 1675−1400 cm^{-1} are attributed to the C−H, C_{ar}–C_{ar}, and C_{ar}=N stretching frequencies of the aromatic group. The series of bands at 1250−1000 cm^{-1} and near 3030−3050 cm^{-1} correspond to the aromatic =C−H stretching vibration.

The thermal stability of **1**–**4** in air and nitrogen atmospheres was investigated. The thermogravimetric analyses reveal the similar behavior of **1**–**4** in each of both atmospheres, confirming their isostructurality (Fig. S8). The summarized thermogravimetric analyses for each compound are presented in the Table S1. The TG results of degradation processes in air and nitrogen atmospheres are very closely resemble each other and reveal the observed total mass losses from room temperature up to 1000 ºC. Degradation processes in air atmosphere of **1** has been taken as representative example. As show in Figure S9, the thermal decomposition process proceeds in one continuous stage. The mass loss observed in the range 291−432 ºC with the total

mass loss of 75.2 % (cal. 75.7 %), which reach their maximum velocity at 308 ºC, associated with a broad exothermic bound on the SDTA (Fig. S9) and DSC curves (Fig. S10a), corresponding to simultaneous decomposition of organic fraction of template and oxalate ligand. The associated mass spectrometry *m/z* 18, 44 and 46 curves are in a good agreement with the TG/dTG curves. The mass spectrometry *m/z* 18, 44 and 46 curves have one common broad maximum at 310 ºC, coinciding with maximum of mass loss in dTG curve, corresponds to continuous structure collapsing and oxidation of ligands. Also, one step degradation process of compounds **1**–**4** was observed in nitrogen atmosphere. In this case, the supramolecular architectures retained their stability up to 210–319 ºC. In representative example **1** the mass loss observed in the range 319–795 ºC with the mass loss of 65.9 % (cal. 78.8 %), which reach their maximum velocity at 385 ºC, associated with endothermic effect on the SDTA (Fig. S9) and DSC curves (Fig. S10b). As shown, simultaneous decomposition of organic fraction of template and oxalate ligand is accompanied with mass losses of *m/z* 15, 18 and 44 and have one common maximum at 385 ºC, coinciding with maximum of mass loss in dTG curve (Fig. S9). Notably that observed and calculated mass loses are different, this phenomena occurred due to formation of carbon solid residues as a product of partial oxidation of organic ligands in nitrogen atmospheres. Finally, the degradation enthalpies for compounds **1**–**4** in nitrogen and air atmospheres ranging from 217 to 366 $J \cdot g^{-1}$ and from -7224 to -9549 $J \cdot g^{-1}$, respectively.

The residual solids of **1**–**4** after their total decomposition in air and nitrogen atmospheres were been identified by powder XRD. The residues powders have been identified as a mixture of Ru metal, Li_2O (for **2** and **4**), Na_2O (for **1** and **3**), $M^{II}{}_2O_3$ (**1** and **2**), $M^{II}O$ (**3** and **4**) and residual carbon (in all cases, also have been confirmed by X-ray microanalysis). The thermal oxidative degradation processes in air atmosphere produce traces which has been identified as a mixture of RuO_2, Li_2O (for **2** and **4**), Na_2O (for **1** and **3**) and $M^{II}{}_2O_3$ (**1** and **2**), $M^{II}O$ (**3** and **4**).

The X-ray thermodiffraction carried under air heating up from 30 ºC to 625 ºC and cooling down to 30 ºC were performed for **1** as the representative example of the family (Fig. S11). The results confirm that no structural changes occurred up 250 ºC. At 300 ºC, a noticeable diffraction intensities drop and peak broadening is observed. In order to continue, at 350 ºC practically no diffraction peaks have been observed. Nevertheless, by heating up to 625 ºC the diffraction patterns have a series of broad peaks corresponding to the formation of oxidative residues. The X-ray thermodiffraction study is consistent with TG analysis and confirms the continuous irreversible decomposition process due to simultaneous degradation of template as well as oxalate ligand of 3D network.

The room-temperature UV-VIS-NIR diffuse reflectance spectra of the powder samples corresponding to **1**–**4** are represented in Figure 6. The spectra consist in three groups of bands: the high energy bands observed between 200 and 330 nm are assigned to $\pi \rightarrow \pi^*$ transition of bpy ligands; the intense broad band at *ca*. 400 nm corresponds to MLCT transition in $[Na/LiRu(C_2O_4)_3]^{2+}$ units, whereas the weaker bands in the VIS-NIR region have been assigned to ligand-field transitions within the $[Fe(bpy)_3]^{2+}$ and $[Ni(bpy)_3]^{2+}$ chromophoric templates in compounds **1**–**4**.

As shows Fig. 6a, the VIS-NIR spectral region of **1** and **2** consist of strong high energy band *ca*. 500 nm corresponding to the spin-allowed $t_{2g} \rightarrow \pi^*$ metal-to-ligand charge transfer transition, and broad band located *ca*. 869 nm assigning to the *d-d* spin-forbidden $^1A_1 \rightarrow {}^3T_1$ transition within low-spin (LS) $[Fe(bpy)_3]^{2+}$ complex.[45] The VIS-NIR spectral region of $[Ni(bpy)3]^{2+}$-contained **3** and **4** characterized by three bands centered at 532, 769 and 833 nm which have been assigned to $^3A_2 \rightarrow {}^3T_1$, $^3A_2 \rightarrow {}^3T_2$ and $^3A_2 \rightarrow {}^1E$ transitions (Fig. 6b).

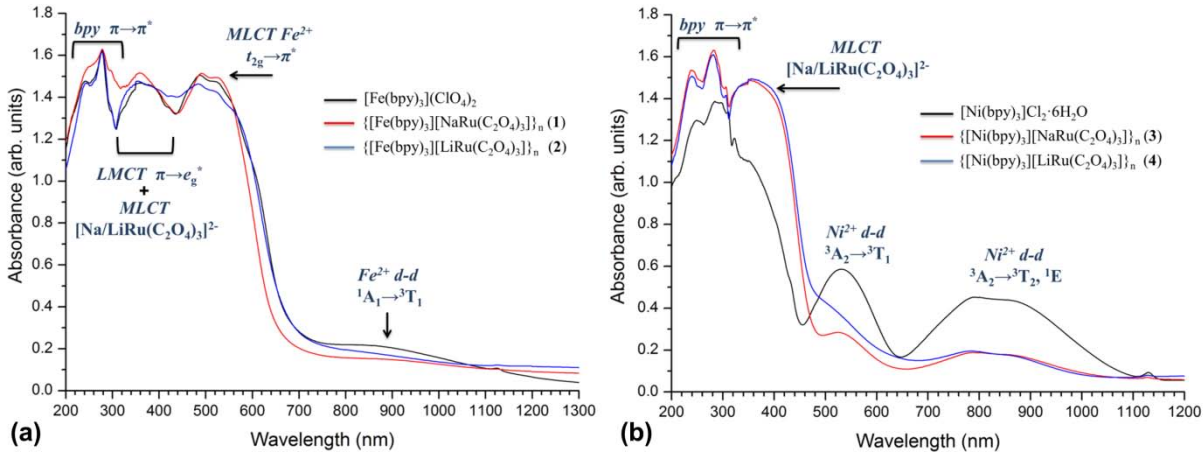

Figure 6. Comparison of the room temperature UV-VIS-NIR diffuse reflectance spectrum for (a) $\{[Fe(bpy)_3][M^IRu(C_2O_4)_3]\}_n$ (M^I = Na (**1**); Li (**2**)) and $[Fe(bpy)_3](ClO_4)_2$; (b) $\{[Ni(bpy)_3][M^IRu(C_2O_4)_3]\}_n$ (M^I = Na (**3**); Li (**4**)) and $[Ni(bpy)_3]Cl_2 \cdot 6H_2O$.

The octahedral crystal-field strength of Ni^{2+} with $^3A_2$ ground state in $[Ni(bpy)_3]^{2+}$ is closed to the exited state crossover $^1E_g \leftrightarrow {}^3T_{2g}$.[45] The characteristic doublet with maxima at 769 nm and 833 nm, which are the result of borrowing the intensity of spin-allowed $^3A_2 \rightarrow {}^3T_2$ transition by $^3A_2 \rightarrow {}^1E$ spin-forbidden transition, exhibit slightly higher absorption for **3** and **4** comparable with $[Ni(bpy)_3]Cl_2 \cdot 6H_2O$ compound.

We have recently reported that the compounds $\{[Co(bpy)_3][M^IRu(ox)_3]\}_n$ (M^I= Na, Li) are highly efficient and selective catalysts for the photocatalytic reduction of CO_2 to CO.[50] Because only few examples of CPs have been reported to date we believed it of interest to check whether the new compounds $\{[M^{II}(bpy)_3][M^IRu(ox)_3]\}_n$ (M^{II} = Fe, Ni; M^I= Na, Li) would affect the catalytic activity. The reduction reactions were performed at mild reaction conditions (20 ºC, 1 atm. of CO_2) using a reactor equipped with refrigerated 500W Hg-lamp (≤ 366 nm) and triethylamine (TEA) as an electron donor and CH_3CN as solvent. As shown in Fig 7a, the heterogeneous catalysts **1**–**4** selectively reduce CO_2 to CO reaching TON of 126 of CO after 10 h of UV irradiation (no traces of H_2, formic acid or methanol were detected).

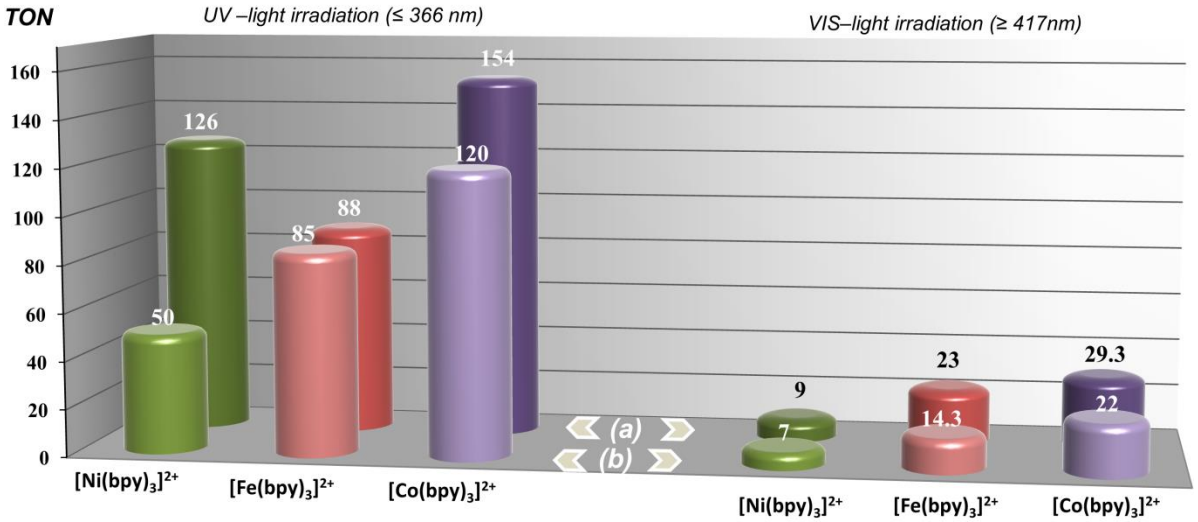

Figure 7. TON values corresponding to CO evolved during the photoreduction of CO_2 using heterogeneous catalysts **1**–**4** and previously reported $\{[Co(bpy)_3][M^IRu(ox)_3]\}_n$ (M^I= Na, Li)[50] which contain $[Ni(bpy)_3]^{2+}$, $[Fe(bpy)_3]^{2+}$ and $[Co(bpy)_3]^{2+}$ cations incorporated in (a) $\{[NaRu(C_2O_4)_3]^{2-}\}_n$ and (b) $\{[LiRu(C_2O_4)_3]^{2-}\}_n$ networks under UV (≤ 366 nm) and VIS-light radiation (≥ 417 nm). Photoreaction mixtures contained 10 µmol of heterogeneous catalyst, 0.5 ml of TEA and 9.5 ml of CH_3CN. Reactions were run for 10 h. TON = mmol of $CO \cdot 10^3$/ 10 µmol of catalyst.

In a similar way to that shown by compounds $\{[Co(bpy)_3][NaRu(ox)_3]\}_n$ and $\{[Co(bpy)_3][LiRu(ox)_3]\}_n$ no CO formation was observed when the reactions are performed in the dark or under UV light without heterogeneous catalyst, proving that the processes are UV-induced and catalysed by **1**−**4**. Photocatalytic reduction of CO_2 was also examined under VIS-light irradiation under the same reaction conditions. As shown in Figure 7 (right), all the compounds also catalyse selectively the reduction of CO_2 to CO albeit with much less efficiently (9, 7, 23, 14, 29 and 22 for **1**–**4**, respectively). It is apparent that the energy transfer from the photosensitizer ruthenium frameworks diminishes by using the VIS-light, which is expected because charge transfer bands within $\{[Na/LiRu(ox)_3]^{2-}\}_n$ networks of **1**–**4** are mostly located in UV region.

Under the same reaction conditions, the precursor compounds $[M^{II}(bpy)_3]X_2$ (M^{II} = Ni, Fe, Co; X = Cl^-, ClO_4^-) as well as a mixture of $K_3[Ru(C_2O_4)_3]$ and $[M^{II}(bpy)_3]X_2$ also catalyse CO_2 reduction (Fig. S12) but with lower yield than that observed for the corresponding coordination polymers.

Recyclability tests performed for compound **3** show after centrifugation and washing with CH_3CN, that the heterogeneous catalysts can be reused, remaining active over three consecutive runs (Fig. S13). Remarkably, the PXRD pattern of the recovered solid of **3** after three runs indicates that no structural change has occurred (Fig S14).

Conclusion

We have reported the synthesis and characterization of photoactive 3D coordination polymers $\{[M^{II}(bpy)_3][M^{I}Ru(ox)_3]\}_n$ (M^{II} = Fe, Ni, Co; M^{I}= Na, Li). The new members M^{II} = Fe, Ni herein reported which are isostructural with the cobalt partner, are also able to photo-catalyze selectively the reduction of CO_2 to CO. The new catalysts remain active for three consecutive runs reaching a total of TON 126, which are among the highest catalytic activity reported to date.[62] The remarkable photo-catalytic activity of this series of compounds demonstrates the potentiality of coordination polymers to be used as heterogeneous catalysts which is a well-known application for a wide range of transition metal compounds.[9–14] It is important to note that among other molecular systems, homogeneous catalysts based on metallomacrocyclic complexes such as $[M^{II}(TPFC)]^{2+}$ (M^{II} =Fe, Co; TPFC = 5,10,15-tris(pentafluorphenyl)corrole) or $[M^{II}(TTP)]^{2+}$ (M^{II} = Fe, Co; TTP = tetrakis(3-methylphenyl)porphyrin)[63] show much lower catalytic activity.

***Acknowledgements*.** The authors thank FEDER and Spanish MINECO for financial support under projects MAT2013-40950-R, UCAN08-4E-008, MAT2012-38664-C02-1 and Consolider ORFEO. A.D. also thanks to Spanish *Ministerio de Educación, Cultura y Deporte* by their pre-doctoral FPU grant (AP2008-03942)

Supporting Information: crystallographic data for the structures reported in this Article have been deposited with the Cambridge Crystallographic Data Center with CCDC # 840551 – 840554, 892008 and 892009. Digital photos of single crystals, SEM images, observed and calculated X-ray powder diffraction patterns, some structure plots, IR spectra, thermodiffractometric results, thermogravimetry plots and summarized TG analysis, results of recyclability plots can be found in Supporting Information.

References

(1) E. E. Benson, C. P. Kubiak, A. J. Sathrum, J. M. Smieja, *Chem. Soc. Rev*., **2009**, *38*, 89−99.
(2) Y. Amao, *Chem.Cat.Chem.*, **2011**, *3*, 458−474.
(3) A. J. Morris, G. J. Meyer, E. Fujita, *Acc. Chem. Res.*, **2009**, *42*, 1983−1994.
(4) B. Kumar, M. Llorente, J. Froehlich, T. Dang, A. Sathrum, C. P. Kubiak, *Annu. Rev. Phys. Chem.*, **2012**, *63*, 541−569.
(5) Y. Izumi, *Coord. Chem. Rev*., **2013**, *257*, 171–186.
(6) F. Hebrard, P. Kalck, *Chem. Rev.*, **2009**, *109*, 4272−4282.
(7) D. Leckel, *Energy Fuels*, **2009**, *23*, 2342−2358.
(8) C. D. Windle, R. N. Perutz, *Coord. Chem. Rev.*, **2012**, *256*, 2562−2570.
(9) S. L.-F. Chan, T. L. Lam, C. Yang, S.-C. Yan and N. M. Cheng, *Chem. Commun*., 2015, **51**, 7799–7801.
(10) J. Hawecker, J. M. Lehn, R. Ziessel, *J. Chem. Soc., Chem. Comm*., **1983**, 536−538.
(11) J. Hawecker, J. M. Lehn, R. Ziessel, *Helv. Chim. Acta*, **1986**, *69*, 1990−2012.
(12) J. Hawecker, J. M. Lehn, R. Ziessel, *J. Chem. Soc., Chem. Commun.*, **1985**, 56−58.
(13) J. M. Lehn, R. Ziessel, *Proc. Natl. Acad. Sci. U.S.A.*, **1982**, *79*, 701−704.
(14) J. L. Grant, K. Goswami, L. O. Spreer, J. W. Otvos, M. Calvin, *J. Chem. Soc., Dalton Trans.*, **1987**, 2105−2109.
(15) T. Hirose, Y. Maeno, Y. Himeda, *J. Mol. Catal. Chem.*, **2003**, *193*, 27−32.
(16) Z. Xie, C. Wang, K. E. deKrafft, W. Lin, *J. Am. Chem. Soc.*, **2011**, *133*, 2056–2059.
(17) T. W. Woolerton, S. Sheard, E. Pierce, S. W. Ragsdale, F. A. Armstrong, *Energy Environ. Sci*., **2011**, *4*, 2393−2399.
(18) S. Sato, T. Arai, T. Morikawa, K. Uemura, T. M. Suzuki, H. Tanaka, T. Kajino, *J. Am. Chem. Soc.*, **2011**, *133*, 15240−15243.
(19) C. D. Windle, M. V. Câmpian, A.-K. Duhme-Klair, E. A. Gibson, R. N. Perutz, J. Schneider, *Chem. Commun.*, **2012**, *48*, 8189−8191.
(20) A. Phan, C. J. Doonan, F. J. Uribe-Romo, C. B. Knobler, M. O'Keeffe, O. M. Yaghi, *Acc. Chem. Res*., **2010**, *43*, 58−67.
(21) J. Li, R. J. Kuppler, H. Zhou, *Chem. Soc. Rev*., **2009**, *38*, 1477−1504.
(22) L. J. Murray, M. Dinca, J. R. Long, *Chem. Soc. Rev*., **2009**, *38*, 1294−1314.
(23) K. Sumida, D. L. Rogow, J. A. Mason, T. M. McDonald, E. D. Bloch, Z. R. Herm, T.-H. Bae, J. R. Long, *Chem. Rev.*, **2012**, *112*, 734–781.
(24) Z. Hu, B. J. Deibert, J. Li, *Chem. Soc. Rev*., **2014**, *43*, 5815–5840.
(25) L. E. Kreno, K. Leong, O. K. Farha, M. Allendorf, R. P. Van Duyne, J. T. Hupp, *Chem. Rev*., **2012**, *112*, 1105–1125.
(26) T. Uemura, N. Yanai, S. Kitagawa, *Chem. Soc. Rev*., **2009**, *38*, 1228−1236.
(27) C.-Y. Sun,C. Qin, X.-L. Wang, Z.-M. Su, *Expert Opin. Drug Delivery*, **2013**, *10*, 89–101.
(28) L. Ma, C. Abney, W. Lin, *Chem. Soc. Rev*., **2009**, *38*, 1248−1256.
(29) J. Lee, O. K. Farha, J. Roberts, K. A. Scheidt, S. T. Nguyen, J. T. Hupp, *Chem. Soc. Rev*., **2009**, *38*, 1450−1459.
(30) E. Coronado, J. R. Galán-Mascarós, C. J. Gómez-García, V. Laukhin, *Nature*, **2000**, *408*, 447−449.
(31) S. Decurtins, H. Schmalle, R. Pellaux, *New. J. Chem.*, **1998**, *22*, 117−121.
(32) S. Decurtins, H. W. Schmalle, P. Schneuwly, J. Ensling, P. Gütlich, *J. Am. Chem. Soc*., **1994**, *116*, 9521−9528.
(33) R. Pellaux, S. Decurtins, H. W. Schmalle, *Acta Cryst.*, **1999**, *C55*, 1075–1079.
(34) R. Sieber, S. Decurtins, H. Stoeckli-Evans, C. Wilson, D. Yufit, J. A. K. Howard, S. C. Capelli and A. Hauser, *Chem.-Eur. J*., **2000**, *6*, 361−368.
(35) S. Decurtins, H. W. Schmalle, R. Pellaux, P. Schneuwly, A. Hauser, *Inorg. Chem*., **1996**, *35*, 1451−1460.
(36) R. Andrés, M. Gruselle, B. Malézieux, M. Verdaguer, J. Vaissermann, *Inorg. Chem.*, **1999**, *38*, 4637−4646.
(37) P. Román, C. Guzmán-Miralles, A. Luque, *Dalton Trans.*, **1996**, 20, 3985−3989.
(38) R. Andrés, M. Brissard, M. Gruselle, C. Train, J. Vaissermann, B. Malézieux, J.-P. Jamet, M. Verdaguer, *Inorg. Chem.*, **2001**, *40*, 4633−4640.
(39) M. Milos, A. Hauser, *J. Luminescence*, **2013**, *133*, 15–20.
(40) M. Milos, A. Hauser, *J. Luminescence*, **2009**, *129*, 1901–1904.

(41) V. S. Langford, M. E. von Arx, A. Hauser, *J. Phys. Chem. A*, **1999**, *103*, 7161–7169.
(42) M. E. von Arx, E. Burattini, A. Hauser, L. van Pieterson, R. Pellaux, S. Decurtins, *J. Phys. Chem. A*, **2000**, *104*, 883–893.
(43) M. E. von Arx, V. S. Langford, U. Oetliker, A. Hauser, *J. Phys. Chem. A*, **2002**, *106*, 7099–7105.
(44) M. E. von Arx, A. Hauser, H. Riesen, R. Pellaux, S. Decurtins, *Phys. Rev. B*, **1996**, *54*, 15800–15807.
(45) R. A. Palmer, T. S. Piper, *Inorg. Chem.*, **1966**, *5*, 864−878.
(46) R. Kaziro, T. W. Hambley, R. A. Bistead, J. K. Beattie, *Inorg. Chim. Acta*, **1989**, *164*, 85−91.
(47) A. Altomare, G. Cascarano, C. Giacovazzo, A. Guagliardi, M. C. Burla, G. Polidori, M. Camalli, *J. Appl. Cryst*., **1994**, *27*, 435.
(48) G. M. Sheldrick, *Acta. Cryst*., **1990**, *A46*, 467–473.
(49) H. D. Flack, G. Bernardinelli, *J. Appl. Crystallogr*., **2000**, *33*, 1143−1148.
(50) A. Dikhtiarenko, R. Valiente, J. A. Blanco, J. Gascon, J. R. García, J. Gimeno, *Chem. Commun*., **2015**, (*submitted*).
(51) S. R. Batten, K. S. Murray, N. J. Sinclair, *Acta Cryst*., **2000**, *C56*, e320.
(52) C. Ruiz-Perez, P. A. L. Luis, F. Lloret, M. Julve, *Inorg. Chim. Acta*, **2002**, *336*, 131−136.
(53) Y. Jing-Cai, M. Lu-Fang, Y. Feng-Juan, *Z. Kristallogr.- New Cryst. Struct*., **2005**, *220*, 483−484.
(54) M. E. Fleet, *Mineral. Mag*., **1976**, *40*, 531−533.
(55) K. Robinson, G. V. Gibbs, P. H. Ribbe, *Science*, **1971**, *172*, 567−570.
(56) V. A. Blatov, A. P. Shevchenko, D. M. Proserpio, *Cryst. Growth Des.*, **2014**, *14*, 3576−3586.
(57) S. T. Hyde, M. O'Keeffe, D. M. Proserpio, *Angew. Chem., Int. Ed*., **2008**, *47*, 7996−8000.
(58) V. M. Russell, D. C. Craig, M. L. Scudder, I. G. Dance, *Cryst. Eng. Comm*., **2000**, *2*, 16−23.
(59) I. A. Baburin, V. A. Blatov, *Acta Cryst*., **2004**, *B60*, 447−452.
(60) E. V. Peresypkina, V. A. Blatov, *J. Mol. Struct.-Theochem*., **1999**, *489*, 225–236.
(61) D. Shriver, P. Atkins, Inorganic Chemistry: Ed. W. H. Freeman; Oxford University Press, Oxford, 2009.
(62) TONs of 120 and 150 have been reported (ref. 49) for the compounds $\{[Co(bpy)_3][M^IRu(C_2O_4)_3]\}$ (M^I = Li, Na).
(63) J. Grodkowski, P. Neta, E. Fujita, A. Mahammed, L. Simkhovish, Z. Gross, *J. Phys. Chem. A*., **2002**, *106*, 4772–4778.

SUPPORTING INFORMATION

Templating 3D Honeycomb-like Coordination Polymers Based on Ruthenium Oxalate Building Unit: Characterization and Catalytic Activity in Carbon Dioxide Photoreduction

Alla Dikhtiarenko,[a] Rafael Valiente,[b] José R. García,[a] and José Gimeno[a]

[a] Departamento de Química Orgánica e Inorgánica, Universidad de Oviedo – CINN, 33006 Oviedo, Spain
[b] MALTA Consolider Team, Departamento de Física Aplicada, Universidad de Cantabria, 39005 Santander, Spain

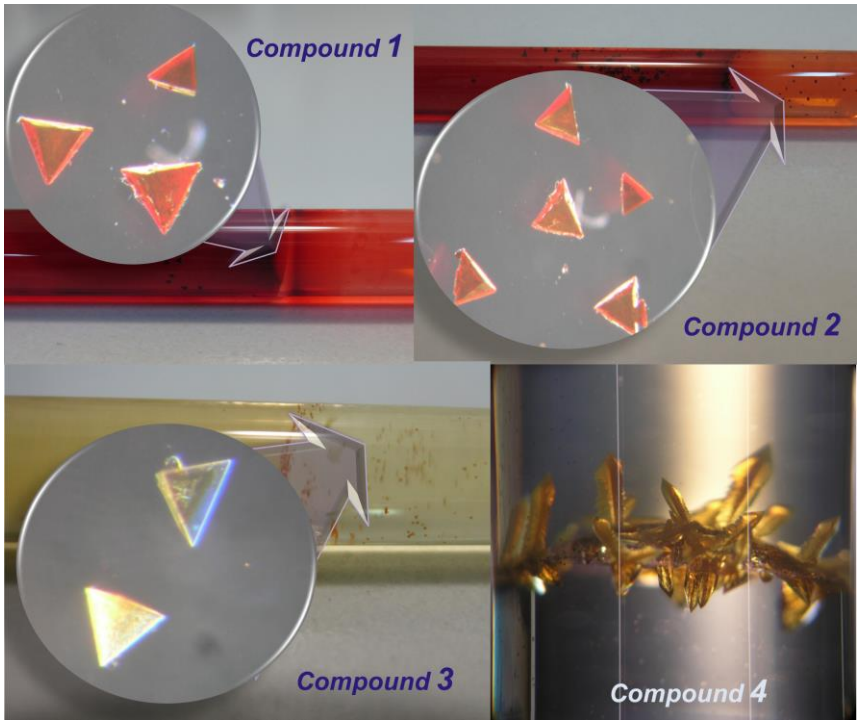

Figure S1. Digital photographs showing the crystal habits of compounds **1**–**4** grown in gel media.

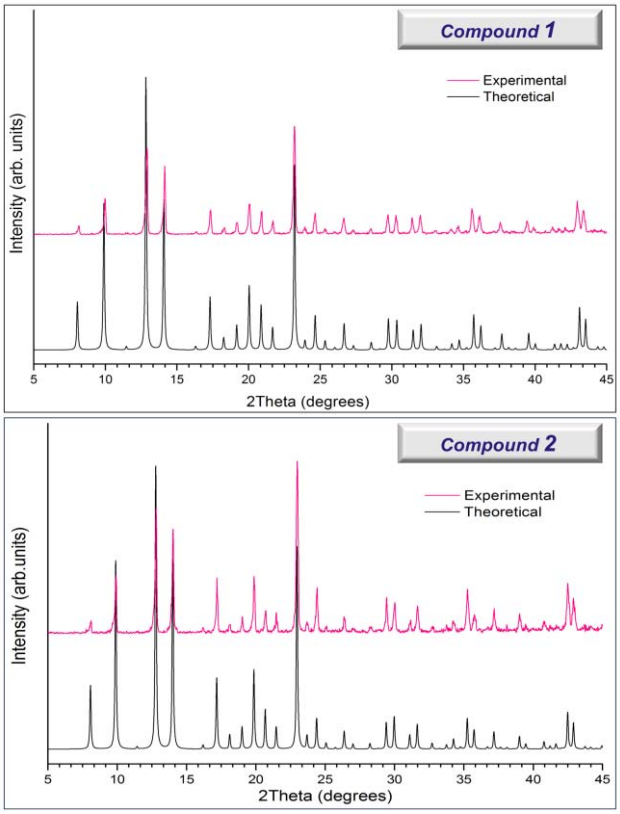

Figure S2. Experimental X-Ray powder diffraction diagrams of compounds $\{[Fe(bpy)_3][NaRu(C_2O_4)_3]\}_n$ (**1**) and $\{[Fe(bpy)_3][LiRu(C_2O_4)_3]\}_n$ (**2**) compared with the calculated ones.

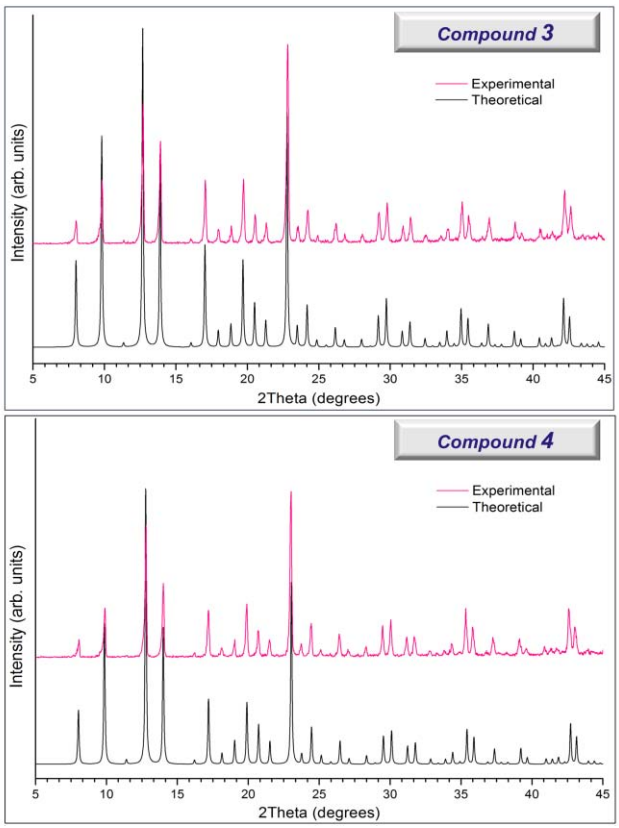

Figure S3. Experimental X-Ray powder diffraction diagrams of compounds $\{[Ni(bpy)_3][NaRu(C_2O_4)_3]\}_n$ (**3**) and $\{[Ni(bpy)_3][LiRu(C_2O_4)_3]\}_n$ (**4**) compared with the calculated ones.

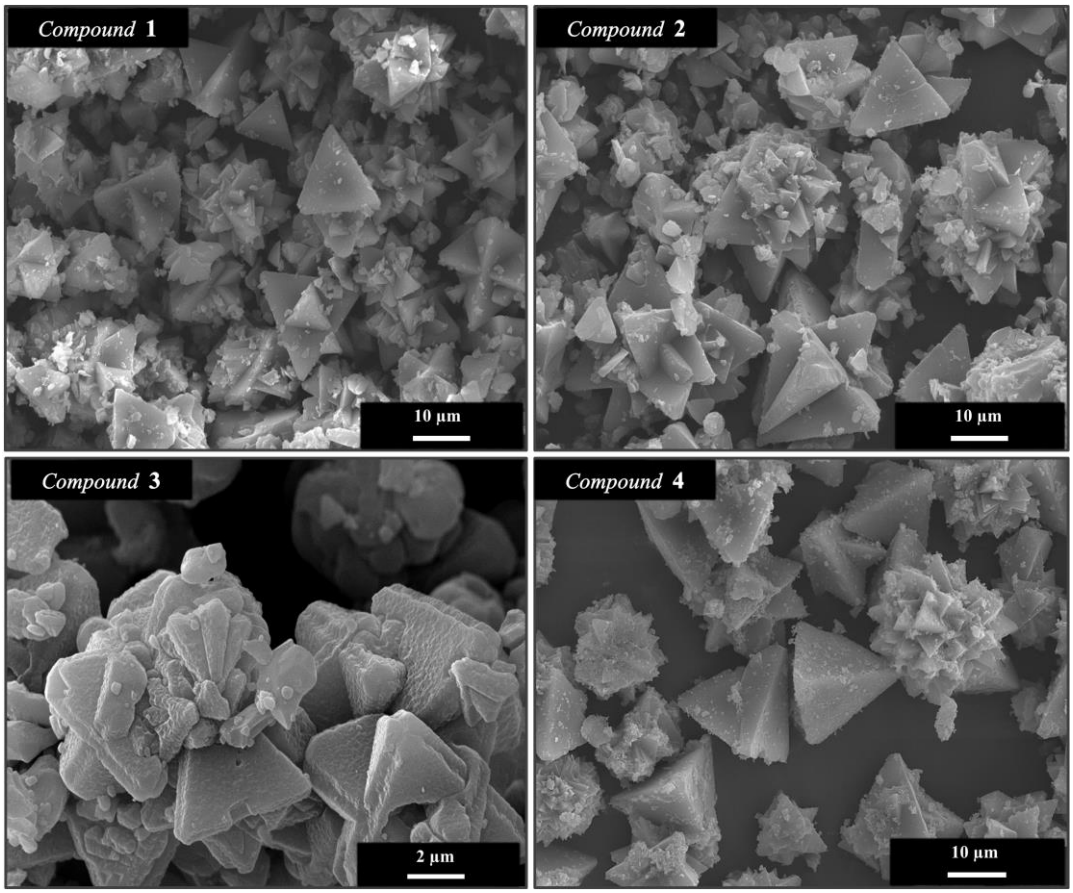

Figure S4. SEM images of compound **1**–**4**

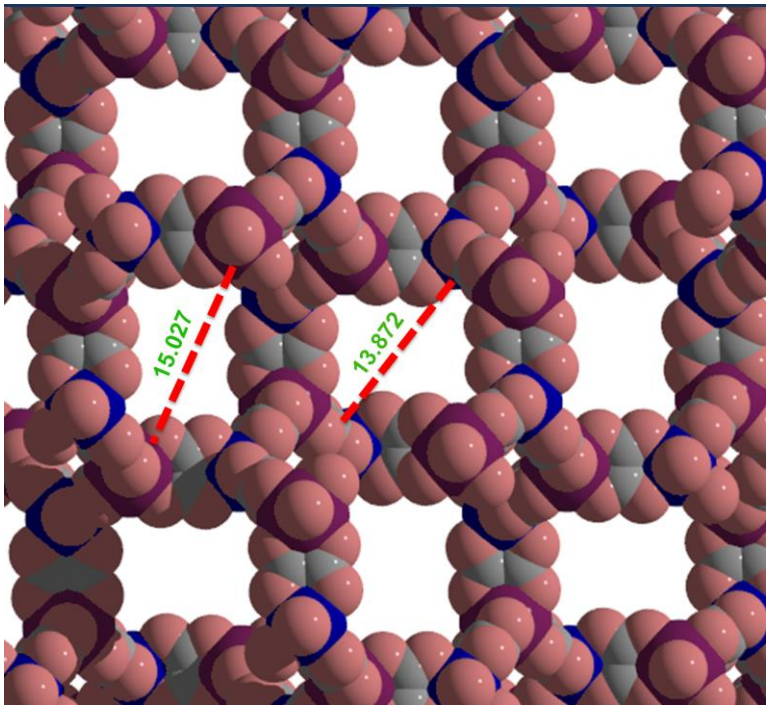

Figure S5. Space filling view of cubic channels along *c*-axis in 3D anionic array of $\{[Fe(bpy)_3][NaRu(C_2O_4)_3]\}_n$ (**1**), showing two porous types: large (15.027(2) Å) and small (13.872(2) Å) ones. The Ru atoms are purple, Na are blue, O are pink and C are grey.

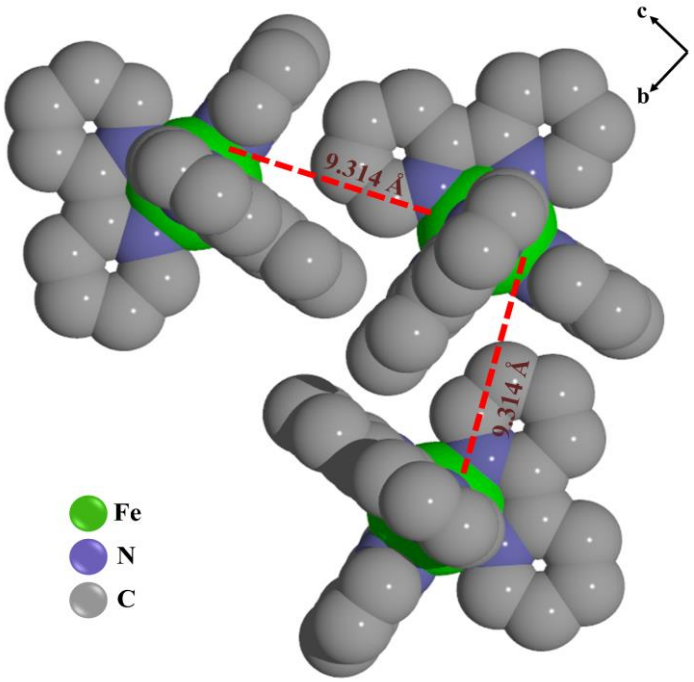

Figure S6. Space filling representation of the packing mode of three $[Fe(bpy)_3]^{2+}$ cationic complexes in 3D anionic network of compound $\{[Fe(bpy)_3][NaRu(C_2O_4)_3]\}_n$ (**1**). The hydrogen atoms have been omitted for clarity.

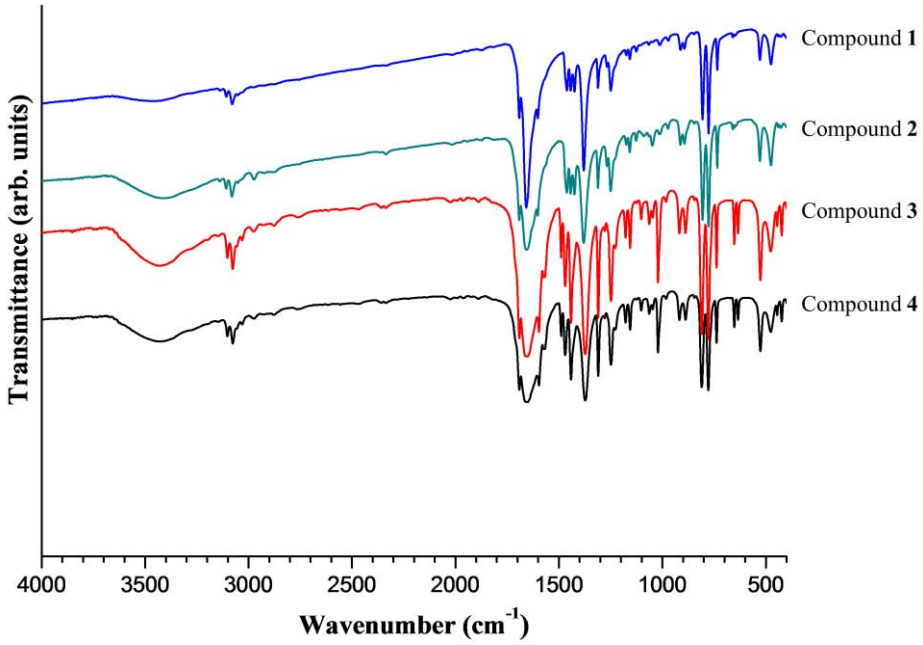

Figure S7. IR spectra of compounds **1**–**4**.

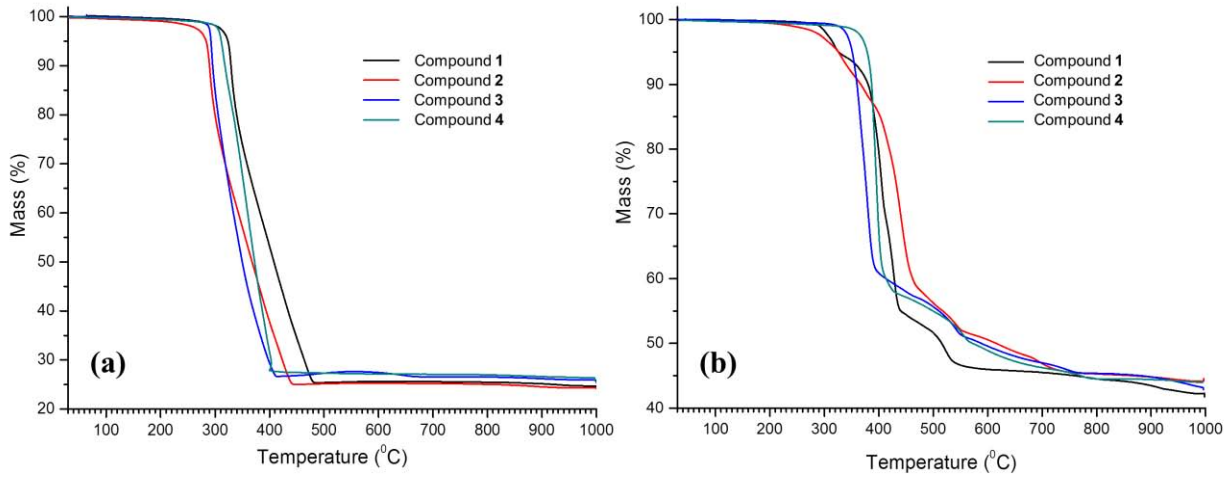

Figure S8. Thermal decomposition curves of compounds **1**–**4** in air (a) and nitrogen (b) atmospheres.

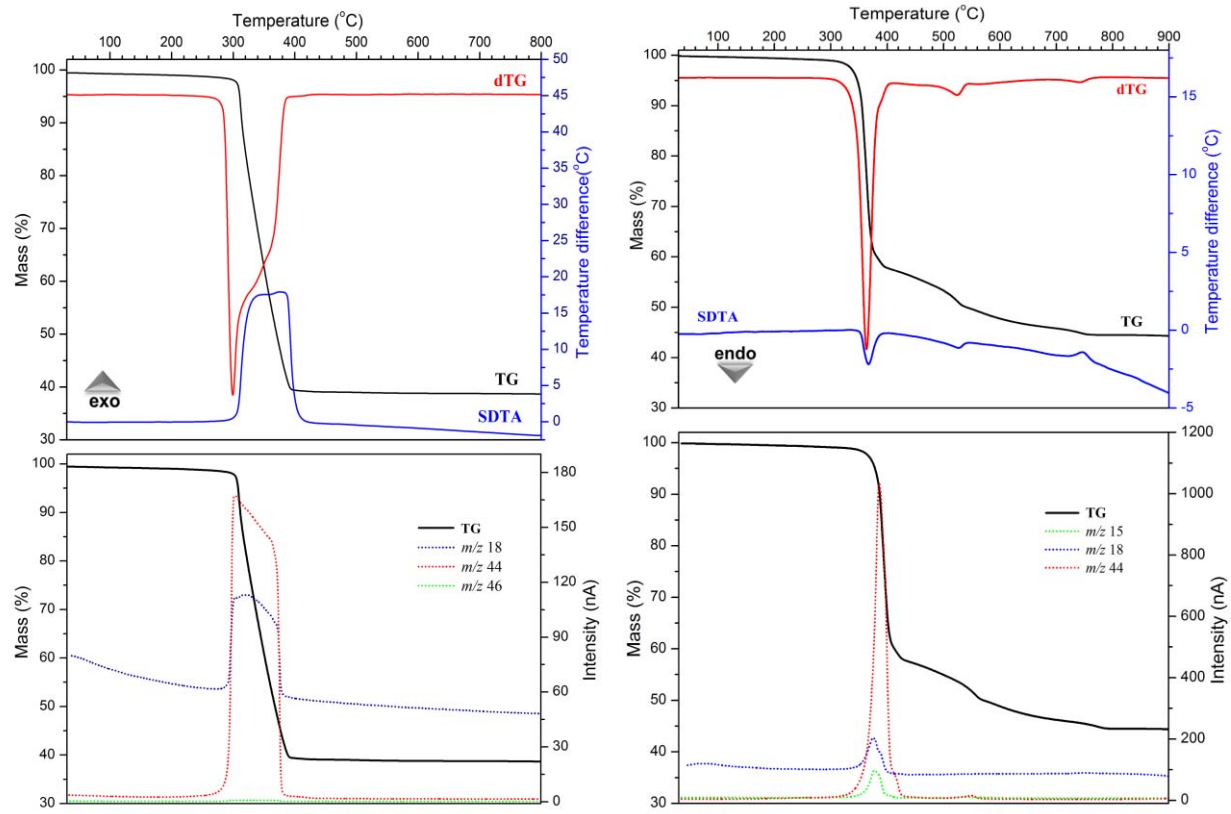

Figure S9. TG, DTG, SDTA and mass spectrometry of evacuated vapors curves for compound $\{[Fe(bpy)_3][NaRu(C_2O_4)_3]\}_n$ (**1**) in air (left) and nitrogen (right) atmosphere.

Table S1. Summary of thermogravimetric data in nitrogen and air atmosphere for compounds **1**–**4**.

Compound	**1**	**2**	**3**	**4**
Formula	$C_{36}H_{24}FeLiN_6O_{12}Ru$	$C_{36}H_{24}FeN_6NaO_{12}Ru$	$C_{36}H_{24}N_6NaNiO_{12}Ru$	$C_{36}H_{24}LiN_6NiO_{12}Ru$
FW	896.47	912.52	915.36	899.31
		Oxygen atmosphere		
T^{range}, °C	215 ÷ 423	281 ÷ 465	225 ÷ 421	291 ÷ 423
T^{max}, °C	295	405	299	308
Weight loss,% obs./calc	74.6 / 74.5	74.1 / 73.8	74.0 / 73.9	75.2 / 75.7
m/z		18 (H_2O), 44 (CO_2), 46 (NO_2)		
Enthalpy (J/g)	- 8680	- 9549	- 7225	- 7281
		Nitrogen atmosphere*		
T^{range}, °C	210 ÷ 799	223 ÷ 625	298 ÷ 760	319 ÷ 795
T^{max}, °C	435	408	381	385
Weight loss,% obs./calc	65.2 / 78.8	64.23 / 76.8	65.1 / 77.4	65.9 / 78.8
m/z		15 (NH_3), 18 (H_2O), 44 (CO_2)		
Enthalpy (J/g)	217	366	224	280

* The difference between observed and calculated mass losses in nitrogen atmosphere due to formation of carbon solid residues as a product of pyrolysis of organic ligands.

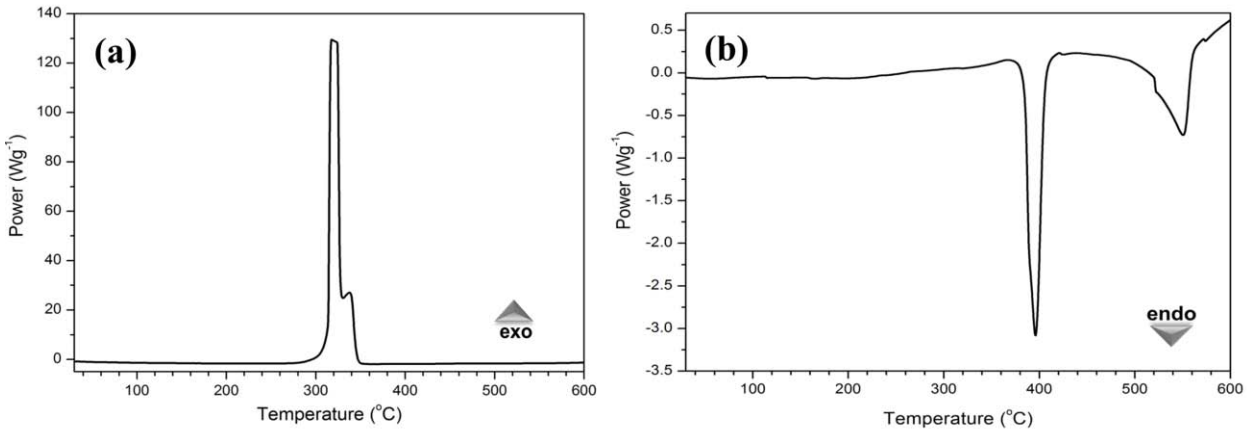

Figure S10. DSC curves of compound $\{[Fe(bpy)_3][NaRu(C_2O_4)_3]\}_n$ (**1**) in air (a) and nitrogen (b) atmospheres.

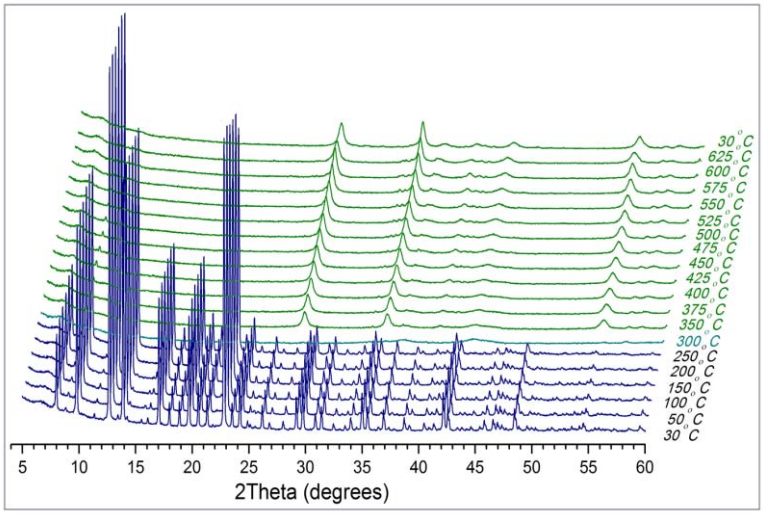

Figure S11. X-Ray thermodiffractogram of $\{[Fe(bpy)_3][NaRu(C_2O_4)_3]\}_n$ (**1**) recorded in air heating up from 30 to 625 °C. Color code corresponds to the structural changes.

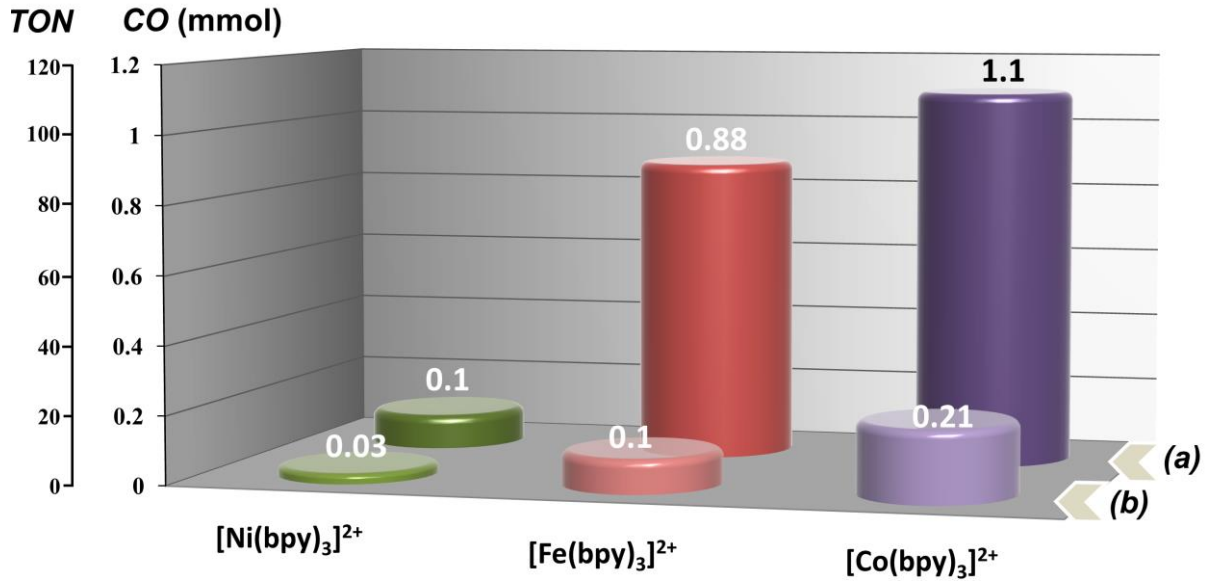

Figure S12. Amounts of CO (mmol) produced by (a) mixture of $K_3[Ru(C_2O_4)_3]$ and $[M^{II}(bpy)_3]X_2$ (M^{II} = Ni, Fe, Co; X = Cl^-, ClO_4^-) complexes or by (b) just $[M^{II}(bpy)_3]X_2$ (M^{II} = Ni, Fe, Co; X = Cl^-, ClO_4^-) precursor compounds in CO_2 photoreduction reaction under 10 h of UV-light irradiation (≤ 366 nm). Left insert scale bars correspond to TON values and can be converted using: TON = mmol of $CO \cdot 10^3$/ 10 µmol of catalyst.

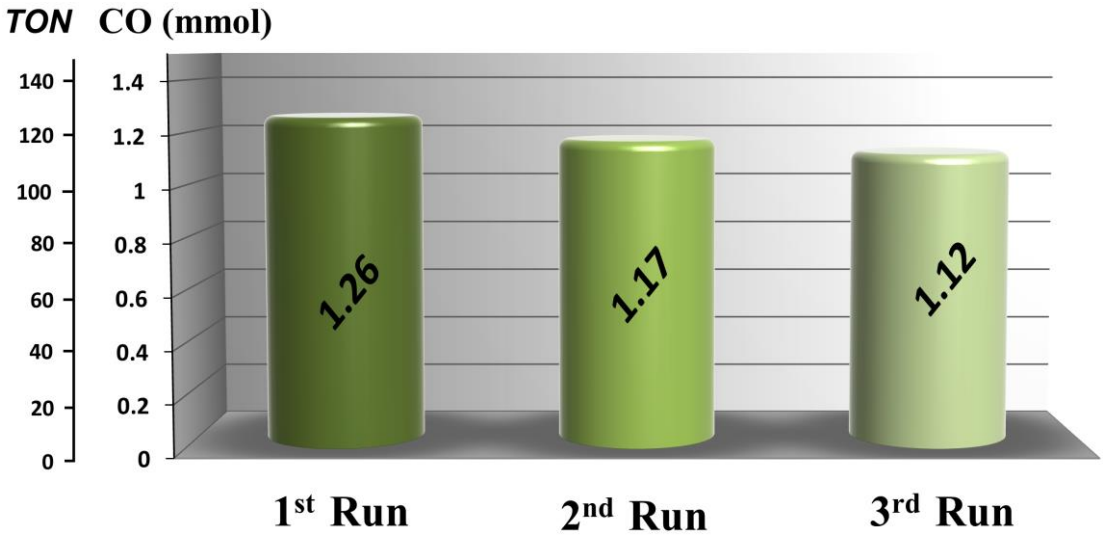

Figure S13. Catalytic activity of $\{[Ni(bpy)_3][NaRu(C_2O_4)_3]\}_n$ (**3**) in CO_2 photoreduction reaction for three consecutive runs. Left insert scale bars correspond to TON values and can be converted using: TON = mmol of $CO \cdot 10^3$/ 10 μmol of catalyst.

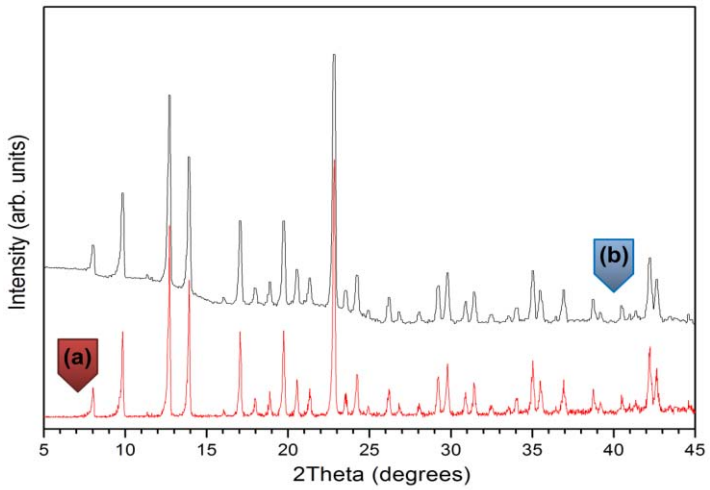

Figure S14. Comparison of powder X-Ray diffraction patterns of compound $\{[Ni(bpy)_3][NaRu(C_2O_4)_3]\}_n$ (**3**) before (a) and after (b) three repeated photocatalytic runs.

Capítulo IX

Polímeros de Coordinación 3D Basados en unidades de Oxalato de Rutenio(III) como Catalizadores Heterogéneos para la Fotoreducción de Agua

El *Capítulo IX* se dedica a la preparación de nuevos polímeros de coordinación tridimensionales de fórmula general $\{[Z^{II}(bpy)_3][M^{I}Ru(C_2O_4)_3]\}_n$ y $\{[Zn^{II}(bpy)_3](H_2O)[LiRu(C_2O_4)_3]\}_n$ (donde Z^{II} = Zn, Cu, Ru, Os; M^{I} = Na, Li; bpy = 2,2´-bipiridina), así como a la caracterización estructural y a la determinación de su actividad como fotocatalizadores heterogéneos en la foto-reducción de agua.

En los últimos años, el agotamiento progresivo de los recursos fósiles, unido a los problemas ambientales causados por su combustión, han estimulado el desarrollo de nuevas tecnologías de producción de energía renovable, incluyendo la síntesis fotocatalítica de hidrógeno a partir de agua.[1–3] Con este fin, la conjunción de materiales orgánicos e inorgánicos ha sido utilizada para el diseño y preparación de fotocatalizadores aplicables a la generación de hidrógeno a partir del agua,[4,5] siendo los polímeros de coordinación (PCs) y las redes metal-orgánicas (MOFs) candidatos potenciales en este campo, en adición a su uso en almacenamiento de gases, tamizado molecular, y catálisis heterogénea.[6–18] Además, en la última década, numerosos estudios han recogido el uso de PCs/MOFs como plataformas para la integración de diferentes componentes funcionales con el fin de lograr el almacenamiento de energía luminosa que propicie su uso en reacciones fotocatalíticas.[19,20] A día de hoy, se conocen PCs/MOFs capaces de provocar la foto-reducción de CO_2, la fotogeneración de las nanopartículas metálicas, la oxidación de compuestos orgánicos, la fotodegradación de colorantes orgánicos, así como otras muchas transformaciones orgánicas. En comparación con otros sistemas fotocatalíticos, los fotocatalizadores basados en PCs/MOFs presentan la ventaja de que las múltiples combinaciones de enlazadores orgánicos y centros metálicos permite el diseño racional de estos materiales a nivel molecular. En este contexto, se han alcanzado recientes logros sintéticos con la preparación de redes poliméricas robustas que hacen posible la disociación fotocatalítica del agua con producción de hidrógeno molecular.[21,22] La mayoría de los PCs/MOFs fotoactivos han sido obtenidos mediante introducción de sus componentes funcionales en varios procesos post-sintéticos sucesivos. Este método presenta las desventajas derivadas de la dificultad de

(1) A. Kudo,Y. Miseki, *Chem. Soc. Rev*., **2009**, *38*, 253–278.
(2) S. J. A. Moniz, S. A. Shevlin, D. J. Martin, Z.-X. Guob, J. Tang, *Energy Environ. Sci.*, **2015**, *8*, 731–759.
(3) M. Matsuoka, M. Kitano, M. Takeuchi, K. Tsujimaru, M. Anpo, J. M. Thomas, *Catal. Today*, **2007**, *122*, 51–61.
(4) Y. Horiuchi, T. Toyao, M. Takeuchi, M. Matsuoka, M. Anpo, *Phys. Chem. Chem. Phys*., **2013**, *15*, 13243–13253.
(5) B. X. Wei, K.-X. Wang, X.-X. Guo, J.-S. Chen, *Proc. R. Soc. A*, **2012**, *468*, 2099–2112.
(6) J.-R. Li, R. J. Kuppler, H.-C. Zhou, *Chem. Soc. Rev*., **2009**, *38*, 1477–1504.
(7) K. Sumida, D. L. Rogow, J. A. Mason, T. M. McDonald, E. D. Bloch, Z. R. Herm, T.-H. Bae, J. R. Long, *Chem. Rev*., **2012**, *112*, 734–781.
(8) J. Liu, P. K. Thallapally, B. P. McGrail, D. R. Brown, J. Liu, *Chem. Soc. Rev*., **2012**, *41*, 2308–2322.
(9) B. Van de Voorde, B. Bueken, J. Denayer, D. De Vos, *Chem. Soc. Rev*., **2014**, *43*, 5766–5788.
(10) N. C. Burtch, H. Jasuja, K. S. Walton, *Chem. Rev.*, **2014**, *114*, 10575–10612.
(11) C. K. Brozek, M. Dincă, *Chem. Soc. Rev*., **2014**, *43*, 5456–5467.
(12) W. Zhang, R.-G. Xiong, *Chem. Rev*., **2012**, *112*, 1163–1195.
(13) P. Ramaswamy, N. E. Wong, G. K. H. Shimizu, *Chem. Soc. Rev*., **2014**, *43*, 5913–5932.
(14) T. Yamada, K. Otsubo, R. Makiura, H. Kitagawa, *Chem. Soc. Rev*., **2013**, *42*, 6655–6669.
(15) J. Gascon, A. Corma, F. Kapteijn, F. X. Llabrés i Xamena, *ACS Catal*., **2014**, *4*, 361–378.
(16) A. Corma, H. García, F. X. Llabrés i Xamena, *Chem. Rev*., **2010**, *110*, 4606–4655.
(17) J. Y. Lee, O. K. Farha, J. Roberts, K. A. Scheidt, S. T. Nguyen, J. T. Hupp, *Chem. Soc. Rev*., **2009**, *38*, 1450–1459.
(18) L. Ma, C. Abney, W. Lin, *Chem. Soc. Rev.*, **2009**, *38*, 1248–1256.
(19) T. Zhang, W. Lin, *Chem. Soc. Rev.*, **2014**, *43*, 5982–5993.
(20) M. A. Nasalevich, M. van der Veen, F. Kapteijn, J. Gascon, *Cryst. Eng. Comm*, **2014**, *16*, 4919–4926.
(21) K. Meyer, M. Ranocchiari, J. A. van Bokhoven, *Energy Environ. Sci*., **2015**, *8*, 1923–1937.
(22) Y. Ren, G. H. Chia, Z. Gao, *Nano Today*, **2013**, *8*, 577–597.

determinar el grado de modificación alcanzado y la distribución heterogénea de los centros catalíticos. Así, polímeros de coordinación tridimensionales, $\{[Z^{II}(bpy)_3][M^IM^{III}(C_2O_4)_3]\}_n$,[23–32] $\{[Z^{II}(bpy)_3](H_2O)[M^IM^{III}(C_2O_4)_3]\}_n$,[33] $\{[Z^{III}(bpy)_3](X)[M^IM^{III}(C_2O_4)_3]\}_n$[29–31,34–38] ($M^I = Li^+$, Na^+; $M^{III} = Al^{3+}$, Cr^{3+}, Rh^{3+}, Ru^{3+}, Fe^{3+}; $Z^{II} = Fe^{2+}$, Co^{2+}, Ni^{2+}, Zn^{2+}, Ru^{2+}, Os^{2+}; $Z^{III} = Rh^{3+}$, Cr^{3+}, Co^{3+}; X = ClO_4^-, PF_6^-, BF_4^-; bpy = 2,2´-bipyridine), y PCs/MOFs funcionales con moléculas fotoactivas encapsuladas,[39] son competidores a considerar, actuando los cationes $[Z^{II}(bpy)_3]^{2+}$ como huéspedes moleculares, homogénea y selectivamente distribuidos en las cavidades de la red aniónica tridimensional, $\{[M^IM^{III}(C_2O_4)_3]^{2-}\}_n$, mientras el catalizador se obtiene directamente mediante auto-ensamblaje, obviando la necesidad de implementar funcionalidades mediante complicadas vías post-sintéticas.

Inspirados en las descripciones realizadas por el grupo de Decurtins de los compuestos $\{[M^{II/III}(bpy)_3][NaCr(C_2O_4)_3]\}_n$ ($M^{II} = Ru^{2+}$, Zn^{2+}, Os^{2+}, Fe^{2+}; $M^{III} = Rh^{3+}$, Cr^{3+})[29–32,37], que indican migración resonante de energía, asistida por iluminación VIS o UV, entre los fragmentos $[Cr(C_2O_4)_3]^{3-}$ y $[M^{II/III}(bpy)_3]^{2+/3+}$, el estudio realizado en el presente Capitulo de esta Tesis se dedica a la preparación y caracterización de una familia de nuevos polímeros de coordinación basados en oxalato de rutenio, $\{[Z^{II}(bpy)_3][M^IRu(C_2O_4)_3]\}_n$ y $\{[Zn^{II}(bpy)_3](H_2O)[LiRu(C_2O_4)_3]\}_n$ (donde M^{II} = Zn, Cu, Ru, Os; M^I = Na, Li; bpy = 2,2´-bipiridina), con especial atención al estudio de su actividad fotocatalítica en la generación de hidrógeno a partir de agua. Los resultados obtenidos se recogen en la *Publicación VIII*, que se presenta a continuación, y forma parte del contenido de esta Tesis.

Los compuestos $\{[Z^{II}(bpy)_3][M^IRu(C_2O_4)_3]\}_n$ y $\{[Zn^{II}(bpy)_3](H_2O)[LiRu(C_2O_4)_3]\}_n$ (donde Z^{II} = Zn, Cu, Ru, Os; M^I = Na, Li; bpy = 2,2´-bipiridina) se originan mediante auto-ensamblaje de sus componentes en medio acuoso a temperatura ambiente. Todos los polímeros de coordinación descritos en este Capítulo presentan relativamente alta estabilidad térmica, tanto en atmósfera reactiva (aire) como inerte (nitrógeno). La degradación térmica de cada miembro de la serie procede en única etapa, en rangos de temperaturas comprendidos entre 180 °C y 300 °C, sin revelar cambios estructurales previos al colapso irreversible de la red polimérica.

Las estructuras cristalinas de todos los miembros de la serie fueron determinadas mediante datos de difracción de rayos X de monocristal, presentando simetría cúbica y naturaleza polimérica. Los datos recogidos en este trabajo indican que todos estos compuestos son isoestructurales, diferenciándose en la composición química de la plantilla catiónica,

(23) R. Pellaux, S. Decurtins, H. W. Schmalle, *Acta Cryst.*, **1999**, *C55*, 1075–1079.
(24) S. Rabaste, N. Amstutz, A. Hauser, A. Pillonnet, *Appl. Phys. Lett.*, **2005**, *87*, 251904(1)–(3).
(25) R. Sieber, S. Decurtins, H. Stoeckli-Evans, C. Wilson, J. A. K. Howard, S. C. Capelli, A. Hauser, *Chem. Eur. J.*, **2000**, *6*, 361–368
(26) P. Roman, C. Guzman-Miralles, A. Luque, *Dalton Trans.*, **1996**, *20*, 3985–3989.
(27) M. Milos, T. Penhouet, P. Pal, A. Hauser, *Inorg. Chem.*, **2010**, *49*, 3402–3408
(28) S. Decurtins, H. W. Schmalle, P. Schneuwly, J. Ensling, P. Gütlich, *J. Am. Chem. Soc.*, **1994**, *116*, 9521–9528.
(29) M. Milos, A. Hauser, *J. Luminescence*, **2013**, *133*, 15–20.
(30) M. Milos, A. Hauser, *J. Luminescence*, **2009**, *129*, 1901–1904.
(31) M. E. von Arx, A. Hauser, H. Riesen, R. Pellaux, S. Decurtins, *Phys. Rev. B*, **1996**, *54*, 15800–15807.
(32) M. E. von Arx, E. Burattini, A. Hauser, L. van Pieterson, R. Pellaux, S. Decurtins, *J. Phys. Chem. A*, **2000**, *104*, 883–893
(33) R. Andrés, M. Gruselle, B Malézieux, M. Verdaguer, J. Vaissermann, *Inorg. Chem.*, **1999**, *38*, 4637−4646.
(34) M. Milos, P. Pal, A. Hauser, *Chem. Phys. Chem.*, **2010**, *11*, 3161–3166.
(35) A. Hauser, H. Riesen, R. Pellaux, S. Decurtins, *Chem. Phys. Lett.*, **1996**, *261*, 313–317.
(36) S. Decurtins, H. W. Schmalle, R. Pellaux, P. Schneuwly, A. Hauser, *Inorg. Chem.*, **1996**, *35*, 1451–1460.
(37) V. S. Langford, M. E. von Arx, A. Hauser, *J. Phys. Chem. A*, **1999**, *103*, 7161–7169.
(38) M. E. von Arx, V. S. Langford, U. Oetliker, A. Hauser, *J. Phys. Chem. A*, **2002**, *106*, 7099–7105.
(39) R. W. Larsen, L. Wojtas, *J. Phys. Chem. A*, **2012**, *116*, 7830−7835.

$[Z^{II}(bpy)_3]^{2+}$ (Z^{II} = Zn, Cu, Ru, Os; bpy = 2,2´-bipiridina), y en el catión alcalino que constituye la red polimérica. Sus estructuras cristalinas constan de la plantilla molecular catiónica, $[Zn^{II}(bpy)_3]^{2+}$, que reside en las cajas de la red aniónica, $\{[Na/LiRu(C_2O_4)_3]^{2-}\}_n$, construida alternando poliedros octaédricos, $\{Na/LiO_6\}$ y $\{RuO_6\}$, enlazados mediante ligandos oxalato. Considerando los enlaces covalentes en la red polimérica, y dado que cada centro metálico muestra una conectividad similar, la estructura tridimensional aniónica, $\{[Na/LiRu(C_2O_4)_3]^{2-}\}_n$, presenta una topología tipo "panal de abeja", caracterizada por el símbolo 10^3 de Schläfli. El compuesto $\{[Zn^{II}(bpy)_3](H_2O)[LiRu(C_2O_4)_3]\}_n$ constituye un caso excepcional, donde una molécula de agua se incorpora a la estructura, acomodándose en el espacio disponible en una caja formada por tres pares de ligandos 2,2´-bipiridina procedentes de tres complejos $[Zn^{II}(bpy)_3]^{2+}$ adyacentes. En estos compuestos, las características electrónicas de las especies moleculares huésped son función de su interacción electrostática con la red anfitriona, discutiéndose las diferencias observadas a la luz de los datos experimentales obtenidos mediante espectroscopia UV-VIS y cálculos teóricos basados en datos estructurales.

La actividad catalítica de los polímeros de coordinación $\{[Z^{II}(bpy)_3][M^{I}Ru(C_2O_4)_3]\}_n$ y $\{[Zn^{II}(bpy)_3](H_2O)[LiRu(C_2O_4)_3]\}_n$ (Z^{II} = Zn, Cu, Ru, Os; M^{I} = Na, Li; bpy = 2,2´-bipiridina) fue evaluada en la fotogeneración de hidrógeno a partir del agua bajo luz incidente ultravioleta (UV, $\lambda \leq 366$ nm) y visible (VIS, $\lambda \geq 366$ nm). Los polímeros de coordinación estudiados demostraron capacidad para generar H_2 a partir del H_2O, alcanzando a producir 123 μmol de H_2 en 8 h de irradiación con luz UV, mientras que bajo irradiación en la región VIS los PCs exhibieron menor eficiencia. Es interesante reseñar que, bajo irradiación UV, la actividad catalítica de los compuestos de la serie disminuye al aumentar el salto de energía prohibida (*band gap*), indicando una relación directa entre la estructura electrónica y el comportamiento fotocatalítico.

En todos los casos, el reciclaje del catalizador muestra una disminución irrelevante de su actividad catalítica intrínseca, ya que la menor eficiencia observada debe relacionarse con pérdidas del catalizador heterogéneo en los procesos de recuperación y lavado. Además, se confirmó que la actividad catalítica no es consecuencia de las especies solubles que puedan aparecer en procesos de descomposición del polímero de coordinación. La compilación de todos los datos experimentales indica que la actividad fotocatalítica de los polímeros de coordinación $\{[Z^{II}(bpy)_3][M^{I}Ru(C_2O_4)_3]\}_n$ y $\{[Zn^{II}(bpy)_3](H_2O)[LiRu(C_2O_4)_3]\}_n$ (Z^{II} = Zn, Cu, Ru, Os; M^{I} = Na, Li; bpy = 2,2´-bipiridina) es función de la plantilla catiónica molecular y de sus características electrónicas, siguiendo el orden $Os^{2+} > Ru^{2+} > Zn^{2+} > Cu^{2+}$ (bajo luz UV) y $Os^{2+} > Ru^{2+} > Cu^{2+} \approx Zn^{2+}$ (bajo luz VIS). Además, la comparación de las actividades fotocatalíticas de la serie de compuestos presentada en este Capítulo de la Tesis con las actividades exhibidas en la fotoreducción del agua por los PCs/MOFs descritos previamente en bibliografía revelan mayores eficiencias fotocatalíticas bajo irradiación UV.

En resumen, los resultados obtenidos ponen de manifiesto que la síntesis racional de arquitecturas aniónicas tridimensionales proporciona un camino adecuado para la preparación de polímeros de coordinación multifuncionales con una topología estructural previsible y las propiedades deseadas.

Publication VIII

"Tris(bipyridine)Metal(II)-Templated Assemblies of 3D Ruthenium Oxalate Coordination Frameworks: Structures, Characterization and Photocatalytic Activity in Water Reduction"

Crystal Growth & Design

(in preparation)

*Year **2015***

Tris(bipyridine)Metal(II)-Templated Assemblies of 3D Alkali-Ruthenium Oxalate Coordination Frameworks: Structures, Characterization and Photocatalytic Activity in Water Reduction

Alla Dikhtiarenko,[a] Rafael Valiente,[b] José R. García,[a] and José Gimeno[a]

[a] Departamento de Química Orgánica e Inorgánica, Universidad de Oviedo – CINN, 33006 Oviedo, Spain
[b] MALTA Consolider Team, Departamento de Física Aplicada, Universidad de Cantabria, 39005 Santander, Spain

Abstract

Series of 3D oxalate bridged ruthenium-based coordination polymers with the formula of $\{[Z^{II}(bpy)_3][M^{I}Ru(C_2O_4)_3]\}_n$ ($Z^{II} = Zn^{2+}$ (**1**), Cu^{2+} (**3**, **4**), Ru^{2+} (**5**, **6**), Os^{2+} (**7**, **8**); $M^{I} = Li^{+}$, Na^{+}; bpy = 2,2′-bipyridine) and $\{[Zn^{II}(bpy)_3](H_2O)[LiRu(C_2O_4)_3]\}_n$ (**2**), have been synthesized at room temperature through self-assembly reaction in aqueous media and characterized by single crystal and powder X-ray diffraction, elemental analysis, infrared and diffuse reflectance UV-VIS spectroscopy, thermogravimetric analysis. The crystal structures of all compounds comprise chiral 3D honeycomb-like polymeric net with *srs*-type which poses of triangular anionic cages where $[Z^{II}(bpy)_3]^{2+}$ cationic templates selectively embedded. Structural analysis reveals that the electronic configuration of the cationic guests is affected by electrostatic interaction with anionic framework. Moreover, the MLCT bands gaps values for **1**–**8** can be tuned in rational way by judicious choice of $[Z^{II}(bpy)_3]^{2+}$ guests. The 3D host-guest polymeric architectures can be used as self-supported heterogeneous photocatalysts in reductive water splitting reaction, and as have been shown exhibit high photocatalytic behavior towards H_2 evolution under UV-light irradiation.

Keywords: water splitting, hydrogen evolution, coordination polymers, photocatalysis.

Introduction

In recent years, the depletion of fossil fuels and the environmental problems caused by their combustion have stimulated research on the development of new renewable energy production technologies. So far, several approaches have been proposed in order to satisfy the requirements. Among those explored, the system combining photocatalysts and solar energy as a clean and abundant energy resource is recognized to be of great promise. Currently, enormous attention has been paid to photocatalytic hydrogen production from water which is promising way to produce hydrogen as a potential clean energy source.[1] In this line, the hybridization of organic and inorganic materials opens up a new potential field in design and preparation of applicable photocatalysts for water splitting reaction by the integration of useful organic and inorganic characteristics within a single composite.[2]

In this sense, metal-organic frameworks (MOFs) and porous coordination polymers (CPs), which are organic-inorganic hybrid materials consisting of organic linkers and metal centers, clusters or metal-oxo clusters, have been received great interest due to their beneficial properties such as extremely high surface areas, well-ordered porous architectures and structure designability.[3] Taking advantages of these interesting properties, MOFs/CPs are widely studied for many potential applications to gas storage, molecular sieving, ion conductivity and catalysis.[4] Additionally, in recent years an increasing number of studies have been explored to indicate that MOFs serve as platform for integrating different functional components to achieve light harvesting[5] and to drive various photocatalytic reactions[6] such as carbon dioxide reduction to CO,[7a,b] formic acid[7c–e] or methanol,[7f,g] synthesis of metallic nanoparticles[8a] or metallic nanostructures for lithographic pattering,[8b] oxidation of organic compounds,[9] degradation of organic dyes,[10] and various organic transformations.[7b,11] Compared to the other photocatalytic systems, the MOFs photocatalysts have advantages that variety of combinations of bridging organic linkers[12a,b] and metallic centers[12c,d] allow for fine-tuning and rational design of these photocatalysts at the molecular level. In this context, recent synthetic achievements have been delivered to robust MOFs/CPs displaying photocatalytic activity in photocatalytic water splitting reaction towards H_2 production.[13]

In 2009, Kataoka *et al*. firstly applied the ruthenium-based MOFs as heterogeneous catalyst for photo-promoted H_2 production.[14] Under VIS-light irradiation, the photocatalytic system containing $[Ru^{II,III}{}_2(BDC)_2BF_4]_n$ MOF (BDC = benzene-1,4-dicarboxylate) acting as catalysts, $[Ru(bpy)_3]^{2+}$ (bpy = 2,2´-bipyridine) as photosensitizer, EDTA (ethylenediaminetetraacetate) and MV^{2+} (N,N´-dimethyl-4,4´-bipyridinium) as electron donors, was able to photosplit a water molecules generating H_2 with high rates. Later, this study was extended on series of analogous $[Ru^{II,III}{}_2(BDC)_2X]_n$ (X = BF_4^-, Cl^-, Br^-) MOFs based on the diruthenium paddle-well structural units, with attempt to determine the effect of incorporated anion on the photocatalytic behavior of the materials.[15] Among more recent studies, the photocatalytic activity of NH_2-MOF-Ti[16,17] and NH_2-UiO-66(Zr)[18] was improved through post-synthetic deposition within the framework of Pt nanoparticles which in turn behave as co-catalysts in reductive water splitting reaction. Similarly, the MIL-101(Cr) MOF with embedded CdS nanoparticles shows high catalytic activity towards H_2 generation upon VIS-light.[19] Moreover, several photocatalytic MOFs for hydrogen evolution were prepared *via* post-modification of organic linkers incorporating photosensitizer molecule or photoactive complex, such as in case of UiO-66(Zr) framework sensitized with rhodamine B,[20] UiO-67(Zr) with target $[Ir(ppy)_2(bpy)]^+$ (ppy = 2-phenylpyridine, bpy = 2,2´-bipyridine) complex,[21] MOF-253(Al) with post-synthetically immobilized Pt-complex,[22] or UiO-66(Zr) with [[FeFe]-(dcbdt)$(CO)_6$] (dcbdt = 1,4-dicarboxylbenzene-2,3-dithiolate) loaded functional groups.[23] Moreover, since implex, laborious and multistep way of post-synthetic functionalization, several photocatalytically active MOFs/CPs for hydrogen evolution were obtained through easiest one-pot syntheses. For instance, $\{[Ln_2Cu_5(OH)_2(pydc)_6(H_2O)_8]\cdot I_8\}_n$ (Ln = Sm, Eu, Gd and Tb) MOF templated by iodine anions,[24] polyoxometalete-based $\{(TBA)_2[Cu^{II}(BBTZ)_2(x\text{-}Mo_8O_{26})]\}_n$ (TBA = tetrabuthylammonium cation; BBTZ = 1,4-bis(1,2,4-triazol-1ylmethyl)-benzene; $x = \beta$ and α))

anionic frameworks,[25] or porphyrin-based $\{[Al(OH)]_2H_2TCPP(DMF_3\text{-}(H_2O)_2\}_n$ (H_2TCPP = tetra(4-carboxyl-phenyl)porphyrin).[26]

Regarding to beneficious one-pot synthesis path for preparation of photocatalytically active MOF/CPs and taking into account disadvantages of post-synthetic way to introduce desired functionality, such as inhomogeneous distribution and doubtful rate of functionalization degrees, we envisioned that known host-guest oxalate-bridged 3D frameworks with general formula of $\{[Z^{II}(bpy)_3][M^IM^{III}(C_2O_4)_3]\}_n$,[27] $\{[Z^{II}(bpy)_3](H_2O)[M^IM^{III}(C_2O_4)_3]\}_n$,[28] $\{[Z^{III}(bpy)_3](X)[M^IM^{III}(C_2O_4)_3]\}_n$[27g–i,29] ($M^I = Li^+$, Na^+; $M^{III} = Al^{3+}$, Cr^{3+}, Rh^{3+}, Ru^{3+}, Fe^{3+}; $Z^{II} = Fe^{2+}$, Co^{2+}, Ni^{2+}, Zn^{2+}, Ru^{2+}, Os^{2+}; $Z^{III} = Rh^{3+}$, Cr^{3+}, Co^{3+}; $X = ClO_4^-$, PF_6^-, BF_4^-; bpy = 2,2´-bipyridine) could be positioned as deserving competitors along with those functional MOFs which encapsulate photoactive guest molecules in pores of the framework.[30] In this class of compounds, the $[Z^{II}(bpy)_3]^{2+}$ cations tingly fit vacant cavities provided by the three-dimensional anionic $\{[M^IM^{III}(C_2O_4)_3]^{2-}\}_n$ network. Thereby, tris-bipyridine complexes are quantitatively and homogeneously distributed within the polymeric framework. Moreover, the chemical variation and combination of the metal ions in oxalate backbone as well as in tris-bipyridine cation offer unique opportunities for rational design of photoactive coordination polymer with desired photochemical and photophysical properties, such as light-induced electron transfer and excitation energy transfer in the solid state.

Thus, herein we present the study focused on the synthesis of series of 3D-dimensional ruthenium-based oxalate-bridged anionic networks $\{[M^IRu^{III}(C_2O_4)_3]^{2-}\}_n$ ($M^I = Na^+$, Li^+) in which the large honeycombed channels occupied by $[Z^{II}(bpy)_3]^{2+}$ (bpy = 2,2´-bipyridine, $Z^{II} = Zn^{2+}$, Cu^{2+}, Ru^{2+}, Os^{2+}) cationic templates, which photocatalytic properties in hydrogen evolution reaction is also discussed as potential application.

Experimental Section

Materials. The complexes $[Z^{II}(bpy)_3](ClO_4)_2$ (where Z^{II} = Zn, Cu, Ru), $[Os^{II}(bpy)_3](PF_6)_2$ and $K_3[Ru(C_2O_4)_3]\cdot 4.5H_2O$ were prepared according to the literature methods.[31] The other chemicals are commercially available and were used as purchased.

Synthesis of $\{[Z^{II}(bpy)_3][NaRu(C_2O_4)_3]\}_n$ ($Z^{II} = Zn^{2+}$ (1), Cu^{2+} (3), Ru^{2+} (5), Os^{2+} (7)), $\{[Z^{II}(bpy)_3][LiRu(C_2O_4)_3]\}_n$ ($Z^{II} = Cu^{2+}$ (4), Ru^{2+} (6), Os^{2+} (8)) and $\{[Zn(bpy)_3](H_2O)[LiRu(C_2O_4)_3]\}_n$ (2) series of compounds (where bpy = 2,2´-bipyridine). The synthesis process was performed in accordance with a previously published procedure for the $\{[Fe^{II}(bpy)_3][M^ICr(C_2O_4)_3]\}$ (where $M^I = Na^+$, Li^+) compounds[27f] introducing $[Ru(C_2O_4)_3]^{3-}$ moiety instead of $[Cr(C_2O_4)_3]^{3-}$. In a typical synthesis, 141 mg (0.25 mmol) of $K_3[Ru(C_2O_4)_3]\cdot 4.5H_2O$ and 30 mg (0.5 mmol) of NaCl or 20 mg (0.5 mmol) of LiCl were dissolved in 5 mL of water, and 0.25 mmol of the $[Z^{II}(bpy)_3](ClO_4)_2$ salt ($[Zn^{II}(bpy)_3](ClO_4)_2$, 183 mg; $[Cu^{II}(bpy)_3](ClO_4)_2$, 183 mg; $[Ru^{II}(bpy)_3](ClO_4)_2$, 192 mg; $[Os^{II}(bpy)_3](PF_6)_2$, 237 mg) dissolved in water/ethanol mixture was added dropwise, after few minutes a precipitates appeared, and the suspensions was stirred for 1 h. The resulted precipitates were filtered, washed with ethanol and air-dried.

Yellow precipitates of **1** and **2** yield 90 % and 74 %, respectively. Anal. Calc. for $C_{36}H_{24}N_6NaO_{12}RuZn$ (**1**): C, 46.85%; H, 2.60%; N, 9.11%. Found: C, 47.0%; H, 2.85%; N, 9.1%. Anal. Calc. for $C_{36}H_{26}LiN_6O_{13}RuZn$ (**2**): C, 46.75%; H, 2.81%; N, 9.09%. Found: C, 46.8%; H, 2.9%; N, 9.1%.

Greenish precipitates of **3** and **4** yield 81 % and 77 %, respectively. Anal. Calc. for $C_{36}H_{24}CuN_6NaO_{12}Ru$ (**3**): C, 46.94%; H, 2.83%; N, 9.13%. Found: C, 50.0%; H, 2.9%; N, 9.2%. Anal. Calc. for $C_{36}H_{24}CuLiN_6O_{12}Ru$ (**4**): C, 47.78%; H, 2.87%; N, 9.29%. Found: C, 47.8%; H, 2.9%; N, 9.3%.

Red-orange precipitates of **5** and **6** yield 62 % and 78 %, respectively. Anal. Calc. for $C_{36}H_{24}N_6NaO_{12}Ru_2$ (**5**): C, 45.11%; H, 2.51%; N, 8.77%. Found: C, 45.0%; H, 2.7%; N, 8.8%.

Anal. Calc. for $C_{36}H_{24}LiN_6O_{12}Ru_2$ (**6**): C, 45.87%; H, 2.55%; N, 8.92%. Found: C, 46.5%; H, 2.8%; N, 9.2%.

Dark green precipitates of **7** and **8** yield %, respectively. Anal. Calc. for $C_{36}H_{24}N_6NaO_{12}OsRu$ (**7**): C, 41.26%; H, 2.29%; N, 8.02%. Found: C, 41.4%; H, 2.3%; N, 8.2%. Anal. Calc. for $C_{36}H_{24}LiN_6O_{12}OsRu$ (**8**): C, 41.91%; H, 2.33%; N, 8.15%. Found: C, 42.1%; H, 2.3%; N, 8.3%.

Single Crystal Growth. Single crystals of all compounds were obtained by crystallization in a tetramethoxysilane gel containing $K_3[Ru(C_2O_4)_3]\cdot 4.5H_2O$ (0.01 M). When the gel is formed, the stoichiometric quantities of a water solution containing $[Z^{II}(bpy)_3]^{2+}$ (Z^{II} = Zn, Cu, Ru, Os) and $M^{I}Cl$ (M^{I} = Li or Na) were added. After one month, the color tetrahedral shaped crystals of **1**−**8** are formed (Fig. S1, Supporting Information).

X-ray Structure Determinations. Tetrahedral shaped single crystals of compounds **1**−**8** were selected for single-crystal X-ray diffraction analyses. The intensity data were collected at room temperature on an Oxford-Gemini X-ray diffractometer using for compounds **2** and **4** graphite-monochromatic Mo-K_α (λ = 0.71073 Å) and for **1**, **3**, **5**−**8** Cu-K_α (λ = 1.54184 Å) radiations. The CrysAlisPro program was used for cell refinement and data reduction. Images were collected at a 55 mm fixed crystal-detector distance, using the oscillation method, with 1° oscillation and variable exposure time per image.

The structures were solved by direct methods using the SIR92 program.[32] The refinement was performed by SHELX-97[33] using full-matrix least squares on F^2. All non-H atoms were anisotropically refined. The hydrogen atoms of the 2,2´-bipyridine ligand were placed geometrically, and the hydrogen atoms of the water molecule in compound **2** could not be located but were included in the formula. The Flack`s absolute parameter[34] (*x*) was used to determine the space group of compounds.

Crystallographic data for **1**−**8** (CCDC#1404961–1404964, #1404970–1404973) have been deposited with Cambridge Crystallographic Data Centre. The detailed crystallographic data are summarized in the Table 1. Topological and geometrical analysis of **1**−**8** was obtained using TOPOS 4.0 software.[35]

X-Ray powder diffraction patterns were collected with a X´Pert Philips X-ray diffractometer (CuK_α radiation, λ = 1.5418 Å) at room temperature. The powder diffraction patterns indicate that all compounds are isostructural and show analogous patterns to the simulated patterns from the atomic coordinates of the crystal structures of **1**−**8** (Figs. S2–S5, Supporting Information).

Characterization Instruments. The IR spectra were recorded on a Bruker Tensor-27 spectrophotometer as KBr pellets in the 4000-500 cm^{-1} region.

Microanalyses (C, H, N) were carried out by the use of a Perkin-Elmer model 2400B elemental analyzer. X-ray microanalysis (SEM/EDX) confirmed the ratio Ru:Z^{II} to be 1:1 (Z^{II} = Zn, Cu, Os), by using JEOL JSM-6100 scanning microscopy (SEM) coupled with an INCA Energy-200 dispersive X-ray microanalysis system (EDX) with a PentaFET ultrathin window detector. As show Figure S6 (Supporting Information), the microcrystalline texture of the samples consists of microcrystals that repeat the same habit as those obtained single crystals, indicating that powder products have been obtained as pure phases.

A Mettler-ToledoTGA/SDTA851 were used for the thermal analyses in nitrogen and air dynamic atmosphere (50 mL/min) at a heating rate of 10°C/min. Approximately 10 mg of powder sample was thermally treated, and blank runs were performed. An Pfeiffer Vacuum TermoStar™ GSD301T mass spectrometer was used to determine the evacuated vapours. The masses 15 (NH_3), 18 (H_2O), 44 (CO_2) and 46 (NO_2) were tested by using a detector C-SEM, operating at 1200 V, with a time constant of 1 s.

A Cary 6000i (Varian) spectrophotometer was used to measure diffuse reflectance spectra in the range 200–1800 nm using a polytetrauoroethylene (PTFE)-coated integrating sphere.

Table 1. Crystallographic data and structure refinements for compounds **1**–**8**.

Compound	**1**	**2**	**3**	**4**	**5**	**6**	**7**	**8**
Formula	$C_{36}H_{24}N_6NaO_{12}RuZn$	$C_{36}H_{26}LiN_6O_{13}RuZn$	$C_{36}H_{24}CuN_6NaO_{12}Ru$	$C_{36}H_{24}CuLiN_6O_{12}Ru$	$C_{36}H_{24}N_6NaO_{12}Ru_2$	$C_{36}H_{24}LiN_6O_{12}Ru_2$	$C_{36}H_{24}N_6NaO_{12}OsRu$	$C_{36}H_{24}LiN_6O_{12}OsRu$
FW (g mol^{-1})	922.06	924.03	920.22	904.17	957.74	941.69	1046.9	1030.85
T (K)	293(2)	293(2)	298(1)	293(2)	293(2)	293(2)	293(2)	293(2)
Wavelength (Å)	1.54184	0.71073	1.54184	0.71073	1.54184	1.54184	1.54184	1.54184
Crystal system	cubic	cubic	cubic	cubic	cubic	cubic	cubic	cubic
Space group	$P2_13$	$P2_13$	$P2_13$	$P2_13$	$P2_13$	$P2_13$	$P2_13$	$P2_13$
a (Å)	15.7549(2)	15.3337(4)	15.6236(2)	15.3725(1)	15.5466(1)	15.3785(1)	15.5139(1)	15.34426
α (°)	90.0	90.0	90.0	90.0	90.0	90.0	90.0	90.0
V (Å^3)	3910.70(8)	3605.3(3)	3813.67(8)	3632.73(6)	3757.56(4)	3636.99(4)	3733.90(4)	3612.75(8)
Z	4	4	4	4	4	4	4	4
Dcalcd (g/cm^3)	1.566	1.699	1.603	1.653	1.693	1.720	1.862	1.895
F(000)	1852	1852	1848	1816	1908	1876	2036	2004
μ (mm^{-1})	4.589	1.160	4.602	1.075	7.247	7.363	10.346	10.567
Crystal size (mm^3)	0.21× 0.16 × 0.14	0.61× 0.49 × 0.22	0.15× 0.08 × 0.03	0.29× 0.26 × 0.16	0.14 × 0.12 × 0.08	0.26 × 0.25 × 0.14	0.08 × 0.06 × 0.03	0.07 × 0.03 × 0.02
Theta range data collect. (°)	4.0 to 70.3	3.8 to 31.2	4.0 to 70.4	3.2 to 31.3	4.0 to 70.4	4.1 to 70.5	4.0 to 70.4	4.1 to 70.7
Index ranges	$-17 \le h \le 14$, $-11 \le k \le 11$, $-15 \le l \le 19$	$-15 \le h \le 15$, $-21 \le k \le 10$, $-4 \le l \le 20$	$-17 \le h \le 17$, $-18 \le k \le 13$, $-18 \le l \le 10$	$-6 \le h \le 22$, $-17 \le k \le 13$, $-11 \le l \le 21$	$-12 \le h \le 12$, $0 \le k \le 13$, $1 \le l \le 18$	$-12 \le h \le 12$, $0 \le k \le 13$, $1 \le l \le 18$	$-17 \le h \le 17$, $-8 \le k \le 18$, $-13 \le l \le 10$	$-18 \le h \le 8$, $-12 \le k \le 18$, $-15 \le l \le 18$
Reflection collected	4945	7387	7070	7220	7080	9446	4956	2302
Independent reflections	2371[R_{int} = 0.082]	3525[R_{int} = 0.034]	2396[R_{int} = 0.065]	3586[R_{int} = 0.028]	2367[R_{int} = 0.049]	2335[R_{int} = 0.040]	2323[R_{int} = 0.046]	2302[R_{int} = 0.053]
T_{max} and T_{min}	1 and 0.802	0.837 and 0.626	0.883 and 0.672	1 and 0.957	0.625 and 0.471	0.389 and 0.320	0.081 and 0.064	0.817 and 0.699
Data/restraints/parameters	2371 / 0 / 173	3525 / 0 / 176	2396 / 0 / 172	3586 / 0 / 172	2367 / 0 / 172	2335 / 0 / 172	2323 / 0 / 172	2302 / 0 / 172
Final R indices [I>2σ(I)]	R_1=0.074, wR_2=0.211	R_1=0.052, wR_2=0.144	R_1=0.039, wR_2=0.078	R_1=0.039, wR_2=0.108	R_1=0.029, wR_2=0.074	R_1=0.025, wR_2=0.068	R_1=0.035, wR_2=0.088	R_1=0.029, wR_2=0.066
R indices (all data)	R_1=0.092, wR_2=0.235	R_1=0.055, wR_2=0.146	R_1=0.061, wR_2=0.085	R_1=0.046, wR_2=0.112	R_1=0.034, wR_2=0.077	R_1=0.025, wR_2=0.068	R_1=0.042, wR_2=0.091	R_1=0.032, wR_2=0.067
Flack parameter	0.43(3)	0.15(3)	0.007(14)	-0.006(18)	-0.007(14)	0.021(12)	-0.03(2)	0.00(2)
GOF on F^2	1.082	1.17	1.002	1.105	1.031	1.101	1.037	1.057

Hydrogen Evolution Experiments. Reactions were carried out at room temperature in a 100 mL gastight photolysis photoreaction cell that was custom-designed in order to allow purging and irradiation of the suspension. The gastight cell was a 100 mL two-necked, flat-bottomed flask with water refrigerator. The cell volume was 100 mL, of which gases occupied 83 mL. In each experiment, 10 μmol of heterogeneous catalyst was dispersed in mixture contained 10 mL H_2O and 7 mL TEA (triethylamine). Reaction mixtures were deoxygenated with three cycles of evacuation and purging with argon. The samples' solution were illuminated with UV light at room temperature by 500 W mercury lamp (HELIOS ITALQUARTZ Apparatus, model UV50F – 85P503I5, ≤ 366 nm) for 12 h. During reaction, a magnetic stirring was used to prevent sedimentation of the catalyst. For experiments performed with visible light irradiation the xenon lamp (150 W, ≥ 417 nm) was used as light source. Reaction products were analyzed by mass spectrometry taking regular aliquots (0.5 mL) of the reactor headspace gas through a septum using gastight syringe. Mass spectrometry analyses were performed using an OmniStar™ (Pfeiffer Vacuum) gas analysis module connected to AutoChem II 2920 (Micromeritics) catalyst characterization system. A cold trap was used with Ar as the carrier gas. Each gas aliquot were quantified using the calibration graph which have been previously obtained using standard 10 % (v/v) H_2 in Ar and 5 % (v/v) O_2 in He gas mixtures (AirLiquid).

Results and Discussion

The compounds **1**–**8** present the 3D three-connected decagon oxalate-bridged anionic network $\{[M^{I}Ru(C_2O_4)_3]^{2-}\}_n$ (M^{I} = Na^+, Li^+), which selective templates $[Z^{II}(bpy)_3]^{2+}$ (where Z^{II} = Zn^{2+}, Cu^{2+}, Ru^{2+}, Os^{2+}; bpy = 2,2´-bipyridine) cationic complex. The single-crystal X-ray analysis of ruthenium based 3D oxalate bridged polymers reveal that the CPs **1**, **3**–**8** are isostructural with $\{[Z^{II}(bpy)_3][M^{I}M^{III}(C_2O_4)_3]\}_n$ (Z^{II} = Co^{2+}, Zn^{2+}, Ni^{2+}, Fe^{2+}, Ru^{2+}; M^{I} = Na^+, Li^+; M^{III} = Rh^{3+}, Ru^{3+}, Al^{3+}, Cr^{3+}, Fe^{3+}) families of compounds.[27] However, compound **2** is isomorphic with $\{[Z^{II}(bpy)_3](H_2O)[LiCr(C_2O_4)_3]\}_n$ (Z^{II} = Ni^{2+}, Ru^{2+}) family of 3D oxalate networks.[28]

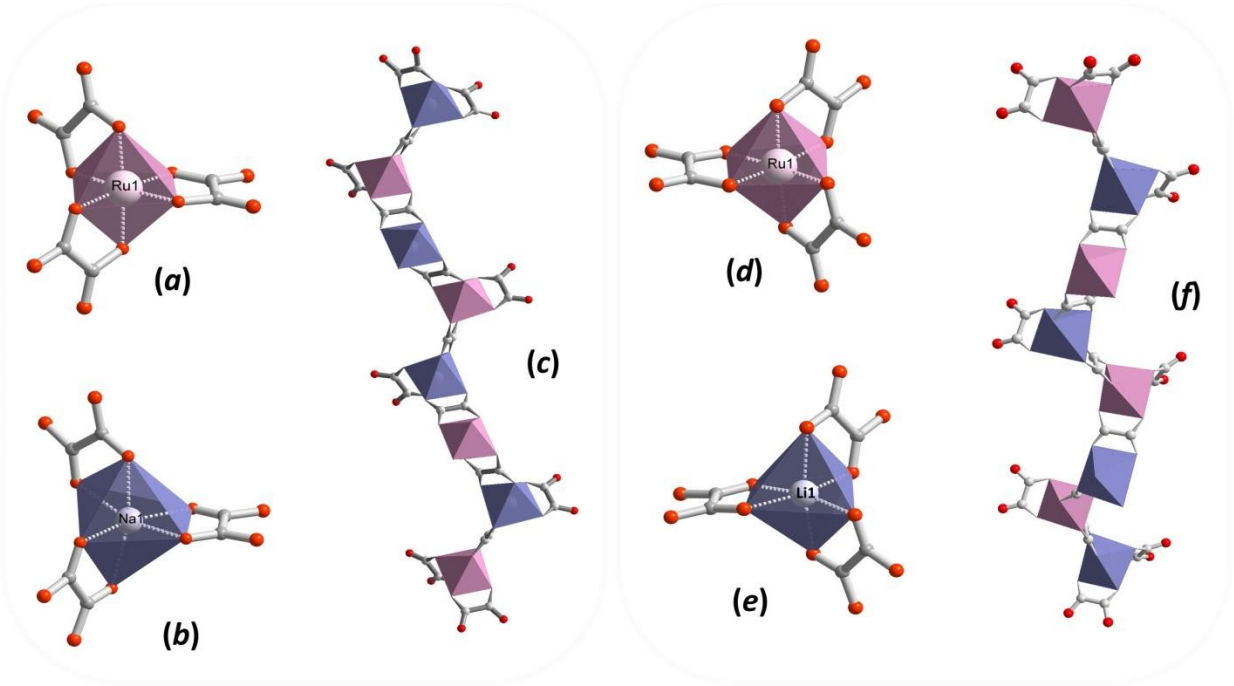

Figure 1. Representation of octahedral coordination environments of (a) Ru^{III} and (b) Na^{I} in **1** exhibiting Λ-conformation with corresponding (c) left-handed helix substructure formed. Representation of octahedral coordination environments of (d) Ru^{III} and (e) Li^{I} in **1** exhibiting Δ-conformation with corresponding (f) right-handed helix substructure formed. Red and grey spheres represent oxygen and carbon atoms, respectively.

The detailed crystal data and structure determination parameters of ruthenium based coordination polymers **1**–**8** are summarized in Table 1. The CPs **1**–**8** crystalize in the cubic chiral space group $P2_13$ with the asymmetric unit consisting of a complete oxalate ligand, Ru^{3+} and Na^+/Li^+ ions of the anionic network, Z^{II} metal center (Z^{II} = Zn^{2+}, Cu^{2+}, Ru^{2+}, Os^{2+}) and the complete bpy ligand of the cationic template (Fig. S7a).

Each Ru^{3+} and Na^+/Li^+ ions surrounded by six oxygen atoms of oxalate ligand forming distorted octahedral coordination environment (Fig.1a,b,d,e) with the mean Ru−O and Na/Li−O bond lengths which are within the range observed for analogous compounds.[27a] Selected bond distances and distortion parameters of Ru^{III}, Z^{II} and M^I coordination environments for compounds **1**−**8** given in Table 2. Interestingly, that the $\{Ru(C_2O_4)_3\}$ and $\{M^I(C_2O_4)_3\}$ structural units (SBU) manifest the same Δ or Λ-configuration in the chiral 3D anionic networks (Fig. 1a, b and d, e). Thus the compounds **1**, **4**–**6** and **8** build of SBU with Λ-form configuration, while **2**–**3** and **7** constructed of Δ-form.

Table 2. Selected bond length (Å) for $\{[Z^{II}(bpy)_3][NaRu(C_2O_4)_3]\}_n$ (Z^{II} = Zn^{2+} (**1**), Cu^{2+} (**3**), Ru^{2+} (**5**), Os^{2+} (**7**)), $\{[Zn^{II}(bpy)_3](H_2O)[LiRu(C_2O_4)_3]\}_n$ (**2**) and $[Z^{II}(bpy)_3][LiRu(C_2O_4)_3]\}_n$ (Z^{II} = Cu^{2+} (**4**), Ru^{2+} (**6**), Os^{2+} (**8**)) coordination polymers, the configuration and structural distortion parameters of $[Z^{II}(bpy)_3]^{2+}$ (Z^{II} = Zn^{2+}, Cu^{2+}, Ru^{2+}, Os^{2+}) guests compared with corresponding $[Z^{II}(bpy)_3]^{2+}$ cation in salts.

Bonds	$\{[Zn(bpy)_3][M^IRu(C_2O_4)_3]\}_n$		$\{[Cu(bpy)_3][M^IRu(C_2O_4)_3]\}_n$		$\{[Ru(bpy)_3][M^IRu(C_2O_4)_3]\}_n$		$\{[Os(bpy)_3][M^IRu(C_2O_4)_3]\}_n$	
	M^I = Na	M^I = Li (H_2O)	M^I = Na	M^I = Li	M^I = Na	M^I = Li	M^I = Na	M^I = Li
Ru–O1	2.013(7)	2.047(3)	2.017(3)	2.034(2)	2.021(3)	2.029(2)	2.027(5)	2.038(4)
Ru–O2	2.036(5)	2.050(3)	2.030(3)	2.044(2)	2.023(3)	2.043(3)	2.045(5)	2.049(4)
M^I–O3	2.336(9)	2.110(9)	2.336(4)	2.136(6)	2.319(4)	2.214(4)	2.306(6)	2.140(9)
M^I–O4	2.375(9)	2.232(9)	2.339(4)	2.235(5)	2.330(4)	2.220(5)	2.312(6)	2.236(9)
Z^{II}–N1	2.126(8)	2.028(4)	2.116(4)	2.100(3)	2.059(3)	2.052(2)	2.057(5)	2.060(4)
Z^{II}–N2	2.141(8)	2.034(4)	2.125(3)	2.101(3)	2.063(3)	2.059(2)	2.064(5)	2.062(4)
Z^{II}–N_{av}	2.133(6)	2.031(2)	2.121(4)	2.100(4)	2.061(2)	2.055(3)	2.061(3)	2.061(1)
Δ /Λ $_{form}$	Λ	Δ	Δ	Λ	Λ	Λ	Δ	Λ
[b] σ^2	68.0	37.3	60.9	56.2	49.1	48.5	53.9	53.5
[c] λ	$1.2\cdot10^{-5}$	$2.2\cdot10^{-6}$	$4.5\cdot10^{-6}$	$5.0\cdot10^{-8}$	$9.4\cdot10^{-7}$	$2.9\cdot10^{-6}$	$2.8\cdot10^{-6}$	$2.3\cdot10^{-7}$

Bond length and distortion parameters of $[Z^{II}(bpy)_3]^{2+}$ cation in salts [a]

	$[Zn(bpy)_3]^{2+}$	$[Cu(bpy)_3]^{2+}$	$[Ru(bpy)_3]^{2+}$	$[Os(bpy)_3]^{2+}$
Z^{II}–$N_{rang.}$	2.110(5)–2.240(3)	2.020(2) –2.454(2)	2.056(1)–2.060(1)	2.062(1)–2.062(1)
Z^{II}–N_{av}	2.159(10)	2.136(11)	2.058(2)	2.062
[b] σ^2	95.6	85.1	57.6	63.9
[c] λ	$4.8\cdot10^{-4}$	$5.7\cdot10^{-3}$	$6.8\cdot10^{-7}$	$3.7\cdot10^{-6}$

[a] The M^{II}-N bonds lengths for $[Zn(bpy)_3](ClO_4)_2$,[36a] $[Cu(bpy)_3](ClO_4)_2$,[36b] $[Ru(bpy)_3](ClO_4)_2$,[36c] and $[Os(bpy)_3](PF_6)_2$ salts[36d] were taken from the published crystallographic data.

[b] The bond angle variance: $\sigma^2 = \frac{1}{11}\sum_{n=1,12}(\theta_n - 90°)^2$, where θ_n is one of the twelve N-Z^{II}-N angles in the coordination sphere.[37]

[c] The mean quadratic elongation: $\lambda = \frac{1}{6}\sum_{n=1,6}\left[\frac{(d_n-\langle d\rangle)}{\langle d\rangle}\right]^2$, where ‹*d*› and d_n are the mean Z^{II}-N bond length and the six Z^{II}-N bond lengths in coordination polyhedra, respectively.[38]

In this type of structures, the oxalate ligand exhibiting μ-coordination mode (Fig. S7b) links in alternate manner Ru^{3+} and Na^+/Li^+ metal centers to form a helical substructures where Ru···Na/Li distances ranged from 5.46 to 5.63 Å. As shown in Fig. 1(c,f), helical substructures with 3-fold axis interpretation spread along *b*-axis and depending on the $\{Ru(C_2O_4)_3\}$ and $\{M^I(C_2O_4)_3\}$ SBUs conformations (Δ or Λ) exhibit left- or right-handed rotation. Repeatedly connected adjacent helices form a porous anionic 3D framework with honeycomb-like channels running along [111] crystallographic direction (Fig. 2a). According to topological analysis performed using TOPOS 4.0 software[35] resulting 3D anionic networks are three-connected uninodal nets with 10^3-*a* array topology (Fig. 2b, also denoted as **srs**-type net).[39]

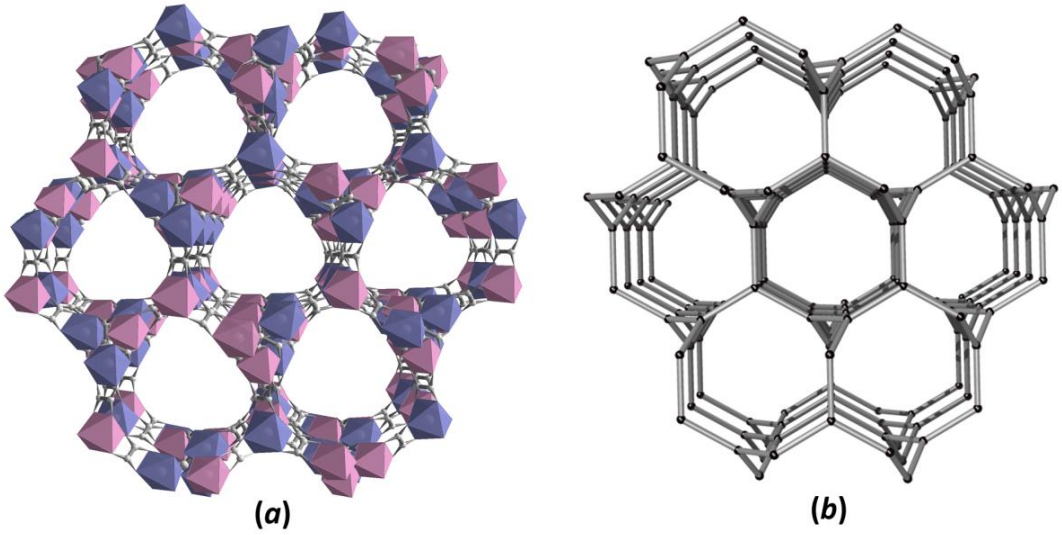

Figure 2. The 3D three-connected decagon anionic network $\{[M^{I}Ru(C_2O_4)_3]^{2-}\}_n$ (M^{I} = Na, Li): (a) view of honeycombed channels along [111] direction and (b) its' simplified topological representation, where black spheres represent a node of equivalent Ru^{III} and M^{I} centers.

In fact, $\{[M^{I}Ru(C_2O_4)_3]^{2-}\}_n$ (M^{I} = Na^{+}, Li^{+} anionic frameworks are cage-like structures with 3-fold cavities formed as a result of helical substructures interconnection. The tris-chelating cationic $[Z^{II}(bpy)_3]^{2+}$ (where Z^{II} = Zn^{2+}, Cu^{2+}, Ru^{2+}, Os^{2+}; bpy = 2,2´-bipyridine) complex acting as charge balanced template fit the large anionic cavities in a specific and highly symmetrical manner (Fig. 3a). Interestingly, the cationic entity acts as a structural (appropriate size/shape), stoichiometric and chiral template which repeat homochiral conformational characteristics (Δ or Λ) such as SBUs in the polymeric network, resumed in Table 2. The role of bulky $[Z^{II}(bpy)_3]^{2+}$ cations in oxalate-based anionic coordination arrays have been previously investigated and have a significant effect on the network structure formation.[29c,40]

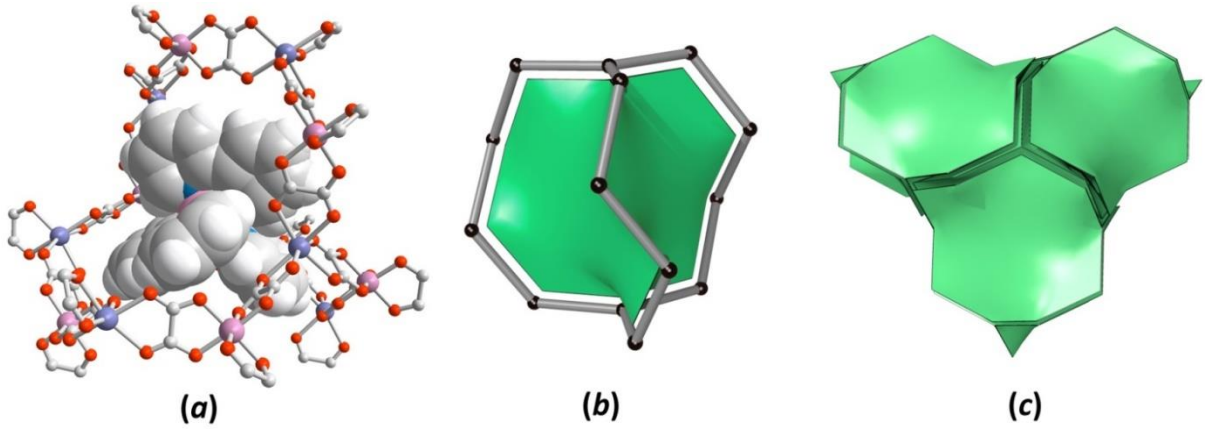

Figure 3. Perspective view of $[Z^{II}(bpy)_3]^{2+}$ (Z^{II} = Zn^{2+}, Cu^{2+}, Ru^{2+}, Os^{2+}) complex hosted in the anionic 3-fold cage. (b) Simplified topological representation of anionic cage (black nodes are Ru^{III} and M^{I} metal centers, grey rods is oxalate ligand) with ***srs*** triangular tile. (c) Tile packing which reconstruct cage structure in 3D honeycomb-like framework.

In course of topological simplification of the 3D framework structures, the anionic cavities are generalized as self-dual natural tile characteristic for 10,3-net topologies and can be described as triangle vertex figure with 14 vertices and 3 faces (Fig. 3b). As illustrated in Figure 3c, the $[10^3]$ tiles sharing one face reconstruct porous spaces of the anionic network to form 3D honeycombed architecture.

Applying the models of Voronoi-Dirichlet polyhedra,[41,42] an accessible volume of 3-fold anionic cages in $\{[M^{I}Ru(C_2O_4)_3]^{2-}\}_n$ (M^{I} = Na^{+}, Li^{+}) nets, the volume of cation $[Z^{II}(bpy)_3]^{2+}$ (Z^{II}

= Zn^{2+}, Cu^{2+}, Ru^{2+} and Os^{2+}) incorporated in the networks and their volume in free salts were calculated and summarized in Figure 4.

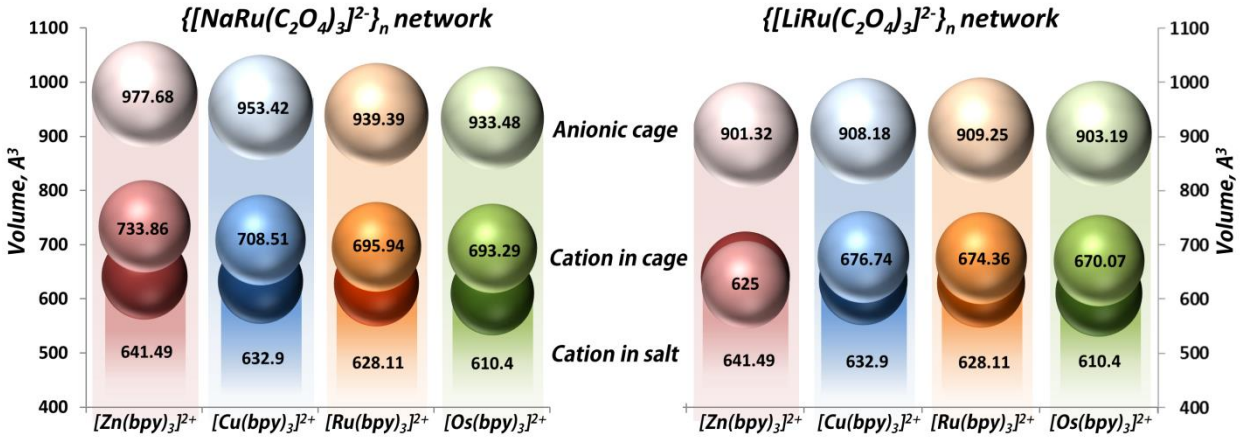

Figure 4. Representation of accessible volumes of anionic cages in $\{[NaRu(C_2O_4)_3]^{2-}\}_n$ (right) and networks$\{[LiRu(C_2O_4)_3]^{2-}\}_n$ (left), the volumes of $[Z^{II}(bpy)_3]^{2+}$ (Z^{II} = Zn^{2+}, Cu^{2+}, Ru^{2+},Os^{2+}) cationic complexes in their salt forms (darker spheres) and incorporated in corresponding 3D polymeric nets (medium spheres). The volume calculation for $[Z^{II}(bpy)_3]^{2+}$ complex in salt forms have been performed using the published crystallographic data.[36]

The volume of anionic cages in $\{[NaRu(C_2O_4)_3]^{2-}\}_n$ framework slightly bigger that those in the $\{[LiRu(C_2O_4)_3]^{2-}\}_n$ which is caused by the difference between the ionic radii of Na and Li metal centers incorporated in the framework. Notably that the cationic template $[Z^{II}(bpy)_3]^{2+}$ (where Z^{II} = Zn^{2+}, Cu^{2+}, Ru^{2+}, Os^{2+}) selectively residing in the anionic cages of **1**, **3**–**8** undergo 6.9–14.4% expansion comparing to the corresponding cationic complex in the free salt forms.

Exceptional case of compound **2** where the volume of $[Zn(bpy)_3]^{2+}$ template is smaller (2.6%) than in the free salt consists in the slight structural distinction from **1**, **3**–**8**. Such difference is related to incorporation of additional water molecule per formula unit which expressed by formulation of $\{[Zn^{II}(bpy)_3](H_2O)[LiCr(C_2O_4)_3]\}_n$ and was observed in analogous compounds $\{[Z^{II}(bpy)_3](H_2O)[LiCr(C_2O_4)_3]\}_n$ (Z^{II} = Ni^{2+}, Ru^{2+})[28] and $\{[Z^{III}(bpy)_3](X)[NaM^{III}(C_2O_4)_3]\}_n$ (M^{III} = Cr^{3+}, Al^{3+}, Rh^{3+}; Z^{III} = Cr^{3+}, Rh^{3+}, Co^{3+}; X = ClO_4^-, PF_6^-),[27g–i,29] the special packing arrangement of $[Z^{III}(bpy)_3]^{3+}$ o $[Z^{II}(bpy)_3]^{2+}$ cations create a cubic-shaped cavities able to encapsulate small anions (ClO_4^- or PF_6^-) or neutral molecules (H_2O). In case of **2**, three pairs of parallel aligned, adjacent bpy ligands, perpendicularly oriented to each other, form the cubic-shaped vacancies in which the water molecules reside with full occupancy of this site. However, in the actual case of the structure **2**, the capture of water molecules into these cavities is expected taking into account that the preparation of the compound realizes from aqueous solution. Figure 5 show the packing arrangement of three adjacent tris-chelated $[Zn^{II}(bpy)_3]^{2+}$ cations exhibiting the cubic-shaped cavity which is drawn with the frontal bpy-ligand partially omitted in order to have a free view into the cage where H_2O molecule is entrapped. The volume of this cubic cage in compound **2** is about 45 $Å^3$ (Fig. S8). Consequently, the size decreasing of $[Zn^{II}(bpy)_3]^{2+}$ cationic template observed in **2** can be explained as a result of a steric pressure effect introduced by incorporation of additional water molecules into the cubic-shaped cavities.

The IR spectrums of **1**–**8** are very similar (Fig. S9) showing the characteristic absorption bands of the oxalate ligand in regions 1610–1625 cm^{-1} ($\nu_{as\ O–C–O}$), 1305–1315 cm^{-1}, 1350–1365 cm^{-1} ($\nu_{s\ O–C–O}$), and 795–805 cm^{-1} ($\delta_{\ O–C–O}$). The bands between 540 cm^{-1} and 490 cm^{-1} are assigned to Ru−O, Li/Na−O and M^{II}−N stretching vibrations. The bands between 3100 cm^{-1} and 2800 cm^{-1} and 1675–1400 cm^{-1} are attributed to the C–H, C_{ar}–C_{ar}, and C_{ar}=N stretching frequencies of the aromatic group. The series of bands at 1250–1000 cm^{-1} and near 3030–3050 cm^{-1} correspond to the aromatic =C–H stretching vibration.

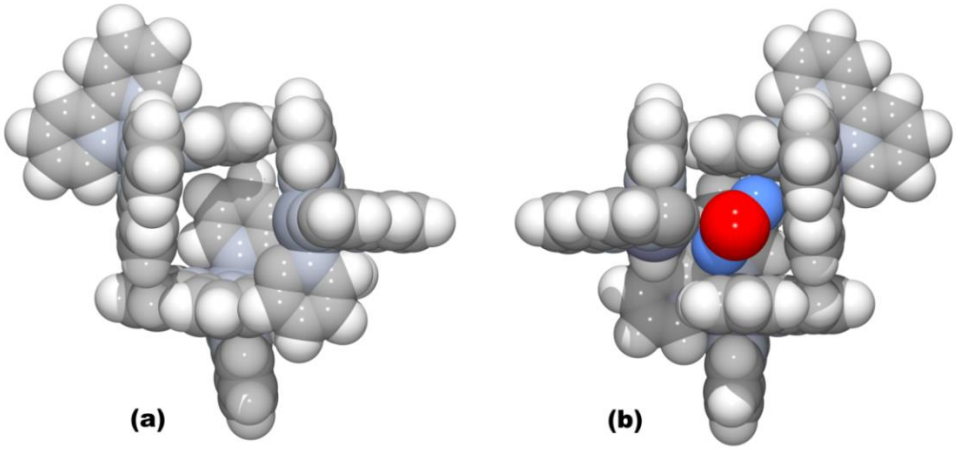

Figure 5. Space filling representation of cubic-shaped cages formed by three pairs of parallel oriented bipyridine ligands proceeding from three adjacent $[Zn^{II}(bpy)_3]^{2+}$ template cations: (a) view to empty space of the cubic cage in compound **1**; (b) view to the cubic cage in compound **2** where the water molecule is located. Part of the bipyridine ligand located at the top of the cage is omitted for clarity.

The thermal stability of **1**–**8** in air and nitrogen atmospheres was investigated. The thermogravimetric curves (TG and derivative TG), SDTA and mass spectrometry analysis of evacuated vapors for **1**–**8** in both air and nitrogen atmospheres are depicted in Figures S10–S11 and S13–S14 (Supporting Information), respectively. As represented, the thermogravimetric analysis results emphasis on similar decomposition behaviors what confirm isomorphic nature of compounds **1**–**8**. The degradation processes occurred in one single step simultaneously in both air and nitrogen atmospheres are very closely resemble each other and reveal the observed total mass losses from room temperature up to 1000 ºC. As summarized in Table S1 (Supporting Information), in air atmosphere degradation process of **1**–**8** proceeds in one continuous stage in which mass loss of 63.6–75.2% (depending on the compositional characteristics) generally observed in the range 180–600 ºC associated with a broad exothermic peaks on the SDTA and DSC curves (Figs. S10–S12, Supporting Information) and correspond to simultaneous decomposition of organic fraction of template and oxalate ligand. The associated mass spectrometry *m/z* 18, 44 and 46 curves are in a good agreement with the TG/dTG curves and occur as one broad maximum coinciding with maximum of mass loss in dTG curves suggesting continuous structure collapsing and oxidational degradation of the ligands.

Oppositely, in nitrogen atmosphere, the pyrolysis of compounds **1**–**8** proceeds in three continuous stages which generally take place in 200–740 ºC temperature range (Table S2, Supporting Information). As represented in Figures S13–S14 (Supporting Information), these decomposition stages exhibit endothermic effects on the SDTA (Figs. S13–S14, Supporting Information) and DSC curves (Fig. S15, see Supporting Information) which are associated with mass spectrometry *m/z* 15, 18 and 44 peaks indicating stepwise decomposition of the polymeric architectures. Notably, that observed mass losses in nitrogen atmosphere do not correspond to those calculated theoretically (Table S2, Supporting Information). Inconsistence of expected and theoretical mass losses can be attributed to the formation of carbon solid residues which are main formed product in the pyrolysis processes. Additionally, a composition of the residual solids of **1**–**8** after decomposition in air or nitrogen atmospheres was identified applying powder X-ray diffraction technique. As a result, the residues powders formed after decomposition in air atmosphere consist of mixture of RuO_2, Li_2O (for compounds **2**, **4**, **6**, **8**) or Na_2O (compounds **1**, **3**, **5**, **7**) and $M^{II}O$ (M^{II} = Zn (**1**, **2**), Cu (**3**, **4**)) or $M^{IV}O_2$ (M^{IV} = Ru (**5**, **6**), Os (**7**, **8**)), while in nitrogen atmosphere the residual composition have been identified as a mixture of Ru metal, Li_2O (for compounds **2**, **4**, **6**, **8**) or Na_2O (compounds **1**, **3**, **5**, **7**), $M^{II}O$ (M^{II} = Zn (**1**, **2**), Cu (**3**, **4**)) or metallic osmium (**7**, **8**).

The room-temperature UV-VIS-NIR diffuse reflectance spectra of the powder samples corresponding to **1**–**8** are represented in Figure 6. All spectra consist in three groups of bands: the high energy bands observed between 200 and 330 nm are assigned to π→π* transition of bpy ligands; the intense broad band at *ca*. 400 nm corresponds to MLCT transition in $[Na/LiRu(C_2O_4)_3]^{2-}$ units, whereas the weaker bands in the VIS-NIR region have been assigned to ligand-field transitions within the $[Z^{II}(bpy)_3]^{2+}$ cationic templates of compounds **1**–**8**.

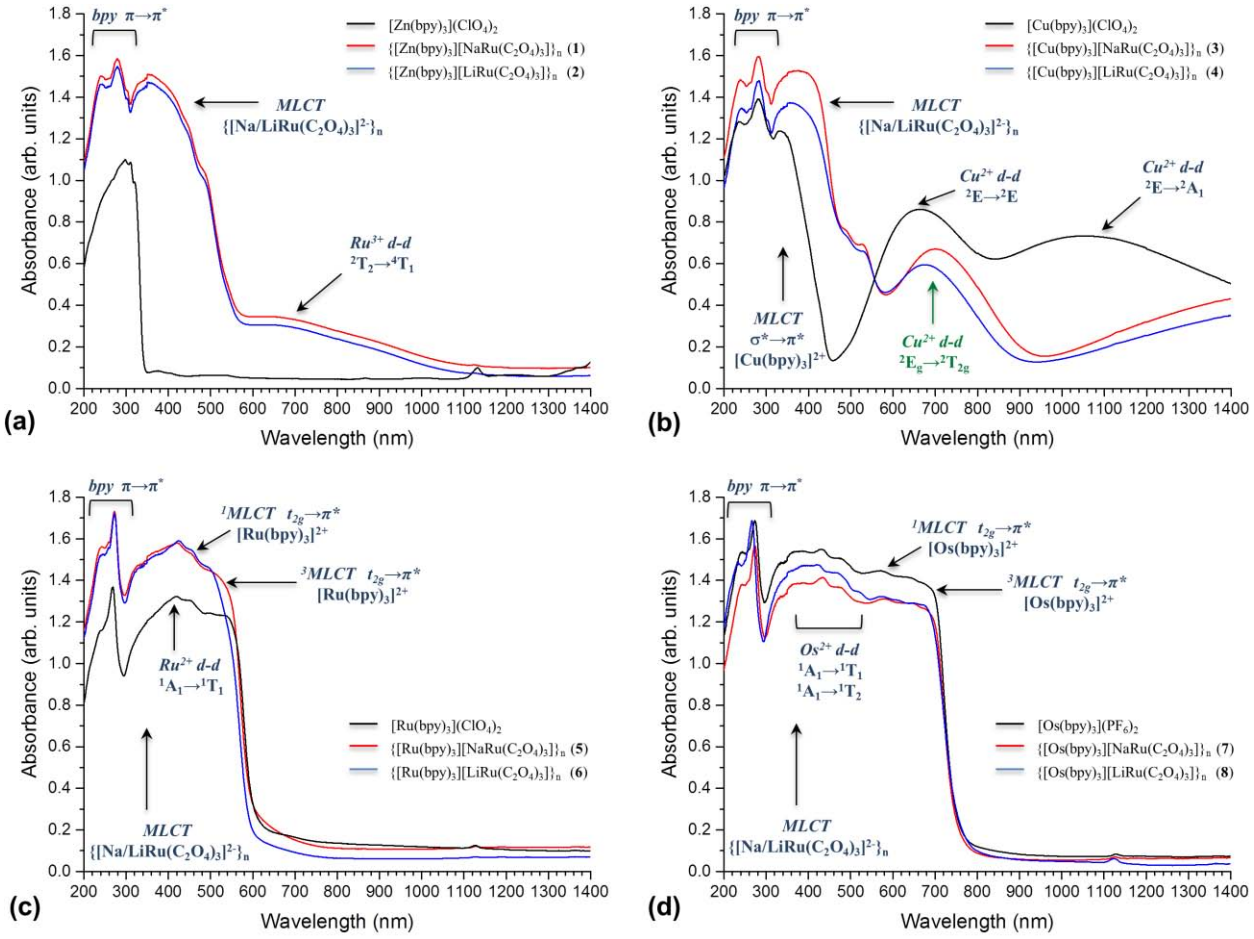

Figure 6. Comparison of room temperature UV-VIS-NIR diffuse-reflectance spectrum for (a) $\{[Zn^{II}(bpy)_3][NaRu(C_2O_4)_3]\}_n$ (**1**), $\{[Zn^{II}(bpy)_3](H_2O)[LiRu(C_2O_4)_3]\}_n$ (**2**) and $[Zn(bpy)_3](ClO_4)_2$; (b) $\{[Cu^{II}(bpy)_3][M^{I}Ru(C_2O_4)_3]\}_n$ and $[Cu^{II}(bpy)_3](ClO_4)_2$ (M^{I} = Na (**3**), Li (**4**)); (c) $\{[Ru^{II}(bpy)_3][M^{I}Ru(C_2O_4)_3]\}_n$ and $[Ru(bpy)_3](ClO_4)_2$ (M^{I} = Na (**5**), Li (**6**)); (d) $\{[Os^{II}(bpy)_3][M^{I}Ru(C_2O_4)_3]\}_n$ and $[Os(bpy)_3](PF_6)_2$ (M^{I} = Na (**7**), Li (**8**)).

Figure 6 shows comparison of diffuse-reflectance spectra of **1**, **2** and $[Zn(bpy)_3](ClO_4)_2$ compounds. As expected, the spectrum of $[Zn(bpy)_3]^{2+}$ complex doesn't appeared to have *d*–*d* transitions due to close shell electronic configuration ($t_{2g}^6e_g^4$) for d^{10} Zn^{2+} ion.[27c,43] However, the spectra of **1** and **2** exhibit broad adsorption band *ca*. 700 nm which was assigned to *d*–*d* (Ru^{3+})[43,44] spin-forbidden $^2T_2 \rightarrow {}^4T_2$ transition within $[Na/LiRu(C_2O_4)_3]^{2-}$ framework units. The VIS-NIR spectral region of **3** and **4** coordination polymers templated by $[Cu(bpy)_3]^{2+}$ cationic complex (Fig. 6b), reveal adsorption band *ca*. 690 nm that was assigned to $^2E_g \rightarrow {}^2T_{2g}$ single electron transition, which is expected in octahedral crystal field for Cu^{2+} ion ($^2T_{2g}$) with $t_{2g}^5e_g^4$ excited electronic state.[45] Normally, the octahedral coordination of Cu^{2+} ions undergoes Jahn-Teller distortion leading to the trigonally distorted pseudo D_3 symmetry, and as can be observed in corresponding spectrum of $[Cu(bpy)_3](ClO_4)_2$ compound (Fig. 6b), where *d*–*d* transitions appeared as medium-strong band *ca*. 680 nm and sharp band *ca*. 1100 nm should be treated as in trigonal field and assigned to $^2E \rightarrow {}^2E$ and $^2E \rightarrow {}^2A_1$ transitions, respectively.[46] Basing on this observations, the fact that the $\{[M^{I}Ru(C_2O_4)_3]^{2-}\}_n$ (M^{I} = Na, Li) anionic framework rigidly

restrict Jahn-Teller distortion in guest $[Cu(bpy)_3]^{2+}$ cationic complex is concluded. Furthermore, the corresponding structural distortion parameters (bond angle variance (σ^2) and mean quadratic elongation (λ)) calculated for $[Cu(bpy)_3]^{2+}$ complex in **3** and **4** frameworks, which are summarized in Table 2, suggest that the coordination environment of Cu^{2+} ion in template cationic complex exhibit more regularized octahedral geometry than that found for corresponding free salt form.

The diffuse-reflectance spectra of compounds **5** and **6** are similar with respect to corresponding $[Ru(bpy)_3](ClO_4)_2$ complex, and the VIS-NIR region consists of several high intensity bands (Fig. 6c), which are attributed to electron transitions within low-spin $[Ru(bpy)_3]^{2+}$ complex where Ru^{2+} ion possess $t_{2g}^5e_g^1$ electronic configuration.[45] Thus, the absorption band *ca*. 450 nm is assigned to $^1A_1 \rightarrow {}^1T_1$ transition. Moreover, the shoulder centered at 480 nm corresponds to $t_{2g} \rightarrow \pi^*$ metal-ligand charge transfer (^{1}MLCT) transition, while the broad shoulder observed at 560 nm belongs to a spin-forbidden third $t_{2g} \rightarrow \pi^*$ metal-ligand charge transfer (^{3}MLCT) transition.[47,48] Similarly, compounds **7** and **8** exhibit diffuse-reflectance spectra close to correspond to $[Os(bpy)_3](PF_6)_2$ complex. As shown in Figure 6d, the VIS-NIR region of spectra consists of several overlapped bands located from 410 nm to 520 nm and was assigned to $^1A_1 \rightarrow {}^1T_2$ and $^1A_1 \rightarrow {}^1T_1$ *d–d* transition, which are expected for low-spin $[Os(bpy)_3]^{2+}$ complex with Os^{2+} ion in $t_{2g}^5e_g^1$ ground state.[45] Similarly to $[Ru(bpy)_3]^{2+}$-contained compounds, the diffuse-reflectance spectra of **7** and **8**, as well as $[Os(bpy)_3](PF_6)_2$, exhibit characteristic shoulders localized from 560 nm to 800 nm which attributed to $t_{2g} \rightarrow \pi^*$ metal-ligand charge transfer (MLCT) along with the spin-forbidden third $t_{2g} \rightarrow \pi^*$ metal-ligand charge transfer (^{3}MLCT) transition.[48,49]

The band gaps of **1**–**8** were estimated from Tauc plots[50] basing on the UV-VIS diffuse-reflectance data transformed by Kubelka-Munk function[51] (Fig. S16). The band gaps (E_g) were determined extrapolating the intersection point between baseline and the linear portion of the adsorption edge in a plot represented as function $(\alpha h\upsilon)^{3/2}$ against energy ($h\upsilon$, eV). The optical adsorption related to E_g in region of MLCT transition, that assumed to be direct forbidden, can be assessed at 2.54 eV for **1**, 2.31 eV for **2**, 2.68 eV for **3**, 2.67 eV for **4**, 2.10 eV for **5**, 2.11 eV for **6**, 1.68 eV for **7** and 1.67 eV for **1**, respectively. Determined values of band gaps for coordination polymers **1**–**8** follow the order **3** ≈ **4** > **1** > **2** > **5** ≈ **6** > **7** ≈ **8**.

Efficiency of photoinduced energy and electron migration processes occurred between photosensible component and catalytically active centers in MOFs/CPs upon light irradiation are essential goals in the rational design of photo-catalytically active MOFs/CPs.[52] Thus, inspired by early study of Kimura *et al*.,[53] that demonstrate efficient intramolecular energy and electron transfer taking place in homogeneous solution between $[Co(C_2O_4)_3]^{3-}$ and $[Ru(bpy)_3]^{2+}$ complexes; and supported by later works of Decurtins *et al*.,[27g–j,29d,29f] which evidenced the existence of *hν*-assisted resonant energy migration between $[Cr(C_2O_4)_3]^{3-}$ and $[M^{II/III}(bpy)_3]^{2+/3+}$ components in $\{[Z^{II/III}(bpy)_3][NaCr(C_2O_4)_3]\}_n$ (Z^{II} = Ru^{2+}, Zn^{2+}, Os^{2+}, Fe^{2+}; M^{III} = Rh^{3+}, Cr^{3+}) coordination networks; we envisioned that the coordination polymers **1**–**8** can act as self-supported photocatalysts.

Herein, we examined the photocatalytic splitting of water for hydrogen production using **1**–**8** coordination polymers under UV (≤ 366 nm) and VIS (≥ 417 nm) light irradiation. In typical experiment, the reactions were performed in reactor equipped with refrigerated 500W Hg-lamp (≤ 366 nm) and using 10 μmol of heterogeneous catalyst **1**–**8** dispersed in water (H_2O)/triethylamine (TEA) mixture (v/v = 1.4 : 1), where TEA acts as electron donor. The amounts of H_2 produced over **1**–**8** photocatalysts under 8 h of UV-light irradiation are depicted in Figure 7.

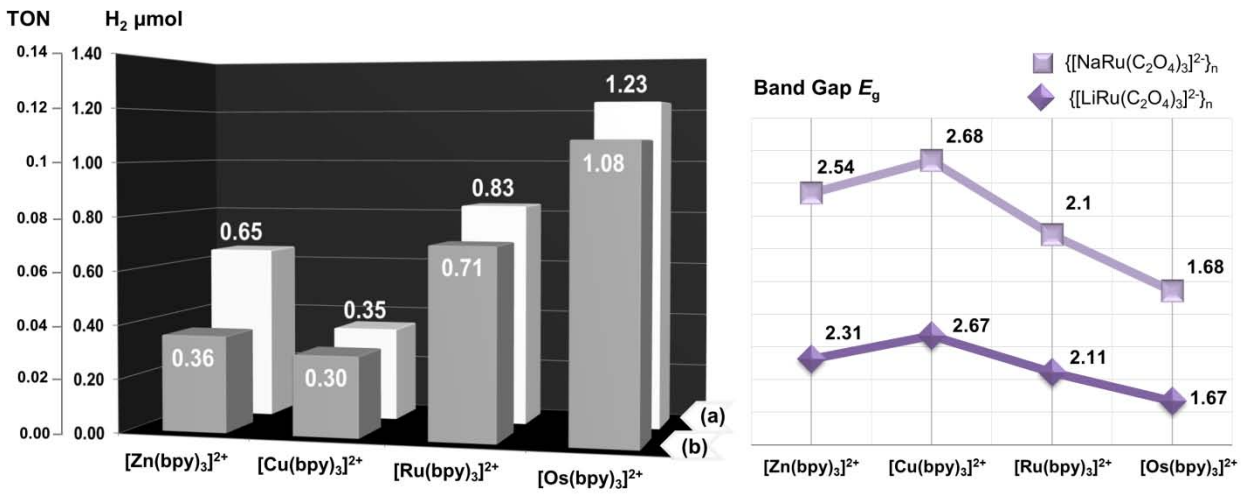

Figure 7. (Left) Amounts and TON values corresponding to H_2 evolved during reductive water splitting reaction using photocatalysts **1**–**8** which contain $[Zn(bpy)_3]^{2+}$, $[Cu(bpy)_3]^{2+}$, $[Ru(bpy)_3]^{2+}$ and $[Os(bpy)_3]^{2+}$ complex cations incorporated in (a) $\{[LiRu(C_2O_4)_3]^{2-}\}_n$ and (b) $\{[NaRu(C_2O_4)_3]^{2-}\}_n$ networks under 8 h of UV (≤ 366 nm) light irradiation (left). Photoreaction mixtures contained 10 µmol of heterogeneous catalyst, 7 ml of TEA and 10 ml of H_2O. TON = µmol of H_2 evolved/ 10 µmol of catalyst. (Right) Values of band gaps determined by diffuse-reflectance measurements for compounds **1**–**8**.

As seen in Figure 7 (left), the heterogeneous catalysts **1**–**8** show to be active in photoreductive water splitting reaction reaching to produce 1.26 µmol (TON of 0.12) of H_2 under 8 h of UV-light irradiation. The results indicate that the catalysts **7** and **8** exhibit the higher photocatalytic performance and its' activities decreases through the sequence **8** > **7** > **6** > **5** > **2** > **1** ≈ **4** > **3**. Interestingly, this sequence of photocatalytic activity is directly opposite to corresponding pathway of the band gaps determined for **1**–**8** (Fig. 7 right). Therefore, the synergistic effects of the smallest band gap and chemical nature of $[Z^{II}(bpy)_3]^{2+}$ cationic template are main factors determining photocatalytic activities of **1**–**8** under UV-light irradiation. Blank reactions were performed to ensure that H_2 production was light-promoted and conducted over heterogeneous catalyst. One blank was UV-illuminated without the catalyst, and another was in the dark with the catalyst under the same experimental conditions. No H_2 was detected in the above two blank tests. "Hot filtration" test was conducted with **6**, in which the heterogeneous catalyst, previously exposed to 8 h of reaction under UV-light, was removed by centrifugation and transparent uncolored reactant solution was returned into photolysis cell (previously degassed and filled with Ar) for additional consecutive photocatalytic run. As a result, no H_2 was detected, which indicate that detected photoactivities are promoted by heterogeneous catalysts rather than by leached soluble species.

Additionally, the photocatalytic activities of **1**–**8** were examined under VIS-light irradiation under the same reaction conditions. As shown in Figure 8, all coordination compounds also catalyze photoreduction of water to H_2 albeit less efficiently. These differences in photocatalytic activities of **1**–**8** under UV and VIS-irradiations can be explained in light of distinct mechanisms of energy transfer taking place within the $\{[Z^{II/III}(bpy)_3][M^{I}M^{III}(C_2O_4)_3]\}_n$ host-guest system, that early was evidenced by Decurtins *et al*. for analogous $\{[Z^{II/III}(bpy)_3][NaCr(C_2O_4)_3]\}_n$ (Z^{II} = Ru^{2+}, Zn^{2+}, Os^{2+}, Fe^{2+}; Z^{III} = Rh^{3+}, Cr^{3+}) compounds.[27i,29b,54] According to the proposed mechanism, the resonant energy migration take place between $[M^{III}(C_2O_4)_3]^{3-}$ and $[Z^{II/III}(bpy)_3]^{2+/3+}$ components of $\{[Z^{II/III}(bpy)_3][M^{I}M^{III}(C_2O_4)_3]\}_n$, in which energy transfer to $[Z^{II/III}(bpy)_3]^{2+/3+}$ component is more efficient that to $[M^{III}(C_2O_4)_3]^{3-}$. Evidently, the UV region of adsorption of **1**–**8**, consist of the bands attributed to MLCT transition within $\{[M^{I}Ru(C_2O_4)_3]^{3-}\}_n$ network which indicate that under UV-light, the $[Ru(C_2O_4)_3]^{3-}$ unit behave as photosensible component, efficiently transferring the energy received upon excitation to $[Z^{II}(bpy)_3]^{2+}$ guests (Z^{II} = Zn^{2+}, Cu^{2+}, Ru^{2+}, Os^{2+}) leading to better photocatalytic performances. Meanwhile, the VIS region of **1**–**8** consist of absorption bands attributing to MLCT transitions

within $[Z^{II}(bpy)_3]^{2+}$ component of the coordination polymers, which suggest that tris-bipyridine guests are photosensible components towards VIS light. Besides the low rate of energy transfer efficiency from $[Z^{II}(bpy)_3]^{2+}$ to $[Ru(C_2O_4)_3]^{3-}$ components of the **1**–**8** frameworks, leads to decreasing of photocatalytic performance in water splitting reaction.

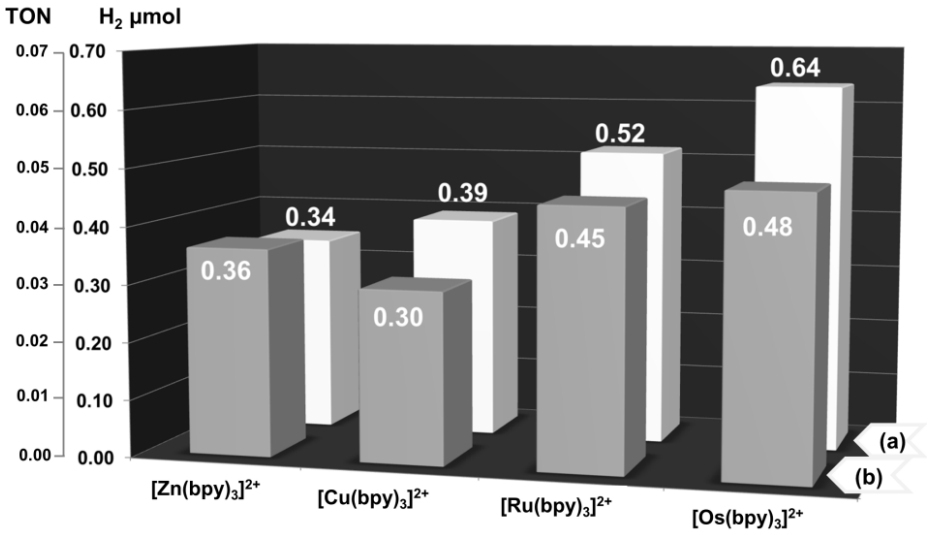

Figure 8. Amounts and TON values corresponding to H_2 evolved during reductive water splitting reaction using photocatalysts **1**–**8** which contain $[Zn(bpy)_3]^{2+}$, $[Cu(bpy)_3]^{2+}$, $[Ru(bpy)_3]^{2+}$ and $[Os(bpy)_3]^{2+}$ complex cations incorporated in (a) $\{[LiRu(C_2O_4)_3]^{2-}\}_n$ and (b) $\{[NaRu(C_2O_4)_3]^{2-}\}_n$ networks under 8 h of VIS ($\geq$ 417 nm) light irradiation (left). Photoreaction mixtures contained 10 µmol of heterogeneous catalyst, 7 ml of TEA and 10 ml of H_2O. TON = µmol of H_2 evolved/ 10 µmol of catalyst.

In order to confirm the recyclability of photocatalysts, the photocatalytic reaction of reductive water splitting was repeated four times with compound **6**, where after each catalytic cycle the heterogeneous solid was separated by centrifugation, washed several times with distillated water and reused in the next consecutive photocatalytic run. As shown in Figure S17, amounts of H_2 evolved after 8 h of UV-light irradiation in each consecutive photocatalytic cycle decrease imperceptible, that probably due to loss of catalyst upon recycling manipulation procedures. Moreover, closely similar photocatalytic activities of recycled catalyst suggest that compound **6** is not undergo photodecomposition or deactivation at least after four repeated catalytic runs. Additionally, to confirm the stability of heterogeneous catalyst, after each recycling run the reused material **6** was checked by XRD, and as evidenced from the comparison of those diffractograms (Fig. S18), photocatalyst **6** maintains its crystallinity and structural integrity during water splitting reaction. These results indicate that coordination polymers **1**–**8** behave as stable, active and reusable heterogeneous catalysts for photoreductive water splitting reaction. Moreover, we compare photocatalytic activities of **1**–**8** with other known MOFs and CPs able to photosplit water to H_2 (Table 3).

Presented results reveal that coordination polymers **1**–**8** show moderate photocatalytic activity towards H_2 generation under VIS-light comparing to known MOFs/CPs, meanwhile under UV-light they exhibit higher photocatalytic efficiencies. It is reasonable to conclude that $\{M^{I}Ru(C_2O_4)_3]^{2-}\}_n$ (M^{I} = Na, Li) anionic frameworks selectively templated by $[Z^{II}(bpy)_3]^{2+}$ (Z^{II} = Zn, Cu, Ru, Os) cationic complexes can be viewed as designable and efficient heterogeneous catalysts for UV-light promoted photoreactions.

Table 3. Comparison of photocatalytic performances of known MOFs/CPs used in photoreduction of water to H_2 under UV and VIS light.

MOF/CP	H_2 (μmol)	*t* (hour)	TON	TOF (TON·h^{-1})	λ (nm)	Ref.
$[Ru^{II,III}_2(p\text{-BDC})_2BF_4]_n$	29.3	4	47.0 [a]	11.7	> 420	[14]
$[Ru^{II,III}_2(p\text{-BDC})_2Cl]_n$ $[Ru^{II,III}_2(p\text{-BDC})_2Br]_n$	13.5 46.7	4	5.38 [b] 18.7 [b]	1.34 4.67	> 420	[15]
Ti-MOF-NH_2@Pt	11.7	3	1.17 [b]	0.39	> 420	[16]
Ti-MOF-NH_2@Pt	15.5	3	1.5 [b]	0.5	> 420	[17]
NH_2-UiO-66(Zr) NH_2-UiO-66(Zr)@Pt	107.1 125	3	2.38 [b] 2.77 [b]	0.93 0.79	370	[18]
MIL-101(Cr)@CdS/Pt	300	1	150 [b]	75.5	> 420	[19]
UiO-66(Zr)@Pt UiO-66(Zr)@RhB UiO-66(Zr)@RhB/Pt	0.97 0.67 1.4	5	19.5 [c] 13.5 [c] 28 [c]	3.9 2.7 5.6	> 420	[20]
UiO-67[$Ir(ppy)_2(bpy)$]@Pt	64.8	6	1620 [a]	270	420	[21]
MOF-253-Pt	3000	34	5.6 [a]	0.17	420	[22]
UiO-66-[FeFe](dcbdt)$(CO)_6$	3.5	2.5	0.7 [b]	0.28	470	[23]
$\{[Sm_2Cu_5(OH)_2(pydc)_6(H_2O)_8]\cdot I_8\}$ $\{[Eu_2Cu_5(OH)_2(pydc)_6(H_2O)_8]\cdot I_8\}$ $\{[Gd_2Cu_5(OH)_2(pydc)_6(H_2O)_8]\cdot I_8\}$ $\{[Tb_2Cu_5(OH)_2(pydc)_6(H_2O)_8]\cdot I_8\}$	979.0 1131.4 1025.2 1052.5	5	9790 [c] 11314 [c] 10252 [c] 10525 [c]	1958.0 2262.8 2050.4 2105.0	420	[24]
$(TBA)_2[Cu^{II}(BBTZ)_2(x\text{-}Mo_8O_{26})]$	4.68	6	0.05 [b]	0.008	< 400	[25]
$\{[AlOH)]_2H_2TCPP(DMF_3\text{-}(H_2O)_2\}$	3.15	8	900 [c]	112.5	420	[26]
$\{[Zn(bpy)_3][NaRu(C_2O_4)_3]\}_n$	0.36	8	0.04 [a c] 36 [b]	0.005 4.5	≥ 417	*This work*
	0.36		0.04 [a c] 36 [b]	0.005 4.5	≤ 366	
$\{[Zn(bpy)_3][LiRu(C_2O_4)_3]\}_n$	0.34		0.03 [a c] 34 [b]	0.004 4.25	≥ 417	
	0.65		0.06 [a c] 65 [b]	0.007 8.12	≤ 366	
$\{[Cu(bpy)_3][NaRu(C_2O_4)_3]\}_n$	0.30		0.03 [a c] 30 [b]	0.004 3.75	≥ 417	
	0.30		0.03 [a c] 30 [b]	0.004 3.75	≤ 366	
$\{[Cu(bpy)_3][LiRu(C_2O_4)_3]\}_n$	0.39		0.04 [a c] 39 [b]	0.005 4.87	≥ 417	
	0.35		0.04 [a c] 35 [b]	0.004 4.37	≤ 366	
$\{[Ru(bpy)_3][NaRu(C_2O_4)_3]\}_n$	0.45		0.04 [a c] 45 [b]	0.005 5.62	≥ 417	
	0.71		0.07 [a c] 71 [b]	0.009 8.75	≤ 366	
$\{[Ru(bpy)_3][LiRu(C_2O_4)_3]\}_n$	0.52		0.05 [a c] 52 [b]	0.006 6.5	≥ 417	
	0.83		0.08 [a c] 83 [b]	0.01 10.4	≤ 366	
$\{[Os(bpy)_3][NaRu(C_2O_4)_3]\}_n$	0.48		0.05 [a c] 48 [b]	0.006 6	≥ 417	
	1.08		0.11 [a c] 108 [b]	0.13 13.5	≤ 366	
$\{[Os(bpy)_3][LiRu(C_2O_4)_3]\}_n$	0.64		0.06 [a c] 64 [b]	0.008 8	≥ 417	
	1.23		0.12 [a c] 123 [b]	0.15 15.4	≤ 366	

[a] TON = μmol H_2·μmol^{-1} MOF; [b] TON = μmol H_2·mg^{-1} MOF; [c] TON = μmol H_2·g^{-1} MOF

Conclusions

The series of $[Z^{II}(bpy)_3]^{2+}$-templated (Z^{II} = Zn (**1**,**2**); Cu (**3**,**4**); Ru (**5**,**6**); Os (**7**,**8**)) assembly of $\{[M^{I}Ru(C_2O_4)_3]^{2-}\}_n$ (M^{I} = Na, Li) anionic frameworks were obtained though self-assembly at room temperature in aqueous media. The anionic framework structures of **1**–**8** achieve the triangular cages which selectively and homogeneously encapsulate $[Z^{II}(bpy)_3]^{2+}$ complex cations. Furthermore, the electronic configuration in cationic guest complexes shows to be influenced by anionic frameworks. In addition, the $[Z^{II}(bpy)_3]^{2+}$ templates embedded within the anionic cages of $\{[M^{I}Ru(C_2O_4)_3]^{2-}\}_n$ (M^{I} = Na, Li) networks undergo 6.9–14.4% expansion as a result of electrostatic interaction between them. The MLCT band gaps in **1**–**8** can easily be tuned by $[Z^{II}(bpy)_3]^{2+}$ cationic guest, and as have been shown follow the order of **3** ≈ **4** > **1** > **2** > **5** ≈ **6** > **7** ≈ **8**. The **1**–**8** CPs exhibit high catalytic activity in UV-light promoted H_2 evolution from water reaching a total TON of 123, and where photocatalytic efficiencies follows the order as **8** > **7** > **6** > **5** > **2** > **1** ≈ **4** > **3**. Under VIS-light irradiation, the CPs **1**–**8** exhibit moderate photocatalytic activities, as have been compared to known MOFs/CPs, with enhanced catalytic rate following the order of **8** > **6** > **7** > **5** > **4** > **1** ≈ **2** > **3** leading to produce H_2 with total TON of 64. Moreover, heterogeneous catalysts remain active for four consecutive usages and preserve structural integrity and crystallinity.

These results highlight that rational synthesis of 3D anionic architectures using a target cationic guest, such as $[Z^{II}(bpy)_3]^{2+}$, provides an insight into construction of multifunctional guest encapsulated CPs with predictable structural topology and desirable properties.

***Acknowledgements*.** The authors thank FEDER and Spanish MINECO for financial support under projects MAT2013-40950-R, UCAN08-4E-008, MAT2012-38664-C02-1 and Consolider ORFEO. A.D. also thanks to Spanish *Ministerio de Educación, Cultura y Deporte* by their pre-doctoral FPU grant (AP2008-03942)

Supporting Information containes digital microgrphas of **1**–**8** crystal habits, SEM images, observed and calculated X-ray powder diffraction patterns, additional structure plots, IR spectra, thermodiffractometric results, thermogravimetry plots and summarized TG analysis, band gap calcultaion results and procedures, results of recyclability tests. Crystallographic data for **1**–**8** structures were deposited in Cambridge Crystallographic Data Center with CCDC # 1404961–1404964, 1404970–1404973.

References

(1) (a) A. Kudo,Y. Miseki, *Chem. Soc. Rev*., **2009**, *38*, 253–278;
(b) S. J. A. Moniz, S. A. Shevlin, D. J. Martin, Z.-X. Guob, J. Tang, *Energy Environ. Sci.*, **2015**, *8*, 731–759;
(c) M. Matsuoka, M. Kitano, M. Takeuchi, K. Tsujimaru, M. Anpo, J. M. Thomas, *Catal. Today*, **2007**, *122*, 51–61.

(2) (a) Y. Horiuchi, T. Toyao, M. Takeuchi, M. Matsuoka, M. Anpo, *Phys. Chem. Chem. Phys*., **2013**, *15*, 13243–13253;
(b) B. X. Wei, K.-X. Wang, X.-X. Guo, J.-S. Chen, *Proc. R. Soc. A*, **2012**, *468*, 2099–2112.

(3) (a) O. M. Yaghi, M. O'Keeffe, N. W. Ockwig, H. K. Chae, M. Eddaoudi, J. Kim, *Nature*, **2003**, *423*, 705–714;
(b) S. Kitagawa, R. Kitaura, S. Noro, *Angew. Chem., Int. Ed*., **2004**, *43*, 2334–2375;
(c) G. Férey, *Chem. Soc. Rev*., **2008**, *37*, 191–214.

(4) (a) J.-R. Li, R. J. Kuppler, H.-C. Zhou, *Chem. Soc. Rev*., **2009**, *38*, 1477–1504;
(b) K. Sumida, D. L. Rogow, J. A. Mason, T. M. McDonald, E. D. Bloch, Z. R. Herm, T.-H. Bae, J. R. Long, *Chem. Rev*., **2012**, *112*, 734–781;
(c) J. Liu, P. K. Thallapally, B. P. McGrail, D. R. Brown, J. Liu, *Chem. Soc. Rev*., **2012**, *41*, 2308–2322;
(d) B. Van de Voorde, B. Bueken, J. Denayer, D. De Vos, *Chem. Soc. Rev*., **2014**, *43*, 5766–5788;
(e) N. C. Burtch, H. Jasuja, K. S. Walton, *Chem. Rev*., **2014**, *114*, 10575–10612;
(f) C. K. Brozek, M. Dincă, *Chem. Soc. Rev*., **2014**, *43*, 5456–5467;
(g) W. Zhang, R.-G. Xiong, *Chem. Rev*., **2012**, *112*, 1163–1195;
(h) P. Ramaswamy, N. E. Wong, G. K. H. Shimizu, *Chem. Soc. Rev*., **2014**, *43*, 5913–5932;
(i) T. Yamada, K. Otsubo, R. Makiura, H. Kitagawa, *Chem. Soc. Rev*., **2013**, *42*, 6655–6669;
(j) J. Gascon, A. Corma, F. Kapteijn, F. X. Llabrés i Xamena, *ACS Catal*., **2014**, *4*, 361–378;
(k) A. Corma, H. García, F. X. Llabrés i Xamena, *Chem. Rev*., **2010**, *110*, 4606–4655;
(l) J. Y. Lee, O. K. Farha, J. Roberts, K. A. Scheidt, S. T. Nguyen, J. T. Hupp, *Chem. Soc. Rev*., **2009**, *38*, 1450–1459;
(m) L. Ma, C. Abney, W. Lin, *Chem. Soc. Rev*., **2009**, *38*, 1248–1256.

(5) (a) F. X. Llabrés i Xamena, A. Corma, H. Garcia, *J. Phys. Chem. C*, **2007**, *111*, 80–85;
(b) J.-L. Wang, C. Wang, W. Lin, *ACS Catal*., **2012**, *2*, 2630–2640;
(c) M. Alvaro, E. Carbonell, B. Ferrer, F. X. Llabrés i Xamena, H. Garcia, *Chem. Eur. J*., **2007**, *13*, 5106–5112.

(6) (a) T. Zhang, W. Lin, *Chem. Soc. Rev*., **2014**, *43*, 5982–5993;
(b) M. A. Nasalevich, M. van der Veen, F. Kapteijn, J. Gascon, *Cryst. Eng. Comm*, **2014**, *16*, 4919–4926.

(7) (a) S. Wang, W. Yao, J. Lin, Z. Ding, X. Wang, *Angew. Chem. Int. Ed*., **2014**, *53*, 1034–1038;
(b) C. Wang, Z. Xie, K. E. deKrafft, W. Lin, *J. Am. Chem. Soc*., **2011**, *133*, 13445–13445;
(c) Y. Fu, D. Sun, Y. Chen, R. Huang, Z. Ding, X. Fu, Z. Li, *Angew. Chem. Int. Ed*., **2012**, *51*, 3364–3367;
(d) D. Sun, Y. Fu, W. Liu, L. Ye, D. Wang, L. Yang, X. Fu, Z. Li, *Chem. Eur. J*., **2013**, *19*, 14279–14285;
(e) D. Sun, W. Liu, Y. Fu, Z. Fang, F. Sun, X. Fu, Y. Zhang, Z. Li, *Chem. Eur. J*., **2014**, *20*, 4780–4788;
(f) J. Li, D. Luo, C. Yang, S. He, S. Chen, J. Lin, L. Zhu, X. Li, *J. Solid State Chem*., **2013**, *203*, 154–159;
(g) Y. Liu, Y. Yang, Q. Sun, Z. Wang, B. Huang, Y. Dai, X. Qin, X. Zhang, *ACS Appl. Mater. Interfaces*, **2013**, *5*, 7654−7658.

(8) (a) S. Han, Y. Wei, B. A. Grzybowski, *Chem. Eur. J*., **2013**, *19*, 11194–11198;
(b) R. Ameloot, M. B. J. Roeffaers, G. De Cremer, F. Vermoortele, J. Hofkens, B. F. Sels, D. E. De Vos, *Adv. Mater*., **2011**, *23*, 1788–1791.

(9) (a) J. R. Choi, T. Tachikawa, M. Fujitsuka, T. Majima, *Langmuir*, **2010**, *26*, 10437–10443;
(b) K. G. M. Laurier, F. Vermoortele, R. Ameloot, D. E. De Vos, J. Hofkens, M. B. J. Roeffaers, *J. Am. Chem. Soc*., **2013**, *135*, 14488–14491;
(c) M.-H. Xie, X.-L. Yang, C. Zou, C.-D. Wu, *Inorg. Chem*., **2011**, *50*, 5318–5320;
(d) L. Shen, S. Liang, W. Wu, R. Liang, L. Wu, *J. Mater. Chem. A*, **2013**, *1*, 11473–11482;

(e) L. Shen, S. Liang, W. Wu, R. Liang, L. Wu, *Dalton Trans*., **2013**, *42*, 13649–13657.
(10) (a) P. Mahata, G. Madras, S. Natarajan, *J. Phys. Chem. B*, **2006**, *110*, 13759–13768;
(b) H.-R. Fu, Y. Kang, J. Zhang, *Inorg. Chem.*, **2014**, *53*, 4209−4214;
(c) S. Zhang, L. Han, L. Li, J. Cheng, D. Yuan, J. Luo, *Cryst. Growth Des*., **2013**, *13*, 5466−5472;
(d) W.-T. Xu, L. Ma, F. Ke, F.-M. Peng, G.-S. Xu, Y.-H. Shen, J.-F. Zhu, L.-G. Qiu, Y.-P. Yuan, *Dalton Trans*., **2014**, *43*, 3792–3798;
(e) J. Gao, J. Miao, P.-Z. Li, W. Y. Teng, L. Yang, Y. Zhao, B. Liu, Q. Zhang, *Chem. Commun*., **2014**, *50*, 3786–3788.
(11) (a) P. Wu, C. He, J. Wang, X. Peng, X. Li, Y. An, C. Duan, *J. Am. Chem. Soc*., **2012**, *134*, 14991–14999;
(b) T. Toyao, M. Saito, Y. Horiuchi, M. Matsuoka, *Catal. Sci. Technol*., **2014**, *4*, 625–628;
(c) J. Long, S. Wang, Z. Ding, S. Wang, Y. Zhou, L. Huang, X. Wang, *Chem. Commun*., **2012**, *48*, 11656–11658.
(12) (a) J. Gascon, M. D. Hernández-Alonso, A. Rita Almeida, G. P. M. van Klink, F. Kapteijn, G. Mul, *Chem. Sus. Chem*., **2008**, *1*, 981–983;
(b) M. A. Nasalevich, M. G. Goesten, T. J. Savenije, F. Kapteijn, J. Gascon, *Chem. Commun*., **2013**, *49*, 10575–10577;
(c) C.-K. Lin, D. Zhao, W.-Y. Gao, Z. Yang, J. Ye, T. Xu, Q. Ge, S. Ma, D.-J. Liu, *Inorg. Chem*., **2012**, *51*, 9039–9044;
(d) L.-M. Yang, G.-Y. Fang, J. Ma, E. Ganz, S. S. Han, *Cryst. Growth Des*., **2014**, *14*, 2532–2541.
(13) (a) K. Meyer, M. Ranocchiari, J. A. van Bokhoven, *Energy Environ. Sci*., **2015**, *8*, 1923–1937;
(b) Y. Ren, G. H. Chia, Z. Gao, *Nano Today*, **2013**, *8*, 577–597.
(14) Y. Kataoka, K. Sato, Y. Miyazaki, K. Masuda, H. Tanaka, S. Naito, W. Mori, *Energy Environ. Sci*., **2009**, *2*, 397–400.
(15) Y. Kataoka, Y. Miyazaki, K. Sato, T. Saito, Y. Nakanishi, Y. Kiatagwa, T. Kawakami, M. Okumura, K. Yamaguchi, W. Mori, *Supramol. Chem*., **2011**, *23*, 287–296.
(16) Y. Horiuchi, T. Toyao, H. Higashimura, M. Saito, M. Anpo, K. Mochizuki, M. Matsuoka, *J. Phys. Chem. C*, **2012**, **116**, 20848−20853.
(17) T. Toyao, M. Saito, Y. Horiuchi, K. Mochizuki, M. Iwata, H. Higashimura, M. Matsuoka, *Catal. Sci. Technol*., **2013**, *3*, 2092–2097.
(18) C. Gomes Silva, I. Luz, F. X. Llabrés i Xamena, A. Corma, H. García, *Chem. Eur. J*., **2010**, *16*, 11133–11138.
(19) J. He, Z. Yan, J. Wang, J. Xie, L. Jiang, Y. Shi, F. Yuan, F. Yu, Y. Sun, *Chem. Commun*., **2013**, *49*, 6761–6763.
(20) J. He, J. Wang, Y. Chen, J. Zhang, D. Duan, Y. Wang, Z. Yan, *Chem. Commun*., **2014**, *50*, 7063–7066.
(21) C. Wang , K. E. deKrafft, W. Lin, *J. Am. Chem. Soc*., **2012**, *134*, 7211–7214.
(22) T. Zhou, Y. Du, A. Borgna, J. Hong, Y. Wang, J. Han, W. Zhang, R. Xu, *Energy Environ. Sci*., **2013**, *6*, 3229–3234.
(23) S. Pullen, H. Fei, A.Orthaber, S. M. Cohen, S. Ott, *J. Am. Chem. Soc*., **2013**, *135*, 16997−17003.
(24) X.-L. Hu, C.-Y. Sun, C. Qin, X.-L. Wang, H.-N. Wang, E.-L. Zhou, W.-E Li, Z.-M. Su, *Chem. Commun.*, **2013**, *49*, 3564–3566.
(25) H. Fu, C. Qin, Y. Lu, Z.-M. Zhang, Y.-G. Li, Z.-M. Su, W.-L. Li, E.-B. Wang, *Angew. Chem. Int. Ed*., **2012**, *51*, 7985–7989.
(26) A. Fateeva, P. A. Chater, C. P. Ireland, A. A. Tahir, Y. Z. Khimyak, P. V. Wiper, J. R. Darwent, M. J. Rosseinsky, *Angew. Chem. Int. Ed*., **2012**, *51*, 7440–7444.
(27) (a) R. Pellaux, S. Decurtins, H. W. Schmalle, *Acta Cryst*., **1999**, *C55*, 1075–1079;
(b) S. Rabaste, N. Amstutz, A. Hauser, A. Pillonnet, *Appl. Phys. Lett*., **2005**, *87*, 251904(1)–(3);
(c) R. Sieber, S. Decurtins, H. Stoeckli-Evans, C. Wilson, J. A. K. Howard, S. C. Capelli, A. Hauser, *Chem. Eur. J*., **2000**, *6*, 361–368;
(d) P. Roman, C. Guzman-Miralles, A. Luque, *Dalton Trans*., **1996**, *20*, 3985–3989;
(e) M. Milos, T. Penhouet, P. Pal, A. Hauser, *Inorg. Chem*., **2010**, *49*, 3402–3408;
(f) S. Decurtins, H. W. Schmalle, P. Schneuwly, J. Ensling, P. Gütlich, *J. Am. Chem. Soc*., **1994**, *116*, 9521–9528;
(g) M. Milos, A. Hauser, *J. Luminescence*, **2013**, *133*, 15–20;
(h) M. Milos, A. Hauser, *J. Luminescence*, **2009**, *129*, 1901–1904;

(i) M. E. von Arx, A. Hauser, H. Riesen, R. Pellaux, S. Decurtins, *Phys. Rev. B*, **1996**, *54*, 15800–15807;
(j) M. E. von Arx, E. Burattini, A. Hauser, L. van Pieterson, R. Pellaux, S. Decurtins, *J. Phys. Chem. A*, **2000**, *104*, 883–893.
(28) R. Andrés, M. Gruselle, B Malézieux, M. Verdaguer, J. Vaissermann, *Inorg. Chem.*, **1999**, *38*, 4637−4646.
(29) (a) M. Milos, P. Pal, A. Hauser, *Chem. Phys. Chem.*, **2010**, *11*, 3161–3166;
(b) A. Hauser, H. Riesen, R. Pellaux, S. Decurtins, *Chem. Phys. Lett.*, **1996**, *261*, 313–317;
(c) S. Decurtins, H. W. Schmalle, R. Pellaux, P. Schneuwly, A. Hauser, *Inorg. Chem.*, **1996**, *35*, 1451–1460;
(d) V. S. Langford, M. E. von Arx, A. Hauser, *J. Phys. Chem. A*, **1999**, *103*, 7161–7169;
(f) M. E. von Arx, V. S. Langford, U. Oetliker, A. Hauser, *J. Phys. Chem. A*, **2002**, *106*, 7099–7105;
(30) R. W. Larsen, L. Wojtas, *J. Phys. Chem. A*, **2012**, *116*, 7830−7835.
(31) (a) D. A. Thornton, G. M. Watkins, *J. Coord. Chem.*, **1992**, *25*, 299−315;
(b) J. A. Broomhead, C. G. Young, *Inorganic Synthesis*, **1982**, *21*, 127−128;
(c) F. H. Burstall, F. P. Dwyer, E. C. Gyarfas, *J. Chem. Soc*., **1950**, 953−955;
(d) R. Kaziro, T. W. Hambley, R. A. Bistead, J. K. Beattie, *Inorg. Chim. Acta*, **1989**, *164*, 85–91.
(32) A. Altomare, G. Cascarano, C. Giacovazzo, A. Guagliardi, M. C. Burla, G. Polidori, M. Camalli, *J. Appl. Cryst*., **1994**, *27*, 435.
(33) G. M. Sheldrick, *Acta. Cryst*., **1990**, *A46*, 467–473.
(34) H. D. Flack, G. Bernardinelli, *J. Appl. Crystallogr*., **2000**, *33*, 1143−1148.
(35) V. A. Blatov, A. P. Shevchenko, D. M. Proserpio, *Cryst. Growth Design*, **2014**, *14*, 3576−3586.
(36) (a) X.-M. Chen, R.-Q. Wang, X.-L. Yu, *Acta Cryst*., **1995**, *51*, 1545−1547;
(b) P. Majumdar, A. K. Ghosh, L. R. Falvello, S.-M. Peng, S. Goswami, *Inorg. Chem*., **1998**, *37*, 1651−1654;
(c) J. M. Harrowfield, A. N. Sobolev, *Aust. J. Chem*., **1994**, *47*, 763−767;
(d) M. M. Richter, B. Scott, K. J. Brewer, R. D. Willett, *Acta Cryst.*, **1991**, *C47*, 2443−2444.
(37) (a) M. E. Fleet, *Mineral. Mag*., **1976**, *40*, 531−533;
(b) K. Robinson, G. V. Gibbs, P. H. Ribbe, *Science*, **1971**, *172*, 567−570.
(38) I. D. Brown, R. D. Shannon, *Acta Crystallogr*., **1973**, *A29*, 266.
(39) S. T. Hyde, M. O'Keeffe, D. M. Proserpio, *Angew. Chem., Int. Ed*., **2008**, *47*, 7996−8000.
(40) (a) V. M. Russell, D. C. Craig, M. L. Scudder, I. G. Dance, *Cryst. Eng. Comm*., **2000**, *2*, 16−23;
(b) S. Decurtins, H. Schmalle, R. Pellaux, *New. J. Chem*., **1998**, *22*, 117–121.
(41) I. A. Baburin, V. A. Blatov, *Acta Cryst*., **2004**, *B60*, 447–452.
(42) E. V. Peresypkina, V. A. Blatov, *J. Mol. Struct.-Theochem*., **1999**, *489*, 225–236.
(43) Chr. K. Jørgensen, In *Advance in Chemical Physics*; Vol. 5: Spectroscopy of Transition-Group Complexes, John Wiley & Sons, LTD, 1963.
(44) R. W. Olliff, A. L. Odell, *J. Chem. Soc.*, **1964**, 2417–2421.
(45) A. B. P. Lever, In *Inorganic Electronic Spectroscopy, Studies in Physical and Theoretical Chemistry*, Amsterdam, Elsevier, 1984.
(46) R. A. Palmer, T. S. Piper, *Inorg. Chem.*, **1966**, *5*, 864−878.
(47) H. Riesen, L. Wallace, E. Krausz, *Chem. Phys. Lett*., **1994**, *228*, 605–609.
(48) T. Otsuka, N. Takahashi, N. Fujigasaki, Y. Ohashi, Y. Kaizu, *Inorg. Chem.*, **1999**, *38*, 1340–1347.
(49) F. Barigelletti, L. De Cola, V. Balzani, R. Hage, J. G. Haasnoot, J. Reedijk, J. G. Vos, *Inorg. Chem.*, **1991**, *30*, 641–645.
(50) D. L. Wood, J. Tauc, *Phys. Rev. B*, **1972**, *5*, 3144–3151.
(51) P. Kubelka, *J. Opt. Soc. Am*., **1948**, *38*, 449–457.
(52) R. W. Larsen, L. Wojtas, *J. Mater. Chem. A*, **2013**, *1*, 14133–14139.
(53) M. Kimura, T. Yamashita, S. Nishida, *Inorg. Chim. Acta*, **1984**, *89*, 193−198.
(54) S. Decurtins, R. Pellaux, *Comments Inorg. Chem*., **1998**, *20*, 143−161.

SUPPORTING INFORMATION

Tris(bipyridine)Metal(II)-Templated Assemblies of 3D Alkali-Ruthenium Oxalate Coordination Frameworks: Structures, Characterization and Photocatalytic Activity in Water Reduction

Alla Dikhtiarenko,[a] Rafael Valiente,[b] José R. García,[a] and José Gimeno[a]

[a] Departamento de Química Orgánica e Inorgánica, Universidad de Oviedo – CINN, 33006 Oviedo, Spain
[b] MALTA Consolider Team, Departamento de Física Aplicada, Universidad de Cantabria, 39005 Santander, Spain

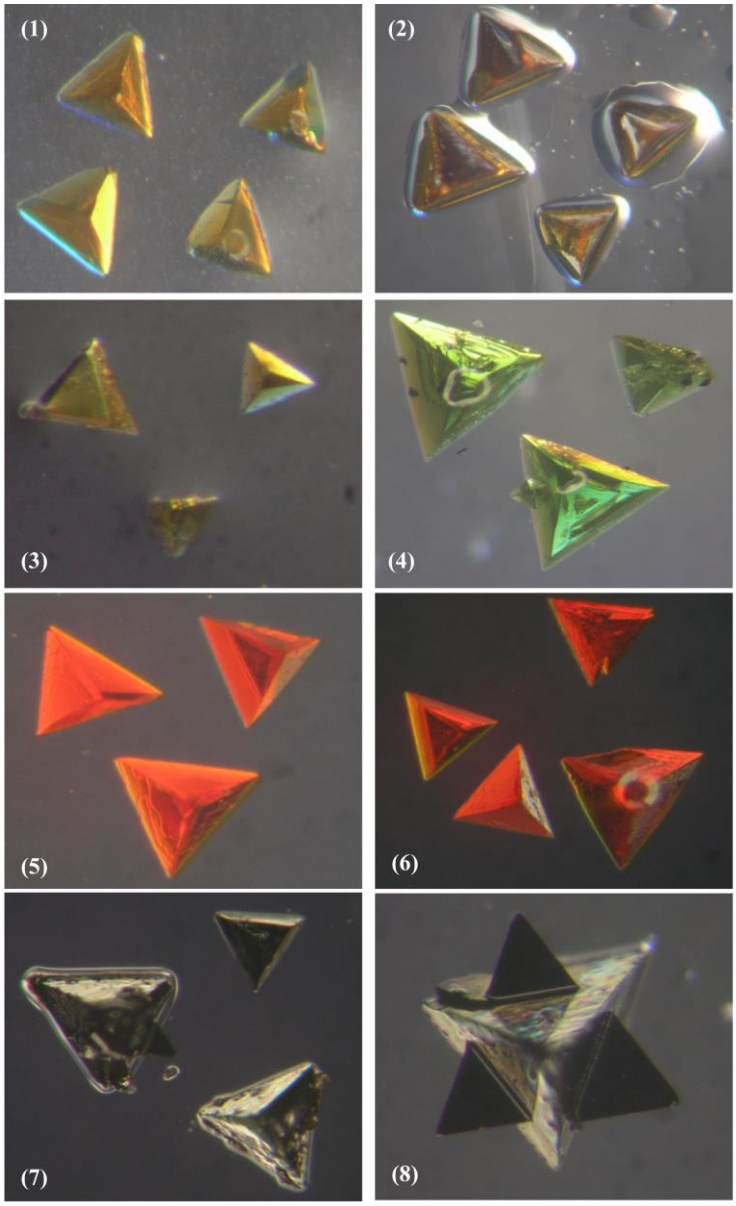

Figure S1. Digital photographs showing the crystal habits of compounds **1**–**8** grown in gel media.

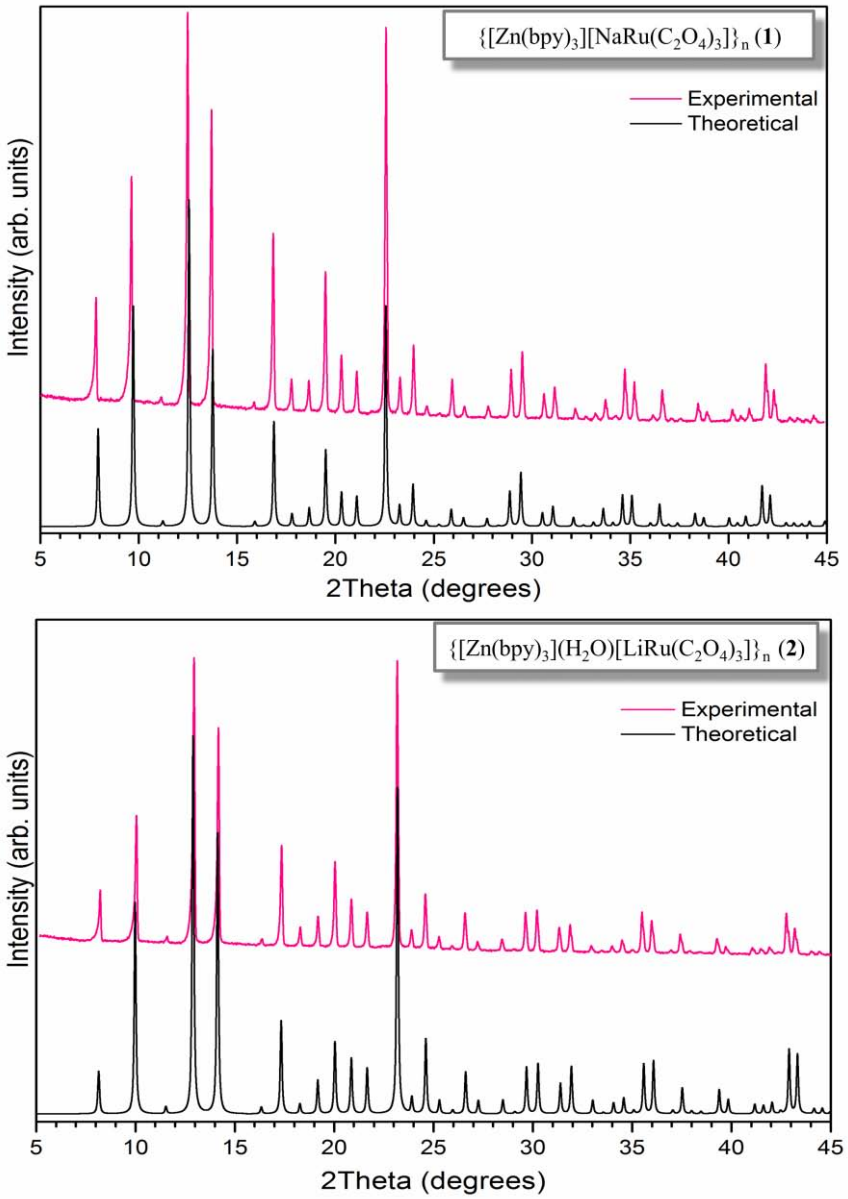

Figure S2. Experimental and theoretical powder X-Ray diffraction patterns for $\{[Zn^{II}(bpy)_3][NaRu(C_2O_4)_3]\}_n$ (**1**) and $\{[Zn^{II}(bpy)_3](H_2O)[LiRu(C_2O_4)_3]\}_n$ (**2**), indication the phase purity.

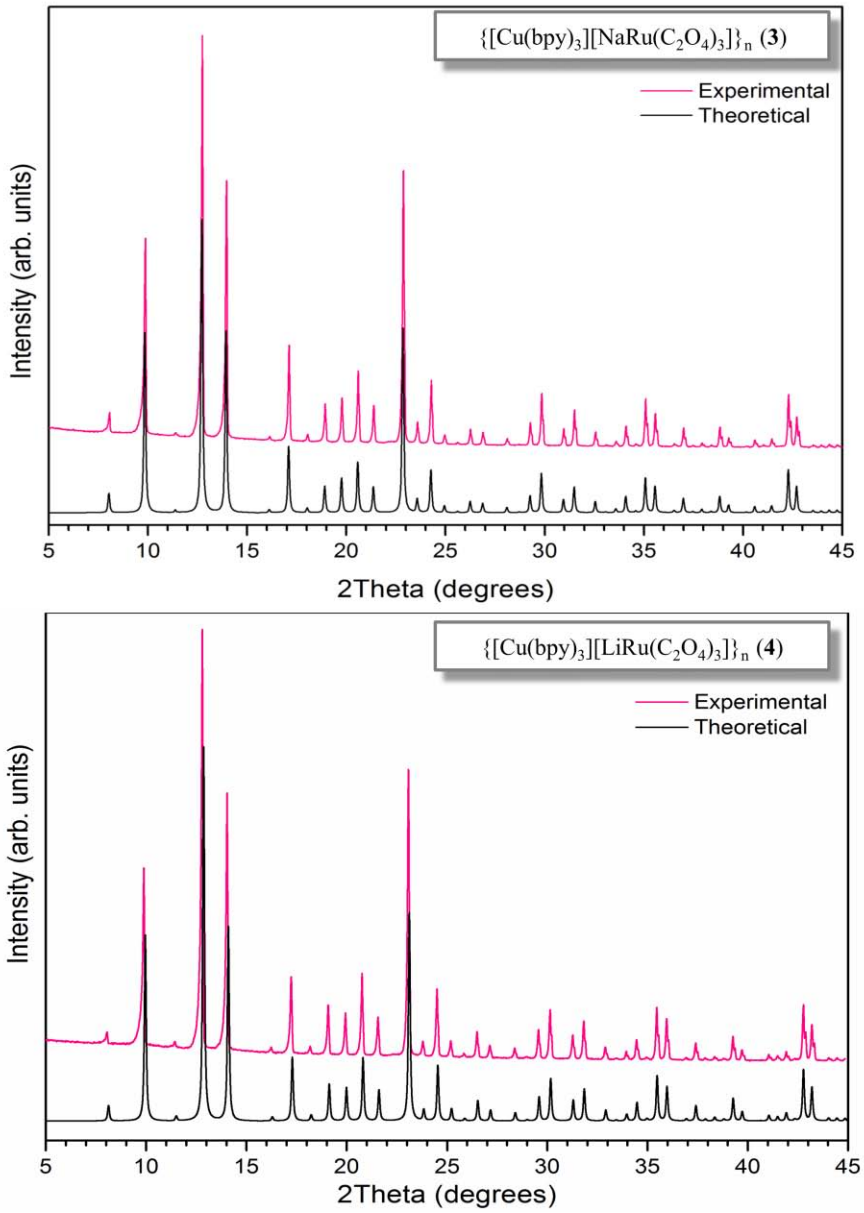

Figure S3. Experimental and theoretical powder X-Ray diffraction patterns for $\{[Cu^{II}(bpy)_3][NaRu(C_2O_4)_3]\}_n$ (**3**) and $\{[Cu^{II}(bpy)_3][LiRu(C_2O_4)_3]\}_n$ (**4**), indication the phase purity.

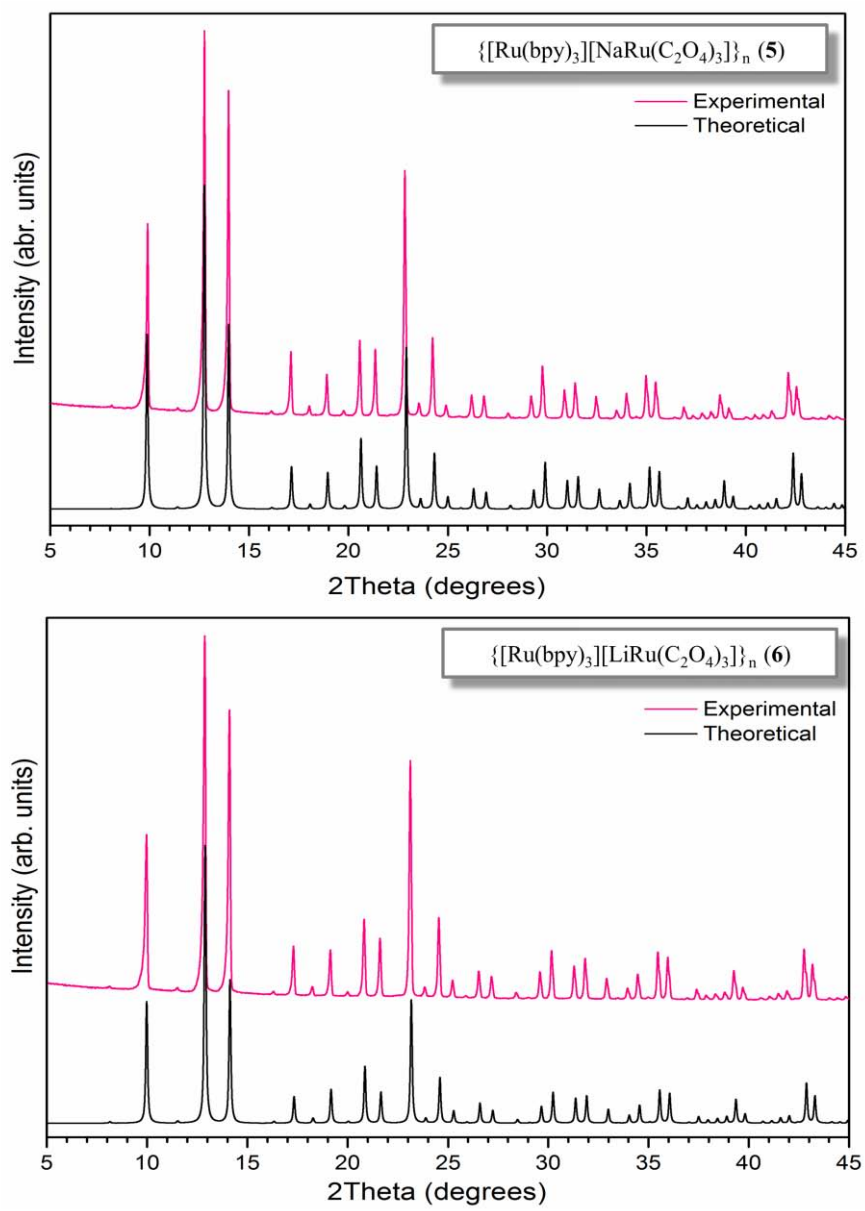

Figure S4. Experimental and theoretical powder X-Ray diffraction patterns for $\{[Ru^{II}(bpy)_3][NaRu(C_2O_4)_3]\}_n$ (**5**) and $\{[Ru^{II}(bpy)_3][LiRu(C_2O_4)_3]\}_n$ (**6**), indication the phase purity.

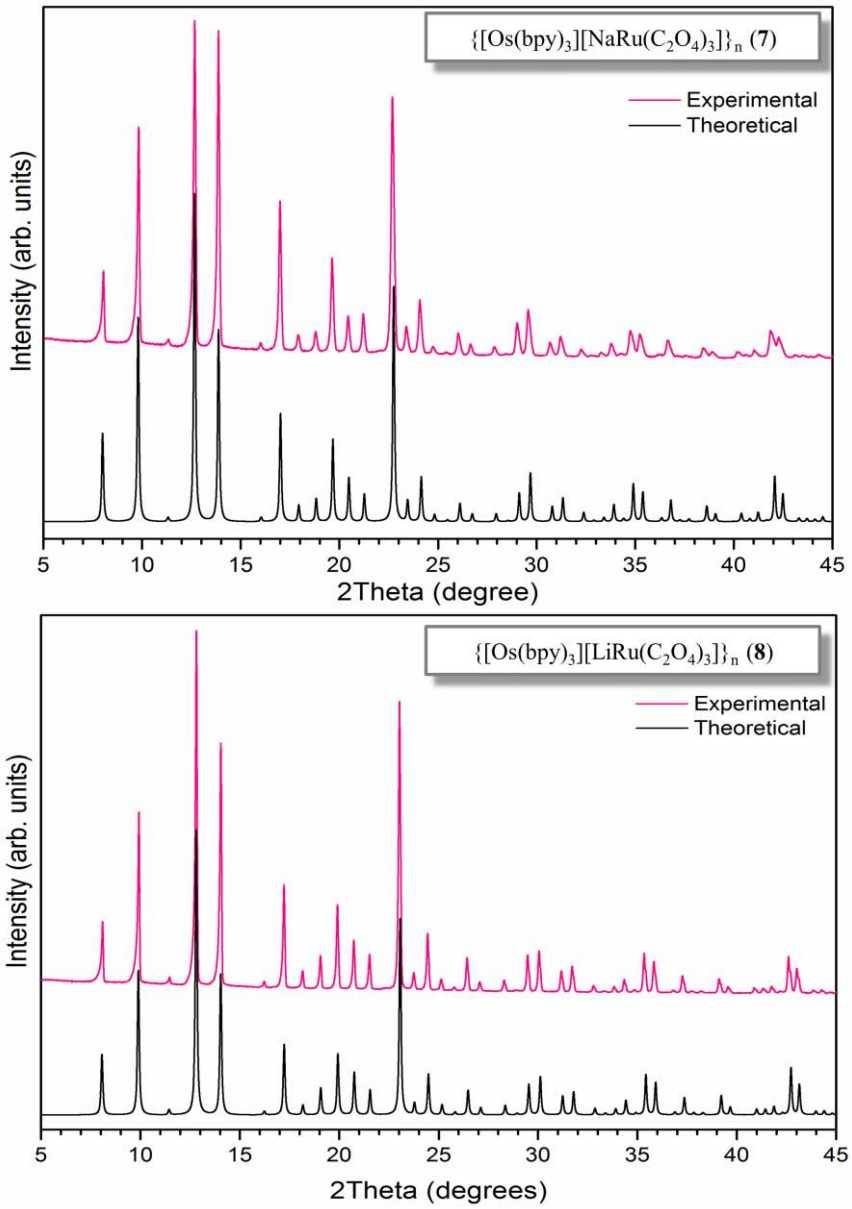

Figure S5. Experimental and theoretical powder X-Ray diffraction patterns for $\{[Os^{II}(bpy)_3][NaRu(C_2O_4)_3]\}_n$ (**7**) and $\{[Os^{II}(bpy)_3][LiRu(C_2O_4)_3]\}_n$ (**8**), indication the phase purity.

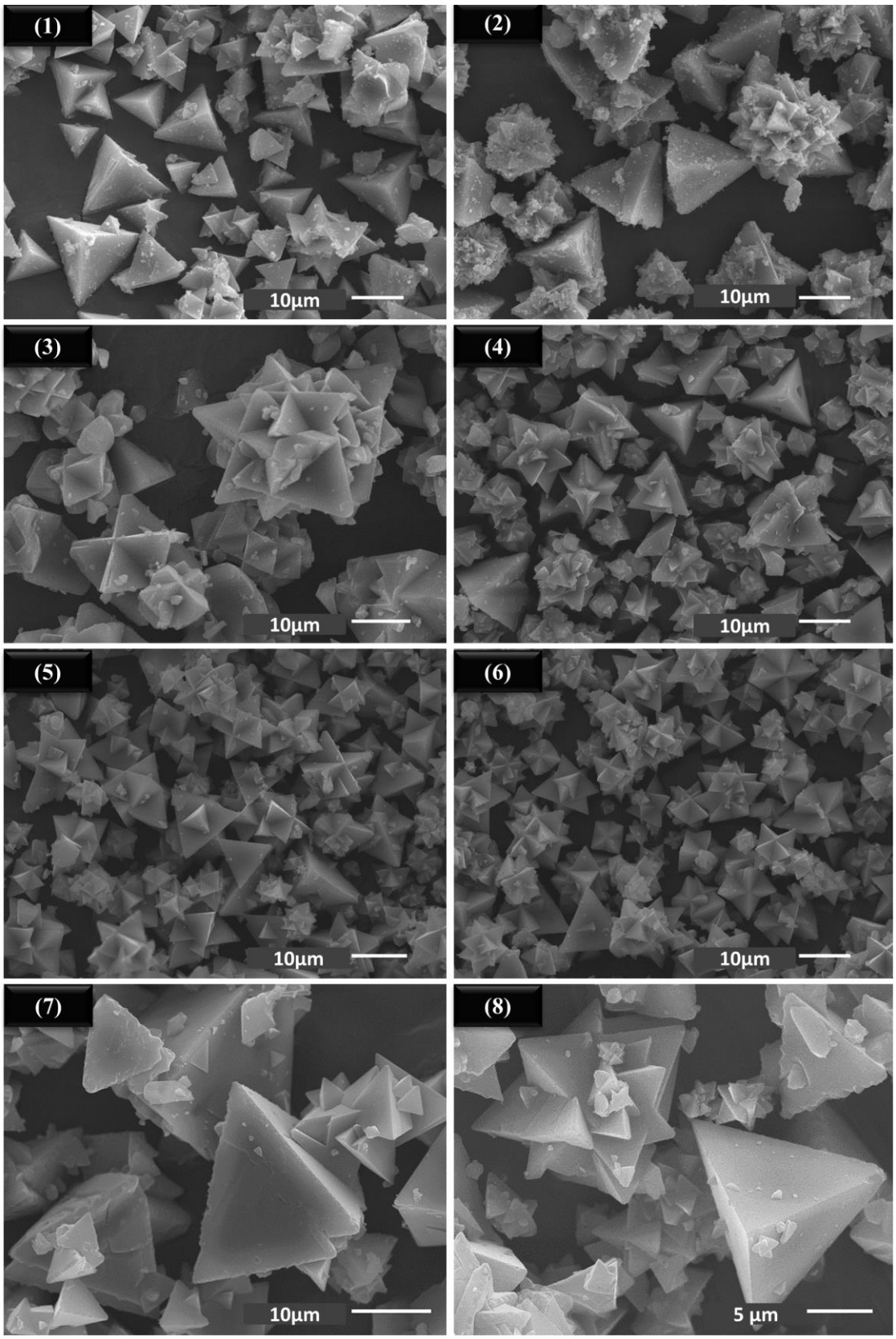

Figure S6. SEM images of compounds **1**–**8**.

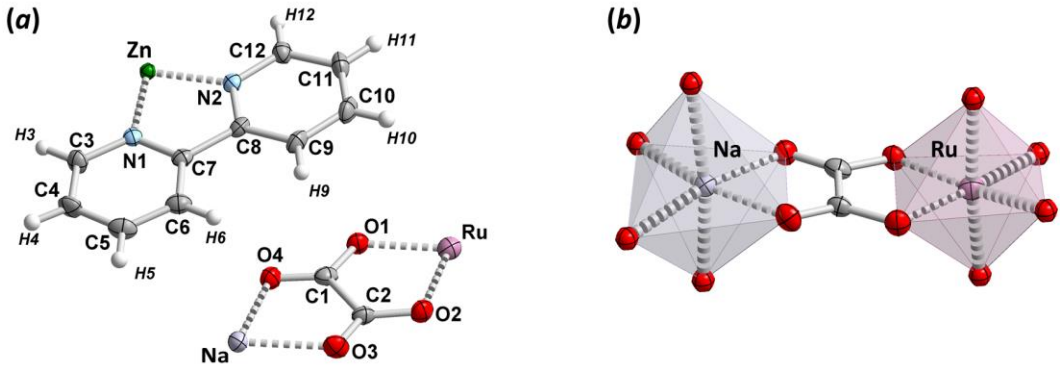

Figure S7. (a) View of the asymmetric unit of **1** with corresponding atom labeling scheme drawn with ellipsoids at the 50% probability level. (b). The bridging mode of oxalate ligand, Ru(III) and Na(I) coordination environment in compound **1**.

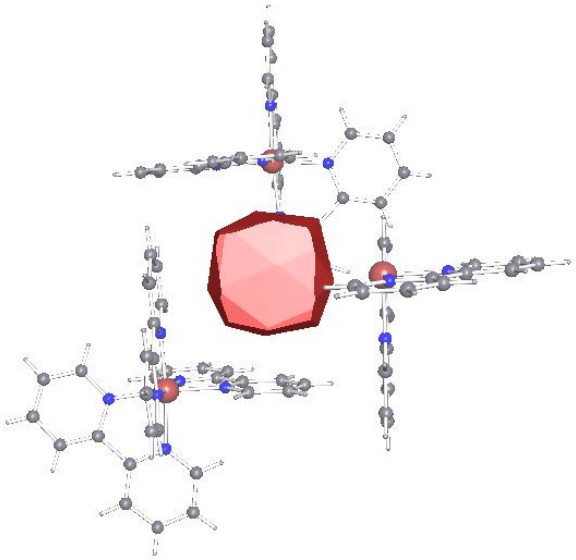

Figure S8. Voronoi-Dirichlet polyhedra representing volume of cubic bpy-cage ocupied by water molecule in **2**.

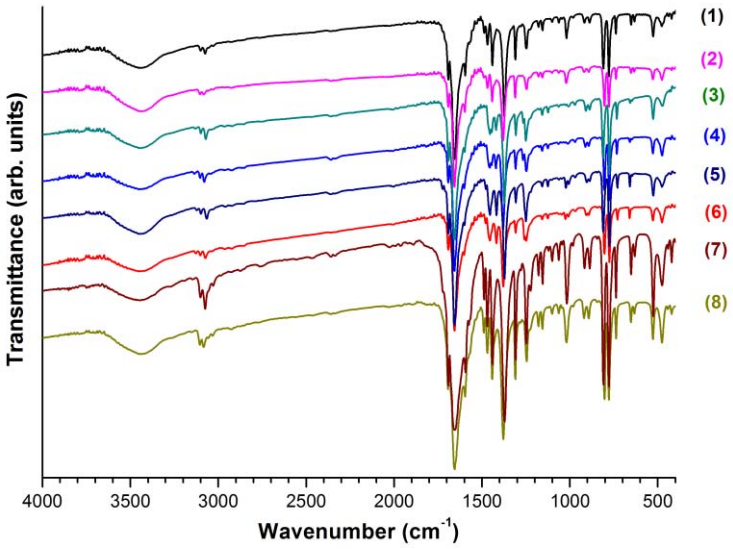

Figure S9. IR spectra of compounds **1**–**8**.

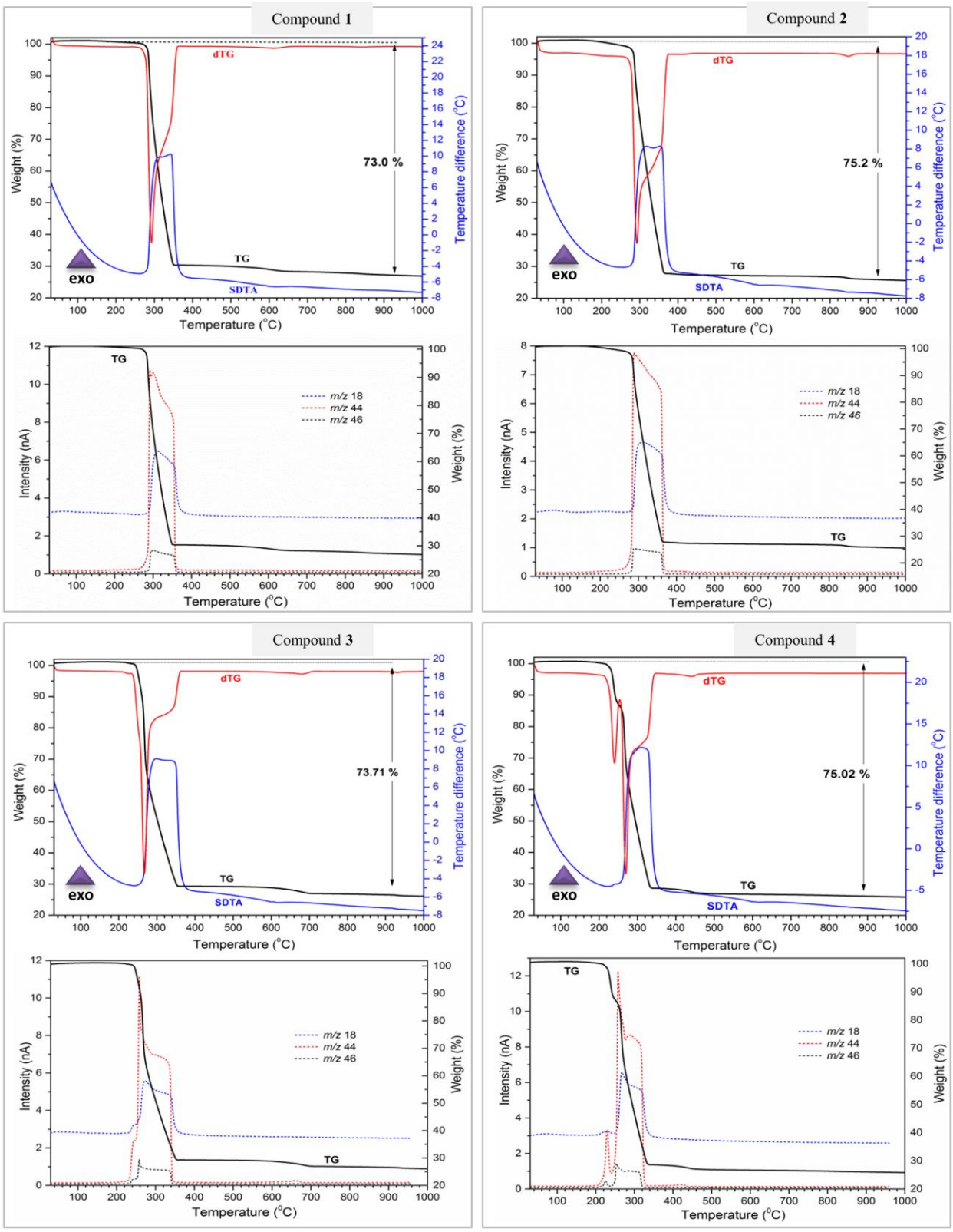

Figure S10. Thermal decomposition (TG, dTG, SDTA) and mass spectrometry of evacuated vapors curves of compounds **1**–**4** in air atmosphere.

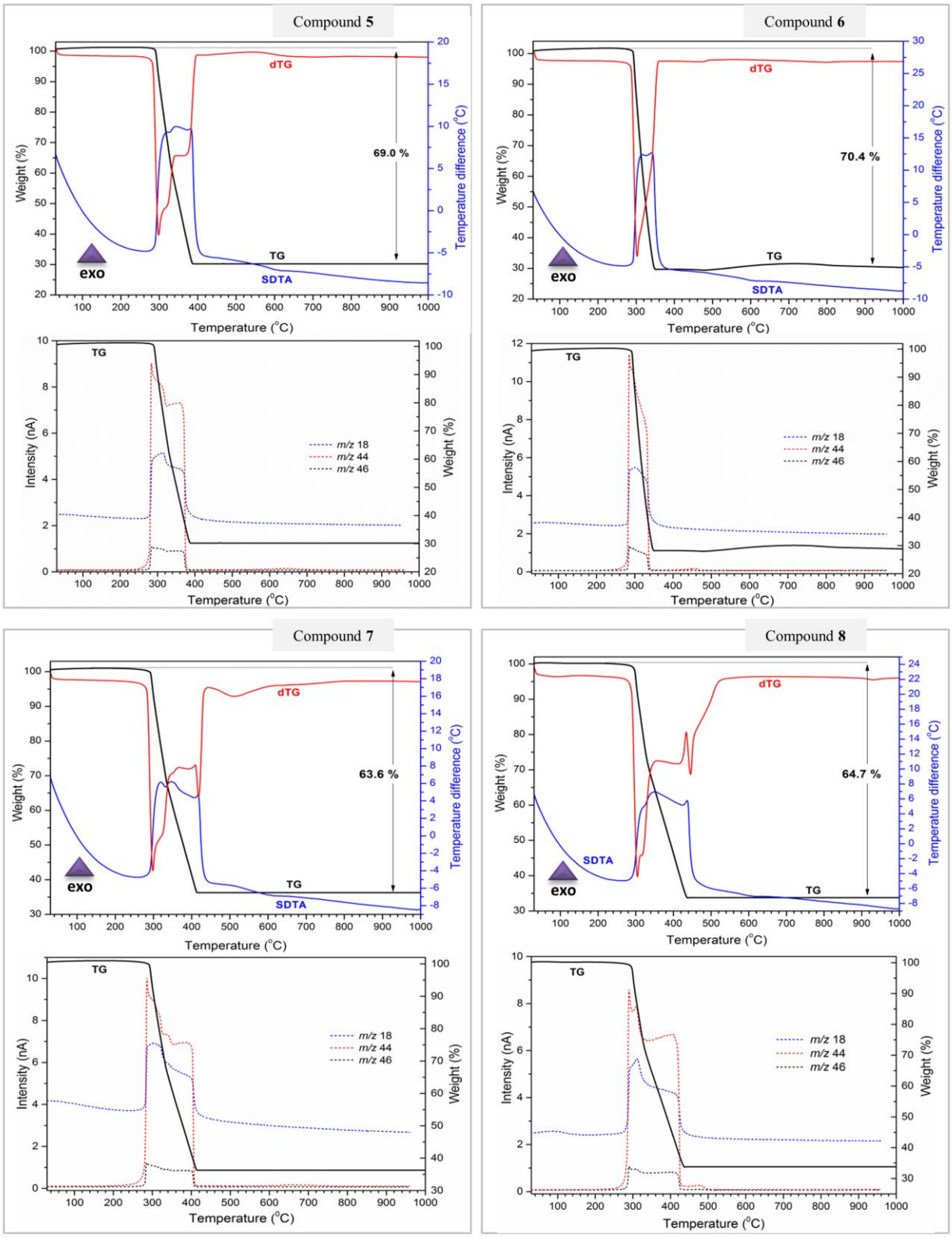

Figure S11. Thermal decomposition (TG, dTG, SDTA) and mass spectrometry of evacuated vapors curves of compounds **5**–**8** in air atmosphere.

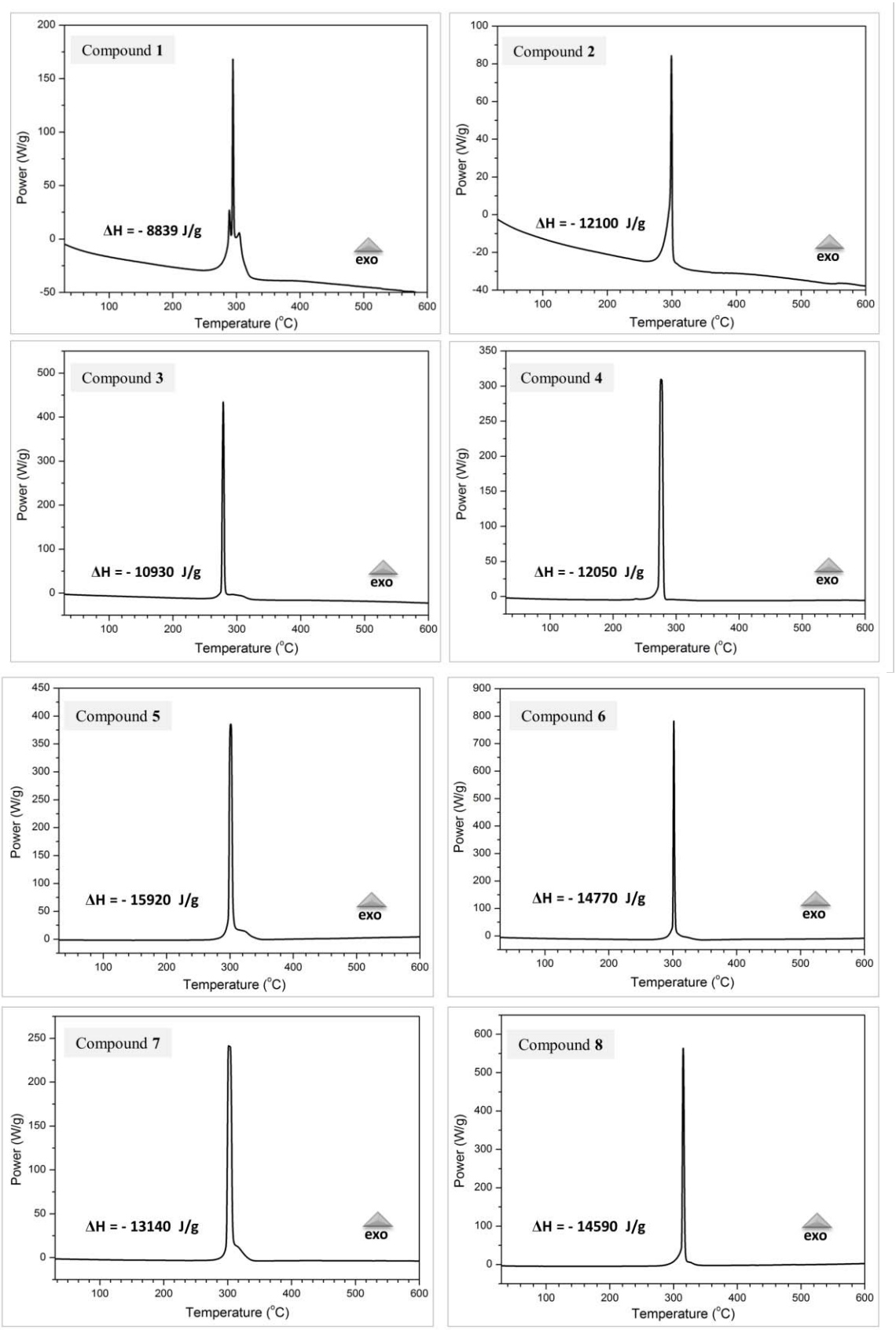

Figure S12. The DSC curves corresponding to thermal decomposition of compounds **1**–**8** in air atmosphere

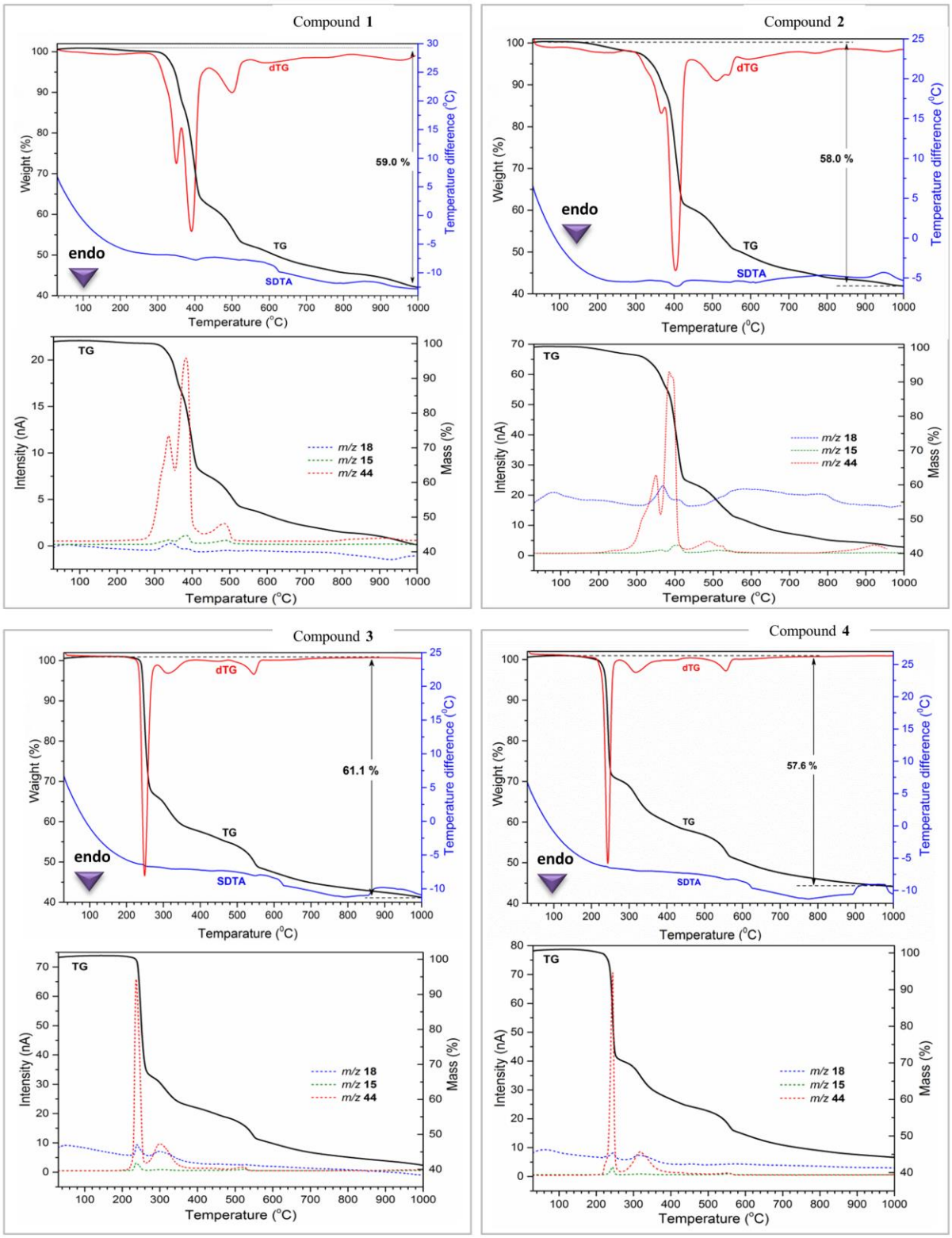

Figure S13. Thermal decomposition (TG, dTG, SDTA) and mass spectrometry of evacuated vapors curves of compounds **1**–**4** in nitrogen atmosphere.

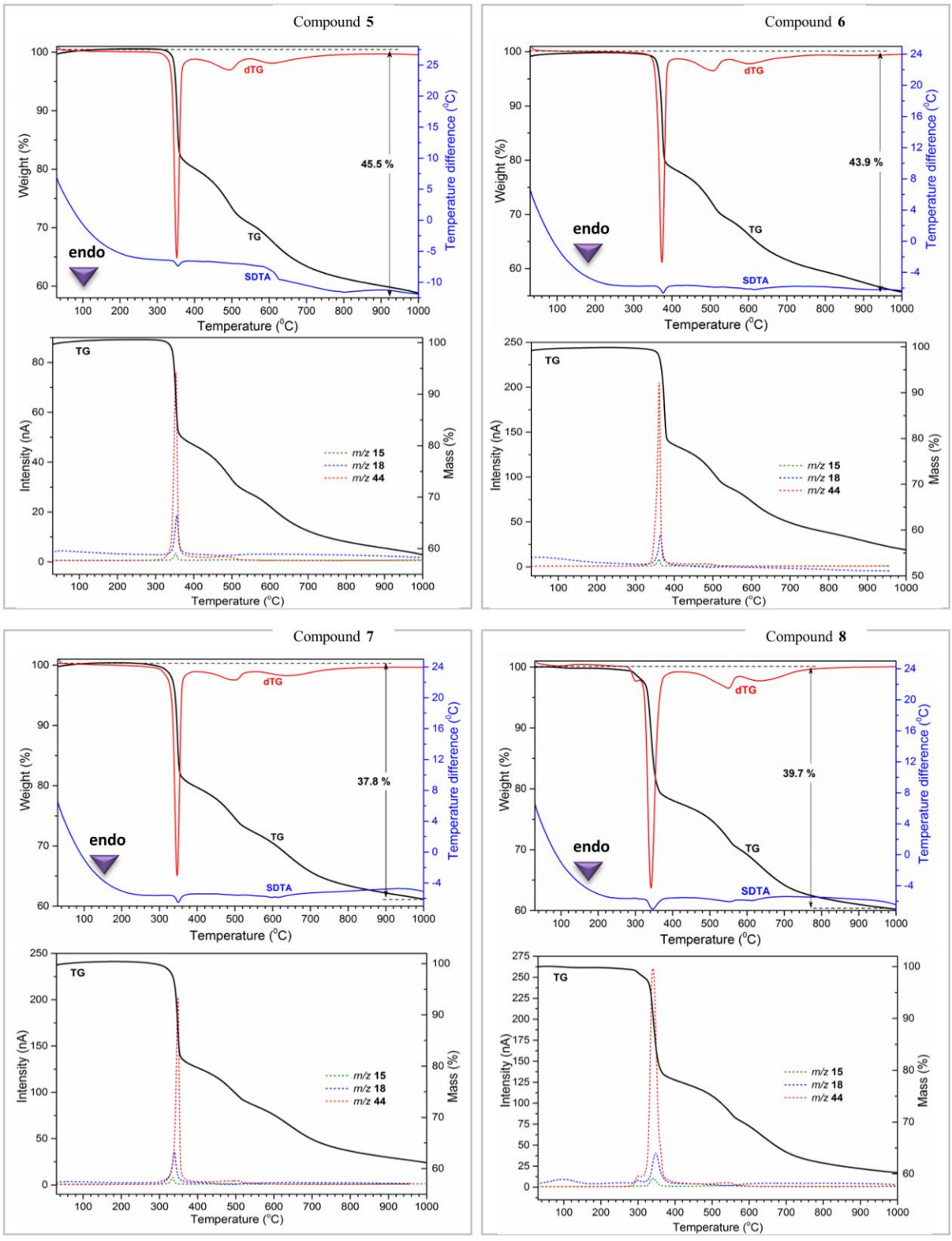

Figure S14. Thermal decomposition (TG, dTG, SDTA) curves of compounds **5**–**8** in nitrogen atmosphere.

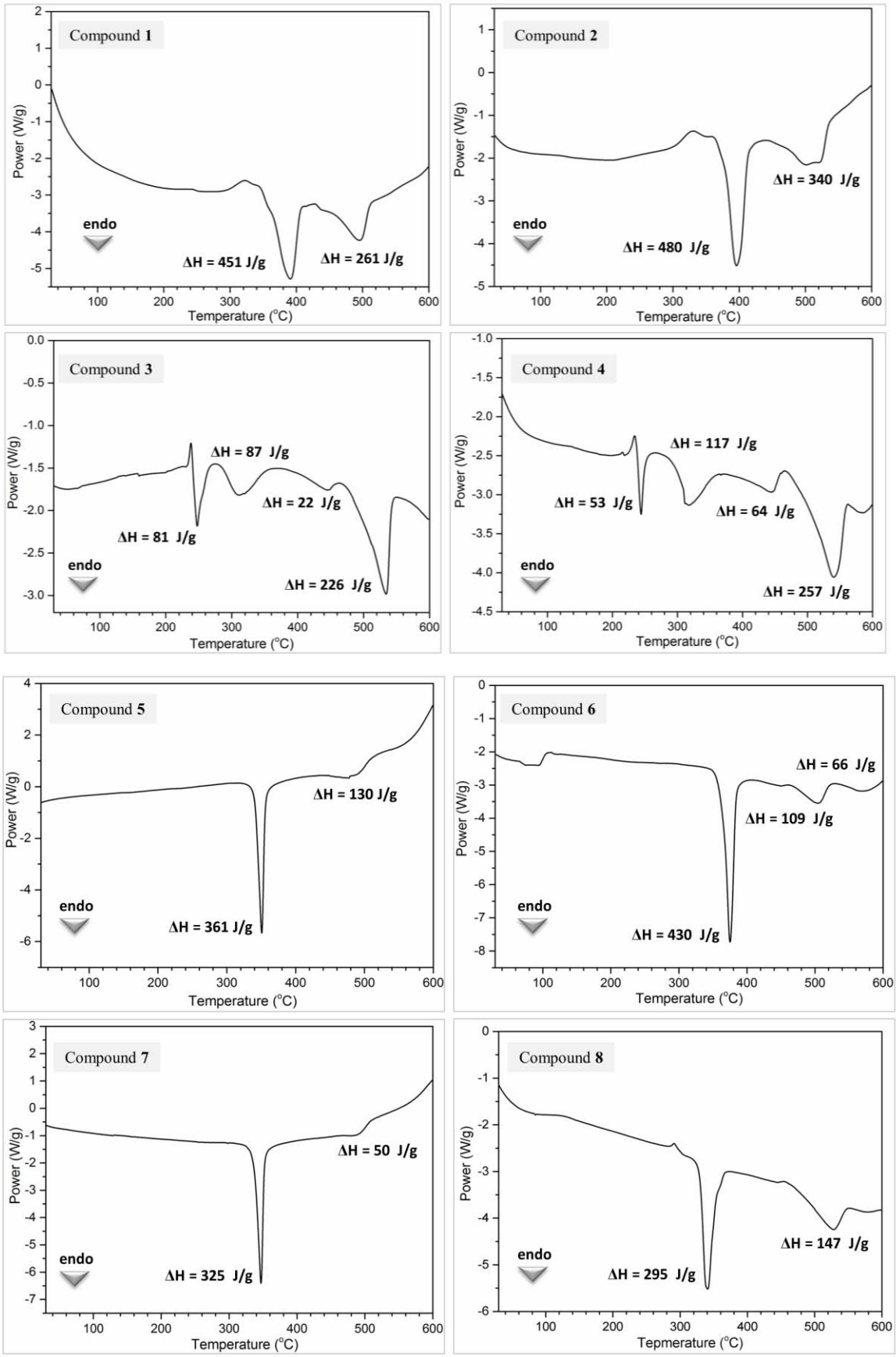

Figure S15. The DSC curves corresponding to thermal decomposition of compounds **1**–**8** in nitrogen atmosphere.

Table S1. Summary of thermogravimetric data in air atmosphere for compounds **1–8**.

Com-d	Formula molecular	FW	T_{range}, °C	T_{max}, °C	Weight loss, % obs. / calc.	m/z	Enthalpy (J/g)	Residue*
1	$C_{36}H_{24}N_6NaO_{12}RuZn$	922.1	240 ÷ 420	295	73.0 / 73.4	H_2O (18), CO_2 (44), NO_2 (46)	- 8839	RuO_2, ZnO, Na_2O
2	$C_{36}H_{26}LiN_6O_{13}RuZn$	923.9	180 ÷ 420	290	75.2 / 75.4		- 12100	RuO_2, ZnO, Li_2O
3	$C_{36}CuH_{24}N_6NaO_{12}Ru$	920.2	200 ÷ 400	270	73.7 / 73.5		- 10930	RuO_2, CuO, Na_2O
4	$C_{36}CuH_{24}LiN_6O_{12}Ru$	904.2	200 ÷ 380	275	75.0 / 74.8		- 12050	RuO_2, CuO, Li_2O
5	$C_{36}H_{24}N_6NaO_{12}Ru_2$	957.7	240 ÷ 440	300	69.0 / 69.6		- 15920	RuO_2, Na_2O
6	$C_{36}H_{24}LiN_6O_{12}Ru_2$	941.7	240 ÷ 400	300	70.4 / 70.2		- 14770	RuO_2, Li_2O
7	$C_{36}H_{24}N_6NaO_{12}OsRu$	1046.9	220 ÷ 460	300	63.6 / 63.8		- 13140	RuO_2, OsO_2, Na_2O
8	$C_{36}H_{24}LiN_6O_{12}OsRu$	1030.8	230 ÷ 600	310	64.7 / 64.1		- 14590	RuO_2, OsO_2, Li_2O

* The residue composition was confirmed by EDX analysis and powder X-ray diffraction

Table S2. Summary of thermogravimetric data in nitrogen atmosphere for compounds **1–8**.

Com-d	Formula molecular	FW	T_{range}, °C	T_{max}, °C	Weight loss, % obs.* / calc.	m/z	Enthalpy (J/g)	Residue**
1	$C_{36}H_{24}N_6NaO_{12}RuZn$	922.1	260 ÷ 360 360 ÷ 430 440 ÷ 550	330 400 520	59.0 / 76.9	NH_3 (15), H_2O (18), CO_2 (44)	451 261	Ru, ZnO, Na_2O
2	$C_{36}H_{26}LiN_6O_{13}RuZn$	923.9	200 ÷ 380 380 ÷ 440 460 ÷ 580	360 400 520	58.0 / 78.6		480 340	Ru, ZnO, Li_2O
3	$C_{36}CuH_{24}N_6NaO_{12}Ru$	920.2	220 ÷ 280 300 ÷ 380 400 ÷ 600	250 330 560	61.1 / 77.0		81 87 226	Ru, CuO, Na_2O
4	$C_{36}CuH_{24}LiN_6O_{12}Ru$	904.2	200 ÷ 280 280 ÷ 380 640 ÷ 600	250 320 570	57.6 / 78.4		53 117 257	Ru, CuO, Li_2O
5	$C_{36}H_{24}N_6NaO_{12}Ru_2$	957.7	300 ÷ 400 440 ÷ 540 560 ÷ 700	360 510 600	45.5 / 75.7		361 130	Ru, Na_2O
6	$C_{36}H_{24}LiN_6O_{12}Ru_2$	941.7	320 ÷ 420 450 ÷ 560 560 ÷ 700	380 520 600	43.9 / 76.9		430 109	Ru, Li_2O
7	$C_{36}H_{24}N_6NaO_{12}OsRu$	1046.9	300 ÷ 420 460 ÷ 550 560 ÷ 740	350 520 640	37.8 / 69.2		325 50	Ru, Os, Na_2O
8	$C_{36}H_{24}LiN_6O_{12}OsRu$	1030.8	260 ÷ 400 460 ÷ 580 580 ÷ 720	340 560 650	39.7 / 70.3		295 147	Ru, Os, Li_2O

* The difference between observed and calculated mass losses in nitrogen atmosphere due to formation of carbon solid residues as a product of partial oxidation of organic ligands.

** The residue composition was confirmed by EDX analysis and powder X-ray diffraction.

Band gap calculations

The band gap energies of **1**–**8** were calculated by Tauc plots of diffuse–reflectance data. According to equation:

$$\alpha h\upsilon = A(h\upsilon - E_g)^{1/n}$$

where α,υ, A and E_g are the absorption coefficient, light frequency, proportionality constant, and band gap, respectively. In the equation, *n* can take on values of 3, 2, 3/2 or 1/2, corresponding to indirect (forbidden), indirect (allowed), direct (forbidden), and direct (allowed) transitions, respectively. The plots of $(\alpha h\upsilon)^n$ versus photon energy $h\upsilon$, so-called Tauc plots, yield the value of the band gap when extrapolated to the baseline.
In case of a diffuse-reflectance measurements ($I = R$), the Kubelka-Munk radiative transfer model can be employed to extract α:

$$f(R) = \frac{(1-R)^2}{2R} = \frac{\alpha}{s}$$

where $f(R)$ is the Kubelka-Munk function and s is the scattering coefficient. Assuming that s is wavelength independent, the $f(R)$ is proportional to α and the Tauc plots can be represented using $f(R)$ in place of α, as follow equation:

$$(f(R)h\upsilon)^n = A(h\upsilon - E_g)$$

Thus, values of band gaps for coordination polymers **1**–**8** were determined as extrapolation to energy axis of point of intersection between baseline and linear fraction of $(f(R)h\upsilon)^{3/2}$ (where n = 3/2 was used as a coefficient characterized direct forbidden MLCT transition).

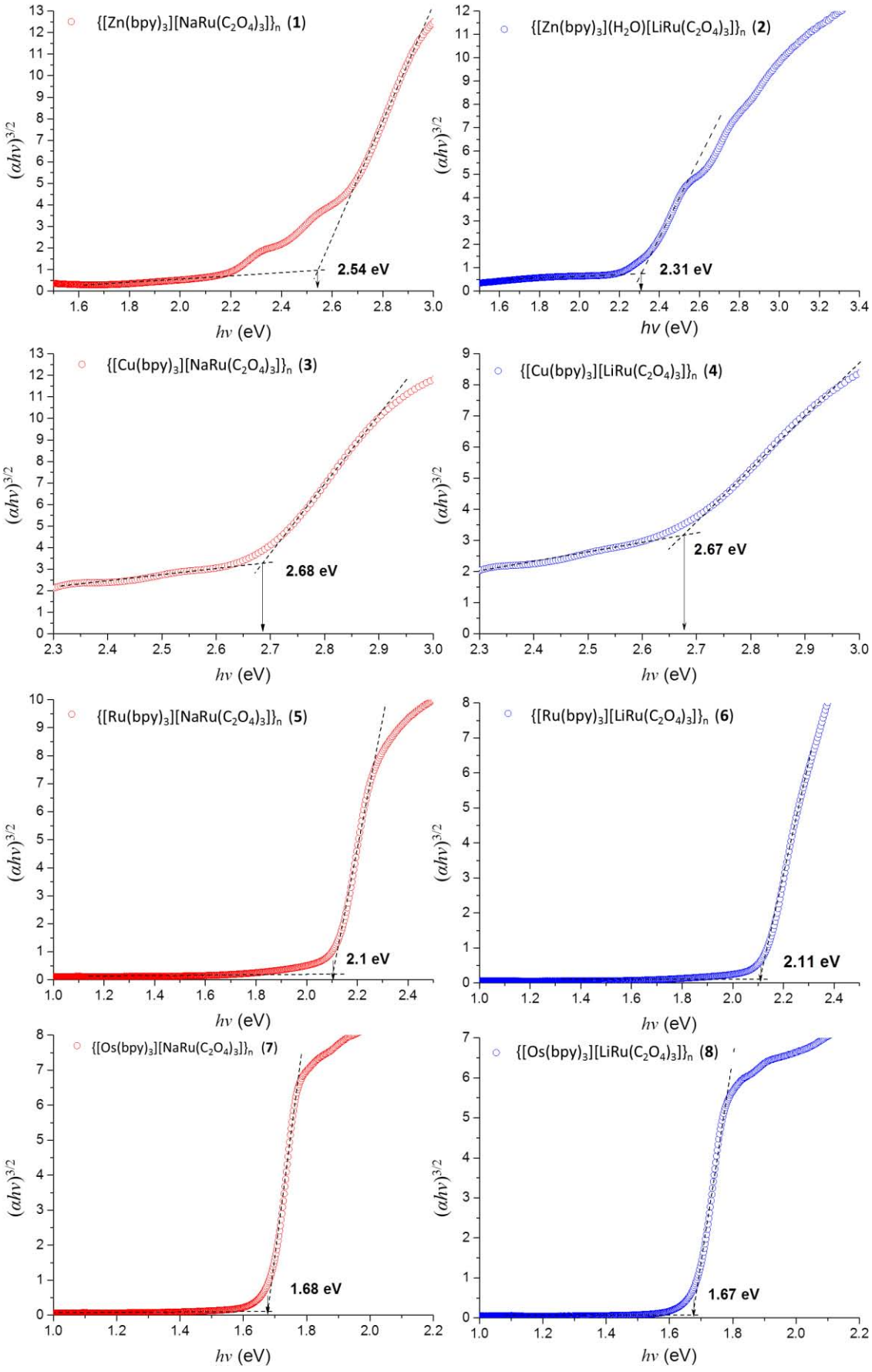

Figure S16. Tauc plots of Kubelka-Munk-transformed diffuse-reflectance spectra of compounds **1**–**8**.

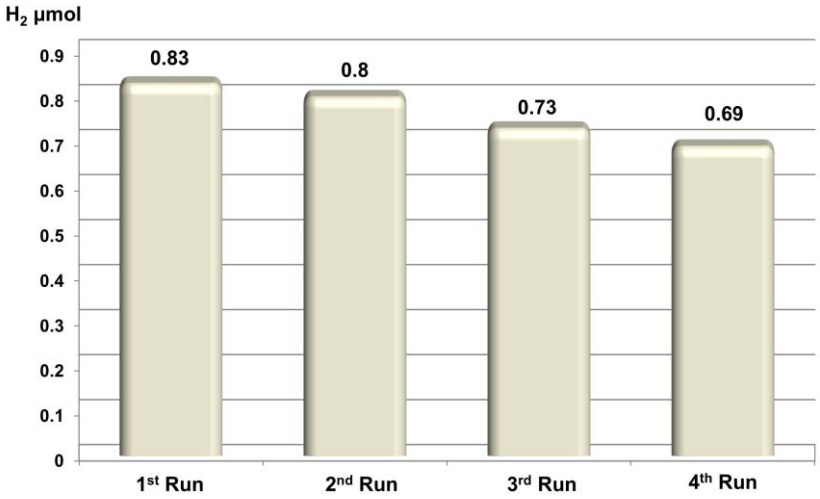

Figure S17. Catalytic activity of $\{[Ru^{II}(bpy)_3][LiRu(C_2O_4)_3]\}_n$ (**6**) in H_2 evolution during water photo-splitting reaction for four consecutive runs.

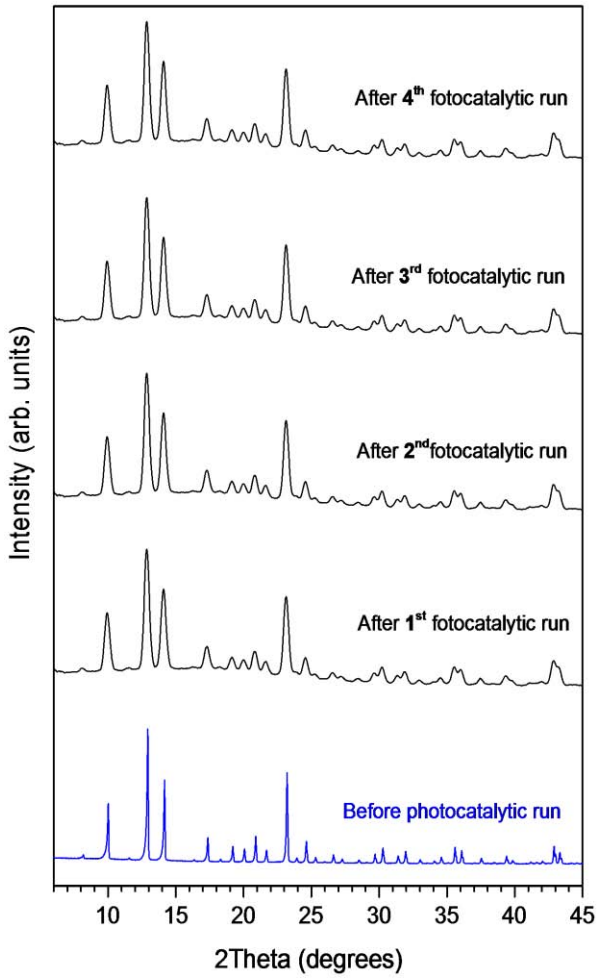

Figure S18. Comparison of powder X-Ray diffraction patterns of compound $\{[Ru^{II}(bpy)_3][LiRu(C_2O_4)_3]\}_n$ (**6**) before and after each repeated photocatalytic runs (four consecutive cycles).

Capítulo X

Conclusiones

Esta Memoria, y los artículos compilados en ella, muestran los resultados obtenidos en el estudio de la síntesis de polímeros de coordinación basados en carboxilatos de rutenio, y su posterior aplicación como catalizadores heterogéneos. A continuación, se presentan las conclusiones más relevantes derivadas de dicho trabajo.

Compuestos Precursores para la Formación de Polímeros de Coordinación Basados en Carboxilatos de Rutenio

- La formación de polímeros de coordinación basados en carboxilatos de rutenio se llevó a término aplicando métodos de síntesis suave (temperatura ambiente, auto-ensamblado molecular) utilizando enlazadores metálicos como precursores moleculares.

- De entre todos los precursores moleculares sintetizados, se ha obtenido un compuesto de estructura cristalina previamente desconocida, que ha podido ser determinada en este trabajo: $[Rh(bpy)_2Cl_2]ClO_4$ presenta simetría ortorrómbica (grupo espacial $P2_12_12_1$, a = 11.0344(2) Å, b = 11.6796(2) Å, c = 17.0884(3) Å).

Preparación de Nanopartículas de Rutenio(0) vía Síntesis Hidrotermal

- Explorando diversas rutas sintéticas para la preparación de polímeros de coordinación basados en carboxilatos de rutenio, se observó que, en condiciones hidrotermales, el uso de $RuCl_3$ como precursor inorgánico en presencia de enlazadores carboxílicos no es apropiado para la formación de redes poliméricas, ya que se produce la reducción del rutenio a su estado elemental.

- La formación de nanopartículas de rutenio en condiciones hidrotermales, usando especies carboxílicas como agentes reductores, puede ser considerada una ruta de "síntesis verde". En función del pH y del anión carboxilato empleado, se detectaron especies intermedias, parcialmente reducidas, que determinan el tamaño y la forma de las nanopartículas obtenidas.

- Las dimensiones de las nanopartículas de rutenio dependen generalmente del pH de la disolución precursora, de la velocidad de nucleación, de la concentración de las especies parcialmente reducidas y del poder reductor de la especie carboxilato utilizada. Sin embargo, su forma está relacionada con el tipo de agente reductor, que determina las especies parcialmente reducidas que actúan como intermediarios de la reacción.

- Las propiedades redox de las nanopartículas de rutenio son función de su tamaño, ya que éste afecta substancialmente a las temperaturas de reducción, lo que debe considerarse en la optimización de los condiciones de trabajo en procesos catalíticos promovidos por rutenio metal.

Clúster de Acetato de Rutenio Trinuclear $[Ru_3^{(II,III,III)}O(CH_3CO_2)_6(H_2O)_3]\cdot 2H_2O$ con Valencia Mixta: Síntesis, Estructura y Actividad Catalítica

- Explorando una ruta indirecta para la síntesis de polímeros de coordinación basados en carboxilatos de rutenio se observó que, en condiciones hidrotermales, el uso de $[Ru_3O(CH_3CO_2)_6(CH_3OH)_3]\cdot CH_3CO_2$ como compuesto precursor en presencia de enlazadores carboxílicos no es apropiado para la formación de redes poliméricas, ya que los ácidos carboxílicos provocan la reducción parcial del rutenio, generando el complejo trinuclear $[Ru_3^{(II,III,III)}O(CH_3CO_2)_6(H_2O)_3]\cdot 2H_2O$.

- El uso de ácidos carboxílicos como reductores suaves, en condiciones hidrotermales, es una vía alternativa adecuada para la preparación de complejos trinucleares de rutenio de valencia mixta, con altos rendimientos y elevada cristalinidad.

- $[Ru_3^{(II,III,III)}O(CH_3CO_2)_6(H_2O)_3]\cdot 2H_2O$ presenta simetría monoclínica (grupo espacial *C*2/*c*, *a* = 27.032(6) Å, *b* = 13.832(3) Å, *c* = 15.257(4) Å, β = 123.62(3)° (293 K), *a* = 26.923(9) Å, *b* = 13.841(3) Å, *c* = 15.165(6) Å, β = 123.13(5)° (100 K)).

- La estructura de $[Ru_3^{(II,III,III)}O(CH_3CO_2)_6(H_2O)_3]\cdot 2H_2O$ contiene un triángulo μ_3-oxo-centrado, con un átomo de rutenio en cada vértice, presentando deslocalización electrónica asimétrica en los átomos de rutenio a temperatura ambiente, estableciéndose Ru^{II} y Ru_2^{III} como estados de oxidación formales a 100 K.

- $[Ru_3^{(II,III,III)}O(CH_3CO_2)_6(H_2O)_3]\cdot 2H_2O$ es un catalizador activo en la hidratación de nitrilos en medio acuso. La reacción es bifásica (benzonitrilo > 3-nitrobenzonitrilo > fenoxiacetonitrilo > 3-clorbenzonitrilo > hexanenitrilo > 3-metilbenzonitrilo), y tanto la naturaleza del grupo electro-aceptor ($Cl > NO_2 > CH_3 > OCH_3$) como su posición en el sustrato (*para* > *meta* > *ortho*) afectan a la eficiencia del proceso y a la actividad catalítica.

- $[Ru_3^{(II,III,III)}O(CH_3CO_2)_6(H_2O)_3]\cdot 2H_2O$ es un catalizador activo en la isomerización de alcoholes alílicos en presencia de $NaHCO_3$.

Polímeros de Coordinación Heterometálicos 2D Basados en Oxalato de Rutenio(III) como Catalizadores Heterogéneos

- Se han aislado cinco miembros de una nueva familia de polímeros de coordinación bidimensionales, $\{[K(18\text{-crown-}6)]_3[M^{II}_3(H_2O)_4\{Ru(ox)_3\}_3]\}_n$ (M^{II} = Mn, Fe, Co, Cu, Zn; ox = C_2O_4), cristalizando todos los compuestos en el grupo espacial *C*2/c (monoclínico) con parámetros de celdilla variando ligeramente en función del metal de transición incorporado a la red polimérica. Las estructuras cristalinas están determinadas por la localización de la especie molecular catiónica $[K(18\text{-crown-}6)]^+$ en el espacio interlaminar aniónico definido por capas $\{[M^{II}_3(H_2O)_4\{Ru(ox)_3\}_3]^-\}_n$ de topología tipo "panal de abeja".

- Los polímeros de coordinación $\{[K(18\text{-crown-}6)]_3[M^{II}_3(H_2O)_4\{Ru(ox)_3\}_3]\}_n$ presentan alta estabilidad térmica, transcurriendo su degradación en tres etapas diferenciadas, con

formación de dos fases cristalinas intermedias, $\{[K(18\text{-crown-6})]_3[M^{II}_3(H_2O)_2\{Ru(ox)_3\}_3]\}_n$ y $\{[K(18\text{-crown-6})]_3[M^{II}_3\{Ru(ox)_3\}_3]\}_n$.

- La deshidratación reversible de $\{[K(18\text{-crown-6})]_3\ [Mn_3(H_2O)_4\{Ru(ox)_3\}_3]\}_n$ origina una fase anhidra, $\{[K(18\text{-crown-6})]_3[Mn_3\{Ru(ox)_3\}_3]\}_n$ (a = 18.52(1) Å, b = 8.58(1) Å, c = 16.00(6) Å), previa formación de una fase parcialmente hidratada, $\{[K(18\text{-crown-6})]_3[Mn_3(H_2O)_2\{Ru(ox)_3\}_3]\}_n$ (a = 19.33(1) Å, b = 11.46(1) Å, c = 14.46(1) Å).

- Todos los compuestos de la serie $\{[K(18\text{-crown-6})]_3[M^{II}_3(H_2O)_4\{Ru(ox)_3\}_3]\}_n$ son catalizadores activos en la reacción de acetalización del benzaldehído, promovida por centros ácidos de Lewis. Las fases anhidras presentan una mayor actividad catalítica que los compuestos hidratados, sugiriendo que los sitios de coordinación vacantes en el centro metálico son los responsables del proceso catalítico.

- Tanto en compuestos hidratados como en anhidros, la actividad catalítica es función del catión divalente integrado en la estructura del material, con una secuencia ($Mn^{2+} < Fe^{2+} < Co^{2+} < Ni^{2+} < Cu^{2+} > Zn^{2+}$) idéntica a la observada para las constantes de formación de la serie de Irving-Williams.

- Los polímeros de coordinación $\{[K(18\text{-crown-6})]_3[M^{II}_3(H_2O)_4\{Ru(ox)_3\}_3]\}_n$ (M^{II} = Mn, Fe, Co, Cu, Zn; ox = C_2O_4) son catalizadores heterogéneos fácilmente reciclables que, a excepción de $\{[K(18\text{-crown-6})]_3[Fe_3(H_2O)_4\{Ru(ox)_3\}_3]\}_n$, no muestran ordenación magnética por encima de 2 K.

Polímeros de Coordinación 3D Basados en Unidades Oxalato de Rutenio(III) como Catalizadores Heterogéneos para la Fotoreducción de CO_2 a CO

- Se obtuvieron seis nuevos polímeros de coordinación tridimensionales, $\{[M^{II}(bpy)_3][M^{I}Ru(C_2O_4)_3]\}_n$ (M^{II} = Ni, Fe, Co; M^{I} = Na, Li; bpy = 2,2´-bipiridina), mediante autoensamblaje de $[Ru(C_2O_4)_3]^{3-}$, $[M^{II}(bpy)_3]^{2+}$ y $[M^{I}]^{+}$ a temperatura ambiente.

- Todos los compuestos presentan simetría cúbica (grupo espacial $P4_13$), con pequeñas variaciones de sus parámetros de celdilla en función del metal de transición incorporado a la plantilla catiónica y del metal alcalino alojado en la red polimérica. Las estructuras consisten en una red aniónica tridimensional, $\{[M^{I}Ru(C_2O_4)_3]^{2-}\}_n$ (M^{I} = Na, Li), con topología tipo "panal de abeja", caracterizada por el símbolo 10^3 de Schläfli, con cajas donde se acomodan las plantillas catiónicas, $[M^{II}(bpy)_3]^{2+}$ (M^{II} = Ni, Fe, Co).

- Los polímeros de coordinación $\{[M^{II}(bpy)_3][M^{I}Ru(C_2O_4)_3]\}_n$ (M^{II} = Ni, Fe, Co; M^{I} = Na, Li) presentan relativamente alta estabilidad térmica, tanto en atmósfera reactiva (aire) como inerte (nitrógeno). La degradación térmica de cada miembro de la serie procede en única etapa, en rangos de temperaturas comprendidos entre 280 °C y 700 °C, sin revelar cambios estructurales previos al colapso irreversible de la red polimérica.

- Estos compuestos presentan bandas de adsorción en las regiones visible (transiciones *d-d* y transferencias de carga en las plantillas catiónicas $[M^{II}(bpy)_3]^{2+}$) y ultravioleta (transferencia de carga de metal-ligando en la red polimérica $\{[M^{I}Ru(C_2O_4)_3]^{2-}\}_n$ (M^I = Na, Li)).

- En $\{[Co(bpy)_3][NaRu(C_2O_4)_3]\}_n$ y $\{[Co(bpy)_3][LiRu(C_2O_4)_3]\}_n$, la plantilla catiónica ($[Co(bpy)_3]^{2+}$) incorporada a la red aniónica muestra equilibrio entre sus estados de alto y bajo espín, exhibiendo diferentes grados de población en función de la temperatura y de la composición de la red polimérica (Na/Li).

- Los compuestos $\{[M^{II}(bpy)_3][M^{I}Ru(C_2O_4)_3]\}_n$ (M^{II} = Ni, Fe, Co; M^I = Na, Li) son catalizadores activos en la foto-reducción de CO_2 a CO bajo irradiación ultravioleta, variando su actividad catalítica en función de la plantilla molecular y del metal alcalino incorporado a la red, siguiendo el orden $Co^{2+} > Ni^{2+} > Fe^{2+}$ (M^I = Na) y $Co^{2+} > Fe^{2+} > Ni^{2+}$ (M^I = Li).

- El mejor comportamiento catalítico en la foto-reducción de CO_2 se observó en los polímeros de coordinación $\{[Co(bpy)_3][NaRu(C_2O_4)_3]\}_n$ y $\{[Co(bpy)_3][LiRu(C_2O_4)_3]\}_n$ que, respectivamente, proporcionan conversiones selectivas a CO de 1.5 mmol (TON = 150) y 1.2 mmol (TON = 120) en 10 h de irradiación UV.

- Se propuso el siguiente mecanismo para la foto-reducción de CO_2: transferencia electrónica desde la especie rutenio(III) foto-excitada al complejo de cobalto(II), con la formación del intermedio $[(Co(bpy)_3]^{+}$ que, tras reducir el CO_2 a CO, retorna al estado de oxidación inicial, $[(Co(bpy)_3]^{2+}$, completándose el proceso con una transferencia electrónica desde la trietilamina (reactivo sacrificante) al centro de rutenio oxidado, regenerándose el componente fotosensible del polímero de coordinación.

- Los polímeros de coordinación $\{[M^{II}(bpy)_3][M^{I}Ru(C_2O_4)_3]\}_n$ (M^{II} = Ni, Fe, Co; M^I = Na, Li) son catalizadores heterogéneos estables bajo irradiación UV y fácilmente reciclables.

Polímeros de Coordinación 3D Basados en Oxalato de Rutenio(III) como Catalizadores Heterogéneos para la Fotoreducción de Agua

- Se han obtenido ocho nuevos polímeros de coordinación tridimensionales, de fórmulas generales $\{[Z^{II}(bpy)_3][M^{I}Ru(C_2O_4)_3]\}_n$ y $\{[Zn(bpy)_3](H_2O)[LiRu(C_2O_4)_3]\}_n$ (donde Z^{II} = Zn, Cu, Ru, Os; M^I = Na, Li; bpy = 2,2´-bipiridina), mediante autoensamblaje de $[Ru(C_2O_4)_3]^{3-}$, $[Z^{II}(bpy)_3]^{2+}$ y $[M^{I}]^{+}$ a temperatura ambiente.

- La estructura cristalina (simetría cúbica, grupo espacial $P4_13$) de estos compuestos consiste en una red aniónica tridimensional, $\{[M^{I}Ru(C_2O_4)_3]^{2-}\}_n$ (M^I = Na, Li), con topología tipo "panal de abeja", caracterizada por el símbolo 10^3 de Schläfli, con espacios vacíos donde se acomoda la plantilla catiónica, $[Z^{II}(bpy)_3]^{2+}$ (Z^{II} = Zn, Cu, Ru, Os).

- Las unidades $[Ru(C_2O_4)_3]^{3-}$ exhiben la misma quiralidad que la plantilla catiónica, $[Z^{II}(bpy)_3]^{2+}$ (Z^{II} = Zn, Cu, Ru, Os), originando redes poliméricas homoquirales.

- Las especies huésped, $[Z^{II}(bpy)_3]^{2+}$, experimentan expansión en el interior de las cajas ofrecidas por las redes aniónicas, $\{[M^{I}Ru(C_2O_4)_3]^{2-}\}_n$ (M^{I} = Na, Li).

- Estos compuestos presentan bandas de adsorción en las regiones visible (transiciones *d-d* y transferencia de carga en $[Z^{II}(bpy)_3]^{2+}$) y ultravioleta (transferencias de carga metal-ligando en la red polimérica, $\{[M^{I}Ru(C_2O_4)_3]^{2-}\}_n$ (M^{I} = Na, Li)), siendo el valor de *band gap* función de la molécula huésped, $[Z^{II}(bpy)_3]^{2+}$.

- $\{[Z^{II}(bpy)_3][M^{I}Ru(C_2O_4)_3]\}_n$ y $\{[Zn(bpy)_3](H_2O)[LiRu(C_2O_4)_3]\}_n$ (Z^{II} = Zn, Cu, Ru, Os; M^{I} = Na, Li) son catalizadores activos, estables, y fácilmente reciclables, en la foto-reducción de agua bajo irradiación ultravioleta y visible, existiendo relación directa entre la estructura electrónica y el comportamiento foto-catalítico, con el orden $Os^{2+} > Ru^{2+} > Zn^{2+} > Cu^{2+}$ (UV) y $Os^{2+} > Ru^{2+} > Cu^{2+} \approx Zn^{2+}$ (VIS).

Chapter X

Conclusions

The current work along with the enclosed publications shows results obtained throughout the study realized on the synthesis of coordination polymers based on the ruthenium carboxylates and their application as heterogeneous catalysts. The most important conclusions derived from this study are summarized below:

Precursor Compounds for the Construction of Coordination Polymers Based on the Ruthenium Carboxylates

- The formation of coordination polymers based on the ruthenium carboxylates was achieved by applying a soft synthetic methods (room temperature, molecular self-assembling) and use of metal-containing linkers as molecular precursors.

- Among all synthesized precursors, a compound of unknown before crystal structure has been obtained and crystallographically characterized: $[Rh(bpy)_2Cl_2]ClO_4$ has orthorhombic symmetry (space group $P2_12_12_1$, a = 11.0344(2) Å, b = 11.6796(2) Å, c = 17.0884(3) Å).

Preparation of Ruthenium(0) Nanoparticles vía Synthesis Hydrothermal

- Having been exploring various synthetic routes for the preparation of coordination polymers based on the ruthenium carboxylates, it was observed that under hydrothermal conditions and in the presence of carboxylic linkers the $RuCl_3$ salt, used as inorganic precursor, undergoes the reduction to ruthenium(0) state that indicates unsuitability of the applied method for the formation of polymeric networks.

- Formation of ruthenium nanoparticles under hydrothermal conditions using carboxylic species as reducing agents can be considered as a green synthesis pathway. The pH and the nature of carboxylate anion used in the reaction determine the type of partially reduced intermediate species and, subsequently, the size and shape of resulted ruthenium nanoparticles.

- The sizes of ruthenium nanoparticles depend on the pH of the precursor solution, the nucleation rate, the concentration of the partially reduced species and the reducing power of used carboxylate. However, the shape of nanoparticles is related to the type of reducing agent which, in turn, determines the partially reduced species that act as intermediates in the reduction process.

- The redox properties of ruthenium nanoparticles based on their size, as it determines the reduction temperatures, which should be considered as optimal conditions for catalytic processes promoted by metallic ruthenium.

Mixed-Valence Trinuclear Ruthenium Acetate Cluster $[Ru_3^{(II,III,III)}O(CH_3CO_2)_6(H_2O)_3]\cdot 2H_2O$: Synthesis, Structure and Catalytic Activity

- Having been exploring the indirect synthetic approach for the synthesis of coordination polymers based on ruthenium carboxylates, the trinuclear ruthenium complex of $[Ru_3^{(II,III,III)}O(CH_3CO_2)_6(H_2O)_3]\cdot 2H_2O$ was formed under hydrothermal conditions as a result of partial reduction of the $[Ru_3O(CH_3CO_2)_6(CH_3OH)_3]\cdot CH_3CO_2$ precursor compound by carboxylic linkers indicating that applied strategy is inappropriate for the construction of polymeric network.

- The use of carboxylic acids behaving as mild reducing agents under hydrothermal conditions is an alternative pathway for the synthesis of mixed-valence trinuclear ruthenium complexes with high yields and outstanding crystallinity.

- $[Ru_3^{(II,III,III)}O(CH_3CO_2)_6(H_2O)_3]\cdot 2H_2O$ have monoclinic symmetry (space group *C*2/*c*, a = 27.032(6) Å, b = 13.832(3) Å, c = 15.257(4) Å, β = 123.62(3)° (293 K), a = 26.923(9) Å, b = 13.841(3) Å, c = 15.165(6) Å, β = 123.13(5)° (100 K)).

- The structure of $[Ru_3^{(II,III,III)}O(CH_3CO_2)_6(H_2O)_3]\cdot 2H_2O$ contains μ_3-oxo-centred triangle with ruthenium atoms at each corner exhibiting the asymmetric valence delocalization between three ruthenium atoms at room temperature, and establishing Ru^{II} and Ru_2^{III} formal oxidation states at 100 K.

- $[Ru_3^{(II,III,III)}O(CH_3CO_2)_6(H_2O)_3]\cdot 2H_2O$ behaves as an active catalyst in the reaction of hydration of nitriles performed in water media. Explored catalytic process is biphasic (benzonitrile > 3-nitrobenzonitrile > phenoxyacetonitrile > 3-clorbenzonitrile > hexanenitrile > 3-methylbenzonitrile), where the nature of electron withdrawing group ($Cl > NO_2 > CH_3 > OCH_3$) as well as its position in substrate (*para* > *meta* > *ortho*) affects the efficiency of a catalysed process and a catalytic activity.

- $[Ru_3^{(II,III,III)}O(CH_3CO_2)_6(H_2O)_3]\cdot 2H_2O$ behaves as an active catalyst in the reaction of isomerization of allylic alcohols in presence of $NaHCO_3$.

2D Heterometallic Coordination Polymers Based on Ruthenium(III) Oxalate Building Units as Heterogeneous Catalysts

- Five members of the family of two-dimensional coordination polymers, $\{[K(18\text{-crown-}6)]_3[M^{II}_3(H_2O)_4\{Ru(ox)_3\}_3]\}_n$ (M^{II} = Mn, Fe, Co, Cu, Zn; ox = $C_2O_4^{2-}$), which crystallized in monoclinic a space group *C*2/c with unit cell parameters slightly varying as a function of a transition metal incorporated in the polymeric network. Crystal structures consist of molecular cationic specie $[K(18\text{-crown-}6)]^+$ located between anionic honeycomb-like layers of $\{[M^{II}_3(H_2O)_4\{Ru(ox)_3\}_3]^-\}_n$.

- The coordination polymers $\{[K(18\text{-crown-}6)]_3[M^{II}_3(H_2O)_4\{Ru(ox)_3\}_3]\}_n$ exhibit high thermal stability with three well defined degradation steps through which two crystalline

intermedium phases, $\{[K(18\text{-crown-}6)]_3[M^{II}_3(H_2O)_2\{Ru(ox)_3\}_3]\}_n$ and $\{[K(18\text{-crown-}6)]_3[M^{II}_3\{Ru(ox)_3\}_3]\}_n$, are formed.

- The coordination polymers $\{[K(18\text{-crown-}6)]_3[M^{II}_3(H_2O)_4\{Ru(ox)_3\}_3]\}_n$ behave as highly active Lewis acid catalysts in the reaction of acetalyzation of benzaldehyde. The dehydrated phases show higher catalytic performance due to the creation of active-accessible Lewis acid centers.

- The hydrated and anhydrous coordination polymers exhibit an increasing catalytic activity in the sequence ($Mn^{2+} < Fe^{2+} < Co^{2+} < Ni^{2+} < Cu^{2+} > Zn^{2+}$) identical to observed in the Irving-Williams series for the formation constants of divalent metal ions.

- Coordination polymers $\{[K(18\text{-crown-}6)]_3[M^{II}_3(H_2O)_4\{Ru(ox)_3\}_3]\}_n$ (M^{II} = Mn, Fe, Co, Cu, Zn; ox = $C_2O_4^{2-}$) show to be recyclable heterogeneous catalysts, and in exceptional case of $\{[K(18\text{-crown-}6)]_3[Fe_3(H_2O)_4\{Ru(ox)_3\}_3]\}_n$ did not show magnetic order above 2 K.

3D Coordination Polymers Based on Ruthenium(III) Oxalate Units as Heterogeneous Catalysts for the Photoreduction of CO_2 to CO

- Series of three-dimensional coordination polymers,$\{[M^{II}(bpy)_3][M^{I}Ru(C_2O_4)_3]\}_n$ (M^{II} = Ni, Fe, Co; M^{I} = Na, Li; bpy = 2,2´-bipiridina), have been obtained by self-assemble of $[Ru(C_2O_4)_3]^{3-}$, $[M^{II}(bpy)_3]^{2+}$ and $[M^{I}]^{+}$ at room temperature.

- The members of the series crystallize in a cubic space group $P4_13$ with unit cell parameters slightly varying as a function of a transition metal in the cationic template and alkali metal incorporated into the polymeric network. Crystal structures consist of anionic three-dimensional framework of the honeycomb-like topology with 10^3 Schläfli symbol and $[M^{II}(bpy)_3]^{2+}$ (M^{II} = Ni, Fe, Co) cationic templates resided in cages of the net.

- Coordination polymers $\{[M^{II}(bpy)_3][M^{I}Ru(C_2O_4)_3]\}_n$ (M^{II} = Ni, Fe, Co; M^{I} = Na, Li) exhibit relatively high thermal stability in either oxidative (air) and inert (nitrogen) atmospheres. Degradation of each member of the series proceeds in one single step within the temperature range 280–700 °C without revealing any structural change before irreversible collapse of the polymeric network.

- These compounds represent adsorption bands in visible region (*d-d* transitions and charge transfers in $[M^{II}(bpy)_3]^{2+}$ cationic templates) and UV (metal-to-ligand charge transfers in the $\{[M^{I}Ru(C_2O_4)_3]^{2-}\}_n$ (M^{I} = Na, Li) polymeric network).

- In $\{[Co(bpy)_3][NaRu(C_2O_4)_3]\}_n$ and $\{[Co(bpy)_3][LiRu(C_2O_4)_3]\}_n$, the cationic templates ($[Co(bpy)_3]^{2+}$) incorporated into the anionic network exhibit spin-crossover between high- and low-spin states possessing different levels of population as a function of the temperature and the composition of the polymeric net (Na/Li).

- The compounds $\{[M^{II}(bpy)_3][M^{I}Ru(C_2O_4)_3]\}_n$ (M^{II} = Ni, Fe, Co; M^{I} = Na, Li) are active catalysts of a CO_2 to CO photoreduction under UV-light irradiation, varying their activity as

a function of the composition of the cationic templates and the nature of the alkali metal incorporated into the net, following the order $Co^{2+} > Ni^{2+} > Fe^{2+}$ (M^I = Na) y $Co^{2+} > Fe^{2+} > Ni^{2+}$ (M^I = Li).

- The best catalytic behavior in the CO_2 photo-reduction was observed for the coordination polymers $\{[Co(bpy)_3][NaRu(C_2O_4)_3]\}_n$ and $\{[Co(bpy)_3][LiRu(C_2O_4)_3]\}_n$ which show conversions to CO reaching up 1.5 mmol (TON = 150) and 1.2 mmol (TON = 120) under 10 h of UV-irradiation, respectively.

- Proposed mechanism for the photo-reduction of CO_2: electron transfer from photo-exited ruthenium(III) species to the complex of cobalt(II), forming $[(Co(bpy)_3]^+$ intermediate that after reducing CO_2 to CO, restore the initial oxidation state $[(Co(bpy)_3]^{2+}$, the process ends with the electronic transfer from triethylamine (sacrificial agent) to the oxidized ruthenium center, regenerating the photo-sensitive component of the polymeric network.

- The coordination polimers $\{[M^{II}(bpy)_3][M^{I}Ru(C_2O_4)_3]\}_n$ (M^{II} = Ni, Fe, Co; M^I = Na, Li) are stable under UV radiation and easily recyclable heterogeneous catalysts.

3D Coordination Polymers Based on Ruthenium(III) Oxalate Units as Heterogeneous Catalysts for the Photoreduction of Water

- Eight tridimensional coordination polymers of a general formula $\{[Z^{II}(bpy)_3][M^{I}Ru(C_2O_4)_3]\}_n$ and $\{[Zn(bpy)_3](H_2O)[LiRu(C_2O_4)_3]\}_n$ (where Z^{II} = Zn, Cu, Ru, Os; M^I = Na, Li; bpy = 2,2´-bipyridine) have been obtained through self-assembly of $[Ru(C_2O_4)_3]^{3-}$, $[Z^{II}(bpy)_3]^{2+}$ and $[M^I]^+$ at room temperature.

- The crystalline structure (cubic symmetry, space group $P4_13$) of these compounds consists of a tridimensional anionic network $\{[M^{I}Ru(C_2O_4)_3]^{2-}\}_n$ (M^I = Na, Li), of a honeycomb-like topology characterized by 10^3 Schläfli symbol, possessing voids, where $[Z^{II}(bpy)_3]^{2+}$ (Z^{II} = Zn, Cu, Ru, Os) cationic templates are located.

- The $[Ru(C_2O_4)_3]^{3-}$ units exhibit the same chirality as the cationic templates $[Z^{II}(bpy)_3]^{2+}$ (Z^{II} = Zn, Cu, Ru, Os), forming homochiral polymeric networks.

- The $[Z^{II}(bpy)_3]^{2+}$ templates, undergo an expansion within the cages provided by the $\{[M^{I}Ru(C_2O_4)_3]^{2-}\}_n$ (M^I = Na, Li) anionic networks.

- These compounds demonstrate adsorption bands in visible region (*d-d* transitions and charge transfers in $[Z^{II}(bpy)_3]^{2+}$ cationic templates) and UV (metal-to-ligand charge transfers in the $\{[M^{I}Ru(C_2O_4)_3]^{2-}\}_n$ (M^I = Na, Li) polymeric network) showing the band gap value as a function of the molecular template $[Z^{II}(bpy)_3]^{2+}$ nature.

- $\{[Z^{II}(bpy)_3][M^{I}Ru(C_2O_4)_3]\}_n$ and $\{[Zn(bpy)_3](H_2O)[LiRu(C_2O_4)_3]\}_n$ (Z^{II} = Zn, Cu, Ru, Os; M^I = Na, Li) are active, stable and easily recyclable catalysts in the water photo-splitting reduction, exhibiting a direct relation between the electronic structure and photo-catalytic

behavior, resulting in the following order: $Os^{2+} > Ru^{2+} > Zn^{2+} > Cu^{2+}$ (UV) and $Os^{2+} > Ru^{2+} > Cu^{2+} \approx Zn^{2+}$ (VIS).